AUSTRALIAN JNL. OF PHY. V 18 1965

7791

गुरुकुल कांगड़ी विश्वविद्यालय, हरिद्वार
पुस्तकालय

R
विषय संख्या 530.5
पुस्तक संख्या M.48A
V.18
आगत पंजिका संख्या 7791

पुस्तक पर किसी प्रकार का निशान लगाना वर्जित है। कृपया १५ दिन से अधिक समय तक पुस्तक अपने पास न रखें।

GULZAR BOOK BINDING HOUSE
[illegible] BAZAR, ROORKEE

7791

COMPILED

सन्दर्भ ग्रन्थ
BOOK

यह पुस्तक वितरित न की जाय
NOT TO BE ISSUED

[illegible] १९८३-१९८४

Stock Verification: 2024

CHECKED 1973
Initial

COMPILED

AUSTRALIAN JOURNAL OF PHYSICS

R530.5, M48A V.18
7791

7791

VOLUME 18

MELBOURNE
1965

AUSTRALIAN JOURNAL OF PHYSICS

Published by the Commonwealth Scientific and Industrial Research Organization. Volumes 1 to 5 of the Australian Journal of Physics and the Australian Journal of Chemistry issued as the Australian Journal of Scientific Research, Series A: Physical Sciences. Issued six times a year, £2 ($A4) per annum.

BOARD OF STANDARDS

The Board of Standards for this Journal is appointed by the Commonwealth Scientific and Industrial Research Organization and the Australian Academy of Science and consists of Professor W. P. Rogers (Chairman), Mr. A. E. Scott (Editor-in-Chief), Professor N. S. Bayliss, Dr. M. F. Day, Professor R. Street, and Professor J. S. Turner.

ADVISORY COMMITTEE

Acceptance of papers for this Journal is in the hands of an Advisory Committee appointed by the Board of Standards in consultation with the Australian Institute of Physics and consisting of Mr. A. E. Scott (Editor-in-Chief and Chairman), Professor A. J. F. Boyle, Dr. J. L. Farrands, Professor C. B. O. Mohr, Dr. C. H. B. Priestley, Professor R. Street, and Professor H. C. Webster.

ऋते ज्ञानान्न मुक्तिः
पुस्तक सं०. ....
आगत नं०. ....
दिनांक.. ....
गुरुकुल पुस्तकालय कांगड़ी

All enquiries and manuscripts should be forwarded to:
The Editor-in-Chief,
Editorial and Publications Section, CSIRO,
Sixth Floor,
372 Albert Street,
East Melbourne, C.2, Victoria

CONTENTS

NUMBER 1, FEBRUARY 1965

PAGE

Electric dipole photon absorption in ^{32}S. By B. M. Spicer 1

Parameters of two levels of the ^{17}F nucleus. By W. Toutenhoofd 7

The photonuclear giant resonance in silicon-28. By A. W. Parker, R. R. Whitehead, and G. G. Shute 15

A spectroscopic study of a decaying hydrogen plasma. By F. E. Irons and D. D. Millar 23

The behaviour of free and attached electrons in oxygen. By J. A. Rees .. 41

Variation of proton flux with atmospheric depth between 10 and 50 g/cm^2 at $\lambda = 47°$ S. geomagnetic. By K. K. M. Wu and B. S. K. Chow 59

The speed and acceleration of the sources of type III and type V solar radio bursts over large distances in the corona. By R. T. Stewart 67

Extended radio sources. II. By P. A. G. Scheuer 77

Short Communications

Some observations at 6 cm wavelength with the Australian 210-ft radio telescope. By N. W. Broten, B. F. C. Cooper, F. F. Gardner, H. C. Minnett, R. M. Price, F. G. Tonking, and D. E. Yabsley 85

A distant HII region in the Galaxy. By K. Akabane and F. J. Kerr 91

On scintillation of radio sources. By J. Aarons 97

Corrigenda 99

NUMBER 2, APRIL 1965

A note on a soluble three-body problem. By L. M. Delves 101

Gauge-independent theory of symmetry. II. By H. A. Buchdahl and L. J. Tassie 109

Monte Carlo calculations of the radial distribution functions for a proton–electron plasma. By A. A. Barker 119

A transmission electron microscope study of amethyst and citrine. By A. C. McLaren and P. P. Phakey 135

Solar radio bursts of spectral type V. By the late A. A. Weiss and R. T. Stewart 143

The nature and velocity of the sources of type II solar radio bursts. By the late A. A. Weiss 167

Short Communications

A preliminary radio survey of planetary nebulae south of declination 24 degrees. By O. B. Slee and D. W. Orchiston 187

Electrical breakdown in polycrystalline sodium chloride at 350°C. By L. A. Butler and J. R. Hanscomb 193

NUMBER 3, JUNE 1965

PAGE

An electromagnetic force theorem for quasi-stationary currents. By W. E. Smith 195

Thermal expansion and other properties of sodium chloride. By D. G. M. Powell and G. C. Fletcher 205

The response of closed channels to wind stresses. By L. M. Fitzgerald and W. W. Mansfield 219

Pre-breakdown ionization in molecular nitrogen in $E \times B$ fields. By F. T. Bagnall and S. C. Haydon 227

Transport coefficients for low energy electrons in crossed electric and magnetic fields. By R. L. Jory 237

Gross discontinuities in the magnetization of type II superconductors. By P. O. Carden 257

Energy level spectra for ^{118}Sn and ^{122}Sn. By N. Kumar, V. Kumar, and V. B. Bhanot 265

Two-stream instabilities in a plasma. By S. K. Kundu 271

Elastic and electromagnetic proton interactions at 3 TeV. By C. B. A. McCusker, L. S. Peak, and R. L. S. Woolcott 277

The polarization structure of type III solar radio bursts. By U. V. Gopala Rao .. 283

NUMBER 4, AUGUST 1965

Energy and dispersion in electromagnetic systems. By W. E. Smith 287

Models of massive stars in homologous gravitational contraction. By S. M. A. Meggitt 297

Vector tetrad in cosmological red shift. By G. L. Gehlot and M. C. Durgapal 303

Equilibrium of a pinch discharge with a transverse rotating magnetic field. By H. A. Blevin and R. B. Miller 309

Backscatter of 16 Mc/s radio waves from land and sea. By J. G. Steele .. 317

The Parkes catalogue of radio sources, declination zone −60° to −90°. By R. M. Price and D. K. Milne 329

Theoretical models for the radiance of contaminant glow clouds in the upper atmosphere. By K. H. Lloyd 349

Magnetohydrodynamic ionizing shock waves in a conducting medium. By B. Green and R. M. May 363

Short Communications

A new kinetic energy correction for capillary tube viscometers. By R. I. Tanner 381

Polarization of 6 cm radiation from the Crab nebula. By F. F. Gardner .. 385

The reactions of ^{6}Li(γ, d) and ^{7}Li(γ, t) below 4 MeV. By P. J. Dallimore, K. S. Lam, and H. H. Thies 389

Corrigenda 393

NUMBER 5, OCTOBER 1965

PAGE

Electromagnetic 2π decay of K_2^0. By S. K. Kundu 395

Reliability of calibrations and comparisons of reference standards with an application to a group of line standards. By E. G. Thwaite 401

Precision measurements of the Townsend energy ratio for electron swarms in highly uniform electric fields. By R. W. Crompton, M. T. Elford, and J. Gascoigne 409

Some experimental observations of the attenuation of Alfven waves in a laboratory plasma. By I. G. Brown 437

The upper limiting primary rigidity of the cosmic ray solar anisotropy. By R. M. Jacklyn and J. E. Humble 451

Harmonic structure and band splitting of type II solar radio bursts. By M. Krishnamurthi, G. Sivarama Sastry, and T. Seshagiri Rao 473

Short Communications

Saint-Venant's principle in anisotropic media. By R. B. Noyes 479

Diffusion of heat from a sphere to a surrounding medium. By A. Brown .. 483

Angular distributions in the reactions $^{11}B(d, p)^{12}B$ and $^{11}B(d, \alpha)^{9}Be$. By D. G. Sargood and G. D. Putt 491

On Bowen's hypothesis. By T. R. Visvanathan 497

Remarks on the paper by T. R. Visvanathan entitled "On Bowen's hypothesis". By G. W. Brier 503

NUMBER 6, DECEMBER 1965

PAGE

A symmetric decomposition of the two-electron wave equation for finite nuclear mass. By T. M. Kalotas 511

A theoretical analysis of the Townsend–Huxley swarm technique for electrons. By C. A. Hurst and B. S. Liley 521

The diffusion and attachment of electrons in water vapour. By R. W. Crompton, J. A. Rees, and R. L. Jory 541

Charged particle motion in a time-dependent axially symmetric magnetic field. By P. W. Seymour, R. B. Leipnik, and A. F. Nicholson 553

The lunar magnetic variations at Toolangi. By H. F. Petersons, D. E. Winch, and L. Slaucitajs 567

Stratospheric temperatures over Australia. By J. G. Sparrow 579

A study of the decimetric emission and polarization of Centaurus A. By B. F. C. Cooper, R. M. Price, and D. J. Cole 589

Identification of extragalactic radio sources between declinations −20° and −44°. By J. G. Bolton, Margaret E. Clarke, and R. D. Ekers 627

A linear polarization survey of the southern sky at 408 Mc/s. By D. S. Mathewson and D. K. Milne 635

Effect of gravitation in the origin of cosmic particles. By M. C. Durgapal and G. L. Gehlot 655

Short Communications

The $^{16}O(\gamma,p_0)^{15}N$ cross section between 14 and 16 MeV. By R. J. J. Stewart, P. H. Cannington, and B. M. Spicer 661

A survey of the southern sky at 30 Mc/s. By D. S. Mathewson, N. W. Broten, and D. J. Cole 665

Identification of two southern quasi-stellar objects. By R. D. Ekers and J. G. Bolton 669

A double radio source with a wide component separation. By F. F. Gardner and J. G. Bolton 671

Index to Volume 18 675

पुस्तकालय
गुरुकुल कांगड़ी विश्वविद्यालय
हरिद्वार

ENERGY AND DISPERSION IN ELECTROMAGNETIC SYSTEMS

By W. E. Smith†

[*Manuscript received March* 25, 1965]

Summary

The total average electromagnetic energy of a loss-free system is expressed in terms of the frequency dependence of the fields on an arbitrary mathematical surface enclosing the system. By introducing scattering, admittance, and impedance matrices the surface integral is reduced and the energy written as quadratic forms involving the frequency derivatives of these matrices. The arguments are of sufficient generality to apply in the presence of inhomogeneous, dispersive, and anisotropic or gyrotropic media. The requirement that the total energy be positive leads to important restrictions on the frequency dependence of the parameter matrices. The application to extensions of Foster's reactance theorem is discussed.

I. Introduction

Energy storage and dispersion in electromagnetic systems are closely related, high energy storage being associated with high dispersion. A detailed examination of the total average electromagnetic energy of loss-free systems shows it to be expressible completely in terms of the frequency dependence of field quantities on an enclosing mathematical surface. The surface integral is reducible to forms involving the frequency dependence of the impedance, admittance, or scattering matrices defined with reference to a set of basis functions on the surface. The result for the simplest system consisting of a single reactance is well known in a.c. circuit theory, namely

$$W = \tfrac{1}{2}I^*I\,\mathrm{d}X/\mathrm{d}\omega, \tag{1}$$

where W is the total average energy when the reactance X is excited by a complex r.m.s. current I of angular frequency ω. The results to be obtained are generalizations of equation (1) for arbitrary linear loss-free electromagnetic systems.

The systems to be considered are general except for the requirement that the media are to have negligible loss. The actual media present may be both anisotropic and gyrotropic (non-reciprocal), and intrinsically dispersive. The Krönig–Kramers dispersion relations imply that dissipation at *some* frequencies is to be associated with dispersion. It will be assumed that the losses at all frequencies of interest are negligible, even though the dispersion is still significant. The limiting case occurs when the entire loss associated with the dispersion is concentrated at a set of resonant frequencies. The inclusion of the possibility of the presence of gyrotropic material leads to very little additional complication to that for anisotropic materials, and the effects of possible conduction currents are described by an effective permittivity tensor. The form of the expression for the energy density which accounts for these conduction currents and for any dispersion present in the basic permittivity and

---

† Department of Applied Mathematics, University of New South Wales, Kensington, New South Wales.

Aust. J. Phys., 1965, **18**, 287–95

permeability tensors is of special importance. The discussion of Landau and Lifshitz (1960, Sec. 61) is made the basis for the evaluation of the total average energy.

Montgomery, Dicke, and Purcell (1948, Sec. 5.21) have given expressions in the form of the final results but under very restricted conditions of excitation and without regard for the implications of the presence of dispersive or other more general media. The results are obtained by considering the frequency dependence of the complex Poynting vector integrated over an enclosing mathematical surface. The surface integral expression obtained for the total energy is of the same form as that obtained in a discussion of average electromagnetic forces (Smith 1961) and may be reduced to impedance, admittance, and scattering matrix (Smith 1964*a*) forms in the same way.

Equation (1) is used in the proof of Foster's reactance theorem (Foster 1924; Montgomery, Dicke, and Purcell 1948, Sec. 5.24) on the form of the analytical dependence of a single reactance X on ω. The relevance of the general results to extensions of Foster's theorem is noted.

II. FUNDAMENTAL EQUATIONS

The system considered is assumed to be excited by exterior sources of angular frequency ω. All field vectors are complex corresponding to the assumed time dependence $\exp(\mathrm{i}\omega t)$. It will be convenient for the amplitudes to be taken as root-mean-square values. The Maxwell equations become (in MKSA rationalized units)

$$\nabla\times\mathbf{E} = -\mathrm{i}\omega\mathbf{B}, \tag{2}$$

$$\nabla\times\mathbf{H} = \mathrm{i}\omega\mathbf{D}+\mathbf{J}, \tag{3}$$

$$\nabla.\mathbf{D} = \rho, \tag{4}$$

$$\nabla.\mathbf{B} = 0, \tag{5}$$

where **E**, **H**, **B**, and **D** are the complex r.m.s. vectors of the electric field, the magnetic intensity, the magnetic induction, and the electric displacement respectively. To preserve generality a current density **J** and charge density ρ are included, although for loss-free systems there are severe restrictions on the form **J** may take.

The usual linear constitutive equations relating **D** and **E**, **B** and **H** are assumed for the media present, together with Ohm's law for the current density, namely

$$\mathbf{D} = [\boldsymbol{\kappa}].\mathbf{E}, \tag{6}$$

$$\mathbf{B} = [\boldsymbol{\mu}].\mathbf{H}, \tag{7}$$

$$\mathbf{J} = [\boldsymbol{\sigma}].\mathbf{E}, \tag{8}$$

where $[\boldsymbol{\kappa}]$, $[\boldsymbol{\mu}]$, and $[\boldsymbol{\sigma}]$ are the second-rank tensors of permittivity, permeability, and conductivity. These tensors may all be dependent on both position and frequency of excitation. For reciprocal media each of these tensors is symmetric but for general gyrotropic media any of them may be asymmetric.

By introducing an effective permittivity tensor $[\boldsymbol{\varepsilon}]$ defined by

$$[\boldsymbol{\varepsilon}] = [\boldsymbol{\kappa}]+[\boldsymbol{\sigma}]/i\omega, \tag{9}$$

the second Maxwell equation (3) may be written

$$\nabla\times\mathbf{H} = i\omega\mathbf{D}', \tag{10}$$

where

$$\mathbf{D}' = [\boldsymbol{\varepsilon}].\mathbf{E} \tag{11}$$

is the effective displacement vector. This device collects together in $i\omega\mathbf{D}'$ all current densities apart from the magnetization current density which is already included in $\mathbf{H}$.

Now consider the surface integral of the complex Poynting vector $\mathbf{E}\times\mathbf{H}^*$ over an arbitrary closed surface S enclosing a volume V of medium, the *inward* normal being regarded as positive:

$$\begin{aligned}\int_S \mathbf{E}\times\mathbf{H}^*.\mathrm{d}\mathbf{A} &= -\int_V \nabla.(\mathbf{E}\times\mathbf{H}^*)\,\mathrm{d}\tau \\ &= \int_V (\mathbf{E}.\nabla\times\mathbf{H}^*-\mathbf{H}^*.\nabla\times\mathbf{E})\,\mathrm{d}\tau \\ &= i\omega\int_V (\mathbf{H}^*.\mathbf{B}-\mathbf{E}.\mathbf{D}'^*)\,\mathrm{d}\tau, \qquad (12)\end{aligned}$$

(using the Maxwell equations (2) and (10)),

$$= i\omega\int_V (\mathbf{H}^*.[\boldsymbol{\mu}].\mathbf{H}-\mathbf{E}.[\boldsymbol{\varepsilon}]^*.\mathbf{E}^*)\,\mathrm{d}\tau, \tag{13}$$

(using equations (7) and (11)).

For a system including only loss-free media the surface integral of the complex Poynting vector must always be purely imaginary. Equation (13) then shows that the quadratic forms $\mathbf{H}^*.[\boldsymbol{\mu}].\mathbf{H}$ and $\mathbf{E}.[\boldsymbol{\varepsilon}]^*.\mathbf{E}^*$ are always real. This implies that $[\boldsymbol{\varepsilon}]$ and $[\boldsymbol{\mu}]$ are Hermitian. In component form,

$$\mu_{kl} = \mu^*_{lk}, \qquad \epsilon_{kl} = \epsilon^*_{lk}.$$

For reciprocal systems in which $[\boldsymbol{\varepsilon}]$ and $[\boldsymbol{\mu}]$ are also symmetric this corresponds to real $[\boldsymbol{\varepsilon}]$ and $[\boldsymbol{\mu}]$. From equation (9) the Hermitian $[\boldsymbol{\varepsilon}]$ corresponds to an anti-hermitian $[\boldsymbol{\sigma}]$. That is,

$$\sigma_{kl} = -\sigma^*_{lk}. \tag{14}$$

A simple illustrative case of equation (14) occurs when conduction is by charge carriers whose only restraint to motion is from inertia or some conservative field of force. The presence of a static magnetic field gives rise to Hall currents and the full generality of equation (14) is then required.

It is clear that, if only because of the inclusion of the effects of conduction currents in the tensor $[\boldsymbol{\varepsilon}]$, the field energy density may not be taken simply as

$$U = \tfrac{1}{2}(\mathbf{E}^*.\mathbf{D}'+\mathbf{H}^*.\mathbf{B}). \tag{15}$$

In general there will also be dispersion from both $[\boldsymbol{\kappa}]$ and $[\boldsymbol{\mu}]$. When dispersion occurs equation (15) does not give the field energy density. However, Landau and Lifshitz (1960, Sec. 61) have derived an expression for the total average energy density when conduction and dispersion are present. Although their treatment refers to isotropic materials, it is readily adapted to general anisotropic materials giving (Landau and Lifshitz 1960, Sec. 76)

$$U = \tfrac{1}{2}[\mathbf{H}^*.\{\mathrm{d}(\omega[\boldsymbol{\mu}])/\mathrm{d}\omega\}.\mathbf{H}+\mathbf{E}^*.\{\mathrm{d}(\omega[\boldsymbol{\varepsilon}])/\mathrm{d}\omega\}.\mathbf{E}], \tag{16}$$

which corresponds to (15) in the absence of dispersion. Equation (16) automatically accounts for all energy associated with the application of the electromagnetic field including any mechanical energy associated with the conduction or polarization processes.

III. BEHAVIOUR OF A SYSTEM WITH VARIATIONS OF FREQUENCY

Suppose the closed mathematical surface S encloses the whole system of interest but not the sources. Consider an integration of the complex Poynting vector $\mathbf{E}\times\mathbf{H}^*$ over S reckoning the *inward* normal positive, together with integrations over the surfaces $S_1, S_2, \ldots$ of any perfect conductors included inside S regarding the *outward* normals as positive, then

$$\int_{S,S_1,S_2,\ldots} \mathbf{E}\times\mathbf{H}^*.\mathrm{d}\mathbf{A} = -\int_V \nabla.(\mathbf{E}\times\mathbf{H}^*)\,\mathrm{d}\tau,$$

where V is the active volume of the system. However, $\mathbf{E}$ is normal to the surfaces $S_1, S_2, \ldots$, therefore

$$\begin{aligned}\int_S \mathbf{E}\times\mathbf{H}^*.\mathrm{d}\mathbf{A} &= -\int_V \nabla.(\mathbf{E}\times\mathbf{H}^*)\,\mathrm{d}\tau\\ &= \mathrm{i}\omega\int_V (\mathbf{H}^*.\mathbf{B}-\mathbf{E}.\mathbf{D}'^*)\,\mathrm{d}\tau, \qquad (17)\\ &\qquad\text{as in equation (12).}\end{aligned}$$

A variation of equation (17) corresponding to a small change $\delta\omega$ of the excitation frequency gives

$$\delta\int_S \mathbf{E}\times\mathbf{H}^*.\mathrm{d}\mathbf{A} = \mathrm{i}\omega\int_V \{\delta(\mathbf{H}^*.\mathbf{B})-\delta(\mathbf{E}.\mathbf{D}'^*)\}\,\mathrm{d}\tau+\mathrm{i}\,\delta\omega\int_V (\mathbf{H}^*.\mathbf{B}-\mathbf{E}.\mathbf{D}'^*)\,\mathrm{d}\tau. \tag{18}$$

Some of the details of the following argument are similar to those used previously in deriving an expression for radiation-pressure forces (Smith 1961), but account must now be taken of the lesser symmetry of $[\boldsymbol{\mu}]$ and $[\boldsymbol{\varepsilon}]$.

From equation (11),

$$\begin{aligned}\delta(\mathbf{E}.\mathbf{D}'^*) &= \mathbf{E}.\delta\mathbf{D}'^*+\delta\mathbf{E}.[\boldsymbol{\varepsilon}]^*.\mathbf{E}^*\\ &= \mathbf{E}.\delta\mathbf{D}'^*+\mathbf{E}^*.[\boldsymbol{\varepsilon}].\delta\mathbf{E},\\ &\qquad\text{since } [\boldsymbol{\varepsilon}] \text{ is Hermitian,}\\ &= \mathbf{E}.\delta\mathbf{D}'^*+\mathbf{E}^*.\delta\mathbf{D}'-\mathbf{E}^*.[\delta\boldsymbol{\varepsilon}].\mathbf{E}. \qquad (19)\end{aligned}$$

Also, from (7),

$$\begin{aligned}\delta(\mathbf{H}^*.\mathbf{B}) &= \delta\mathbf{H}^*.\mathbf{B}+\mathbf{H}^*.[\delta\boldsymbol{\mu}].\mathbf{H}+\mathbf{H}^*.[\boldsymbol{\mu}].\delta\mathbf{H}\\ &= \delta\mathbf{H}^*.\mathbf{B}+\mathbf{H}^*.[\delta\boldsymbol{\mu}].\mathbf{H}+\delta\mathbf{H}.[\boldsymbol{\mu}]^*.\mathbf{H}^*,\\ &\qquad\qquad\text{since } [\boldsymbol{\mu}] \text{ is Hermitian,}\\ &= \delta\mathbf{H}^*.\mathbf{B}+\delta\mathbf{H}.\mathbf{B}^*+\mathbf{H}^*.[\delta\boldsymbol{\mu}].\mathbf{H}. \end{aligned}\tag{20}$$

The terms in $[\delta\boldsymbol{\mu}]$ and $[\delta\boldsymbol{\varepsilon}]$ are direct effects of dispersion in the media.

Substitution of equations (19) and (20) in equation (18) gives

$$\begin{aligned}\delta\int_S \mathbf{E}\times\mathbf{H}^*.\mathrm{d}\mathbf{A} &= \mathrm{i}\,\delta\omega\int_V(\mathbf{H}^*.\mathbf{B}-\mathbf{E}.\mathbf{D}'^*)\,\mathrm{d}\tau+\mathrm{i}\omega\int_V(\mathbf{H}^*.[\delta\boldsymbol{\mu}].\mathbf{H}+\mathbf{E}^*.[\delta\boldsymbol{\varepsilon}].\mathbf{E})\,\mathrm{d}\tau\\ &\quad+\mathrm{i}\omega\int_V\{(\delta\mathbf{H}^*.\mathbf{B}-\mathbf{E}.\delta\mathbf{D}'^*)+(\mathbf{B}^*.\delta\mathbf{H}-\mathbf{E}^*.\delta\mathbf{D}')\}\,\mathrm{d}\tau. \end{aligned}\tag{21}$$

The Maxwell equations may now be used to express the last term in equation (21) in a more useful form. The variation of equation (10) gives

$$\mathrm{i}\omega\,\delta\mathbf{D}' = \nabla\times\delta\mathbf{H}-\mathrm{i}\,\delta\omega\,\mathbf{D}',$$

which together with equation (2) allows the term to be written

$$\begin{aligned}&\int_V\{(\mathbf{E}.\nabla\times\delta\mathbf{H}^*-\delta\mathbf{H}^*.\nabla\times\mathbf{E})+(\delta\mathbf{H}.\nabla\times\mathbf{E}^*-\mathbf{E}^*.\nabla\times\delta\mathbf{H})\}\,\mathrm{d}\tau\\ &\quad+\mathrm{i}\,\delta\omega\int_V(\mathbf{E}.\mathbf{D}'^*+\mathbf{E}^*.\mathbf{D}')\,\mathrm{d}\tau\\ &\qquad= -\int_V\nabla.(\mathbf{E}\times\delta\mathbf{H}^*-\mathbf{E}^*\times\delta\mathbf{H})\,\mathrm{d}\tau+\mathrm{i}\,\delta\omega\int_V(\mathbf{E}.\mathbf{D}'^*+\mathbf{E}^*.\mathbf{D}')\,\mathrm{d}\tau\\ &\qquad= \int_{S,S_1,S_2,\ldots}(\mathbf{E}\times\delta\mathbf{H}^*-\mathbf{E}^*\times\delta\mathbf{H}).\mathrm{d}\mathbf{A}+\mathrm{i}\,\delta\omega\int_V(\mathbf{E}.\mathbf{D}'^*+\mathbf{E}^*.\mathbf{D}')\,\mathrm{d}\tau\\ &\qquad= \int_S(\mathbf{E}\times\delta\mathbf{H}^*-\mathbf{E}^*\times\delta\mathbf{H}).\mathrm{d}\mathbf{A}+\mathrm{i}\,\delta\omega\int_V(\mathbf{E}.\mathbf{D}'^*+\mathbf{E}^*.\mathbf{D}')\,\mathrm{d}\tau, \end{aligned}\tag{22}$$

since $\mathbf{E}$ is normal to the conducting surfaces S_1, S_2, ...

Equations (21) and (22) when combined give

$$\begin{aligned}\int_S(\delta\mathbf{E}\times\mathbf{H}^*+\mathbf{E}^*\times\delta\mathbf{H}).\mathrm{d}\mathbf{A} &= \mathrm{i}\,\delta\omega\int_V(\mathbf{H}^*.\mathbf{B}+\mathbf{E}^*.\mathbf{D}')\,\mathrm{d}\tau\\ &\quad+\mathrm{i}\omega\int_V(\mathbf{H}^*.[\delta\boldsymbol{\mu}].\mathbf{H}+\mathbf{E}^*.[\delta\boldsymbol{\varepsilon}].\mathbf{E})\,\mathrm{d}\tau\\ &= \mathrm{i}\,\delta\omega\int_V[\mathbf{H}^*.\{\mathrm{d}(\omega[\boldsymbol{\mu}])/\mathrm{d}\omega\}.\mathbf{H}+\mathbf{E}^*.\{\mathrm{d}(\omega[\boldsymbol{\varepsilon}])/\mathrm{d}\omega\}.\mathbf{E}]\,\mathrm{d}\tau. \end{aligned}\tag{23}$$

The volume integral on the right-hand side of equation (23) is recognized as being twice the total average energy W derived from the energy density of equation (16). Therefore,

$$2\mathrm{i}\,\delta\omega\,\mathring{W} = \int_S(\delta\mathbf{E}\times\mathbf{H}^*+\mathbf{E}^*\times\delta\mathbf{H}).\mathrm{d}\mathbf{A},\tag{24}$$

which expresses the total average energy W in terms of the frequency dependence (dispersion) of the fields on an arbitrary enclosing surface S. The variations $\delta\mathbf{E}$ and $\delta\mathbf{H}$ on S, of course, are not independent and in the following section reduced forms of the basic equation (24) are obtained.

IV. REDUCTION OF EQUATION (24) TO PARAMETER FORMS

The surface integral in equation (24) is of the same form as that relating to average electromagnetic forces (Smith 1961) and may be reduced in the same ways (Smith 1961, 1964*a*). In the present paper no restriction to reciprocal media has been applied so that care is required in writing the reduced forms, as the scattering, impedance, and admittance matrices **S**, **Z**, and **Y** are not necessarily symmetric.

For loss-free systems the requirement that the complex power to the system be purely imaginary leads to the usual unitarity of **S**, that is

$$\mathbf{S}^{-1} = \mathbf{S}^{\dagger}, \qquad (\dagger \text{ denotes Hermitian conjugate}), \tag{25}$$

and the corresponding antihermitian nature of **Z** and **Y**,

$$\mathbf{Z}^{\dagger} = -\mathbf{Z}, \qquad \mathbf{Y}^{\dagger} = -\mathbf{Y},$$

which for reciprocal systems implies that **Z** and **Y** are purely imaginary.

Equation (24) reduces to the following parameter matrix forms:

(i) *Scattering Matrix Form* (*Smith 1964* a)

$$\mathrm{i}W = -\mathbf{b}^{\dagger}\,\mathrm{d}\mathbf{S}/\mathrm{d}\omega\,\mathbf{a} \qquad (\mathbf{b} = \mathbf{S}\mathbf{a}), \tag{26}$$

a and **b** being column vectors of the incident and scattered partial wave r.m.s. amplitudes. Alternatively equation (26) may be written

$$\begin{aligned}\mathrm{i}W &= -\mathbf{a}^{\dagger}\mathbf{S}^{\dagger}\,\mathrm{d}\mathbf{S}/\mathrm{d}\omega\,\mathbf{a}\\ &= -\mathbf{a}^{\dagger}\mathbf{S}^{-1}\,\mathrm{d}\mathbf{S}/\mathrm{d}\omega\,\mathbf{a} \qquad (\text{from } (25)).\end{aligned} \tag{27}$$

(ii) *Impedance and Admittance Matrix Forms* (*Smith 1961*)

$$2\mathrm{i}W = \mathbf{I}^{\dagger}(\mathrm{d}\mathbf{Z}/\mathrm{d}\omega)\mathbf{I}, \tag{28}$$

$$2\mathrm{i}W = \mathbf{V}^{\dagger}(\mathrm{d}\mathbf{Y}/\mathrm{d}\omega)\mathbf{V}, \tag{29}$$

where

$$\mathbf{V} = \mathbf{Z}\mathbf{I}, \tag{30}$$

$$\mathbf{I} = \mathbf{Y}\mathbf{V}, \tag{31}$$

and **V** and **I** are the "voltage" and "current" column vectors.

The equivalence of equations (26), (28), and (29) is a result of the relationships between admittance or impedance matrices and the scattering matrix (Montgomery, Dicke, and Purcell 1948; Smith 1964*b*). In terms of the reactance matrix **X**, i**X** being defined generally as the loss-free (antihermitian) part of **Z**, we have

$$2W = \mathbf{I}^{\dagger}(\mathrm{d}\mathbf{X}/\mathrm{d}\omega)\mathbf{I} \tag{32}$$

or

$$2W = \mathbf{V}^{\dagger}(\mathrm{d}\hat{\mathbf{B}}/\mathrm{d}\omega)\mathbf{V}, \tag{33}$$

where $\hat{\mathbf{B}}$ is the susceptance matrix related similarly to $\mathbf{Y}$. Clearly $\mathbf{X}$ and $\hat{\mathbf{B}}$ are Hermitian in general, and real for reciprocal systems. For the loss-free systems under consideration,

$$\mathbf{X} = -\hat{\mathbf{B}}^{-1}.$$

V. Discussion and Applications

The total average energy for sinusoidal excitation of a general loss-free system has been expressed as a surface integral of field quantities, and alternatively in algebraic forms involving the frequency dependence of admittance, impedance, reactance, susceptance, or scattering matrices. There has been no restriction on the frequency of excitation, neither has there been any restriction to reciprocal or non-dispersive media. The parameter forms of Section IV illustrate the close connection between energy storage and dispersion, high dispersion implying high energy storage for similar conditions of excitation.

Montgomery, Dicke, and Purcell (1948, Sec. 5.21) have also obtained these parameter forms but for isotropic, non-dispersive media with special excitation such that the fields everywhere are of constant phase. In low-frequency electric circuit theory, results corresponding to equations (32) and (33) for a two-terminal network (one-port), where there is just a single component to each $\mathbf{V}$ and $\mathbf{I}$, are well known (Guillemin 1957).

Since the average energy density U is always positive for non-vanishing fields (Landau and Lifshitz 1960, Sec. 61), the total average energy W is necessarily positive. This leads to important conditions for the parameter matrices. Thus from equations (32) and (33) the matrices $\mathrm{d}\mathbf{X}/\mathrm{d}\omega$ and $\mathrm{d}\hat{\mathbf{B}}/\mathrm{d}\omega$ are positive definite. For a two-terminal network these conditions on $\mathrm{d}X/\mathrm{d}\omega$ and $\mathrm{d}\hat{B}/\mathrm{d}\omega$ together with general considerations of the analytic behaviour and symmetry of reactance functions at complex frequencies (Cauer 1958, Chs. 4 and 5; Landau and Lifshitz 1960, Secs. 58 and 62) lead to Foster's reactance theorem (Bode 1945, Sec. 9.4; Montgomery, Dicke, and Purcell 1948, Sec. 5.24) which expresses $X(\omega)$, $\hat{B}(\omega)$ in the form

$$X(\omega) = -\sum_n r_n\left(\frac{1}{\omega+\omega_n}+\frac{1}{\omega-\omega_n}\right), \tag{34}$$

where r_n and ω_n^2 are real and positive. (If $X(\omega)$ has a pole at infinity a further term $a\omega$, with $a > 0$, may be required in equation (34).)

The results of the present paper immediately extend Foster's theorem to systems containing dispersive or gyrotropic materials. More generally, it may be reasoned similarly that the eigenvalues of $\mathbf{X}$ and $\hat{\mathbf{B}}$ are all of the form (34). Since $\mathbf{X}$ and $\hat{\mathbf{B}} = -\mathbf{X}^{-1}$ are Hermitian, they may be brought simultaneously to diagonal form by a unitary transformation of the terminal voltages $\mathbf{V}$ and currents $\mathbf{I}$ without disturbing power or energy relationships such as equations (32) and (33). The resulting diagonal elements (eigenvalues) of $\mathbf{X}$ and $\hat{\mathbf{B}}$ are real. With this choice of $\mathbf{V}$ and $\mathbf{I}$, $\mathrm{d}\mathbf{X}/\mathrm{d}\omega$ and $\mathrm{d}\hat{\mathbf{B}}/\mathrm{d}\omega$ need not be diagonal, but by a familiar result from matrix theory (Landau and Lifshitz 1959, Sec. 72) their diagonal values are the derivatives of the eigenvalues of $\mathbf{X}$ and $\hat{\mathbf{B}}$. These values must be positive for the quadratic forms of equation (32) and (33) to be positive definite. Foster's theorem may then be extended to apply to each eigenvalue of $\mathbf{X}$ and $\hat{\mathbf{B}}$. For reciprocal systems ($\mathbf{X}$, $\hat{\mathbf{B}}$ real and symmetric) the required diagonalizing transformation is real and orthogonal rather than unitary. Cauer (1931, 1958) and Carlin (1955) have discussed extensions of Foster's theorem for n-terminal pair lumped-element systems.

Zeros of the eigenvalues of $\mathbf{X}$ correspond to poles of the eigenvalues of $\hat{\mathbf{B}}$, and vice versa. The critical frequencies ω_n of equation (34) are resonant frequencies corresponding to zeros of the eigenvalues of $\hat{\mathbf{B}}$, i.e. resonant frequencies with respect to the surface S. It has been assumed in the reductions of Section IV that critical resonant or anti-resonant (zeros of the eigenvalues of $\mathbf{X}$) frequencies are to be avoided in writing equations (30) and (31). The form given in equation (34) may also be obtained by expansion of a general field in terms of the eigenfunction solutions of the system with specified boundary conditions on S. The ω_n^2 are the corresponding eigenvalues of ω^2. This technique is employed for deriving the Wigner–Eisenbud many-level formula for the R matrix in formal nuclear scattering theory (Blatt and Weisskopf 1952; Lane and Thomas 1958). The Wigner–Eisenbud formula of quantum theory giving the energy dependence of the parameter matrices corresponds to Foster's reactance theorem in electromagnetism, although there are important differences of detail.

The result from the scattering matrix formulation (equation (27)) corresponding to the positive reactance or susceptance derivatives is best expressed in terms of a phase shift matrix $\boldsymbol{\eta}$. Since $\mathbf{S}$ is unitary it may be diagonalized by a unitary transformation of the partial wave amplitudes, and each of the eigenvalues is of unit modulus. Thus $\mathbf{S}$ may be expressed as

$$\mathbf{S} = \exp 2\mathrm{i}\boldsymbol{\eta},$$

where $\boldsymbol{\eta}$ is Hermitian with real eigenvalues η_k. Since the total average energy is positive, equation (27) shows that the matrix $\mathrm{i}\mathbf{S}^{-1}\,\mathrm{d}\mathbf{S}/\mathrm{d}\omega$ is positive definite, so that its diagonal elements are always positive. In particular, the diagonal elements in a representation in which $\mathbf{S}$ is diagonal, are positive, that is

$$(\mathrm{i}\mathbf{S}^{-1}\,\mathrm{d}\mathbf{S}/\mathrm{d}\omega)_{kk} > 0.$$

But

$$\begin{aligned}(\mathrm{i}\mathbf{S}^{-1}\,\mathrm{d}\mathbf{S}/\mathrm{d}\omega)_{kk} &= \mathrm{i}\exp(-2\mathrm{i}\eta_k)\{\mathrm{d}(\exp 2\mathrm{i}\boldsymbol{\eta})/\mathrm{d}\omega\}_{kk}\\ &= \mathrm{i}\exp(-2\mathrm{i}\eta_k).\mathrm{d}(\exp 2\mathrm{i}\eta_k)/\mathrm{d}\omega\\ &= -2\,\mathrm{d}\eta_k/\mathrm{d}\omega,\end{aligned}$$

therefore,

$$\mathrm{d}\eta_k/\mathrm{d}\omega < 0. \qquad (35)$$

Equation (35) corresponds to the positive derivatives of the eigenvalues of the reactance or susceptance matrices. In fact the interrelation of $\mathbf{X}$ and $\hat{\mathbf{B}}$ with $\mathbf{S}$ gives

$$\mathbf{X} = \cot \boldsymbol{\eta}, \qquad \hat{\mathbf{B}} = -\tan \boldsymbol{\eta},$$

from which the equivalence follows by differentiation in a diagonal representation.

The time dependence has been taken as harmonic in all of the considerations. This is not an important restriction since the time-averaged energy may be computed by summing over all Fourier components present, it being assumed that the system is without loss at all of these frequencies. Under periodic excitation the average energy is simply the energy averaged over a single period.

VI. References

Blatt, J. M., and Weisskopf, V. F. (1952).—"Theoretical Nuclear Physics." (Wiley: New York.)

Bode, H. W. (1945).—"Network Analysis and Feedback Amplifier Design." (Van Nostrand: New York.)

Carlin, H. J. (1955).—*In* "Proceedings of the Symposium on Modern Network Synthesis." p. 11. (Polytechnic Institute of Brooklyn: New York.)

Cauer, W. (1931).—*S.B. preuss. Akad. Wiss., Physik. math. Kl.* **30**: 673.

Cauer, W. (1958).—"Synthesis of Linear Communication Networks." Vols. I and II. (McGraw-Hill: New York.)

Foster, R. (1924).—*Bell Syst. Tech. J.* **3**: 259.

Guillemin, E. A. (1957).—"Synthesis of Passive Networks." (Wiley: New York.)

Landau, L. D., and Lifshitz E. M. (1959).—"Quantum Mechanics." (Pergamon Press: London.)

Landau, L. D., and Lifshitz, E. M. (1960).—"Electrodynamics of Continuous Media." (Pergamon Press: Oxford.)

Lane, A. M., and Thomas, R. G. (1958).—*Rev. Mod. Phys.* **30**: 257.

Montgomery, C. G., Dicke, R. H., and Purcell, E. M. (1948).—"Principles of Microwave Circuits." (McGraw-Hill: New York.)

Smith, W. E. (1961).—*Aust. J. Phys.* **14**: 152.

Smith, W. E. (1964*a*).—*Aust. J. Appl. Sci.* **15**: 65.

Smith, W. E. (1964*b*).—*Aust. J. Phys.* **17**: 389.

MODELS OF MASSIVE STARS IN HOMOLOGOUS GRAVITATIONAL CONTRACTION

By S. M. A. MEGGITT*

[*Manuscript received February* 15, 1965]

Summary

Nine models of homologously contracting, uniform composition stars have been constructed for $\mu^2M/M_\odot$ in the range 10–80. Apart from the two smallest models, all models have convective cores, the size of core increasing with the mass. The rate of contraction increases with mass up to $\mu^2M/M_\odot = 32$ and decreases thereafter. One set of models covers all compositions.

I. INTRODUCTION

Previous investigations of the contraction of massive stars have been undertaken by Boury (1963) and by Van der Borght (1964). In these investigations it was assumed that contraction was homologous, and the relative distributions of the physical quantities were taken to be the same as in the corresponding main sequence model. This implies that there is no energy generated in the envelope and is a good approximation when there is a large convective core containing most of the mass. This can be expected to be the case for very massive stars, owing to the importance of the radiation pressure. On the other hand smaller stars are wholly radiative in the period immediately preceding nuclear burning.

Models are constructed here in which the energy generation in the radiative region is taken into account. It is shown that the equations of quasi-static equilibrium can be solved directly, independently of the radius, if it is assumed that (i) contraction is homologous, (ii) the energy source is entirely gravitational, (iii) the opacity is due to electron scattering, and (iv) the composition is uniform throughout the model. This leads to models which change from purely radiative at the lower masses to mainly convective at the higher masses. By extending the transformations used in Van der Borght and Meggitt (1963) to the energy equation, a one-parameter set of models suffices for all compositions. These models can be expected to be a good approximation to the structure of a massive star during the time when the surface temperature is high enough to ensure a radiative envelope, but before nuclear energy provides an appreciable proportion of the luminosity.

II. EQUATIONS

The assumptions of uniform composition and of electron scattering opacity imply that μ and κ are constant throughout the model. Also, in the absence of nuclear processes they do not change with time. In the basic differential equations for the stellar interior (Schwarzschild 1958, whose notation is used here), the composition and radius are removed from all equations except the energy equations

---

* Department of Mathematics, School of General Studies, Australian National University, Canberra.

Aust. J. Phys., 1965, **18**, 297–302

((2), (5) below), by the substitutions $m = \mu^2 M_r$, $l = \kappa\mu^2 L_r$, $t = \mu RT$, following the procedure of Van der Borght and Meggitt (1963). Using the equation of state to eliminate the density and pressure, the differential equations become

$$\frac{\mathrm{d}m}{\mathrm{d}x} = \frac{4\pi a}{3\mathscr{R}} \cdot \frac{\beta t^3}{1-\beta} \cdot x^2, \tag{1}$$

$$\frac{\mathrm{d}l}{\mathrm{d}m} = \kappa\epsilon; \tag{2}$$

Convective

$$\left.\begin{aligned} \frac{\mathrm{d}t}{\mathrm{d}x} &= -\frac{G}{\mathscr{R}} \cdot \frac{\beta(8-6\beta)}{32-24\beta-3\beta^2} \cdot \frac{m}{x^2}, \\ \frac{\mathrm{d}\beta}{\mathrm{d}x} &= \frac{G}{\mathscr{R}} \cdot \frac{3\beta^3(1-\beta)}{32-24\beta-3\beta^2} \cdot \frac{m}{x^2 t}; \end{aligned}\right\} \tag{3}$$

Radiative

$$\left.\begin{aligned} \frac{\mathrm{d}t}{\mathrm{d}x} &= -\frac{1}{16\pi c\mathscr{R}} \cdot \frac{\beta}{1-\beta} \cdot \frac{l}{x^2}, \\ \frac{\mathrm{d}\beta}{\mathrm{d}x} &= \frac{1}{4\pi c\mathscr{R}} \cdot \frac{\beta}{x^2 t}\{l - 4\pi c G m(1-\beta)\}; \end{aligned}\right\} \tag{4}$$

together with the expression for the energy released by contraction,

$$\epsilon = \frac{3\mathscr{R}T}{2\mu} \frac{\partial}{\partial\tau}(\ln T - 8y/3 - \tfrac{2}{3}\ln y), \tag{5}$$

where $y = (1-\beta)/\beta$, β is the ratio of gas pressure to total pressure, and τ is the time.

To these equations are added the boundary conditions $m = 0$, $l = 0$ at the centre, and $t = 0$ at the surface. The additional condition necessary at the surface has been taken as

$$\frac{\kappa L}{4\pi c G M(1-\beta)} = 1. \tag{6}$$

This is an approximation to the more precise condition

$$\left(\frac{T}{T_e}\right)^4 = \frac{1}{2\{1 - \kappa L/4\pi c G M(1-\beta)\}},$$

which holds in a radiative region near the surface, in which M_r and L_r are taken as constant and in which $\kappa P R^2/GM$ has the value $\frac{2}{3}$ when $T = T_e$ (effective temperature).

The composition (which enters only through κ and μ) and the radius are removed from the energy equations (2) and (5) in the following way. The assumption of homologous contraction is that $q = M_r/M$ is independent of the time. By Lane's theorem (Chandrasekhar 1939) it follows that RT and β are independent of the time. Define the quantity K by

$$\frac{\mu^2}{\kappa K} = \frac{\mathrm{d}}{\mathrm{d}\tau}\left(\frac{1}{R}\right). \tag{7}$$

Equation (5) then becomes

$$\epsilon = 3\mathscr{R}t/2\kappa K. \tag{8}$$

The surface condition (6) shows that κL is constant during the contraction, that is,

$$\frac{3\mathscr{R}M}{2K}\int_0^1 t\,\mathrm{d}q = \text{constant.}$$

It follows that K is constant, and the contraction follows the usual pattern in which the reciprocal of the radius changes uniformly with time. Combination of (2) and (8) leads to the energy equation

$$\frac{\mathrm{d}l}{\mathrm{d}m} = \frac{3\mathscr{R}t}{2K}. \tag{9}$$

Equations (1), (3), (4), and (9) are now independent of both radius and time, and so may be integrated to give a model in a state of homologous contraction.

III. METHOD OF INTEGRATION

The equations were integrated numerically on an IBM 1620 computer using the classical fourth-order Runge–Kutta method with a step length of 1% of the radius. Starting from the surface the values of two parameters, L and K, need to be chosen. The method described by Sears (1959) was used, in which the run of $U = \mathrm{d}(\ln M_\mathrm{r})/\mathrm{d}(\ln r)$ determines whether the initial choice of L is too large or too small. In a similar manner, a check on the value of K was obtained by observing the quantity $\mathrm{d}(\ln L_\mathrm{r})/\mathrm{d}(\ln M_\mathrm{r})$, which should increase monotonically from zero at the surface to unity at the centre. If this quantity decreases anywhere K is too large, and if it exceeds unity K is too small for the particular value of L chosen.

Each inward integration was terminated at $x = 0\cdot10$, and the central value β_c was estimated from the convective expansion

$$y = y_\mathrm{c} - \frac{x^2}{2}\left(\frac{4\pi G\mu\rho R^2}{\mathscr{R}T}\cdot\frac{y}{5+40y+32y^2}\right)_\mathrm{c} + \frac{x^4}{24}\left(\frac{16\pi^2G^2\mu^2\rho^2R^4y}{5\mathscr{R}^2T^2}\cdot\frac{70+120y+768y^2+1024y^3}{(5+40y+32y^2)^3}\right)_\mathrm{c},$$

while T_c was obtained from constancy of the entropy

$$(\tfrac{2}{3}\ln y + 8y/3 - \ln T)(3\mathscr{R}/2\mu)$$

in the core. These values were used to start an integration from the centre out to the point $x = 0\cdot10$. The differences between the values of β and T at this point from the inward and outward integrations were used to improve the estimates of T_c and β_c, and the differences in M_r and L_r were used to improve the values of the parameters L and K. So long as these differences were less than 1% of the quantities involved, linear extrapolation in two variables gave excellent results.

IV. RESULTS

The results of the integrations are set out in Table 1. With the exception of the models $\mu^2 M/M_\odot = 10$ and $12{\cdot}5$, which are purely radiative, all models were found to have convective cores and radiative envelopes. Interpolation in the Schwarzschild condition shows that convection appears at the centre when $\mu^2 M/M_\odot = 13{\cdot}1$. The subscripts c, f, s refer to the centre, boundary between core and envelope, and surface respectively. The numbers in the row labelled P.E. are the coefficients of $-GM^2/R$ in the expression for the potential energy. Comparison with the value

$$-\frac{3}{5-n}\cdot\frac{GM^2}{R}$$

for a polytrope shows an average polytropic index varying between 2·76 and 2·6.

TABLE 1

RESULTS OF NUMERICAL INTEGRATIONS

$\mu^2 M/M_\odot$	10	12·5	15	20	25	30	40	60	80
$10^{-5}K$	1·122	1·030	0·976	0·920	0·896	0·887	0·891	0·930	0·982
$\log_{10}(\kappa\mu^2 L/L_\odot)$	4·204	4·407	4·563	4·793	4·962	5·094	5·294	5·558	5·735
$\mu R T_c/10^6 R_\odot$	148	173	195	232	264	295	350	447	532
$\rho_c/\bar{\rho}$	31·6	29·7	28·1	26·2	25·3	24·9	24·9	25·6	26·5
x_f	—	—	0·147	0·262	0·327	0·372	0·433	0·504	0·546
q_f	—	—	0·076	0·302	0·458	0·564	0·695	0·818	0·874
L_f/L	—	—	0·122	0·429	0·607	0·713	0·827	0·916	0·949
β_c	0·818	0·769	0·727	0·662	0·614	0·576	0·519	0·444	0·395
β_f	—	—	0·740	0·697	0·662	0·631	0·582	0·509	0·458
β_s	0·879	0·845	0·815	0·765	0·722	0·686	0·627	0·544	0·486
P.E.	1·337	1·319	1·303	1·279	1·265	1·256	1·249	1·250	1·257

The constant K is defined by equation (7), and is tabulated so that κK is in units of (years) × (solar radii) if κ is expressed in cm²/g. It gives a measure of the Helmholtz contraction time in the sense that if the model were to contract from an infinite radius, $\kappa K/\mu^2$ would be the time in years to contract to one solar radius. It can be seen that the rate of contraction reaches a maximum for $\mu^2 M/M_\odot = 32$, more massive models contracting more slowly. In fact, for large masses K will increase in proportion to the square root of the mass. For, as M increases the model approaches a completely convective state in which radiation pressure is dominant. Under these circumstances Hoyle and Fowler (1963) have shown that a good approximation is obtained by using a polytrope of index 3. This satisfies the relation

$$0{\cdot}0031(\mu\beta)^4(M/M_\odot)^2 = 1-\beta, \tag{10}$$

and has potential energy $-3GM^2/2R$. Since only the proportion $\beta/2$ of the energy is available for radiation, we have

$$L = \frac{\beta}{2}\frac{\mathrm{d}}{\mathrm{d}\tau}\left(\frac{3GM^2}{2R}\right).$$

Substitution of K from (7), β from (10), and L from (6) with $1-\beta\approx 1$ leads to

$$K = 7\cdot 7\times 10^3(\mu^2 M/M_\odot)^{\frac{1}{3}}.$$

The models for large masses differ little in relative distribution of β, q, and T from static homogeneous models. The only difference lies in the energy equation.

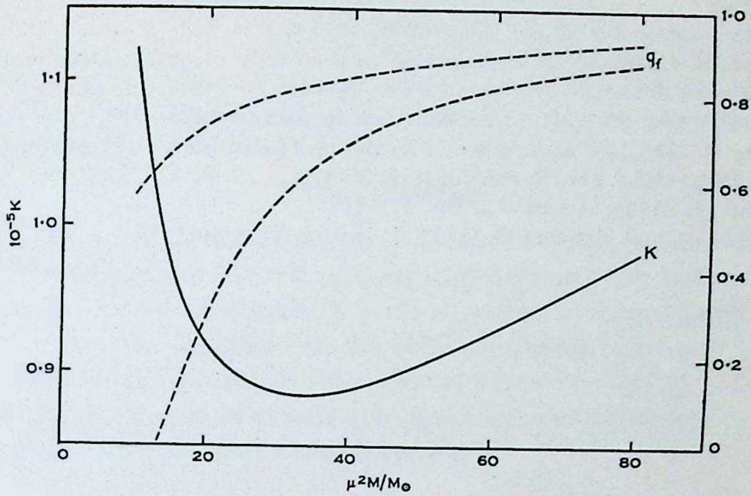

Fig. 1.—Variation of K and q_f with mass. Upper dashed curve: main sequence models (Van der Borght and Meggitt); lower dashed curve: models constructed in the present paper.

In the contracting models part of the energy is produced outside the core; in the static models all of the energy is produced in the core. As the size of the core increases with mass the difference between the two types of models diminishes (Fig. 1). Table 2 compares the properties of the most massive contracting model considered here with those of the corresponding static homogeneous model. The effect of the 5% of the luminosity which is generated in the envelope of the contracting model is seen to be small.

TABLE 2

COMPARISON BETWEEN CONTRACTING AND STATIC HOMOGENEOUS MODELS FOR $\mu^2M/M_\odot=80$

Characteristic	Contracting Model	Static Model
$\log_{10}(\kappa\mu^2L/L_\odot)$	5·735	5·729
$\mu RT_c/10^6R_\odot$	532	528
$\rho_c/\bar{\rho}$	26·5	25·6
x_f	0·546	0·608
q_f	0·874	0·924
L_f/L	0·949	1
β_c	0·395	0·393
β_f	0·458	0·469
β_s	0·486	0·492

V. Acknowledgment

It is a pleasure to express my appreciation to Professor R. Van der Borght for many valuable discussions.

VI. References

Boury, A. (1963).—*Mém. Soc. R. Sci. Liège* (5) **8**: Part 6.
Chandrasekhar, S. (1939).—"An Introduction to the Study of Stellar Structure." (Univ. of Chicago Press.)
Hoyle, F., and Fowler, W. A. (1963).—*Mon. Not. R. Astr. Soc.* **125**: 169.
Schwarzschild, M. (1958).—"Structure and Evolution of the Stars." (Princeton Univ. Press.)
Sears, R. L. (1959).—*Mém. Soc. R. Sci. Liège* (5) **3**: 479.
Van der Borght, R. (1964).—*Aust. J. Phys.* **17**: 165.
Van der Borght, R., and Meggitt, S. (1963).—*Aust. J. Phys.* **16**: 415.

VECTOR TETRAD IN COSMOLOGICAL RED SHIFT

By G. L. GEHLOT* and M. C. DURGAPAL*

[*Manuscript received March* 19, 1965]

Summary

The tetrad formalism is applied to certain cosmological models and it is found that the vector C_ν has the time component associated with Hubble's expansion.

I. INTRODUCTION

Mathematical formulation of the general theory of relativity and cosmology has been given by vector tetrad. This terminology has been used by McCrea and Mikhail (1956) to admit creation of matter in a steady-state universe. Singh and Verma (1962) have applied the formalism to the Schwarzschild interior and exterior solutions. We have used the contracted form of a third-order tensor, $\gamma^{\mu}_{\nu\sigma}$, a tensor associated with Ricci's coefficient of rotation, in certain cosmological models and found its correspondence with the gravitational red shift.

II. $\gamma^{\mu}_{\nu\sigma}$ IN TETRAD

Four mutually orthogonal vectors are said to form an orthogonal tetrad. The vectors of a tetrad may be denoted by $\lambda^{\mu}_{(m)}$, where μ is the contravariant tensor index, and m (0, 1, 2, 3) is a tetrad suffix. With each event in space–time are associated four such contravariant vectors, and μ runs from 0 to 3. The suffix (m) is just a label and has nothing to do with the covariance or contravariance of the vector.

The cofactor of the contravariant vector $\lambda^{\mu}_{(m)}$ in the determinant $|\lambda^{\mu}_{(m)}|$ gives the covariant vector $\lambda^{(m)}_{\mu}$. The following relations are of importance.

$$\left.\begin{aligned} \lambda^{\mu}_{(m)}\,\lambda^{(n)}_{\mu} &= \delta^{n}_{m}, \\ \lambda^{\mu}_{(m)}\,\lambda^{(m)}_{\nu} &= \delta^{\mu}_{\nu}, \end{aligned}\right\} \tag{1}$$

where δ^{n}_{m} and δ^{μ}_{ν} are Kronecker delta symbols. The metric tensor in space–time is

and

$$\left.\begin{aligned} g_{\mu\nu} &= \lambda^{(m)}_{\mu}\,\lambda^{(m)}_{\nu} \\ g^{\mu\nu} &= \lambda^{\mu}_{(m)}\,\lambda^{\nu}_{(m)}. \end{aligned}\right\} \tag{2}$$

A third-order tensor $\gamma^{\mu}_{\nu\sigma}$ is defined as

$$\begin{aligned} \gamma^{\mu}_{\nu\sigma} &= \lambda^{\mu}_{(m)}\,\lambda^{(m)}_{\nu}|_{\sigma} \\ &= \lambda^{\mu}_{(m)}[\lambda^{(m)}_{\nu,\sigma} - \Gamma^{\rho}_{\nu\sigma}\,\lambda^{(m)}_{\rho}], \end{aligned} \tag{3}$$

where $_{|\sigma}$ represents covariant differentiation, and

$$\Gamma^{\rho}_{\nu\sigma} = \tfrac{1}{2}g^{\rho\alpha}[g_{\nu\alpha,\sigma} + g_{\alpha\sigma,\nu} - g_{\nu\sigma,\alpha}]. \tag{4}$$

---

* Department of Physics, University of Jodhpur, Jodhpur, India.

Aust. J. Phys., 1965, **18**, 303–7

Using equations (4), (2), and (1), equation (3) gives

$$\gamma^{\mu}_{\nu\sigma} = \tfrac{1}{2}\lambda^{\mu}_{(m)}[\lambda^{(m)}_{\nu,\sigma} - \lambda^{(n)}_{a,\sigma}\,\lambda^{(n)}_{\nu}\,\lambda^{a}_{(m)} - \lambda^{(n)}_{a,\nu}\,\lambda^{(n)}_{\sigma}\,\lambda^{a}_{(m)}$$

$$-\lambda^{(m)}_{\sigma,\nu} + \lambda^{(n)}_{\nu,a}\,\lambda^{(n)}_{\sigma}\,\lambda^{a}_{(m)} + \lambda^{(n)}_{\nu}\,\lambda^{(n)}_{\sigma,a}\,\lambda^{a}_{(m)}]. \tag{5}$$

Contraction between the suffixes μ and ν of the tensor $\gamma^{\mu}_{\nu\sigma}$ gives

$$\gamma^{\mu}_{\mu\sigma} = 0, \tag{6}$$

while the contraction between μ and σ gives

$$C_{\nu} = \gamma^{\mu}_{\nu\mu} = \lambda^{\mu}_{(m)}[\lambda^{(m)}_{\nu,\mu} - \lambda^{(m)}_{\mu,\nu}]. \tag{7}$$

The vector C_{ν} has been used by Levi-Civita (1929), McCrea and Mikhail (1956), and Singh and Verma (1962), and it is important in the present work also.

III. VALUES OF C_{ν} IN IMPORTANT COSMOLOGICAL MODELS

(a) *Space–Time Conformally Flat*

The metric is given by (Synge 1960)

$$\mathrm{d}s^2 = [\omega(t)]^2(\mathrm{d}t^2 - \mathrm{d}x^2 - \mathrm{d}y^2 - \mathrm{d}z^2), \tag{8}$$

where ω is a function of time. Then

$$g_{\mu\nu} = \mathrm{diag}\{[\omega(t)]^2;\ -[\omega(t)]^2;\ -[\omega(t)]^2;\ -[\omega(t)]^2\},$$

$$\lambda^{(n)}_{\nu} = \mathrm{diag}\{\omega(t);\ \mathrm{i}\omega(t);\ \mathrm{i}\omega(t);\ \mathrm{i}\omega(t)\},$$

$$\lambda^{\mu}_{(m)} = \mathrm{diag}\{1/\omega(t);\ -\mathrm{i}/\omega(t);\ -\mathrm{i}/\omega(t);\ -\mathrm{i}/\omega(t)\},$$

and

$$C_{\nu} = \{-3\omega'(t)/\omega(t);\ 0;\ 0;\ 0\}, \tag{9}$$

where i is the normal complex operator.

The cosmological red shift is given by (Synge 1960)

$$\rho = r_0\,\omega'(t)/\omega(t), \tag{10}$$

where r_0 is the optical distance for all observations made at t. The constant of proportionality comes out to be $-\frac{1}{3}C_0$, that is, $\frac{1}{3}$ times the value of the time component of the vector C_{ν} in the tetrad.

(b) *Spatially Isotropic Universe*

If we assume that the vector C_{ν} in the tetrad, is such that the time component is related to the red shift and the other three components have special isotropy, we should be able to explain the phenomena of a spatially isotropic universe in which the density of the stars is the same in all directions. Let us take the metric for such a universe as (Weber 1961)

$$\mathrm{d}s^2 = (\mathrm{d}x^0)^2 - y^2(1+ar^2)^{-2}[(\mathrm{d}x^1)^2 + (\mathrm{d}x^2)^2 + (\mathrm{d}x^3)^2], \tag{11}$$

where y is a function of time alone, and a is a constant. Then

$$g_{\mu\nu} = \mathrm{diag}\{1;\ -y^2/(1+ar^2)^2;\ -y^2/(1+ar^2);\ -y^2/(1+ar^2)\},$$

$$\lambda^{(m)}_{\mu} = \mathrm{diag}\{1\,;\,\mathrm{i}y/(1+ar^2)\,;\,\mathrm{i}y/(1+ar^2)\,;\,\mathrm{i}y/(1+ar^2)\},$$

and

$$C_\nu = \left\{-3\left(\frac{1}{y}\frac{\partial y}{\partial x^0}\right);\,\frac{4ar}{1+ar^2}\frac{\partial r}{\partial x^1};\,\frac{4ar}{1+ar^2}\frac{\partial r}{\partial x^2};\,\frac{4ar}{1+ar^2}\frac{\partial r}{\partial x^3}\right\}, \tag{12}$$

where

$$r^2 = (x^1)^2+(x^2)^2+(x^3)^2.$$

The form of the vector C_ν agrees with our assumption, as the time component C_0 corresponds to Hubble's expansion $(1/y)(\partial y/\partial x^0)$ and C_1, C_2, C_3 are components of $4a\mathbf{r}/(1+ar^2)$, that is,

$$4ax^1/(1+ar^2);\;\; 4ax^2/(1+ar^2);\;\; 4ax^3/(1+ar^2); \tag{13}$$

corresponding to the isotropy assumed.

This method can safely be extended to other cosmological models.

IV. GRAVITATIONAL FORCE IN TERMS OF $\overline{C}_1$

Approximate gravitational force in terms of $\overline{C}_1$ (the gravitating mass contribution to C_1) has been found for Schwarzschild's exterior and interior fields. Hence, an approximation for force can be obtained from $\overline{C}_1$ for the following fields.

(a) *Schwarzschild's Interior Field in Isotropic Coordinates*

Choosing the metric (Wyman 1946)

$$\mathrm{d}s^2 = e^{\sigma}\,\mathrm{d}t^2 - e^{\mu}(\mathrm{d}r^2+r^2\,\mathrm{d}\theta^2+r^2\sin^2\theta\,\mathrm{d}\phi^2),$$

where

$$e^{\sigma} = \{2a-2m+m(4a-m)r^2/2a^3\}\{(2a+m)(1+mr^2/2a^3)\}^{-1}$$

and

$$e^{\mu} = (1+m/2a)^6(1+mr^2/2a^3)^{-2},$$

we obtain

$$C_\nu = \left\{0\,;-\frac{2}{r}-\frac{mr}{a^3(1+mr^2/2a^3)}\left[2-\frac{2a-m}{2a-2m+m(4a-m)r^2/2a^3}\right];\,-\cot\theta\,;0\right\}. \tag{14}$$

Now the value of C_ν in Schwarzschild's external field (Singh and Verma 1962) is

$$C_\nu = \left\{0;\,-\frac{2}{r}-\frac{M}{r^2}(1-2M/r)^{-1};\;-\cot\theta;\;0\right\}.$$

$$\overline{C}_1 = -\frac{M}{r^2}(1-2M/r)^{-1},$$

where $\overline{C}_1$ is the contribution to C_1 due to the gravitating mass. The other contributions depend only on the choice of the coordinates. For Schwarzschild's internal field, to the first approximation (Singh and Verma 1962),

$$\overline{C}_1 \simeq -4\pi\rho_0 r/3.$$

We see that $\overline{C}_1$ corresponds to the gravitational force. Hence in Schwarzschild's internal field in isotropic coordinates, the gravitational force must be given by (from equation (14))

$$\overline{C}_1 = -\frac{mr}{a^3(1+mr^2/2a^3)}\left[2-\frac{2a-m}{2a-2m+m(4a-m)r^2/2a^3}\right],$$

as the gravitating matter contributes only to the $\overline{C}_1$ term.

(b) *Force in Schwarzschild's External Field for Charged Particles*

The metric is (Eddington 1924)

$$ds^2 = \left(1-\frac{2m}{r}+\frac{4\pi e^2}{r^2}\right)dt^2-\left(1-\frac{2m}{r}+\frac{4\pi e^2}{r^2}\right)^{-1}dr^2-r^2\,d\theta^2-r^2\sin^2\theta\,d\phi^2.$$

The contribution of charge and mass, that is, $\overline{C}_1$ comes out as

$$\overline{C}_1 = -\left(\frac{m}{r^2}-\frac{4\pi e^2}{r^3}\right)\left(1-\frac{2m}{r}+\frac{4\pi e^2}{r^2}\right)^{-1},$$

which must correspond to the force in this field.

(c) *Force in a Spatially Isotropic Universe*

The metric (Weber 1961)

$$ds^2 = (dx^0)^2-y^2(1+ar^2)^{-2}[dr^2+r^2\,d\theta^2+r^2\sin^2\theta\,d\phi^2]$$

gives the value of C_ν as

$$C_\nu = \left\{-3\left(\frac{1}{y}\frac{\partial y}{\partial x^0}\right);\ -\frac{2}{r}\cdot\frac{1-ar^2}{1+ar^2};\ \cot\theta;\ 0\right\}.$$

$$C_1 = -\frac{2}{r}+\frac{4ar}{1+ar^2},$$

or

$$\overline{C}_1 = 4ar/(1+ar^2).$$

Hence the force in a spatially isotropic universe is represented by $4ar/(1+ar^2)$. We see that $\overline{C}_1$ here is the vector whose components are given by C_1, C_2, and C_3 of equation (13).

V. DISCUSSION

We are led to a clear understanding of vector tetrad in a spatially isotropic universe. We can always choose a vector in a tetrad which gives

(i) the Hubble expansion of cosmological red shift in terms of its time component, and

(ii) the gravitational field force.

In other words, we can also say that the x^0 component of the gravitational field force corresponds to Hubble's expansion, and components along x^1, x^2, x^3 are components along space axes.

VI. REFERENCES

EDDINGTON, A. S. (1924).—"Mathematical Theory of Relativity." (Cambridge Univ. Press.)

LEVI-CIVITA, T. (1929).—"A Simplified Presentation of Einstein's Unified Field Equations." (A translated pamphlet.) (Blackie: London.)

MCCREA, W. H., and MIKHAIL, F. I. (1956).—*Proc. R. Soc.* **A235**: 11.

SINGH, K. P., and VERMA, M. P. (1962).—*Proc. Natn. Inst. Sci. India* A **28**: 293.

SYNGE, J. L. (1960).—"Relativity: the General Theory." (Interscience: New York.)

WEBER, J. (1961).—"General Relativity and Gravitational Waves." (Interscience: New York.)

WYMAN, M., (1946).—*Phys. Rev.* **70**: 74.

EQUILIBRIUM OF A PINCH DISCHARGE WITH A TRANSVERSE ROTATING MAGNETIC FIELD

By H. A. Blevin* and R. B. Miller*

[*Manuscript received March* 19, 1965]

Summary

The electron density distribution in a linear pinch discharge with a transverse rotating magnetic field is calculated for partially ionized plasmas. Numerical examples are given for distributions in the plasma with and without externally applied axial magnetic fields, and with different degrees of ionization.

I. Introduction

It has been shown (Blevin and Thonemann 1961, 1962) that a magnetic field rotating about the axis of a cylindrical plasma column can produce large azimuthal current densities in the plasma, provided that the angular frequency of the rotating field lies between the ion and electron cyclotron frequencies. Blevin and Thonemann also calculated the equilibrium electron density distribution when an axial magnetic field is applied so that the radial Lorentz force confines the plasma away from the tube walls. In the present paper we consider the manner in which the equilibrium electron density is modified when an axial current flows through the plasma.

II. Electron Density Distribution

For a plasma column of finite length the experiments described by Blevin and Thonemann indicated that end effects caused a distortion of the rotating magnetic field and modified the equilibrium plasma distribution. This complication could be avoided by using either toroidal discharges of large aspect ratio, or linear discharges for which the ratio of length to diameter is very large.

Consider a cylindrical plasma column, which is sufficiently long so that end effects can be neglected, to which an axial electric field E_z and magnetic fields B_a, B_0 are applied as shown in Figure 1. It is assumed that there is no axial variation of any quantity. Provided that the angular frequency ω of the rotating field lies between the ion and electron cyclotron frequencies and the electron collision frequency is less than the electron cyclotron frequency, then the electrons rotate in synchronism with the rotating field (Blevin and Thonemann 1961), and it follows that (using CGS electromagnetic units)

$$j_\theta = -ner\omega, \tag{1}$$

$$B_z(r) = B_a - 2Ne\omega, \tag{2}$$

$$\mathrm{d}N/\mathrm{d}(r^2) = -\pi n, \tag{3}$$

where n is the electron density, e is the electronic charge, j_θ is the azimuthal current

---

* Department of Physics, University of New England, Armidale, N.S.W.

Aust. J. Phys., 1965, **18**, 309–15

density, and N is the number of electrons per unit length of the discharge which are *outside* a cylinder of radius r, that is,

$$N = 2\pi \int_r^\infty nr\,\mathrm{d}r.$$

When the plasma is in equilibrium $\nabla p = \mathbf{j}\times\mathbf{B}$. Putting $p = nkT$, where $T = T_\mathrm{i}+T_\mathrm{e}$ is the sum of the ion and electron temperatures and is assumed to be constant throughout the plasma, this equilibrium condition becomes

$$kT\,\mathrm{d}n/\mathrm{d}r = j_\theta B_z - j_z B_\theta. \tag{4}$$

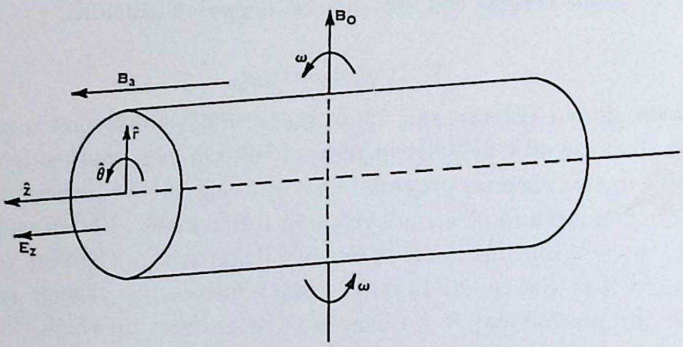

Fig. 1.—Configuration of fields applied to the cylindrical plasma.

Also, neglecting displacement currents, Maxwell's equations give $\nabla\times\mathbf{B} = 4\pi\mathbf{j}$ and, taking the z component of this equation,

$$\frac{1}{r}\frac{\mathrm{d}}{\mathrm{d}r}(rB_\theta) = 4\pi j_z. \tag{5}$$

Substituting (1), (2), (3), and (5) in (4)

$$\frac{\mathrm{d}^2N}{\mathrm{d}(r^2)^2} = -\frac{e\omega}{2kT}\frac{\mathrm{d}N}{\mathrm{d}(r^2)}(B_\mathrm{a}-2Ne\omega)+\frac{2\pi^2 j_z}{kTr^2}\int_0^r j_z r\,\mathrm{d}r. \tag{6}$$

To proceed further, j_z is required as a function of radial position. For a highly ionized plasma the resistivity is nearly independent of electron density (Spitzer 1956), and in the first instance we will assume that

(i) j_z is constant throughout the plasma, and

(ii) the radius of the plasma column is a.

Thus the total axial current $I_z = \pi a^2 j_z$. Putting $(r/a)^2 = x$, (6) becomes (for $x < 1$)

$$\frac{\mathrm{d}^2N}{\mathrm{d}x^2}+\frac{B_\mathrm{a}a^2e\omega}{2kT}\frac{\mathrm{d}N}{\mathrm{d}x}-\frac{(ae\omega)^2}{2kT}\frac{\mathrm{d}N^2}{\mathrm{d}x}-\frac{I_z^2}{kT} = 0,$$

which can be integrated using the boundary conditions $N = 0$ and $\mathrm{d}N/\mathrm{d}x = 0$ when $x = 1$, to give

$$\frac{\mathrm{d}N}{\mathrm{d}x}+\frac{B_{\mathrm{a}}a^2e\omega}{2kT}N-\frac{(ae\omega)^2}{2kT}N^2+\frac{I_z^2}{kT}(1-x) = 0, \tag{7}$$

which is an integrable form of Riccati's equation (McLachlan 1950).

Let

$$z = \exp\left\{-\frac{ae\omega}{2kT}\int(ae\omega N-\tfrac{1}{2}B_{\mathrm{a}}a)\,\mathrm{d}x\right\} \tag{8}$$

and

$$X = 1+(B_{\mathrm{a}}^2a^2/8I_z^2)-x.$$

Then (7) reduces to

$$\frac{\mathrm{d}^2z}{\mathrm{d}X^2}-\frac{1}{2}\left(\frac{I_z ae\omega}{kT}\right)^2Xz = 0$$

with the solution

$$z = A_0X^{\frac{1}{2}}\mathrm{I}_{\frac{1}{3}}(\phi)+A_1X^{\frac{1}{2}}\mathrm{I}_{-\frac{1}{3}}(\phi), \tag{9}$$

where

$$\phi = \frac{\sqrt{2}}{3}\left(\frac{I_z ae\omega}{kT}\right)X^{3/2};$$

A_0, A_1 are constants of integration; and $\mathrm{I}_{\frac{1}{3}}(\phi)$, $\mathrm{I}_{-\frac{1}{3}}(\phi)$ are the modified Bessel functions. From (8) and (9),

$$N = \frac{B_{\mathrm{a}}}{2e\omega}+\frac{kT}{X(ae\omega)^2}\left[1+3\phi\left\{\frac{A_0\mathrm{I}'_{\frac{1}{3}}(\phi)+A_1\mathrm{I}'_{-\frac{1}{3}}(\phi)}{A_0\mathrm{I}_{\frac{1}{3}}(\phi)+A_1\mathrm{I}_{-\frac{1}{3}}(\phi)}\right\}\right],$$

where the prime denotes differentiation with respect to ϕ. Using the boundary condition $N = 0$ when $x = 1$ and the recurrence relations for Bessel functions, it follows that

$$A_0/A_1 = -k_0,$$

where

$$k_0 = \{\mathrm{I}_{-\frac{1}{3}}(\phi_0)+\mathrm{I}_{\frac{2}{3}}(\phi_0)\}\{\mathrm{I}_{\frac{1}{3}}(\phi_0)+\mathrm{I}_{-\frac{2}{3}}(\phi_0)\}^{-1},$$

and

$$\phi_0 = \phi(x = 1) = B_{\mathrm{a}}^3a^4e\omega/48I_z^2kT.$$

Put

$$\chi = \{k_0\mathrm{I}_{-\frac{2}{3}}(\phi)-\mathrm{I}_{\frac{2}{3}}(\phi)\}\{k_0\mathrm{I}_{\frac{1}{3}}(\phi)-\mathrm{I}_{-\frac{1}{3}}(\phi)\}^{-1},$$

then

$$N = \frac{B_{\mathrm{a}}}{2e\omega}+\frac{3kT}{(ae\omega)^2}\phi\chi.$$

Using (2) and (3),

$$B_z = (-2^{3/2}/a)I_z X^{\frac{1}{2}}\chi, \tag{10}$$

$$n = (I_z^2/\pi a^2 kT)X(1-\chi^2), \tag{11}$$

and from (5),

$$B_\theta = (2I_z/a)x^{\frac{1}{2}}, \qquad \text{for } x < 1. \tag{12}$$

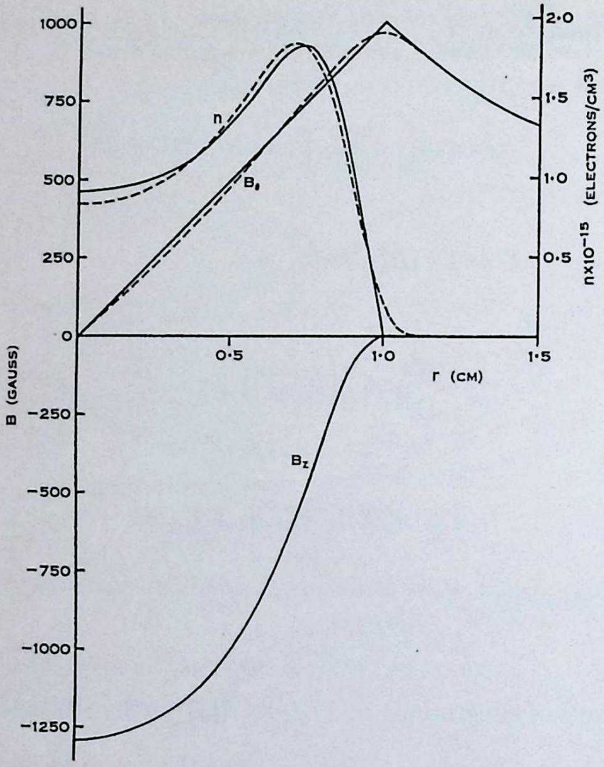

Fig. 2.—Electron density and magnetic field distributions for different values of ionization (—— 100%, --- 16%, at the axis) with $T = 10^5$ °K, $I_z = 5000$ A, $B_a = 0$, and $N_0 = 4 \cdot 05 \times 10^{15}$ electrons/cm.

Equations (10), (11), and (12) give the magnetic field distributions (apart from the rotating field, which does not enter into the pressure balance equation) and the electron density distribution in the plasma. The field distributions can be grouped into three categories.

(i) No externally applied axial field, $B_a = 0$.

(ii) Axial field reversed in the central region of the discharge. Equation (2) shows that this occurs when $B_a < 2N_0 e\omega$, where N_0 $(= N_{r=0})$ is the number of electrons per unit length of the plasma column.

(iii) Axial field in the same direction throughout the discharge. This occurs for $B_a > 2N_0 e\omega$.

Examples of each of these distributions are shown in Figures 2, 3, and 4 using some arbitrarily chosen values of the discharge parameters B_a, I_z, T, and N_0 (in fact

N_0 has been chosen to make $a = 1$ cm in each case). Perhaps the most unrealistic feature of these results is the assumed discontinuity in the electrical conductivity at $r = a$ and, as a consequence of this, the large pressure gradients at the plasma boundary. In practice the current density in the outer regions of the discharge where n has small values is determined either by electron run-away or, if there is an appreciable number of neutral molecules present, by electron collisions with gas molecules. In the latter case the electron density distribution can be determined from (6) by inserting the appropriate expression for the current density j_z as a function of radial position.

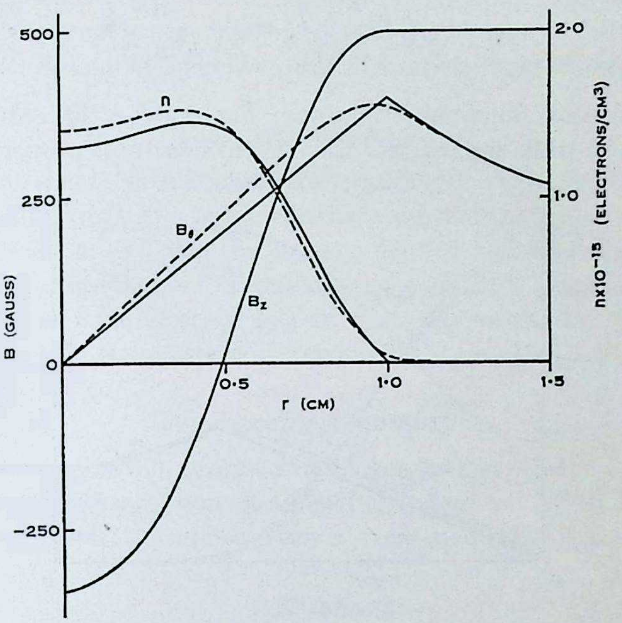

Fig. 3.—Electron density and magnetic field distributions for different values of ionization (—— 100%, – – – 49%, at the axis) with $T = 10^5$ °K, $I_z = 2000$ A, $B_a = 500$ G, and $N_0 = 2\cdot64\times10^{15}$ electrons/cm.

For a partially ionized gas the resistivity η is approximately given by (Allis 1956) $\eta = (m/ne^2)(\nu_i+\nu_n)$, where ν_i, ν_n are the appropriate momentum transfer collision frequencies for electron–ion and electron–neutral collisions respectively, and m is the electron mass. In a *hydrogen* plasma ν_n is approximately constant for electron energies above about 3 eV, and the collision frequencies are given by (Delcroix 1960)*

$$\nu_n \approx 2\times10^{-7}n_n,$$

$$\nu_i \approx 2\cdot6nT_e^{-3/2}\ln\Lambda,$$

where n_n is the neutral gas density and $\ln\Lambda$ is a slowly varying function of n and

---

* Although we will use these values in later numerical examples, it should be noted that this value of ν_n is a rather high approximation.

T_e (Spitzer 1956). Substituting these values in the expression for η, then

$$j_z = \frac{E_z}{\eta} = \frac{e^2 T_e^{3/2} E_z}{2 \cdot 6 m \ln \Lambda} \left\{ \frac{n}{\alpha n_n + n} \right\},$$

where $\alpha \approx 7 \cdot 7 \times 10^{-8} T_e^{3/2} / \ln \Lambda$.

If $\ln \Lambda$ is approximated by a constant with a value of 10 for the electron densities and temperatures considered in the examples of Figures 2, 3, and 4, then using (3)

$$j_z = -K E_z \frac{\mathrm{d}N}{\mathrm{d}(r^2)} \bigg/ \left(\alpha n_n - \frac{1}{\pi} \frac{\mathrm{d}N}{\mathrm{d}(r^2)} \right), \tag{13}$$

where K and α are now functions of T_e alone. For $\alpha n_n \ll n$ this reduces to the former case $j_z =$ constant, while for $\alpha n_n \gg n$ the current density is proportional to n.

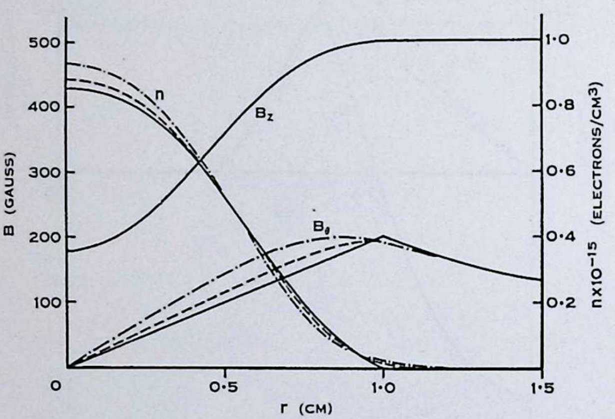

Fig. 4.—Electron density and magnetic field distributions for different values of ionization (—— 100%, - - - 70%, —•— 44%, at the axis) with $T = 10^5$ °K, $I_z = 1000$ A, $B_a = 500$ G, and $N_0 = 1 \cdot 00 \times 10^{15}$ electrons/cm.

Substituting (13) into (6) gives

$$\frac{\mathrm{d}^2 N}{\mathrm{d}(r^2)^2} + \frac{e\omega}{2kT} \frac{\mathrm{d}N}{\mathrm{d}(r^2)} (B_a - 2Ne\omega) - \frac{2\pi^2 (KE_z)^2 \mathrm{d}N/\mathrm{d}(r^2)}{kTr^2 \{\alpha n_n - (1/\pi)\mathrm{d}N/\mathrm{d}(r^2)\}} \int_0^r \frac{\{\mathrm{d}N/\mathrm{d}(r^2)\} \, . \, r \, . \, \mathrm{d}r}{\alpha n_n - (1/\pi)\mathrm{d}N/\mathrm{d}(r^2)} = 0,$$

which can be solved numerically for given discharge parameters.

Examples of the resulting magnetic field and electron density distributions are shown in Figures 2, 3, and 4 for several values of αn_n. The percentage ionization (at any particular position in the plasma) can only be determined from αn_n when T_e is known, and the values indicated on the diagrams were obtained by taking $T_e = T_i = \frac{1}{2} T$. Although the neutral gas density has been assumed to be independent of r in these calculations, it is no more difficult to include a dependence of n_n on radial position. For comparison with the results obtained for $j_z =$ constant, the values of

T, I_z, B_a, and N_0 were held constant in each case. This necessitates a change in the value of E_z for different amounts of neutral gas.

These results show that appreciable neutral particle densities are required to affect the magnetic field profiles to any great extent. For example, in the case considered in Figure 4 the ionization at the tube axis must be less than $\sim 70\%$ for the magnetic field components to change by more than 10% from the case where neutral gas is not present. In addition, the effect of neutral particles on the field profiles depends critically on the nature of the density distribution. This is shown in Figure 2, where the fields are only slightly changed for an ionization as low as 10%. In this case αn_n becomes comparable to n only in a small region near the plasma boundary. For higher temperature plasmas (high α) a lower percentage of neutral molecules is required to produce a comparable effect on the magnetic field distributions.

III. Conclusions

In a pinch discharge with a transverse rotating magnetic field, a measurement of the magnetic fields B_θ, B_z as a function of radius would enable the plasma temperature T to be determined, and also the electron density as a function of radius. For partially ionized plasmas the neutral gas density could also be estimated when the percentage ionization is sufficiently low so that the resistivity of the plasma is appreciably modified by the presence of neutral gas molecules.

IV. Acknowledgments

This work forms part of a program which has been supported by the Australian Institute of Nuclear Science and Engineering. One of us (R.B.M.) gratefully acknowledges the financial assistance received from an I.C.I.A.N.Z. scholarship.

V. References

Allis, W. P. (1956).—"Handbuch der Physik." Vol. 21, pp. 383–444. (Springer–Verlag: Berlin.)

Blevin, H. A., and Thonemann, P. C. (1961).—U.K.A.E.A. Research Report CLM–R12.

Blevin, H. A., and Thonemann, P. C. (1962).—*Nucl. Fusion*, 1962 Suppl., Part I, p. 55.

Delcroix, J. L. (1960).—"Introduction to the Theory of Ionized Gases." (Interscience: New York.)

McLachlan, N. W. (1950).—"Ordinary Non-Linear Differential Equations." (Oxford Univ. Press.)

Spitzer, L. (1956).—"Physics of Fully Ionised Gases." (Interscience: New York.)

BACKSCATTER OF 16 Mc/s RADIO WAVES FROM LAND AND SEA

By J. G. Steele*

[*Manuscript received April* 5, 1965]

Summary

Relative backscatter coefficients for 16 Mc/s backscatter from land and sea at elevation angles between 5 and 30° were obtained using a large ground-based sounder at Brisbane. For both land and sea, as the angle of elevation decreases, the backscatter coefficient at first increases smoothly and then decreases suddenly at a certain angle which has been called the knee angle. This angle is about 13° for land, and smaller for sea. For a given angle of elevation above 13°, backscatter from sea is about 10 dB stronger than from land.

The nature of the scattering irregularities is discussed in the light of the experimental evidence, and it is concluded that the main scattering agents are trees and wave crests. An explanation of the knee effect is advanced.

I. Introduction and Previous Work

Ground backscatter is the process by which radio waves are scattered at the ground so that some of the energy goes back along its original path to the transmitter. This process is used in oblique-incidence sounding of the ionosphere. A pulse of radio energy may undergo backscatter at the ground after one or more reflections from the ionosphere, and the time the echo takes to return is a measure of the range at which backscatter occurs. The various uses of backscatter sounding are outlined by Peterson (1957).

The strength of backscatter echoes depends on the backscatter coefficient at the echoing area of the ground. This coefficient may be expected to vary according to elevation angle and type of ground, and the interpretation of the results of backscatter soundings requires a knowledge of this behaviour.

The backscatter coefficient has been variously defined by different writers, and the definition used here is that given by Cosgriff, Peake, and Taylor (1960),

$$\gamma = \sigma_0/\sin\Delta,$$

where γ is the backscatter coefficient, σ_0 is the radar cross section per unit area of the surface, and Δ is the angle of elevation of the rays with respect to the mean level of the terrain.

The radar cross section occurs as a factor in the radar equation (Clapp 1946; Shearman 1956; Cosgriff, Peake, and Taylor 1960; Nielson *et al.* 1960),

$$P_{\mathrm{R}} = \sigma G^2 P_0 \lambda^2/(4\pi)^3 R^4,$$

where P_0 = power transmitted,
P_{R} = power received,
R = range of target,
G = antenna gain, and
σ = radar cross section.

---

* Physics Department, University of Queensland, Brisbane; present address: Radioscience Laboratory, Stanford Electronics Laboratories, Stanford, California, U.S.A.

Aust. J. Phys., 1965, **18**, 317–27

The radar cross section per unit area of the surface, σ_0, is a parameter commonly used in radar. The backscatter coefficient γ is related to σ_0, and is the radar cross section per unit area normal to the direction of propagation at the scattering area (hence the sin Δ in the definition). The choice of this definition makes the present work easily comparable with the results of Hagn (1962) and Cosgriff, Peake, and Taylor (1960).

Cosgriff, Peake, and Taylor used centimetric radar (about 30 000 Mc/s) to measure backscatter coefficients. At 16 Mc/s, the measurement is rendered more difficult by the great distances involved and the large size of the antennas required. The most direct method is to mount the antennas on an aircraft; this has been done at 32·8 Mc/s by Nielson *et al.* (1960), and the results were given by Hagn (1962). Sea echoes were found to be about 20 dB stronger than land echoes for the same angle of elevation. The disadvantages of this method include uncertainties due to the motion of the aircraft, difficulty in calibrating the antennas, and radio noise from the aircraft ignition system.

The present method is less direct, as it involves oblique ionospheric reflections between the sounder and the point of ground scatter. The main disadvantage is that the precise nature of the ionospheric reflections cannot be determined. The advantages are that a large antenna system can be used, with high azimuthal directivity and a well-known vertical radiation pattern; that large echoing areas at great ranges can be investigated; and that the fading of the backscatter echoes can be attributed to effects in the ionosphere and at the target area, and not to the motion of the sounder.

Previous observations using ground-based sounders have been qualitative, and gave conflicting results. Villard and Peterson (1952*a*, 1952*b*) working at 3–30 Mc/s, and Shearman (1956) at 10–27 Mc/s, found no noticeable difference in echo amplitude between land and sea echoes, while Ranzi and Dominici (1959) at 22·3 Mc/s estimated that sea echoes were perhaps 10 dB stronger than land echoes of comparable range.

II. EXPERIMENTAL TECHNIQUE

In the present investigation, the 16 Mc/s backscatter sounder at Brisbane was used. It has been described by Thomas and McNicol (1960). It employs an array of four horizontally polarized Yagi antennas mounted half a wavelength above the ground, the whole array being rotatable in azimuth. The antennas were directed to the east and to the west, to obtain echoes from the sea and the land in turn. Rectangular pulses of 600 μs duration were transmitted, with a pulse repetition frequency of 25 pulses per second and a peak power of 5 kW. Backscatter echoes to a range of 4500 km were displayed on an oscilloscope screen by brightness modulation of the time-base trace, and were recorded on film moving continuously past the trace at $\frac{1}{2}$ in/min. An example is shown in Plate 1, Figure 1. The strong horizontal lines are at intervals of 1000 km. The range–time display thus generated was modified by the use of a swept-gain unit, by means of which the receiver gain was varied through 40 dB in a series of 12 stages. This cycle was repeated every minute, as shown in Plate 1, Figure 2.

Neglecting any variation in range during one gain sweep, we can regard each frame of the swept-gain records as a range–amplitude display, similar in format to a type A presentation of the echo pulse, with a logarithmic amplitude scale. Successive pulses are returned with different shapes as a result of fading, which makes ordinary type A presentation difficult to interpret. The present method provides a useful type of averaging of the echo shape, and some estimate of the fading rate can also be obtained.

Plate 1, Figure 2, is a record of backscatter from the sea to the east of Brisbane. The regular fading (about 0·8 c/s) is fairly typical of sea scatter. It is constant in phase across the range spread of the echo, and appears in both the $1F$ echo (leading edge at 1300 km), backscattered after one hop via the F region of the ionosphere, and the $1E_s$ echo (leading edge at 700 km), backscattered after propagation via the sporadic E layer.

Backscatter echoes from the land fade less regularly, as illustrated in Plate 1, Figure 1, where the $1F$ echo was backscattered at a range of 1300 km to the west of Brisbane.

Backscatter records for comparison with calculations were carefully selected to minimize the uncertainties due to the unknown ionospheric path of the echoes. The following criteria were adopted:

(1) E_s-propagated echoes should not be present.

(2) Both backscatter and vertical-incidence data should be simultaneously available and clearly recorded.

(3) Travelling ionospheric disturbances should not be present. These could usually be detected on the records, if they were present.

(4) Radio interference should be at a minimum.

(5) D-region absorption should be negligible.

(6) The F region should approximate to a simple parabolic layer.

Conditions (5) and (6) were best fulfilled in the late afternoon.

After suitable records had been selected, $1F$ echoes only were used for analysis, and the peak echo power only was considered, as this could be calculated with greater certainty than other parts of the echo pulse.

III. Calculation of Echo Power

For comparison with the range–amplitude records, the relative peak power of a given backscatter echo was calculated using a method outlined by Shearman (1956). The backscatter coefficient was assumed to be independent of angle of elevation and type of terrain. This assumption is not true, but when the results of calculations based on this assumption were compared with the corresponding observed backscatter records, the relative backscatter coefficient, at the calculated angle of elevation and for the given terrain, could be deduced.

The calculation involves the vertical radiation pattern of the antenna array, which had been measured by means of a balloon-borne transmitter (Steele 1965).

The calculation also requires a knowledge of the base height, semi-thickness, and critical frequency of the ionospheric layer, which is assumed parabolic. The base height and critical frequency were obtained from vertical-incidence data taken at Brisbane, and extrapolated east and west along the paths of the backscatter echoes. This extrapolation was achieved by assuming that the ionospheric parameters remain fairly constant at a given subsolar point as the Earth rotates. In particular, it was assumed that the parameters at the control point of the skip ray, say 1000 km east of Brisbane, were the same as those measured by vertical-incidence sounding at Brisbane at some time up to an hour later. The actual time lag applicable was determined by superimposing a set of theoretical curves, of minimum calculated echo range versus corresponding ground range to the control point, upon a curve giving minimum observed echo range versus Eastern Australian Standard Time at Brisbane. The point of intersection of the appropriate curves identified the particular backscatter record to be paired with a given vertical-sounding record.

For east–west propagation, magneto-ionic splitting of the echoes was not resolvable on the records, as the ordinary and extraordinary rays formed echoes at about the same range, with a sharp leading edge. The range of this leading edge enabled the semi-thickness of the layer to be deduced from the base height and critical frequency, using charts based on the equations of Appleton and Beynon (1940).

Owing to skip-distance focusing, most of the power of a backscatter echo is associated with rays very close to the skip ray. The angle of elevation of this ray at the ground, Δ_s, was obtained in the course of the calculations. The difference (in dB) between the calculated and observed peak echo powers was taken as a measure of the relative backscatter coefficient γ at the angle calculated and for the given terrain.

IV. RESULTS

As the critical frequency decreased in the late afternoon, Δ_s decreased, and γ was plotted against Δ_s. As most of the power is associated with rays at angles near Δ_s, γ was effectively plotted against Δ. Figure 1 shows two such graphs, the upper curve being for backscatter from the sea to the east of Brisbane, and the lower curve for backscatter from the land to the west. A total of 12 curves for sea and 9 for land were obtained, although not all showed such definite trends as in Figure 1.

The horizontal scale for Δ is reversed in Figure 1 because it has been conventional in the literature to plot the angle of incidence from left to right, and the angle of elevation Δ from right to left. This has the advantage that measurements at normal incidence, which may be useful for calibration purposes, can be plotted on the left. Hagn (1962) also follows this convention.

There are three main results, namely: (1) at angles of elevation near 20°, sea scatter is stronger than land scatter by about 10 dB; (2) as the angle of elevation decreases, the backscatter coefficient decreases rapidly at some angle near grazing incidence, known as the knee angle; and (3) at angles of elevation above this knee angle, the curves for both sea and land follow a law approximating to $\gamma \propto 1/\sin^2\Delta$. These three points will now be discussed in more detail.

7791

(1) The curves above 15° are approximately parallel, but there is a 10 dB difference between land and sea. This difference is much greater than any likely errors in the antenna patterns or in the choice of the ionospheric parameters, and is therefore largely due to a difference in γ. The asymmetry of east and west propagation at sunset could have conceivably affected the result, so a sample calculation was done using morning data, when the asymmetry was reversed; sea scatter was still stronger than land scatter by about 10 dB. Morning calculations were not as reliable as those of the evening, owing to the presence of the morning F_1 layer, which rendered the Appleton and Beynon (1940) formulae not strictly applicable. Nevertheless, the morning results were sufficiently accurate to show that the difference in γ for land and sea is independent of ionospheric asymmetry.

R
530.5
M48A
V.18
7791

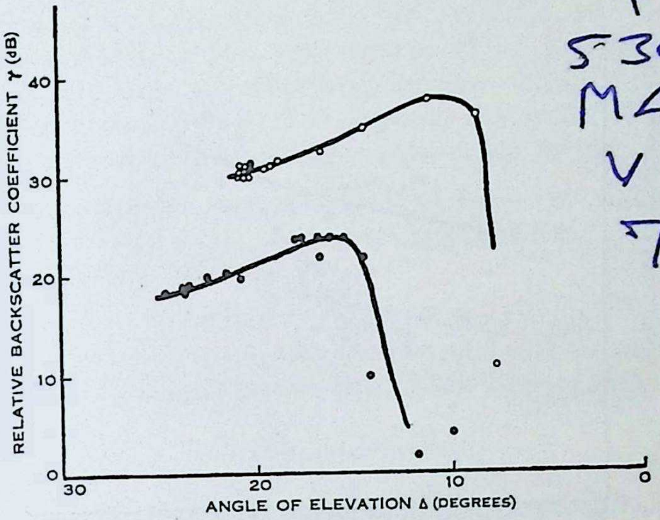

Fig. 1.—Relative backscatter coefficient as observed on two days. ○ March 23, 1963, sea; ● April 14, 1963, land.

(2) For most of the curves obtained, as Δ decreases γ decreases suddenly at some angle. This effect, also described by Hagn (1962), is called the knee effect. For land, the angle at which the knee occurs is usually between 14 and 12°. In view of the closeness of these limits, the variation is likely to be due to experimental errors, and 13° may be taken as the knee angle for the given terrain.

Two possible doubts arise concerning the reality of the knee. First, the knee may be due to failure of the propagation path. As the critical frequency falls, Δ_s approaches zero, and the echo vanishes as virtually all rays penetrate the ionosphere. This failure may appear to be a knee if the calculations erroneously give values of Δ_s that are too large. But investigations show that Δ_s would not be in error by as much as 13°. In the present work, as Δ_s decreases, the most rapidly varying ionospheric parameter is the critical frequency. Above 10°, assuming other ionospheric parameters to be constant, an error of $\pm 0 \cdot 2$ Mc/s (as is likely) would give rise to an error of only $\pm 1°$ in the calculated value of Δ_s. Below 10°, the rate of change of Δ_s with critical frequency increases, and when Δ_s is 5°, an error of $\pm 0 \cdot 2$ Mc/s may introduce an error of $\pm 5°$ in Δ_s.

Secondly, the terrain may not be uniform to long ranges. Perhaps at some range there is an abrupt change in the terrain, so that γ becomes very small at long ranges (corresponding to low angles of elevation); but reference to maps shows that there is no range at which the terrain in the illuminated region changes abruptly.

For sea, the knee angle is less constant than for land, and in half of the cases plotted the knee (if it existed) was at an angle below those for which data were available. When the knee was observed, it occurred at angles ranging from 14 to 9°. The presence of a knee at 14° shows that in some cases, at least, the knee is a real effect, although at angles below 10° it could possibly be due to errors in calculating Δ_s as mentioned above. Probably the knee is always present, and the knee angle varies according to the state of the sea.

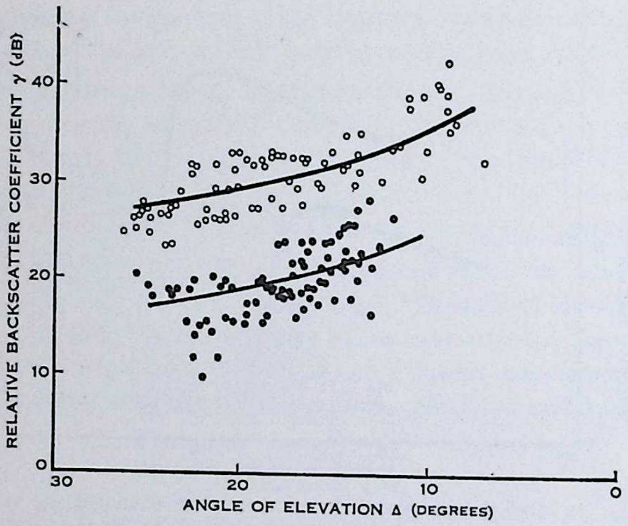

Fig. 2.—Variation of relative backscatter coefficient with elevation angles above the knee. The curves superimposed represent the function $\gamma \propto 1/\sin^2\Delta$. ○ sea; ● land.

(3) The points plotted for various days are collected in Figure 2; points which fell below the knee are omitted. The curves superimposed on the points represent the relation $\gamma \propto 1/\sin^2\Delta$. For both sea and land echoes, this fitted better than $1/\sin\Delta$ or $1/\sin^3\Delta$, although on individual days one of the latter relations sometimes fitted better. In Figure 2, the scatter of points about their respective means is not as large as may appear, as the γ scale is merely relative. Owing to day-to-day changes in transmitter output, sea roughness, receiver gain, and oscilloscope brightness, the points for various days probably have slight zero errors differing from one day to the next, and therefore can legitimately be moved up or down the γ axis for better agreement. When this was done, it was found that if indeed $\gamma \propto 1/\sin^2\Delta$, the scatter of points falls within 3 dB of the curves of Figure 2. This is about the accuracy to be expected if the probable errors are 2 dB in reading the echo power and 1 dB in calculating it.

V. The Nature of the Scattering Irregularities

At any range and time, the intensity of a backscatter echo depends on the density of scattering irregularities on the ground, and also on the extent to which the individual echoes from these irregularities reinforce one another on arrival at the receiver.

In the work described here, the instantaneous echoing area was a portion of a circular annulus about 100 km wide, and about 15° in azimuthal extent, corresponding to a length of about 250 km at a range of 1000 km. This represents quite a large sample of the terrain, much larger than that sampled by Nielson *et al.* (1960). In their work, any large irregularities such as mountains had a marked effect on the echo strengths, and for the sake of clarity only comparatively smooth surfaces were selected when deriving the backscatter coefficient. In the present work, that restriction is not necessary and, in fact, not possible. The echoes received contained components from both large and small irregularities. This may explain why the backscatter coefficient for land here, and in Ranzi and Dominici (1959), was only 10 dB below that for sea, whereas in Hagn (1962) it was 20 dB below.

The individual scatterers may be assumed to be upright objects such as trees and wave crests (Goldstein 1951; Katz and Spetner 1958). This assumption is supported by the following observations:

(1) The observed relationship $\gamma \propto 1/\sin^2\Delta$ shown in Figure 2 is consistent with a theory of backscatter from vertical cylinders proposed by Katz and Spetner (1958). The theory, as quoted by Cosgriff, Peake, and Taylor (1960), is of the form

$$\gamma \propto 1/\sin \Delta\,(A+\sin^2\Delta),$$

which, depending on the value of A, will be between $1/\sin \Delta$ and $1/\sin^3\Delta$. Shearman (1956) predicted the equivalent of $1/\sin \Delta$ for a model consisting of hemispherical bosses on a flat conducting plane. The observed relationship therefore suggests that the scatterers are more rugged than hemispheres. Trees, which approximate to vertical cylinders, and wave crests, which are roughly conical, would seem to fulfil this requirement.

(2) The results in Figure 2, in which γ increased as Δ decreases, are similar to Hagn's (1962) results for vertical polarization, but quite different from his results for horizontal polarization, which show the opposite trend. In the present work, the polarization of the outgoing waves is initially horizontal, but becomes elliptical at the echoing area after propagation through the ionosphere. It seems probable that the backscatter echoes are due largely to the vertical component of the waves at the scattering area. This would be true if the scattering irregularities were vertically polarized.

(3) The fading of backscatter echoes may be attributed largely to the movement of the scattering irregularities. For land, the random fading can be explained in terms of the wind in the trees, as mentioned by Clapp (1946); the phase relationships between the various components of the backscatter echo are continually changing in a random fashion.

For the sea, the regular fading observed is due to the fact, observed by Crombie (1955), that backscatter echoes are most effectively returned by sea waves moving radially with respect to the sounder and of length about half the radio wavelength. Such waves will always exist as components of the complex structure of the sea. A train of such waves behaves as an array, returning echo components in phase with one another.

Sea waves of a given length have characteristic velocities, causing characteristic Doppler shifting of the radio frequency of the echoes, and the fading rate represents the beat between the resulting frequencies. Dowden (1957) observed the regular fading of backscatter echoes from the sea, but his explanation, based on the beat between Doppler-shifted echoes from opposite directions, will not suffice here as the sea is viewed in only one direction. The explanation is probably that, in a Fourier analysis of the sea surface, there will be two components with a wavelength $L = \frac{1}{2}\lambda$. These will have velocities $\pm v$, where

$$v = (gL/2\pi)^{\frac{1}{2}},$$

and g is the acceleration due to gravity. Doppler shifts will be

$$\begin{aligned}\Delta f &= 2v/\lambda \\ &= \pm 0\cdot 41 \text{ c/s}\end{aligned}$$

for radio waves of 16 Mc/s. The fading rate would therefore be 0·82 c/s, which agrees with the observed rate.

Such an explanation is in accord with the observations of Ingalls and Stone (1957), who measured the Doppler power spectrum of sea echoes at 18 and 24 Mc/s and found spectrum peaks at the carrier frequency and two narrow sidebands shifted by the appropriate value of Δf. In the present work the carrier frequency component appears to be small, as the fading rate is $2\Delta f$ and not Δf.

VI. AN INTERPRETATION OF THE KNEE EFFECT

It may be possible to explain the knee in the curve for the backscatter coefficient, assuming that the scattering irregularities are upright objects such as trees and wave crests, and that the polarization is effectively vertical at the echoing area.

Explanations have been offered by Hagn (1962) and at u.h.f., by Katzin (1957) and Spizzichino (Beckmann and Spizzichino 1963).

(1) Hagn's first suggestion was that the knee is caused by the absorption of the signal by the ground. He suggested that for vertical polarization, which he found to be more important than horizontal near grazing incidence, absorption could be a Brewster-angle effect. For land, the Brewster angle is about 17° for dry land or rocky soil, and for sea the pseudo Brewster angle for 16 Mc/s is about 0·5° (Burrows and Attwood 1949). At the Brewster angle, all the energy is absorbed and the reflection coefficient is zero (or nearly zero in the case of the pseudo Brewster angle). In the present work, however, these angles respectively are too high and too low to explain the knee. The Brewster angle is defined for smooth surfaces, but here we

have a situation where the irregularities cannot be neglected and, in fact, appear to be essential to the backscattering mechanism.

(2) Hagn's second suggestion was that there is some critical angle below which the energy is practically all reflected in the forward direction and so is not observed in the back direction.

(3) Katzin's suggestion, slightly modified by Spizzichino, is that, if H is the height of the scattering irregularities above the mean horizontal plane, the knee angle Δ_k could be defined as $\Delta_k = \lambda/4H$. For Δ less than Δ_k there would always be destructive interference between the direct field and that reflected by the surface surrounding the scatterer.

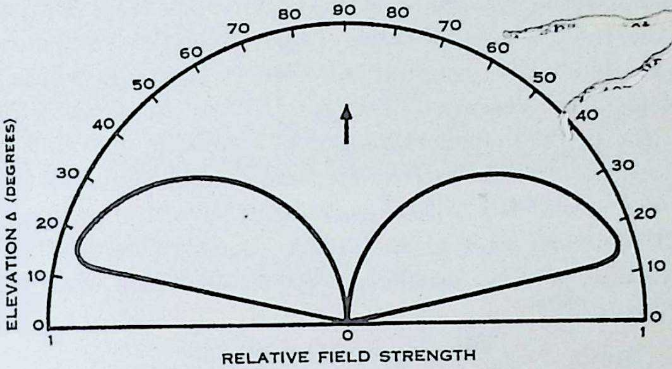

Fig. 3.—Vertical-plane radiation pattern of a short vertical cylinder standing on a smooth horizontal surface for which the Brewster angle is 17°. The arrow indicates the polarization of the cylinder.

In the present work, destructive interference is a possibility, as vertically polarized waves can exhibit phase reversal on reflection at low angles. But the formula given for Δ_k does not satisfactorily predict the knee angle. To make Δ_k equal to 13°, H would have to be about 17 m, which is too large for the trees in the area considered. To make Δ_k less than 10°, as for backscatter from the sea, H would have to be impossibly large. In contrast, Katzin (1957) concluded from his observations that H had to be much less than the measured wave height to account for Δ_k.

The suggestion made here is a combination of (1), (2), and (3). For the land, the scatterers may be regarded as vertical cylinders standing on a smooth horizontal plane. Consider the cylinders first as receiving antennas. The energy reaching a scatterer is a combination of direct and ground-reflected rays. For vertical polarization, the ground-reflected component is small above the Brewster angle and falls to zero at the Brewster angle, so the energy received is largely due to the vertical component of the direct rays. The reception pattern in the vertical plane will be similar to that of an elementary dipole in free space, provided that H is small compared with λ. Below the Brewster angle there is a phase reversal on reflection and the amplitude of the reflected wave increases. The resultant electric field close to the surface is then small. This may account for the sharpness of the knee and the fact that the knee angle occurs some degrees below the Brewster angle. Allowing for the

Brewster angle effect, the reception pattern of a vertical cylinder will be like that shown in Figure 3.

Now consider the cylinders as transmitting antennas. The radiation pattern for transmission will be the same as that for reception. As backscatter echoes require both reception and transmission by the scatterers, they are doubly affected by the radiation pattern of the scatterers.

On this view, the knee angle would not greatly depend on the height of the trees. All that is required is that H should be appreciably less than $\lambda/4\Delta_k$, that is, less than 17 m when $\Delta_k = 13°$, and this is true of the vegetation in central Australia.

For backscatter from the sea, the pseudo Brewster angle is too small to account for the knee if a smooth horizontal reflecting plane is assumed. But, as noted above, in backscatter the radio waves effectively "see" only those sea waves with crests $\frac{1}{2}\lambda$ apart. It seems likely that between these crests, the radio waves "see" only the broad trough of a "pure" sea wave of length $\frac{1}{2}\lambda$. We should therefore consider the scatterers to be sharp wave crests rising out of a smooth, curved reflecting surface. It is possible that rays of elevation, say 10°, undergo reflections in the wave troughs and reach the wave crests after reflection at angles below the pseudo Brewster angle, causing destructive interference at the crests. In this case the knee angle would depend on the theoretical wave profile between crests, which would be a function of H and λ.

VII. ACKNOWLEDGMENTS

Thanks are due to Professor H. C. Webster, Dr. J. D. Whitehead, and Dr. J. A. Thomas. The author is a recipient of a Commonwealth Postgraduate Award. The work was financially assisted by the Australian Radio Research Board and made use of equipment purchased with funds supplied under Research Contract AF 64(500)–9 by the United States Air Force.

VIII. REFERENCES

APPLETON, E. V., and BEYNON, W. J. G. (1940).—*Proc. Phys. Soc.* **52**: 518–33.

BECKMANN, P., and SPIZZICHINO, A. (1963).—"The Scattering of Electromagnetic Waves from Rough Surfaces." p. 417. (Pergamon Press: Oxford.)

BURROWS, C. R., and ATTWOOD, S. S. (1949).—"Radio Wave Propagation." p. 118. (Academic Press: New York.)

CLAPP, R. E. (1946).—A theoretical and experimental study of radar ground return. M.I.T. Radiation Laboratory Rep. No. 1024.

COSGRIFF, R. L., PEAKE, W. H., and TAYLOR, R. C. (1960).—Terrain scattering properties for sensor system design (Terrain Handbook II). Engineering Experiment Station Bull. No. 181, Ohio State University.

CROMBIE, D. D. (1955).—*Nature* **175**: 681–2.

DOWDEN, R. L. (1957).—*J. Atmos. Terr. Phys.* **11**: 111–7.

GOLDSTEIN, H. (1951).—*In* "Propagation of Short Radio Waves." (Ed. D. E. Kerr.) pp. 481–527. (McGraw-Hill: New York.)

HAGN, G. (1962).—An investigation of the direct backscatter of high-frequency radio waves from land, sea water, and ice surfaces. Stanford Research Institute Project 2909, Final Report II.

INGALLS, R. P., and STONE, M. L. (1957).—*Trans. Inst. Radio Engrs* **AP-5**: 164. (Abstract.)

KATZ, I., and SPETNER, L. M. (1958).—A program to investigate radar terrain return. Appl. Phys. Lab. Report CF-2700, Johns Hopkins University.

BACKSCATTER FROM LAND AND SEA

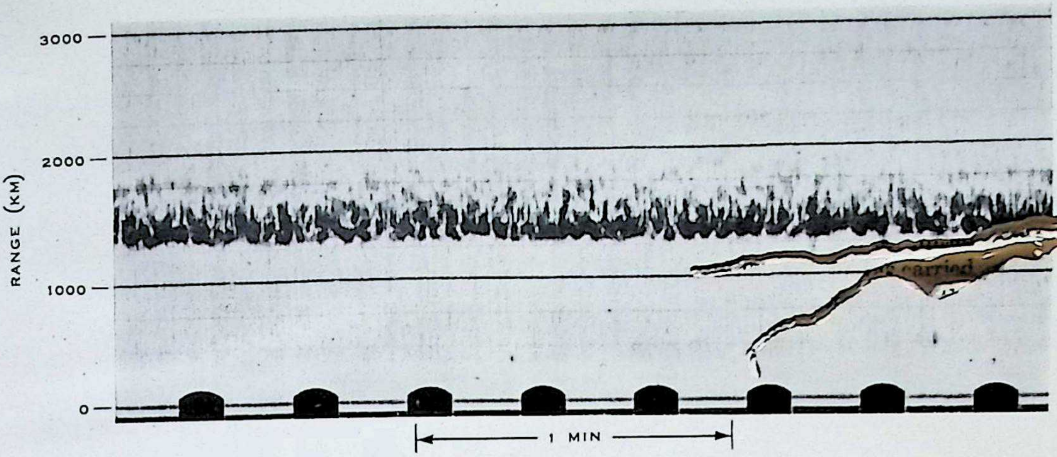

Fig. 1.—Backscatter echoes from land, April 9, 1963, at 1800 hr, with antennas directed westwards. The leading edge is at 1300 km, and propagation is by one hop in the F region ($1F$).

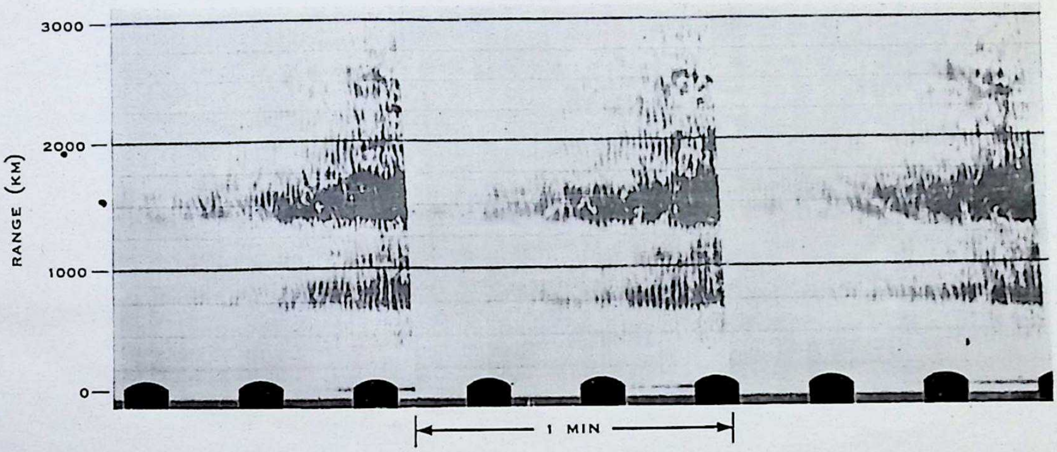

Fig. 2.—Backscatter echoes from sea, April 5, 1963, at 1620 hr, with antennas directed eastwards. The duration of each gain sweep is 1 min, and the fading rate is about 48 cycles/min. The echoes with leading edge at 700 km are $1E_s$, and those at 1300 km are $1F$.

Aust. J. Phys., 1965, **18**, 317–27

THE PARKES CATALOGUE OF RADIO SOURCES DECLINATION ZONE −60° TO −90°

By R. M. Price* and D. K. Milne†

[*Manuscript received April 28, 1965*]

Summary

A catalogue of 247 radio sources between declinations −60° and −90° is presented. In the zone −60° to −75°, the sources were selected from an initial finding survey at 408 Mc/s, while from −75° to −90° a 1410 Mc/s survey was carried out. The survey covers an area of 0·8 steradians, omitting the region near the galactic plane. Flux densities determined from source measurements at 408, 1410, and 2650 Mc/s are presented together with suggested optical identifications, radio spectra, and preliminary polarization information.

I. Introduction

This paper reports the results of a survey of radio sources in the declination zone −60° to −90° carried out at the Australian National Radio Astronomy Observatory at Parkes, New South Wales, as part of the source survey program. The results of the survey for the declination zone −20° to −60° have been reported by Bolton, Gardner, and Mackey (1964), hereafter referred to as BGM.

The zone reported in the present catalogue was divided into two zones for the purpose of the observations, namely declinations −60° to −75° and declinations −75° to −90°. The region of the Magellanic Clouds was surveyed by D. S. Mathewson of this laboratory and we are indebted to him for information on sources in this region. For further information concerning Magellanic Cloud sources the reader is referred to Mathewson and Healey (1964*a*, 1964*b*). Portions of the regions near the galactic plane were not covered in this survey since it was designed primarily for the detection of extragalactic sources.

The initial survey and the subsequent measurements at 408, 1410, and 2650 Mc/s are described. Measurements in the investigation consist of fluxes and positions for all sources, and where possible such parameters as polarization and spectra. Optical identifications are suggested for several of the sources. South of declination −75°, it is thought that the present catalogue is substantially complete for sources greater than 0·5 flux units at 1410 Mc/s (1 flux unit (f.u.) = 10^{-26} W m^{-2} (c/s)$^{-1}$). From −75° to −60° declination, the catalogue is complete for sources greater than 1 f.u. at 1410 Mc/s.

Since the limit of flux density investigated in this survey was lower than that of BGM, the log N–log S curve for the lower flux density sources is compared with the results of BGM.

---

* Mount Stromlo Observatory, Australian National University, Canberra, and Division of Radiophysics, CSIRO, University Grounds, Chippendale, N.S.W.

† Division of Radiophysics, CSIRO, University Grounds, Chippendale, N.S.W.

Aust. J. Phys., 1965, 18, 329–47

II. The Finding Survey

(a) *Declinations —60° to —75°*

In this zone the survey techniques were the same as reported by BGM except that declination scans were made at intervals of 4^{m} of right ascension. Therefore the scans were 30′ of arc apart at —60° declination and 15′·5 apart at —75° declination.

The finding survey in this zone was carried out at 408 Mc/s (~ 75 cm wavelength), where the beam of the 210-ft telescope is 48′ of arc. The receiver used is a switched radiometer using a conventional crystal mixer with no r.f. amplification (Mackey 1964). The survey was not extended into regions near the plane of the Galaxy where the level of the background was high and confusion due to galactic structure likely. The criteria for selection of sources were the same as those adopted by BGM, i.e. sources with flux densities greater than 4 f.u. at 408 Mc/s which did not noticeably broaden the 48′ beam of the telescope were selected for further study.

(b) *Declinations —75° to —90°*

In this circumpolar zone, the finding survey was carried out using both the 408 and 1410 Mc/s receivers, a dual-feed system allowing simultaneous operation at the two frequencies. At 1410 Mc/s (~ 21 cm wavelength) the beamwidth of the telescope is 14′ of arc. The parametric-type receiver used (Gardner and Milne 1963) has a system temperature of approximately 100°K. With a 10 Mc/s bandwidth and the output time constant of 1 s used in the finding survey, the peak-to-peak noise observed was 0·2 degK of aerial temperature.

The observations were made by scanning the region in declination at fixed values of right ascension. Because of the rapid convergence of lines of constant right ascension on the celestial sphere in this region of the sky, scans were made from —75° to —83° declination at intervals of 3^{m} of right ascension, and from —82° to —87° declination at intervals of 6^{m} of right ascension. The region —87° to the pole was surveyed in altazimuth coordinates, scanning in azimuth at 10′ intervals of zenith angle.

Scans were made at drive rates of approximately 2°/min, allowing about 7 s for passage of the 14′ beam over a point. At the frequency of 1410 Mc/s the survey was sensitivity limited, nevertheless a source of 0·15°K (approximately 0·2 f.u.) was detected if the beam passed directly over it. This detection limit rises to approximately 0·25°K for a source lying between two scans at their maximum separation of 11′·6 at declination —75°.

It is thought that nearly all point sources greater than 0·5 f.u. at 1410 Mc/s in the region have been detected. All the sources discovered in this region by the finding survey were later investigated again at 1410 Mc/s for more accurate flux and position determinations.

III. Measurements

(a) *1410 Mc/s*

All sources selected from the finding survey were observed at 1410 Mc/s for position, size, and flux measurements. The observational procedure used follows BGM.

Some sources selected from the 408 Mc/s finding survey were rejected when 1410 Mc/s observations showed them to be due to background variations. Of the probable sources located in the 1410 Mc/s finding survey, some 35% were found to be too weak for accurate measurements to be made and have been omitted from the catalogue.

(*b*) *2650 Mc/s*

All sources greater than 1·5 f.u. at 1410 Mc/s were observed at 2650 Mc/s (~ 11 cm wavelength). The receiver used is a degenerate parametric switched radiometer (Cooper, Cousins, and Gruner 1964) with an overall system temperature of approximately 150°K and an i.f. bandwidth of 40 Mc/s. Peak-to-peak noise fluctuations are about 0·15 degK with a 2 s output time constant. The selection requirements set for sources from the 1410 Mc/s observations meant that most of the sources measured at 2650 Mc/s had aerial temperatures greater than 0·4°K.

Table 1

ESTIMATES OF AVERAGE ERROR

Frequency (Mc/s)	R.M.S. Error	
408 (75 cm)	±1·2 f.u.	±5%
1410 (21 cm)	±0·2 f.u.	±6%
2650 (11 cm)	±0·15 f.u.	±7%

IV. Determination of Flux Densities

The procedure of BGM was followed in establishing the scales of flux density from observations of sources whose flux values had been given by Conway, Kellermann, and Long (1963). Standard sources were observed on most nights for a determination of flux-density scale factors, which varied slightly with different aerial feeds and different cables used between the feed and the receiver input. Where necessary, corrections were made to flux-density values on the basis of these daily observations.

In determining the accuracy with which the flux measurements can be made there are two types of possible error which have to be considered. The first type is an error proportional to the flux density of the source. This can be due to an error in the flux scale factors adopted, unnoticed non-linearities in the system, partial resolution of the sources, or polarization of the source radiation. For extended or resolved sources, given flux densities determined from peak values of aerial temperature observed represent a lower limit of flux density. Sources of up to 3′ of arc diameter whose broadening effect on the beam was not measurable may have had their fluxes underestimated correspondingly by up to 16%. On the average, the errors due to unknown polarization of the sources are not expected to amount to more than 2% (this applies only to 1410 and 2650 Mc/s measurements, not to 408 Mc/s where the effect is negligible).

The second type of error is fixed in flux value, being due to noise fluctuations on the records and, in some cases (particularly at 408 Mc/s), to background confusion. Peak errors due to noise amount to 0·1 f.u. at 1410 and 2650 Mc/s, and 0·5 f.u. at

TABLE 2

PARKES CATALOGUE OF RADIO SOURCES −60° TO −90°

Catalogue Number	Position (1950·0)		Annual Precession		Flux Density (10^{-26} W m^{-2} (c/s)$^{-1}$)				Spectrum			Remarks	Galactic Coordinates		MSH Cat. No.
	R.A. h m s	Dec. ° ′	Δα s	Δδ ″	350	75	21	11	75→ 350	21→ 75	11→ 21		l^{II} °	b^{II} °	
0004−83	00 04 09	−83 22·5	−2·88	+20·04		7·9	2·5	1·3		0·9	1·0		304	−34	
0013−63	00 13 35	−63 27·6	+2·89	20·00	27	7·4	1·9	0·7	0·8	1·1	1·6		310	−53	00−61
0016−77	00 16 39	−77 00·1	−2·65	20·02			0·8					conf. with 0017−77	305	−40	
0017−71	00 17 30	−71 13	+2·77	19·98		2·0	1·0			0·5		ext. at 21cm	307	−46	
0017−77	00 17 44	−77 08·1	−2·60	20·02			0·8					conf. with 0016−77	305	−40	
0020−74	00 20 30	−74 44	+2·64	19·96			1·0						306	−44	
0021−68·6	00 21 48	−68 38·4	2·74	19·95		3·7	1·0					Not resolved at 75 cm	307	−49	
0021−68·2	00 21 53	−68 10·4	2·76	19·95			0·7						307	−49	
0022−74	00 22 00	−74 13	2·62	19·95		1·5	0·6			0·7			306	−43	
0022−60	00 22 53	−60 46·6	2·83	19·93		3·5	1·4	0·7		0·7	1·0		309	−56	
0032−63	00 32 47	−63 36·7	2·66	19·82		3·0	1·2			0·8			306	−54	
0036−62	00 36 30	−62 48·2	2·65	19·77		3·1	1·4	0·8		0·6	0·9		305	−55	
0037−68	00 37 00	−68 49	2·52	19·78			1·2						305	−50	
0038−72	00 38 30	−72 00	+2·39	19·76			1·2						304	−45	
0041−76	00 41 13	−76 05·7	−2·09	19·71		3·2	0·6			1·3			304	−41	
0041−84	00 41 53	−84 39·0	−0·25	19·72		1·5	0·9			0·4			303	−33	
0043−63	00 43 52	−63 51·1	+2·54	19·64		2·4	1·2			0·6			304	−54	
0048−83	00 48 11	−83 22·3	−0·45	19·60			0·8						303	−34	
0055−73	00 55 00	−73 00	+2·04	19·47	550	110	67		1·0	0·4		see Mathewson and Healey 1964*a* Centroid of SMC	302	−44	00−71
0101−80	01 01 03	−80 12·6	−1·05	+19·30		1·9	0·4			1·2			302	−37	

0101−76	01 01 09	−76 01·6	−1·62	+19·30			0·5						302	−41	
0106−84	01 06 40	−84 20·1	−0·72	19·20			0·6						302	−33	
0110−69	01 10 01	−69 17·2	+2·02	19·12		5·5	2·0	1·0		0·8	1·1		300	−48	
0113−80	01 13 50	−80 53·5	−0·28	19·00		2·3	0·7			1·0			302	−36	
0118−68	01 18 00	−68 26·2	+1·95	18·89		2·5	1·1			0·7			299	−50	
0119−63	01 19 58	−63 25·9	+2·08	18·83	22	5·1	1·6	0·7	0·9	0·9	1·3		297	−54	01−61
0122−75	01 22 34	−75 32·0	−1·33	18·80		2·1	0·7			0·9			300	−42	
0125−61	01 25 57	−61 34·2	+2·15	18·63	17	4·0	1·1		0·9	1·0			295	−55	01−62
0127−81	01 27 56	−81 24·4	0·31	18·60		1·9	0·8			0·7			301	−36	
0130−62	01 30 39	−62 02·6	2·09	18·47		3·4	1·1			0·9			294	−55	
0133−69	01 33 00	−69 46	1·64	18·41	22	3·2	0·6		1·2				297	−49	01−63
0141−69	01 41 00	−69 59	+1·51	18·13			0·8						296	−49	
0152−76	01 52 14	−76 29·8	−0·40	17·70		3·9	0·8			1·3			298	−40	
0155−82	01 55 14	−82 41·5	−2·25	17·60			0·6						300	−34	
0156−78	01 56 15	−78 39·7	−0·55	17·50			0·7						299	−38	
0157−78	01 57 33	−78 55·3	−0·45	17·50			1·2						299	−38	
0158−74	01 58 52	−74 46·8	+0·65	17·40		4·0	1·6			0·7			296	−43	
0202−76	02 02 00	−76 34·1	−0·15	17·30	18	8·0	2·6	1·3	0·6	0·9	1·0		297	−40	01−71?
0210−62	02 10 04	−62 12·5	+1·87	17·29	11	2·5	1·0		0·9	0·7			287	−53	02−62
0223−71	02 23 08	−71 12·5	0·78	16·25	30	5·0	1·5		1·2	1·0			292	−45	02−71?
0224−70	02 24 00	−70 05·5	+0·77	16·20		3·2	0·6			1·3			292	−45	
0230−83	02 30 23	−83 31·4	−3·92	16·10		1·7	0·7			0·7			300	−33	
0230−66	02 30 51	−66 40·1	+1·17	15·84	13	4·7	1·4	0·6	0·6	1·0	1·3		288	−48	02−63
0244−69	02 44 32	−69 22·3	+0·74	15·09		2·5	1·0			0·7			288	−45	
0247−77	02 47 56	−77 16·9	−0·89	14·90			0·5						295	−38	
0251−67	02 51 11	−67 30·4	+0·84	14·59	34	6·2	1·2		1·1	1·3		>35″ EW ext. in δ 20′S 74 II	286	−46	02−65
0252−71	02 52 19	−71 17·2	+0·39	14·63	7	14·0	5·9			0·7		350 cm flux uncertain	290	−43	02−72?
0312−77	03 12 46	−77 05·3	−1·27	13·36		2·0	0·8			0·7			293	−38	
0315−68	03 15 41	−68 31·9	+0·52	13·16		4·6	1·5			0·9			284	−44	
0324−70	03 24 10	−70 23·8	+0·16	+12·60		1·5	0·6			0·7			286	−42	

TABLE 2 (*Continued*)

Catalogue Number	Position (1950·0)		Annual Precession		Flux Density (10^{-26} W m^{-2} (c/s)$^{-1}$)				Spectrum			Remarks	Galactic Coordinates		MSH Cat. No.
	R.A. h m s	Dec. ° ′	Δα s	Δδ ″	350	75	21	11	75→ 350	21→ 75	11→ 21		l^{II} °	b^{II} °	
0324−77	03 24 13	−77 10·4	−1·49	+12·60			0·6						293	−37	
0325−76	03 25 21	−76 39·9	−1·33	12·52			0·9						292	−37	
0344−85	03 44 25	−85 35·1	−11·29	11·18			0·6					ext. in δ at 21 cm	299	−31	
0349−88	03 49 00	−88 26·4	−38·21	10·83		6·8	1·5			1·2			302	−29	
0354−76	03 54 52	−76 33·2	−1·70	10·41			0·5						291	−36	
0355−66	03 55 24	−66 50	+0·40	10·37		2·3	1·2			0·5			279	−42	
0359−76	03 59 36	−76 14·3	−1·65	10·05			0·6						290	−36	
0401−64	04 01 06	−64 11	+0·68	9·94	14	4	<0·5		0·8			75 cm position	277	−42	04−61?
0408−65	04 08 06	−65 49	+0·45	9·40	36	45	15		−0·2	0·9		<15″ EW	277	−42	04−62
0410−75	04 10 11	−75 15·3	−1·43	9·24	87	40	13·5	7·5	0·5	0·8	1·0	peculiar spectrum <20″ EW P < 1% 74I	289	−36	04−71
0411−75	04 11 10	−75 39·9	−1·58	9·16			0·5						289	−36	
0416−65	04 16 15	−65 01·9	+0·49	8·76			0·7						277	−40	
0420−62	04 20 30	−62 30	+0·75	8·43	38	9	3		0·9	0·9		20″ EW	273	−41	04−63
0423−68	04 23 06	−68 41	−0·05	8·22		2·4	0·8			0·9			280	−39	
0425−72	04 25 00	−72 48	−0·88	8·07	11	4·7	1·7		0·5	0·9			284	−37	04−72
0428−67	04 28 12	−67 52	+0·05	7·81		2·3	0·9			0·7			278	−39	
0429−61	04 29 48	−61 34	+0·80	7·69	35	6·5	1·7		1·1	1·1			271	−41	04−64
0437−74	04 37 02	−74 54·8	−1·56	7·10		1·4	0·8			0·5			288	−35	
0437−65	04 37 06	−65 03	+0·39	7·09	16	4·5	1·4		0·8	0·9			276	−38	04−65
0443−59	04 43 26	−59 29·7	0·93	6·55		3·6	1·3	0·6		0·8	1·2		269	−39	
0448−62	04 48 24	−62 20	+0·65	6·16	9	2·7	0·8		0·8	1·0		ext. at 21 cm	272	−38	04−66
0450−70	04 50 36	−70 53	−0·61	5·98		2·3	1·0			0·7			281	−36	
0454−81	04 54 43	−81 06·2	−5·12	5·63			1·1						294	−31	
0458−75	04 58 43	−75 12·1	−1·80	5·30		3·0	0·6			1·3			287	−33	
0506−61	05 06 13	−61 12·5	+0·71	+4·64	14	6·1	2·2	1·5	0·5	0·8	0·6		270	−36	05−61

0507−62	05 07 36	−62 44	+0·55	+4·54	11	3·4	1·1		0·7	0·8			271	−36	05−62?
0513−83	05 13 52	−83 38·5	−8·68	4·01			0·5						296	−30	
0522−69	05 22 00	−69 00	−0·36	3·31	4000	1100	620		0·8	0·5		Centroid of LMC see Mathewson and Healey 1964*a*	280	−33	05−63
0525−78	05 25 15	−78 39·6	−3·51	3·03			0·6						291	−31	
0525−66	05 26 00	−66 08	+0·09	2·96	34	9	1·3		0·9	1·5		Supernova remnant ~30″	276	−33	05−64
0532−63	05 32 48	−63 50	0·37	2·37	10	2·2	0·8		1·0	0·8			271	−33	05−65
0534−61	05 34 30	−61 22	+0·64	2·23		3·2	1·3			0·7			269	−33	
0539−69	05 39 00	−69 07	−0·41	1·83	108							30 Doradus see Mathewson and Healey 1964*a*	279	−32	05−66
0540−82	05 40 11	−82 04·4	−6·49	1·73		2·7	0·6			1·2			294	−29	
0546−83	05 46 47	−83 48·3	−9·22	+1·16			0·5						296	−29	
0601−70	06 01 12	−70 38·5	+0·73	−0·10			0·7						281	−30	
0602−64	06 02 24	−64 43	+0·25	−0·21		3·4	1·4			0·7			273	−29	
0606−79	06 06 41	−79 33·6	−4·18	−0·58		3·8	1·4			0·8			291	−29	
0607−60	06 07 24	−60 31·5	+0·71	−0·65	16	3·0	1·0		1·1	0·9		ext.?	269	−28	06−62
0608−65	06 08 48	−65 49	+0·10	−0·77	14	2·7	1·4		1·1	0·5			274	−29	06−61
0611−74	06 11 36	−74 30	−1·77	−1·01		2·6	1·1			0·7		ext.?	284	−29	
0613−77	06 13 48	−77 50·4	−3·12	−1·21		3·0	0·8			1·1			289	−29	
0617−80	06 17 30	−80 43·7	−5·09	−1·53			0·6						293	−28	
0620−82	06 20 58	−82 34·7	−7·14	−1·83		4·3	1·2			1·0			295	−28	
0623−64	06 23 14	−64 34·5	+0·28	−2·04			0·8						274	−27	
0624−62	06 24 45	−62 39·8	+0·50	−2·16		4·0	0·7			1·4			272	−27	
0637−75	06 37 20	−75 14·4	−1·93	−3·28	20	9·7	6·7	4·9	0·4	0·3	0·5	P 3·6% 74 II	286	−27	06−71
0642−78	06 42 06	−78 12·1	−3·22	−3·66		2·7	1·1			0·7			290	−27	
0651−60	06 51 08	−60 19·0	+0·77	−4·45	9	3·7	1·4	0·7	0·6	0·8	1·1		270	−23	06−63
0654−79	06 54 23	−79 47·2	−4·14	−4·71			0·8						292	−27	
0658−65	06 58 16	−65 41·2	+0·21	−5·05	17		2·2						276	−24	06−64
0702−78	07 02 17	−78 24·6	−3·20	−5·38		1·7	0·6			0·8			290	−26	
0702−75	07 02 50	−75 46·9	−2·00	−5·43			0·6						287	−26	
0714−76	07 14 20	−76 15·6	−2·11	−6·39		2·3	0·7			0·9			288	−25	
0714−78	07 14 52	−78 12·4	−2·99	−6·43		3·3	0·8			1·1			290	−25	

TABLE 2 (*Continued*)

Catalogue Number	Position (1950·0)		Annual Precession		Flux Density (10^{-26} W m^{-2} (c/s)$^{-1}$)				Spectrum			Remarks	Galactic Coordinates		MSH Cat. No.
	R.A. h m s	Dec. ° ′	Δα s	Δδ ″	350	75	21	11	75→ 350	21→ 75	11→ 21		l^{II} °	b^{II} °	
0744−67	07 44 04	−67 19·7	+0·20	−8·79		11·7	5·3			0·6			279	−20	
0752−78	07 52 32	−78 03·0	−2·49	−9·45		2·5	0·6			1·1		ext. at 21 cm	290	−24	
0802−80	08 02 50	−80 49·8	−4·04	−10·23		2·5	0·7			1·0			293	−24	
0814−77	08 14 22	−77 53·6	−2·12	−11·09			0·6						291	−22	
0818−74	08 18 57	−74 44·6	−0·95	−11·42			0·6						288	−21	
0831−77	08 31 23	−77 45·4	−1·79	−12·30			0·5						291	−22	
0841−83	08 41 56	−83 34·1	−5·94	−13·01		3·9	1·0					conf. at 21 cm	297	−24	
0842−75	08 42 12	−75 29·5	−0·85	−13·04	58	10·5	4·3	2·4	1·1	0·7	0·9	<20″ EW P < 2·5% 74 III	289	−20	08−71
0846−81	08 46 13	−81 07·2	−3·33	−13·29		4·4	1·1			1·1			295	−23	
0859−77	08 59 53	−77 07·1	−1·06	−14·16			0·7						291	−20	
0905−68	09 05 59	−68 16·9	+1·00	−14·66		6·1	1·7	0·9		1·0	1·0		285	−14	
0910−63	09 10 46	−63 40·7	+1·15	−14·78	15	4·4	1·1		0·9	1·1			281	−11	09−62?
0916−79	09 16 48	−79 07·9	−1·47	−15·17		4·2	0·7			1·4			294	−21	
0918−76	09 18 58	−76 47·8	−0·61	−15·29			0·8						292	−19	
0924−76	09 24 16	−76 42·6	−0·48	−15·59			0·6						292	−19	
0925−81	09 25 31	−81 31·8	−2·53	−15·66			0·7						296	−22	
0926−70	09 26 50	−70 00·6	+0·80	−15·74		4·4	0·6					conf. at 75 cm?	287	−14	
0928−78	09 28 44	−78 46·3	−1·05	−15·83		3·2	1·2			0·8			294	−20	
0936−62	09 36 25	−62 16·1	+1·58	−16·21	16	3·5	0·7		0·9	1·3			283	−8	09−63
0943−76	09 43 25	−76 06·7	0·04	−16·59		6·6	2·1	1·2		0·9	0·9		292	−17	
0944−75	09 44 38	−75 44·5	0·15	−16·65			0·6						292	−17	
0953−75	09 53 25	−75 14·4	+0·13	−16·71			0·7						292	−16	
0958−84	09 58 06	−84 52·3	−4·48	−17·27			0·7						299	−24	
1010−64	10 10 49	−64 43·4	+1·76	−17·82	19	5·3	2·6	1·4	0·8	0·6	1·0		287	−7	10−61
1029−85	10 29 29	−85 27·0	−3·39	−18·50			0·7						300	−24	

1033−80	10 33 48	−80 31·3	+0·13	−18·64		3·5	0·8			1·2			297	−19	
1036−72	10 36 21	−72 51·0	1·53	−18·72		2·6	0·9			0·8			293	−13	
1036−69	10 36 57	−69 47·9	1·70	−18·75		6·9	2·4	1·2		0·8	1·1		292	−10	
1057−79	10 57 48	−79 48·0	1·08	−19·31		2·5	0·9			0·8			298	−18	
1136−67	11 36 17	−67 55·2	2·74	−19·93	34	6·6	3·1	1·7	1·0	0·6	1·0	>35″ EW	296	−6	11−64
1150−72	11 50 24	−72 23·4	2·88	−20·02		2·2	1·3	0·7		0·4	1·0	conf. at 75 cm?	299	−10	
1151−69	11 51 48	−69 28·9	2·96	−20·03	15	5·0	2·0	0·9	0·7	0·7	1·3		298	−7	11−66
1208−75	12 08 18	−75 10·7	3·26	−20·03			0·5						300	−13	
1221−82	12 21 30	−82 56·3	4·08	−19·95			0·6						302	−20	
1221−66	12 21 39	−66 34·3	3·35	−19·95		>2·0	2·0	1·2			0·8	conf. at 75 cm	300	−4	
1225−81	12 25 57	−81 37·2	4·10	−19·91		3·2	0·7			1·2			302	−19	
1239−81	12 39 00	−81 51·3	4·65	−19·75			0·5						303	−19	
1239−75	12 39 46	−75 17·7	3·95	−19·74			0·7						302	−13	
1242−84	12 42 44	−84 56·7	5·87	−19·69			1·2						303	−22	
1244−82	12 44 59	−82 46·3	5·13	−19·66			0·9						303	−20	
1251−71	12 51 46	−71 21·8	3·97	−19·69		3·0	1·0			0·9			303	−9	
1259−76	12 59 23	−76 56·3	4·55	−19·37			1·2						303	−14	
1301−86	13 01 47	−86 20·6	8·64	−19·32			0·7						303	−24	
1302−82	13 02 51	−82 42·9	5·90	−19·29			1·3						303	−20	
1305−74	13 05 08	−74 52·6	4·42	−19·36			0·5						304	−12	
1308−76	13 08 09	−76 56·9	4·76	−19·16			0·9					ext. in δ at 21 cm	304	−14	
1347−76	13 47 10	−76 24·8	5·57	−17·89		>2	0·6						306	−14	
1416−86	14 16 05	−86 43·1	16·11	−16·61			0·5						304	−24	
1420−74	14 20 12	−74 29·7	5·84	−16·28		3·9	1·1			1·0			309	−13	
1432−69	14 32 22	−69 22·6	5·22	−15·70		4·6	0·8			1·4			312	−9	
1445−74	14 45 35	−74 56·7	6·36	−15·03		4·8	1·3			1·0			310	−14	
1514−81	15 14 00	−81 52·4	10·08	−13·28			0·7						308	−21	
1514−86	15 14 13	−86 01·4	17·48	−13·27			1·0						305	−24	
1517−75	15 17 33	−75 16·8	6·93	−13·05			0·9						312	−15	
1540−82	15 40 28	−82 49·6	+11·78	−11·46			1·0						308	−22	

TABLE 2 (*Continued*)

Catalogue Number	Position (1950·0)		Annual Precession		Flux Density $(10^{-26}\ \mathrm{W\ m^{-2}\ (c/s)^{-1}})$				Spectrum			Remarks	Galactic Coordinates		MSH Cat. No.
	R.A. h m s	Dec. ° ′	Δα s	Δδ ″	350	75	21	11	75→ 350	21→ 75	11→ 21		l^{II} °	b^{II} °	
1540—73	15 40 43	−73 02·9	+6·70	−11·45		5·2	1·8			0·8			315	−15	
1545—76	15 45 53	−76 04·1	7·56	−11·07			0·6						313	−17	
1547—79	15 47 45	−79 32·6	8·40	−10·77			4·0	2·8			0·6	Not resolved	311	−20	
1549—79	15 49 36	−79 06·3	8·49	−10·69			6·2	4·9			0·4	at 75 cm 74 III	311	−20	
1602—63	16 02 05	−63 22·2	5·37	−9·75		14·6	5·4			0·8			323	−8	
1606—84	16 06 19	−84 11·2	14·62	−9·54			1·7						308	−24	
1606—83	16 06 48	−83 42·5	13·74	−9·50			0·7						308	−23	
1610—60	16 10 47	−60 48·2	5·19	−9·10	1190		56·0					P < 1% ⩾70″ EW shoulder in δ at 21 cm 74 II	325	−7	16—61
1610—77	16 10 56	−77 10·4	8·29	−9·19		6·0	5·0	5·2		0·1	0	shoulder in α at 21 cm	313	−19	
1619—63	16 19 43	−63 29·2	5·50	−8·31			0·7						324	−10	
1624—75	16 24 45	−75 01·8	7·65	−8·09	38	3·2	1·2			0·8			316	−18	16—71??
1632—68	16 32 48	−68 08·4	5·59	−7·26		5·0	1·3			1·1			322	−14	
1637—77	16 37 09	−77 10·3	8·56	−7·12		13·5	6·5	4·0		0·6	0·8		314	−20	
1640—76	16 40 56	−76 32·7	8·33	−6·78			0·6						315	−20	
1649—78	16 49 00	−78 53·7	9·56	−6·11			0·8						313	−21	
1655—77	16 55 13	−77 37·1	8·92	−5·62		~4	2·5					conf. at 75 cm 74 I	315	−21	
1700—85	17 00 47	−85 26·9	19·30	−5·12			0·6						307	−25	
1706—73	17 06 23	−73 39·8	7·46	−4·65		4·1	0·9			1·2			319	−20	
1707—81	17 07 10	−81 10·0	11·44	−4·58			0·6						312	−23	
1716—80	17 16 22	−80 02·2	10·54	−3·79		6·8	2·5			0·8			313	−23	
1720—83	17 20 34	−83 40·8	14·96	−3·43			1·0						309	−25	
1721—78	17 21 57	−78 12·0	9·38	−3·31			0·8						315	−23	
1726—77	17 26 42	−77 23·9	8·99	−2·90			0·5						316	−22	
1728—76	17 28 16	−76 48·9	8·72	−2·77			0·6						316	−22	
1737—60	17 37 33	−60 54·8	+5·47	−1·84		7·4	3·3			0·6			332	−16	

1740−64	17 40 20	−64 42·5	+5·91	−1·36		4·0	0·7					Not resolved at 75 cm	328	−18	
1746−64	17 46 12	−64 58·5	5·91	−1·21			1·2						328	−18	
1754−59	17 54 37	−59 46·3	5·38	−0·43	25	15	3·9	1·5	0·4	1·1	1·5	P 3·2%	334	−17	17−*51*
1814−63	18 14 49	−63 46·9	5·79	+1·40	71	34	14·2	7·5	0·5	0·7	1·0	≤20″ EW	331	−21	18−*61*
1815−76	18 15 17	−76 36·8	8·68	1·34			0·7						318	−25	
1819−67	18 19 18	−67 20·3	6·28	1·75		4·4	2·1			0·6			327	−22	
1833−77	18 33 32	−77 13·1	8·90	2·92			0·9						317	−26	
1833−78	18 33 59	−78 59·1	9·86	2·96			0·6						315	−26	
1835−79	18 35 08	−79 44·2	10·37	3·06			0·6						314	−26	
1843−69	18 43 43	−69 02·1	6·73	3·82		4·9	0·8			1·4			326	−25	
1848−79	18 48 12	−79 38·2	10·22	4·18			0·7						315	−27	
1848−81	18 48 59	−81 09·9	11·47	4·25			0·5						313	−27	
1853−87	18 53 30	−87 31·5	33·15	4·64			0·7						306	−27	
1855−66	18 55 01	−66 20·6	6·07	4·87		4·3	1·2			1·0			329	−26	
1904−80	19 04 33	−80 15·4	10·55	5·57		5·6	1·5					Not resolved at 75 cm	314	−28	
1909−80	19 09 55	−80 05·7	10·37	6·02			0·9						314	−28	
1922−62	19 22 46	−62 47·3	5·51	7·18	12	6·0	2·4		0·5	0·7			334	−28	19−*61*?
1928−74	19 28 03	−74 55·3	7·67	7·51			0·8						320	−32	
1934−63	19 34 49	−63 49·2	5·57	8·14		5·0	16·0	11·8				Peculiar spectrum 74 II P < 1%	333	−29	
1950−79	19 50 29	−79 26·3	9·42	9·29			0·7						315	−30	
1954−87	19 54 40	−87 56·2	35·61	9·61			1·2						305	−28	
2000−79	20 00 40	−79 22·5	9·23	10·07			0·7						316	−30	
2025−77	20 25 38	−77 02·0	7·74	11·90			1·0						317	−32	
2028−73	20 28 26	−73 14·5	6·66	12·18	18	6·2	1·6		0·8	1·0			321	−33	20−*71*
2033−75	20 33 44	−75 43·8	7·19	12·46			0·6					2nd source 15′N at 21 cm	318	−34	
2041−63	20 41 03	−63 10·7	5·09	12·95		2·4	0·6			1·1			333	−37	
2041−60	20 41 19	−60 29·7	4·87	13·02	55	10·5	2·8	0·9	1·1	1·1	1·8	<15″ EW 74 I	336	−37	20−*61*.
2043−67	20 43 25	−67 04·4	5·53	13·08			1·1						328	−36	
2050−75	20 50 39	−75 09·7	6·78	13·58			0·9						318	−34	
2059−64	20 59 06	−64 09·1	+5·04	+14·11	17	3·1	0·9		1·0	1·0			331	−39	20−62

TABLE 2 (*Continued*)

Catalogue Number	Position (1950·0)		Annual Precession		Flux Density (10⁻²⁶ W m⁻² (c/s)⁻¹)				Spectrum			Remarks	Galactic Coordinates		MSH Cat. No.
	R.A. h m s	Dec. ° ′	Δα s	Δδ ″	350	75	21	11	75→ 350	21→ 75	11→ 21		l^{II} °	b^{II} °	
2059−78	20 59 48	−78 40·6	+7·80	+14·16			0·8						314	−33	
2118−64	21 18 18	−64 16·4	4·91	15·31		≥2·3	1·7	0·8			1·2	conf. at 75 cm	330	−40	
2127−75	21 27 45	−75 57·0	6·37	15·78			0·5						316	−36	
2132−84	21 32 34	−84 23·7	11·24	16·04			0·6						308	−31	
2141−81	21 41 14	−81 46·6	8·34	16·48		10	3·1	1·7		0·9	1·0		310	−33	
2141−75	21 41 57	−75 50·8	6·08	16·51		≥2	1·8	1·2			0·6	conf. at 75 cm	316	−37	
2142−76	21 42 34	−76 36·9	6·24	16·54			0·7						315	−36	
2145−78	21 45 43	−78 20·6	6·66	16·70			0·6						313	−35	
2152−76	21 52 41	−76 03·8	5·91	17·03			0·6						315	−37	
2152−69	21 52 58	−69 55·8	4·98	17·09	253	80	32	17·5	0·8	0·7	0·9	25″EW P 2–3% 74I	321	−41	21−64
2155−83	21 55 26	−83 53·1	9·52	17·15		≥2	1·0					conf. at 75 cm	308	−32	
2201−77·9	22 01 28	−77 51·4	6·14	17·42			0·5						313	−36	
2201−77·4	22 01 29	−77 26·9	6·04	17·42			0·6						313	−36	
2204−63	22 04 51	−63 40·8	4·39	17·65		4·1	1·1			1·1			327	−45	
2223−62	22 23 31	−62 54·3	+4·08	+18·31		1·8	1·0					conf. at 75 cm	326	−47	

2227—66	22 27 25	—66 34·7	+4·24	+18·48		5·2	1·0					conf. at 75 cm	322	—45	
2238—61	22 38 58	—61 00·4	3·95	18·82	14	3·7	1·2	0·5	0·9	0·9	1·4		327	—50	22—62
2239—80	22 39 34	—80 00·7	5·68	18·82			0·5						309	—36	
2253—65	22 53 48	—65 17·1	3·90	19·24	19		0·9						320	—48	22—63
2255—70	22 55 00	—70 31·0	4·13	19·29			1·3	0·6			1·2		316	—44	
2258—81	22 58 08	—81 42·5	5·52	19·32		2·1	0·7			0·9			308	—35	
2259—76	22 59 04	—76 59·3	4·59	19·34			0·5						311	—39	
2315—81	23 15 17	—81 14·3	4·75	19·66		2·2	0·7			0·9			307	—35	
2326—80	23 26 43	—80 35·4	4·24	19·83			0·6						307	—36	
2332—66	23 32 15	—66 54·4	3·41	19·91	26	7·8	2·5	1·3	0·8	0·9	1·0		314	—49	23—63
2336—80	23 36 53	—80 36·5	3·89	19·94			0·5						307	—36	
2351—77	23 51 01	—77 14·5	3·31	20·03			0·5					ext. to N in δ ∼ 30′	307	—40	
2353—68	23 53 31	—68 37·6	3·16	20·03		2·1	1·5	1·0			0·6	conf. at 75 cm	310	—48	
2353—79	23 53 36	—79 41·0	3·28	20·03			0·8						306	—37	
2356—61	23 56 29	—61 12·3	3·12	20·04	296	66	23·7	10·4	1·0	0·8	1·3	P 5% 40″EW 74I	314	—55	23—64
2358—75	23 58 03	—75 27·5	3·12	20·04			0·6						307	—42	
2358—83	23 58 19	—83 07·4	3·16	20·04			0·7						305	—34	

408 Mc/s. At 408 Mc/s effects of confusion could contribute an additional peak error of 1·0 f.u. in unpolarized areas, and in regions where the background is appreciably polarized (see Mathewson and Milne 1964) the errors could exceed 2 f.u.

The reader is referred to BGM for a more complete discussion of the errors. Table 1, p. 331, shows estimates of average error which apply to this survey.

V. POSITION MEASUREMENTS

The pointing errors of the 210-ft telescope have been discussed by BGM. The corrections mentioned there have been applied to all sources in the declination zone −60° to −75°. It is thought that 90% of the positions given for this zone are correct to within 1′·5 of arc. This has been estimated from internal consistency of several measurements of the same sources and in a few cases on new optical identifications in the region (see Section IX).

In the declination zone −75° to −90° position corrections were not applied. In these cases, inadequate knowledge of corrections leaves an uncertainty of approximately 2′·0 of arc in positions.

In the entire region of this survey, mean precession only was applied to the positions in obtaining 1950·0 coordinates from the positions observed in 1962–63. Effects due to nutation, aberration, and second-order precession were neglected and are additional sources of error in the positions given.

Considering the above sources of error we believe that r.m.s. errors in the catalogue positions do not exceed 1′·5 of arc in the region −60° to −75°, and 2′·5 for sources from declination −75° to −90°.

VI. CATALOGUE

The Source Catalogue (Table 2) is largely self-explanatory, additional information concerning its use being given below.

Column 1.—Catalogue number.

Columns 2 and 3.—Right ascension and declination for epoch 1950·0.

Columns 4 and 5.—Annual precession in right ascension (seconds of time) and declination (seconds of arc).

Columns 6, 7, 8, and 9.—Flux densities at the indicated wavelengths, in units of 10^{-26} W m^{-2} (c/s)$^{-1}$.

Columns 10, 11, and 12.—Spectral indices for indicated wavelength ranges.

Column 13.—Remarks and miscellaneous data. Abbreviations used are as follows.

> 74 I, 74 II, 74 III, 74 IV: Harris–Roberts field class of identification on Mount Stromlo 74-in. plate; I, the error rectangle about the source position includes a galaxy brighter than $m_{pg} \doteq 17$; II, the area includes a galaxy or galaxies for which $17 < m_{pg} < 19 \cdot 5$; III, the area includes no galaxies above the plate limit; IV, the field is heavily obscured.

ext. = extended; P = polarized at 1410 Mc/s, percentage indicated; conf. = confused; N = north; S = south; EW = east–west angular size.

Columns 14 and 15.—New galactic coordinates.

Column 16.—MSH catalogue number, where applicable. (MSH = 85 Mc/s survey by Mills, Slee, and Hill (1961).)

VII. Polarization

All sources greater than 2 f.u. at 1410 Mc/s were observed for linear polarization by F. F. Gardner and R. D. Davies as part of an investigation of the polarization in radio sources. A full account of this investigation will be published separately. The present catalogue includes the percentage polarization for sources with measured polarization at 1410 Mc/s.

VIII. Spectra of Sources

The spectral index has been derived from $S \propto f^{-\alpha}$, where α is the spectral index. This definition avoids the continual use of a minus sign with each spectral index.

Table 3

SOURCES WITH CURVED SPECTRA

Positive curvature:	0013−63	0202−76	0410−75
	0506−61	1151−69	1814−63
	2028−73		
Negative curvature:	0210−62		
Positive curvature with maximum in observed frequency range:	(0252−71?)	(0408−65?)	1934−63

Figure 1 shows the distribution of spectral indices taken from columns 10, 11, and 12 of the source catalogue. The number of sources for which spectral indices could be derived was less than half the number in the catalogue. This was due to two factors: (i) MSH fluxes are available for only 47 sources in the region; (ii) many of the sources have flux densities between 0·5 and 1 f.u. at 1410 Mc/s, and are therefore too weak in most cases for observation at 2650 Mc/s and likely to be below the confusion limit at 408 Mc/s. Spectral indices are not indicated in the catalogue when flux values are questioned. Figure 1 shows that spectra over the frequency range 1410–2650 Mc/s are appreciably steeper than at lower frequencies. The median spectral index for this range is 0·97, whereas for the 408–1410 Mc/s range it is 0·88, and for the 85–408 Mc/s range it is 0·82. This effect has been noted by previous authors (e.g. BGM).

In addition to sources with approximate power law spectra, some source spectra exhibit curvature. Several such cases of curvature were noted in the sources in the present catalogue and are classified in Table 3.

IX. Identifications

Positions of all the sources reported have been compared with those of NGC and IC objects and with the objects reported by de Vaucouleurs (1956) (with the exception of the areas of the Magellanic Clouds, in which case the reader is referred to radio studies of the clouds themselves, e.g. Mathewson and Healey (1964*b*)). For four sources, approximate positional agreement has been noted and they are considered as possible identifications. Further optical study of these sources has not been undertaken, and they are considered as identifications on the strength of positional agreement only.

Positions of 13 additional sources from the catalogue were observed with the Mount Stromlo 74-in. reflector, and were classified according to the field in the error rectangle of the radio position (Harris and Roberts 1960). From the sources with Class I or Class II fields, six are considered probable identifications. Table 4 lists suggested identifications; types and magnitudes for the objects listed are tentative. Further information on these objects has been compiled by Westerlund and Smith (unpublished data).

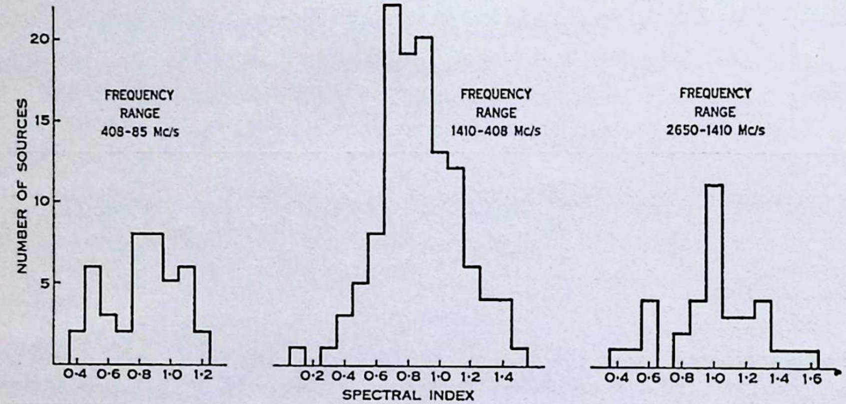

Fig. 1.—Histograms of the distribution of spectral indices.

X. Source Counts

It is thought that the present catalogue is substantially complete south of declination −75° for sources with flux density greater than 0·5 f.u. at 1410 Mc/s. Because different observing techniques were used north and south of declination −75° (see Section II), some sources with flux density between 0·5 and 1 f.u. at 1410 Mc/s have been omitted from the catalogue north of declination −75°.

The limited number of sources available makes it difficult to derive precise conclusions about the number-count–flux-density distribution, but it is of interest to see whether the distribution differs significantly from that obtained from previous work, most of which has been done at lower frequencies.

Figure 2 shows the 135 sources in the 0·27 steradians south of declination −75° plotted in the conventional manner as a log N–log S distribution, in which N is the number of sources observed with flux density greater than S. When allowance is made for the statistical error due to the small number of sources with flux density greater than 2 f.u., and for uncertainty in the flux-density determination of the

TABLE 4

SUGGESTED OPTICAL IDENTIFICATIONS

Catalogue Number	Radio Position		Optical Position		Remarks
	R.A.	Dec.	R.A.	Dec.	
	h m s	° ′	h m s	° ′ ″	
0251−67	02 51 11	−67 30·4	02 51 32	−67 28 57 (Westerlund–Smith)	cluster 17–18^{m}
0410−75	04 10 11	−75 15·3	04 09 36·4 04 09 57·9	−75 15 42 −75 14 06 (Westerlund–Smith)	E4 16^{m} SO 15^{m} } two bright members of cluster
1655−77	16 55 13	−77 37·1	16 55 12·4	−77 37 33 (Westerlund–Smith)	EO $16·5^{m}$
1716−80	17 16 22	−80 02·2	17 15 30	−80 01·3 (IC)	IC 4640
1746−64	17 46 12	−64 58·5	17 46 12	−64 58 (de Vaucouleurs)	IC 4662 A
1934−63	19 34 49	−63 49·2	19 34 48·3	−63 49 37 (Ekers)	stellar image with jet(?) 18^{m}
2028−73	20 28 26	−73 14·5	20 30 15	−73 06·3 (IC)	IC 5016
2041−60	20 41 19	−60 29·7	20 41 12·7	−60 30 20 (Westerlund–Smith)	E $17+^{m}$
2152−69	21 52 58	−69 55·8	21 52 57·8	−69 55 40 (Westerlund–Smith)	E3 14^{m}
2238−61	22 38 58	−61 00·4	22 38 18	−61 01·1 (IC)	IC 5238
2356−61	23 56 29	−61 12·3	23 56 29·3	−61 11 40 (Westerlund–Smith)	E3 16^{m}

weaker sources, it is found that the distribution can be fitted by a straight line which has a slope of $-1·7\pm0·3$. This value does not differ significantly from that obtained in earlier more extensive measurements (BGM, and Scott and Ryle 1961). This slope appears to be maintained down to flux density values of 0·5 f.u. at 1410 Mc/s.

XI. Comparison with MSH Sources

The survey of sources at 85 Mc/s by Mills, Slee, and Hill (1961) extends as far south as declination −80°. However, in the zone which overlaps the present survey, −60° to −80°, the MSH survey suffers from difficulty with spurious responses due to side lobes and foreshortening of the north–south arm of the cross-type aerial used.

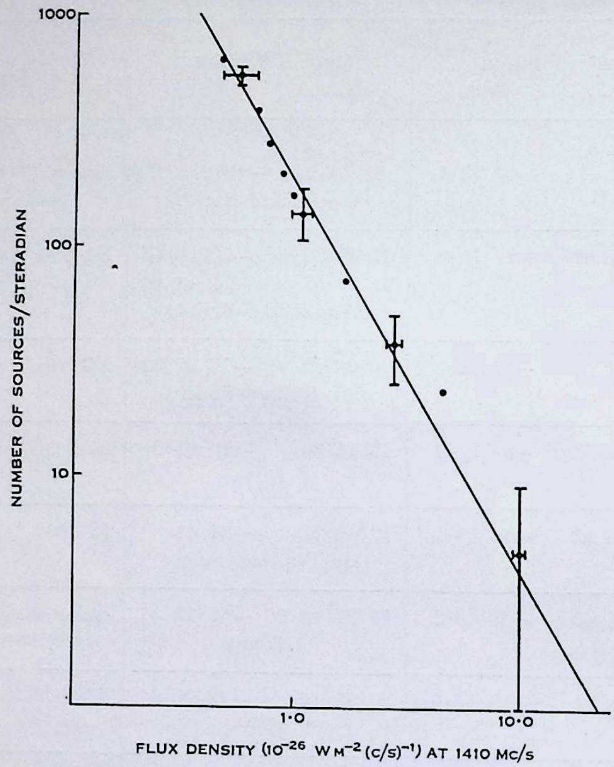

Fig. 2.—Source count for the declination zone −75° to −90°. Error bars in the ordinate indicate statistical error in the number of sources, while error bars in the abscissa are average flux-density errors.

The MSH survey reports 77 sources in the area common to the two surveys, 9 of which are listed as uncertain, possibly due to background variations or side-lobe effects. The present survey lists 40 sources considered to be the same as sources detected by MSH, and another 7 which are considered probable but are questioned on the basis of poor positional agreement. Those sources that are questionable are marked by a (?) after the MSH number in Column 16 of the present catalogue.

Figure 3 shows the differences between the MSH positions and positions given in the present catalogue. The median difference is 12′ of arc (6′·7 of arc in right ascension and 9′·8 of arc in declination). On an overall average, MSH positions tend to have an earlier right ascension (by 3′ of arc) and a more northerly declination (by 3′ of arc) than the source positions determined in the present survey.

Searches were undertaken in the region of 15 of the remaining 30 MSH sources and, in an area of 1° square, centred on the MSH position, disclosed nothing greater than the level set for the finding survey at 408 Mc/s.

Background irregularities at 408 Mc/s were noted near the positions of 07—6*1*, 15—7*1*, and 16—6*3*.

Weak sources (< 1 f.u. at 1410 Mc/s) were found within 15′ of the positions of 02—6*1*, 02—6*2*, 21—6*3*, 22—6*1*, and 23—6*1*. The region of 17—6*1* is a complex of extended weak sources at 1410 Mc/s.

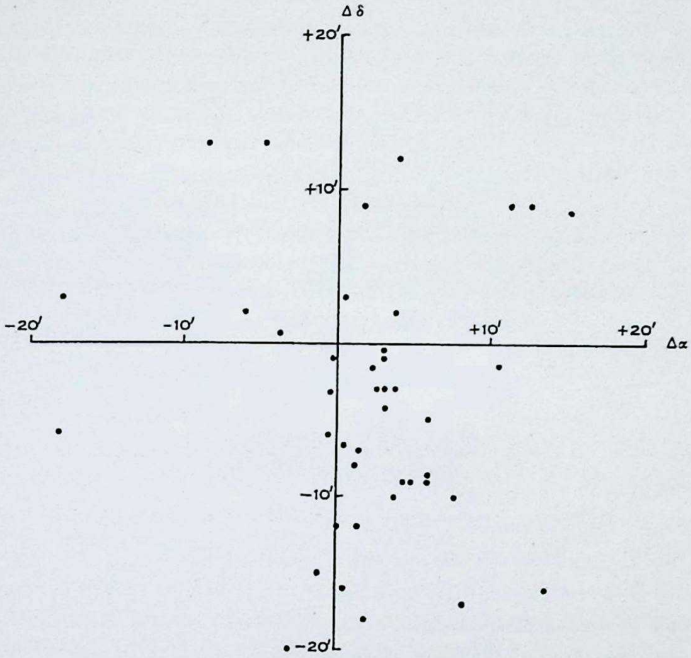

Fig. 3.—Differences between MSH positions and positions of the present catalogue, measured at 1410 Mc/s. Six sources lie outside the limits of the diagram.

XII. References

Bolton, J. G., Gardner, F. F., and Mackey, M. B. (1964).—*Aust. J. Phys.* **17**: 340.

Conway, R. G., Kellermann, K. I., and Long, R. J. (1963).—*Mon. Not. R. Astr. Soc.* **125**: 261.

Cooper, B. F. C., Cousins, T. E., and Gruner, L. (1964).—*Proc. Instn Radio Engrs Aust.* **25**: 221.

Gardner, F. F., and Milne, D. K. (1963)—*Proc. Instn Radio Engrs Aust.* **24**: 127.

Harris, D. E., and Roberts, J. A. (1960).—*Publs Astr. Soc. Pacif.* **72**: 427.

Mackey, M. B. (1964).—*Proc. Instn Radio Engrs Aust.* **25**: 515.

Mathewson, D. S., and Healey, J. R. (1964*a*).—*In* "The Galaxy and the Magellanic Clouds", IAU–URSI Symposium No. 20 (Eds. F. J. Kerr and A. W. Rodgers). p. 245. (Aust. Acad. Sci.: Canberra.)

Mathewson, D. S., and Healey, J. R. (1964*b*). —*In* "The Galaxy and the Magellanic Clouds", IAU–URSI Symposium No. 20 (Eds. F. J. Kerr and A. W. Rodgers). p. 283. (Aust. Acad. Sci.: Canberra.)

Mathewson, D. S., and Milne, D. K. (1964).—*Nature* **203**: 1273.

Mills, B. Y., Slee, O. B., and Hill, E. R. (1961).—*Aust. J. Phys.* **14**: 497.

Scott, P. C., and Ryle, M. (1961).—*Mon. Not. R. Astr. Soc.* **122**: 389.

de Vaucouleurs, G. (1956).—*Mem. Commonw. Sol. Obs. Mt Stromlo*, No. 13.

THEORETICAL MODELS FOR THE RADIANCE OF CONTAMINANT GLOW CLOUDS IN THE UPPER ATMOSPHERE

By K. H. Lloyd*

[*Manuscript received May* 19, 1965]

Summary

A discussion is given of the time variation in radiance which would be observed across a diffusing glow cloud released in the upper atmosphere. A Gaussian distribution for the contaminant number density is used, and it is assumed that, when chemical reactions occur, either the contaminant density is everywhere very small, or an insignificant quantity of contaminant is consumed.

The cases of chemiluminescence and scattering of the Sun's rays are examined, and the effects on the observed radiance of absorption, re-emission, and scattering of radiation within the cloud are considered. The results may be used to interpret observations on upper atmosphere contaminant releases. It is found that if the cloud is optically thin the radiance distribution is Gaussian for both chemiluminescent and sunlit glow clouds, and the radiance is proportional to the number of cloud particles along the line of sight. Optically thick glow clouds will not be Gaussian, and it is inadmissible to use a method based on a Gaussian distribution in analysis of these clouds.

I. Introduction

This paper is concerned with the derivation of theoretical expressions for the radiance variation across diffusing, contaminant clouds released in the upper atmosphere. Marmo, Pressman, and Aschenbrand (1961) and Shklovskii and Kurt (1960) have used observations on the radiance of contaminant releases to find diffusion coefficients from which the upper atmospheric density is derived. However, these and other workers in the field have paid little attention to the theoretical derivation of cloud radiance from the number density of the cloud particles. In general an expression has been used for radiance which, as will be seen, is equivalent to assuming the cloud to be optically thin. This assumption is not always valid and can lead to serious errors in determining upper atmospheric properties.

The general properties of a spherically symmetric cloud which reacts with the ambient atmosphere are discussed in Section II. Section III contains the derivation of the radiance variation across chemiluminescent glow clouds for which the emission is a result of a chemical reaction of the contaminant with the ambient atmosphere. The number density of the diffusing cloud particles is assumed to be Gaussian, as is done by other workers, and both optically thin and optically thick clouds are treated. In Section IV, the same is done for sunlit glows; in this case, the emission results from scattering of sunlight that is incident on the cloud. Expressions for the total flux from each type of cloud are derived in Section V.

The quantities that describe the radiation field within the cloud, namely integrated intensity I, emission coefficient j, absorption coefficient κ, and albedo

---

* Weapons Research Establishment, Department of Supply, Salisbury, S. Aust.

for single scattering $\tilde{\omega}_0$, are as defined by Chandrasekhar (1960). Following Chamberlain (1961), the integrated intensity from the cloud that is received by an observer will be named the surface radiance, R. The total flux escaping from the cloud as a whole will be denoted by P.

II. Statement of the Problem

The number density of the emitting particles in the diffusing cloud will be taken as (Johnson and Lloyd 1963, eqn. (2))

$$n(r,t) = \frac{N_0}{\pi^{3/2}(r_0^2+4Dt)^{3/2}}\exp\left(-\frac{r^2}{r_0^2+4Dt}\right), \tag{1}$$

where r = radial coordinate,

D = diffusion coefficient,

t = time,

r_0 = initial effective radius,

N_0 = total number of cloud particles.

Equation (1) is the solution of the spherically symmetric diffusion equation which neglects depletion or creation of contaminant particles, namely

$$\frac{\partial^2 n}{\partial r^2}+\frac{2}{r}\frac{\partial n}{\partial r} = \frac{1}{D}\frac{\partial n}{\partial t},$$

with the initial Gaussian radial distribution

$$n = n(0,0)\exp\{-r^2/r_0^2\}. \tag{2}$$

Introducing the dimensionless parameters $\rho = r/r_0$ and $b^2 = [1+4Dt/r_0^2]^{-1}$ simplifies the analysis, and equation (1) can be rewritten

$$n(\rho,b) = n(0,0)\,b^3\exp\{-b^2\rho^2\}, \tag{3}$$

where $n(0,0)$ is the initial peak number density.

Equation (3) assumes that there is no change in the total number of cloud particles with time. A reaction of the form

$$(\text{cloud}) + (\text{ambient}) \xrightarrow{k} (\text{product}) + h\nu \tag{4}$$

will result in a loss of cloud particles at a rate $kn_{\mathrm{C}}n_{\mathrm{A}}$, where k is the reaction rate constant, n_{C} is the number density of the reacting cloud particles, and n_{A} is the number density of the reacting portion of the ambient atmosphere. This loss means that the contaminant number density n given by equation (3) is not correct when reactions are occurring, although there are certain limiting cases for which simple solutions expressible in terms of n are obtainable.

(i) *Case* $n_{\mathrm{C}} \ll n_{\mathrm{A}}$.—Since the absolute changes in n_{C} and n_{A} are of the same order of magnitude, the fractional change in n_{A} is very much less than the fractional change in n_{C}. Therefore the ambient particle density can be assumed to remain constant at its initial value $n_{\mathrm{A}0}$. With this assumption, the relation between n_{C} and n is $n_{\mathrm{C}} = n\exp(-kn_{\mathrm{A}0}t)$, and the reaction rate is $knn_{\mathrm{A}0}\exp(-kn_{\mathrm{A}0}t)$.

(ii) *Case* $4D/r_0^2 \gg kn_A$.—The change in n_C resulting from reaction with the atmosphere is negligible compared with the change in n_C due to diffusion, and is therefore ignored. The cloud particle density is given by its reaction-free approximation, viz. n. Simple general expressions for n_A, and hence the reaction rate $kn_C n_A$, cannot be obtained. However, if changes in n_A resulting from diffusion only need be included, then n_A can be considered a (known) function of time. The reaction rate is now given by the product of n and some function of time. Another sub-case is $4D/r_0^2 \ll kn_C$, which implies that $n_C \gg n_A$, i.e. changes in n_A result almost entirely from reaction with n_C. It can be shown that $n_A = n_{A0}\exp\left(-k\int_0^t n\,dt\right)$, and the reaction rate is therefore $knn_{A0}\exp\left(-k\int_0^t n\,dt\right)$, which is not directly proportional to n.

The emission from the reaction given by (4) is proportional to the reaction rate $kn_C n_A$. Therefore, provided that either $n_C \ll n_A$ or chemical reaction effects are small (kn_A, kn_C both much less than $4D/r_0^2$), the emission is directly proportional to n and the solution of a diffusion equation, omitting reaction terms, can be used in calculating emission even when chemical reactions are present. The first case, $n_C \ll n_A$, seems to be the most important since no restriction is placed on kn_A. The fact that the total number of contaminant cloud particles, and therefore the total flux, may change significantly with time must not be overlooked; that is, when $n_C \ll n_A$ the total flux is proportional to $\exp(-kn_{A0}t)$.

III. CHEMILUMINESCENT CLOUDS

(*a*) *Simple Emission with No Absorption*

It will be assumed that the emission due to chemiluminescence by an element of volume dv of the cloud is given by

$$4\pi j_c n\,dv, \tag{5}$$

where j_c is the emission coefficient for chemiluminescence.

The dimensions of the cloud are much less than the distance of the cloud from the observer, so the surface radiance R is given by the line-of-sight integration

$$R = \int_{-\infty}^{\infty} j_c n\,dl. \tag{6}$$

Using n from equation (3), this gives

$$R = R_0 b^2 \exp(-b^2\sigma^2), \tag{7}$$

where $R_0 = \pi^{\frac{1}{2}} j_c r_0 n(0,0)$ is the zero-time peak radiance for the cloud, $\alpha = Dt/r_0^2$ and $b^2 = (1+4\alpha)^{-1}$ are dimensionless time parameters, s is the coordinate perpendicular to the line of sight, and $\sigma = s/r_0$. The coordinate system is shown in Figure 1.

The time variation in radiance across the cloud, given by equation (7), is plotted in Figure 2. These curves reduce to a single curve if $(1/b^2)(R/R_0)$ is plotted against $b^2\sigma^2$, as has been done in Figure 3. The value of R corresponding to any value of α, σ, and R_0 may be determined from this line when it is used in conjunction with the relation between α and b^2.

(*b*) *Simple Emission and Absorption, with No Re-emission of Absorbed Radiation*

In this case some of the chemiluminescent flux is absorbed by the cloud. It will be assumed that the decrease in intensity as a result of absorption is given by Beer's Law,

$$\mathrm{d}I = -\kappa n \,\mathrm{d}h, \tag{8}$$

where κ is the absorption coefficient.

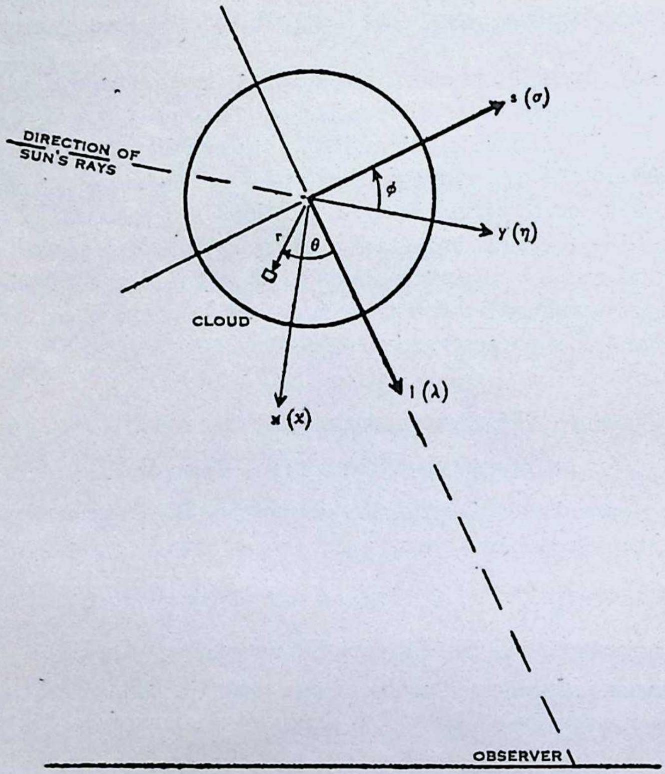

Fig. 1.—Coordinate system. The $z(\zeta)$ axis is perpendicular to the plane of the diagram.

Equation (6) is now replaced by the expression

$$R = \int_{-\infty}^{\infty} j_c n \exp\left(-\int_{l}^{\infty} \kappa n \,\mathrm{d}h\right) \mathrm{d}l. \tag{9}$$

The exponent in the integral represents absorption between the element at l and the observer.

By substituting

$$\tau = \int_l^\infty \kappa n \, \mathrm{d}h,$$

where τ is the optical thickness of the cloud between l and infinity, equation (9) can be integrated to give the radiance as

$$R = (R_0/g)[1 - \exp\{-gb^2 \mathrm{e}^{-b^2\sigma^2}\}], \tag{10}$$

where $g = (\kappa R_0/j_c)$ is a measure of the total optical thickness of the cloud along a line of sight. This equation is illustrated in Figure 3.

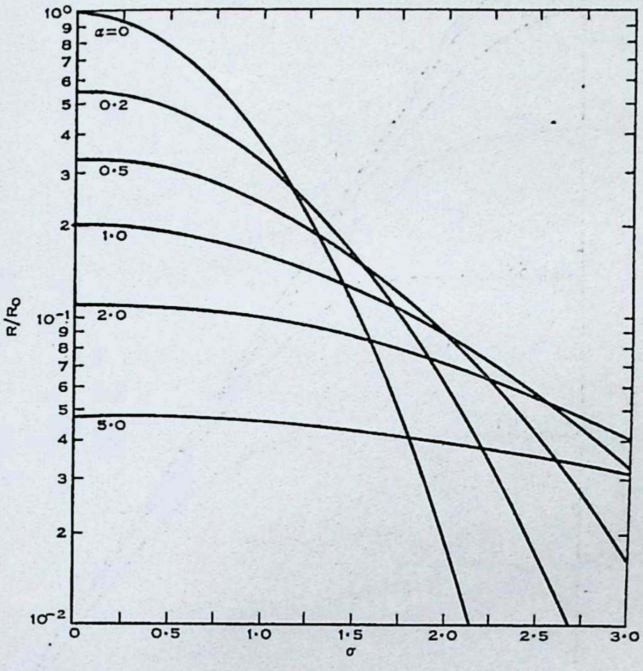

Fig. 2.—Variation with time of the radiance across a non-absorbing chemiluminescent cloud (equation (7)).

When the cloud is optically thin ($gb^2 \ll 1$), the exponential in equation (10) may be expanded giving, to the first order in g,

$$R = R_0 b^2 \exp(-b^2\sigma^2)\,[1 - \tfrac{1}{2} g b^2 \exp(-b^2\sigma^2)]. \tag{11}$$

In the limit of great optical thickness ($gb^2 \gg 1$), equation (10) reduces to

$$R = \frac{R_0}{g} = \frac{j_c}{\kappa}. \tag{12}$$

Plots of equation (10) with $g = 10$ are given in Figure 4 and compared with the radiance variation predicted by equations (7) and (11) for the case $\alpha = 0$. Note that, for optically thick clouds, equation (12) is valid at the centre, while equation (11) tends to the correct result at the edges, which are optically thin. Figure 5 shows how the radiance of an optically thick cloud varies with absorption coefficient. The time variation of centre point radiance ($R_{\max}$) for clouds of different optical thickness is shown in Figure 6.

It is of interest to examine the error introduced by using the first-order optically thin approximation for an absorbing cloud (eqn. (11)). The maximum error in the cloud radiance, which occurs at the centre of the cloud, is given in Table 1 as a percentage of its exact value for different values of gb^2, which may be regarded as an optical thickness parameter.

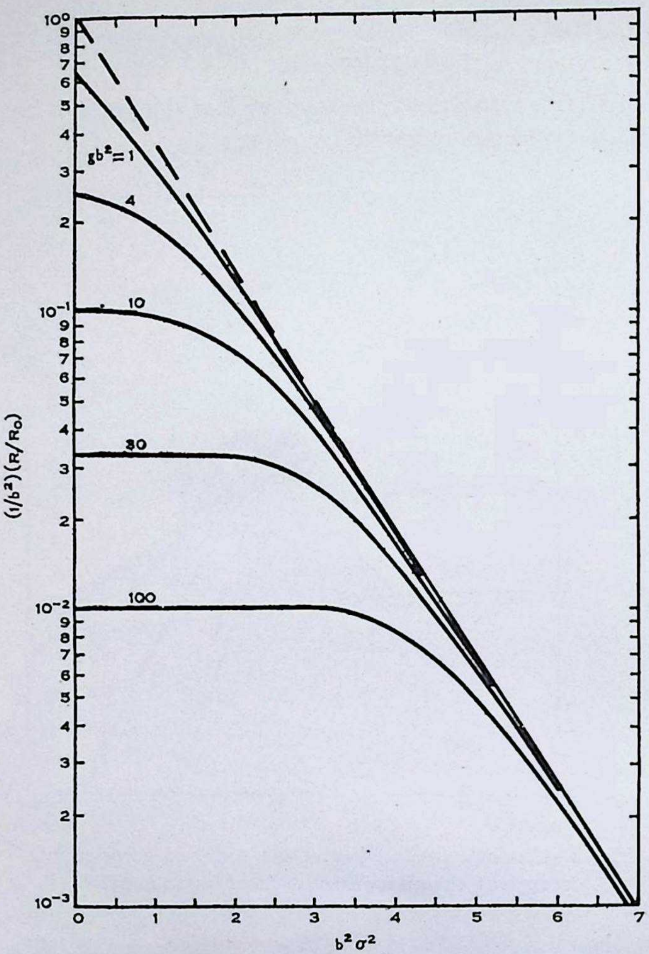

Fig. 3.—Variation of $(1/b^2)(R/R_0)$ with $b^2\sigma^2$ for chemiluminescent glow clouds. — — non-absorbing (equation (7)); —— absorbing (equation (10)).

(c) *Simple Emission and Absorption, with Re-emission of Absorbed Radiation*

In this section it is assumed that a fraction $\tilde{\omega}_0$ of the radiation absorbed by an element of the cloud is re-emitted isotropically; $\tilde{\omega}_0$ is called the albedo for single scattering. For perfect scattering $\tilde{\omega}_0 = 1$.

The emission j from an element of the cloud is the sum of the chemiluminescent emission, given by (5), and the re-emission of absorbed radiation (i.e. scattered radiation), thus:

$$j = j_c + j_s. \tag{13}$$

The emission due to scattering, j_s, is given by

$$j_s = \frac{\kappa\tilde{\omega}_0}{4\pi}\int_{\mathbf{r}'\neq\mathbf{r}} \frac{j(\mathbf{r}')\,n(\mathbf{r}')}{|\mathbf{r}-\mathbf{r}'|^2} \exp\left(-\int_{\mathbf{r}'}^{\mathbf{r}} \kappa n \,\mathrm{d}h\right) \mathrm{d}v'. \tag{14}$$

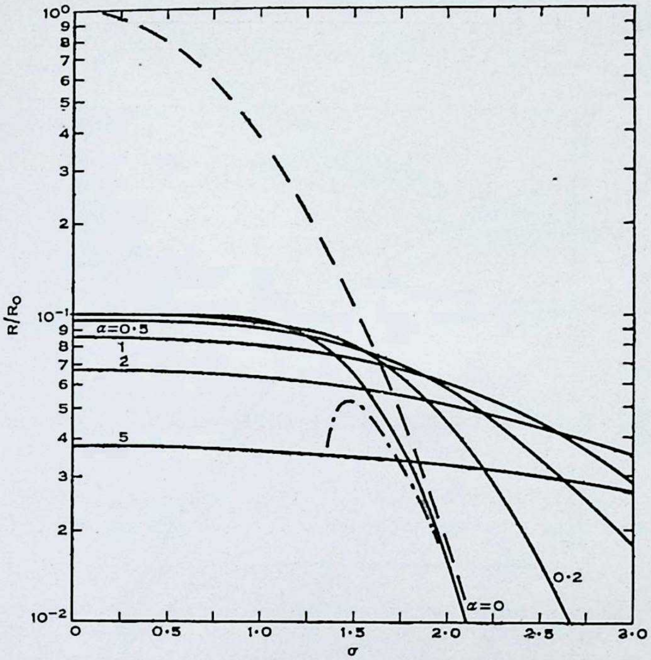

Fig. 4.—Variation with time of the radiance across an absorbing chemiluminescent cloud: —— equation (10) for the case $g = 10$; - - - optically thin approximation (equation (11) with $g = 10$); — — non-absorbing cloud (equation (7)).

Substitution of equation (14) into equation (13) gives a singular integral equation of the second kind in j. The equation does not admit of a general solution. However, if it is assumed that the cloud is optically thin and that, of the two contributions to emission from an element, chemiluminescence is by far the larger, a solution may be found for j by iteration. An outline of the steps made in solving equations (13) and (14), and in integrating equation (15) below, is given by Lloyd (1963).

Equation (9) relates j to the radiance of the cloud, that is,

$$R = \int_{-\infty}^{\infty} jn\left\{1-\kappa\int_{l}^{\infty} n\,\mathrm{d}h + \frac{\kappa^2}{2}\left(\int_{l}^{\infty} n\,\mathrm{d}h\right)^2\right\} \mathrm{d}l, \tag{15}$$

where the exponential has been expanded to second order in κ since the glow-cloud is assumed to be optically thin. Integration of equation (15) gives the variation in radiance across an optically thin chemiluminescent glow cloud with time, including the effects of absorption and re-emission correct to the second order of small quantities in κ, as follows:

$$R/R_0 = b^2\exp(-b^2\sigma^2)-\tfrac{1}{2}b^4\exp(-2b^2\sigma^2)[g-(\tilde{\omega}_0\kappa/j_c)R_0K_1] \\ +\tfrac{1}{4}gb^6\exp(-3b^2\sigma^2)[\tfrac{2}{3}g-(\tilde{\omega}_0\kappa/j_c)R_0\{K_1+K_2\}], \qquad (16)$$

where
$$K_1 = \int_0^1 \frac{\exp a^2b^2\sigma^2}{(2-a^2)^{\frac{1}{2}}}\,\mathrm{d}a, \qquad (17)$$

and
$$K_2 = \int_0^1\int_0^1 \frac{\exp\{-b^2\sigma^2(c^2-1)(1+a)^2(1+a^2)^{-1}\}}{(1+a^2)^{\frac{1}{2}}[3+(c^2-1)(1+a)^2(1+a^2)^{-1}]}\,\mathrm{d}a\,\mathrm{d}c. \qquad (18)$$

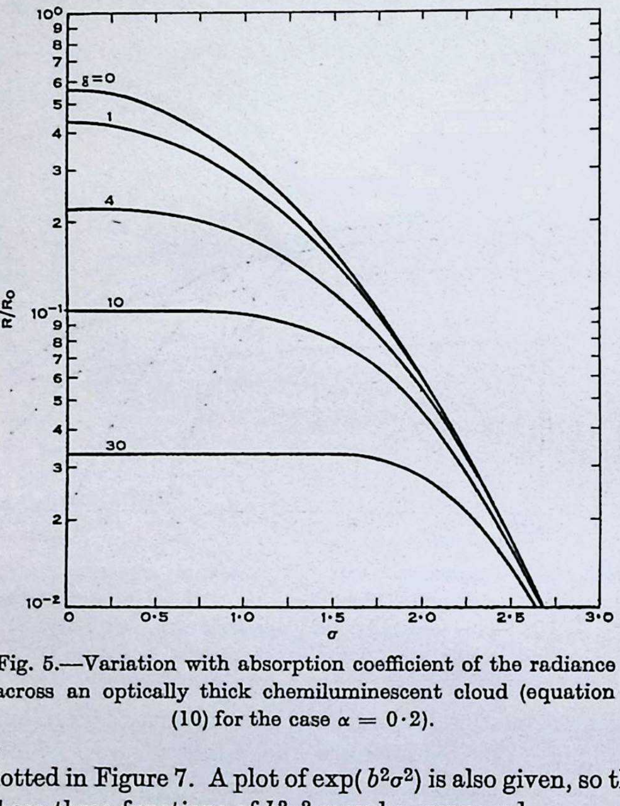

Fig. 5.—Variation with absorption coefficient of the radiance across an optically thick chemiluminescent cloud (equation (10) for the case $\alpha = 0\cdot2$).

K_1 and K_2 are plotted in Figure 7. A plot of $\exp(b^2\sigma^2)$ is also given, so that the relative magnitudes of these three functions of $b^2\sigma^2$ may be compared.

IV. Sunlit Clouds

It will be assumed in this section that the radiance of the diffusing cloud is due to isotropic scattering (or absorption and re-emission) of the Sun's incident rays. If I_∞ is the intensity of the Sun's radiation falling on the cloud, then the intensity of radiation at an element of the cloud whose coordinates are (x, y, z) is I_s, where

$$I_s = I_\infty\exp\left(-\int_{-\infty}^{y}\kappa n\,\mathrm{d}y\right), \qquad (19)$$

and y is the coordinate in the direction of the Sun's rays (see Fig. 1). The emission from this element is

$$\kappa\tilde{\omega}_0 I_s n \,\mathrm{d}v. \tag{20}$$

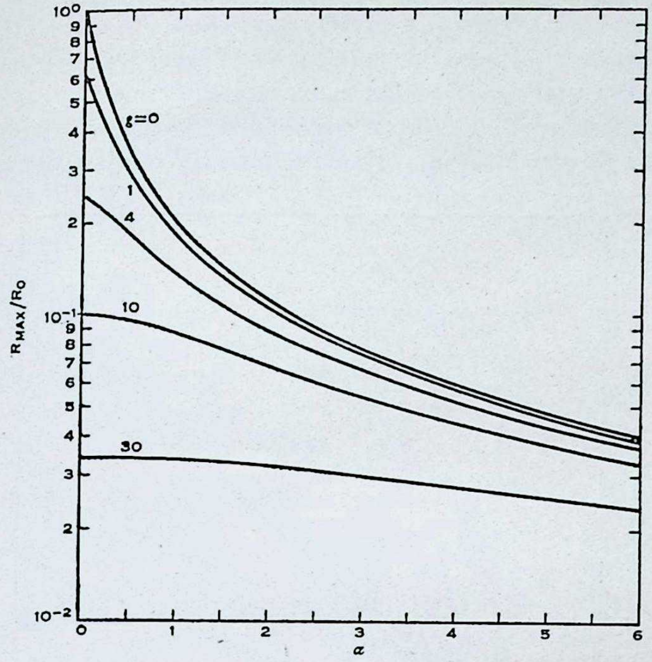

Fig. 6.—Variation of centre-point radiance with time for an absorbing chemiluminescent cloud (equation (10) with $\sigma = 0$).

TABLE 1

ERROR IN FIRST-ORDER APPROXIMATION FOR CLOUD RADIANCE

gb^2	Error (%)
1·25	35
1·00	21
0·75	12
0·5	6
0·25	2
0·00	0

Secondary scattering will be neglected. With this assumption the radiance distribution across a sunlit glow cloud is given, from equations (9) and (19), and from (20), as

$$R = \frac{\tilde{\omega}_0 \kappa I_\infty}{4\pi j_c}\frac{R_0 b^2}{\pi^{\frac{1}{2}}}\mathrm{e}^{-b^2\sigma^2}\int_{-\infty}^{\infty}\mathrm{e}^{-\lambda^2}\exp\Big[-\tfrac{1}{2}gb^2\,\mathrm{e}^{-b^2(\sigma^2+\zeta^2)}$$

$$\times\Big(\operatorname{erfc}\lambda+(\mathrm{e}^{b^2\sigma^2\cos^2\phi}\,\mathrm{e}^{-\lambda\cos\phi(\lambda\cos\phi-2b\sigma\sin\phi)}\{1+\operatorname{erf}(\lambda\sin\phi+b\sigma\cos\phi)\}\Big)\Big]\,\mathrm{d}\lambda, \tag{21}$$

where ϕ is the angle between the direction of the Sun's rays and the normal to the observer's line-of-sight, and $\zeta = z/r_0$. The equation has been written in terms of the peak radiance of the equivalent chemiluminescent cloud so that a comparison between the radiance profiles of chemiluminescent and sunlit glow clouds may be easily made. The factor $(\tilde{\omega}_0 \kappa I_\infty / 4\pi j_c)$ is the ratio of the emission by a given number of cloud particles for sunlit and chemiluminescent glow clouds.

It is not possible to obtain an analytic expression for the integral in equation (21). The equation may be integrated numerically, and Figure 8 presents the result for the case $\phi = 0$, $g = 10$, and $\alpha = 0 \cdot 2$. The asymmetrical, crescent shape of the isophots results from a reduction of intensity of the incident Sun's rays by absorption as they pass through the cloud. Also shown in the figure are the isophots and the radiance cross section for the equivalent chemiluminescent cloud (eqn. (10)); this has the same radiance gradient in the optically thin regions. The radiance contour for the sunlit cloud in Figure 8 is qualitatively similar to that observed by Groves (1963, Fig. 5) for a sunlit cloud produced by the release of 18 kg of explosive at 103 km altitude, i.e. a non-Gaussian radiance distribution with an asymmetric peak. This large contaminant release therefore produced an optically thick glow cloud.

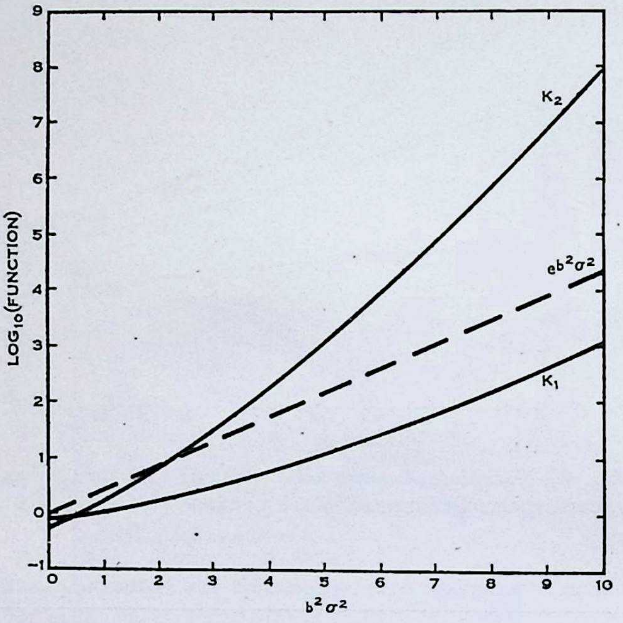

Fig. 7.—The functions K_1 and K_2 (equations (17) and (18)).

An approximation for optically thin clouds is obtained by expanding the exponential in equation (21) and retaining terms to first order in g. This may be integrated to give

$$R = \frac{\tilde{\omega}_0 \kappa I_\infty}{4\pi j_c} R_0 b^2 \exp\{-b^2(\sigma^2+\zeta^2)\}\Big(1-\tfrac{1}{2} g b^2 \exp\{-b^2(\sigma^2+\zeta^2)\}$$

$$\times [1+(\epsilon/\sqrt{2})\sec\phi \exp(\epsilon^2 b^2 \sigma^2)\{1+\operatorname{erf}\epsilon b\sigma\}]\Big), \qquad (22)$$

where $\epsilon^2 = 2(1+\sec^2\phi)^{-1}$.

Isophots for an optically thin sunlit cloud, and the radiance contour in the direction of the Sun's rays for $\phi = 0$, $g = 10$, and $\alpha = 5$, are presented in Figure 9. Also shown in the figure are the isophots and radiance contour for the equivalent chemiluminescent glow cloud (eqn. (11) with $g = 10$, $\alpha = 5$). Note that the isophots for the sunlit glow cloud are very nearly circular. The circles are not concentric but are displaced in the direction of the Sun, the brighter isophots being displaced further. Comparison of the radiance contours for sunlit and chemiluminescent clouds shows that the two are very similar, and therefore optically thin sunlit clouds may be analysed to a first approximation using the equivalent expression for chemiluminescent clouds. This is, in fact, what other workers have done without having justified their action.

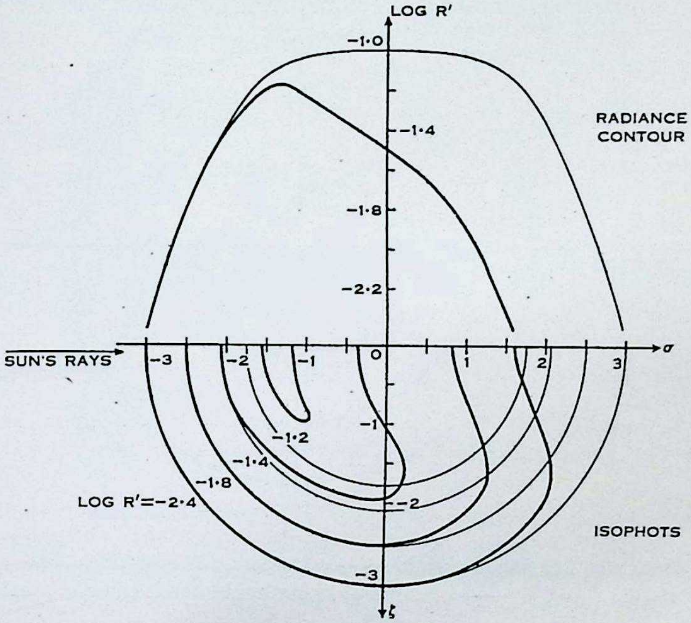

Fig. 8.—Optically thick sunlit cloud: —— equation (21) with $R' = R[4\pi j_c/\kappa\tilde{\omega}_0 I_\infty R_0]$, $g = 10$, $\alpha = 0\cdot2$, $\phi = 0°$; —— equivalent chemiluminescent cloud (equation (10) with $R' = R/R_0$, $g = 10$, $\alpha = 0\cdot2$).

The maximum error introduced by the first-order approximation (eqn. (22)) is given by Table 1 with g replaced by $2g[1+(1/\pi)\cot^{-1}(\sec\phi)]$.

V. Total Flux Emitted by the Cloud

For a glow whose emission is direction independent, the total flux emitted, P, is given by

$$P = 4\pi \int_{-\infty}^{\infty} \int_{-\infty}^{\infty} R \,\mathrm{d}s\,\mathrm{d}z. \tag{23}$$

Since the chemiluminescent clouds considered are spherically symmetric, equation (23) may be applied to them. It may also be applied to optically thin sunlit clouds, when the intensity of the Sun's incident rays is not decreased appreciably by scattering within the cloud.

For a non-absorbing chemiluminescent cloud, substitution of equation (7) into (23) shows that the total flux has the time-independent value

$$P_0 = 4\pi^2 r_0^2 R_0. \tag{24}$$

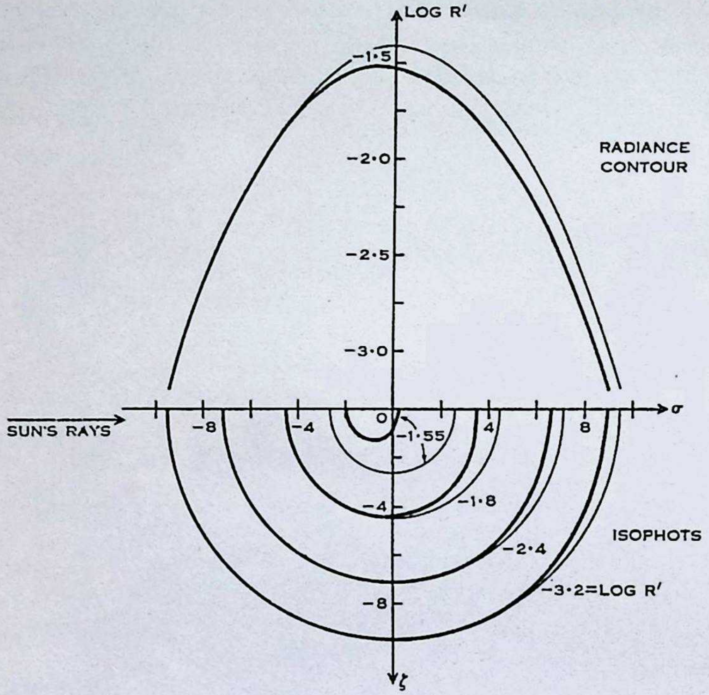

Fig. 9.—Optically thin sunlit cloud: —— equation (22) with $R' = R[4\pi j_c/\kappa\tilde{\omega}_0 I_\infty R_0]$, $g = 10$, $\alpha = 5$, $\phi = 0°$; —— equivalent chemiluminescent glow (equation (11) with $R' = R/R_0$, $g = 10$, $\alpha = 5$).

For an absorbing chemiluminescent cloud of arbitrary optical thickness with no re-emission of absorbed radiation, represented by equation (10), the integration is effected by making the substitution

$$\xi = gb^2 \mathrm{e}^{-b^2\sigma^2}, \tag{25}$$

which reduces the integral to

$$P = \frac{P_0}{gb^2}\int_0^{gb^2} \frac{1-\mathrm{e}^{-\xi}}{\xi}\,\mathrm{d}\xi. \tag{26}$$

This gives the total flux emitted by an absorbing chemiluminescent cloud of arbitrary optical thickness as

$$P = (P_0/gb^2)[C + \ln gb^2 - \mathrm{ei}(-gb^2)], \tag{27}$$

where C is Euler's constant $(0\cdot577\,215\ldots)$, and $\mathrm{ei}(-x) = -\int_x^\infty \frac{\mathrm{e}^{-\xi}}{\xi}\,\mathrm{d}\xi$ is the exponential integral (Lowan 1940). For an optically thin cloud ($gb^2 \ll 1$) equation (27) reduces to

$$P = P_0(1-\tfrac{1}{4}gb^2). \tag{28}$$

Plots of equation (27) for different values of g are given in Figure 10.

It should be noted that the total flux emitted by an optically thick chemiluminescent cloud is not the same as the sum of the chemiluminescent fluxes emitted by all the elements of the cloud. However, as the cloud expands, the total amount of such self-absorption decreases, and the total flux emitted tends to the value for a non-absorbing cloud. It is seen that the time dependence of the total flux can give indications both of the optical thickness of the cloud and of the rate of the reactions, if any, occurring within the cloud. For re-emission with $\tilde{\omega}_0 = 1$ (i.e. perfect scattering) there is no net absorption of radiation, and the total flux emitted is the same as for a non-absorbing cloud. Of course, the radiance variation across the cloud is not the same as in the non-absorbing case.

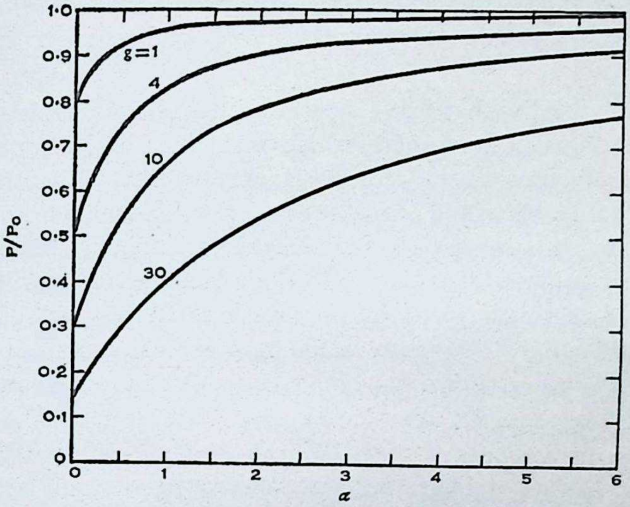

Fig. 10.—Variation with time of the total flux emitted by optically thick chemiluminescent clouds (equation (27)). Note: For sunlit clouds $g \to 2g\{1+(1/\pi)\cot^{-1}(\sec\phi)\}$

For the optically thin sunlit cloud which was considered in Section IV, the relevant integration is effected by changing to polar coordinates. The result obtained is

$$P = \left(\frac{\kappa\tilde{\omega}_0 I_\infty}{4\pi j_c}\right)P_0\left[1-\frac{gb^2}{2}\left\{1+\frac{\cot^{-1}(\sec\phi)}{\pi}\right\}\right]. \tag{29}$$

Note the formal similarity of equation (29) to the optically thin approximation for chemiluminescent clouds (eqn. (28)); the effective optical thickness for an optically thin sunlit glow cloud is greater than for the equivalent optically thin chemiluminescent glow cloud by the factor $2\{1+(1/\pi)\cot^{-1}(\sec\phi)\}$.

It is of interest to note that the sunlit sodium cloud observed at 430 km altitude by Shklovskii and Kurt (1960) behaved as predicted by equation (29), i.e. there is a rapid initial increase in total flux, tending to an asymptotic value at large time.

VI. Discussion

The results of Sections III, IV, and V all ignore consumption of the contaminant particles. Care must be taken when the results in these sections are used that one of the restrictive conditions given in Section II is obeyed. In particular, when the contaminant particle density is small, all results in Sections III, IV, and V must be multiplied by the time-dependent factor $\exp(-kn_{A0}t)$ (see Section II). Even when the restrictive conditions are not satisfied, the results of Sections III, IV, and V will give an indication of the form of the results that may be expected for more general and more complex reaction mechanisms. In particular, the continual re-occurrence of dimensionless parameters (e.g. b, g, $\kappa\tilde{\omega}_0 I_\infty/4\pi j_c$) and the grouping of these parameters into expressions such as gb^2 and $b^2\exp(-b^2\sigma^2)$ should be noted; these parameters, and similar groupings, are likely to be present in a more general treatment.

Most of the results that have been derived above involve rather complex functions of the diffusion coefficient, which makes the use of such expressions in analysing results of observations on the radiance of glow clouds very difficult. A simple test for whether the cloud is non-absorbing, or optically very thin, is indicated by equation (7), and involves plotting $\log R$ against s^2. Should the cloud be optically thin, i.e. the cloud radiance distribution be Gaussian, the points will lie on a straight line. An example of this is given by Johnson and Lloyd (1963, Fig. 2). It is, in practice, very difficult to determine whether a non-Gaussian cloud radiance distribution is due to optical thickness effects or to reaction mechanisms that are not of the simple type considered in Section II.

VII. Acknowledgments

The author wishes to thank Mr L. M. Sheppard of the Weapons Research Establishment for many helpful discussions pertaining to this work, and the Chief Scientist, Department of Supply, for permission to publish this paper.

VIII. References

Chamberlain, J. W. (1961).—"Physics of the Aurora and Airglow." (Academic Press: London.)

Chandrasekhar, S. (1960).—"Radiative Transfer." (Dover Publications: New York.)

Groves, G. V. (1963).—*J. Geophys. Res.* **68**: 3033–47.

Johnson, E. R., and Lloyd, K. H. (1963).—*Aust. J. Phys.* **16**: 490–9.

Lloyd, K. H. (1963).—Weapons Research Establishment Tech. Note HSA 84.

Lowan, A. N. (1940).—"Tables of Sine, Cosine and Exponential Integrals." Vol. I. (Federal Works Agency: New York.)

Marmo, F. F., Pressman, J., and Aschenbrand, L. M. (1961).—*Planet. Space Sci.* **3**: 139–57.

Shklovskii, I. S., and Kurt, V. G. (1960).—*ARS Jl.* **30**: 662–7.

MAGNETOHYDRODYNAMIC IONIZING SHOCK WAVES IN A CONDUCTING MEDIUM

By B. Green* and R. M. May*

[*Manuscript received March* 9, 1965]

Summary

We present numerical calculations for the flow parameters (velocity, density, pressure, etc.) in a magnetohydrodynamic shock wave propagating in a conducting medium. The effect of ionization in the shock front is included. The results are presented graphically for a complete range of the initial magnetic field strength and direction, and for several arbitrary values of the ionization energy of the downstream fluid.

I. Introduction

Kemp and Petschek (1959) (hereafter called K.P.) have made a detailed investigation of the propagation of a magnetohydrodynamic shock wave in a conducting medium. Following methods made familiar by the study of ordinary gas dynamic shocks, K.P. divide the flow into four regions: the undisturbed gas ahead of the shock front; the steady flow region behind the shock front (containing the high temperature gas sample suitable for plasma studies); the expansion wave; and the steady flow region behind the expansion wave, which joins to the boundary conditions at the end of the shock tube. K.P. derive quantitative results for the variation of all flow parameters (velocity, density, temperature, etc.) throughout all these regions. They consider arbitrary orientation of the magnetic field ahead of the shock front: in this regard their work is an extension of that of Bazer (1958), who considers a purely axial field ahead of the front.

In the present paper, we extend the work of K.P. by including the possibility of a change in internal energy of the gas through the shock front. Such an internal energy change would occur, for example, if the conducting gas were further ionized by the passage of the shock wave.

It is to be emphasized that both K.P. and the present work assume that the gas ahead of the shock front is "conducting". The case of an ionizing magnetohydrodynamic shock wave propagating into a "non-conducting" medium, is much more complex (Kulikovski and Lyubimov 1960; Gross and Kunkel 1962; Chu 1964; May and Tendys 1965). We need only note that the criterion (May and Tendys 1965) for the undisturbed gas ahead of the front to be deemed "conducting" is that its magnetic diffusivity $1/\sigma\mu$ be very much less than its viscosity ν and thermal conductivity κ (see Lehnert 1958 for a table giving ν, κ, and $1/\mu\sigma$ for several gases at various densities and temperatures), that is,

$$1/\mu\sigma \ll \nu,\ \kappa. \tag{1}$$

This criterion can well be fulfilled even if the gas ahead of the shock front is only

---

* Theoretical Department, School of Physics, University of Sydney.

partly ionized (e.g. in a gas of hydrogen at density 10^{16} molecules/cm^3, the criterion is fulfilled at 2% ionization). Thus there is some practical point in extending the analysis of K.P. to include the possibility of further ionization of an already "conducting" gas by the passage of a magnetohydrodynamic shock wave.*

In Section II we describe the equations and method of treatment used to derive our results for the various flow parameters. Since the analysis is very similar to that of K.P., we confine ourselves to an outline. In Section III, the results are presented and discussed. These results are mainly in the form of a series of graphs for the various flow quantities.

Before proceeding to the results, we mention the recent work of Taussig (1964), who has also introduced the internal energy change term into a study of magnetohydrodynamic ionizing shock waves. However, Taussig considers only "normal" shocks in which the magnetic field in the undisturbed region ahead of the shock front is perpendicular to the front; while we (as did K.P.) consider arbitrary orientations of this field, that is, we have $\frac{1}{2}\pi \geqslant \theta \geqslant 0$ (Taussig has $\theta = 0$), where θ is defined by equation (2) in Section II. On the other hand, we restrict ourselves to conducting media, so that ahead of the shock front we must have the electric field zero; whereas Taussig considers the general case where the medium ahead of the shock front need not be conducting, and hence the electric field need not be zero. The relation between the present work and that of Taussig and earlier authors is summarized schematically in Table 1.

TABLE 1

COMPARISON OF PRESENT WORK WITH THAT OF EARLIER AUTHORS

Authors	Angle of Initial Magnetic Field θ (from eqn. (2))	Conductivity ahead of Shock Front	Internal Energy Change through Shock Front
Bazer (1958)	0	∞	0
Kemp and Petschek (1959)	$0<\theta<\frac{1}{2}\pi$	∞	0
Taussig (1964)	0	finite	finite
Present work	$0<\theta<\frac{1}{2}\pi$	∞	finite

II. ANALYSIS

Since our program differs from that of K.P. only by the inclusion of a change in internal energy through the shock front, we present only an outline of the method of analysis and refer to K.P. for details.

We consider plane flow in the X–Y plane, with all the flow quantities being functions only of the variable X. This idealization gives a reasonable approximation to the usual experimental conditions of flow in the annulus between two concentric cylinders. X corresponds to the axial, Y to the azimuthal, and Z to the radial direction. It is also assumed that the gas pressure is isotropic, and that the criterion (1) is satisfied so that the medium is conducting ahead of the shock front. All calculations are made in a reference frame attached to the shock front.

---

* In the AVCO experiments considered by K.P., and all other similar experiments so far performed, the analysis that ignores internal energy changes is adequate, either because the gas ahead of the front is already fully ionized, or because the temperatures behind the front are sufficiently large to dwarf the internal energy change.

The analytical solution of the problem has five parameters which may be chosen as:

(*a*) The angle of orientation θ of the initial magnetic field,

$$\theta = \tan^{-1}(B_{Y1}/B_X), \tag{2}$$

where B_{Y1} is the azimuthal magnetic field ahead of the shock (region 1), and B_X is the axial field, which is constant ($\nabla . \mathbf{B} = 0$).

(*b*) The ratio of the shock speed U_S to the fast sound speed c_f in the undisturbed gas ahead of the shock front, i.e. the ratio U_S/c_f.

(*c*) The ratio of gas pressure to magnetic pressure in the undisturbed gas, i.e. the ratio $p_1/(B_1^2/2\mu)$. B_1 is the modulus of the magnetic field in region 1, or $B_1^2 = B_{Y1}^2 + B_X^2$.

(*d*) The ratio of specific heats γ in the ionized gas behind the shock.

(*e*) The ratio P of the change in internal energy through the shock front to the magnetic energy ahead of the front,

$$P = \rho_1 \, \mu(\Delta e)/B_1^2. \tag{3}$$

In the limit $P = 0$, our calculations reduce to those of K.P.

Although the general theory is valid for arbitrary values of these parameters, in order to perform the numerical computations, we have specified the parameters (*c*) and (*d*) by choosing

$$p_1/(B_1^2/2\mu) = 0 \tag{4}$$

and

$$\gamma = 5/3. \tag{5}$$

Both these choices will be good approximations to most experimental conditions. Notice that the choice (4) implies that the fast sound speed c_f is now the Alfven speed, that is, $c_f = (B_1^2/\rho_1 \, \mu)^{\frac{1}{2}}$.

With the simplifications described above, the flow becomes one of a perfect gas with infinite conductivity. In the reference frame we have chosen, physical quantities vary only with X; the velocity and magnetic field vectors have only X components (u, B_X) and Y components (v, B_Y); the fluid pressure and density are p and ρ respectively. (We use rationalized MKS units, with μ denoting the permeability of free space.) The appropriate differential equations for the flow and the magnetic field are now Maxwell's equations and the compressible, perfect gas, fluid-flow equations with the magnetic force and energy terms added.

Figure 1 is a displacement–time diagram showing the various flow regions of the shock wave. For the equations relating quantities ahead of the shock front (region 1) to those behind the front (region 2), we have the usual jump relations, which express conservation of mass, longitudinal and transverse momentum, and energy. Our inclusion of a change in internal energy through the front alters only the energy equation; all the other equations remain as in K.P. Allowing for a change in internal energy, Δe, the energy conservation equation (K.P. equation (24)) now reads

$$\rho_1 u_1\left\{\frac{\gamma}{\gamma-1}\frac{p_1}{\rho_1}+\tfrac{1}{2}(u_1^2+v_1^2)\right\}+\frac{B_{Y1}}{\mu}(B_{Y1}u_1-B_X v_1)$$

$$=\rho_2 u_2\left\{\frac{\gamma}{\gamma-1}\frac{p_2}{\rho_2}+\tfrac{1}{2}(u_2^2+v_2^2)+\Delta e\right\}+\frac{B_{Y2}}{\mu}(B_{Y2}u_2-B_X v_2). \qquad (6)$$

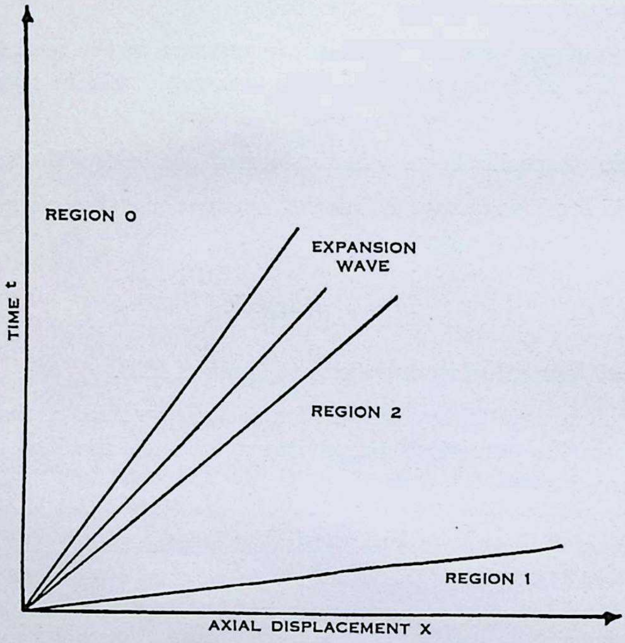

Fig. 1.—X–t diagram showing flow regions.

The suffix 1 denotes region 1 ahead of the front, and the suffix 2 denotes region 2. The other jump relations connecting the flow parameters in region 1 to those in region 2 are identical with K.P. equations (19)–(23).

The steady flow region 2 behind the shock front is joined to the back of the shock tube (region 0) by a simple expansion wave. We assume that no further change in internal energy takes place behind the shock front.* Thus the expansion wave is described by the K.P. set of three simultaneous first-order differential equations, together with one algebraic equation (K.P. equations (9)–(12)). This set of equations is solved by numerical integration, beginning from region 2 and terminating with a boundary condition enforced by the back wall of the shock tube, namely, that in the laboratory frame there should be no axial motion in region 0. This boundary condition can be achieved either

---

* This point is discussed further by Taussig (1965).

(i) by a vacuum in region 0 ($p_0 = 0$, $\rho_0 = 0$), or

(ii) by having no axial flow in region 0 ($u_0 = U_S$ in the shock-centred frame).

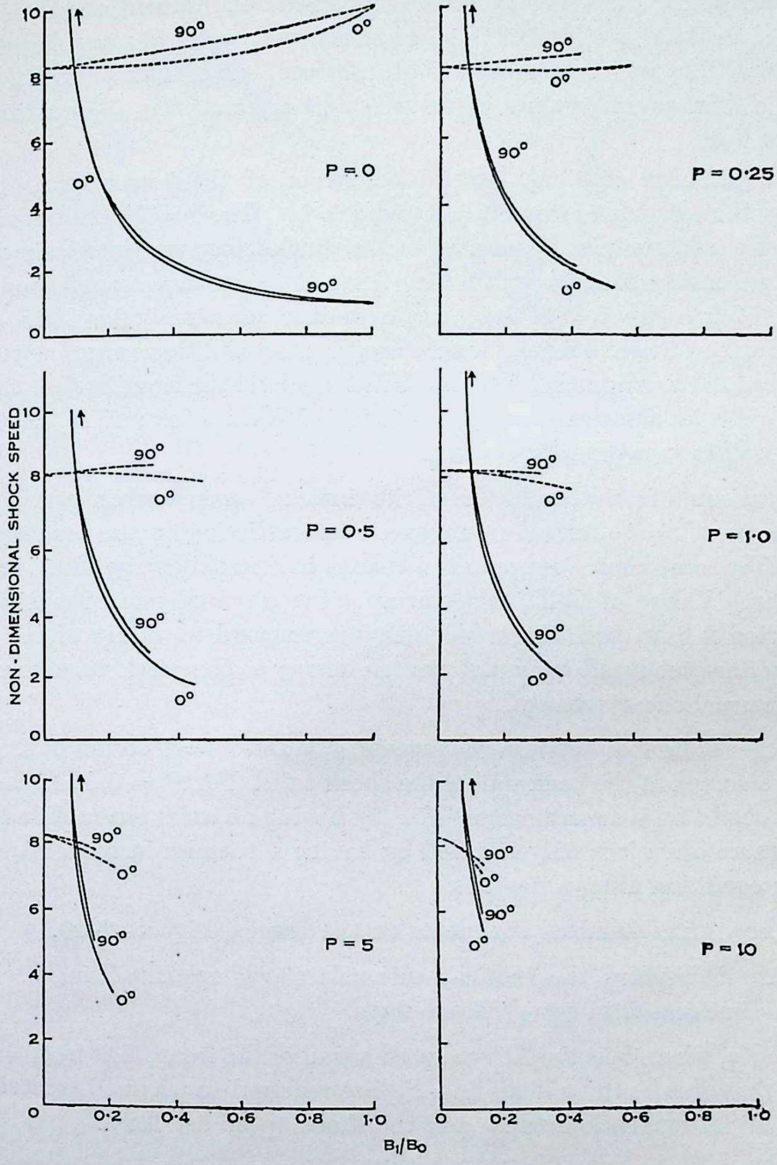

Fig. 2.—Non-dimensional shock speed U_S/b_1 (solid curves) and $10U_S/b$ (dashed curves) versus B_1/B_0 for $\theta = 0$ and 90°, and various values of P.

Thus a complete solution for the flow parameters in all regions is obtained by first specifying the five parameters (*a*)–(*e*) above, then obtaining the flow in region 2 behind the shock front by using the jump relations described above, and finally obtaining the flow in region 0 by integration through the expansion wave. We now proceed to the results obtained from this program.

III. Results

The results for the significant flow parameters in various regions are plotted against the ratio B_1/B_0, where B_1 is the magnitude of the field ahead of the shock front, and B_0 is the magnitude of the field at the back wall. We occasionally refer to the "drive field", by which we mean the difference $B_0 - B_1$. Each parameter is plotted against B_1/B_0 for several values of the remaining parameters θ (equation (2)) and P (equation (3)).

The qualitative and quantitative behaviour of the flow with $\frac{1}{2}\pi > \theta > 0$ is bounded by the extreme cases of $\theta = 0$ and $\theta = \frac{1}{2}\pi$. The $\theta = \frac{1}{2}\pi$ case, corresponding to a magnetic field completely parallel to the shock front, presents a simple picture, namely, a piston-like shock wave moving down the tube causing axial motion of the gas ahead of it. The $\theta = 0$ case, corresponding to a magnetic field completely perpendicular to the wave front, is more complicated and there are now two possible flow regimes. If the azimuthal field B_{Y2} is finite behind the front, we get the "switch-on" shock with its associated fluid rotation behind the front; if $B_{Y2} = 0$, the flow is as in an ordinary gas dynamic shock.

Comparison of the results for finite internal energy changes, $P \neq 0$, with the special case $P = 0$ shows the existence of a restriction on the permissible values of B_1/B_0. (We recall that P represents a change in internal energy, due to an increase in ionization.) Values of B_1/B_0 that correspond to a non-physical negative temperature in region 2 have been discarded; they correspond to values of the drive field $B_0 - B_1$ that are too small to impart enough energy to the shock wave to provide the required internal energy change.

Another difference between the cases $P \neq 0$ and $P = 0$ occurs in the boundary condition enforced at the back wall of the shock tube. For $P = 0$, K.P. find that this boundary condition is sometimes satisfied by having no axial gas motion in region 0, although more often it is only satisfied by having a vacuum in region 0; for $P \neq 0$ the latter condition always prevails.

We now make itemized comments on the graphs, Figures 2–10.

Figure 2 displays the (non-dimensional) shock speed. This shock speed is made non-dimensional in two different ways.

(i) U_S/b_1, where b_1 is the Alfven speed ahead of the front, that is, $b_1 = (B_1^2/\rho_1 \mu)^{\frac{1}{2}}$. It is seen that greater drive fields (B_0–B_1) are required to produce greater ionization when the initial magnetic field B_1 and the shock speed are fixed.

(ii) U_S/b_*, where $b_* = (B_0^2/\rho_1 \mu)^{\frac{1}{2}}$. These curves show small variation with B_1/B_0. However, for a fixed U_S and B_0, smaller initial fields B_1 (i.e. greater drive fields, as before) are required to produce greater ionization. As in K.P., the limiting value of this quantity for $B_1/B_0 = 0$ can be calculated. For $P = 0$ this limit is approximately 8·16, and for $P \neq 0$ and increasing, this limit decreases slowly.

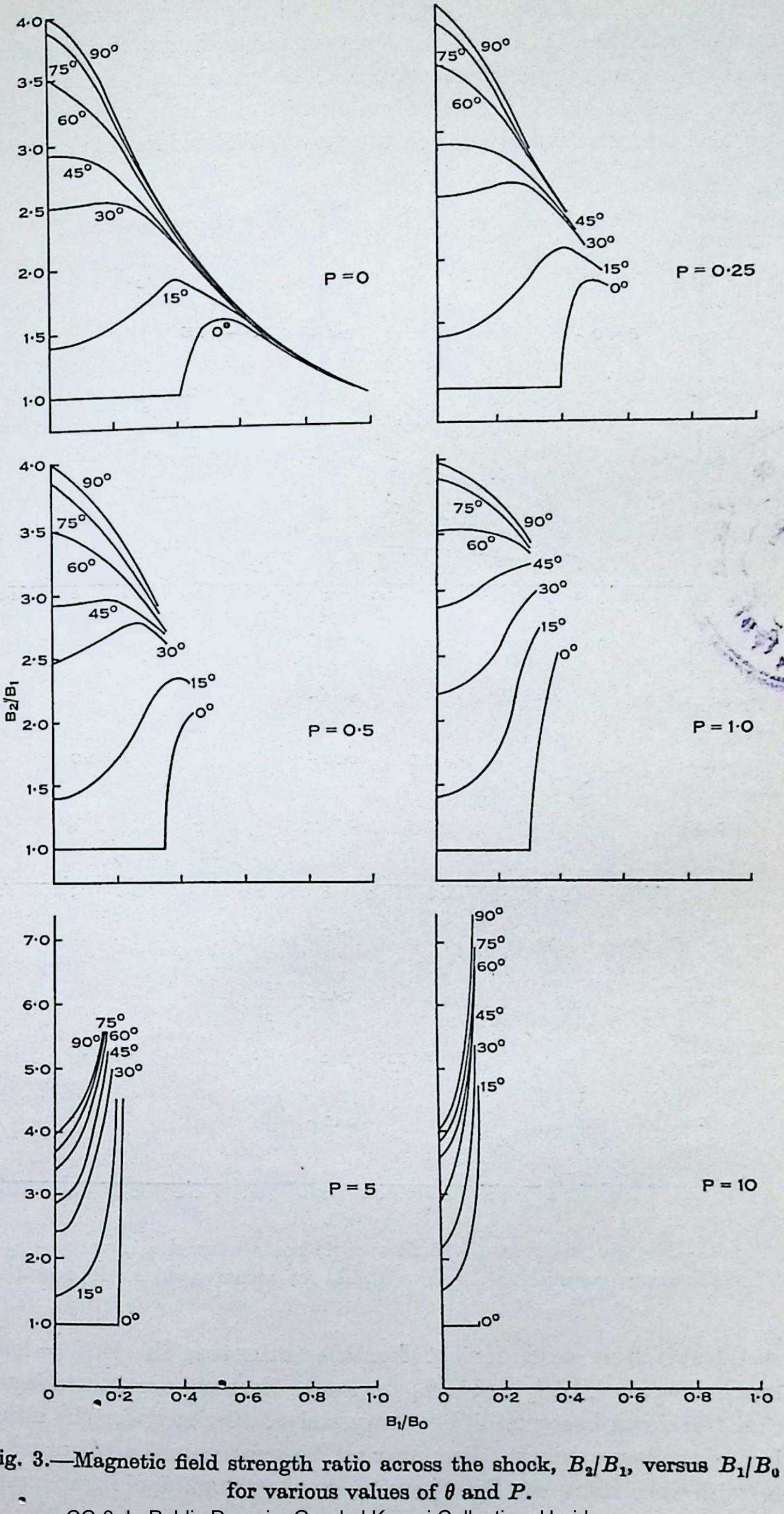

Fig. 3.—Magnetic field strength ratio across the shock, B_2/B_1, versus B_1/B_0 for various values of θ and P.

The "knee" in the B_2/B_1 curves (Fig. 3), clearly seen for most of the $\theta = 0$ cases, gives the transition between the switch-on and ordinary shock regions. These latter regions lie towards lower B_1/B_0 values. This transition cannot be seen for the $P = 10$ curve, because the physical switch-on region is now very small; the non-physical portion continually expands as the value of P is increased, until it almost

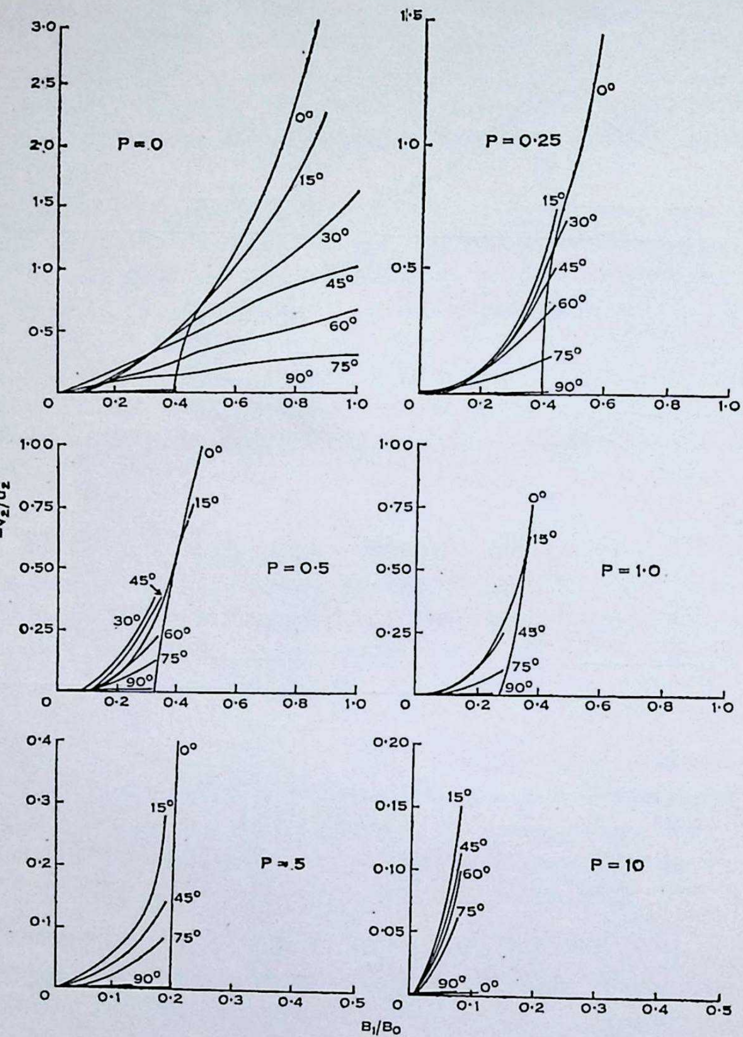

Fig. 4.—Negative tangent of the flow angle behind the shock wave, $-v_2/u_2$ (in laboratory coordinates), versus B_1/B_0 for various values of θ and P.

fills the total switch-on shock region. For the transverse shock ($\theta = 90°$), there is a stage reached where B_2/B_1 and ρ_2/ρ_1 no longer decrease for increasing B_1/B_0 but increase, i.e. the shock becomes highly compressive. Similarly for the other θ values, the maxima of the lower θ curves disappear as P increases until all θ curves are strictly increasing with increasing B_1/B_0. Conversely, very high ionization energy values

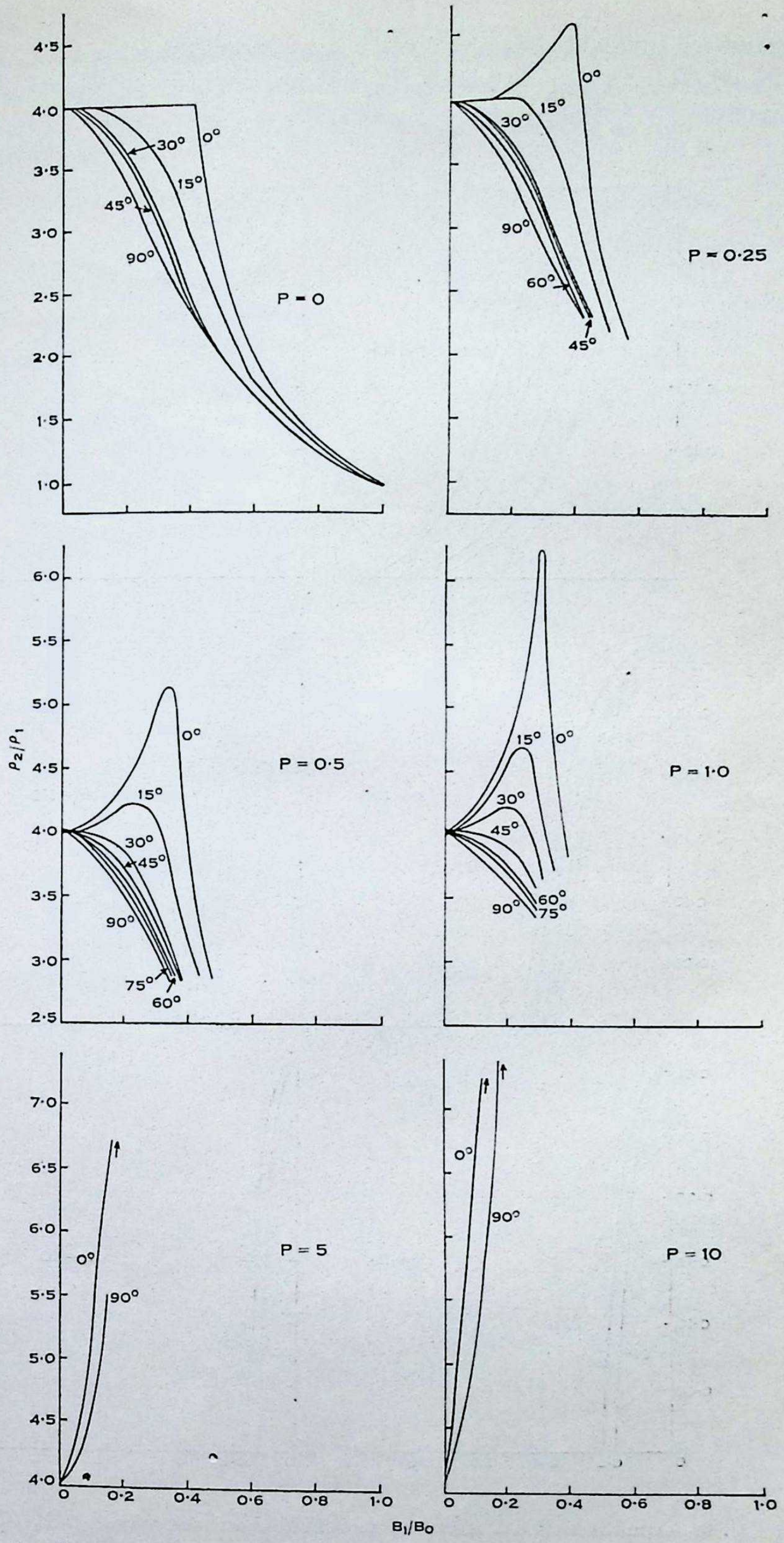

Fig. 5.—Density ratio across the shock wave, ρ_2/ρ_1, versus B_1/B_0 for various values of θ and P.

can be produced by highly compressive (i.e. very strong) shock waves. The limiting values for B_2/B_1 and ρ_2/ρ_1 when $B_1/B_0 = 0$ are slightly increased on increasing P (all $\theta \neq 0$).

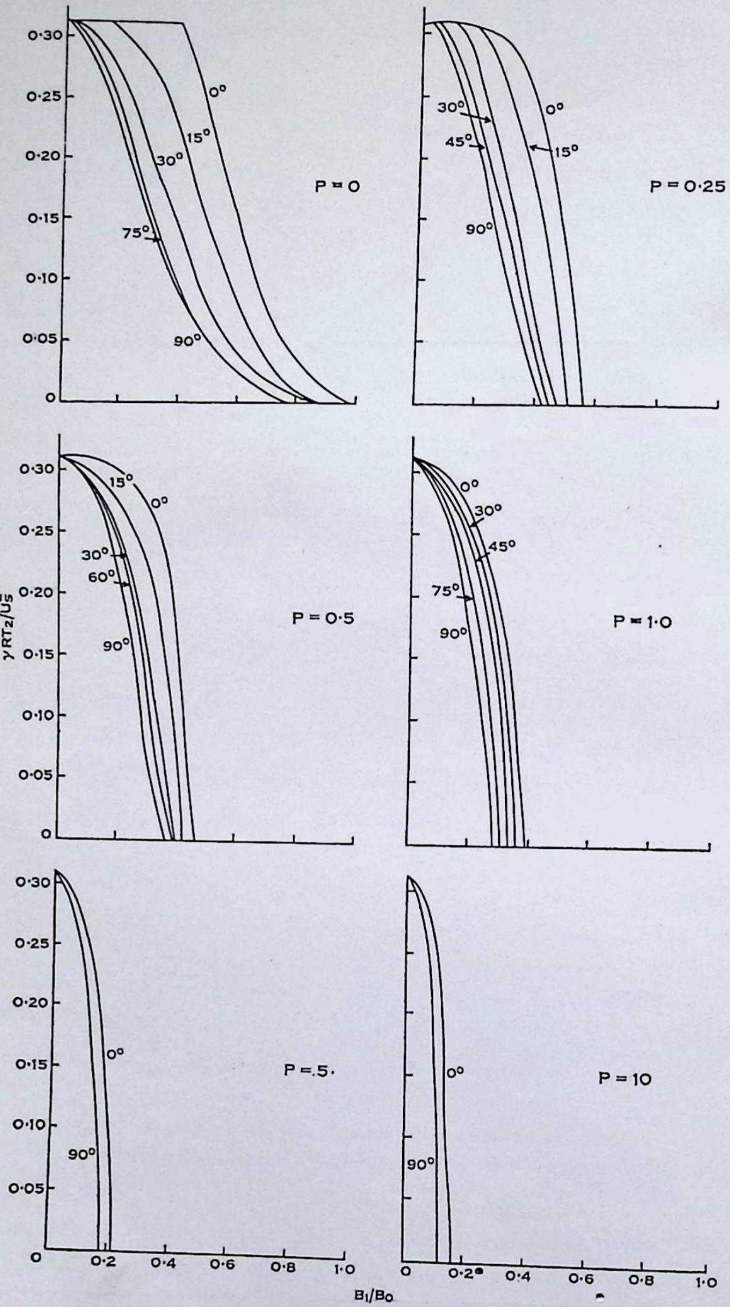

Fig. 6.—Non-dimensional temperature behind the shock wave, $\gamma RT_2/U_S^2$ (R is the gas constant per unit mass), versus B_1/B_0 for various values of θ and P.

In Figure 4, the negative tangent of the angle of downstream flow, in the laboratory reference frame, is shown, i.e. the ratio $-v_2/u_2$ in laboratory coordinates. (By the choice of sign convention this is a positive quantity.) In the transverse case there is no azimuthal flow at all, but as θ decreases the amount of rotation, or azimuthal flow, increases. For the normal shock in the switch-on region, the flow is increasingly rotational for increasing P, whereas under ordinary shock flow conditions the flow is entirely axial. Thus for the switch-on shock, a higher ionization will

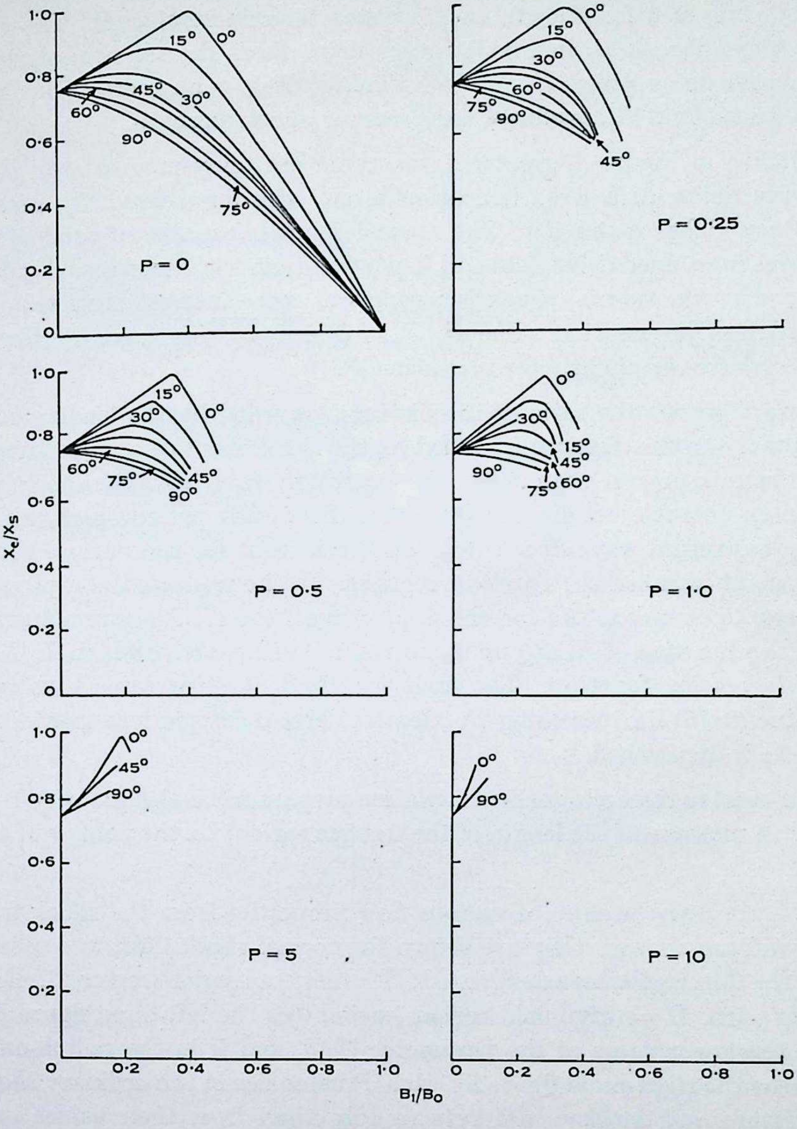

Fig. 7.—Ratio of distance travelled by the leading edge of the expansion wave, X_e, to distance travelled by the shock wave, X_S at a given time versus B_1/B_0 for various values of θ and P.

be obtained by a flow in which there is as much rotation as possible. This explains the present interest in the study of rotating plasmas in thermonuclear research.

The density ratio ρ_2/ρ_1 across the shock front is a measure of the shock strength; this ratio is presented in Figure 5. In the ordinary gas dynamic limit $(B_1/B_0 = 0)$ the density ratio is 4 for $P = 0$, and increases with increasing P. The curves are similar to those for B_2/B_1 in that stronger drive fields do not necessarily produce stronger shocks for a given P. We see that for $P \gtrsim 5$ an increase in drive field, with fixed initial field B_1, produces a decrease in shock strength.

As shown in Figure 6, greater downstream gas temperatures are produced by greater drive fields, at a fixed ionization level; also for a fixed T_2, greater drive fields produce higher ionization. The normal shock is capable of producing greater temperatures for a fixed drive field and ionization than the transverse shock, showing once again why the normal shock is perhaps of more interest than the transverse shock in plasma preparation. The $B_1/B_0 = 0$ limit of this quantity for $P = 0$ is $0 \cdot 3125$, and decreases slightly for increasing P.

Figure 7 graphs the ratio of the distance travelled by the leading edge of the expansion wave to the distance travelled by the shock front at a given time (X_e/X_S). When this ratio is greater than unity, the expansion wave leads the shock, producing an inherently unstable condition. However, this is not present here, although for $P = 0$ the expansion wave does catch the shock front for the normal shock at the transition point between the two flow regimes. In the neglected non-physical cases, X_e/X_S becomes complex. As for the ρ_2/ρ_1 curves, the X_e/X_S curves have maxima (regarded as a function of B_1/B_0) up to a certain P value, above which X_e/X_S becomes a strictly increasing function. The limit for $B_1/B_0 = 0$ increases slightly from its $P = 0$ value $(0 \cdot 75)$ for increasing P. Greater drive fields produce greater ionization when X_e/X_S is diminished.

Of interest to research workers in plasma preparation is the quantity $1-(X_e/X_S)$, which gives a measure of the length of the test gas region, i.e. the volume of the plasma produced.

In Figure 8 the profiles of various flow properties from the shock front (S) to the back wall are shown; they are shown for normal shock flow, two cases for each P value. The flow regions are designated: T = test gas region (region 2), E = expansion wave region, D = drive field region (region 0). The left-hand figure for each P value has the lower value of the parameter U_S/b_1 and is in the switch-on region of flow, whereas the right-hand figure for each P value lies in the ordinary shock region. As the pressure and density drop very rapidly away from their values in region 2, the test gas is well defined. The approximate linearity of the velocity components in the expansion wave, as noted in K.P., is evident here.

Figs. 8(*a*) to 8(*l*).—Profiles of flow properties between the shock front and the rear wall of the shock tube for $\theta = 0°$ and two values of the parameter U_S/b_1, so that the switch-on and ordinary flow regions are shown; S = shock front, T = test gas region (region 2), E = expansion wave region, D = drive field region (region 0). The profile numbers refer to flow properties as follows: 1 to $p/\rho_1 U_S^2$; 2 to U/U_S; 3 to $B^2/2\mu\rho_1 U_S^2$; 4 to $-v/U_S$; 5 to $(\rho/4\rho_1)^2$; 6 to $-E_Z/U_S B_{Y0}$.

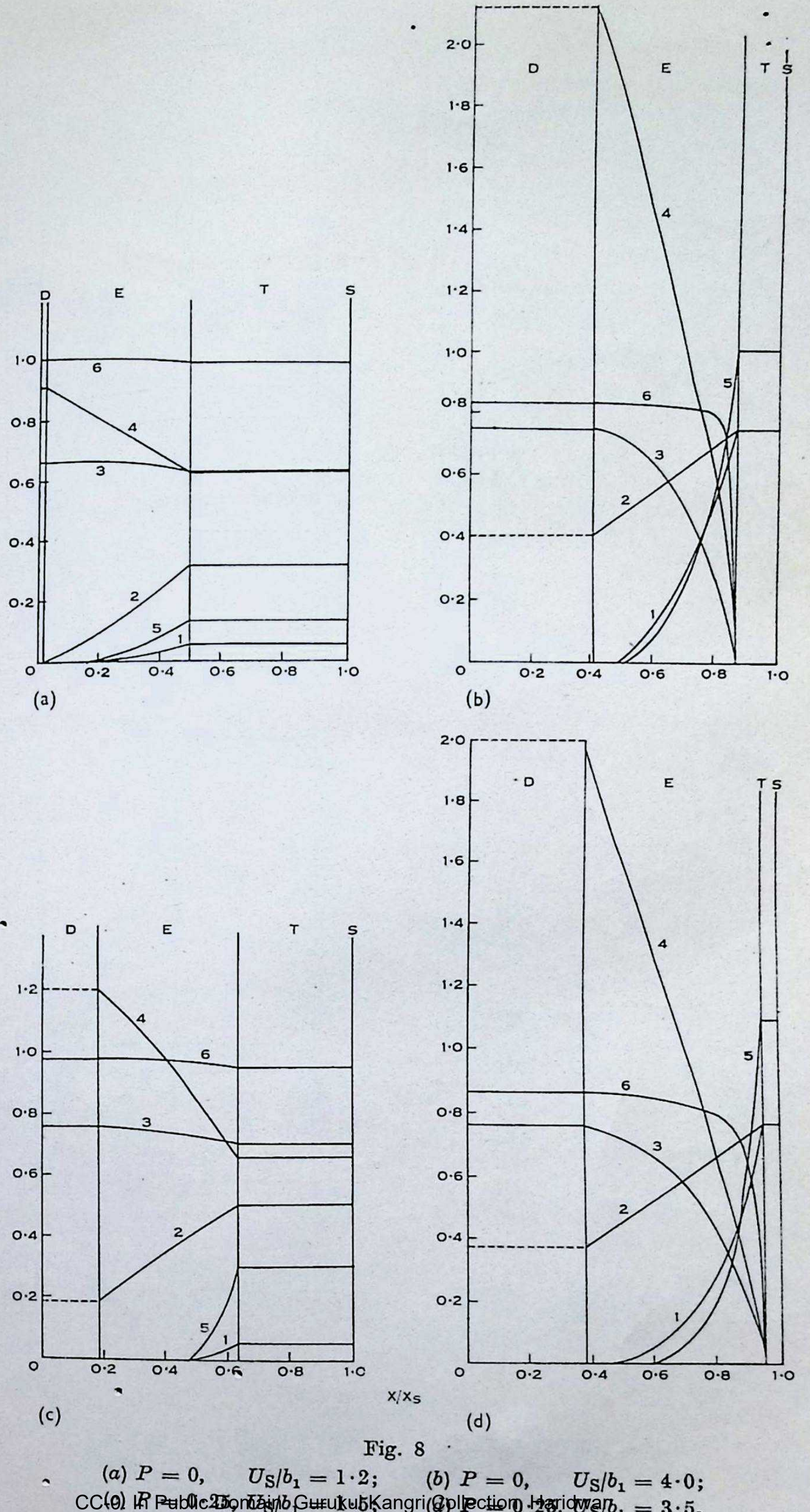

Fig. 8

(*a*) $P = 0$, $U_S/b_1 = 1 \cdot 2$; (*b*) $P = 0$, $U_S/b_1 = 4 \cdot 0$;
(*c*) $P = 0 \cdot 25$, $U_S/b_1 = 1 \cdot 5$; (*d*) $P = 0 \cdot 25$, $U_S/b_1 = 3 \cdot 5$.

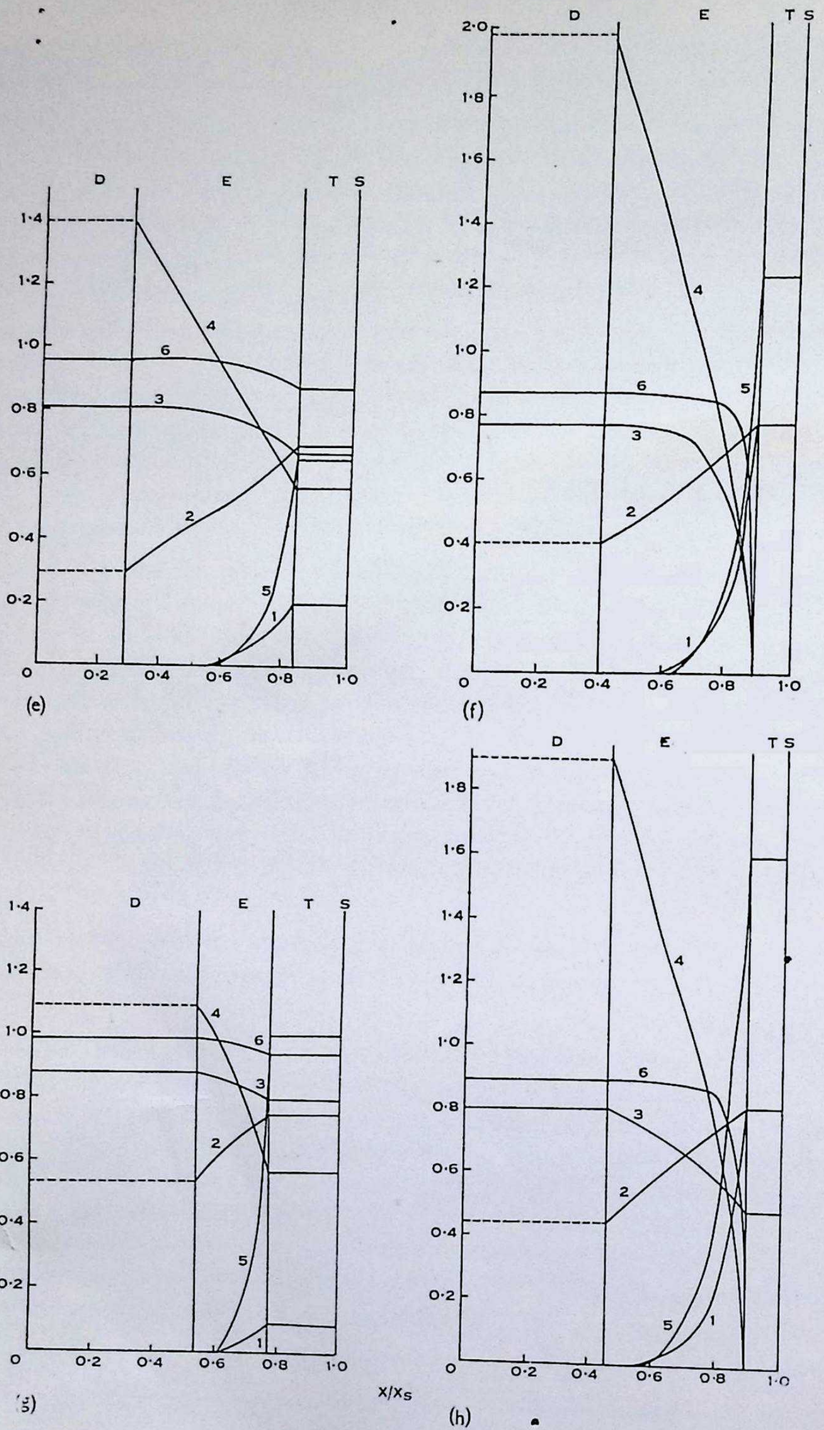

Fig. 8 (*Continued*)

(*e*) $P = 0\cdot 5$, $U_S/b_1 = 1\cdot 8$; (*f*) $P = 0\cdot 5$, $U_S/b_1 = 3\cdot 5$;
(*g*) $P = 1\cdot 0$, $U_S/b_1 = 2\cdot 0$; (*h*) $P = 1\cdot 0$, $U_S/b_1 = 3\cdot 5$.

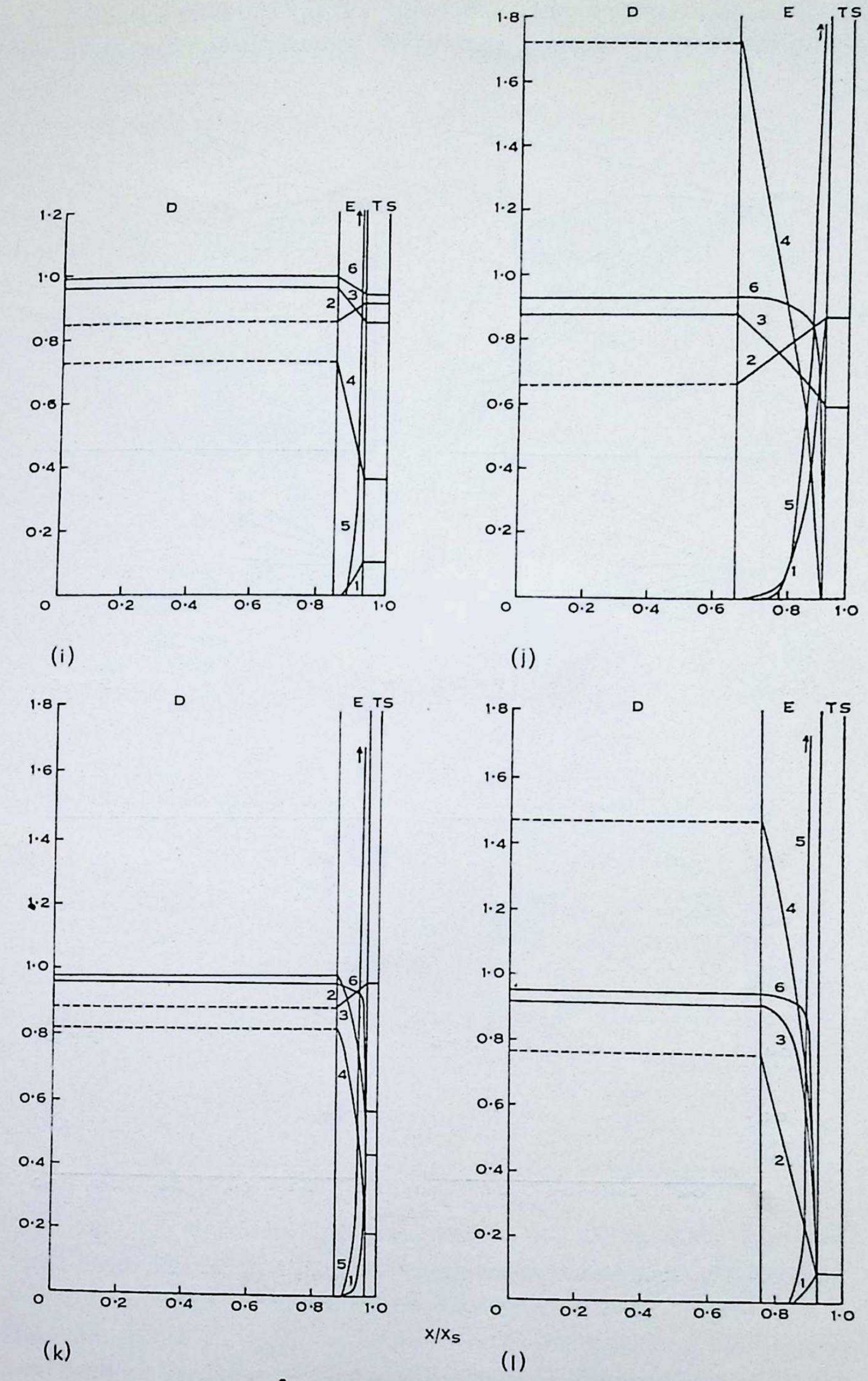

Fig. 8 (*Continued*)

(*i*) $P = 5$, $U_S/b_1 = 3\cdot 5$; (*j*) $P = 5$, $U_S/b_1 = 5\cdot 0$;
(*k*) $P = 10$, $U_S/b_1 = 4\cdot 86$; (*l*) $P = 10$, $U_S/b_1 = 6\cdot 0$.

Figure 9 essentially gives the radial (Z) component of the electric field at the electrode at the back of the tube as a function of B_1/B_0. This electric field can be used to calculate the impedance as seen by the circuit that drives the flow. For a

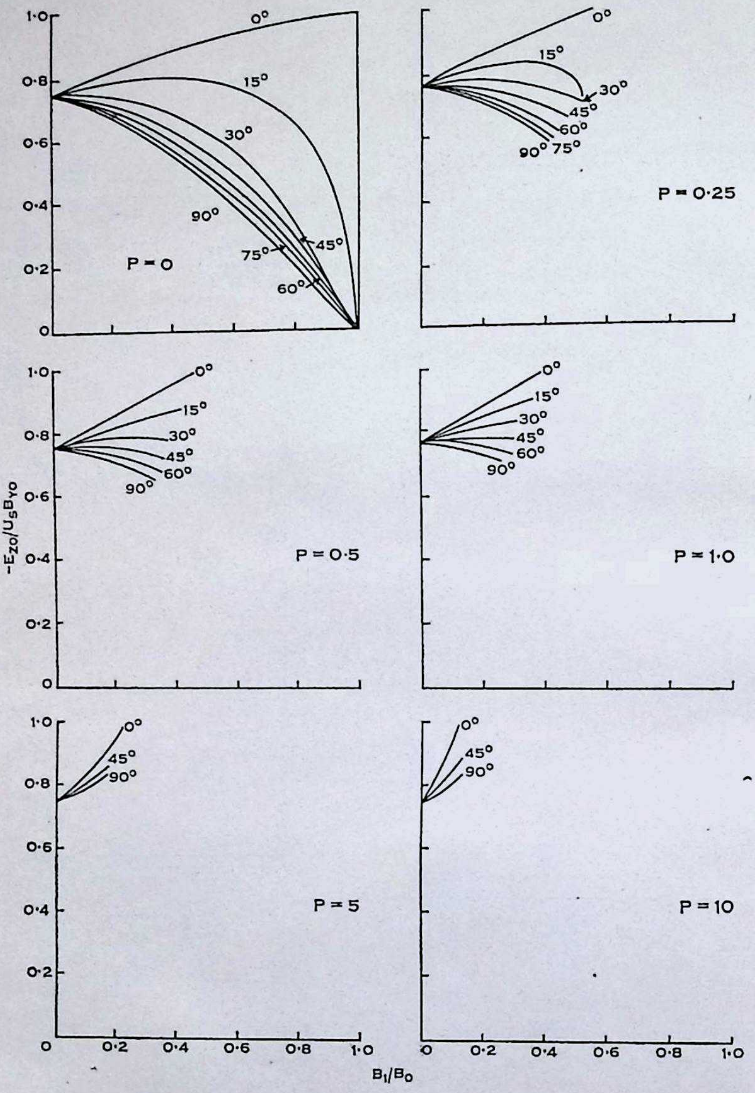

Fig. 9.—Non-dimensional electric field $-E_{Z_0}/U_S B_{Y0}$, in the drive field region (region 0), versus B_1/B_0 for various values of θ and P.

fixed electric field, a greater magnetic drive field is required to produce greater ionization. The $B_1/B_0 = 0$ limit behaves with P in the same way as does that of Figures 7 and 10.

The axial component of the drive field gas velocity U_0 is considered as a function of B_1/B_0 in Figure 10. When it is not zero, the pressure and the density in this region must vanish to satisfy the zero axial mass motion boundary condition

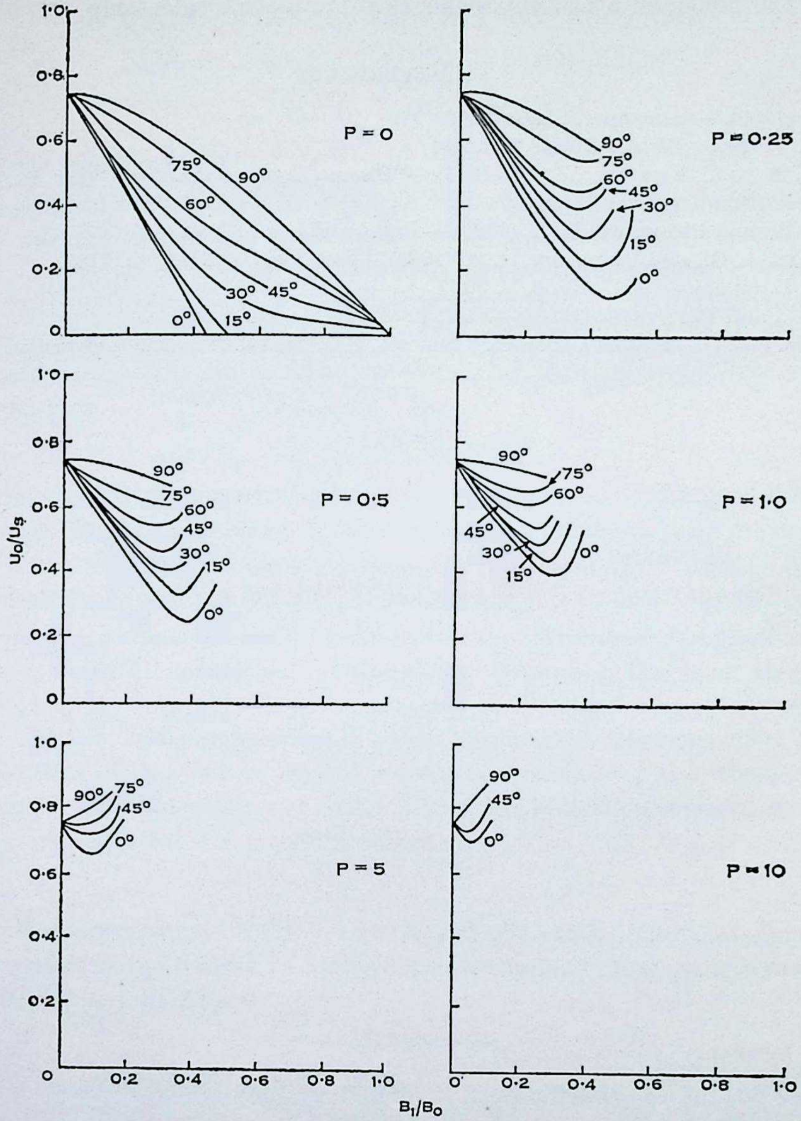

Fig. 10.—Non-dimensional axial component of gas velocity at the rear edge of the expansion wave, U_0/U_S, versus B_1/B_0 for various values of θ and P.

of the rear wall. When $U_0 = 0$, the pressure and density need not vanish, and the gas present remains in the region with no axial motion. As is shown in Figure 10, the condition $U_0 = 0$ is achieved only for $P = 0$; in all other cases there is a vacuum in the drive field region.

IV. ACKNOWLEDGMENTS

The authors wish to thank Professor C. N. Watson-Munro for helpful discussion, and Professor H. Messel for the facilities provided. This work was supported in part by the Nuclear Research Foundation within the University of Sydney. One of us (B.G.) is the holder of a CSIRO Senior Post-graduate Studentship.

V. REFERENCES

BAZER, J. (1958).—*Astrophys. J.* **128**: 686.

CHU, C. K. (1964).—*Physics Fluids* **7**: 1349.

GROSS, R. A., and KUNKEL, W. B. (1962).—"Plasma Hydromagnetics." (Ed. D. Bershader.) p. 58. (Stanford Univ. Press.)

KEMP, N. H., and PETSCHEK, H. E. (1959).—*Physics Fluids* **2**: 599.

KULIKOVSKI, A. G., and LYUBIMOV, G. A. (1960).—*Sov. Phys. Doklady* **4**: 1185.

LEHNERT, B. (1958).—I.A.U. No. 6, p. 50.

MAY, R. M., and TENDYS, J. (1965).—*Nucl. Fusion* 5 (2): (In press.)

TAUSSIG, R. (1964).—Plasma Laboratory Reports, Nos. 12, 14, Columbia University.

SHORT COMMUNICATIONS

A NEW KINETIC ENERGY CORRECTION FOR CAPILLARY TUBE VISCOMETERS*

By R. I. TANNER†

Source of the New Correction

The work of Caw and Wylie (1961) on viscometers with special capillary tubes of slowly varying radius has enabled the usual kinetic energy corrections to be reduced to a very small fraction of those with abrupt-ended capillaries. Thus one of the uncertainties in the use of such tubes is eliminated; also, the remaining small effect is rendered amenable to calculation (Tanner and Linnett 1965). It has been shown theoretically that the relation between viscosity and flow time is expected to be of the form

$$\nu = At + Ct^{-3} + O(t^{-7}), \tag{1}$$

where A is a positive constant, and C may be positive or negative. Relation (1) is valid up to Reynolds numbers (based on capillary diameter and mean velocity) of 100 or more with typical flared viscometers (Caw and Wylie 1961). Agreement between experiment and equation (1) is satisfactory up to such Reynolds numbers.

However, the value of the Ct^{-3} term now makes it necessary to consider another correction, of order t^{-1}, which can be completely ignored in the usual abrupt-ended tube because of the relatively large uncertainty in the usual correction term, which is also of order t^{-1} (Merrington 1943). This apparently new correction is due to the unsteadiness of the flow in typical viscometers caused by the variable head in the instrument. The calculation of such a correction is straightforward, and is given below for a capillary tube of constant radius R.

Calculation

To a first approximation the head of liquid (H) varies exponentially with time —the viscometer is equivalent to a capacitor discharging through a linear resistor. Hence if H_0 is the initial head,

$$H = H_0 \exp(-kt), \tag{2}$$

where k is a constant, which may be evaluated from a single test on the viscometer. Thus, to a first approximation, the velocity components in the capillary vary in a similar manner with time, and we seek an axi-symmetric solution of the Navier–Stokes equations in cylindrical polar coordinates (r, θ, z) (Rosenhead 1963) in which the velocity components vary exponentially with time. Assume the velocity vector V is given by

$$\mathrm{V} = \{0, 0, u(r)\exp(-kt)\}, \tag{3}$$

---

* Manuscript received February 10, 1965.

† Mechanical Engineering Department, University of Sydney.

Aust. J. Phys., 1965, 18, 381–3

then the Navier–Stokes equations reduce to

$$\frac{\partial p}{\partial z} = \mu\left(\frac{\partial^2 u}{\partial r^2}+\frac{1}{r}\frac{\partial u}{\partial r}\right)-\rho\frac{\partial u}{\partial t}, \tag{4}$$

where the pressure $p = p(z,t)$, the viscosity of the fluid is μ, and ρ is the fluid density. Explicitly,

$$\frac{\partial p}{\partial z} = -\frac{\rho g H_0}{l_c}\exp(-kt), \tag{5}$$

where l_c is the capillary length and g is the acceleration of gravity. Hence, substituting in (4) one obtains

$$\frac{\mathrm{d}^2 u}{\mathrm{d}r^2}+\frac{1}{r}\frac{\mathrm{d}u}{\mathrm{d}r}+\frac{\rho k}{\mu}u = -\frac{\rho g H_0}{\mu l_c}. \tag{6}$$

The solution for (6) finite on the axis and zero at $r = R$ is given by

$$u = \left(\frac{g H_0}{k l_c}\right)\left\{1-\frac{\mathrm{J}_0(\alpha r)}{\mathrm{J}_0(\alpha R)}\right\}, \tag{7}$$

where $\alpha = (\rho k/\mu)^{\frac{1}{2}}$. For small αR, which is the case of interest, the Bessel function J_0 may be represented by a few terms of the series. Integration to find the total volume discharge $\mathscr{V}$ in a time of flow t gives, to the second approximation,

$$\mathscr{V} = \frac{\pi\rho g H_0 R^4 t}{8\mu l_c}\left\{1+\frac{\rho k R^2}{6\mu}\right\}\left\{1-\tfrac{1}{2}kt\right\}. \tag{8}$$

Hence, since $k = t^{-1}\ln(H_0/H)$, (8) may be rearranged to give the relation

$$\nu = \frac{\pi g H_0 R^4 t}{8\mathscr{V} l_c}\left\{1-\ln(H_0/H)\right\}\left\{1+\frac{R^2}{6\nu t}\ln(H_0/H)\right\}, \tag{9}$$

which, substituting for ν in the right-hand side of (9), is seen to be of the form

$$\nu = At+B/t, \tag{10}$$

where

$$B = \tfrac{1}{6}R^2\ln(H_0/H). \tag{11}$$

B is thus positive, in contrast to the usual kinetic energy correction.

Discussion

The new correction is easily calculated on the assumption that the parallel capillary is the only source of flow resistance. For flaring capillaries, which are the cases of interest, no difficulty will arise provided the parallel portion is the main source of resistance. If this is not the case, then at low Reynolds numbers one may apply equation (5) in differential form, and then define the equivalent radius (R_e^2) as the ratio

$$R_e^2 = \int R^{-2}\,\mathrm{d}z \Big/ \int R^{-4}\,\mathrm{d}z. \tag{12}$$

The integrals are taken over the length of the viscometer. R_e^2 should then be used in equation (11).

For the viscometers used by Caw and Wylie (1961) the new correction is negligible. However, as an example of the orders of magnitude that may be involved, consider viscometers of the BS/U types G and H (British Standards Institution 1957) used at Reynolds numbers of 50; the steady flow kinetic energy errors from a flared version of these viscometers would be at most of the order of 0·1% while the calculation presented here would give an error of the order of 1%. Thus, particularly with flared capillaries of larger bore, the two effects should be considered together.

References

British Standards Institution (1957).—British Standard 188: 1957.

Caw, W. A., and Wylie, R. G. (1961).—Viscometers of negligible kinetic energy effect. *Br. J. Appl. Phys.* **12**: 94–8.

Merrington, A. C. (1943).—"Viscometry." (Arnold: London.)

Rosenhead, L. (1963).—"Laminar Boundary Layers." (Oxford Univ. Press.)

Tanner, R. I., and Linnett, I. W. (1965).—Pressure losses in viscometric capillary tubes of varying diameter. Proc. 2nd Australasian Conf. on Hydraulic and Fluid Mech. (Auckland). (In press.)

POLARIZATION OF 6 CM RADIATION FROM THE CRAB NEBULA*

By F. F. Gardner†

Linear polarization measurements at 6 cm wavelength with the 210-ft Parkes radio telescope have shown that the polarization of the Crab nebula is concentrated in an area under $2'$ in angular extent centred $0'.5 \pm 0'.2$ to the west and $1'.1 \pm 0'.2$ to the south of the centre of the total emission.

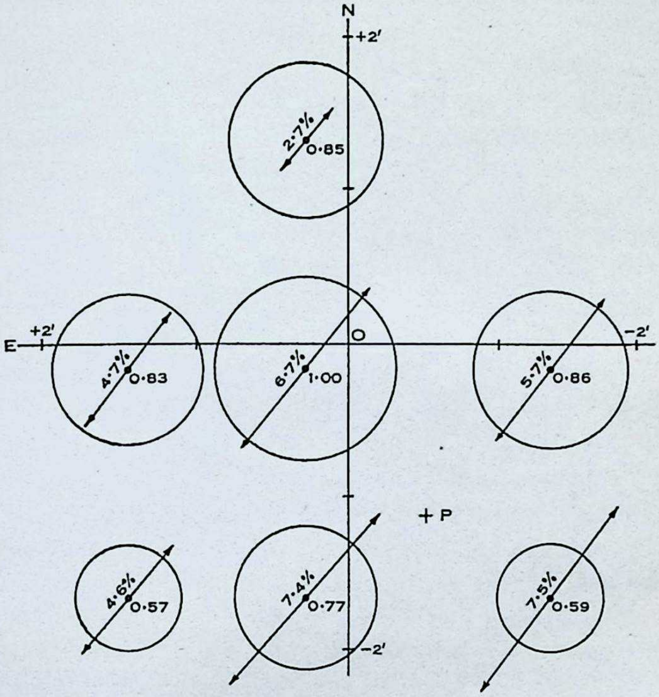

Fig. 1.—Variation of 6 cm intensity and polarization across the Crab nebula. At each point measured the total intensity is given as a fraction of the central intensity and is proportional to the diameter of the surrounding circle, while the arrows show the direction and degree of polarization expressed as a percentage of the central intensity. The total intensity is centred at O and the polarized emission at point P.

The results of the observations‡ made in October 1963 are shown in Figure 1. For each point observed the total intensity is expressed as a fraction of the central intensity and is indicated by the diameter of the surrounding circle; the arrows show the direction and degree of polarization expressed as a percentage of the central intensity.

---

* Manuscript received April 7, 1965.

† Division of Radiophysics, CSIRO, University Grounds, Chippendale, N.S.W.

‡ The experimental method and the procedure for evaluating spurious effects will be discussed in a forthcoming paper by Davies and Gardner.

Aust. J. Phys., 1965, 18, 385–7

Within the accuracy of the measurements the position angle of the polarization is the same at all points, namely 141±3°. It is apparent that the centre of the polarized emission, P, is displaced from the centre of total emission, O. With centre P, determined on the assumption of circular symmetry, the angular distribution of polarization is not significantly broader than the aerial beam. (The best estimate of polarization half-width is 4′·2 compared to the beamwidth of 4′·1, while the observed total intensity half-width of Taurus A is slightly over 5′·0 in both coordinates.) The actual percentage polarizations of the small-diameter source must be high (probably over 20%), since the apparent percentage polarization, shown by the ratio of the arrow length to the circle diameter, increases progressively along the radius from O to P, reaching 12·7% (= 7·5/0·59) at the furthermost point measured, compared with 6·7% near O. Should the polarization source be extended to the south-west, and observations further out are required to settle this, the apparent percentage polarization would be even higher in the extension.

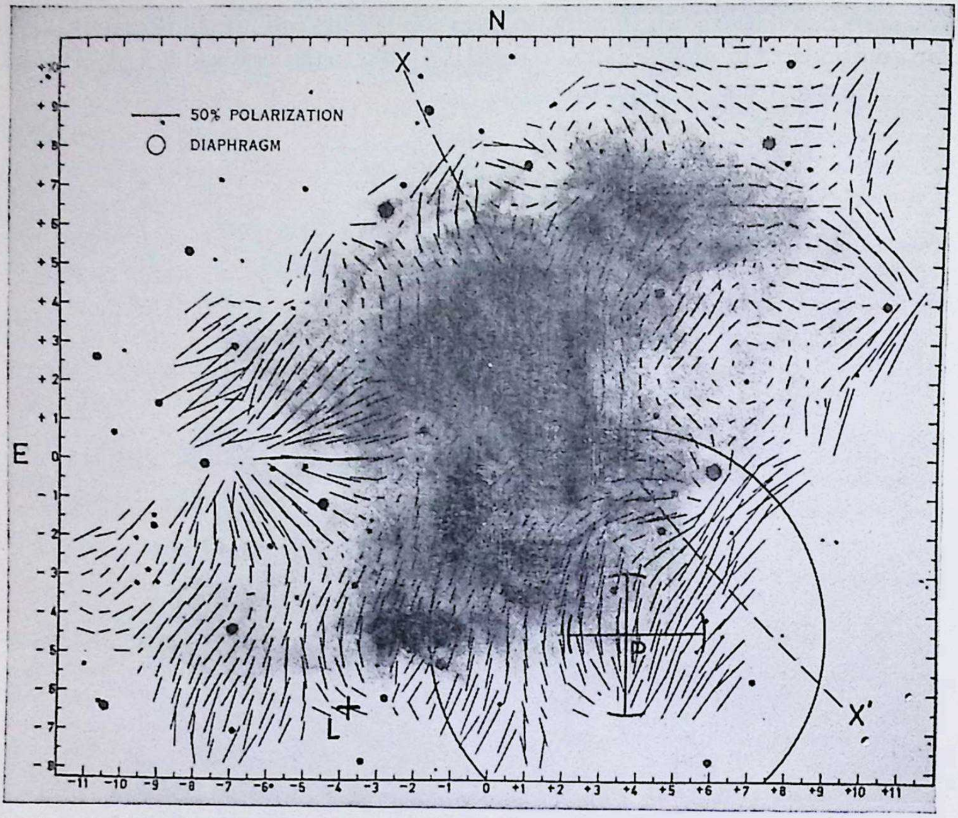

Fig. 2.—The centre P of the 6 cm polarization distribution and a circle showing the approximate extent of the polarization superposed on the distribution of optical polarization given by Woltjer (1957). The small diameter 26 Mc/s source is shown as L; the X-ray source lies along the line X–X′. The origin of Woltjer's diagram is the south-west component of the central double star, R.A. $05^{\rm h}\,31^{\rm m}\,31^{\rm s}\cdot5$, dec. +21° 58′ 55″ (1950). Scale: 1′ arc = 5·4 units.

The existence of a polarization concentration is in agreement with the observations at 3 cm at Pulkovo by Soboleva, Prozorov, and Pariiskii (1963) and at 10 cm at Caltech by Morris, Radhakrishnan, and Seielstad (1964). However, the result of the former workers was that the polarized emission was east of the total-intensity peak observed with a fan-beam antenna, and that the position angle varied markedly across the source, both of which conflict with our results; but Pariiskii (personal communication) has indicated that more recent observations at Pulkovo are consistent with those reported here. The result of Morris, Radhakrishnan, and Seielstad was that the polarization was uniform in direction and confined to an area about 1′.9 in diameter in which the percentage polarization was 8–10%. They did not measure a position.

In Figure 2 the position of the polarization centre P is shown on Woltjer's (1957) distribution of optical polarization. The radio-optical superposition is made on the basis of coincidence between the centres of radio and optical emission. Lunar occultations observed at 408 Mc/s by Seeger and Westerhout (1957), and more recently at 400 and 1400 Mc/s by Davies, Hazard, Gardner, and Mackey (unpublished data), show that the two agree to within 0′.2. From the optical distribution in Figure 2 there is no reason to expect that the polarized emission would be displaced to one side of the nebula, although in the region around P the optical percentage polarization is high and fairly uniform in direction. The average optical position angle in this area is 160–170° east of north compared with the radio intrinsic polarization angle of 150–155° (141° corrected for a Faraday rotation of -27 rad/m^2; see Gardner and Whiteoak 1963).

Figure 2 also shows the position L of a small-diameter (20″ arc) source with a steep spectral index found by Andrews, Branson, and Wills (1964) at 26 Mc/s. It does not appear to be related to the polarized source. Recently Bowyer *et al.* (1964) have detected an X-ray source about 1′ in diameter which is located along the line X–X′ in Figure 2 (their 230 sec line). This line X–X′ is displaced from P by a little more than the estimated position errors. The future determination of the location of the X-ray source along X–X′ will show whether there is any possiblity of a relationship between the two phenomena.

It is difficult to explain the rapid change in the prominence of the polarization feature with increasing radio wavelength by Faraday rotation (the polarization drops from 15–20% at 6 cm to below 3% at 20 cm in the occultation observations of Davies *et al.*), in view of the small overall rotation measure which would change the position angle by only 60° between 6 and 20 cm. In addition it is necessary to explain why some regions, highly polarized at optical wavelengths, are not polarized at 6 cm. It is evident that the radiation processes in the Crab nebula are not fully understood. As far as the radio measurements are concerned there is a definite need for higher resolution measurement of polarization over a range of frequencies.

References

Andrews, B. H., Branson, N. J. B. A., and Wills, D. (1964).—*Nature* **203**: 171.

Bowyer, S., Byram, E. T., Chubb, T. A., and Friedman, H. (1964).—*Science* **146**: 912.

Gardner, F. F., and Whiteoak, J. B. (1963).—*Nature* **197**: 1162.

Morris, D., Radhakrishnan, V., and Seielstad, G. A. (1964).—*Astrophys J.* **139**: 551.

Seeger, C. L., and Westerhout, G. (1957).—*Bull. Astr. Insts Neth.* **13**: 312.

Soboleva, N. S., Prozorov, V. A., and Pariiskii, Yu. N. (1963).—*Soviet Astron.–A. J.* **7**: 1.

Woltjer, L. (1957).—*Bull. Astr. Insts Neth.* **13**: 301.

THE REACTIONS ^{6}Li(γ, d) AND ^{7}Li(γ, t) BELOW 4 MEV*†

By P. J. DALLIMORE,‡§ K. S. LAM,‡ and H. H. THIES‡

In the present experiment the reactions $^6\mathrm{Li}(\gamma,\mathrm{d})$ and $^7\mathrm{Li}(\gamma,\mathrm{t})$ were investigated with bremsstrahlung from a linear accelerator by detecting the charged reaction products in coincidence with solid-state surface barrier detectors.‖

Earlier experiments with monochromatic γ-rays (Glenn 1952; Titterton and Brinkley 1952; Jensen and Gis 1953; Däublin, Bertholt, and Jensen 1959) have shown the reaction $^6\mathrm{Li}(\gamma,\mathrm{d})$ below 4 MeV to be extremely weak. The reaction $^7\mathrm{Li}(\gamma,\mathrm{t})$ below 4 MeV has not been investigated previously. It is likely to be extremely weak too, as there are no known levels in ^{7}Li between 4 MeV and the reaction threshold (Ajzenberg-Selove and Lauritsen 1959). Assuming an "alpha+triton" model of the ^{7}Li nucleus, Czyż (1955) predicted on theoretical grounds a resonance peak of order $3\cdot5\times10^{-27}$ cm^2 near the reaction threshold. However, in a more complete report of his investigation (Czyż 1956), the applicability of this model for the energy region below 4 MeV was questioned. Using a Breit–Wigner formula (Peaslee 1952) we have calculated the cross section of $^7\mathrm{Li}(\gamma,\mathrm{t})$ below 4 MeV. We have assumed that this reaction takes place via the known states at $0\cdot478$ and $4\cdot63$ MeV. The partial radiative width of the $4\cdot63$ MeV level was estimated from known $^7\mathrm{Li}(\gamma,\mathrm{t})$ cross-section data of Erdös *et al.* (1954). Other parameters were taken from the compilation of Ajzenberg-Selove and Lauritsen (1959). We estimate on the basis of this calculation that the cross section of $^7\mathrm{Li}(\gamma,\mathrm{t})$ below 4 MeV is $\sim5\times10^{-31}$ cm^2.

The purpose of the present experiments was to confirm with bremsstrahlung the extreme weakness of the $^6\mathrm{Li}(\gamma,\mathrm{d})$ and $^7\mathrm{Li}(\gamma,\mathrm{t})$ reactions below 4 MeV. The investigation of $^7\mathrm{Li}(\gamma,\mathrm{t})$ is of particular interest also for the following reason. E_{Q}, the energy at which photodisintegration becomes possible energetically, is usually slightly less, by an amount ΔE, than E_1, the energy of the first virtual state, i.e. the energy of the first level above E_{Q}. In general ΔE is some tens of keV or less. It is of interest to know whether photodisintegration cross sections occur at E_{Q}, E_1, or some intermediate value. Such knowledge is required, for example, for the precision calibration of the energy scale of accelerators by measurement of empirical photonuclear thresholds.¶ ^{7}Li is unique inasmuch as here ΔE has the anomalously large value of $2\cdot1$ MeV. The photodisintegration becomes possible via $^7\mathrm{Li}(\gamma,\mathrm{t})$ at $E_{\mathrm{Q}} = 2\cdot47$ MeV, whereas the first virtual state occurs at $E_1 = 4\cdot63$ MeV (Ajzenberg-Selove and Lauritsen 1959). Thus the investigation of $^7\mathrm{Li}(\gamma,\mathrm{t})$ below $4\cdot1$ MeV can decide unambiguously whether a photonuclear reaction can occur below the first virtual state.

---

* This work was supported by an Australian Atomic Energy Commission Contract.

† Manuscript received May 21, 1965.

‡ Physics Department, University of Western Australia.

§ Present address: Physics Department, University of Oxford, England.

‖ A detailed account of these experiments is given by Lam (1964).

¶ Such calibrations naturally presume that, within experimental accuracy, cross sections have a reasonably sharp "cut-off" point.

Aust. J. Phys., 1965, 18, 389–92

The same experimental arrangement was used for the investigation of ^{6}Li(γ, d) and ^{7}Li(γ, t), and it is shown diagrammatically in Figure 1. A linear accelerator (Linac) produced 4 MeV bremsstrahlung. The output of this machine is about 120 r/min at 1 m, and its beam is pulsed, giving 500 two-microsecond pulses per second. The γ-beam first passed through a 3·5 cm aluminium absorber to relatively enhance the high energy end of the bremsstrahlung spectrum. It then passed through two calibrated transmission ionization chambers, one to measure the instantaneous dose rate and one to measure the integrated dose, and, via an aligned $0 \cdot 8 \times 0 \cdot 3$ cm aperture in a 20 cm lead collimator, entered the brass target chamber, which had 0·16 cm Perspex entrance and exit windows. The target consisted of lithium hydroxide films supported by thin carbon backings; for ^{6}Li(γ, d), 190 μg/cm^2 of lithium enriched to 95·6% in ^{6}Li on 20 μg/cm^2 of carbon; for ^{7}Li(γ, t), 370 μg/cm^2 of natural lithium supported by 40 μg/cm^2 of carbon. Target films were held at 15° to the beam axis by stainless steel frames with 1·9 cm central openings. This method of support ensured that the direct γ-beam traversed the lithium hydroxide–carbon film without striking the supporting frame or the detectors, which were mounted as close as possible to the γ-irradiated part of the targets. Great care was taken in the design of the chamber target geometry to prevent photo electrons and Compton electrons from hitting the detector surfaces. The two detectors were conventional solid-state surface barrier detectors made from 1000 ohm-cm silicon with 100 μg/cm^2 gold "windows" of 0·52 and 0·40 cm diameter respectively, possessing a resolution of better than 100 keV to 5 MeV α-particles. The detector bias was kept so low that the thickness of the sensitive depletion layer was only slightly greater than the range of the most energetic deuterons to be detected. As the charged reaction

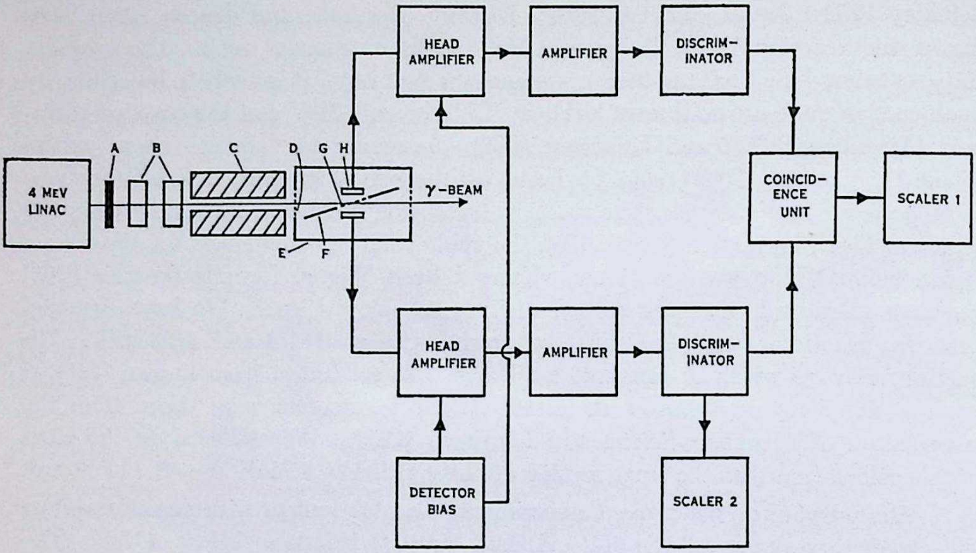

Fig. 1.—Diagrammatic experimental arrangement for the investigation of ^{6}Li(γ, d) and ^{7}Li(γ, t). A, aluminium absorber; B, transmission ionization chambers; C, lead collimator; D, Perspex window; E, target chamber (evacuated to 0·1 torr); F, target support; G, target film; H, solid-state detector.

products from ^{6}Li(γ, d) and ^{7}Li(γ, t), i.e. α-particles, deuterons, and tritons, have much smaller ranges than electrons at corresponding energies, "electron pile-up" pulses were only relatively small. By severely differentiating in the head amplifiers it was possible to reduce the rate of pile-up pulses entering the main amplifier to a tolerable non-coincident count rate. The electronic arrangement used was conventional (see Fig. 1). Coincident signals were to be recorded by scaler 1, and non-coincident signals by scaler 2. The count rate of scaler 2 thus permitted calculation of the random coincidence rate to be expected.

Each target was irradiated with 50 000 r during continuous 9 hr runs. No coincidences were recorded.* The random coincidence count rate to be expected was 0·05 counts per 9 hr. Before and after each run the complete counting system was tested by applying appropriate coincident test pulses from a pulse generator to the head amplifiers and, in its non-coincident mode, by bringing an α-source close to the detectors. Upper limits for the weighted average reaction cross section between E_Q and 4·1 MeV were calculated. In this calculation, account was taken of the exact detector–target geometry. Allowance was made for energy losses of the charged particles in the target films and in the solid-state detectors. The bremsstrahlung spectrum used was calculated with a Schiff formula modified at the high energy end to the corrected Sauter–Fano value (Fano, Koch, and Motz 1958). Attenuation in the ionization chambers and the aluminium filter was allowed for.

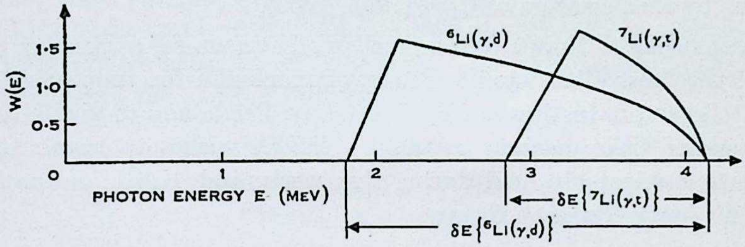

Fig. 2.—Weighting functions employed in the calculation of upper limits of the average reaction cross sections $\bar{\sigma}$, where

$$\bar{\sigma} = \frac{1}{\delta E}\int_{4\cdot1\ \mathrm{MeV}-\delta E}^{4\cdot1\ \mathrm{MeV}} W(E)\sigma(E)\,\mathrm{d}E.$$

The weighting functions that were used in calculating an upper limit for the weighted average cross sections are shown in Figure 2. They take account of the spectral distribution of the photons at the target and the losses in the finite-size targets and detectors, and may be interpreted as hypothetical photon spectra in ideal equivalent experiments with infinitesimal targets and ideal detectors. The calculated weighted average cross-section values are: for ^{6}Li(γ, d)

$$\bar{\sigma}\{^6\mathrm{Li}(\gamma,\mathrm{d})\} < (6\cdot70\pm1\cdot00)\times10^{-31}\ \mathrm{cm}^2,$$

---

* This does not preclude that the only reaction competing below 4·1 MeV, namely ^{6}Li(γ, np)α, has an appreciable cross section in this region. E_Q for this reaction occurs at 3·70 MeV, but even for 4·1 MeV photons corresponding p–α pairs have insufficient energies to be recorded in coincidence in the present experiment.

and for ^{7}Li(γ, t)

$$\bar{\sigma}\{^{7}\mathrm{Li}(\gamma,\mathrm{t})\} < (1\cdot 55\pm 0\cdot 20)\times 10^{-30}\ \mathrm{cm}^2.$$

Errors indicated are estimated systematic errors. The < sign implies here that there was a 65% probability that actual weighted average cross sections are smaller than the stated values.

The result for ^{6}Li(γ, d) confirms the extreme weakness of this reaction below 4·1 MeV, as was found previously with some monochromatic γ-rays by Glenn (1952), Titterton and Brinkley (1952), Jensen and Gis (1953), and Däublin, Bertholt, and Jensen (1959). It is in agreement with the theoretical calculation of Vashakidze and Chilashvili (1954).

The result for ^{7}Li(γ, t) shows that an empirical photonuclear threshold need not coincide with the energy at which the corresponding reaction becomes energetically possible. The observed extreme weakness of the reaction ^{7}Li(γ, t) below 4·1 MeV is in agreement with a theoretical estimate reported in the present paper. It does not confirm the existence of a resonance peak near E_Q, as was predicted, with reservations, by a calculation of Czyż (1955, 1956).

We would like to thank Professor E. W. Titterton for suggesting these experiments, and the Australian Atomic Energy Commission for supporting the project. We are grateful to the Institute of Radiotherapy, Perth, and to the linear accelerator crew for making their machine available. P.J.D. wishes to thank CSIRO for a Post-graduate Studentship held during this work, and K.S.L. acknowledges with thanks a University Research Grant.

References

AJZENBERG-SELOVE, F., and LAURITSEN, T. (1959).—*Nucl. Phys.* **11**: 1.
CZYŻ, W. (1955).—*Nuovo Cim.* **2**: 320.
CZYŻ, W. (1956).—*Acta Phys. Pol.* **15**: 129.
DÄUBLIN, F., BERTHOLT, F., and JENSEN, P. (1959).—*Z. Naturf.* **14a**: 208.
ERDÖS, P., STOLL, P., WÄCHTER, W., and WATAGHIN, V. (1954).—*Nuovo Cim.* **12**: 639.
FANO, U., KOCH, H. W., and MOTZ, J. W. (1958).—*Phys. Rev.* **112**: 1679.
GLENN, H. B. (1952).—*Phys. Rev.* **88**: 418.
JENSEN, P., and GIS, K. (1953).—*Z. Naturf.* **8a**: 137.
LAM, K. S. (1964).—M.Sc. Thesis, University of Western Australia.
PEASLEE, D. C. (1952).—*Phys. Rev.* **88**: 812.
TITTERTON, E. W., and BRINKLEY, T. A. (1952).—*Proc. Phys. Soc.* A **65**: 1052.
VASHAKIDZE, I. SH., and CHILASHVILI, G. A. (1954).—*Zh. Eksper. Teor. Fiz.* **26**: 254.

CORRIGENDA

VOLUME 17, NUMBER 4

"Transient heat conduction between a sphere and a surrounding medium of different thermal properties." By J. R. Philip. pp. 423–30

Professor A. Brown has kindly pointed out to the author that brackets were omitted from equation (4.1) of the above paper, and that the consequences of this omission carried on to some later equations, namely, (4.2), (4.4), (5.2), (5.3), (7.1), (7.2), (7.3), and (7.4). All the terms that appear before the summation sign in the numerator of the right-hand member of equation (4.1) should be enclosed in square brackets. The error affects the higher terms of a number of "small time" expansions, but does not influence the conclusions of the paper.

VOLUME 18, NUMBER 3

"Transport coefficients for low energy electrons in crossed electric and magnetic fields." By R. L. Jory. pp. 237–56

Page 252, Table 3:

The values attributed to Engelhardt, Phelps, and Risk in the last column of the table are incorrectly quoted. Their values (calculated at 300°K), which were plotted correctly in Figure 4, should read down the table as follows: 1·60, 1·58, 1·53, 1·49, 1·41, 1·36, 1·31, 1·28, 1·22, 1·18, 1·13, 1·11, 1·09, 1·09, 1·09, 1·10, 1·11, 1·12, 1·15.

ELECTROMAGNETIC 2π DECAY OF K_2^0

By S. K. Kundu*

[*Manuscript received April 22, 1965*]

Summary

As alternatives to the observed $K_2^0 \rightarrow 2\pi$ decay we consider the processes (i) $K_2^0 \rightarrow 2\pi+\gamma$ and (ii) $K_2^0 \rightarrow K_1^0$ magnetic conversion. It is shown that the former process is quite unlikely with the photon energy as suggested from experiment, while the second one is not so unlikely. Also suitable experiments are suggested to observe the processes considered here.

INTRODUCTION

Experimentalists (Abashian *et al.* 1964; Christenson *et al.* 1964) have observed a process which could be $K_2^0 \rightarrow 2\pi$ decay with a branching ratio $\sim 2\times10^{-3}$, corresponding to a partial decay rate $(1/\tau)(K_2^0 \rightarrow 2\pi) \approx 3\times10^4\ s^{-1}$. If this is the case, then the process violates CP invariance. In the following we try to consider what they have found as 2π decay with one real or virtual photon which conserves CP invariance. There are two possibilities: (i) radiative decay and (ii) $K_2^0 \rightarrow K_1^0$ conversion on passage through inhomogeneities in a magnetic field. Mechanism (i) appears to be ruled out by the absence of observed γ-rays exceeding about 10 MeV; mechanism (ii) seems also improbable but is not so obviously excluded by the experimental conditions.

Both types of mechanism may be within possible observation in experiments specifically designed for the purpose.

RADIATIVE DECAY, $K_2^0 \rightarrow 2\pi+\gamma$

An approximate estimation of the partial decay rate can be made as follows. Comparison of $K_2^0 \rightarrow 2\pi+\gamma$ with $K_1^0 \rightarrow 2\pi$ gives

$$\frac{1}{\tau}(K_2^0 \rightarrow 2\pi+\gamma) \sim \left(\frac{\alpha}{2\pi}\right)\left\{\frac{\rho(K_2^0 \rightarrow 2\pi+\gamma)}{\rho(K_1^0 \rightarrow 2\pi)}\right\}\frac{1}{\tau(K_1^0 \rightarrow 2\pi)} \approx 10^6\ s^{-1},$$

where ρ represents the phase volume for the respective processes.

Similarly from the comparison with $K_2^0 \rightarrow 3\pi$, we get

$$\frac{1}{\tau}(K_2^0 \rightarrow 2\pi+\gamma) \sim \left(\frac{\alpha}{2\pi}\right)\left\{\frac{\rho(K_2^0 \rightarrow 2\pi+\gamma)}{\rho(K_2^0 \rightarrow 3\pi)}\right\}\frac{1}{\tau(K_2^0 \rightarrow 3\pi)} \approx 10^5\ s^{-1}.$$

The preceding estimates show that

$$\tau(K_2^0 \rightarrow 2\pi+\gamma) \approx 10^{-5} \text{ to } 10^{-6}\ s.$$

---

* Research School of Physical Sciences, Australian National University, Canberra.

Aust. J. Phys., 1965, 18, 395–400

We now consider a dynamical model, as shown in Figure 1, where the $K_2^0\gamma K_1^{0*}$ vertex has the same structure as the $\pi\gamma\rho$ vertex from the unitary symmetry scheme. The effective interaction Hamiltonians for the two vertices are given by

$$H(K_2^0\gamma K_1^{0*}) = \tfrac{1}{2}(G/\kappa_1)\epsilon_{\alpha\beta\sigma\tau}F_{\alpha\beta}\Psi_\sigma\,\partial\Phi/\partial x_\tau \tag{1}$$

and

$$H(K_1^{0*}\pi\pi) = 2^{-\frac{1}{2}}g\Psi_\mu(\partial_\mu\phi^*\phi-\phi^*\partial_\mu\phi), \tag{2}$$

where $F_{\alpha\beta}$ is the electromagnetic field of the photon, Ψ the K_1^{0*}-meson amplitude, Φ the K_2^0 amplitude, ϕ the pion amplitude, κ_1 the K_1^{0*} mass, $G^2/4\pi \sim 0\cdot02$ in accordance with a $\rho\rightarrow\pi+\gamma$ decay width of $\frac{1}{2}$ MeV (Adler and Drell 1964; Berman and Drell 1964), $g = 1\cdot26\times10^{-11}\,M_0^2$ (M_0 has the dimension of mass in MeV) is the usual beta decay coupling.

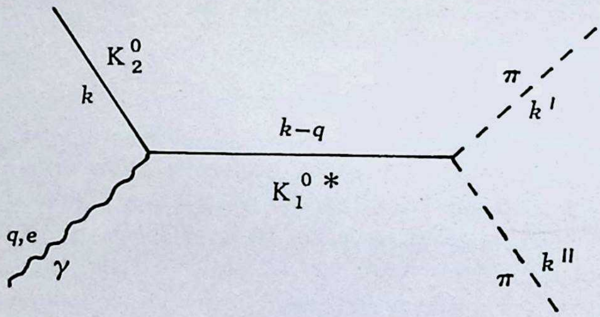

Fig. 1.—Radiative 2π decay process for K_2^0 meson.

For the propagator of the intermediate boson we use the expression

$$\delta_{\mu\sigma}/\{(k-q)^2-\kappa_1^2\}. \tag{3}$$

The decay rate for $K_2^0\rightarrow 2\pi+\gamma$ in the K_2^0 rest frame is given by

$$(1/\tau)(K_2^0\rightarrow 2\pi+\gamma) = \int (2\pi)^4\,\delta(k'+k''-q)|\mathscr{M}|^2\rho_E\,\mathrm{d}\rho_E, \tag{4}$$

where by equations (1), (2), and (3)

$$\mathscr{M} = \frac{1}{\sqrt{(2M)}}\cdot\frac{1}{\sqrt{(2q)}}\cdot\frac{G}{\kappa_1}\epsilon_{\alpha\beta\sigma\tau}e_\alpha q_\beta k_\tau\frac{\delta_{\mu\sigma}}{(k-q)^2-\kappa_1^2}\cdot\frac{g(k'-k'')_\mu}{\sqrt{(2)}\sqrt{(2\omega')}\sqrt{(2\omega'')}}$$

with four-vectors $(M,0)$, $(q,\mathbf{q})$, $(\omega',\mathbf{k}')$, and $(\omega'',\mathbf{k}'')$ for the K_2^0, γ-ray, and two π mesons; furthermore,

$$\rho_E\,\mathrm{d}\rho_E = \frac{\mathrm{d}^3k'}{(2\pi)^3}\cdot\frac{\mathrm{d}^3k''}{(2\pi)^3}\cdot\frac{\mathrm{d}^3q}{(2\pi)^3}\delta(E_i-E_f), \qquad E_f = \omega'+\omega''.$$

Replacing $\mathbf{k}'+\mathbf{k}'' = \mathbf{q}$, $\mathbf{k}'-\mathbf{k}'' = 2\mathbf{p}$ with $\mathrm{d}^3k'\mathrm{d}^3k'' = \mathrm{d}^3p\mathrm{d}^3q$, we find

$$\frac{1}{\tau} = \int (2\pi)^{-5}\frac{g^2G^2M}{8\omega'\omega''\kappa_1^2}\cdot\frac{p^4q^3\sin^2\theta}{(M^2-2Mq-\kappa_1^2)^2}\left|\frac{\mathrm{d}p}{\mathrm{d}E_f}\right|_{E_i=E_f}\mathrm{d}q\mathrm{d}\Omega_p\mathrm{d}\Omega_q, \tag{5}$$

where we put

$$|\epsilon_{\alpha\beta\sigma\tau} e_\alpha q_\beta k_\tau (2p)_\sigma|^2 = 4p^2 q^2 M^2 \sin^2\theta$$

(θ is the angle between **p** and **q**).

Now

$$\frac{p^4}{\omega'\omega''}\left|\frac{\mathrm{d}p}{\mathrm{d}E_f}\right|_{E_i=E_f} = \frac{(M-q)^4(M^2-2Mq-4m^2)^{3/2}}{8(M^2-2Mq+q^2\sin^2\theta)^{5/2}},$$

where m is the π-meson mass. Putting

$$\mathrm{d}\Omega_p = 4\pi, \qquad \mathrm{d}\Omega_q = 2\pi\sin\theta\,\mathrm{d}\theta,$$

and performing the θ-integration, we find from (5)

$$\frac{1}{\tau} = \int \frac{(2\pi)^{-3}g^2G^2}{24\kappa_1^2}\cdot\frac{M(M^2-2Mq-4m^2)^{3/2}q^3\,\mathrm{d}q}{(M^2-2Mq-\kappa_1^2)^2(M^2-2Mq)^{\frac{1}{2}}},$$

and, after the following substitution

$$q/M = x, \qquad m/M = y, \qquad \text{and } \kappa_1/M = z,$$

the decay rate ($\mathrm{K}_2^0 \to 2\pi+\gamma$) reduces to

$$\frac{1}{\tau} = \frac{g^2G^2}{(2\pi)^3\,24z^2M}\int_0^{(0\cdot5-2y^2)}\frac{x^3(1-2x-4y^2)^{3/2}\,\mathrm{d}x}{(1-2x-z^2)^2(1-2x)^{\frac{1}{2}}} = 7\times10^4\ \mathrm{s}^{-1},$$

where we have used

$$g = 1\cdot5\times10^{-5}, \text{ corresponding to } M_0 = 1\cdot1 \text{ GeV},$$
$$M = 496 \text{ MeV},\ y = 0\cdot276, \text{ and } z = 1\cdot51.$$

Thus the value of $\tau(\mathrm{K}_2^0 \to 2\pi+\gamma) \approx 1\cdot4\times10^{-5}$ s, as obtained from the present dynamical model, is consistent with the approximate estimation made at the beginning of the paper.

The photon energy spectrum in the K_2^0 rest frame is given by

$$f(x) = \frac{x^3(1-2x-4y^2)^{3/2}}{(1-2x-z^2)^2(1-2x)^{\frac{1}{2}}}, \tag{6}$$

as shown in Figure 2.

From experiment (Abashian *et al.* 1964; Christenson *et al.* 1964) we have

$$(\mathrm{K}_2^0 \to 2\pi)/(\mathrm{K}_2^0 \to \text{all decay modes}) = 2\times10^{-3}.$$

This ratio corresponds to about half the radiative events, according to the above estimates, or hence to an average photon energy of not quite 100 MeV. Thus, if the γ-ray energy is really $\lesssim 10$ MeV, the possibility for the interpretation that the observed event is $\mathrm{K}_2^0 \to 2\pi+\gamma$ is very slight. Conversely, if the γ-ray energy could happen to be as large as 100 MeV, such interpretation may be possible.

This suggests the importance of the experimental study of $\mathrm{K}_2^0 \to 2\pi+\gamma$. The energy distribution is approximately a parabola peaked at 120 MeV, and the angular correlation is approximately proportional to $\sin^2\theta$.

MAGNETIC $K_2^0 \rightarrow K_1^0$ CONVERSION

The fact that $K_2^0 \rightarrow K_1^0 +$ odd γ is in principle only inhibited but not forbidden (Peaslee and Vaughn 1960) suggests a possible interaction of the form

$$H_{\text{int}} = eA_\mu f(\Box^2)[\phi_4 \partial_\mu \phi_3 - \phi_3 \partial_\mu \phi_4] \tag{7}$$

$$= ieA_\mu f(\Box^2)[\phi^* \partial_\mu \phi - \partial_\mu \phi^* \phi], \tag{8}$$

where $\phi = (\phi_3 + i\phi_4)/\sqrt{2}$ represents a K^0 meson.

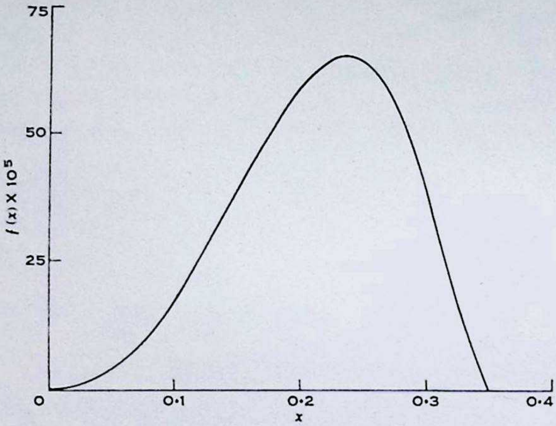

Fig. 2.—Photon energy spectrum associated with $K_2^0 \rightarrow 2\pi + \gamma$, where x measures the photon energy in units of average baryon mass.

Electrical neutrality of the K^0 meson assumes by equation (8) that $f(0) = 0$ but tells nothing about higher moments. If $f(\Box^2)$ does not vanish identically, the possibility exists of $K_2^0 \rightarrow K_1^0$ conversion on passage through an external magnetic field. One-photon conversion can involve only scalar photons because the K^0 meson has spin zero. We write

$$f(\Box^2) = f_0 + f_2(\Box^2/M_0^2) + f_4(\Box^4/M_0^4) + \ldots, \tag{9}$$

where $f_0 = 0$ and $M_0 = 1 \cdot 1$ GeV is the baryon mass.

Now

$$\Box^2 A_\mu = -j_\mu, \text{ source of the magnetic field,}\dagger \tag{10}$$

and from equations (7), (9), and (10) we find

$$H_{\text{int}} = \frac{ef_2}{M_0^2} \cdot \frac{\mathbf{k} . \mathbf{j}(\kappa)}{\omega(2\pi)^{3/2}} \Psi^2(R),$$

where we use

$$\mathbf{k} \approx \mathbf{k}' = K^0\text{-meson momentum},$$

$$\omega \approx \omega' = K^0\text{-meson energy},$$

$$\mathbf{j}(x) = (2\pi)^{-3/2} \int \mathbf{j}(\kappa)\, e^{-i\kappa \cdot x}\, d^3\kappa,$$

---

† In the present calculation only the transverse fringe of the beam, which actually passes through the current coils of the magnets, produces regeneration. The entire beam is taken coherent in the transverse dimension, and the coil acts as the edges of a gigantic slit.

with $\kappa =$ wave vector of magnetic field. Here $\Psi(R)$ is a function describing the spread of the beam, considered as a coherent wave packet in the transverse dimensions (cf. Appendix). The momentum of this wave packet is negligibly disturbed by the $K_2^0 \rightarrow K_1^0$ transition; therefore the $K_1^0 \rightarrow 2\pi$ decay occurs principally in the centre of the beam, although the converting interaction was located in the fringes. If the total path length through the magnetic field is L, the probability of $K_2^0 \rightarrow K_1^0$ conversion is given by

$$P = (L/\tau)(\omega/k), \tag{11}$$

where

$$\frac{1}{\tau} = \tfrac{1}{3}(2\pi)^{-2}\left(\frac{ef_2}{M_0^2}\right)^2 \frac{k^2}{\omega^2}\, j^2(\kappa)\left(\frac{\mathrm{d}^3k'}{\mathrm{d}E}\right)\left|\Psi^2(R)\right|^2.$$

Integrating over all wave vectors $\boldsymbol{\kappa}$ present in the field, we get

$$P = \tfrac{1}{3}(2\pi)^{-2}\left(\frac{ef_2}{M_0^2}\right)^2 \frac{Lk}{\omega}\int j^2(\kappa)\,\mathrm{d}^3\kappa\left(\frac{\mathrm{d}^3k'}{\mathrm{d}E}\right)\left|\Psi^2(R)\right|^2. \tag{12}$$

Now put

$$\int j^2(\kappa)\,\mathrm{d}^3\kappa = \int \kappa^2(\mathbf{j}\,.\,\mathbf{A})\,\mathrm{d}^3\kappa = \langle\kappa^2\rangle 4\pi\epsilon_t,$$

where ϵ_t is the total energy in the magnetic field $H(\approx 10^3$ to 10^4 gauss) and $\langle\kappa^2\rangle = (2\pi n/l)^2$, with l the mean transverse wavelength in the magnetic field and n a numerical factor depending on the nonuniformity of the magnetic field. With $\mathrm{d}^3k'/\mathrm{d}E = 4\pi k\omega$, the expression for the probability of magnetic conversion becomes (after inserting the $\hbar c$ factors)

$$P = \tfrac{1}{3}(4\pi n)^2 f_2^2\left(\frac{L}{l^2}\cdot\frac{e^2}{M_0c^2}\right)\left(\frac{\epsilon_t}{M_0c^2}\right)\left(\frac{p_\kappa}{M_0}\right)^2\left|\Psi^2(R)\right|^2, \tag{13}$$

where $p_\kappa = \hbar k$, and each term in the brackets is dimensionless.

For $L = 10$ ft, $H = 10^4$ gauss, $\Psi^2(R) = 10^{-3}$,* $p_\kappa = 1\cdot 1$ GeV/c, $nf_2 = 3$, and $(L/l^2)\epsilon_t = (1/4\pi)(HL)^2$, we get from equation (13)

$$P = 10^{-5}.$$

This is about the same as for radiative decay with $E_\gamma \lesssim 3$ MeV and is about 10^2 short of the observed value. On the other hand, $nf_2 \approx 30$ would explain the observations. (See Peaslee and Vaughn (1960) for a possible value of f_2.)

The presence of magnetic conversion $K_2^0 \rightarrow K_1^0$ seems feasible to observe by changing the magnetic field, length of the field, and n. Such a measurement might be of interest even if the mechanism is not responsible for the previous observations (Abashian *et al.* 1964; Christenson *et al.* 1964).†

Failure of CP invariance as a local effect due to dissymmetry of the environment was also suggested by Bell and Perring (1964).

---

* According to the Appendix this corresponds to a magnetic field at a distance of order $R = 0\cdot 97R_0$ from a beam of radius R_0.

† The results of Christenson *et al.* have been repeated independently at CERN and in England. In every case the decay fraction of $(K_2^0 \rightarrow 2\pi)/K_2^0$ was $\epsilon = 2\times 10^{-3}$, although the experimental set-ups must have differed greatly. All electromagnetic regeneration effects vary as $(p_\kappa/M_0)^2 \rightarrow \gamma^2 = 1/(1-\beta^2)$. Christenson *et al.* had already made preliminary measurements showing the *absence* of any γ^2 effect.

ACKNOWLEDGMENT

The author is grateful to Professor D. C. Peaslee for initiating the investigation and for many helpful discussions.

REFERENCES

ABASHIAN, A., ABRAMS, R. J., CARPENTER, D. W., FISHER, G. P., NEFKENS, B. M. K., and SMITH, J. H. (1964).—*Phys. Rev. Lett.* **13**: 243.

ADLER, R. J., and DRELL, S. (1964).—*Phys. Rev. Lett.* **13**: 349.

BELL, J. S., and PERRING, J. K. (1964).—*Phys. Rev. Lett.* **13**: 348.

BERMAN, S., and DRELL, S. (1964).—*Phys. Rev.* **133**: B791.

CHRISTENSON, J. H., CRONIN, J. W., FITCH, V. L., and TURLAY, R. (1964).—*Phys. Rev. Lett.* **13**: 138.

PEASLEE, D. C., and VAUGHN, M. T. (1960).—*Phys. Rev.* **119**: 460.

APPENDIX

Transverse beam function $\Psi(R)$, corresponding to a uniform momentum distribution, is

$$\Psi(R) = \frac{1}{2\pi}\int_0^{K_0} \{\exp(\mathrm{i}KR\cos\theta)\}K\,\mathrm{d}K\,\mathrm{d}\theta$$

$$= \int_0^{K_0} K\,\mathrm{d}K\mathrm{J}_0(KR)$$

$$= (K_0/R)\mathrm{J}_1(K_0R).$$

Thus

$$\Psi(R) = C(R_0/R)\mathrm{J}_1(3\cdot 83R/R_0),$$

where R_0 = beam radius, and $3\cdot 83$ = 1st zero of J_1, the Bessel function of order one. The constant C is fixed by the condition

$$2\pi\int_0^{R_0} \frac{R\mathrm{d}R}{R_0^2}\Psi^2(R) = 1.$$

Hence, after numerical integration, we get

$$C = 0\cdot 64,$$

and accordingly

$$\Psi(R) = 0\cdot 64(R/R_0)^{-1}\mathrm{J}_1(3\cdot 83R/R_0).$$

RELIABILITY OF CALIBRATIONS AND COMPARISONS OF REFERENCE STANDARDS WITH AN APPLICATION TO A GROUP OF LINE STANDARDS

By E. G. Thwaite*

[*Manuscript received April* 26, 1965]

Summary

The problem discussed is that of combining interrelated data which refer to the calibration and intercomparison of a group of standards, to give best estimates for the values of the standards together with their reliabilities. A résumé is given of least squares in matrix notation, which is particularly suited to computations using automatic computers, and this technique is applied to results obtained over a period of 15 years at the Bureau International des Poids et Mesures and the National Standards Laboratory, in the calibration and intercomparison of five 1 m reference line standards of length. One of these scales was a platinum-iridium prototype (No. 20), while the remainder were in nickel or 58% nickel-steel. The analysis yields time-dependent values, where appropriate, for the lengths of the scales together with their variances, and an estimate of the observational variance. The estimate of the observational variance, $(0\cdot077\ \mu\text{m})^2$, is based in part on "external consistency", as the data used in the analysis were obtained in more than one laboratory.

I. Introduction

Where a number of reference standards have been in use for some time, and have been individually calibrated on a number of occasions and compared with each other from time to time, the questions naturally arise of the best values to be associated with the standards, and the reliabilities of these values. The answers to these questions are of particular interest when the observations come from more than one laboratory, since the results can then lead to reliable estimates of consistency between laboratories and to more realistic estimates of accuracy.

The interrelationships between the various observations can be very complex, particularly in the case where the standards are unstable. To arrive at the "best" values for the standards at any time, it is necessary to combine all the information available, while making allowance for particular circumstances such as instability, unequal reliability, or correlations between the observations.

The appropriate way of arriving at the "best" estimates in the situation described above would seem to be by a least-squares treatment. Further, and this is perhaps more relevant here, the sizes of the residuals from any least-squares solution, or statistics calculated from them, are an excellent guide to the reliability of the measurements.

The technique of least squares has been used for decades in adjusting and combining observations. However, solutions involving even small numbers of

---

* Division of Applied Physics, National Standards Laboratory, CSIRO, University Grounds, Chippendale, N.S.W.

Aust. J. Phys., 1965, **18**, 401–8

unknowns require formidable computations and, while for small numbers it is reasonable to undertake solutions using a desk calculator, the use of an automatic computer considerably lightens the task and makes it possible readily to undertake solutions involving very large numbers of unknowns.

The size of problem that can be handled on a digital computer is limited by the memory capacity of the machine and by the accuracy required in the solution, together with the amount of machine time available. There are several ways in which limitations of memory capacity and accuracy can be overcome, and so the effective limitation is that of machine time.

For the purpose of computation on a digital computer, the formulation of the least-squares solutions in matrix notation is ideal. Not only does the matrix approach lead to a highly systematic and general set of relationships for the design and for the solutions, but also it gives the variances and covariances of the improved estimates with very little additional calculation once the solutions have been obtained.

In the following sections, a brief résumé of the matrix formulation of least squares is given, and an analysis is made of a comprehensive set of data relating to observations made over a period of 15 years, at the Bureau International des Poids et Mesures and the National Standards Laboratory, on a group of 1 m reference line standards.

The approach adopted here is a general one and suitable for application to any set of data that shows the type of dependencies already discussed. The data could refer to any one of a number of different types of standards, such as resistance, capacitance, mass, etc.

II. LEAST SQUARES IN MATRIX NOTATION

Let the results $y_1, y_2, \ldots, y_m$ of m observations be related to the quantities $x_1, x_2, \ldots, x_n$ by the expectations

$$\epsilon(y_i) = \sum_{j=1}^{n} a_{ij} x_j \qquad (i = 1, 2, \ldots, m),$$

where the a_{ij} are constants and form the design matrix $[a_{ij}]$, A say, of order $m \times n$.

Writing

$$\mathbf{x} = [x_1, x_2, \ldots, x_n]^T,$$

$$\mathbf{y} = [y_1, y_2, \ldots, y_m]^T,$$

both column matrices, we have in matrix notation

$$\epsilon(\mathbf{y}) = \mathbf{A}\mathbf{x}.$$

Making the restriction that the observed values y are independent and have equal variances σ^2, we may write the dispersion matrix in the form

$$\mathbf{D} = \sigma^2 \mathbf{I};$$

the least-squares solutions are then

$$\hat{\mathbf{x}} = (\mathbf{A}^T\mathbf{A})^{-1}\mathbf{A}^T\mathbf{y},$$

with the variance–covariance matrix given by

$$\mathbf{D}_x = \sigma^2(\mathbf{A}^T\mathbf{A})^{-1}.$$

In general σ^2 is unknown, and its unbiased estimate s^2 is given by

$$s^2 = \frac{\mathbf{y}^T\mathbf{y}-\hat{\mathbf{x}}^T\mathbf{A}^T\mathbf{y}}{m-n}.$$

Rigorous treatments using matrix notation of least squares in the linear case will be found in the works of Plackett (1960) and Guest (1961), and these include the important case of dependent observations.

III. LEAST-SQUARES ANALYSIS FOR A GROUP OF REFERENCE LINE STANDARDS

Since 1948 the National Standards Laboratory (N.S.L.) has maintained a number of 1 m line standards as reference standards of length. Until the introduction of the wavelength standard these line standards embodied the primary standard of length for the Commonwealth of Australia.

The information relating to the lengths of these scales is contained in a complex set of relationships between the lengths of the scales, which are the result of direct comparisons made from time to time at N.S.L., and also in their relationships with the prototype metre, determined through calibrations at the Bureau International des Poids et Mesures (B.I.P.M.) and on one occasion by the National Physical Laboratory (N.P.L.). The complexity of the information lies in the fact that the scales are of unequal age, and the periods they have been under surveillance vary. Further, the majority of the scales are known to be unstable in length, and this adds greatly to the difficulty of determining the appropriate value for their length at any time.

At the beginning of the period, the set consisted of a pair of 58% nickel-steel scales, 4028 and 4756(I), both calibrated by B.I.P.M. The original set was augmented, firstly by a nickel scale 79, then by another 58% nickel-steel scale 172/62, and finally by the reruled platinum-iridium prototype No. 20. The nickel scale and, of course, the prototype, were initially calibrated by B.I.P.M. Owing to corrosion damage, one of the original pair of nickel-steel scales required to be reruled, and this resulted in an unfortunate discontinuity in the knowledge of its behaviour. The reruled scale is designated 4756(II).

Details of the calibration and intercomparison of the set of scales are given in Table 1, together with additional information which will be discussed later.

We now proceed to obtain the solutions for the data given in Table 1.

The error in the length of a scale is assumed to be given by an equation of the form

$$L_i(d) = a_i+b_i(d-1948),$$

where L_i is the error at 20°C in the length of the ith scale at date d (expressed in years and decimals of a year), and the a_i and b_i are constants of the expression that are to be estimated by the least-squares solution. The lengths of all the scales are assumed to be adequately represented by this form of expression, with the exception of prototype No. 20 which is assumed to be stable and so lacks the time-dependent term. It is known that the nickel-steel scales are unstable, and it would be unwise to assume stability for the nickel scale. In the absence of information other than the data alone about the degree of the curve to be fitted, the justification of a model is its success in fitting the data points, the model of least degree that adequately fits the data being the one chosen. While in the present case the data are hardly adequate to fit anything but a linear model, as will be seen later, the fit is good. Under these conditions extrapolation will be as good as is possible.

TABLE 1

OBSERVED AND CALCULATED VALUES* (ELEMENTS OF **y**)

Observational standard deviation 0·077 μm

Scale	Authority	Date	Observed Value (μm)	Calculated Value (μm)	Residual (μm)
4028	B.I.P.M.	1948·96	−2·19	−2·253	−0·063
4028	B.I.P.M.	1957·04	−3·02	−2·988	0·032
4756(I)	B.I.P.M.	1952·71	−0·67	−0·635	0·035
4756(II)	B.I.P.M.	1961·96	−0·13	−0·130	0·000
79	B.I.P.M.	1957·25	2·11	2·115	0·005
79	N.P.L.	1957·54	2·06	2·108	0·048
20	B.I.P.M.	—†	1·31	1·253	−0·057
4028–4756(I)	N.S.L.	1957·21	1·94	1·956	0·016
4028–4756(I)	N.S.L.	1955·87	2·05	1·957	−0·093
4028–4756(I)	N.S.L.	1957·96	1·93	1·956	0·026
4028–79	N.S.L.	1957·96	−5·18	−5·170	0·010
79–4756(I)	N.S.L.	1957·96	3·23	3·214	−0·016
4028–4756(II)	N.S.L.	1962·37	−3·31	−3·261	0·049
4028–172/62	N.S.L.	1962·37	−5·62	−5·566	0·054
4028–79	N.S.L.	1962·37	−5·55	−5·468	0·082
4756(II)–172/62	N.S.L.	1962·37	−2·26	−2·305	−0·045
4756(II)–79	N.S.L.	1962·37	−2·30	−2·206	0·094
172/62–79	N.S.L.	1962·37	0·09	0·098	0·008
172/62–79	N.S.L.	1961·62	0·24	0·206	−0·034
172/62–4028	N.S.L.	1961·62	5·59	5·624	0·034
20–79	N.S.L.	1963·79	−0·64	−0·708	−0·068
20–4028	N.S.L.	1963·79	4·73	4·855	0·125
79–4028	N.S.L.	1963·79	5·51	5·564	0·054

* Referred to 20°C.

† See text.

Prototype No. 20 is of the same melt as the original prototypes, and it can be reasonably assumed that, in the very short period between the B.I.P.M. calibration (June–September 1960 and January 1963) and its inclusion in the N.S.L. series (1963·79), any drift will be negligible.

From the data of Table 1, the design matrix is the 23 row by 11 column matrix

$$\mathbf{A} = \begin{bmatrix}
1 & 0\cdot96 & 0 & 0 & 0 & 0 & 0 & 0 & 0 & 0 & 0 \\
1 & 9\cdot04 & 0 & 0 & 0 & 0 & 0 & 0 & 0 & 0 & 0 \\
0 & 0 & 1 & 4\cdot71 & 0 & 0 & 0 & 0 & 0 & 0 & 0 \\
0 & 0 & 0 & 0 & 1 & 13\cdot96 & 0 & 0 & 0 & 0 & 0 \\
0 & 0 & 0 & 0 & 0 & 0 & 1 & 9\cdot25 & 0 & 0 & 0 \\
0 & 0 & 0 & 0 & 0 & 0 & 1 & 9\cdot54 & 0 & 0 & 0 \\
0 & 0 & 0 & 0 & 0 & 0 & 0 & 0 & 0 & 0 & 1 \\
-1 & -9\cdot21 & 1 & 9\cdot21 & 0 & 0 & 0 & 0 & 0 & 0 & 0 \\
-1 & -7\cdot87 & 1 & 7\cdot87 & 0 & 0 & 0 & 0 & 0 & 0 & 0 \\
-1 & -9\cdot96 & 1 & 9\cdot96 & 0 & 0 & 0 & 0 & 0 & 0 & 0 \\
1 & 9\cdot96 & 0 & 0 & 0 & 0 & -1 & -9\cdot96 & 0 & 0 & 0 \\
0 & 0 & -1 & -9\cdot96 & 0 & 0 & 1 & 9\cdot96 & 0 & 0 & 0 \\
1 & 14\cdot37 & 0 & 0 & -1 & -14\cdot37 & 0 & 0 & 0 & 0 & 0 \\
1 & 14\cdot37 & 0 & 0 & 0 & 0 & 0 & 0 & -1 & -14\cdot37 & 0 \\
1 & 14\cdot37 & 0 & 0 & 0 & 0 & -1 & -14\cdot37 & 0 & 0 & 0 \\
0 & 0 & 0 & 0 & 1 & 14\cdot37 & 0 & 0 & -1 & -14\cdot37 & 0 \\
0 & 0 & 0 & 0 & 1 & 14\cdot37 & -1 & -14\cdot37 & 0 & 0 & 0 \\
0 & 0 & 0 & 0 & 0 & 0 & -1 & -14\cdot37 & 1 & 14\cdot37 & 0 \\
0 & 0 & 0 & 0 & 0 & 0 & -1 & -13\cdot62 & 1 & 13\cdot62 & 0 \\
-1 & -13\cdot62 & 0 & 0 & 0 & 0 & 0 & 0 & 1 & 13\cdot62 & 0 \\
0 & 0 & 0 & 0 & 0 & 0 & -1 & -15\cdot79 & 0 & 0 & 1 \\
-1 & -15\cdot79 & 0 & 0 & 0 & 0 & 0 & 0 & 0 & 0 & 1 \\
-1 & -15\cdot79 & 0 & 0 & 0 & 0 & 1 & 15\cdot79 & 0 & 0 & 0
\end{bmatrix}$$

The column vector $\mathbf{x}$ is given by

$$\mathbf{x} = [a_1, b_1, a_2, b_2, a_3, b_3, a_4, b_4, a_5, b_5, a_6]^T,$$

where the correspondence between the scales and the constants is as given in Table 2.

TABLE 2

ESTIMATES OF COEFFICIENTS AT 20°C

Scale	i	a_i (μm)	b_i (μm m^{-1} yr^{-1})
4028	1	$-2\cdot166$	$-0\cdot0910$
4756(I)	2	$-0\cdot204$	$-0\cdot0915$
4756(II)	3	$2\cdot649$	$-0\cdot1991$
79	4	$2\cdot333$	$-0\cdot0235$
172/62	5	$4\cdot497$	$-0\cdot1672$
20	6	$1\cdot253$	—

The observational vector is

$$\mathbf{y} = [-2\cdot19, -3\cdot02, -0\cdot67, \ldots, 5\cdot51]^T.$$

It is assumed that the elements of y have equal weights, that is, that they are independent and have equal variances. While the data have been obtained over a considerable length of time and at different laboratories, techniques applied in the comparison of line standards differ little, and should have remained sufficiently stable for the assumption of equal variances to be reasonably made. The results of the solution can be used to test this assumption, but unfortunately in this case the test is necessarily inexact. The solutions are then given by the last three equations of Section II.

The whole of the least-squares solution was carried out on a digital computer. The core of the solution is the inversion of the matrix $\mathbf{A}^T\mathbf{A}$, and this was undertaken by the "elimination" method (see, for example, Kunz 1957).

On post-multiplication by $\mathbf{A}^T\mathbf{y}$ the inverse yields the estimates $\hat{\mathbf{x}}$, the components of which are listed in Table 2.

The estimate of the observational variance s^2 was $0\cdot005917\ \mu\mathrm{m}^2$, giving a standard deviation of $0\cdot077\ \mu\mathrm{m}$, the estimate being based on 12 degrees of freedom.

Multiplication of the inverse by s^2 then gives the dispersion matrix $\mathbf{D}_{\hat{x}}$, the diagonal elements corresponding to the variances and the off-diagonal elements to the covariances.

$$\mathbf{D}_{\hat{x}} = (10^{-7}\mu\mathrm{m}^2)\begin{array}{c}
\begin{array}{ccccccccccc}
\multicolumn{2}{c}{\overbrace{\hspace{6em}}^{4028}} & \multicolumn{2}{c}{\overbrace{\hspace{6em}}^{4756(\mathrm{I})}} & \multicolumn{2}{c}{\overbrace{\hspace{6em}}^{4756(\mathrm{II})}} & \multicolumn{2}{c}{\overbrace{\hspace{6em}}^{79}} & \multicolumn{2}{c}{\overbrace{\hspace{6em}}^{172/62}} & 20 \\
a_1 & b_1 & a_2 & b_2 & a_3 & b_3 & a_4 & b_4 & a_5 & b_5 & a_6
\end{array} \\
\left[\begin{array}{rrrrrrrrrrr}
56608 & & & & & & & & & & \\
-5123 & 642 & & & & & & & & & \\
1290 & -1184 & 233872 & & & & & & & & \\
638 & 208 & -27592 & 3551 & & & & & & & \\
548924 & -131862 & 524589 & -119890 & 14492452^{*} & & & & & & \\
-39321 & 9446 & -37578 & 8588 & -10232902 & 722681 & & & & & \\
40171 & -5676 & -6692 & 742 & 1639543 & -117446 & 223235 & & & & \\
-3856 & 649 & -585 & 186 & -210687 & 15092 & -19357 & 1828 & & & \\
48389 & -5400 & -2700 & 689 & 5667879 & -406008 & 131698 & -11606 & 18268155 & & \\
-4489 & 645 & -884 & 197 & -507075 & 36323 & -12516 & 1238 & -1301547 & 92983 & \\
-15000 & 3193 & -11110 & 2534 & -1073465 & 76896 & -43956 & 5298 & -29475 & 4245 & 44764
\end{array}\right]
\end{array}$$

* The accuracy of the solution is not sufficient to give the value of this last place.

As the matrix $\mathbf{D}_{\hat{x}}$ is symmetric about the diagonal, only the lower triangular matrix has been reproduced here.

Substitution of the estimates $\hat{\mathbf{x}}$ in the expressions $\mathbf{Ax}$ gives estimates of the observed values, and these, together with the residuals from the observed values, are given in Table 1.

IV. Discussion and Conclusion

The variances to be associated with the estimates from the regression lines are, of course, time-dependent and are given by the propagation of variance formula

$$\mathrm{Var}(L_i) = \mathrm{Var}(a_i) + (d-1948)^2 \,.\, \mathrm{Var}(b_i) + 2(d-1948) \,.\, \mathrm{Cov}(a_i, b_i).$$

Substitution then leads to the following:

$$\begin{aligned}
\mathrm{Var}(4028) &= 0\cdot005661+0\cdot0000642(d-1948)^2-0\cdot0010246(d-1948),\\
\mathrm{Var}(4756\ \mathrm{I}) &= 0\cdot023387+0\cdot0003551(d-1948)^2-0\cdot0055184(d-1948),\\
\mathrm{Var}(4756\ \mathrm{II}) &= 14\cdot492452+0\cdot0722681(d-1948)^2-2\cdot0465804(d-1948),\\
\mathrm{Var}(79) &= 0\cdot022324+0\cdot0001828(d-1948)^2-0\cdot0038714(d-1948),\\
\mathrm{Var}(172/62) &= 1\cdot826816+0\cdot0092983(d-1948)^2-0\cdot2603094(d-1948),
\end{aligned}$$

where the unit is $\mu\mathrm{m}^2$.

On first inspection of the time-dependent variance equations, the impression may be gained that the variances, in some cases, are very large indeed. Since a common time, the year 1948, has been chosen as the origin for all the regression equations, the constant terms in the right-hand side of the variance equations will be large in those cases where the first observations occur at times much later than 1948. In these cases, however, the covariance term has a substantial negative value during the observational period, and the variances over these periods are much smaller than the values at the origin.

The expressions for the time-dependences of the lengths have a varying degree of usefulness that depends primarily upon the length of time that the scale has been under observation. The values of the variances for 4756(II) and 172/62 show that these two scales have been under observation for much too short a period for any reliability to be placed upon the predictions from their regression lines.

The results of the adjustments do not answer unequivocably the question of the stability of the nickel scale 79. A test of the slope of this regression line against the hypothesis of zero slope showed it to be almost significant at the 10% level. The normal interpretation of this result would be that there is insufficient evidence to say that the scale is unstable; the effect on the model, however, is small.

The sizes of the individual residuals are all satisfactorily small. The estimate of the observational standard deviation, $0\cdot077\ \mu\mathrm{m}$, is to be compared with the value $0\cdot1\ \mu\mathrm{m}$ which is usually spoken of as the ultimate accuracy with which line standards can be compared using visual microscopes. This estimate of the observational standard deviation is of some importance as it is based, in the main, on data from two laboratories, that is, it is an estimate based in part on "external consistency" rather than purely "internal consistency". Birge (1957) and Youden (1962) have discussed at some length the importance of estimates based on external, rather than internal, consistency.

The form of the design matrix in this case does not lend itself to a rigorous test of the assumption of equal variance for the results of the different laboratories. However, estimation of the variances for B.I.P.M. and N.S.L. separately from the residuals, using degrees of freedom based on a partitioning of the total number of degrees of freedom in the ratio 7 : 16, leads to an F ratio of $2\cdot16$. To be significant at the 5% level this ratio is required to be of the order 6, while to be significant at the 1% level it would have to reach 15. It is certain then that, whatever the actual degrees of freedom for the two estimates, the F ratio would not reach a significant value, and it must be concluded that the results show no evidence to contradict the assumption of equal variance for the observed values.

The result of the present adjustment indicates that it would be practicable and indeed desirable to undertake an adjustment on a much wider basis. The inclusion of the prototype metres in a least-squares adjustment would appear to be valuable at present, when the relationship between lengths based on the prototypes and on the wavelength definition are under discussion.

V. Acknowledgments

The least-squares solution was carried out on the I.B.M. 7090 computer, at Weapons Research Establishment, Salisbury, S. Aust. The author wishes to thank Mr. M. J. Puttock and Dr. R. T. Leslie for their comments on the manuscript.

VI. References

Birge, R. T. (1957).—*Nuovo Cim.* (10) **6** (Suppt.): 39–67.

Guest, P. G. (1961).—"Numerical Methods of Curve Fitting." (Cambridge Univ. Press.)

Kunz, K. S. (1957).—"Numerical Analysis." pp. 234–5. (McGraw-Hill: New York.)

Plackett, R. L. (1960).—"Regression Analysis." Ch. III. (Oxford Univ. Press.)

Youden, W. J. (1962).—N.B.S. Miscellaneous Publ. 248. (Pap. 5.1, Proc. 1962 Stds Lab. Conf.) (U.S. Dept. of Commerce.)

PRECISION MEASUREMENTS OF THE TOWNSEND ENERGY RATIO FOR ELECTRON SWARMS IN HIGHLY UNIFORM ELECTRIC FIELDS

By R. W. Crompton,* M. T. Elford,* and J. Gascoigne*

[*Manuscript received May* 31, 1965]

Summary

A detailed account is given of the solution to the problems associated with the use of the Townsend–Huxley method of measuring the ratio of drift speed to diffusion coefficient for very low energy electron swarms. The elimination of radial components of the electric field within the diffusion chamber is shown to be the major experimental problem, especially in the case of the comparatively weak electric fields which must be used for some of the measurements in the near-thermal region. The experimental techniques and procedures, which are described in some detail, enable measurements to be made in this region with an accuracy comparable to that which has been achieved at higher electron energies.

I. Introduction

One of the methods of examining collision phenomena between low energy electrons and gas molecules is to measure the ratio of the drift velocity W to the diffusion coefficient D of an electron swarm moving under the influence of an electric field E in a gas at a pressure p. Since W/D is a pressure-dependent quantity, the experimental results are always given either in terms of D/μ, where μ is defined as the ratio W/E, or of k_1, a parameter closely related to the Townsend energy factor, k_T, which is defined as the ratio of the mean energy of agitation of the electrons to the mean thermal energy of the molecules of the gas through which the electron swarm moves. These quantities are related by the expression

$$k_1 = \frac{D/\mu}{kT/e} = \frac{eE/kT}{W/D}, \tag{1}$$

where

k = Boltzmann's constant,

e = electronic charge,

T = absolute gas temperature.

Both k_1 and D/μ are functions of the ratio E/N and are also, in general, functions of the gas temperature.

An examination of a number of possible sources of error in the Townsend–Huxley method for measuring k_1 has been made by Crompton and Jory (1962), who showed that, by careful attention to the choice of experimental parameters and conditions, results with errors of less than 1% can be achieved for measurements of k_1 in hydrogen at 293°K over the range in E/p of $0\cdot1$–$5\cdot0$ V cm^{-1} torr^{-1}, for which the lowest value of k_1 is approximately 2. If the measurements are to be extended to lower values of E/p, the data lose much of their significance unless at least comparable accuracy is achieved in the face of increasing experimental difficulties. Improved accuracy is in fact desirable for the following reason. When the data from these experiments are used to investigate inelastic collision processes for quasi-thermal electrons in molecular gases (see, for example, Huxley 1959; Frost and Phelps 1962), the parameters which assume importance are not simply k_1 and D/μ but rather the difference terms (k_1-1) and $(D/\mu-kT/e)$, both of which approach zero as E/p approaches zero. Clearly, small errors in the determination of W/D can lead to serious errors in analyses which rely on these difference terms, and it is for this reason that an attempt has been made in the present work to achieve a high order of accuracy and to understand the factors that limit the accuracy of experiments of this type.

---

* Ion Diffusion Unit, Australian National University, Canberra.

Although the results of a number of workers (Townsend and Bailey 1921; Crompton and Sutton 1952; Cochran and Forester 1962; Warren and Parker 1962; Rees 1964; Rees and Jory 1964) are in reasonable agreement when the mean energy of the electron swarm is in excess of about 0·5 eV, the agreement is not satisfactory when the electron energy approaches the energy of the gas molecules. Our own experience and that of Warren and Parker (1962) have shown that considerable difficulties exist in obtaining reliable, and therefore significant, data in this low energy region. In the recent extensive investigation carried out by Warren and Parker (1962), these difficulties were so severe that it was necessary to calibrate the apparatus empirically, the results obtained using the empirical calibration and those obtained from the mathematically derived calibration differing by up to 30%. Such a procedure is clearly undesirable where $k_1-1 \lesssim 0\cdot 10$, in view of the discussion above. In the present investigation no such procedure was necessary. In other investigations (e.g. Cochran and Forester 1962) it is apparent that large systematic errors were present but that it was not possible to take account of them.

In what follows, an account is given of the outcome of an extensive investigation into the factors that must be considered in order to obtain measurements of W/D at 293°K, to within 1%, down to a value of E/p of 0·006 where, for example in hydrogen, $(k_1-1) \approx 0\cdot 03$. The results from these investigations have been published previously in summary (Crompton and Elford 1963), and will be published in detail in due course together with an extension of the work to other gases and other temperatures.

II. PRINCIPLE OF THE METHOD

The method of measuring the ratio W/D has been described in detail elsewhere (e.g. Crompton and Jory 1962), and will be considered only briefly here.

Electrons enter the diffusion chamber (Fig. 1) through a small hole in the cathode, and diffuse and drift under the influence of the electric field E towards the anode. The anode is divided into a disk and annulus, and the ratio R of the electron currents received by these electrodes is measured.

The diffusion equation that describes the motion of an electron swarm is

$$\nabla^2 n = (W/D)\,\partial n/\partial z = 2\lambda\,\partial n/\partial z, \tag{2}$$

where n is the electron number density, and the z axis is parallel to the electric field E. If the electrons originate from a point source, two solutions of equation (2) are (Huxley 1940):

$$n = A\,\mathrm{e}^{\lambda z}\left(\frac{\mathrm{e}^{-\lambda r}}{r}\right) \tag{3}$$

and

$$n = A\,\mathrm{e}^{\lambda z}\frac{z}{r}\frac{\mathrm{d}}{\mathrm{d}r}\left(\frac{\mathrm{e}^{-\lambda r}}{r}\right), \tag{4}$$

where r is the distance measured from the origin, and A is a constant.

The boundary conditions normally applied are that $n = 0$ everywhere at the cathode and anode except at the origin. No radial boundary condition need be imposed since it can be shown that, with the most widely divergent electron stream used in our experiments, less than $0\cdot004\%$ of the electron swarm is found outside a radial distance of 4 cm. The electron concentration at the surface of the guard electrodes of the apparatus shown in Figure 2 is therefore negligible, and hence the presence of the guard electrodes cannot significantly affect the electron concentration elsewhere. Thus for this apparatus, and for others of the same type which have been used in this laboratory for similar experiments, it is unnecessary to take into account the effect of the walls of the diffusion chamber as has been suggested by Warren and Parker (1962). When the boundary conditions are imposed on the dipole solution (equation (4)), the ratio of the current i_b received by the disk of diameter $2b$ to the total current i arriving at the receiving electrode is given by

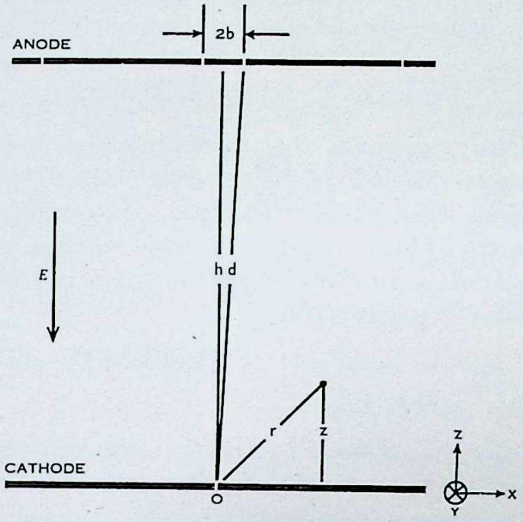

Fig. 1.—Geometry of diffusion chamber.

$$R = i_b/i = 1-(h/d-1/\lambda h+h/d^2\lambda)(h/d)\,\mathrm{e}^{-\lambda(d-h)}, \tag{5}$$

where h is the distance between anode and cathode, and $d^2 = h^2+b^2$.

It has been found that the experimental measurements do not always agree accurately with values calculated from equation (5), but that the expression

$$R = 1-(h/d)\,\mathrm{e}^{-\lambda(d-h)} \tag{6}$$

is consistent with experimental results over a wide range of experimental parameters. This expression follows from the use of the solution for n given in equation (3) together with the boundary conditions discussed by Huxley and Crompton (1955).

The expressions (5) and (6) for the ratio R have been discussed by Huxley and Crompton (1955) and by Crompton and Jory (1962), who show that, for certain experimental conditions, there is a negligible difference between the results obtained using these two expressions. These experimental conditions are certainly fulfilled where maximum accuracy is required in the experiments described in this paper.

III. THE CHOICE OF PARAMETERS IN THE DESIGN OF THE DIFFUSION APPARATUS

The design of the diffusion chamber that was finally adopted is shown in Figure 2. In choosing the dimensions of the chamber careful attention has to be paid to a number of parameters, although the final choice is in fact a compromise.

(a) *Length of Chamber,* h, *and Radius of Collector Disk,* b

The most obvious requirement that determines the choice of h and the ratio b/h is the need to measure the ratio of the currents received by the disk and annulus with adequate precision. The use of the current measuring equipment described in Section VIII(b) enables this to be done provided R lies between 0·2 and 0·9. The effect of this restriction on the choice of b and h can be seen by examining equation (6), which may be rewritten as

$$R = 1-\{(b/h)^2+1\}^{-\frac{1}{2}}\,\mathrm{e}^{-\lambda h}[\{(b/h)^2+1\}^{\frac{1}{2}}-1], \tag{7}$$

where $\lambda = W/2D = (e/2kT)(E/k_1)$.

When k_1 is greater than about 5 it can be shown, with the aid of equation (7), that no great difficulty exists in choosing suitable values for b and h which will lead to current ratios in the centre of the prescribed range when field strengths of 10 V/cm or more are used. The pressure can then be chosen to obtain the value of E/p appropriate to the required value of k_1. Cross checks can subsequently be made by either increasing or decreasing E and p, keeping E/p constant and the current ratio within the range.

The choice of parameters becomes more difficult, however, as k_1 approaches unity, and as the gas temperature is lowered. Calculations show that reasonable divergence of the electron stream can be obtained only with small values of the electric field; on the other hand, as will be discussed in Section V(b)(ii), significant experimental errors may arise from contact potential differences for values of E less than about 3 V/cm. The lower limit which must be placed on the value of E requires that small values of b and large values of h be used if a significant fraction of the electron stream is to arrive at the receiving electrode outside the central disk, but practical difficulties dictate a compromise in the choice of these two parameters. In practice it is difficult to achieve the required tolerance of ±0·1% in the effective diameter of the central disk for diameters less than about 1 cm, owing partly to difficulties in measurement but chiefly to the finite size of the air gap between disk and annulus (Section III(d)). Furthermore, errors resulting from the finite size of the source hole (Section III(c)) become more significant as the diameter of the disk is reduced. The use of a diffusion chamber of length $h = 10$ cm in conjunction with a disk of radius $b = 0\cdot5$ cm leads to a value of R as high as $0\cdot5$ for thermal electrons at room temperature (293°K) with $E = 3\cdot0$ V/cm, still larger ratios resulting from

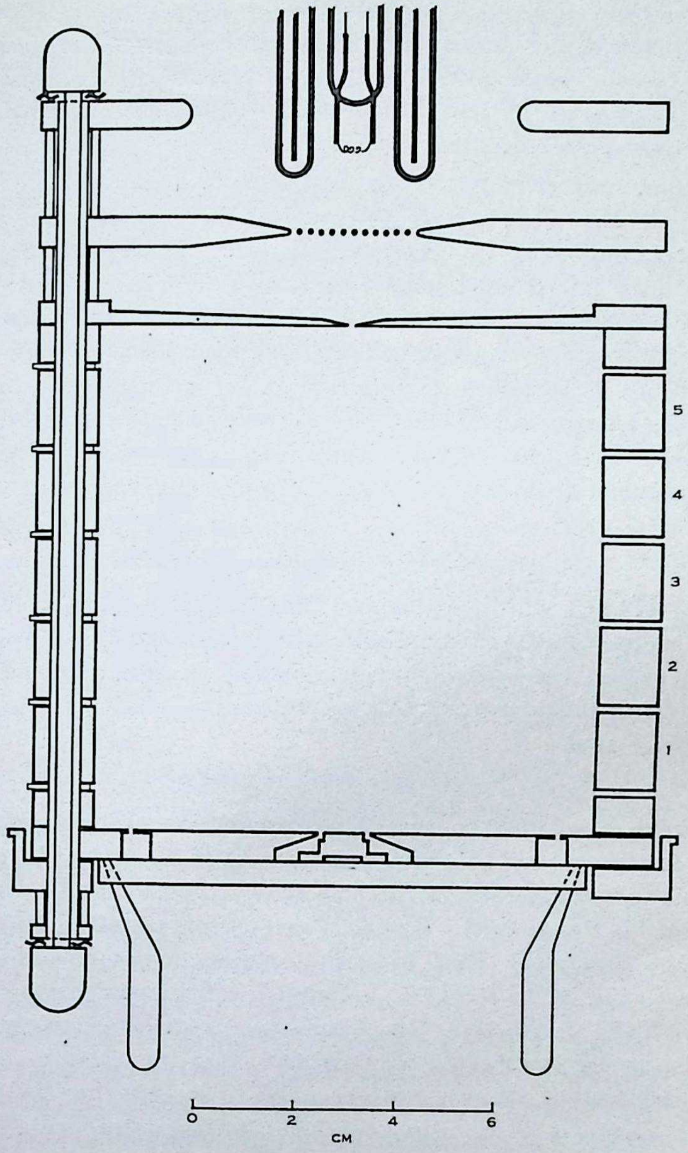

Fig. 2.—Cross section of diffusion chamber.

the use of lower gas temperatures or higher field strengths. If R is to remain within the prescribed range it is, in fact, impossible to use values of E higher than approximately $9\cdot0$ V/cm at 293°K or $2\cdot5$ V/cm at 78°K. Thus, even with this choice of the values of b and h, measurements can be made only at relatively low field strengths, and this restriction leads to enhanced experimental difficulties and larger experimental errors, as will be discussed subsequently.

Some improvement to the situation can be achieved by increasing h, but there are factors which make such an increase undesirable. A significant improvement would be obtained only by a large increase in h, which would then add considerably to the difficulty of conducting the experiments at low temperatures. These difficulties result from the length of vacuum envelope to be immersed in the refrigerant and the increase in the already large quantity of gas of high purity required to perform the experiment at pressures of the order of 500 torr, such pressures being necessary to obtain the lowest values of E/p.

One further requirement governing the choice of b and h is already satisfied with this choice of dimensions, namely, the removal of a possible source of significant error in the interpretation of the experimental results in terms of the ratio W/D. Crompton and Jory (1962) have shown that with $h = 10$ cm and $b = 0 \cdot 5$ cm, equations (5) and (6) lead to values of W/D that differ by less than $0 \cdot 2\%$ when $R > 0 \cdot 5$. The discrepancy between theory and experiment, which is discussed fully in their paper, is therefore unimportant in the present work. Furthermore, uncertainty in the interpretation of the results arising from the spatial dependence of W/D, as discussed by Parker (1963), would also appear to be insignificant using the criterion suggested by Parker.

(b) *Diameter of the Diffusion Chamber*

The diameter of the diffusion chamber must be large enough to ensure that the electric field is uniform to the required tolerance (see Section VI(b)) over the volume of the chamber where the electron number density is significant. A diameter of 10 cm satisfies the requirements of field uniformity with the particular guard electrode structure used.

(c) *Diameter of Source Hole*

In obtaining a solution to the diffusion equation the assumption is made that the hole in the cathode acts as a point source of electrons. In practice there is a lower limit to the diameter of the hole set by the requirement that sufficient electron current be transmitted. The diameter chosen was $0 \cdot 1$ cm. Calculations made by Crompton and Jory (1962) indicate that, for a source hole of this diameter, the error in the value of W/D will be a function of R and will vary from $0 \cdot 05\%$ at $R = 0 \cdot 1$ to $0 \cdot 8\%$ at $R = 0 \cdot 8$. These calculations almost certainly overestimate the error, owing to the assumption which is made that the electron number density across the hole is constant. However, it is possible to observe the effect of this source of error in the experimental measurements, and its magnitude will be discussed in Section XI.

(d) *Width of Annular Gap*

Equation (7) may be used to show that an error of $0 \cdot 0005$ cm in b leads to an error of $0 \cdot 2\%$ in the determination of W/D, but a difficulty arises in the determination of b apart from that associated with measurement. The effective diameter of the central disk is normally taken as the actual diameter plus the width of the gap between disk and annulus, on the assumption that the electrons arriving at the gap divide equally between disk and annulus. The accuracy of this assumption is difficult to assess, since the way in which electrons diffuse in the essentially field-free region within the gap is unknown. Any error arising from the incorrectness of this assumption may obviously be minimized by making the gap as narrow as possible.

The use of an extremely narrow gap leads to a high inter-electrode capacitance which may add to the difficulty of determining the current ratio R. The capacitance can be reduced by undercutting the edges of the electrodes, but there is a limit to the thinness of the edges set by the need to maintain a truly plane surface across the face of the whole electrode (Section V(*b*)(i)).

As a compromise, a gap width of $0\cdot005$ cm was used. The maximum error arising from the uncertainty in the effective diameter of the disk is therefore $\pm1\%$, although experiments in which the gap width was varied indicate that this figure greatly overestimates the error from this cause. The width of the gap between the annulus and the outer earthed annular ring is not critical and was chosen to be $0\cdot1$ cm.

(*e*) *Preliminary Field Region*

In order to ensure that the energy distribution of the electrons entering the diffusion chamber approximates closely the equilibrium energy distribution throughout the chamber, the electrons are made to traverse a region 2 cm in length, immediately above the cathode, where the field is maintained at the same value as in the diffusion chamber (Fig. 2). To obtain some estimate of the distance required for an electron to reach its equilibrium energy the following expression was used (Loeb 1955):

$$x_\eta = \frac{1}{2a}\ln\frac{1+\eta}{1-\eta}, \tag{8}$$

where η is the fraction of its equilibrium energy attained by an electron in travelling a distance x_η in the direction of the electric field, and a is a parameter given by

$$a^2 = 5\cdot32(m/M)(1/l^2),$$

where

m = electronic mass,
M = mass of the gas molecules,
l = mean free path.

The factor $5\cdot32\ (m/M)$ is twice the mean fractional energy lost by electrons in elastic collisions. In the calculation which follows for the case of electrons in hydrogen this factor has been replaced by the value obtained experimentally, since inelastic collisions significantly alter its value.

If the following experimental conditions are assumed

$$E/p = 1\cdot0\ \text{V}\,\text{cm}^{-1}\,\text{torr}^{-1},$$
$$p = 10\ \text{torr},$$
$$\eta = 0\cdot99,$$

then the value of x_η is approximately $0\cdot1$ cm.

Owing to the assumptions that have been made in the derivation of the expression for x_η, these calculations are approximate only. Nevertheless, they show that the length of the preliminary field region is adequate, and in any case no variation in the measured values of W/D could be found on varying the initial field over a wide range.

(*f*) *Diameter of Outer Collector*

The diameter of the outer annulus must be sufficiently large that only a negligible proportion of the electron current falls outside this electrode. In Section II it was stated that for the most divergent electron stream used (i.e. at the lowest values of E and p), less than 0·004% falls outside a diameter of 8 cm in a diffusion chamber 10 cm in length. The diameter chosen for the outer annulus was 8·5 cm.

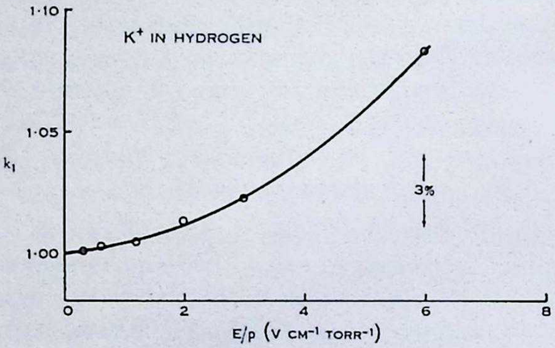

Fig. 3.—The variation of k_1 with E/p for K⁺ ions in H_2.

IV. Tests for Sources of Systematic Error

There are two tests that can be made to detect the presence of systematic errors. In the first test, use is made of the fact that, at a constant temperature, k_1 is a function of E/p only, so that the same value of k_1 should be obtained at the same value of E/p regardless of the value of p. When experimental results are taken, both E and p are varied over the widest possible range and the results tabulated as a function of E/p and p. A pressure dependence of the experimental results at a fixed value of E/p indicates the presence of systematic errors.

The second and most stringent test that can be made is to determine the value of k_1 for positive alkali ions at values of E/p where the ions are virtually in thermal equilibrium with the gas molecules. At low values of E/p the value of k_1 increases very slowly as E/p increases. From Figure 3 it can be seen that, in the case of potassium ions in hydrogen, k_1 remains within approximately 0·2% of unity (corresponding to thermal equilibrium) for values of E/p less than 0·5. The procedure is, therefore, to take measurements with potassium ions in the range of values of E/p for which $k_1 = 1$ to within say 0·2%, that is, in the case of hydrogen, for $E/p < 0.5$. If the value of k_1 obtained differs significantly from unity then an error is present in the measurements.

When this second test employing positive ions was used with one of the early experimental tubes the results were found to be in error by 4%, and the cause of this error was traced to distortion of the electric field. The type of field distortion responsible for errors of this magnitude was therefore investigated and the causes of such distortion determined.

V. DISTORTION OF THE ELECTRIC FIELD AS A SOURCE OF ERROR

(a) *Types of Field Distortion*

The distortion of an electric field that has cylindrical symmetry can take two forms. It is possible (for example, by applying non-equal potential differences to adjacent members of an infinite set of thin, equally-spaced guard electrodes) to produce an electric field that is everywhere axial but in which the field strength is not everywhere equal. The set of equipotential planes is then "bunched" in some regions and widely spaced in others. More often the distortion of the field arises from curvature of the equipotential planes so that the field lines are not everywhere axial. Thus, if the distortion results in a series of surfaces that are dished, the electric field at any point may be resolved into an axial and a radial component.

It has been found that the measured values of k_1 are sensitive to field distortion introduced, for example, through contact potential differences between the guard electrodes and the source and receiving electrodes. It is important to establish whether the divergence of the stream is affected by variations in the axial field strength, by the presence at some places within the diffusion chamber of radial fields, or by a combination of both effects.

In order to find out something about the relative importance of these effects the following experiments were performed. Considerable distortion was introduced by connecting the lowest full guard electrode in the electrode system shown in Figure 2 to the receiving electrode. The lead to this guard electrode was disconnected from the voltage divider so that each of the other guard electrodes had the correct potential applied to it. The total voltage applied to to the diffusion chamber remained unaltered during the test.

The value of k_1 obtained for potassium ions in hydrogen when the electrodes were connected in this way was 16% higher than that obtained when the electrodes were correctly connected. A similar change (15%) was obtained for electrons in hydrogen at $E/p = 1$.

A qualitative and semi-quantitative estimate of the electric field within the diffusion chamber was made from a two-dimensional analogue, using conducting paper, for conditions equivalent to those used in the experiments described above. From the spacing of the equipotential lines along the axis of the system, the average value of the axial component of the field over intervals of 1 cm between source and receiving electrodes was found to be as follows:

Interval (cm)	1	2	3	4	5	6	7	8	9	10
Average field strength (V/cm)	9·33	9·73	9·80	10·0	10·2	10·42	10·4	10·4	10·37	10

Interval 1 began at the receiving electrode, and the nominal field strength was 10 V/cm.

From this table it can be seen that there are some regions in which the field is below the nominal value and some in which the field is above this value; furthermore, the lowest field strength is only 7% below the nominal value.

The effect of this variation in the axial component of the field can be estimated as follows. For positive ions near thermal equilibrium, as in this experiment, the value of W in each of the 10 regions will be proportional to the value of E in that region, whereas the diffusion coefficient will be practically independent of it. Thus, in region 1 the value of W/D, which determines the divergence of the stream, is smaller than the nominal value, while in region 7 it is larger. It might be expected, therefore, that the final divergence of the stream, and hence the value of k_1 determined from it, would be little affected. This is not so, and in fact the value of k_1 lies well outside the value it would have in the extreme case of the field being everywhere at the lowest value. If this were the case k_1 would be subject only to a 7% error and not the 15% error recorded. Furthermore, the regions of high field strength would reduce the 7% error, so that it appears that axial non-uniformity is not the main contributor to the spurious divergence.

Further evidence is afforded by the results for electrons. The value of $E/p = 1 \cdot 0$ was purposely chosen to lie in the region where W/pD is largely independent of E/p. This was confirmed by altering the value of E/p, when it was found that a 7% change in E/p altered W/pD by about $1 \cdot 5$%. If non-uniformity of the axial field were to lead to the spurious divergence, then the error in k_1 would be expected to be far less for electrons at this value of E/p than for ions, for which a 7% change in E/p caused a 7% change in W/pD. Since the errors introduced are almost identical, the results of this experiment confirm the conclusions drawn from the experiment with positive ions.

It seems, therefore, that the results quoted above must be attributed to the introduction of radial field components. Further examination of the equipotential plot showed the lines to have very appreciable abnormal curvature towards the edges of the field, and just appreciable curvature in the region above the annular gap between the disk and the annular electrode, where any radial component of the field is likely to have the greatest effect in determining the distribution of current between these electrodes. It is necessary, therefore, to examine the ways in which radial components of the electric field could be introduced.

(b) *Causes of Field Distortion*

(i) *Field Distortion Introduced by Incorrect Geometry.*—Distortion of the electric field can be introduced by geometrical inaccuracy in the guard electrode structure, in the source electrode, or in the receiving electrode. Incorrect voltage division in the potential divider supplying the potentials to the guard electrodes is equivalent to a displacement of the guard electrodes and may therefore be included in this category.

The most serious error introduced by geometrical inaccuracy results from the surface of the collecting electrode not being a true geometrical plane. Radial fields arising from relatively abrupt changes in contour are more likely to occur in the vicinity of the annular gap than elsewhere. Furthermore, this is the region where such fields would have maximum effect since they would cause a spurious distribution of current about the gap. For example, in a series of experiments with one particular apparatus a systematic error of the order of 1·5% was consistently observed. The cause of this error could not be traced to any of the other effects discussed in the present paper. When the region around the gap of the collecting electrode of this apparatus was examined it was found that a small lip of the order of 0·0004 cm in height existed at the inner edge of the outer annulus. This lip resulted from the extreme fragility of the inner edge of the annulus, which had been undercut to reduce interelectrode capacitance. Another electrode was constructed in which the thickness of the copper at the edge was increased. Optical tests showed that no lip existed after lapping and polishing. When this collecting electrode was inserted in the apparatus the 1·5% systematic error previously observed was no longer present.

If the distortion arises from either geometrical inaccuracy or insufficiently accurate division in the voltage divider feeding the guard electrodes, the percentage error in k_1 will be largely independent of both the divergence of the stream and the way in which W/D varies with E/p. This form of field distortion will therefore be characterized by an error which does not scale with E.

(ii) *Field Distortion Produced by Contact Potential Differences.*—Non-uniformity of the electric field can arise from contact potential differences either over a surface or between different surfaces. There may be contact potential differences between different parts of the anode or cathode surfaces, or between sections of the surface of the guard electrode structure. Furthermore, difficulty has been experienced in obtaining cathode and anode surfaces between which the average contact potential difference is zero even when vacuum coated simultaneously, and similar remarks apply to the guard electrodes. However, provided that the contact potential differences remain constant, the errors arising from field distortion introduced by them can always be recognized by the fact that the magnitude of the error is approximately inversely proportional to the magnitude of the applied field. For example, in experiments in which this type of field distortion has been simulated by imposing a constant additional potential, either on the guard electrodes or on the central disk, doubling the field has in each case approximately halved the error. Conversely, numerous tests have shown that the magnitude of the percentage error introduced is directly proportional to the magnitude of the potential applied at a given value of the main field.

Table 1 shows the additional potentials which, when applied to the respective electrodes of an apparatus of the form shown in Figure 2, lead to a 1% change in k_1 for a main field of 3 V/cm.

(c) *A Method of Distinguishing the Types of Error Caused by Field Distortion*

The magnitude and type of error can be found by measuring the variation of the error with increasing electric field strength E at one fixed value of E/p. From the discussion in the previous sections (V(*b*), (i) and (ii)) it can be seen that errors arising from field distortion owing to geometrical inaccuracy (to be called type 1) are independent of the magnitude of E, whereas those arising from contact potential differences (to be called type 2) are inversely proportional to E apart from second order effects due to the variation in R.

If, in measurements with electrons, errors of both type 1 and type 2 are present the variation of the error with E is as shown in curve (*a*) of Figure 4. If, instead of electrons, positive ions are used, errors of type 1 remain unchanged, while errors of type 2 reverse in sign but remain unchanged in magnitude at the same value of E (curve (*b*)). At high values of E errors of type 2 become negligible and the residual error (ϵ_1) arising from geometrical inaccuracy can therefore be found. This error can then be subtracted from the total error in order to obtain the magnitude of errors of type 2 at any given value of E. It should be noted that the signs of the errors shown in the figure are chosen only as an example.

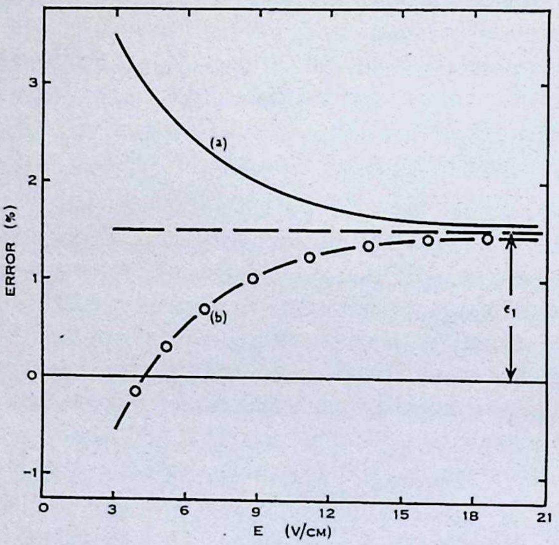

Fig. 4.—Variation of errors in k_1 with electric field strength (E/p fixed).

In practice the situation illustrated by Figure 4 is to some extent obscured by two other factors. The first is the variation with R of the errors from contact potential differences, which will be discussed in Section IX; the second arises from the effect of the finite size of the source hole and is also dependent on R (Sections III(*c*) and XI). Nevertheless, when used with care this method enables errors of both types to be identified and measured.

VI. Production of a Uniform Electric Field

(*a*) *Alternative Methods of Producing a Uniform Electric Field*

A longitudinal electric field is often held uniform by employing a series of guard electrodes maintained at voltages appropriate to their position along the length of the field. For diffusion chambers used in these experiments, it is also necessary to ensure that no penetration can occur through the guard electrodes of stray fields outside the electrode structure. Although adequate shielding from wall effects was achieved in the apparatus described by Crompton and Jory (1962), more closely spaced guard electrodes had to be employed to give adequate shielding when an attempt was made to construct an apparatus of smaller diameter suitable for immersion in a refrigerant for measurements at low gas temperatures. In the latter apparatus the guard electrodes had an internal diameter of 3·7 cm and were spaced at 0·5 cm intervals. To avoid distortion caused by the finite thickness of the electrodes each was made 0·06 cm in thickness. The length of the diffusion chamber was 10 cm and the value of b/h was 0·05. When this apparatus was tested for systematic errors, as outlined in Section IV, using potassium ions in hydrogen, the measured values of k_1 were consistently less than unity by 2–3%. This error was thought to be due to the existence of field distortion in the diffusion chamber caused by warping of the thin guard electrodes.

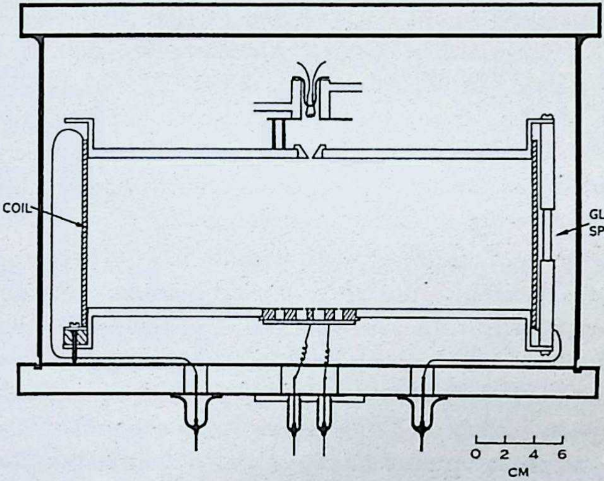

Fig. 5.—Apparatus designed to minimize field distortion produced by the guard electrode structure.

To test whether field distortion was in fact the cause of the incorrect values of k_1 a second apparatus (Fig. 5) was constructed in which the internal diameter of the diffusion chamber was increased from 3·7 to 25 cm. By increasing the ratio of diameter to length in this way the role of the guard electrode structure becomes less important. In addition an alternative form of guard electrode structure, theoretically superior to the more conventional type, was used, the design of which was based on the following considerations.

An electric field uniform over the entire volume of the diffusion chamber could be produced if it were possible to place the appropriate voltage across a uniform conducting surface forming the cylindrical wall of the diffusion chamber. In practice, there are a number of difficulties involved in producing a uniform field in this way. The conductivity of the surface must be uniform to a high degree and the current flowing through the conductor must be small to avoid ohmic heating. When high values of field are required these restrictions are such that no material could be found which adequately met the requirements, and an alternative approach was adopted.

The ideal case of a continuous and linear variation of potential along a cylindrical wall parallel to its axis may be approximated by using a coil of fine wire. The resistance of the coil must be chosen to ensure that, at the maximum electric field strength used, the magnetic field and the ohmic heating produced by the current flowing through the coil will not significantly affect the results. The coil used in this second, large diameter apparatus (Fig. 5) consisted of 300 turns of nichrome wire wound on the inside of an epoxy resin former. The coil was placed inside a steel cylinder which formed the vacuum envelope. Measurements made with potassium ions in hydrogen gave values of k_1 which were within 0·25% of the true value of unity. The conclusion from the results of this and the previous experiment is, therefore, that a high degree of uniformity in the electric field is essential to obtain the required accuracy.

The epoxy resin used in the construction of this experimental tube resulted in the gas being contaminated to a level which would normally be regarded as unacceptable. However, gas purity cannot affect the values of k_1 for positive ions at low values of E/p, since the value of k_1 for any ion species in any gas approaches unity as E/p approaches zero. Because of the unacceptable impurity level and the size of the apparatus, it was considered to be unsuitable for measurements with electrons at room or low temperatures.

If the same degree of uniformity of electric field is to be maintained in an apparatus of reduced diameter, it is necessary to increase the number of turns in the coil. Another apparatus employing this guard system was constructed with the electric field held uniform by a coil of 10 cm diameter, consisting of 1000 turns of Karma wire which was both insulated and held in position by polyurethane. The coil was vacuum baked for 2 hr at 100°C before being assembled into the apparatus. Vapour pressure tests on the polyurethane indicated that it would not significantly add to the impurity level in the gas samples used. The resistance of the coil was 86 kΩ, and the variation from linearity in the potential drop along its length was less than 0·25%. The contact potential difference between Karma wire and a gold surface in air was measured as 0·22 V, and appropriate allowance was made when voltages were applied to the apparatus.

Measurements made using potassium ions in hydrogen were found to be alarmingly inaccurate (9% error at $E = 3$ V/cm), and the error was found to decrease as the electric field strength was increased. This behaviour is consistent with the presence of field distortion resulting from contact potential differences within the diffusion chamber (Section V(*b*)(ii)), and it was assumed that the distortion had been introduced as a result of incorrect compensation for the contact potential difference between the Karma wire and the gold surfaces of the anode and cathode. An apparatus employing the Kelvin method (Kelvin 1898) was constructed to measure the contact potential difference between the Karma wire and a gold surface under various atmospheres. It was found that changing the atmosphere from air to hydrogen caused a considerable change in the contact potential difference between these two metal surfaces. The inescapable conclusion would therefore seem to be that all surfaces exposed to the diffusing electron swarm must be of the same material. Since gold had been chosen as the best material for coating the anode and cathode, this conclusion means that a coil cannot be used for the purpose of establishing a uniform electric field, as the resistance of a coil of gold wire or even gold-coated wire would be far too low.

The use of thin guard electrodes and of a coil to produce uniform electric fields were thus both unsuccessful, owing to insufficient mechanical rigidity in the first case and to the effects of contact potential differences in the second. Both these approaches were attempts to ensure that field distortion was made negligible throughout the whole diffusion chamber. An alternative approach is to ensure that the amount of field distortion is made negligible in the region in which the electron or ion concentration is appreciable but to allow a certain known degree of distortion elsewhere. An electrode system that can be made to fulfil these requirements is one consisting of thick cylindrical guard electrodes. Such a system has the following advantages. First, each element of the system has a high degree of mechanical stability; secondly, this system shields the diffusion chamber completely from stray electrical fields exterior to it; and thirdly, the effects of dielectric soakage in the glass spacers separating the electrodes can be eliminated.* Since this electrode structure was used in the final apparatus the field produced by such a structure will be discussed more fully.

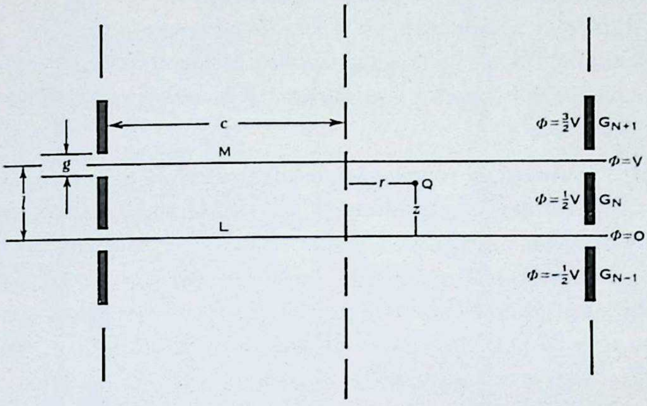

Fig. 6.—Geometry of guard electrode system whose electric potential distribution is as given by equation (9).

(*b*) *An Analysis of the Field Produced by Guard Electrode Systems*

The potential field generated by a system of identical guard electrodes spaced at regular intervals (Fig. 6) can be examined by considering the field within any module of the system. The planes L and M of the system shown in Figure 6 define such a module. If the potentials of the electrodes G_{N-1}, G_N, and G_{N+1} are $-\frac{1}{2}V$,

---

* A slow change of the current ratio R with time following a change of the electric field from a high to a low value was incorrectly attributed to surface effects at the receiving electrode (Crompton and Jory 1962). Subsequently it was shown that the effect was due to field distortion resulting from dielectric soakage in the glass spacers.

$\frac{1}{2}V$, and $\frac{3}{2}V$ respectively, the potentials of the planes L and M will be 0 and V respectively, and the solution to the Laplace equation with these boundary conditions is (Hurst 1960)

$$\phi = \frac{Vz}{l} + \sum_{N} \frac{2V}{N\pi} \frac{\mathrm{I}_0(N\pi r/l)}{\mathrm{I}_0(N\pi c/l)} \sin(N\pi z/l) \frac{\sin(N\pi g/2l)}{N\pi g/2l}, \tag{9}$$

where

ϕ = potential of the point Q at distances z from L and r from the axis of the system,
l = length of the module,
c = inner radius of the guard electrodes,
g = thickness of the gap between the guard electrodes,
I_0 = modified Bessel function of zero order,
N = summation index, the summation being carried out for all even values of N.

In the electrode structure of the apparatus described in Section VII, $l = 10/6$ cm and $c = 5$ cm, and the use of equation (9) shows that the potential at any point within an axial cylindrical volume of 6 cm diameter is within 0·05% of the value corresponding to a uniform field. From equation (6) it can be shown that for a current ratio R greater than 0·2, 99·9% of the electron stream arrives at the anode within a circular area of this diameter. It can be seen, therefore, that it is possible to obtain a high degree of uniformity within a volume of adequate dimensions without the use of a large number of electrodes or of a large diameter, even though there is considerable distortion in the vicinity of the electrodes. By contrast, the use of the more conventional guard electrode structure, while theoretically providing uniformity over a larger volume in an apparatus of the same dimensions, is unlikely to produce a high degree of uniformity anywhere because of geometrical distortion of the electrodes.

The use of equation (9) shows that the deviation from a linear variation of potential along a line parallel to the central axis of the guard electrodes, and at a radial distance r from it, is a periodic function whose amplitude depends on r and the ratio of the thickness of the module to the internal radius. As a check on calculations based on this formula, a series of plots was made using an electrolytic tank to measure the deviation from a linear variation of potential at a radial distance of 4·5 cm. This radial distance was chosen to ensure that the distortion was easily measurable. The deviations observed agreed with the predicted values to within the experimental error (approximately 2%).

(c) *Production of Surfaces of Sufficient Uniformity in Contact Potential Difference*

To obtain an electric field of adequate uniformity it is necessary not only to minimize distortion resulting from geometrical inaccuracy in the guard electrode structure and elsewhere, but also to minimize distortion produced by contact potential differences. Table 1 shows that contact potential differences will have the greatest effect if they occur over the surface of the collecting electrode. Since very small differences in potential between adjacent areas of the surface of the collecting electrode can lead to large errors in the measured current ratios, it is essential to produce a gold surface for which these differences are reduced to a minimum. In order to test the uniformity of these surfaces an apparatus (Fig. 7) was built to measure contact potential differences. The surface to be examined is supported by insulating glass blocks on a table that can be rotated by a shaft passing through the baseplate. The probe can be raised and lowered by means of a sliding rod and can also be moved through an arc of 45°. By the movement of the probe and turntable any small area $0 \cdot 6$ cm in diameter (the diameter of the probe) on a surface 10 cm in diameter can be examined. The contact potential difference between the probe and the surface could be determined to within approximately ±1 mV. The vacuum conditions under which the apparatus was operated were chosen to approximate those of the diffusion apparatus. For this reason no attempt was made to outgas the contact potential apparatus or to obtain extremely clean surfaces by ion bombardment, etc.

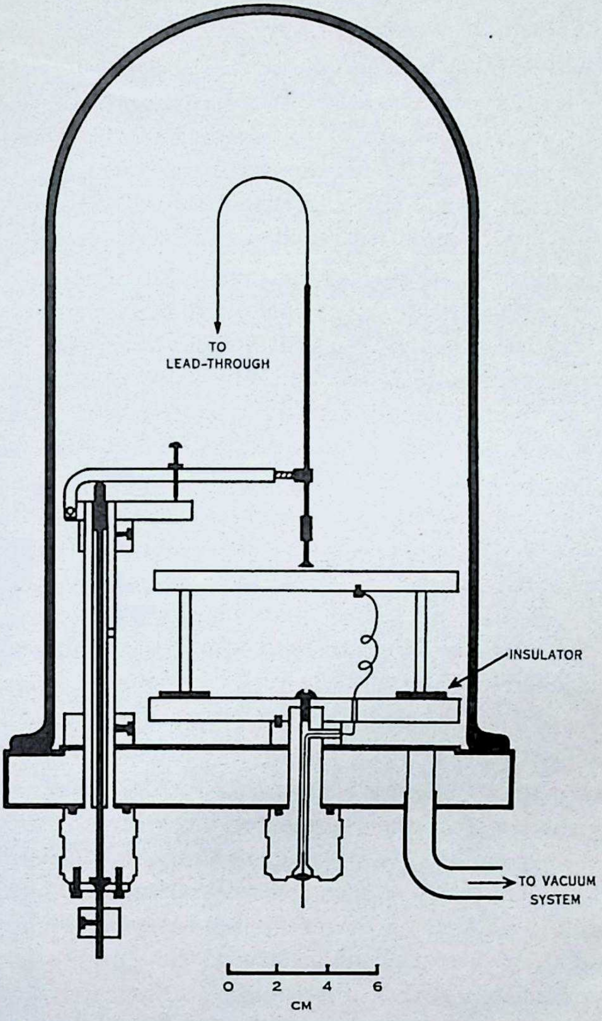

Fig. 7.—Apparatus used to measure contact potential differences.

The first measurements were made with electroplated gold surfaces. Large variations of up to 150 mV were found in the contact potential difference as the probe traversed the surface. In general the variation was randomly distributed over the surface. Parker and Warren (1962) have observed a similar behaviour for unbaked electroplated surfaces. Since it seemed impossible to make a significant improvement to the uniformity of electroplated gold surfaces, attention was turned to surfaces coated with gold by vacuum deposition.

The first of these surfaces was produced with either a short filament or a boat, and in general poor results were obtained. To improve the uniformity of the coating over the surface and within the gaps of the electrode, a triple-strand ring filament was later used which was placed below the surface and at a distance from it equal to the radius of the ring (Bond 1954; Holland 1961). Care was taken to ensure that the filament was still covered with gold when the evaporation was terminated.

Measurements made with the contact potential apparatus established that the vacuum coated surfaces were in general more uniform than the gold plated surfaces, but that a small potential gradient across the surface often occurred, the effect of which is clearly undesirable (Section V). It was also found that, when more than one surface was coated simultaneously with the same filament, the contact potential difference between the surfaces differed by 30–100 mV. Furthermore, the coating procedure was found to have a marked effect on the uniformity of the surfaces. Nevertheless, by careful attention to the conditions under which the vacuum deposition took place and after a large number of trials, a method was developed for producing surfaces of acceptable uniformity and stability. The maximum contact potential difference between any two areas of the collecting electrode used in the diffusion apparatus was 8 mV, with differences of only 3 mV occurring in the central region.

Measurements of k_1 made with this new surface confirmed the superiority of the gold anode and cathode surfaces prepared by vacuum deposition. Although a discrepancy of just over 1% existed between the results taken at extreme values of E for the same value of E/p, this represented a considerable improvement on the previous attempt to use surfaces prepared in this way, when discrepancies in excess of 5% were found. The results were now more reproducible than previously, showing little or no variation with time or the previous history of the apparatus. Because of this reproducibility, and of the uniformity of the surfaces as demonstrated by preliminary direct measurement, it was considered that the most likely cause of the 1% variation was a contact potential difference between the vacuum-deposited gold surfaces of the anode and cathode, and the electroplated surfaces of the guard electrodes. No attempt was made to gild the guard electrodes by vacuum deposition because of the risk of producing non-uniform surfaces with the techniques available.*

To allow for the contact potential difference between the guard rings and anode and cathode surfaces, a compensating potential of the order of 100 mV was placed between the set of guard electrodes and the anode and cathode. The procedure for determining the correct compensating potential and the magnitude of the errors involved is discussed in Section IX.

---

* In order to eliminate contact potential differences arising from the position of the surface relative to the evaporating source it would have been necessary to rotate the guard electrodes about an axial filament to ensure adequate uniformity.

VII. THE CONSTRUCTION OF THE DIFFUSION APPARATUS

The final form of the experimental tube is shown in Figures 2 and 8. The main electrode structure was made of copper, the only other metals used being nonmagnetic stainless steel and nichrome. The use of nonmagnetic materials, together with other precautions, ensured that the magnetic field strength within the diffusion chamber was only that due to the Earth's field. The limits to the experimental parameters imposed by the other considerations discussed in this paper ensure that the effect of this field is negligible.

With the exception of the receiving electrode, the electrode structure is designed to withstand a temperature range of 80–520°K, while the arrangement of the electrometer leads enables measurements to be made at the lowest temperatures in this range. Since the principal aim of the experiments described in this paper was the precise determination of k_1 when k_1 approaches unity, no attempt was made to heat the experimental tube to accelerate outgassing because of the attendant risk of changing the contact potential differences within the chamber. Consequently, the use of Apiezon W 100 vacuum wax and Apiezon N grease was permissible for sealing the demountable joints. It is shown in Section X that the contamination of the gas samples from this procedure was negligible.

Two filaments are attached to the filament support. Electrons are produced from a platinum filament, and potassium ions from a heated potassium aluminosilicate bead (Blewett and Jones 1936). This arrangement enabled the changeover from measurements with electrons to those with ions to be made without changing the gas sample, thus avoiding any possibility of changes in contact potential differences within the apparatus. As a

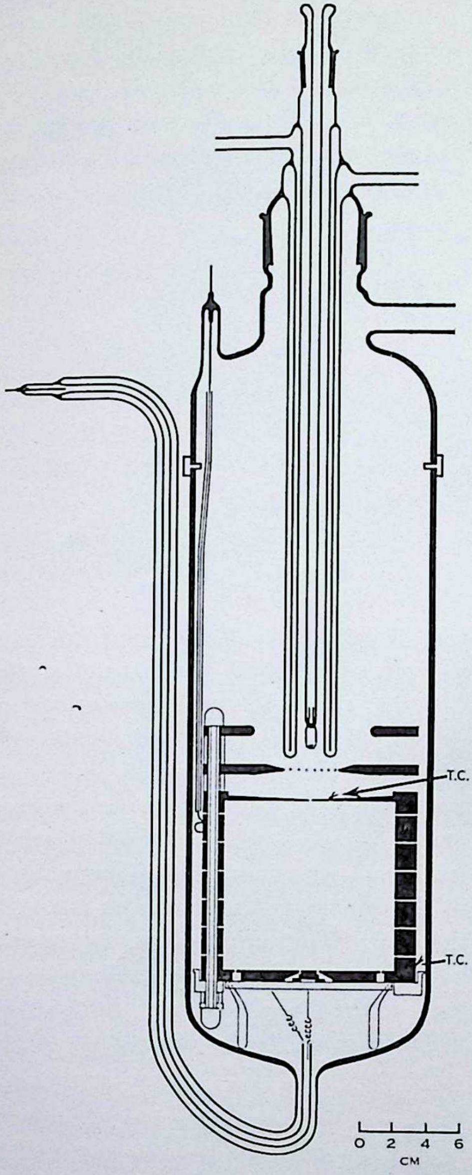

Fig. 8—The experimental tube.

control on the electron or ion current, the inner surface of the water jacket in the region of the filament was coated with a layer of platinum, the potential of which could be varied with respect to the filament.

The construction of the receiving electrode proved unsatisfactory below 90°K, when differential contraction of its components caused the disk and annulus to touch. This was not unexpected in view of the gap of only 0·005 cm between them. An alternative design employing concentric ceramic–metal seals successfully overcame this difficulty but introduced an equally serious one. As a result of the distortion of the annulus during cooling, a vertical displacement of the order of 0·005 cm occurred between the disk and the neighbouring section of the annulus. A solution has yet to be found to the problem of maintaining adequate mechanical stability over this temperature range to meet the requirements laid down in Section V(*b*)(i).

The dimensions of the apparatus are as follows:

length h of diffusion chamber	$10 \pm 0 \cdot 005$ cm
effective radius b of central collector disk	$0 \cdot 5 \pm 0 \cdot 002$ cm
diameter of central collector disk	$0 \cdot 9955 \pm 0 \cdot 0005$ cm
internal diameter of annulus of collector	$1 \cdot 0050 \pm 0 \cdot 0005$ cm
width of gap between disk and annulus	0·005 cm
external diameter of annulus of collector	8·5 cm
internal diameter of guard electrodes	10 cm
diameter of source hole	$0 \cdot 1 \pm 0 \cdot 005$ cm
thickness of full guard electrodes	$1 \cdot 616 \pm 0 \cdot 003$ cm
thickness of glass spacers	$0 \cdot 051 \pm 0 \cdot 002$ cm.

The tolerances to which the individual components of the apparatus are machined ensure adequate precision in the separation and parallelism of the cathode and anode, but considerable care has to be paid to the procedure of assembling the apparatus to obtain accurate alignment of the cathode and anode with respect to the principal axis of the diffusion chamber. In developing this procedure, it was necessary to recognize that the guard electrodes, rather than the cathode and anode, were principally responsible for generating the field and were therefore responsible for establishing the axis. The principal axis used for alignment was therefore taken as the axis originating from the centre of the receiving electrode whose direction was parallel to the axis of the guard electrodes rather than normal to the receiving electrode. In practice the difference in these directions is unimportant, apart from small anomalies which may be present in the plane surface of the electrode or which may arise from an accumulation of tolerances in the dimensions of the guard electrodes and spacers.

A Taylor–Hobson Micro-Alignment Telescope was used for the alignment. This instrument can be used to set up an axis normal to a plane surface and to measure deviations from this axis. In this instance the axis was parallel to the axis of the guard electrodes and incident on an indentation 0·01 cm in diameter marking the centre of the disk of the receiving electrode. When the cathode was placed in position it was moved laterally until the centre of the source hole coincided with the principal axis, after which a final check on the position of the anode was made by sighting through the source hole. The maximum error in the alignment of the apparatus is less than 0·005 cm.

VIII. THE MEASUREMENT OF EXPERIMENTAL QUANTITIES

(*a*) *The Measurement of* E/p

The potentials of the electrodes were derived from a voltage divider in which the resistors were matched to better than 0·05%. The voltage to the divider was supplied by a Fluke 301 E power supply, the output of which is accurate to within 0·1%. Since the chamber length of 10 cm was known to within ±0·005 cm, the value of the electric field strength E could be determined to within 0·15%.

The gas pressure was measured by means of two capsule gauges (Crompton and Elford 1957), which were calibrated against a C.E.C. type 6-201 primary pressure standard. The gas pressure can be measured with an error of less than 1% at 500 torr and 0·25% at 40 torr. The larger errors at high gas pressures are due to hysteresis effects in the capsules of the gauges. Fortunately, it is necessary to use high pressures only when measurements are being made at the lowest values of E/p, where small errors in the pressure measurement have little effect on the value of k_1. This insensitivity to errors in pressure measurement is due to the value of k_1 varying only slowly with E/p; for example, for electrons in hydrogen at $E/p = 0{\cdot}006$, if the measurement of the gas pressure of 500 torr were in error by 5% the error in k_1 would be only 0·2%. At higher values of E/p, k_1 changes rapidly with E/p, but the lower pressures which are then used can be measured with adequate precision.

(*b*) *The Measurement of the Ratio* R

(i) *Double Induction Balance.*—In order to avoid the effects of Coulomb repulsion in electron or ion swarms it is necessary to ensure that the particle number density is very low. It may be necessary, therefore, for the total current arriving at the collector to be as small as 10^{-12} A. The ratio of the currents received by the disk and annulus must be determined with high accuracy if an error in this measurement is to contribute less than 1% to the error in the measured value of k_1. Furthermore, in order to avoid effects similar to those described in Section V(*b*)(ii), arising from non-uniformity in potential over the collecting electrode, the potential of the disk and annulus must not depart significantly from earth potential in the course of the measurement.

The method adopted to measure the ratio is a modification of that used by Crompton and Sutton (1952). Their method employed a pair of integrating induction balances and was developed from the method originated by Townsend (1914). A simplified circuit diagram of the modified system is shown in Figure 9. The potentiometer P_1 is a 12 kΩ Colvern potentiometer, cam-corrected to give an output within ±0·05% of linear when loaded by the 450 kΩ 10-turn helipot P_2. A voltage V, continuously variable from 1 to 10 V, is applied to P_1 from a highly stabilized d.c. power supply of low impedance. When P_1 is driven at a constant rate of 1 rev/min by a synchronous motor, a highly linear sweep voltage is generated at A while a similar signal, the relative amplitude of which is determined by the setting of P_2, appears at B. The two potentials are applied to the capacitors C_1 and C_2, which have been designed to eliminate leakage currents from dielectric soakage (Crompton and Sutton 1952). Each capacitor has a capacitance of approximately 30 pf, and the pair is matched to within 0·01%. With this arrangement, two constant displacement currents i_1 and i_2 are generated, the ratio of which is determined simply by the setting of P_2. Since the resolution and accuracy of the helipot is better than 1 part in 1000, the error incurred in k_1 due to this limit of resolution is 0·4% at $R = 0{\cdot}2$ and 0·9, and 0·07% at $R = 0{\cdot}5$.

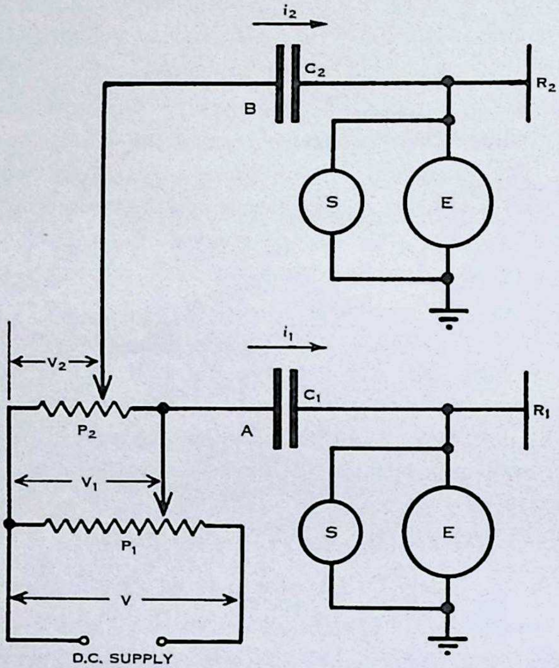

Fig. 9.—Simplified circuit of the double induction balance.

When measuring the ratio of the currents received by the segments R_1 and R_2 of the receiving electrode, the potential difference between each segment and earth is measured by the electrometers E. Adjustment of the voltage V, followed by adjustment of the potentiometer P_2, is made until R_1 and R_2 are maintained at earth potential to within 0·2 mV. The ratio R is then the required ratio of the currents.

Full advantage can be taken of the method only by making it an integrating one, with the integration commencing when $V_1 = V_2 = 0$ and terminating just before $V_1 = V$. To effect this, a correctly phased cam operates a microswitch which in turn activates the electromagnetic earthing switches S (EIL type 33124C). The switches are designed to inject minimum charge into the electrometer circuits on opening as a result of contact potential differences between the moving contacts.

(ii) *Electrometers.*—To enable the ratio R to be measured to the required accuracy when currents of the order of 10^{-12} A are being compared, it is necessary to detect currents of the order of 10^{-15}–10^{-16} A. The electrometers that are used as null indicators must therefore have a high order of stability over the period of integration, adequate sensitivity, and leakage currents less than 10^{-16} A. These requirements can be met by using selected double electrometer valves (Ferranti BDM 20) operated under closely specified and controlled conditions.

The grid current in the valve can be made vanishingly small by operating the valve at the grid voltage corresponding to the crossover point A in Figure 10, at the expense of greater difficulty in achieving stability in the grid current. One major advantage of using electrometer tubes in this way is that by suitable adjustments of the grid bias a leakage current of either sign can be introduced. Any small residual leakage current arising in either electrometer circuit, generated either internally or externally, can therefore be annulled. Before each measurement of the ratio R, one complete integration is taken with no current being received by the collecting electrode to ensure that the leakage currents in each electrometer circuit are negligible.

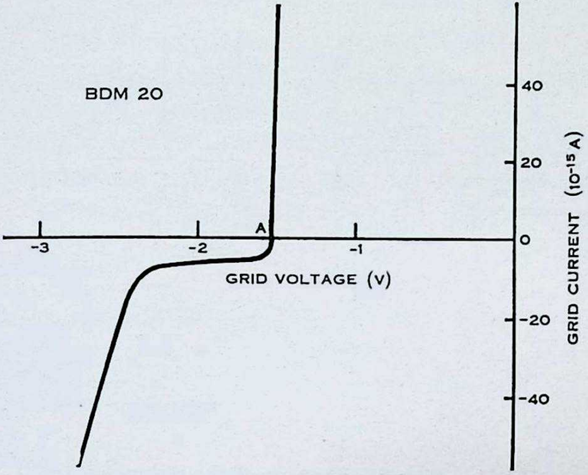

Fig. 10.—Typical grid current characteristic of the BDM 20 electrometer valve.

The circuit of the double electrometer unit is shown in simplified form in Figure 11. All resistors are high precision wire-wound types, and the cathode and plate voltages are supplied by a bank of 1·5 V dry cells. The sensitivity of the electrometers is such that an input of one millivolt causes a deflection of 5 mm of the galvanometer spot. By use of the procedure described above, the leakage rate for each of the electrometers can be made less than approximately 10^{-16} A over a period of several hours without adjustment of the grid bias controls. During the same period the zero drift is less than ±0·2 mV.

(c) *Temperature Control and Measurement*

The temperature at which the measurements are made can affect the measured values of k_1 either directly (Section I) or indirectly through its effect on the gas number density N, since the gas pressure p rather than N is measured to determine E/N. In the region of low electron energy, that is as $E/p \to 0$ and $k_1 \to 1$, the error in the measured value of k_1 resulting from an uncertainty of 1 degC in the gas temperature may be as large as 0·3% when $T \approx 293°\text{K}$, and in excess of 1% when $T \approx 80°\text{K}$. By measuring the quantity D/μ it is not possible, of course, to avoid the consequences of errors of this magnitude when using these data in subsequent analyses. Although D/μ can be determined accurately without knowledge of the gas temperature, the relevant quantity $(D/\mu - kT/e)$, which expresses the energy excess, is subject to the same percentage error as its equivalent (k_1-1) through any error in the estimate of the temperature. Therefore, it is necessary to exercise considerable care in both the control and measurement of the gas temperature.

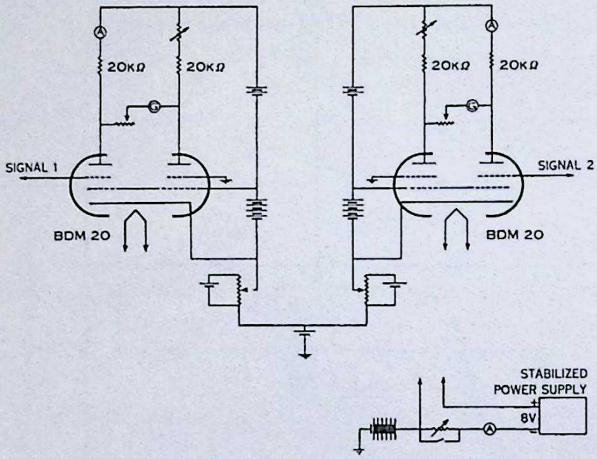

Fig. 11.—Simplified circuit of the electrometers.

To assist in the maintenance of constant gas temperature, the temperature of the laboratory was controlled to ±1 degC, and the experimental tube was surrounded by a 2-in. thick jacket of "Styrofoam". The heat generated by the platinum filament was removed by means of the cooling jacket, through which water was circulated in a closed system by a small pump.

To measure the gas temperature two copper–constantan fine-wire thermocouples were attached to the earthed ring of the collector electrode and to the cathode (Fig. 8). To avoid the danger of thermal e.m.f.'s being produced at conventional tungsten seals, hollow Kovar tube seals were used. The temperature as recorded by the two thermocouples showed a variation of the order of 0·1 degC over a period of 1 hr when measurements were being taken continuously.

IX. METHODS OF COMPENSATING FOR RESIDUAL ERRORS DUE TO CONTACT POTENTIAL DIFFERENCES

When care has been taken to eliminate as far as possible all the sources of systematic error discussed in this paper, a residual error of the order of ±1% is usually present at the lowest value of E. This error results from the existence of contact potential differences within the diffusion chamber despite the attention given to this problem. A simple method of compensating for these contact potential differences has been used which largely removes this residual error. It has been shown in Section VI(c) that, with the present techniques for gilding the surfaces, the most likely place for large contact potential differences to occur is between the internal surface of the guard electrode structure and the surfaces of the anode and cathode. On the other hand, although contact potential differences across the surface of the anode are known to be small they have a much greater influence (see Table 1). The most exact method of compensation for these effects would therefore be to place compensating potentials between the guard electrode structure and the anode and cathode and between the disk and annulus of the collecting electrode. In practice the first of these methods is the simpler of the two, so that, if practicable, it is advantageous to compensate for contact potential differences occurring anywhere in the apparatus by this method alone. This procedure is adequate only if, for a given value of E, the percentage error in k_1 resulting from a contact potential difference of either type is either independent of R or varies with R in a similar way for each type.

TABLE 1

VALUES OF ADDITIONAL POTENTIAL WHICH, WHEN APPLIED TO A GIVEN ELECTRODE, CHANGE THE MEASURED VALUE OF k_1 BY 1%

Electrode	Potential Difference (mV)
Central disk (or annulus)	6
Central disk and annulus	100
Collecting electrode and adjacent half guard electrode	170
Source electrode and adjacent half guard electrode	500
Guard electrode 1	350
Guard electrode 2	500
Guard electrode 5	2500
Set of guard electrodes	130

In order to test the validity of this procedure, a potential difference of 10 mV was first placed between the disk and annulus and the change in the measured value of k_1 for electrons obtained when the potential was reversed, the value of E in this and subsequent tests being 3 V/cm. With $p = 500$ torr, R was approximately 0·5 and the change in k_1 was $3\frac{1}{2}$%. On the other hand with $p = 10$ torr the ratio was approximately 0·2 and the change in k_1 was then $2\frac{1}{2}$%, that is, the magnitude of the error is to some extent dependent on R.

The same experiments were repeated with a potential difference now applied between the guard electrodes and the cathode and anode. This time the percentage change was found to be independent of the value of R.

Finally, a comparison was made between the two experiments with quasi-thermal electrons ($p = 500$ torr, $E = 3\cdot 0$ V/cm, i.e. $E/p = 0\cdot 006$) and those performed using positive ions with $E = 3\cdot 0$ V/cm, the ratio R for the ions then being essentially the same as that for the electrons. The percentage change in k_1 was in each case found to be the same for the ions as for the electrons.

Two conclusions can be drawn from this set of experiments. First, the use of positive ions to adjust the value of the compensating potential is justified since, as might be expected, the measurements with ions and electrons are equally sensitive to contact potential differences provided the value of R is similar in each case. The use of positive ions takes obvious precedence since the value of k_1 is known. Secondly, regardless of where contact potential differences exist in the apparatus, they can be compensated for accurately when studying quasi-thermal electrons by applying a potential difference between the guard electrodes and the anode and cathode, the magnitude of this potential difference being adjusted by using positive ions. Furthermore, although the compensation using this method is less precise when the electrons are non-thermal it is still adequate. If, as in the present experiments, the residual error to be compensated for is only 1%, then the error resulting from the use of this method when non-thermal electrons are being studied is at most 0·3%.

X. Effect of Gaseous Impurities

Some of the most commonly considered sources of error in experiments on electronic and atomic collision processes are those arising from the presence of gaseous impurities. While the effects of small traces of impurity may be significant in some swarm experiments, as for example the effect of molecular impurities in argon when the mean energy of the swarm is near the Ramsauer minimum (Bowe 1960; Uman 1964), it is necessary to recognize that in other circumstances larger errors may be introduced in reducing the impurity level than would be present if the impurity remained. The present investigation was aimed at obtaining maximum precision in the measurement of k_1 for quasi-thermal electrons in molecular gases. Calculations show that, for nitrogen and hydrogen, impurity levels of the order of 100 p.p.m. or less will have negligible effect on the results. Experience has shown that the level of impurity as a result of the outgassing of the tube can be kept well below this amount without baking. On the other hand, it seems highly probable that significant errors could be introduced through changes of the contact potential differences within the apparatus if the tube were subjected to elevated temperatures. The outgassing was therefore reduced to an insignificant level by employing long periods of pumping. Following pumping with a 5 l/s Vacion pump, isolation tests made without using liquid air traps showed that the rate of rise of pressure was of the order of 5×10^{-6} torr/hr, which corresponds to a gas influx rate of 8×10^{-8} torr-litres/s. When using samples at 500 torr the rate of rise of impurity level is therefore 1 part in 10^8 per hour. Measurements of k_1 taken over a period of 24 hr showed no change with time, indicating that the background level of gaseous impurity had a negligible effect.

The gases for which results have been published to date using the techniques described in this paper are hydrogen and nitrogen (Crompton and Elford 1963). The hydrogen was obtained by diffusion through palladium using the apparatus and technique described by Crompton and Elford (1962). This method is capable of producing hydrogen with an impurity level which is certainly less than 0·1 p.p.m. (Young 1963). Nitrogen was obtained from a cylinder of Airco Reagent Grade gas.

TABLE 2

TYPICAL RESULTS FOR ELECTRONS IN HYDROGEN AT 293°K, SHOWING THE RESIDUAL VARIATION OF k_1 WITH GAS PRESSURE

p (torr) E/p (V cm^{-1} torr^{-1})	500	400	300	200	150	100
0·01	1·049	1·047	1·047			
0·02	1·131	1·129	1·130	1·128	1·125	
0·03			1·217	1·217	1·216	1·213
0·04				1·305	1·305	1·305

XI. RESIDUAL ERRORS DUE TO THE FINITE SIZE OF THE SOURCE HOLE

Part of a typical set of results for k_1 is shown in Table 2. These results were taken using a compensating potential of 100 mV between the guard electrodes and the cathode and anode. The use of this potential, the magnitude of which was set using the procedure discussed in Section IX, eliminates errors from contact potential differences of not more than 0·7% at the lowest field strengths used.

The table shows that the values of k_1 decrease slightly as the pressure is decreased at a fixed value of E/p. This variation is similar to that predicted when account is taken of the finite size of the source hole (Crompton and Jory 1962). However, as discussed in Section III(c), the magnitude of the variation of the results with pressure from this source of error cannot be accurately estimated, and for this reason the best estimate for k_1 at any given value of E/p was obtained by averaging the results taken over a range of pressures. The maximum error incurred using this procedure is less than 0·5%.

XII. ACKNOWLEDGMENTS

The authors wish to thank their colleagues in the Ion Diffusion Unit, and in particular Dr. J. A. Rees and Dr. R. L. Jory, for their contribution to this work.

XIII. REFERENCES

BLEWETT, J. P., and JONES, E. J. (1936).—*Phys. Rev.* **50**: 464.
BOND, W. L. (1954).—*J. Opt. Soc. Am.* **44**: 429.
BOWE, J. C. (1960).—*Phys. Rev.* **117**: 1411.
COCHRAN, L. W., and FORESTER, D. W. (1962).—*Phys. Rev.* **126**: 1785.

CROMPTON, R. W., and ELFORD, M. T. (1957).—*J. Scient. Instrum.* **34**: 405.

CROMPTON, R. W., and ELFORD, M. T. (1962).—*J. Scient. Instrum.* **39**: 480.

CROMPTON, R. W., and ELFORD, M. T. (1963).—Proc. 6th Intern. Conf. on Ionization Phenomena in Gases, Paris, 1963. Vol. 1, p. 337.

CROMPTON, R. W., and JORY, R. L. (1962).—*Aust. J. Phys.* **15**: 451.

CROMPTON, R. W., and SUTTON, D. J. (1952).—*Proc. R. Soc.* A **215**: 467.

FROST, L. S., and PHELPS, A. V. (1962).—*Phys. Rev.* **127**: 1621.

HOLLAND, L. (1961).—"Vacuum Deposition of Thin Films." (Chapman and Hall: London.)

HUXLEY, L. G. H. (1940).—*Phil. Mag.* **30**: 396.

HUXLEY, L. G. H. (1959).—*J. Atmos. Terr. Phys.* **16**: 46.

HUXLEY, L. G. H., and CROMPTON, R. W. (1955).—*Proc. Phys. Soc.* B **68**: 381.

KELVIN, LORD (1898).—*Phil. Mag.* **46**: 82.

LOEB, L. B. (1955).—"Basic Processes of Gaseous Electronics." p. 225. (Univ. of California Press: Berkeley.)

PARKER, J. H. (1963).—*Phys. Rev.* **132**: 2096.

PARKER, J. H., and WARREN, R. W. (1962).—*Rev. Scient. Instrum.* **33**: 948.

REES, J. A. (1964).—*Aust. J. Phys.* **17**: 462.

REES, J. A., and JORY, R. L. (1964).—*Aust. J. Phys.* **17**: 307.

TOWNSEND, J. S. (1914).—"Electricity in Gases." (Oxford Univ. Press.)

TOWNSEND, J. S., and BAILEY, V. A. (1921).—*Phil. Mag.* **42**: 873.

UMAN, M. A. (1964).—*Phys. Rev.* **133**: A 1266.

WARREN, R. W., and PARKER, J. H. (1962).—*Phys. Rev.* **128**: 2661.

YOUNG, J. R. (1963).—*Rev. Scient. Instrum.* **34**: 891.

SOME EXPERIMENTAL OBSERVATIONS OF THE ATTENUATION OF ALFVEN WAVES IN A LABORATORY PLASMA

By I. G. Brown*

[*Manuscript received June 2, 1965*]

Summary

An experiment is described in which the velocity and attenuation of torsional, azimuthally symmetric, hydromagnetic waves are measured in a hydrogenous plasma, from low frequencies where ion–neutral collisions are unimportant to the wave damping, to frequencies where such collisions profoundly affect the damping. A theory including both ion–electron and ion–neutral collisions is outlined, and the attenuation results are compared with the theoretical values. An estimate is made, from the frequency dependence of the attenuation, of the hydrogen ion–atom collision cross section for momentum transfer.

I. Introduction

A conducting fluid contained in a magnetic field is capable of supporting a large number of different types of wave motions. The type that results from the interaction of electromagnetic and hydrodynamic forces is known, at frequencies below ion cyclotron frequency, as a hydromagnetic wave. The case of propagation parallel to the static magnetic field was first considered theoretically by Alfvén (1942) in an attempt to explain the zone velocity and long period of sunspots. The theory was carried further by Åström (1950*a*, 1950*b*) and Herlofson (1950), and since then by many authors.

The first laboratory demonstrations of Alfven waves, as these waves are also called, were carried out by Lundquist (1949) in mercury, and by Lehnert (1954) in sodium. The wave attenuation in these liquid metals is quite high; a much lower attentuation is possible when the wave is propagated in a plasma. Bostik and Levine (1952) observed standing hydromagnetic waves in a toroidal helium plasma.

More recently, Alfven wave experiments have been conducted at Berkeley, California, at Tohoku, Japan, and at Culham, England. At Berkeley, Allen *et al.* (1959) launched waves in a cylindrical deuterium plasma and measured the velocity and attenuation; the velocity results were consistent with theory, but the attenuation results were not explained at that time. De Silva (1961) carried the experiment further, and for waves of frequency much less than the ion–neutral collision frequency was able to explain the attenuation in terms of ion–electron collisions. Spillman (1963) extended the measurements to frequencies comparable with the ion–neutral collision frequency; his results, however, were in only qualitative agreement with the theory that took these collisions into account. Nagao and Sato (1960, 1961), at Tohoku, using an air plasma, have also demonstrated the propagation of these waves. At Culham, Jephcott and Stocker (1962) investigated their propagation in helium and argon plasmas for frequencies approaching the ion cyclotron frequency.

---

* Wills Plasma Physics Department, School of Physics, University of Sydney.

Aust. J. Phys., 1965, **18**, 437–49

They obtained good agreement for both velocity and attenuation with the theory of Woods (1962) if a loss of particles from the plasma is assumed.

In the experiment described here, the wave velocity and attenuation in a hydrogen plasma are measured, from low frequencies to frequencies where ion–neutral collisions significantly affect the wave attenuation. The attenuation results are compared with a theory that includes both ion–electron and ion–neutral collisions. Further, the measured frequency-dependence of the attenuation allows an estimate to be made of the ion–neutral collision cross section for momentum transfer.

II. Theory

The attenuation or damping length L is defined as that distance in the direction of propagation in which the amplitude of the wave field decreases by a factor e. If the wave is propagating in the z (axial) direction, is of angular frequency ω, and has propagation constant p, then all wave variables vary as $\exp i(pz-\omega t)$; for propagation in a cylindrical geometry, azimuthal symmetry is assumed. The real and imaginary parts of p are respectively the wave number κ and the attenuation constant ϵ, that is, $p = \kappa + i\epsilon$; κ and ϵ are related to the wavelength λ and the attenuation length L by $\kappa = 2\pi/\lambda$ and $\epsilon = 1/L$. If one obtains the dispersion relation for hydromagnetic waves in a cylindrical plasma, then the wave attenuation can be predicted in terms of the various plasma parameters.

The theoretical model assumed is as follows. A partially ionized hydrogenous plasma of finite conductivity is contained in a cylindrical, perfectly conducting waveguide, infinite in one direction. The plasma is uniform throughout its volume, except for perhaps a thin layer of vacuum (cold gas) between it and the wall. A steady axial magnetic field exists throughout the entire region, and the wave magnetic field is a small perturbation on this. Electron–neutral collisions are neglected and only azimuthally symmetric ($m = 0$) waves are considered.

(a) *Dispersion Relation*

The dispersion relation is derived in the Appendix. It is obtained by eliminating in turn all variables but one (here, the wave magnetic field **b**) from the equations of motion for ions, electrons, and neutral atoms, Maxwell's equations, and various conservation laws and definitions. The condition for a non-trivial solution to the resulting equation in **b**, i.e. that the determinant of coefficients vanishes, gives the dispersion relation.

The dispersion relation is

$$ap^4+bp^2+c = 0,$$

where a, b, c are algebraic functions of the plasma parameters and are defined in the Appendix. This equation is quadratic in p^2 and so has two distinct roots, corresponding to two wave types. These are known variously as:

(i) Torsional, shear, T-type, or slow wave. This wave is left-hand polarized, that is, its electric field vector rotates about the static magnetic field in the same sense as the ions. It hence has a resonance at the ion cyclotron frequency; and is heavily damped for higher frequencies. For frequencies much less than the ion cyclotron frequency this wave is the ordinary Alfven wave.

(ii) Compressional, TLA-type, or fast wave. This wave has, in a cylindrical geometry, a low frequency cut-off for angular frequencies less than $\omega_c = \nu V_A$, where ν is the radial wave number and V_A the Alfven speed. Its polarization is right-handed and hence it has a resonance at the electron cyclotron frequency. For frequencies approaching this frequency it is known as the Whistler wave.

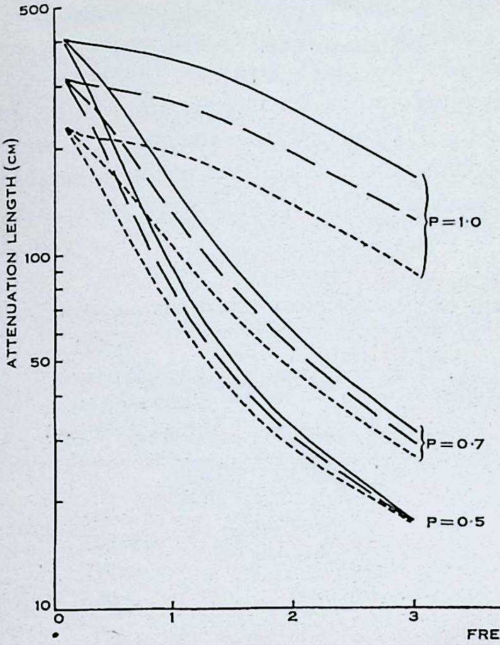

Fig. 1

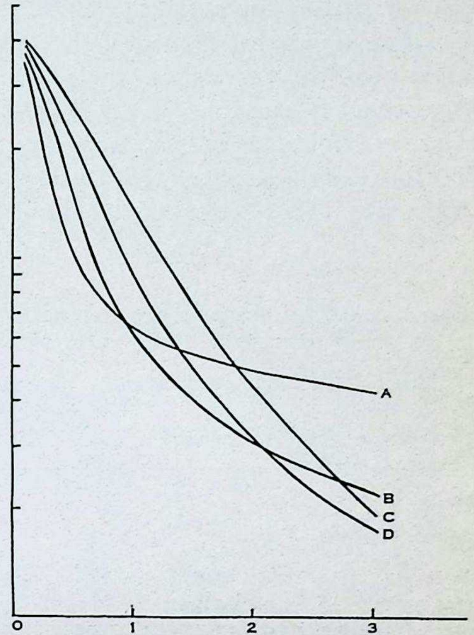

Fig. 2

Fig. 1.—Theoretical attenuation length as a function of frequency for variation of fractional ionization and temperature. Fractional ionizations are 1·0, 0·7, 0·5 and temperatures are 1·2 (——), 1·0 (— —), 0·8 (- - -) $\times 10^4$ °K. Other parameters are: axial magnetic field 12·8 kG, total particle density $2 \cdot 1 \times 10^{15}$ cm^{-3}, radial wave number 36·5 m^{-1}, cross section $1 \cdot 0 \times 10^{-14}$ cm^2.

Fig. 2.—Theoretical attenuation length as a function of frequency for variation of cross section. Cross sections are: A 2·0, B 5·0, C 20·0, D $10 \cdot 0 \times 10^{-15}$ cm^2. Other parameters are: axial magnetic field 12·8 kG, total particle density $2 \cdot 1 \times 10^{15}$ cm^{-3}, radial wave number 36·5 m^{-1}, fractional ionization 0·5, temperature $1 \cdot 2 \times 10^4$ °K.

The torsional hydromagnetic wave is the one studied in the present experiment. For the plasma parameters employed here the fast wave is cut off (i.e. is highly attenuated) for frequencies less than 3·5 Mc/s, which is greater than the maximum frequency used.

The dispersion relation for the torsional mode has been numerically evaluated using the English–Electric KDF9 computer. In particular, the damping length has been plotted as a function of frequency for many different sets of plasma parameters. Some of these curves, demonstrating the general trends, are shown in Figures 1 and 2. It should be noted that the dispersion relation used here differs from that of De Silva (1961) and Spillman (1963) in that the parallel and transverse resistivities are not approximated to equality. This assumption of equality gives rise to quite different attenuations, especially at high percentage ionizations when there is little neutral damping; for a fully ionized plasma at a temperature of 1 eV the error is nearly a factor of two at a few megacycles per second.

(b) *Wave Radial Mode Number*

The attenuation length (and to a considerably smaller extent the phase velocity) is dependent on the radial mode number; higher-order modes are damped out more rapidly than are lower modes. For comparison with theory then, it is necessary to know with which mode we are dealing, or, if there are more than one, what percentages of the various modes are present. Three points of relevance here are: (i) the relative amplitudes at the launching electrode, (ii) the relative attenuations, and (iii) the relative amplitudes of the various modes at the radius of the probe (owing to different radial variations of the azimuthal component of the wave magnetic field, b_θ).

TABLE 1

RELATIVE AMPLITUDES OF FIRST FIVE RADIAL MODES OF THE TORSIONAL HYDROMAGNETIC WAVE

Radial Mode Number	Max. Amplitude at $z = 0$	Attenuation Length at 1 Mc/s (cm)	Max. Amplitude at $z = 50$ cm	Amplitude at Radius of Probe (for $z = 50$ cm)
1	$+1$	75	$+1$	$+1$
2	$-0\cdot37$	52	$-0\cdot28$	$-0\cdot096$
3	$-0\cdot15$	35	$-0\cdot07$	$+0\cdot037$
4	$-0\cdot46$	26	$-0\cdot13$	$+0\cdot047$
5	$+0\cdot34$	19	$+0\cdot048$	$+0\cdot018$

(i) The relative amplitudes at the launching electrode are determined by the radii of the inner and outer electrodes, and by the boundary condition imposed on b_θ (or its equivalent, E_r) at the quartz plate at the launching end. These have been calculated and are given in the second column of Table 1.

(ii) The radial wave number ν_n appropriate to the nth radial mode is obtained as the solution to $J_1(\nu_n R) = 0$, where J_1 is the Bessel function of the first kind and order, and R is the vessel radius. This results from the boundary condition imposed on b_θ by the conducting walls. If there is a layer of cold gas between plasma and wall, this simple expression is replaced by a more complicated one; but it happens that for a thin vacuum layer the change in ν_n is small, smaller than would be obtained from a direct reduction in the value of R to the plasma radius. Hence, with the vessel radius for R, and using the simple expression to find the appropriate ν_n, the attenuation lengths for the present plasma have been calculated from the dispersion relation and are shown in the third column of Table 1 for a typical frequency. The effect of different attenuation lengths on the relative amplitudes, at a distance of 50 cm, is shown in the fourth column of the table.

(iii) The magnetic probe is inserted into the plasma at a radial distance for which the lowest-order mode of b_θ has a maximum; higher modes have their maxima elsewhere. This further reduced the amplitudes of the monitored wave fields of higher modes, as is shown by the values given in the final column of Table 1. It is clear from this table that for the experimental arrangement used the wave field monitored is, to a good approximation, only the lowest mode.

III. Experimental Method

(*a*) *Apparatus*

The experiment was carried out in a cylindrical plasma source (Supper II—see Fig. 3), which has been described in detail by Brennan, Lehane, *et al.* (1963). It consists of a stainless steel vacuum vessel, through which hydrogen at a pressure of 70 μmHg is circulated. It is immersed in a uniform axial magnetic field of 12·8 kG. One end of the machine is sealed with a quartz plate that has a central molybdenum electrode. The other end is sealed with a Pyrex glass plate to which a stainless steel mesh is attached on the inside. There are 16 radial diagnostic ports along the machine, in 4 groups of 4.

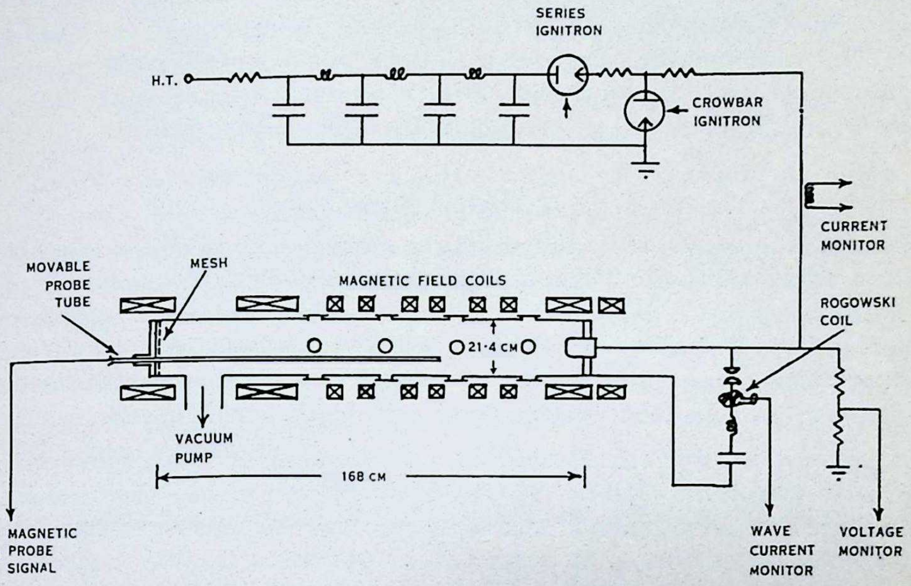
SERIES IGNITRON
H.T.
CROWBAR IGNITRON
CURRENT MONITOR
MOVABLE PROBE TUBE
MESH
MAGNETIC FIELD COILS
ROGOWSKI COIL
21·4 CM
VACUUM PUMP
168 CM
MAGNETIC PROBE SIGNAL
WAVE CURRENT MONITOR
VOLTAGE MONITOR

Fig. 3.—Schematic diagram of experimental apparatus (Supper II).

To prepare the plasma, a pulse line of impedance 0·7 Ω, charged to +20 kV, is discharged through a series resistance of 1·05 Ω to the end electrode; the gas breaks down and a hydromagnetic ionizing shock front, driven by the discharge current of 6·3 kA, travels down the tube. The characteristics of the shock front have been studied here and are reported by Brennan, Brown, *et al.* (1963). Behind the front the plasma is left rotating. This rotation is removed by the "self crowbarring" that occurs when the front hits the stainless steel mesh at the far end (a time of about 50 μs after breakdown). The sudden cessation of rotation of the plasma causes a large-amplitude standing Alfven wave to be set up; this is evidenced by a ringing voltage appearing on the electrode. The plasma preparation current is crowbarred (by an ignitron) on the first positive swing of the electrode, at about 60 μs after breakdown. It has been found from framing camera photographs that a less turbulent plasma is produced if the mesh does the plasma crowbarring, rather than the ignitron; hence the above order of events is used.

(*b*) *Wave Excitation*

The waves are launched at times of 150, 200, or 250 μs after initial breakdown. The wave launcher consists of a condenser of from $0\cdot2\ \mu$F (at 265 kc/s) to $0\cdot01\ \mu$F (at $2\cdot5$ Mc/s), charged to $+20$ kV, in series with a suitable inductance, and discharges via a spark gap to the end electrode and plasma. The ringing circuit is sufficiently isolated from the shorted crowbar ignitron by the inductance of a long coaxial cable. The wave-inducing current is monitored by a Rogowski coil encircling the lead to the spark gap. The peak current for the various condenser–coil combinations is from 1 to 5 kA, and the Q of the circuit varies from about 10 to 20.

(*c*) *Wave Detection*

The wave is detected by a magnetic probe, which is placed inside a quartz tube to isolate it from the plasma. This tube is inserted axially through a hole in the far end plate and mesh at a radius of 5 cm. The probe consists of 30 turns of 40 S.W.G. copper wire on a 2 mm diameter former. It is orientated to pick up the azimuthal component of the wave field, which, theoretically, is the biggest of the three components; this has been confirmed by measuring the other two components.

The wave velocity and attenuation are determined by making measurements of the wave phase and amplitude as a function of axial position. In making these measurements, the probe and the tube are moved together in order to eliminate any possible effect of the tube on the attentuation. Measurements were typically made at five or six different axial positions. For each axial position and time of firing of the waves, between 3 and 12 shots were taken. This was necessitated by the large shot-to-shot variation inherent in the present method of plasma preparation. This scatter increases with frequency and with the axial position of the probe. The stainless steel mesh at the far end did reduce the scatter quite considerably, but still the scatter is as great as (in extreme cases) $\pm50\%$ of the mean value.

(*d*) *Plasma Properties*

To compare the experimental results with the theory outlined in Section II, it is necessary to know the values of the various plasma parameters that occur in the dispersion relation. These parameters are the total particle density, the percentage ionization, the plasma temperature (it is assumed that $T_{\mathrm{e}} = T_{\mathrm{i}}$), and the ion–neutral momentum transfer cross section. Curves of attenuation length *v.* frequency have been drawn from the computed dispersion relation for various sets of these parameters, and the experimental points have been compared with these to find the curve of best fit. The fitting process gives fairly good estimates of the temperature, percentage ionization, and cross section, since the structure of the curves varies in different ways for these three parameters.

Independent estimates of the plasma properties can be obtained. The average ion density across a diameter has been found by measuring the Stark broadening of the Hβ line. A value of about $1\cdot6\times10^{15}$ cm^{-3} is obtained. This is in reasonable agreement with that expected from the results of Irons and Millar (1965), who have made a detailed investigation of the density and temperature distributions in a similar but smaller machine (Supper I). Their results also enable an estimate to be made of the temperature in Supper II, which has not been measured spectroscopically. This estimated value is $1\cdot0$–$1\cdot2\times10^{4}$ °K.

These independent estimates of density and temperature are taken only as indications of the correct values. The values obtained from the measured wave velocity and the curve-fitting process described above are thought to be more reliable.

IV. Results

(a) *Velocity*

The wave velocity has been measured for three different wave times (150, 200, and 250 μs after breakdown) and for 12 different frequencies. A least squares fit to a straight line has been made for the three wave times and the mean velocity in the low frequency limit has been found. This is 60 ± 3 cm/μs; a small variation of velocity with frequency is expected theoretically, but this is masked by the scatter in the points. The particle density ρ may be obtained from this low frequency velocity using the simple expression for the Alfven speed, $V_A = B_0(\mu\rho)^{-\frac{1}{2}}$, where B_0 is the static magnetic flux density; in the low frequency limit, the exact dispersion relation yields the same density as the simple expression. The density obtained in this manner is $2\cdot1\times10^{15}$ cm^{-3}. This is the total particle density, since in the low frequency limit the neutral atoms are closely coupled into the wave motion via ion–neutral collisions.

The density of the unionized gas is $4\cdot6\times10^{15}$ atoms/cm^{3}, more than twice the measured density of the plasma at the wave time. Spectral measurements made on Supper I can be explained by assuming a large radial drift of particles to the wall during plasma preparation by the $J\times B$ process; this loss of particles is sufficient to account for the difference in densities. The value of $2\cdot1\times10^{15}$ cm^{-3} for the total particle density has been used in the selection of a curve of best fit for the attenuation results. The shape of the theoretical attenuation–frequency curve is, however, very insensitive to the total particle density.

(b) *Attenuation*

The measured attenuation lengths for two wave times, 150 and 250 μs, are shown in Figures 4(*a*) and 4(*b*), together with the finally selected curves of best fit. The plasma parameters appropriate to these curves are:

Total particle density	$2\cdot1\times10^{15}$ cm^{-3}
Temperature	$1\cdot2\times10^{4}$ °K
Radial wave number	$36\cdot5$ m^{-1}
Percentage ionization	50%
Collision cross section	$5\cdot0$–$10\cdot0\times10^{-15}$ cm^{2}

The manner in which the shape of the curve varies with the different parameters ensures the selection of the correct value; the low frequency damping is determined almost entirely by the temperature alone (i.e. by ion–electron collisions), and the fitting of the curve at the low frequency end ensures the correct temperature. The damping of a low frequency Alfven wave is a good diagnostic for temperature; such a technique has been used in this laboratory.

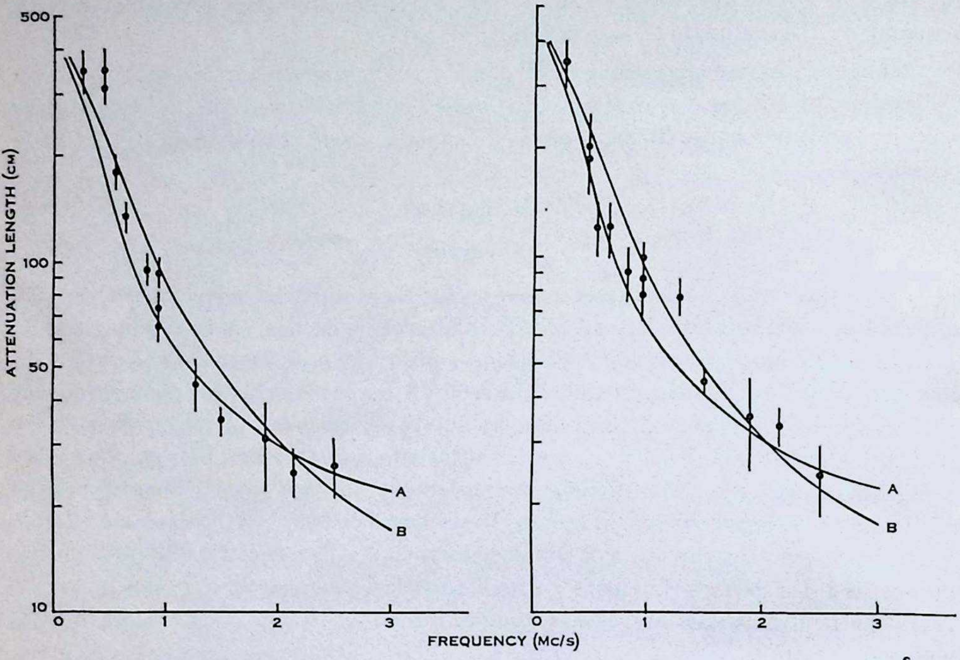

(a) (b)

Fig. 4.—Measured attenuation lengths as a function of frequency, for the wave launching times of (*a*) 150 μs and (*b*) 250 μs after plasma preparation. Also shown are the finally selected theoretical curves; these have the following parameters: total particle density $2 \cdot 1 \times 10^{15}$ cm^{-3}, fractional ionization $0 \cdot 5$, temperature $1 \cdot 2 \times 10^{4}$ °K, cross sections A $5 \cdot 0$, B $10 \cdot 0 \times 10^{-15}$ cm^{2}.

It is at first surprising that the percentage ionization is about the same for all three wave times; one may have expected this to fall off with time. Irons and Millar (1965) have shown that the plasma decay process occurs much faster in the outer, cooler layers of the plasma, and this leads to a shrinkage in diameter of the central plasma column, within which the density and temperature fall off very slightly during the times of interest. Framing camera photographs show no apparent change in the diameter of the central core. As discussed in Section II(*b*), this results in only a small change in the radial wave number, and the attenuation change is expected to be small.

V. Discussion

It is of interest to compare the momentum transfer cross section obtained here ($7 \cdot 5 \pm 2 \cdot 5 \times 10^{-15}$ cm^{2}) with other experimental and theoretical estimates. Fite, Smith, and Stebbings (1962) have measured the hydrogen ion–atom charge exchange cross section down to 20 eV ($2 \cdot 3 \times 10^5$ °K) by the modulated crossed beams technique. Their points fall more or less uniformly on a straight line that extrapolates back to $5 \cdot 5 \times 10^{-15}$ cm^2 at 1 eV ($1 \cdot 16 \times 10^4$ °K), with rather large error here. Dalgarno (1960) states that the momentum transfer cross section is equal to twice the charge exchange cross section, and so Fite would predict a momentum transfer cross section of $1 \cdot 1 \times 10^{-14}$ cm^2, again with rather large error. Dalgarno arrives at a theoretical value of $1 \cdot 0 \times 10^{-14}$ cm^2. Swanson (1963) has conducted a Fourier analysis of the impulse response of a plasma to the compressional hydromagnetic wave. He does not state a cross section, but a calculation based on his results gives the value 5×10^{-15} cm^2 at ~ 5000°K; the associated error is probably ± 2–3×10^{-15} cm^2. The cross section varies slowly with temperature, and the expected difference in values at 5000°K and at 12000°K is only about 10%.

The present experiment, then, yields a momentum transfer cross section that is consistent with both theoretical values and the little experimental data available. The dispersion relation used here, with the deduced value for the cross section, is able to predict the measured attenuation lengths quite well, from frequencies where neutral atoms are unimportant to the wave damping, to frequencies where ion–neutral collisions affect the damping greatly. From equation (11) of the Appendix it can be shown that the momentum vector has a quadrature component, introduced by the neutral particles lagging in phase, varying from less than 1% to nearly 40% of the real component, for the frequency range covered. Thus one can conclude that the roles of ion–electron and ion–neutral collisions have been well identified.

VI. Acknowledgments

The author is grateful to Professor C. N. Watson-Munro and the late B. E. Swire for discussion in the course of this work, to the Institute of Nuclear Science and Engineering for financial support, and to Professor H. Messel for the provision of research facilities in the School of Physics.

VII. References

Alfvén, H. (1942).—*Ark. Mat. Astr. Fys.* **29B**: 1.

Allen, T. K., Baker, W. R., Pyle, R. V., and Wilcox, J. M. (1959).—*Phys. Rev. Lett.* **2**: 383.

Åström, E. (1950*a*).—*Nature* **165**: 1019.

Åström, E. (1950*b*).—*Ark. Fys.* **2**: 443.

Bostik, W. H., and Levine, M. A. (1952).—*Phys. Rev.* **87**: 671.

Brennan, M. H., Brown, I. G., Millar, D. D., and Watson-Munro, C. N. (1963).—*J. Nucl. Energy* C **5**: 229.

Brennan, M. H., Lehane, J. A., Millar, D. D., and Watson-Munro, C. N. (1963).—*Aust. J. Phys.* **16**: 340.

Dalgarno, A. (1960).—*Proc. Phys. Soc.* **75**: 374.

De Silva, A. W. (1961).—Ph.D. Thesis, Univ. Calif. Radiation Lab. Rep. 9601.

Fite, W. L., Smith, A. C. H., and Stebbings, R. F. (1962).—*Proc. Roy. Soc.* A **268**: 527.

Herlofson, N. (1950).—*Nature* **165**: 1020.

Irons, F. E., and Millar, D. D. (1965).—*Aust. J. Phys.* **18**: 23.

Jephcott, D. F., and Stocker, P. M. (1962).—*J. Fluid Mech.* **13**: 587.

Lehnert, B. (1954).—*Phys. Rev.* **94**: 815.

Lundquist, S. (1949).—*Phys. Rev.* **76**: 1805.

Nagao, A., and Sato, T. (1960).—*J. Phys. Soc. Japan* **15**: 735.

Nagao, A., and Sato, T. (1961).—Res. Rept Tohoku University, Sendai, Japan.
Spillman, G. R. (1963).—Ph.D. Thesis, Univ. Calif. Radiation Lab. Rep. 10990.
Spitzer, L. (1962).—"Physics of Fully Ionised Gases." (Interscience: New York.)
Swanson, D. G. (1963).—Calif. Inst. Tech., Tech. Rep. No. 1.
Woods, L. C. (1962).—*J. Fluid Mech.* **13**: 570.

APPENDIX

Derivation of Dispersion Relation for Hydromagnetic Waves

The plasma model assumed is as stated in Section II. We consider azimuthally symmetric waves in a hydrogenous plasma and neglect all terms of order $(m_e/m_i)^{\frac{1}{2}}$ or less.

The equations of motion for ions, electrons, and neutral particles are obtained from the Boltzmann equation (Spitzer 1962), and are written here as

$$n_i m_i \partial \mathbf{v}_i/\partial t = n_i e\mathbf{E} + n_i e\mathbf{v}_i \times \mathbf{B} + \mathbf{P}^{ie} + \mathbf{P}^{in}, \tag{1}$$

$$n_e m_e \partial \mathbf{v}_e/\partial t = -n_e e\mathbf{E} - n_e e\mathbf{v}_e \times \mathbf{B} + \mathbf{P}^{ei}, \tag{2}$$

$$n_n m_n \partial \mathbf{v}_n/\partial t = \mathbf{P}^{ni}, \tag{3}$$

where subscripts i, e, n refer to ions, electrons, and neutral atoms respectively. n, m, e are the particle densities, particle masses, and the electronic charge; $\mathbf{v}$ is the macroscopic particle velocity vector, $\mathbf{E}$ and $\mathbf{B}$ are the total electric field and magnetic flux density present, and $\mathbf{P}^{ij}$ is the momentum transfer vector—the momentum transferred per unit time and volume from species j to species i. In the derivation of these equations, all non-linear, pressure gradient, and gravitational potential-like terms have been neglected. Electron–neutral collisions have been neglected since $\mathbf{P}^{en} \sim (m_e/m_i)^{\frac{1}{2}}\mathbf{P}^{in}$.

Using the conservation of momentum

$$\mathbf{P}^{ei} = -\mathbf{P}^{ie}, \tag{4}$$

the definition of current density $\mathbf{j}$

$$\mathbf{j} = en(\mathbf{v}_i - \mathbf{v}_e), \tag{5}$$

and the condition of charge neutrality for a hydrogenous plasma

$$n_e = n_i = n, \tag{6}$$

one can obtain from (1) and (2)

$$\rho_i \partial \mathbf{v}_i/\partial t = \mathbf{j} \times \mathbf{B} + \mathbf{P}^{in}, \tag{7}$$

where $\rho_i = n_i m_i$, and terms of order m_e/m_i, ω/ω_{ce} have been neglected (ω_{ce} = electron cyclotron frequency $= eB_0/m_e$). Now define the ion–neutral collision frequency per neutral, ν_{ni}, by

$$\mathbf{P}^{in} = mn_n \nu_{ni}(\mathbf{v}_n - \mathbf{v}_i), \tag{8}$$

where m is taken to be either the neutral or ion mass. The cross section for momentum transfer σ_{ni} is defined in terms of ν_{ni} through the usual expression

$$\nu_{ni} = n_i \sigma_{ni} v_i.$$

Combining (8) and (3)

$$\mathbf{P}^{\mathrm{in}} = \frac{\mathrm{i}\omega\rho_{\mathrm{n}}}{1-\mathrm{i}\tau}\,\mathbf{v}_{\mathrm{i}}, \tag{9}$$

where now $-\mathrm{i}\omega$ replaces the time derivative $\partial/\partial t$, $\rho_{\mathrm{n}} = m_{\mathrm{n}} n_{\mathrm{n}}$, and $\tau = \omega/\nu_{\mathrm{ni}}$. Substituting (9) in (7) gives the required complex equation of motion,

$$-\mathrm{i}\omega\rho_1\,\mathbf{v}_{\mathrm{i}} = \mathbf{j}\times\mathbf{B}, \tag{10}$$

where

$$\rho_1 = \rho_0(1+\mathrm{i}\xi), \tag{11}$$

$$\rho_0 = \rho_{\mathrm{i}} + \frac{\rho_{\mathrm{n}}}{1+\tau^2}, \tag{12}$$

and

$$\xi = \frac{\rho_{\mathrm{n}}}{\rho_0}\cdot\frac{\tau}{1+\tau^2}. \tag{13}$$

The physical significance of the equation (10) is evident in that ρ_1 is complex, expressing the fact that the neutrals introduce an out-of-phase component to the momentum vector.

Now using (5) in (1) to eliminate $\mathbf{v}_{\mathrm{e}}$, and again neglecting terms of order $m_{\mathrm{e}}/m_{\mathrm{i}}$, $\omega/\omega_{\mathrm{ce}}$, one obtains the generalized Ohm's law,

$$\mathbf{E}+\mathbf{v}_{\mathrm{i}}\times\mathbf{B} = (1/en)\mathbf{j}\times\mathbf{B}+\boldsymbol{\eta}\,.\,\mathbf{j}, \tag{14}$$

where $\boldsymbol{\eta}$ is the resistivity tensor defined by

$$\boldsymbol{\eta}\,.\,\mathbf{j} = \mathbf{P}^{\mathrm{ei}}/ne. \tag{15}$$

The resistivity is related to the temperature by the formulae of Spitzer.

The complex equation of motion, equation (10), the generalized Ohm's law, equation (14), and Maxwell's equations,

$$\nabla\times\mathbf{B} = \mu_0\,\mathbf{j}, \tag{16}$$

$$\nabla\times\mathbf{E} = -\partial\mathbf{B}/\partial t, \tag{17}$$

constitute the set to be solved.

Now let $\mathbf{B} = \mathbf{B}_0+\mathbf{b}$, where $\mathbf{B}_0$ is the static axial field, and $\mathbf{b}$ the perturbation wave field. Putting (10) in (14) and using (16) and (17) to eliminate all wave variables but $\mathbf{b}$, and neglecting all second-order terms, one obtains

$$\mathbf{b}+\frac{V^2}{\omega^2}\nabla\times[\{(\nabla\times\mathbf{b})\times\hat{\mathbf{z}}\}\times\hat{\mathbf{z}}]+\frac{\mathrm{i}}{\omega\mu_0}\nabla\times\{\boldsymbol{\eta}\cdot(\nabla\times\mathbf{b})\}+\frac{\mathrm{i}V^2}{\omega\omega_{\mathrm{ci}}}\cdot\frac{\rho_1}{\rho_{\mathrm{i}}}\nabla\times\{(\nabla\times\mathbf{b})\times\hat{\mathbf{z}}\} = 0, \tag{18}$$

where $V^2 = B_0^2/\mu_0\rho_1$, and $\hat{\mathbf{z}}$ is the unit vector in the axial direction.

Equation (18) can best be solved by making use of a type of vector notation. For any vector $\mathbf{A}$ with a dependence like $\exp\mathrm{i}(pz+m\theta-\omega t)$, with $m = 0$, then in cylindrical coordinates

$$\nabla\times\mathbf{A} = \begin{bmatrix} 0 & -ip & 0 \\ ip & 0 & -\dfrac{\partial}{\partial r} \\ 0 & \dfrac{1}{r}\dfrac{\partial}{\partial r}r & 0 \end{bmatrix}\mathbf{A} \tag{19}$$

and

$$\mathbf{A}\times\hat{\mathbf{z}} = \begin{bmatrix} 0 & 1 & 0 \\ -1 & 0 & 0 \\ 0 & 0 & 0 \end{bmatrix}\mathbf{A}. \tag{20}$$

Using these relations, and taking $\boldsymbol{\eta}$ to be of the form

$$\boldsymbol{\eta} = \begin{bmatrix} \eta_\perp & 0 & 0 \\ 0 & \eta_\perp & 0 \\ 0 & 0 & \eta_\parallel \end{bmatrix}, \tag{21}$$

equation (18) can be reduced to a matrix equation in $\mathbf{b}$, containing in the matrix coefficients $\partial/\partial r$ type operators. Now assume a solution of the form

$$\mathbf{b} = (AJ_1(\nu r), BJ_1(\nu r), CJ_0(\nu r)). \tag{22}$$

This is the solution expected from the boundary conditions imposed on $\mathbf{b}$ (that $b_r = 0$ at the wall), and also it is the solution given by the cold, collisionless plasma theory. Equation (22) is substituted in the matrix equation for $\mathbf{b}$, and so three equations are obtained in the three unknowns A, B, and C.

Using $\nabla\,.\,\mathbf{b} = 0$ on equation (22), one obtains

$$\nu A = -ipC, \tag{23}$$

which can be used to eliminate C. One then has three equations, two of which are identical; this has arisen as a result of dropping the pressure gradient term from the linearized equation of motion, and corresponds to the loss of a further wave type. For sound speeds much less than the Alfven speed (as is the case in the present experiment), this mode is physically irrelevant.

For a non-trivial solution, the two remaining equations in A and B must have zero determinant, and one thus obtains the desired dispersion relation

$$ap^4+bp^2+c = 0, \tag{24}$$

where

$$a = \Omega^2-(1-i\alpha_\perp)^2,$$

$$b = \nu^2(\Omega^2-1)+\nu^2(\alpha_\perp^2+\alpha_\perp\alpha_\parallel)+2(\omega^2/V^2)(1-i\alpha_\perp)+i\nu^2(2\alpha_\perp+\alpha_\parallel),$$

$$c = -\frac{\omega^4}{V^4}+\frac{\omega^2\nu^2}{V^2}+\alpha_\perp\alpha_\parallel\nu^4+i\alpha_\parallel\left\{\nu^4-\frac{\omega^2\nu^2}{V^2}\left(1+\frac{\alpha_\perp}{\alpha_\parallel}\right)\right\},$$

and $$\Omega = (\rho_1/\rho_i) \cdot (\omega/\omega_{ci}),$$

$$\alpha_\perp = \omega\eta_\perp/\mu_0 V^2, \qquad \alpha_\parallel = \omega\eta_\parallel/\mu_0 V^2.$$

For the simplification $\eta_\perp = \eta_\parallel$, this reduces to the same expression as that used by De Silva (1961) and by Spillman (1963).

THE UPPER LIMITING PRIMARY RIGIDITY OF THE COSMIC RAY SOLAR ANISOTROPY

By R. M. Jacklyn* and J. E. Humble†

[*Manuscript received June 8, 1965*]

Summary

A method of determining the upper limiting rigidity of the solar diurnal variation of the cosmic ray primaries in free space is described. It involves a comparison of the response to the anisotropy of neutron monitors at sea level and of meson telescopes underground. Making use of the model for the free-space first harmonic proposed by Rao, McCracken, and Venkatesan, the annual average value for the upper limiting rigidity (R_u) in 1958 is estimated to have been 95 GV with an error of estimate of about 10–20 GV. Changes in the observed annual mean daily variation between 1958 and 1962 indicate that R_u may have decreased by about 20–40 GV over this period, but a more refined analysis is needed to confirm this.

Changes in R_u could also influence a sidereal daily variation as observed at the Earth. Evidence is presented for such an effect, from the observations underground at Hobart.

It is shown that the annual average pressure-corrected solar diurnal variation observed at a depth of 40 m.w.e. must be largely under the control of the solar anisotropy. The most significant evidence presented comes from observations in three different directions underground at Hobart during 1961 and 1962. The first harmonics of the solar daily variations observed in these directions have been found to be broadly compatible with the model for the anisotropy proposed by Rao, McCracken, and Venkatesan.

We also present the results of an investigation of the response of an underground telescope to generalized free-space first and second harmonics, for different approximations to the geomagnetic field and for small and large sets of arrival directions.

I. Introduction

Recent theories of modulation of galactic cosmic rays within the interplanetary medium (Ahluwalia and Dessler 1962; Parker 1964; Axford 1965) have indicated that charged particles approaching the Earth's orbit with gyro-radii greater than about 1 a.u. would be too energetic to take part in the cosmic ray solar anisotropy, which appears to be responsible for most of the observed pressure-corrected solar daily variation at the Earth. Consequently it has been predicted that the upper limiting rigidity R_u (the rigidity above which the solar daily variation in free space vanishes) would have been approximately in the vicinity of 10^2 GV at the recent maximum of solar activity when the average interplanetary magnetic field strength at the Earth's orbit was a few gammas. At solar minimum R_u should be somewhat smaller, depending on the nature of the minimum. This solar-cycle dependence should be reflected in changes in amplitude and phase of the solar daily variation.

---

* Antarctic Division, Department of External Affairs, Melbourne, and Physics Department, University of Tasmania, Hobart.

† Department of Physics, University of Tasmania, Hobart.

Aust. J. Phys., 1965, **18**, 451–71

It is also reasonable to suppose that R_u might be the threshold rigidity for observations at the Earth's orbit of any sidereal anisotropy of the charged primaries, and there could be a significant relationship between the solar and sidereal daily variations because of this common dependence on R_u. In short, there are a number of reasons why experimental determinations of R_u are needed at various stages of the solar cycle, in addition to the more fundamental one, that it is one of the constants that characterize the region of modulation. It is proposed to describe here a method of determining annual average values of R_u within reasonably narrow limits and to report a provisional value for 1958, the year of minimum cosmic ray intensity in the present cycle. This follows an earlier estimate of 200 GV, to within a factor of two, given by Rao, McCracken, and Venkatesan (1963), based on the Hobart underground observations in 1958. The present method depends on the fact that changes in the value of R_u would have a much greater effect on the solar daily variation observed underground than on the daily variation observed with neutron monitors at high latitude sea level stations.

Towards the end of 1960 two inclined telescopes began operating at the Hobart underground site, in addition to the two vertical semi-cubes. Their axial directions were 30° north of the zenith and 45° south of the zenith respectively, in the plane of the geographic meridian. The whole arrangement would permit a simultaneous scan of the southern sky along three broadly overlapping asymptotic latitude strips. Some results from the three directions during 1961–62 are presented here, partly to indicate how R_u may have changed since 1958, and also to demonstrate that the first harmonics observed underground at about 40 m.w.e. must have been produced in the greater part by an extraterrestrial anisotropy.

It should be emphasized that the following treatment concerns only the first harmonic of the solar anisotropy. However, it does appear, notably from the work of Sarabhai and his associates (Sarabhai and Subramanian 1963*a*; Subramanian 1963), that a second harmonic must be considered when attempting to describe some of the characteristics of the anisotropy as a whole. There is also evidence that the second harmonic is greater at higher rigidities. We wish to make the point here that, although the free-space daily variation may not be completely described by a first harmonic as Rao, McCracken, and Venkatesan had tentatively concluded, they have shown that the first harmonic has certain definite characteristics that enable an upper limiting rigidity to be worked out for it quite simply. In this instance what is true for the first harmonic might reasonably be expected to apply to the free-space daily variation as a whole.

It is also important to note the argument (Sarabhai and Subramanian 1963*b*) that annual-averaged daily variations fail to provide a realistic picture of the solar anisotropy because the daily variations observed on individual days tend to fall into distinct groups that are attributed to solar anisotropies of differing character. Thus, although on the annual average the index β of variation spectrum may be almost zero, it seems that it is not characteristically zero on individual days. On the other hand, annual averages of upper and lower limiting rigidities and of the amplitude constant of the anisotropy are not open to misinterpretation in the same way. It appears that the two methods of approach are complementary and should lead to conclusions that are compatible, provided the limitations of each method are understood. Perhaps the greatest single advantage of using an annual average of the solar daily variation is that the influence of a sidereal anisotropy is thereby completely averaged out.

II. OUTLINE OF A METHOD OF DETERMINING R_u

The first harmonic of the pressure-corrected daily variation observed underground in 1958 can now be related to the solar anisotropy of the primaries with some degree of confidence. In the first instance, Rao, McCracken, and Venkatesan, making careful allowance for the asymptotic cones of acceptance of particle detectors, were able to delineate the free-space first harmonic of the anisotropy in 1958, at least so far as to account for the manner in which the first harmonic of the observed annual mean daily variation of neutron intensity depended on the geographic location of the detector. Since adequate coupling coefficients that could be applied to underground detectors of charged particles were not available then, the authors could make only a rough estimate of R_u. However, recent calculations have indicated that underground telescopes have a mean energy of response that is lower than had been previously thought. Specifically, Fenton (1963) has worked out the yield functions for the pions that are thought to be responsible for the μ-meson intensity at the underground depth of 40 m.w.e. Thereby he has obtained the differential coupling coefficients, which give the fraction of the observed counting rate underground due to primaries of any given energy E. He has found that the coupling coefficients are similar to those derived by Mathews (1963) from an empirical response curve extrapolated from latitude–intensity data. Fenton calulates the mean energy of response to be about 200 GeV, and that less than 10% of the counting rate is due to primaries of energy < 50 GeV. From such information the cone of acceptance technique enables the first harmonic underground to be estimated as a function of R_u, in relation to the given free-space first harmonic.

Rao, McCracken, and Venkatesan could find no convincing evidence from the neutron data that a semi-diurnal component of extraterrestrial origin existed. Accordingly they specified the anisotropic component of intensity in free space for primaries of rigidity R, and for a very narrow angle detector, as being simply a first harmonic $\alpha_1 I_0(R)\cos\lambda\cos(\psi-\psi_0)$, where α_1 is the amplitude constant, $I_0(R)$ is the omnidirectional differential intensity of primaries, λ is the ecliptic latitude of the detector, ψ is the direction of viewing in the plane of the ecliptic, measured eastward of the Earth–Sun line, and ψ_0 is the direction of maximum intensity. Initially the expression given by them also contained the factor R^β, denoting the dependence of amplitude on rigidity, but one of their most important findings was that the annual average amplitude was independent of rigidity in 1958, so that $\beta = 0$. On transforming to rotating terrestrial coordinates it can be shown (Jacklyn 1963*a*) that the corresponding free-space solar diurnal variation is, to a sufficient degree of approximation,

$$\Delta I(R)/I_0(R) = \alpha_1 \cos\delta\cos(\phi-\phi_0), \qquad (1)$$

where δ is the geographic latitude of viewing, ϕ is the time of day relative to noon, in angular measure (or longitude east of the observer's meridian at noon), and

ϕ_0 ($\simeq \psi_0$) is the time of maximum intensity. In this context, free space, or the asymptotic region, is the region of modulation situated beyond the effective limits of the Earth's magnetic field.

Now, the fraction of the observed first harmonic underground that is due to anisotropic primaries of rigidity R will differ considerably from $\Delta I(R)/I_0(R)$, partly because at any instant the primaries involved do not approach the Earth's magnetic field from a single direction (δ, ϕ) but from a cone of directions that will allow them to arrive at the meson production level within the solid angle of viewing of the recorder, after penetrating the field. The cone is the asymptotic cone of acceptance of which the concept and general method of application to an anisotropy have been fully outlined by Rao, McCracken, and Venkatesan. The present treatment differs somewhat in detail from theirs and is perhaps only appropriate when dealing with high energy primaries. The cone of acceptance is divided up into N segments specified by intervals of asymptotic latitude. These intervals can be conveniently defined so that each segment of the cone contributes about the same amount to the fraction of the counting rate that is due to primaries of the given rigidity. The contribution $v(R)$ to the first harmonic of the daily variations underground from primaries of rigidity R is then approximated by the summation

$$v(R) = \alpha_1 \frac{Y_R}{N} \sum_{n=1}^{N} A_{Rn} \cos \delta_{Rn} \cos(\phi - \phi_0 + \phi_{Rn}). \tag{2}$$

In this expression Y_R is the differential coupling coefficient and A_{Rn} is an amplitude reduction factor determined by the manner in which the contributions to Y_R from the nth segment of the cone are distributed in asymptotic longitude. An individual contribution will be defined more precisely below as the "differential radiation sensitivity" $I(R, \omega)$. The distribution also determines an effective longitude of viewing ϕ_{Rn} (east of the observer's meridian) with respect to a first harmonic of the anisotropy. The mean asymptotic latitude δ_{Rn} is obtained from distribution in asymptotic latitude of the contributions to Y_{Rn} from the nth segment of the cone.

The total first harmonic v is estimated as

$$\begin{aligned} v &= \sum_{R=R_c}^{R_u} v(R) \\ &= \alpha_1 \sum_{R=R_c}^{R_u} \sum_{n=1}^{N} \frac{Y_R}{N} A_{Rn} \cos \delta_{Rn} \cos(\phi - \phi_0 + \phi_{Rn}), \end{aligned} \tag{3}$$

where R_c is the lowest primary rigidity to which the recorder can respond, provided it is greater than R_L, the lower limiting rigidity of the anisotropy. In practice the vector form of $v(R)$ is more useful, being denoted by

$$\mathbf{v}_R = |v_R| \boldsymbol{\rho}_R = \frac{\alpha_1 Y_R}{N} \sum_{n=1}^{N} A_{Rn} \cos \delta_{Rn} \boldsymbol{\rho}_{Rn}, \tag{4}$$

where ρ_{Rn} is the phase angle on the harmonic dial. In turn, the total first harmonic vector is

$$\mathbf{v} = |v|\boldsymbol{\rho} = \sum_{R=R_c}^{R_u} |v_R|\boldsymbol{\rho}_R. \tag{5}$$

Considerable use is also made of the relative harmonics $\mathbf{v}_R/\alpha_1$ and $\mathbf{v}/\alpha_1$, whose amplitudes are denoted by B_{1R} and B_1 respectively.

If one substitutes for v with a reliable observed first harmonic (notably one that is as free as possible from contributions of atmospheric origin), the free-space amplitude α_1 may be estimated from equation (3) for a given value of R_u. It will be shown that, in relation to the underground observations, α_1 is a steeply varying function of R_u when R_u is in the vicinity of 100 GV. On the other hand, when the form of equation (3) that applies to a high latitude neutron monitor is worked out and v is replaced by the first harmonic of an observed daily variation of neutron intensity, one finds that the variation of α_1 with R_u flattens off as R_u increases above 100 GV. Therefore, if R_u is thought to be about 200 GV, the neutron monitor observations can be used to determine the free-space amplitude α_1 regardless of the exact value of R_u. This is what Rao, McCracken, and Venkatesan have done. However, the result is less precise if R_u is closer to 100 GV. In general it is more profitable to find the intersection of the curve specifying α_1 as a function of R_u, relating to observations of high latitude neutron intensity (curve B in Fig. 3), with the corresponding curve relating to simultaneous observations of meson intensity underground (curve A in Fig. 3). The sharp intersection gives the values of both α_1 and R_u that apply to the observations. This is the method that shall be used in estimating R_u for 1958.

III. Method of Determining $\mathbf{v}/\alpha_1$ as a Function of R_u

To calculate the response underground to a first harmonic of the anisotropy we determine sets of values of A_{Rn}, δ_{Rn}, and ϕ_{Rn} for selected rigidities so that by curve-fitting they may be read off as functions of R. It should be noted that A_{Rn}, δ_{Rn}, and ϕ_{Rn} are constants of the detector at the given location and may be used to determine the response to any free-space first harmonic, either solar or sidereal. Corresponding quantities A_{2Rn}, δ_{2Rn}, and ϕ_{2Rn} relating to a second harmonic may be obtained by the same procedures, and so on for higher harmonics.

Consider the μ-mesons, due to isotropic primaries of rigidity R, which arrive at the detector within a small solid angle ω_r specified by zenith angle Z_r and azimuth a_r. They constitute a fraction of the total counting rate that is known as the differential radiation sensitivity $I(R, \omega_r)$ given by

$$I(R, \omega_r) = Y_R F(\omega_r) \cos^n Z_r.$$

The factor $F(\omega_r)$, the geometric sensitivity (see Parsons 1957), is the fraction of the total counting rate apportioned to ω_r by virtue of the geometry of the telescope, while $\cos^n Z_r$ expresses the well-known zenith angle dependence of intensity. The primaries of rigidity R that are responsible for $I(R, \omega_r)$ will have approached the Earth's magnetic field from directions within some asymptotic volume element $(\Omega_r)_R$ specified by latitude $(\delta_r)_R$ and longitude $(\phi_r)_R$. Such asymptotic coordinates are usually found either by computing the trajectories of the primaries outward from the direction (Z_r, a_r) at the geomagnetic location of the recorder (see McCracken, Rao, and Shea 1962), or else from observations of the deflections of charged particles in a physical simulation of the geomagnetic field (see the terrella experiments of Brunberg and Dattner 1953). When $I(R, \omega_r)$ and the associated asymptotic coordinates $(\delta_r)_R$ and $(\phi_r)_R$ have been calculated for each of the volume elements ω_r that make up the solid angle of the recorder, the distribution of the fractional μ-meson intensity due to primaries of rigidity R can be determined with respect to both asymptotic latitude and asymptotic longitude of the primaries. The distribution with latitude can be simply divided up amongst N latitude intervals giving equal contributions to the differential counting rate, thereby defining the N segments of the total asymptotic cone. The mean latitudes δ_{Rn} are obtained from the latitude distributions within the individual segments. The distribution with respect to longitude within each segment, when applied to a first harmonic $\cos\phi$, provides the amplitude reduction factor A_{Rn} and the longitude displacement angle ϕ_{Rn}. However, it should be noted that the distributions themselves are derived on the assumption of isotropic primaries and an average cosmic ray spectrum.

When the constants A_{Rn}, δ_{Rn}, and ϕ_{Rn} are applied to a particular model for the anisotropy, the important simplification in the present treatment is that the mean value δ_{Rn} replaces a latitude distribution. This suggests that the latitude intervals specifying the segments of the asymptotic cones should be small. Several factors are involved in the choice of intervals, one of them being the manner of variation of the longitude distribution with respect to asymptotic latitude. As far as the underground vertical semi-cube is concerned, the final result does not seem to depend at all markedly on the number of latitude intervals used.

IV. Application to the Cosmic Ray Detectors

(a) *The Vertical Semi-cube Underground*

The solid angle of the semi-cube was divided up into 576 elements (ω_r) of dimensions 5° in azimuth and 7·5° in zenith angle. In calculating the values of $I(R, \omega_r)$, Fenton's (1963) coupling coefficients and the geometric sensitivity characteristics calculated by Parsons (1957) were used. Both $n = 2 \cdot 0$ and $n = 2 \cdot 2$ were tried for the $\cos^n Z$ zenith angle dependence of intensity, but for all practical purposes they each led to the same final asymptotic distribution.

Since about 90% of the counting rate underground appears to be due to primaries of energy > 50 GeV, it was considered that a centred dipole was a sufficient approximation to the real geomagnetic field for calculations of the asymptotic coordinates $(\delta_r)_R$ and $(\phi_r)_R$. (Calculations using a more complex representation of the field tended to confirm this view and will be mentioned again below.) Consequently, the particle deflections were estimated from the diagrams of Brunberg and Dattner (1953) for the geomagnetic southern latitude of 50°. Considerable interpolation was necessary and for this reason it was found more convenient to express the asymptotic latitude and longitude data in the form of deflections in zenith angle and azimuth.

At the higher rigidities the differential cones of acceptance change rather slowly with rigidity, and therefore it was decided to work them out only for the three most important rigidities, namely, 50 GV (a practical lower limiting rigidity of response), 150 GV (near the mean rigidity of response), and infinite rigidity (providing an asymptote for the response constants).

Each cone of acceptance was initially divided up into three segments defined by intervals of asymptotic geographic latitude. For example, it was found that, of the 50 GV primaries contributing to the counting rate, one-third came from the latitude range 90° S. to 46° S., one-third from the range 45° S. to 28° S., and the remainder from the range 27° S. to 20° N. These high, middle, and low latitude intervals were found to be almost exactly the same at the higher rigidities.

The mean latitude δ_{Rn} was worked out for each segment from the distribution $I(R, \omega_r)$ versus $(\delta_r)_R$, after the data had been grouped at 3° intervals of latitude. The distribution $I(R, \omega_r)$ versus $(\phi_r)_R$ was based on longitude intervals of 20° and provided the amplitude constant A_{Rn} and phase constant ϕ_{Rn} when a first harmonic $\cos\phi$ was impressed on it. In addition, constants A_R, δ_R, and ϕ_R were obtained for the total (undivided) cone. Values of the asymptotic constants for individual segments and for the total cone are given in Table 1 for each of the three rigidities. It can be seen that (*a*) above 150 GV the cone of acceptance does not change with increasing rigidity except for a gradual displacement towards the observer's meridian, and that (*b*) the distribution $I(R, \omega_r)$ versus $(\phi_r)_R$ changes only slightly with latitude, as would be expected.

TABLE 1

ASYMPTOTIC CONSTANTS* FOR THE VERTICAL SEMI-CUBE UNDERGROUND AT 50° S. GEOMAGNETIC LATITUDE

Primary Rigidity (GV):	50			150			∞		
	A_{Rn}	δ_{Rn}	ϕ_{Rn}	A_{Rn}	δ_{Rn}	ϕ_{Rn}	A_{Rn}	δ_{Rn}	ϕ_{Rn}
High latitude range (H)	0·84	−56°	25°	0·75	−60°	12°	0·74	−62°	0°
Mid latitude range (M)	0·86	−36	35	0·86	−38	10	0·86	−41	0
Low latitude range (L)	0·91	−13	33	0·90	−15	12	0·89	−18	0
Total cone	0·87	−34	30	0·83	−39	11	0·83	−39	0

* The constants specify the differential response to a free-space first harmonic at the given primary rigidities.

Curves of fit, from which A_{Rn}, δ_{Rn}, and ϕ_{Rn} could be read off against rigidity R, were drawn using the results from Table 1. The vectors $\mathbf{v}_R/\alpha_1$, relating to the free-space model of Rao, McCracken, and Venkatesan, were then estimated in accordance with equation (4) as the mean sums of the individual vectors $(\mathbf{v}_R)\mathrm{H}/\alpha_1$, $(\mathbf{v}_R)\mathrm{M}/\alpha_1$, and $(\mathbf{v}_R)\mathrm{L}/\alpha_1$. Finally, the total first harmonic vector $\mathbf{v}/\alpha_1$ was estimated as the sum of differential vectors $\mathbf{v}_R/\alpha_1$ for different values of R_u.

Now, it was found that if the total vectors $\mathbf{v}/\alpha_1$ were derived from undivided cones of acceptance, characterized by the constants given in the last line of Table 1, they were practically indistinguishable from those calculated from cones that had been divided up into three segments. This greatly simplified the procedure for estimating the response of the vertical semi-cube to free-space harmonics. However, as we shall see below, such a drastic simplification would not be justifiable in the case of the south-pointing cube underground.

Curves of fit were drawn through the total-cone values A_R, δ_R, and ϕ_R given in Table 1 and are shown in Figure 1. These curves were used in all subsequent calculations requiring values of the asymptotic constants as functions of R.

It is of interest at this stage to enquire whether the asymptotic constants would have been very different (*a*) if approximations to the geomagnetic field other than a centred dipole had been used, and (*b*) if the solid angle of the semi-cubical telescope had comprised fewer and larger volume elements. We also note how the response to a free-space second harmonic would be affected. It was decided to compare three representations of the field: the centred dipole; the Finch and Leaton sixth-order field (Finch and Leaton 1957), as used by Rao, McCracken, and Venkatesan; and the same field ignoring second-order terms and above (approximating an off-centred dipole). In the last two cases the facilities of an Elliott 503 computer were used in the determination of the asymptotic coordinates. For each representation of the field we tried volume elements ω_r of small size (about 10^{-2} sr, employed throughout the present paper) and of large size (about 10^{-1} sr, centred on the azimuth 0°, 45°, 90°, . . . 315° and zenith angles 5°, 10°, 20°, 30°, 40°, 50°, and 60°, 56 elements making up the solid angle of the telescope). Consequently, with three representations of the geomagnetic field and a small and a large number of arrival directions available we were able to compare six sets of the constants δ_R, A_R, ϕ_R, A_{2R}, and ϕ_{2R}, the last two constants characterizing the differential response to a generalized second harmonic of an anisotropy. Attention was confined to a primary rigidity of 50 GV,

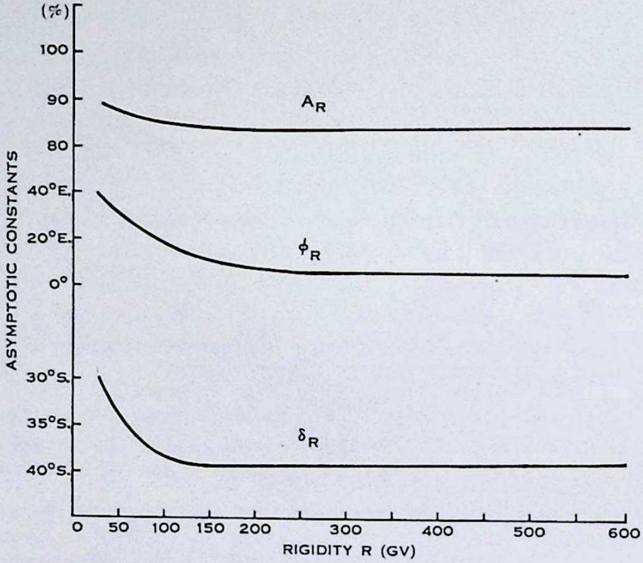

Fig. 1.—The differential asymptotic constants of response to a diurnal variation of the primaries in free space for a vertical semi-cubical telescope at a depth of 40 m.w.e. at $\lambda = 50°$ S.

the lowest effective rigidity of response, where the greatest discrepancies would be expected. The first result was that the estimates of δ_R, ϕ_R, and ϕ_{2R} were essentially unaffected. On the other hand, it can be seen from Table 2 that the estimated values of the amplitude factors A_R and A_{2R} tended to be smaller when a large number of arrival directions was used, and larger when more complex representations of the Earth's magnetic field were used. The differences relating to the volume elements could depend on the particular arrival directions that are chosen, as well as on the number. We conclude that it is generally advisable to use a large number of arrival directions, particularly for the estimation of the second harmonic constant A_{2R}. It also appears that the centred dipole field, and specifically the results of the terrella experiments of Brunberg and Dattner, should suffice for present calculations of the response underground to a free-space first harmonic, introducing uncertainties of not more than 2 or 3% in estimates of A_R.

Table 2

ESTIMATES OF RELATIVE AMPLITUDES FOR DIFFERENT GEOMAGNETIC FIELD REPRESENTATIONS AND FOR SMALL AND LARGE NUMBERS (N) OF ARRIVAL DIRECTIONS

Values are estimated for the response of a vertical semi-cube at Hobart to first and second harmonics of an anisotropy in the intensity of 50 GV primaries

Geomagnetic Field Representation	First Harmonic A_R		Second Harmonic A_{2R}	
	$N = 56$	$N = 576$	$N = 56$	$N = 576$
Brunberg and Dattner (1953), centred dipole	0·893	0·874	0·633	0·589
Finch and Leaton (1957), first-order terms only	0·915	0·899	0·676	0·635
Finch and Leaton (1957), sixth order	0·915	0·915	0·704	0·663

In curve 1 of Figures 2(*a*) and 2(*b*) the relative amplitude B_1 and the phase angle ρ_1 of the estimated relative first harmonic v/α_1 are shown as functions of the upper limiting rigidity R_u. The phase angle ρ_1 is measured east of the direction of maximum intensity of the free-space first harmonic, so that negative values denote earlier times of maximum. The curves 1 demonstrate that changes in R_u have a much greater effect on the estimated amplitude of the first harmonic than on the phase. For example, if R_u decreases from 200 to 100 GV the amplitude decreases by 50% while there is a phase shift to an earlier time of maximum of only about $\frac{1}{2}$ hr.

(*b*) *The Inclined Telescopes Underground*

There is an average of about 35 m.w.e. of material absorber within the viewing cone of the north-pointing telescope. This has been estimated from the difference in counting rate between the inclined cube and the vertical semi-cube, having regard to their respective radiation sensitivity patterns. The axial direction of the telescope was set 30° north of the zenith, the equivalent latitude being 13° S. In the axial direction, the telescope views upwards along the magnetic field at Hobart and at the same time this represents a low latitude of viewing. It is for this reason that the asymptotic acceptance cones are relatively compact, centred only slightly east of the observer's meridian, and are not strongly dependent on rigidity, while the distribution of $I(R, \omega_r)$ with asymptotic longitude is virtually independent of asymptotic latitude. Consequently the constants A_R, δ_R, and ϕ_R can be computed from the undivided cones of acceptance with rather less loss of accuracy than in the case of the vertical semi-cube. Following the same procedures as in Section IV(a) above, we determine B_{1N} and ρ_{1N} as functions of R_u. The result is shown in curves 2 of Figure 2.

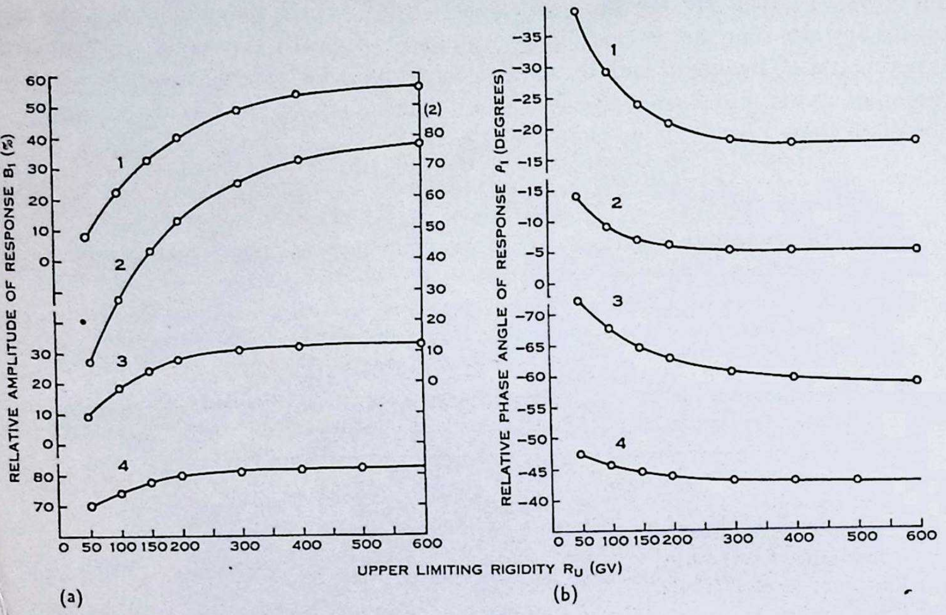

Fig. 2.—(a) The estimated amplitude of the solar diurnal variation, relative to the amplitude of the average free-space first harmonic, and (b) the estimated direction of the solar diurnal variation, measured east of the direction of maximum intensity of the free-space first harmonic, versus upper limiting rigidity for

1, a vertical semi-cube at a depth of about 40 m.w.e. at Hobart;
2, a cube inclined 30° north of the zenith at a depth of about 40 m.w.e. at Hobart;
3, a cube inclined 45° south of the zenith at a depth of about 40 m.w.e. at Hobart; and
4, a high latitude neutron monitor at sea level.

Open circles indicate calculated values. The model for the free-space first harmonic is that proposed by Rao, McCracken, and Venkatesan.

It suffices to note here that, in comparison with the response of the vertical telescope, the amplitude of the first harmonic in the north-pointing direction depends more steeply on R_u, while the phase is rather less dependent on R_u.

The south-pointing cube underground has an average of about 42 m.w.e. of earth and shale absorber within its field of view. The axial direction of the telescope is 45° south of the zenith and this corresponds to a geographic latitude of 88° S. The situation is the reverse of that in the north-pointing direction. Directions of arrival tend to be transverse to the magnetic field and at higher zenith angles are accessible from all 360° of asymptotic longitude. The cones of acceptance are centred far to the east of the observer's meridian and change very markedly with primary rigidity. The cones were divided into high, middle, and low latitude segments from which the constants A_{Rn}, δ_{Rn}, and ϕ_{Rn} were derived, leading finally to the evaluation of B_{1S} and ρ_{1S} versus R_u, shown in curves 3 of Figure 2. It is clear that the transition from low to high axial latitudes of viewing with a cubical telescope is accompanied by the following changes in response to a first harmonic of the anisotropy:

(1) The amplitude increases less steeply with increasing R_u. This is reflected in the potentially useful relationship B_{1S}/B_{1N} versus R_u, which would enable R_u to be determined independently of α_1, given a simultaneous pair of observations in the north and south directions. Unfortunately the statistical inaccuracies in the observed ratios are far too great for this method to be of any use at present.

(2) There is a pronounced shift to later times of maximum and a greater dependence of the time of maximum on R_u.

(c) *A High Latitude Neutron Monitor*

Rao, McCracken, and Venkatesan have calculated the diurnal relative amplitudes B_1 and the times of maximum for the neutron monitors (see their Table 1) over a rigidity range from near cut-off to 500 GV. In effect then, they have put R_u equal to 500 GV. The actual value was of little consequence in their work, provided it was not much less than about 200 GV. In what follows we show approximately how B_1 and ρ_1 are affected as R_u decreases from 500 to 50 GV.

For rigidities > 50 GV the difference of response between a high latitude neutron monitor and the underground semi-cube is due essentially to the very great differences in the coupling coefficients. The differences in the cones of acceptance are relatively minor. Therefore, since a refined treatment for a neutron monitor is unnecessary at this stage, it suffices to apply the same values of A_R, δ_R, and ϕ_R at the higher rigidities as have been worked out for the semi-cube. Accordingly, the differential first harmonic vectors $\mathbf{v}_R/\alpha_1$ were estimated from equation (4) for the rigidities 75, 125, 175, 250, 350, and 450 GV as they were for the semi-cube except that the values of Y_R were those calculated by Dorman (1957) for a high latitude monitor. The amplitude and the time of maximum of the estimated relative first harmonic v/α_1 for Mt Wellington are given by Rao, McCracken, and Venkatesan in their Table 1 and are the values for $R_u = 500$ GV. Estimates of v/α_1 for lower values of R_u were therefore obtained by successive subtraction of the differential vectors $\mathbf{v}_R/\alpha_1$ from the total vector specified in their table. Thereby the values of B_1 and ρ_1 versus R_u that are shown in curves 4 of Figure 2 were obtained. It can be seen that the estimated relative amplitude begins to fall off rather significantly as R_u decreases below about 150 GV, but of course much less steeply than the relative amplitude underground. A comparison is given in Table 3.

V. 1958 EVALUATION OF α_1 AND R_u

(a) α_1 *versus* R_u *from the Underground Observations at Hobart*

The relative amplitude B_1 in curve 1, Figure 2(*a*), is $|v|/\alpha_1$, where $|v|$ is the amplitude of that part of the observed first harmonic that is caused by the primary anisotropy. Given a value of $|v|$ for 1958, estimates of the free-space amplitude α_1 for different values of R_u can be obtained directly from this curve.

The amplitude of the first harmonic of the annual mean pressure-corrected daily variation underground in 1958 was $(0 \cdot 095 \pm 0 \cdot 008$ S.E.)% and the time of maximum was (1712 ± 20 min) local solar time. It appears that if there were contributions to the first harmonic from daily variations of atmospheric temperature they must have been very small. This is discussed in a paper on the sidereal effect (Jacklyn 1965). We also present evidence below that the diurnal variations observed in three different directions underground are compatible with the model for the free-space first harmonic put forward by Rao, McCracken, and Venkatesan. It is concluded that the result in 1958 was at least very largely of extraterrestrial origin. With $|v| = 0 \cdot 095\%$, we obtain curve A in Figure 3, giving the estimate of α_1 versus R_u from the underground observations in 1958. The dashed lines give the limits of error arising from the S.E. of estimate of $|v|$.

TABLE 3

ESTIMATED CHANGES IN RELATIVE AMPLITUDE B_1 OF THE FIRST HARMONIC AS UPPER LIMITING RIGIDITY R_u DECREASES

	$\Delta B_1/B_1$ (%)			
R_u	250–200	200–150	150–100	100–50 (GV)
Neutron intensity at Mt Wellington	−1	−2	−4	−8
Meson vertical intensity underground at Hobart	−10	−18	−32	−68

(b) α_1 *versus* R_u *from Neutron Monitor Observations*

Having virtually assumed R_u to be 500 GV, Rao, McCracken, and Venkatesan obtained $0 \cdot 4\%$ as their estimate of α_1 for 1958, this being the average of individual estimates from the records of 17 neutron monitors distributed globally. Looking at their Figure 12, for $\beta = 0$, $g(\lambda) = \cos\lambda$, we see that the end-points of all but three of the individual estimates of the free-space vector are grouped within a circle of radius $0 \cdot 067\%$, this being 3σ, where σ is the S.E. of estimate of amplitude of the diurnal variation at a single station. It seems that, if we regard the radius of the circle as being about twice the S.E. of estimate of α_1 from a single station, it would fairly take account of other random errors. Thus the estimate of $0 \cdot 4\%$ would have a S.E. of about $0 \cdot 008\%$. Clearly, if we use the averaged estimate of α_1, in the product $\alpha_1 B_1$ we have a much more accurate indication of the amplitude of the first harmonic at Mt Wellington to be expected from the model than would be given by the actual observation at the station. From Table 1 of their paper, we see that B_1 for Mt Wellington is $0 \cdot 813$, so that the estimated amplitude at that station is $(0 \cdot 325 \pm 0 \cdot 006)\%$. Their Figures 9 and 12 show that the observed amplitude at Mt Wellington was in fact very close to this estimate. Proceeding as in Section V(a) and substituting $0 \cdot 325\%$ for $|v|$, we obtain estimates of α_1 for different values of R_u from curve 4, Figure 2(a). The result is shown as curve B in Figure 3. It indicates how the estimate of free-space amplitude at a high latitude station, derived from world-wide observations of neutron intensity in 1958, would depend on the value assigned to R_u. The errors due to counting rate statistics would be very small and are not shown. The intersection of curves A and B gives values of R_u and α_1 that would satisfy the observations of the solar diurnal variation both underground at Hobart and at the neutron monitor stations, in relation to the model. The intersection value of R_u is 95 GV with an error tail due to counting rate statistics of perhaps 5 GV. The free-space amplitude is about 0·43%, slightly higher than the estimate given by Rao, McCracken, and Venkatesan.

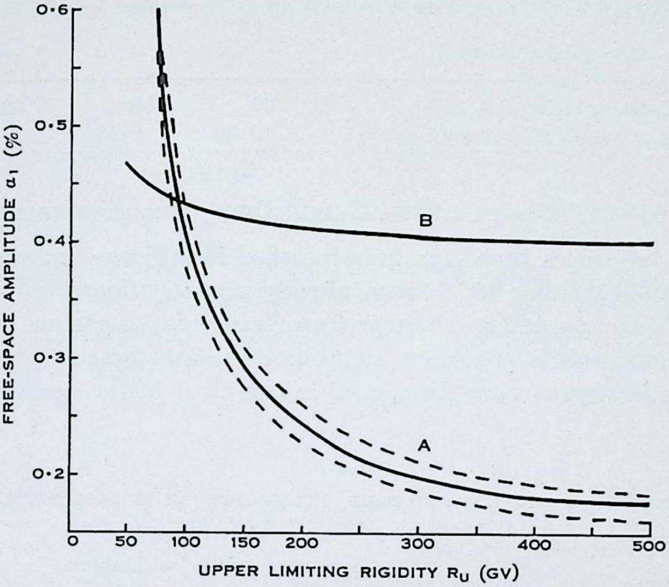

Fig. 3.—Estimates of the amplitude of the average free-space solar diurnal variation of the primaries in 1958 for different values of the upper limiting rigidity based on: A, observations with a vertical semi-cubical telescope at a depth of 40 m.w.e. at Hobart; B, the estimated solar diurnal variation of neutron intensity at a high-latitude sea level station, deduced from world-wide observations of neutron intensity. The average values of R_u and α_1 for 1958 are given by the intersection of the two curves. All the estimates derive from the model for the free-space first harmonic proposed by Rao, McCracken, and Venkatesan. The dashed lines represent the standard errors of estimate of individual points on curve A.

This result only holds if the average free-space first harmonic is independent of rigidity. Supposing the free-space amplitude to vary as R^β, Rao, McCracken, and Venkatesan showed that β was $0{\cdot}00 \pm 0{\cdot}05$, averaged over 1958. Therefore we have to find out how our estimates of α_1 and R_u would be affected if $|\beta|$ was about 0·05. Accordingly, the curves A and B of Figure 3 were recalculated, starting from equation (3) which now contains the factor R^β, for $\beta = +0{\cdot}05$ and for $\beta = -0{\cdot}05$. Essentially the result was that in each case curve A became much steeper for values of R_u below about 150 GV while curve B was displaced towards lower values of α_1 for $\beta = 0{\cdot}05$ and towards higher values for $\beta = -0{\cdot}05$. The intersection values of α_1 and R_u are shown in Table 4. Note that we now have to refer to α_1 as the free-space amplitude constant since it only becomes the free-space amplitude itself when $\beta = 0$.

From these considerations it appears that the error in estimation of R_u would be about 15 GV. This might even take care of uncertainties in the calculation of curve B that do not apply to curve A. These uncertainties will be mentioned in the Discussion, but it is clear that they would affect the determination of α_1 rather than R_u.

Table 4

ESTIMATES OF THE UPPER LIMITING RIGIDITY AND THE FREE-SPACE AMPLITUDE CONSTANT FOR THREE VALUES OF THE RIGIDITY DEPENDENCE INDEX

Values are estimated for the first harmonic of the solar anisotropy in 1958

Rigidity Dependence Index β:	$-0\cdot05$	$0\cdot00$	$+0\cdot05$
Upper limiting rigidity R_u (GV)	105	95	90
Free-space amplitude constant α_1 (%)	0·50	0·43	0·38

VI. 1961–62. Results from Three Directions Underground

The four telescopes that have been installed in a disused railway tunnel near Hobart (geographic latitude 43° S.) have already been mentioned in Section I, but it may be useful to summarize here the main features of the arrangement during 1961–62. While the tunnel itself is not quite in the north–south direction, the axes of the inclined telescopes were accurately aligned in the plane of the geographic meridian.

Table 5

CHARACTERISTICS OF THE UNDERGROUND TELESCOPES AT HOBART DURING 1961–62

Telescope Type:	North Single Cube	Vertical Duplex Semi-cube	South Single Cube
Inclination of axis to the zenith	30° N.	0°	45° S.
Approximate mean asymptotic latitude of response	17° S.	39° S.	60° S.
Effective absorber excluding atmosphere (m.w.e.)	35	40	42
Particles/hr	16700	70000	8700

Each telescope registered triple coincidences, and individual trays were of 1 square metre sensitive area. Other characteristics of the telescopes are tabulated in Table 5. At the end of 1962 the north-pointing telescope was elongated to give 20° half angle of aperture and the axis was inclined 70° north of the zenith.

The pressure-corrected first harmonic vectors averaged over the two calendar years 1961 and 1962 are shown in Figure 4. The radius of each error circle is 2σ so that even in the south-pointing direction the first harmonic is significant. To show that the vector distribution was broadly consistent with an extraterrestrial origin for the diurnal variation underground, it was tested against the model for the anisotropy on the assumption that $\beta = 0$ and neither α_1 nor ψ_0 had changed appreciably since 1958. Estimates of the first harmonics to be expected in the three directions were calculated as functions of R_u. The results are shown as dashed lines in the figure. It can be seen that the phase differences between **V**, **N**, and **S** are compatible with the model although the observed time of maximum for **N** is later than expected. The amplitudes are also those to be expected from the model but they indicate that the average value of R_u must have been about 70 GV during 1961–62 if the other constants had not changed. Alternatively, if α_1 alone had changed, it must have decreased by about 40% since 1958. The estimates of α_1 versus R_u that were derived from each result demonstrate the interrelationships more clearly (Fig. 5). It is quite clear that the same estimate is given by each of the three independent experiments, involving detectors of different geometry and greatly different effective latitudes of scan.

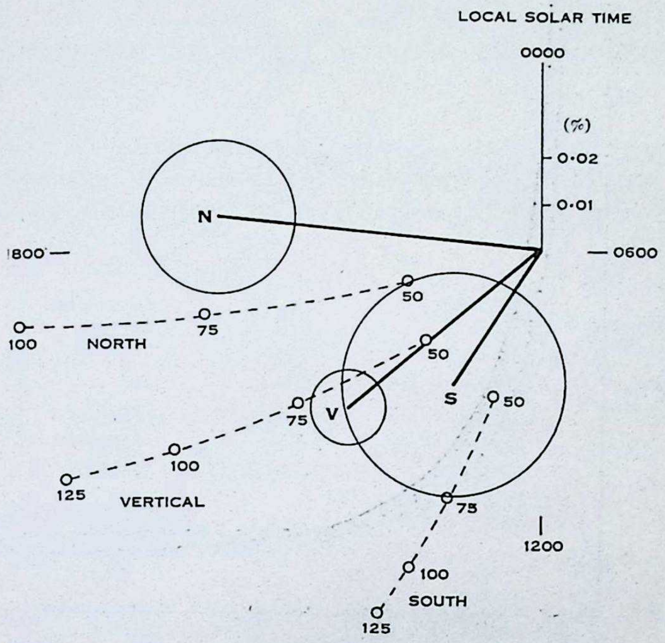

Fig. 4.—The first harmonic vectors of the pressure-corrected daily variations observed in the north (N), vertical (V) and south-pointing (S) directions underground at Hobart, averaged over the years 1961 and 1962. The radius of each error circle is 2σ. The dashed lines give estimates of the first harmonics to be expected in each of the three directions, for different values of upper limiting rigidity. Some values of interest are shown in GV. The estimates are based on the model for the free-space solar diurnal variation of the primaries proposed by Rao, McCracken, and Venkatesan.

VII. 1958–62. Some Results from Other Places

The large decrease of amplitude of the solar diurnal variation that has taken place at the Hobart underground site since 1958 was confirmed by results from the vertical semi-cubical telescopes located at a depth of 40 m.w.e. at Budapest (geographic coordinates 47·5° N., 18·9° E., geomagnetic latitude 46·4° N.). The only complete years available from Budapest were 1959 and 1961. The comparison with Hobart for these 2 years, given in Table 6, shows unmistakable agreement except for the differences in time of maximum in 1961.

Also of relevance are some interesting results reported by Sarabhai and Subramanian (1963*a*). They have found that the peak-to-peak amplitude of the total solar daily variation (sum of first and second harmonics) of neutron intensity at a low latitude station (Huancayo) had decreased by about 35% between 1958 and 1961–62, while at a high latitude station (Churchill) it had decreased by about only 5%. There were also interesting shifts of the times of maximum and minimum to earlier hours at Huancayo but not at Churchill. The results from a cubical meson telescope at Churchill were between those from the two neutron monitors. Sarabhai and Subramanian suggested that the observed changes could have come about if β had become increasingly negative or if R_u had decreased, but that a decrease in the lower limiting rigidity R_L could not have been the main cause. Also, their results do not seem to be consistent with a large decrease in the amplitude constant α_1. This would have produced similar decreases of total amplitude at all stations, bearing in mind that the part played by the second harmonic in their observations is unknown. Finally, changes in the galactic spectrum that might have been expected over the period (see Mathews and Kodama 1964) would clearly not have been responsible for an effect that seems to increase with increasing primary rigidity of response.

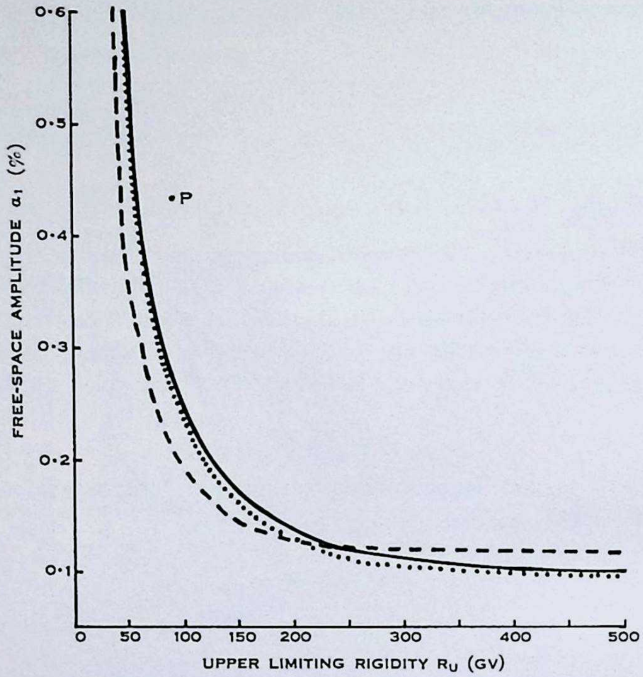

Fig. 5.—Estimates of the amplitude of the free-space solar diurnal variation of the primaries, averaged over 1961 and 1962, for different values of R_u and for $\beta = 0$, based on observations underground at Hobart with (*a*) the vertical semi-cubes, full line; (*b*) the north-pointing cube, dotted line; (*c*) the south-pointing cube, dashed line. The point P represents the intersection of curves A and B for 1958 (Fig. 3).

VIII. Relevant Changes in the Apparent Sidereal Effect observed Underground

Every year since experiments commenced at the Hobart underground site a significant daily variation in sidereal time has been observed. A general account of the results obtained over the period 1958–62 inclusive has been published recently (Jacklyn 1965). It is submitted in that paper that most, if not all, of the sidereal effect observed at the depth of 40 m.w.e., is genuine. Figure 6 shows the annual running averages of the amplitudes of the total daily variations in solar and sidereal time. As noted in Sections VI and VII, the amplitude in solar time has decreased considerably over the period and it is evident that most of the change took place after December 1960. It seems that the amplitude in sidereal time also decreased somewhat after 1958, but that it began to increase again during 1961 and passed through quite a conspicuous maximum at the same time as the amplitude of the solar daily variation passed through a minimum, and a few months before the daily intensity reached a maximum value. Over a period of about 6 months centred on the turning points of the two amplitude curves the genuineness of the sidereal effect was strikingly demonstrated; the time of maximum of the monthly mean daily variation in solar time changed from 1500 to 0700 solar time and became earlier month by month at about the rate of 2 hr each month, in the manner of a sidereal daily variation expressed in solar times. In other words, the sidereal component of the daily variation was dominating the solar component over this period. Accounts of this phase anomaly have been given elsewhere (Jacklyn 1963*b*, 1965). Now, the point we wish to make here is that the changes in amplitudes of the solar and sidereal components over this period were probably not negatively correlated by chance but were connected through opposite dependences on changes in R_u. On the one hand, a decrease in R_u is a decrease in upper limiting rigidity leading to a decrease of amplitude of the solar component. On the other hand, it is a decrease in threshold rigidity leading to an increase of amplitude of the sidereal component. The effect on the sidereal component (assumed to be observable over a very wide range of rigidities above R_u) would not be expected to be very great until R_u had decreased to values below 100 GV,

Table 6

FIRST HARMONICS OF MEAN PRESSURE-CORRECTED SOLAR DAILY VARIATION OF VERTICAL INTENSITY AT BUDAPEST AND HOBART DURING 1959 AND 1961

Values were obtained from semi-cubical telescopes at a depth of 40 m.w.e.

	1959		1961	
	Amplitude (%)	$T_{\max}$ (local solar time)	Amplitude (%)	$T_{\max}$ (local solar time)
Budapest*	0·1114	1640	0·0389	1554
S.E.	±0·0054	±12 min	±0·0054	±34 min
Hobart†	0·1062	1638	0·0389	1408
S.E.	±0·0058	±12 min	±0·0058	±34 min

* Geomagnetic latitude 46° N.

† Geomagnetic latitude 50° S.

where the differential response of the underground detector is greatest. Calculations based on a simple model for the sidereal anisotropy show that the observed increase of amplitude could be explained if R_u had decreased from, say, 85 to 50 GV over the period of increase, although it might be necessary for the spectrum of variation (for the sidereal effect) to be somewhat negatively dependent on rigidity.

If, alternatively, the changes in amplitude of the solar component were primarily due to β becoming increasingly negative on the average, then there would be no simple explanation for the correlated changes in amplitude of the sidereal component.

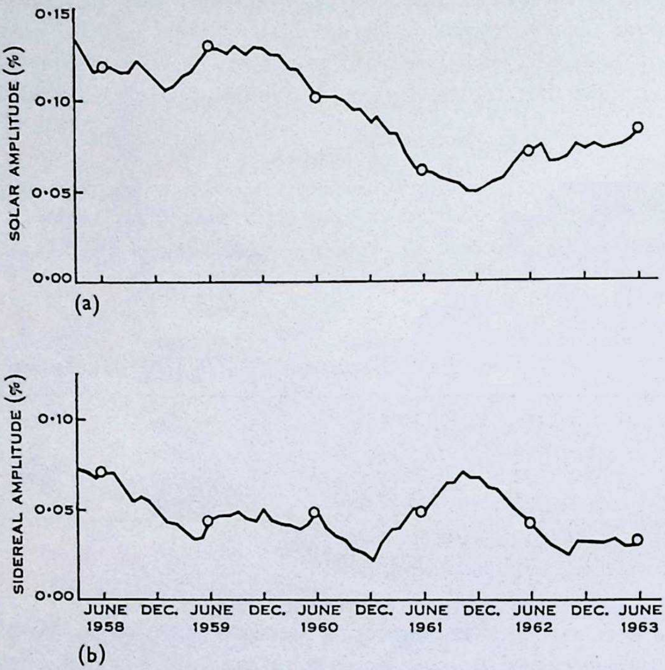

Fig. 6.—Long-term changes observed with the vertical semi-cubical telescopes at the Hobart underground station; month by month annual running averages of (*a*) amplitude of the solar daily variation, (*b*) amplitude of the apparent sidereal daily variation. The dates refer to the central months and the open circles indicate the conventional annual mean values.

IX. Discussion

The fact that the amplitude, but not the phase, of the first harmonic of the solar daily variation underground changed so greatly between 1958 and 1962 is itself evidence that the observed daily variation at this depth must be very largely of extraterrestrial origin. Of greater significance, however, is the evidence that the amplitudes and times of maxima in all three directions underground are compatible with the model for the free-space first harmonic derived from the neutron monitor data. In addition to this there were indications in 1961 that simultaneous changes in the solar and apparent sidereal daily variations were connected. Overall, it seems reasonable to assume that the observed pressure-corrected first harmonic at 40 m.w.e.

is almost entirely due to the anisotropy, a prerequisite for the present method of determining R_u. We have seen that the method depends essentially on the fact that the differential coupling coefficients (Y_R) for the underground semi-cube differ very greatly from the coupling coefficients that apply to a high latitude neutron monitor. This is the main reason for the difference between curves A and B in Figure 3. Moreover, the nature of the difference is such that quite sizeable errors in curve B will not greatly affect the estimation of R_u.

It would seem that more accurate knowledge of the deflections of high energy particles in the Earth's magnetic field, improved estimates of the radiation sensitivity patterns of the underground telescopes, or a more refined treatment of the asymptotic cones of acceptance are not likely to affect curve A very much. The reliability of the coupling coefficients is a more important factor. It seems unlikely that the coefficients used here would be greatly in error since the values worked out by Fenton (1963) are in reasonable agreement with Mathews's (1963) results obtained by empirical methods. The coefficients are only strictly applicable at vertical incidence where the meson threshold energy at production, for detection at 40 m.w.e. underground, is 15 GeV. However, in the case of the vertical semi-cube they should apply quite well up to the limiting zenith angle of about 60°, where the meson threshold energy has only increased to 18 GeV.

The accuracy of estimation of curve B, relating to the Mt Wellington neutron monitor, should be sufficient for this provisional determination of R_u. However, in a detailed study of year to year changes in R_u, α_1, and β, other quantities would be important at the low rigidities of response. It is evident from the work of Mathews and Kodama (1964), for example, that the differential coupling coefficients at rigidities below 15 GV must change considerably during the cycle of solar activity. Therefore, at the least, it might be necessary to use different average cosmic ray spectra at solar maximum and solar minimum when analysing the neutron monitor data.

It is conceivable that β, the index of the variational spectrum, changes with increasing rigidity, although *a priori* there is no reason to suppose that this happens. Indeed, Rao, McCracken, and Venkatesan showed that any trend of this kind in 1958 would have been difficult to detect since β was found to be within the limits $0\cdot0\pm0\cdot05$ at least over the rigidity range 1–100 GV. To provide against the possibility, however, it would be an advantage to have additional estimates of α_1 versus R_u from detectors whose mean primary rigidities of response were between those of neutron monitors and the telescopes at 40 m.w.e. Unfortunately, as the amount of material absorber decreases, the atmospheric negative temperature effect in particular contributes increasingly to the daily variation of meson intensity. At many places, daily variations of atmospheric structure are difficult to estimate and may vary greatly from place to place (see Kane 1963). One way to avoid this problem is to make use of results from the crossed telescopes that operate at Hobart, Mawson, and a number of other places. Even then such data may prove to be of limited value until the differential responses of inclined telescopes at sea level to primaries of rigidity > 15 GV are more reliably known.

So far it has been tacitly assumed that R_u represents both the upper limiting rigidity of the solar anisotropy and the threshold rigidity for observation of a sidereal effect. This is not necessarily true of course. In the case of the sidereal anisotropy we are interested to know the rigidity above which primaries have access to the Earth's orbit from some particular direction in space, without having been appreciably scattered. On the other hand, if we accept Parker's recent theory (Parker 1964) that the solar diurnal variation is produced essentially by streaming of cosmic rays with an azimuthal velocity of rigid rotation with the Sun, then, as he points out, two conditions for the upper limiting rigidity must be satisfied. R_u must be such that (*a*) the gyro-radius is less than 1 a.u., so that the guiding centre approximation holds for the motion of particles along the spiralling interplanetary field, and (*b*) the gyro-radius is small enough to allow the particles to be scattered several times beyond the orbit of the Earth as they approach, so that a density gradient of intensity would be largely destroyed. In these circumstances there are clearly several possibilities whereby R_u could differ from the threshold rigidity for observation of a sidereal effect. Nevertheless, it seems reasonable to assume as a starting point that the two are not very different and that changes in R_u would be accompanied by similar changes in the sidereal threshold rigidity, but perhaps not vice versa. Moreover, judging from the evidence for a sidereal effect obtained from neutron monitor data by Conforto and Simpson (1957) at the previous sunspot minimum, the average threshold rigidity for observation should usually exceed the lower limiting rigidity of the sidereal anisotropy.

X. CONCLUSION

The pressure-corrected solar daily variation at 40 m.w.e. appears to be very largely under the control of the primary anisotropy, as evidenced by the nature of the year to year variations of the first harmonic observed at Hobart and Budapest in the vertical direction and by the characteristics of the first harmonic observed in three different directions underground at Hobart. It would follow that a component of atmospheric origin must be small and this is supported by other evidence, which is discussed in an earlier paper (Jacklyn 1965).

The provisional estimate of the average value of R_u in 1958 is 95 GV, this being the average primary rigidity above which a first harmonic of the anisotropy would become unimportant. The uncertainty of 10–20 GV in the estimate refers only to the method of measurement and has nothing to do with any inherent variability in R_u.

It appears that changes in the annual average solar diurnal variation between 1958 and 1962 would have been effected mainly through one or more of the constants R_u, R_L, α_1, β, and ψ_0 of the average free-space first harmonic, and through the average primary spectrum from which the coupling coefficients are derived. All these quantities may have varied to some extent, but it is interesting to note that only a decrease in R_u (of about 20–40 GV) could by itself have brought about the observed decrease in amplitude of the solar diurnal variation underground, the negatively correlated effects in solar and sidereal time underground in 1961, and the type of change observed in the solar daily variation of neutron intensity at Huancayo relative to that at Churchill.

A more refined analysis of long-term changes should take into account the variability of each of the parameters specifying the free-space first harmonic. It would also be necessary to clarify the part played by the second harmonic. Some of the factors (e.g. changes in R_L) should only affect the daily variation of neutron intensity, while others (e.g. changes in R_u) produce the most noticeable effects underground. Therefore a comprehensive comparative study of year to year changes in the daily variation of neutron intensity and of the underground meson intensity should permit the most important of these factors to be identified and estimated. A project of this type is being undertaken at Hobart. To achieve the desired result many years of continuous and reliable data are needed. Of particular importance are the records from the few neutron monitors at the very high and very low latitudes.

XI. ACKNOWLEDGMENTS

The authors wish to thank Dr. A. G. Fenton for providing the coupling coefficients for the underground telescopes in advance of publication. We thank the Director of the Cosmic Ray Department of the Central Research Institute of Physics of the Hungarian Academy of Sciences for the underground data from Budapest, made available through World Data Centre WDC 2. One of us (J.E.H.) is grateful to General Motors–Holden's Ltd. for the award of a Research Fellowship during the period of the present work. We are indebted to the Hydro–University Computing Centre at Hobart for the use of the facilities of the Elliott computer.

XII. REFERENCES

AHLUWALIA, A. S., and DESSLER, A. J. (1962).—*Planet. Space Sci.* **9**: 195.

AXFORD, W. I. (1965).—*Planet. Space Sci.* **13**: 115.

BRUNBERG, E. A., and DATTNER, A. (1953).—*Tellus* **5**: 269.

CONFORTO, A. M., and SIMPSON, J. A. (1957).—*Nuovo Cim.* **6**: 1052.

DORMAN, L. I. (1957).—"Cosmic Ray Variations." p. 117. (State Publishing House for Technical and Theoretical Literature, Moscow.) (Translation by Technical Document Liaison Office, U.S. Air Force.)

FENTON, A. G. (1963).—Proc. Int. Conf. Cosmic Rays, Jaipur, India. Vol. 2, p. 185.

FINCH, H. P., and LEATON, B. R. (1957).—*Mon. Not. R. Astr. Soc., Geophys. Suppl.* **1**: 314.

JACKLYN, R. M. (1963*a*).—*Nature* **200**: 1306.

JACKLYN, R. M. (1963*b*).—Proc. Int. Conf. Cosmic Rays, Jaipur, India. Vol. 2, p. 345.

JACKLYN, R. M. (1965).—*Nuovo Cim.* **37**: 1135.

KANE, R. P. (1963).—*Ind. J. Phys.* **37**: 151.

MCCRACKEN, K. G., RAO, U. R., and SHEA, M. A. (1962).—Tech. Rep. Lab. Nucl. Sci. Engng M.I.T. No. 77 (NYO–2670).

MATHEWS, T. (1963).—*Phil. Mag.* **8**: 387.

MATHEWS, T., and KODAMA, M. (1964).—*J. Geophys. Res.* **69**: 4429.

PARKER, E. N. (1964).—*Planet. Space Sci.* **12**: 735.

PARSONS, N. R. (1957).—*Rev. Scient. Instrum.* **28**: 265.

RAO, U. R., MCCRACKEN, K. G., and VENKATESAN, D. (1963).—*J. Geophys. Res.* **68**: 345.

SARABHAI, V. A., and SUBRAMANIAN, G. (1963*a*).—Proc. Int. Conf. Cosmic Rays, Jaipur, India. Vol. 2, p. 307.

SARABHAI, V. A., and SUBRAMANIAN, G. (1963*b*).—Proc. Int. Conf. Cosmic Rays, Jaipur, India. Vol. 2, p. 405.

SUBRAMANIAN, G. (1963).—Proc. Int. Conf. Cosmic Rays, Jaipur, India. Vol. 2, p. 302.

HARMONIC STRUCTURE AND BAND SPLITTING OF TYPE II SOLAR RADIO BURSTS

By M. Krishnamurthi,*† G. Sivarama Sastry,* and T. Seshagiri Rao*

[*Manuscript received April* 15, 1965]

Summary

An analysis of single-frequency records of type II solar radio bursts at 29 Mc/s has been made. Such characteristic features as harmonic structure and band splitting due to coronal magnetic fields have been identified. Calculations indicate that the shock fronts generating the type II bursts experience a deceleration as they move outwards. Existing theories have been used to estimate the magnetic field strengths, which come out to be of the order of 3–8 G at a height of 0·7 solar radius above the photosphere at the time of occurrence of these bursts.

I. Introduction

Correlation of optical solar flare data with the solar radio emission at metre wavelengths obtained from single-frequency records and swept-frequency methods has been established by Shain and Mitra (1954), Dodson (1958), Roberts (1959), and others. The authors have reported (Krishnamurthi, Sivarama Sastry, and Seshagiri Rao 1962*a*) a close correlation between flares of importance 3 or 3± which occurred during the IGY period for the year 1958 and the related effects in the 29 Mc/s cosmic noise observations at Hyderabad, India (lat. 17°26′ N.; long. 78°27′ E.). In another paper the authors (Krishnamurthi, Sivarama Sastry, and Seshagiri Rao 1962*b*) have indicated a new method of obtaining the velocities of the shock fronts generating type II bursts, from an analysis of the single-frequency records. On a re-examination of these records for the year 1958, the authors have observed that information regarding the other features of type II bursts, such as harmonic structure and band splitting, can also be derived from the single-frequency data. Data obtained from such an analysis are presented in the present paper.

II. Experimental Results and Discussion

(*a*) *Velocities of Shock Fronts*

The equipment used for obtaining the single-frequency records employs a radio telescope, operating at 29 Mc/s, consisting of a broadside array of 30 full-wave dipoles giving a half-power beamwidth of 8·8° in the east–west direction and 18° in the north–south direction. The other details of the equipment have been described in an earlier paper (Krishnamurthi, Sivarama Sastry, and Seshagiri Rao 1958). For the period January–December 1958, nine sudden cosmic noise absorptions (SCNA's) have been recorded in these single-frequency records, and they have been correlated with the optical flares of importance 3 or 3± occurring at the same time.

---

* Department of Physics, Osmania University, Hyderabad 7, India.

† Present address: Defence Electronics Research Laboratories, Hyderabad, India.

Aust. J. Phys., 1965, 18, 473–8

In each of these SCNA's, an intense outburst of solar radio noise has been observed at about the maximum phase of the flare. These outbursts have been identified as type II bursts by virtue of their high intensity and their duration (a few minutes). Since the start of the SCNA has been closely identified with the start of an optical flare, the time elapsed for the appearance of the type II burst is used to estimate the velocity of the shock fronts generating these bursts. The method of calculation is described in an earlier paper (Krishnamurthi, Sivarama Sastry, and Seshagiri Rao 1962*b*). By this procedure it has become possible to obtain the velocities of shock fronts in the solar corona without the aid of elaborate swept-frequency methods.

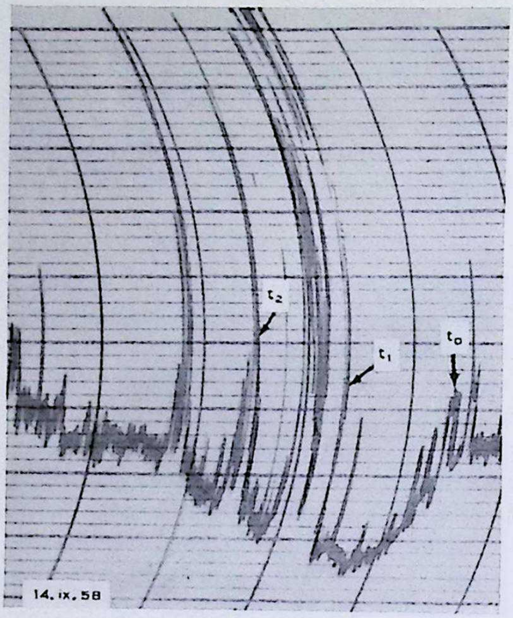

Fig. 1.—Sudden Cosmic Noise Absorption, September 14, 1958. t_0, beginning of SCNA; t_1, start of the first type II event; t_2, start of the second-harmonic burst.

(*b*) *Harmonic Structure*

Ordinarily, it is not possible to describe the harmonic structure of the type II bursts from single-frequency records. In fact, only since the advent of swept-frequency methods has the occurrence of harmonic bands for the type II events been established, together with such other characteristic features as band splitting and herring-bone structure in some cases (Roberts 1959).

Roberts has reported the presence of fundamental and second-harmonic bands in 60% of the type II bursts observed by him and in a larger proportion in the case of moderate and high-intensity bursts. The type II bursts recorded at 29 Mc/s by the authors occur at about the maximum phase of an intense SCNA, and are therefore of very high intensity. A closer examination of these records has shown that in all these events there is another distinct outburst occurring a few minutes after the first intense outburst. The intensity of this second outburst is comparable with that of the first. Since the receiver is tuned to the single frequency of 29 Mc/s all the time, it cannot receive the second-harmonic frequency of 58 Mc/s. Therefore, the burst occurring at the time t_2 shown in Figure 1 can be due to the second harmonic of a burst whose fundamental frequency is half that of the receiver frequency. In other words, if the shock front in its travel outwards in the solar corona reaches a level where the electron density is appropriate to excitation of 14·5 Mc/s radiation, then at the same instant the second harmonic of this fundamental radio wave will also be excited, and may be recorded by the radio telescope which is kept tuned to this second-harmonic frequency.

TABLE 1

VELOCITIES OF SHOCK FRONTS IN THE SOLAR CORONA, DERIVED FROM SECOND-HARMONIC BURSTS

Serial No.	Date	Start of SCNA (U.T.) h	m	t_1-t_0 (s)	t_2-t_0 (s)	$V_{\text{fund.}}$ (km/s)	$V_{\text{2nd harm.}}$ (km/s)	Deceleration $(\mathrm{km/s^2})$
1.	3. iii.58	10	10	710	1279	567	556	0·043
2.	23. iii.58	09	51	568	1042	709	682	0·119
3.	5. v.58	04	10	474	853	851	834	0·093
4.	6. vi.58	04	36	521	947	774	751	0·112
5.	29. vii.58	03	00	616	947	655	751	—
6.	16.viii.58	04	45	379	758	1063	938	0·668
7.	14. ix.58	08	53	900	1658	448	429	0·052
8.	19. x.58	07	27	379	710	1063	1001	0·383
9.	3. xii.58	07	02	805	—	501	—	—

On this assumption, since shock fronts are generating 14·5 Mc/s radiation at the appropriate level in the corona at a time t_2 after the start of the flare, their velocities may be estimated. On the basis of the Baumbach–Allen model, the height of the layer in the solar corona where the 14·5 Mc/s radiation is excited is estimated to be $1{\cdot}022\ R_{\odot}$, where $R_{\odot}$ is the radius of the Sun's visible disk ($0{\cdot}6957 \times 10^6$ km). The velocities thus obtained are given in Table 1, and are compared with the velocities calculated earlier for the same events from the fundamental outburst occurring at time t_1 after the start of the flare (Fig. 1). The times given in this table are determined to within ± 10 s.

It can be seen that the two values for the velocities agree closely, justifying the above procedure. In the last event occurring on December 3, 1958, the second burst is not recorded. For the event occurring on July 29, 1958, the value for $V_{\text{2nd harm.}}$ is much higher than $V_{\text{fund.}}$. In this case, therefore, it is not clear whether or not the second burst at t_2 is the second-harmonic burst. For all the other cases the value for $V_{\text{2nd harm.}}$ comes out to be smaller than $V_{\text{fund.}}$. Since it is likely that the shock wave experiences a deceleration in its travel outwards in the corona, $V_{\text{2nd harm.}}$ will always be less than $V_{\text{fund.}}$. Assuming uniform deceleration for the shock wave, values of deceleration may be calculated from the distances travelled during the time intervals (t_1-t_0) and (t_2-t_0), and are given in Table 1.

A different type of calculation has also been made in the following manner. Assuming that the shock front continues to travel with a uniform velocity as obtained from the time interval (t_1-t_0) corresponding to the fundamental outburst, the height at which the harmonic outburst is generated is calculated using the time interval (t_2-t_0). The plasma frequency f_p corresponding to this level is calculated in the usual way. The ratio of this frequency to the receiver frequency gives the harmonic ratio. Table 2 gives these values for the different events.

TABLE 2

CALCULATED VALUES OF HARMONIC RATIO

Date	$V_{\text{fund.}}$ (km/s)	t_2-t_0 (s)	Height h ($R_\odot$)	f_p for Height h (Mc/s)	Harmonic Ratio
3. iii.58	567	1279	1·042	14·16	2·05
23. iii.58	709	1042	1·062	13·83	2·10
5. v.58	851	853	1·043	14·14	2·05
6. vi.58	774	947	1·053	13·97	2·08
29. vii.58	655	947	0·892	17·17	1·69
16.viii.58	1063	758	1·158	12·43	2·33
14. ix.58	448	1658	1·068	13·72	2·11
19. x.58	1063	710	1·085	13·45	2·16
3. xii.58	501	..	No harmonic observed		..

Wild, Murray, and Rowe (1954) were the first to record the harmonic type II bursts, and they showed that the ratio of peak frequencies in the two bands was usually somewhat less than 2. This was explained by assuming that the lower frequencies in the fundamental band were unable to escape from the Sun in the direction of the Earth, and because of this the harmonic ratio varies with the position of the burst on the Sun's disk. Later observations by Roberts (1959) have shown that the harmonics could be received from any position on the disk and that the harmonic ratio does not vary significantly with the position of the burst.

It can be seen from Table 2 that the harmonic ratio is slightly greater than 2 in all cases except for the event of July 29, 1958. This clearly establishes that the burst occurring at time t_2 must be the second harmonic of the plasma frequency appropriate to that level. It is noteworthy that the harmonic ratio is always greater than 2. This higher value is obtained because it is assumed that the shock wave is travelling with uniform velocity, namely $V_{\text{fund.}}$.

(c) *Band Splitting*

For all the events listed in Table 1, except for the one on May 5, 1958, a doubling of the fundamental burst has been observed. A typical record is reproduced in Figure 2. This feature, observed in the structure of all the type II bursts, is considered to be analogous to the band splitting noticed in the swept-frequency records. In swept-frequency records a splitting of the fundamental and harmonic bursts into two components, separated in frequency by a few percent, has been observed by Roberts. Since the plasma region where the flare occurs is permeated by a general magnetic field of the sunspot group, a magnetic splitting analogous to the Zeeman effect may be responsible for the observed band splitting. Westfold (1949) has suggested that such a plasma region has three frequencies for which the refractive index is zero. These are given by the plasma frequency f_p and the frequencies

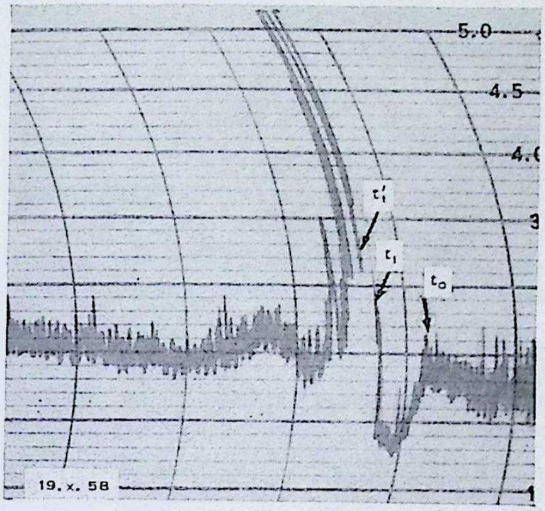

Fig. 2.—Sudden Cosmic Noise Absorption, October 19, 1958. t_0, beginning of SCNA; t_1, start of the first type II event; t_1', start of the burst due to band splitting.

$(f_p^2+\frac{1}{4}f_H^2)^{\frac{1}{2}}\pm\frac{1}{2}f_H$, where f_H is the gyro frequency $(eH/2\pi mc)$. The lower of these cannot escape from the plasma region. On the other hand, from the dispersion relation

$$\omega^2 = \tfrac{1}{2}[\omega_p^2+\omega_H^2\pm(\omega_p^4+\omega_H^4-2\,\omega_p^2\,\omega_H^2\cos 2\theta)^{\frac{1}{2}}],$$

Sturrock (1961) has recently obtained the frequencies that can be observed in band splitting. By imposing the condition $d\omega/d\theta = 0$, the frequencies of the lowest group velocity modes that are preferentially excited are obtained as ω_p and $(\omega_p^2+\omega_H^2)^{\frac{1}{2}}$, and their separation is nearly equal to $\frac{1}{2}(\omega_H^2/\omega_p)$, $(\omega_p \gg \omega_H)$.

In the present calculation, the procedure followed is to determine the frequency corresponding to the level where the burst at t_1' (Fig. 2) has occurred. The difference between this frequency and the receiver frequency of 29 Mc/s gives the band separation appropriate to the level where the burst at t_1' is excited. For these calculations the velocities $V_{\text{fund.}}$ given in Table 1 are used. The height h' of these levels, their appropriate frequencies f_p', the band separation $(29-f_p')$, and the associated magnetic field strengths H are presented in Table 3. The magnetic field strengths are calculated using both the theories mentioned above.

The values of magnetic field strength calculated using the expressions given by Westfold and by Sturrock compare favourably with the values indicated by Roberts earlier. Sturrock has estimated a magnetic field of 20 G at a height corresponding to 80 Mc/s radiation. The lower field strengths arrived at in the present analysis give an indication of how the associated magnetic field decreases in intensity with increasing height in the solar corona. However, the values obtained in this investigation are much higher than the average magnetic fields at these heights for a Baumbach–Allen corona over a Chapman model sunspot field of 3000 G. This might perhaps be expected for the coronal streamer regions over highly intense sunspot fields that give rise to flares of importance 3 or 3±.

TABLE 3

OBSERVED BAND SPLITTING AND ASSOCIATED MAGNETIC FIELDS CORRESPONDING TO TYPE II BURSTS

Date	$V_{\text{fund.}}$ (km/s)	$t_1'-t_0$ (s)	Height h' ($R_\odot$)	f_p' (Mc/s)	Band Separation (Mc/s)	f_H* (Mc/s)	f_H† (Mc/s)	H* (G)	H† (G)
3. iii.58	567	899·5	0·735	21·79	7·21	12·62	19·14	4·5	6·8
23. iii.58	709	662·8	0·677	24·06	4·94	9·04	16·19	3·2	5·8
5. v.58	851	..	..	No band splitting observed			..	..	..
6. vi.58	774	663·1	0·738	21·69	7·31	12·77	19·25	4·6	6·9
29. vii.58	655	758·1	0·714	22·58	6·42	11·41	18·20	4·1	6·5
16.viii.58	1063	592·1	0·906	16·86	12·14	19·20	23·60	6·9	8·4
14. ix.58	448	1113·1	0·717	22·46	6·54	11·61	18·35	4·2	6·6
19. x.58	1063	473·7	0·725	22·15	6·85	12·09	18·72	4·3	6·7
3. xii.58	501	947·1	0·682	23·84	5·16	9·40	16·51	3·4	5·9

* Values calculated using the formula given by Westfold (1949).

† Values calculated using the formula given by Sturrock (1961).

While the swept-frequency techniques have established the various features of type II bursts such as harmonic structure and band splitting, the foregoing analysis of single-frequency records seems to give more accurate data, once these features are seen to be characteristic of type II bursts.

III. REFERENCES

DODSON, H. W. (1958).—*Proc. Inst. Radio Engrs* **46**: 149.

KRISHNAMURTHI, M., SIVARAMA SASTRY, G., and SESHAGIRI RAO, T. (1958).—*J. Scient. Ind. Res.* **17A**: 71.

KRISHNAMURTHI, M., SIVARAMA SASTRY, G., and SESHAGIRI RAO, T. (1962*a*).—*Aust. J. Phys.* **15**: 20.

KRISHNAMURTHI, M., SIVARAMA SASTRY, G., and SESHAGIRI RAO, T. (1962*b*).—*Aust. J. Phys.* **15**: 120.

ROBERTS, J. A. (1959).—*Aust. J. Phys.* **12**: 327.

SHAIN, C. A., and MITRA, A. P. (1954).—*J. Atmos. Terr. Phys.* **5**: 316.

STURROCK, P. A. (1961).—*Nature* **192**: 58.

WESTFOLD, K. C. (1949).—*Aust. J. Scient. Res.* A **2**: 169.

WILD, J. P., MURRAY, J. D., and ROWE, W. C. (1954).—*Aust. J. Phys.* **7**: 439.

SHORT COMMUNICATIONS

SAINT-VENANT'S PRINCIPLE IN ANISOTROPIC MEDIA*

By R. B. Noyes†

Saint-Venant's principle may be stated (Sternberg 1954): "An equilibrated system of external forces applied to an elastic body, all of the points of application lying within a given sphere, produces deformations of negligible magnitude at distances from the sphere which are sufficiently large compared to its radius."

Although Saint-Venant's principle has been known and used for over 100 years, a general proof and a method of estimating the distance from the disturbance at which deformations become small in specific cases has only recently been given for isotropic media (Boley 1958). Boley showed that Saint-Venant's principle is a consequence of the elliptic character of the governing differential equations, and estimated the "smoothing distance", or distance from the disturbance at which deformations become small, by making use of an upper bound to the Green's function for the problem. In a later paper (Boley 1960), it was shown that in certain cases in which the differential equation of the problem is parabolic Saint-Venant's principle may still apply.

It does not appear to be well known, however, that anisotropy may cause significant changes in the smoothing distance of a disturbance. For example, Lenkhnitskii (1963) remarks in the early pages of his book that he will invoke Saint-Venant's principle in order to simplify the statement of certain problems, but does not comment upon the effect of anisotropy on Saint-Venant's principle.

Because of the high degree of anisotropy of certain structural materials (e.g. fibre-reinforced composites), it appears desirable to investigate the order of magnitude of smoothing distance necessary to the application of Saint-Venant's principle in such media.

We choose in the first instance to examine this problem in a very simple case of steady-state heat transfer. Consider the problem of two-dimensional heat conduction in a semi-infinite bar of width b, thin in the z direction. Let the principal axes of thermal conductivity coincide with the bar axes, and let the sides and edges of the bar be insulated. The differential equation for the problem is (Carslaw and Jaeger 1959, p. 41)

$$K_x \frac{\partial^2 T}{\partial x^2} + K_y \frac{\partial^2 T}{\partial y^2} = 0,$$

and its solution can be shown to be

$$T_{(x,y)} = \sum_{n=0}^{\infty} a_n \exp\left\{-\frac{n\pi y}{b}\left(\frac{K_x}{K_y}\right)^{\frac{1}{2}}\right\}\cos\frac{n\pi x}{b},$$

---

* Manuscript received May 4, 1965.

† Department of Mechanical Engineering, University of Western Australia, Nedlands, W.A.

where T is temperature, K_x and K_y are the thermal conductivities in the x and y directions respectively, and b is the breadth of the bar.

Let us impose at the end of the bar a disturbance

$$T_{(x,0)} = T_0 \cos \frac{2\pi x}{b},$$

which has null net heat input and, because of its symmetry about the bar centre line, has also null net "moment" of heat input. (This disturbance could be superimposed upon any specified temperature distribution $T^*_{(x,0)}$ at the end of the bar to obtain a new temperature distribution $T^{**}_{(x,0)}$ which would be "statically equivalent" to $T^*_{(x,0)}$.)

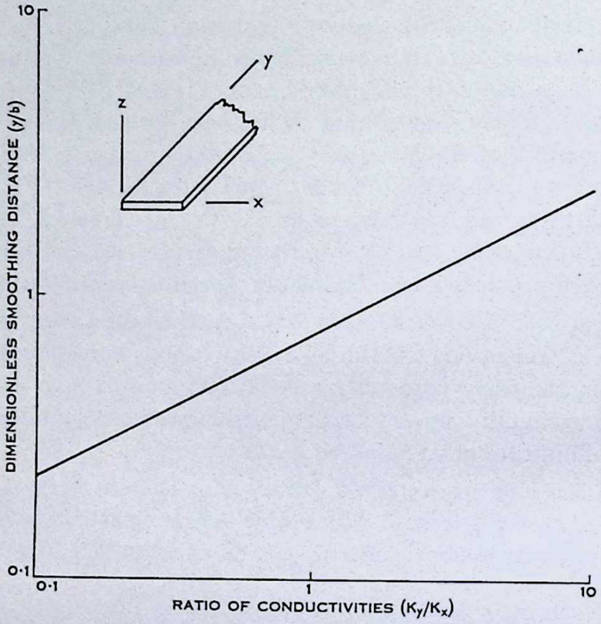

Fig. 1.—Position in a semi-infinite anisotropic thin bar at which the disturbance $T_{(x,0)} = T_0 \cos(2\pi x/b)$ has essentially (99%) disappeared.

The solution corresponding to the specified disturbance is

$$T_{(x,y)} = T_0 \exp\left\{-\frac{2\pi y}{b}\left(\frac{K_x}{K_y}\right)^{\frac{1}{2}}\right\} \cos \frac{2\pi x}{b}.$$

We are particularly interested in the maximum temperature which occurs for any value of x at a specified distance from the end of the bar, and which is given by

$$T_{\max(y)} = T_0 \exp\left\{-\frac{2\pi y}{b}\left(\frac{K_x}{K_y}\right)^{\frac{1}{2}}\right\}.$$

Selecting some particular value for $T_{\max}$ (for example, 1% of T_0), which we will consider to have reduced the disturbance to negligible magnitude, we may calculate the smoothing distance for the problem. These distances are shown in Figure 1.

This simple example is given to illustrate the existence of, and to give some idea of, the magnitude of the effect of anisotropy upon Saint-Venant's principle. In geometrically complicated anisotropic heat conduction problems, where an exact solution is not so easily given, an upper bound to the smoothing distance may be constructed by using the transformation suggested by Carslaw and Jaeger (1959, p. 44) and the method of Boley (1958).

Discussion and Conclusion

Provided that the principal thermal conductivities are non-zero, anisotropy does not change the elliptic character of the equation of steady-state heat conduction, and Saint-Venant's principle applies. It will be noted from Figure 1 that in an isotropic material the disturbance in question has essentially (99%) disappeared in about three-quarters of a bar width.

However, as Figure 1 shows, anisotropy may significantly increase or decrease the smoothing distance, depending upon the orientation of the higher conductivity axis with respect to the bar axis. It may be noted that in the limiting case where K_y becomes zero, Saint-Venant's principle holds with a smoothing distance of zero. If K_x becomes zero, Saint-Venant's principle does not apply.

References

Boley, B. A. (1958).—*In* "Proceedings of the Third U.S. National Congress of Applied Mechanics". pp. 259–63. (Am. Soc. Mech. Engrs: New York.)

Boley, B. A. (1960).—*Quart. Appl. Math.* **18**: 205.

Carslaw, H. S., and Jaeger, J. C. (1959).—"Conduction of Heat in Solids." 2nd Ed. (Clarendon Press: Oxford.)

Lenkhnitskii, S. G. (1963).—"Theory of Elasticity of an Anisotropic Elastic Body." (Trans. P. Fern.) (Holden Day: San Francisco.)

Sternberg, E. (1954).—*Quart. Appl. Math.* **11**: 393–401.

DIFFUSION OF HEAT FROM A SPHERE TO A SURROUNDING MEDIUM*

By A. Brown†

In a recent paper, Philip (1964) discussed a heat flow problem in which, as an idealization, spherical symmetry is assumed and the medium is regarded as composite, with a spherical core of one material embedded in a larger mass of a second material. One application in mind was to laccoliths, where an intrusion of igneous rock in sedimentary material can produce dome-shaped bulging at the surface. The idea of treating this as a problem involving spherical symmetry was put forward by Lovering (1935), who gave a solution for the case where the core and its surroundings are taken as uniform. In a subsequent paper, Lovering (1936) considered in more detail what variations in the thermal conductivity and diffusivity are to be expected. From the figures he quotes, a composite model should give a better approximation, though remaining a considerable simplification of the physical problem.

In Philip's model, the outer region is taken to be infinite in extent, and at time $t = 0$ the core and the outer region are each at a constant temperature, with the core at a higher temperature than its surroundings. Philip showed that solutions for the temperature and the heat flux at the interface between the two regions could be developed as series expansions, and gave the first few terms of these expansions both for small and large values of t.

The present paper gives some additional results for the same problem. In particular, the temperature at any point is given as an infinite integral. Although this integral converges for any time t greater than zero, the convergence is more rapid when t is large. For small values of t, a more convenient solution is obtained in the special case where the thermal conductivity of the two materials is the same although their diffusivities differ. It is possible to extend this solution to a number of related problems, and these extensions are outlined in the final section of the present paper.

Notation and Method of Solution

We take the spherical core as the region $0 \leqslant r \leqslant a$, where r is the distance from the centre, and use K_1, k_1, T_1 for the conductivity, diffusivity, and temperature in the core, with K_2, k_2, T_2 as the corresponding quantities in the outer region. The relevant equations for T_1 and T_2 are then:

$$\frac{\partial T_1}{\partial t} = k_1\left(\frac{\partial^2 T_1}{\partial r^2} + \frac{2}{r}\frac{\partial T_1}{\partial r}\right) \qquad 0 < r < a; \tag{1}$$

$$\frac{\partial T_2}{\partial t} = k_2\left(\frac{\partial^2 T_2}{\partial r^2} + \frac{2}{r}\frac{\partial T_2}{\partial r}\right) \qquad r > a; \tag{2}$$

$$T_1 = T_2, \qquad K_1(\partial T_1/\partial r) = K_2(\partial T_2/\partial r), \qquad \text{at } r = a;$$

$$T_1 = T_0, \qquad T_2 = 0, \qquad \text{at } t = 0.$$

---

* Manuscript received May 24, 1965.

† Aeronautics Division, California Institute of Technology; on leave from Department of Applied Mathematics, School of General Studies, Australian National University, Canberra.

Aust. J. Phys., 1965, **18**, 483–9

For convenience, the initial temperature in the outer region has been taken as the zero level for T_1 and T_2, and we shall take T_0 to be a positive constant. Additional restrictions which affect the form of T_1 and T_2 are that T_1 must be finite at $r = 0$, and T_2 must tend to zero as r approaches infinity.

If $\bar{T}_1$ and $\bar{T}_2$ are the Laplace transforms of T_1 and T_2 with respect to t, that is,

$$\bar{T}_i = \int_0^\infty T_i(r,t)\exp(-pt)\,\mathrm{d}t \qquad (i = 1, 2),$$

then it can be shown that

$$\bar{T}_1 = \frac{T_0}{p}\left[1 - \frac{K_2(1+q_2 a)\sinh q_1 r}{r\{K_1 q_1 \cosh q_1 a + (K_2 q_2 + K)\sinh q_1 a\}}\right], \tag{3}$$

$$\bar{T}_2 = \frac{T_0}{p}\left[\frac{K_1(q_1 a \cosh q_1 a - \sinh q_1 a)\exp\{-q_2(r-a)\}}{r\{K_1 q_1 \cosh q_1 a + (K_2 q_2 + K)\sinh q_1 a\}}\right], \tag{4}$$

where

$$q_1 = (p/k_1)^{\frac{1}{2}}, \qquad q_2 = (p/k_2)^{\frac{1}{2}}, \tag{5}$$

$$K = (K_2 - K_1)/a. \tag{6}$$

Equations (3) and (4) are equivalent to equations (3.6) and (3.7) of Philip's paper (Philip 1964). However, the notation follows more closely that of Carslaw and Jaeger (1939), who considered a somewhat similar problem of heat transfer in a composite system with spherical symmetry.

Carslaw and Jaeger (1939) also used the Laplace transform method, and obtained transforms with essentially the same denominator as in $\bar{T}_1$ and $\bar{T}_2$ above. To invert these transforms, they used the standard inversion integral (Churchill 1958, p. 176), and integrated around a suitable contour in the (complex) p-plane. In this way, they obtained solutions for the temperature in a form involving real integrals. In the present problem, their procedure can be taken over with only minor variations, and this gives solutions for T_1 and T_2 in the form

$$\frac{T_1}{T_0} = \frac{2Qa}{\pi r}\int_0^\infty \frac{(\sin u - u\cos u)\sin(ur/a)\exp(-k_1 u^2 t/a^2)}{(u\cos u + L\sin u)^2 + (Qu\sin u)^2}\,\mathrm{d}u, \tag{7}$$

$$\frac{T_2}{T_0} = \frac{2a}{\pi r}\int_0^\infty \frac{(\sin u - u\cos u)\,F(u)\exp(-k_1 u^2 t/a^2)}{(u\cos u + L\sin u)^2 + (Qu\sin u)^2}\,\frac{\mathrm{d}u}{u}, \tag{8}$$

where

$$F(u) = (u\cos u + L\sin u)\sin\{u(r-a)/\sigma a\} + Qu\sin u\cos\{u(r-a)/\sigma a\},$$

$$Q = K_2/K_1\sigma, \qquad L = (K_2 - K_1)/K_1, \qquad \sigma = (k_2/k_1)^{\frac{1}{2}}.$$

It will be seen that the integrals involved are of Fourier type, in that separable solutions of equations (1) and (2) are combined in suitable proportions to satisfy the boundary conditions and initial conditions. For example, equation (7) is of the form

$$T_1 = \int_0^\infty G(u)\,\{(1/r)\sin(ur/a)\exp(-k_1 u^2 t/a^2)\}\,\mathrm{d}u,$$

where the expression in braces is a separable solution of equation (1) for all values of u, and $G(u)$ can be regarded as an amplitude factor.

Temperature and Heat Flow at Interface

The temperature at the interface, which we denote by T^*, can be obtained by putting $r = a$ in either equation (7) or equation (8). This gives

$$T^* = (2QT_0/\pi) \int_0^\infty (1/D^2)(\sin u - u\cos u)\sin u \exp(-k_1 u^2 t/a^2)\, du, \tag{9}$$

where $D^2 = (u\cos u + L\sin u)^2 + (Qu\sin u)^2$.

Similarly, the heat flux from the core to the exterior region can be obtained from either of equations (7) and (8). If we use $H'(t)$ for this heat flux, then

$$\begin{aligned} H'(t) &= -4\pi K_1 a^2(\partial T_1/\partial r)_{r=a} = -4\pi K_2 a^2(\partial T_2/\partial r)_{r=a} \\ &= 8T_0 aK_1 Q \int_0^\infty \{(\sin u - u\cos u)^2/D^2\} \exp(-k_1 u^2 t/a^2)\, du. \end{aligned} \tag{10}$$

By integrating from 0 to t, we get the heat loss from the core after time t as

$$H(t) = 8T_0 a^3 K_1 Q/k_1 \int_0^\infty \{(\sin u - u\cos u)^2/u^2D^2\}\{1-\exp(-k_1 u^2 t/a^2)\}\, du.$$

As $t \to \infty$, the temperature in the core will tend to zero, and $H(t)$ must approach H_0, where H_0 is the total amount of energy which the core can lose by heat flow to the surrounding material. Now

$$\begin{aligned} H_0 &= (\text{core volume})\times(\text{density})\times(\text{specific heat})\times(\text{initial temperature difference}) \\ &= (4\pi/3)a^3(K_1/k_1)T_0. \end{aligned} \tag{11}$$

The density and specific heat here are those appropriate to the core and, since

$$\text{diffusivity} = (\text{thermal conductivity})/(\text{density}\times\text{specific heat}),$$

we can use K_1/k_1 instead of (density × specific heat) in equation (11). It follows that

$$\int_0^\infty \{(\sin u - u\cos u)^2/u^2D^2\}\, du = \pi/6Q,$$

and

$$\begin{aligned} (H_0 - H)/H_0 &= \text{fraction of total heat flux from core that has yet to occur at time } t \\ &= (6Q/\pi) \int_0^\infty \{(\sin u - u\cos u)^2/u^2D^2\} \exp(-k_1 u^2 t/a^2)\, du. \end{aligned} \tag{12}$$

For large values of t, the integrals in equations (9), (10), and (12) can be approximated by an asymptotic expansion in descending powers of t. In the case of equation (9), for example, the asymptotic expansion is obtained by expressing $(1/D^2)(\sin u - u\cos u)\sin u$ as a power series in u, and integrating the new form of the integrand term by term. The resulting expansion for T^* agrees exactly with the asymptotic expansion given by Philip (1964, equation (6.4)). Similarly, the asymptotic expansion for $H'(t)$ from equation (10) agrees with Philip's equation (6.5), and the asymptotic expansion for $(H_0 - H)/H_0$ confirms Philip's conclusions regarding the equilibration time of the composite system.

Temperature Distribution for $K_1 = K_2$

The expressions for T_1 and T_2 given by equations (7) and (8) are valid for all positive values of t, but it is clear that they converge more rapidly when t is large than when t is small. In the case where $K_1 = K_2$, equations (7) and (8) can be supplemented by series solutions which converge more rapidly for small values of t.

If we put $K_1 = K_2$ in equations (3)–(6), then $K = 0$ and

$$\bar{T}_1 = \frac{T_0}{p}\left[1 - \frac{(1+q_2 a)\sinh q_1 r}{rq_1\{\cosh q_1 a + (1/\sigma)\sinh q_1 a\}}\right], \tag{13}$$

$$\bar{T}_2 = \frac{T_0}{p}\left[\frac{(q_1 a\cosh q_1 a - \sinh q_1 a)\exp\{-q_2(r-a)\}}{rq_1\{\cosh q_1 a + (1/\sigma)\sinh q_1 a\}}\right], \tag{14}$$

since $\sigma = (k_2/k_1)^{\frac{1}{2}} = q_1/q_2$. These Laplace transforms can be inverted to give solutions for T_1 and T_2 in terms of the error function and its integral. One way of inverting $\bar{T}_1$ and $\bar{T}_2$ is to express the hyperbolic functions in terms of exponentials and replace $\{\cosh q_1 a + (1/\sigma)\sinh q_1 a\}^{-1}$ by a series expansion in powers of $\exp(-2q_1 a)$. An example of this procedure is given by Carslaw and Jaeger (1959, Chap. XII, § 12.5). An alternative method, which leads into some interesting by-ways, is to use the result that, if

$$\bar{G}(p) = (\pi/p)^{\frac{1}{2}}\,\bar{F}(p^{\frac{1}{2}}),$$

then

$$G(t) = t^{-\frac{1}{2}}\int_0^\infty F(u)\exp(-u^2/4t)\,du \qquad (t > 0),$$

where $\bar{F}(p)$ is the Laplace transform of $F(t)$. However, the first method is simpler and more direct.

To write the solutions for T_1 and T_2 compactly, we introduce the notation

$$E_0(x) = \operatorname{erfc} x, \qquad E_1(x) = \operatorname{ierfc} x = \int_x^\infty E_0(u)\,du,$$

$$P_N = \{Na+\tfrac{1}{2}(a-r)\}/(k_1 t)^{\frac{1}{2}}, \qquad Q_N = \{Na+\tfrac{1}{2}(a+r)\}/(k_1 t)^{\frac{1}{2}},$$

$$R_N = \{N\sigma a+\tfrac{1}{2}(r-a)\}/(k_2 t)^{\frac{1}{2}}.$$

Then

$$\frac{T_1}{T_0} = 1 - \frac{(a/r)}{1+\sigma}\sum_{N=0}^{\infty}\left(\frac{1-\sigma}{1+\sigma}\right)^N\left[E_0(P_N) - E_0(Q_N) + \frac{2(k_2 t)^{\frac{1}{2}}}{a}\{E_1(P_N) - E_1(Q_N)\}\right], \tag{15}$$

$$\frac{T_2}{T_0} = \frac{\sigma(a/r)}{1+\sigma}\left\{E_0(R_0) - \frac{2(k_1 t)^{\frac{1}{2}}}{a}E_1(R_0)\right\}$$
$$+ \frac{2\sigma(a/r)}{(1+\sigma)^2}\sum_{N=1}^{\infty}\left(\frac{1-\sigma}{1+\sigma}\right)^{N-1}\left\{E_0(R_N) + \frac{2(k_2 t)^{\frac{1}{2}}}{a}E_1(R_N)\right\}. \tag{16}$$

Equations (15) and (16) agree with the solution given by Lovering (1935). As mentioned earlier, he treated the core and its surroundings as if they were of the same material. (In his numerical work, he used an average value of the thermal conductivity and of the diffusivity.) With this assumption, $k_1 = k_2$ and hence $\sigma = 1$, so the series for T_1 and T_2 terminate, giving

$$T_1/T_0 = 1-(a/2r)\{E_0(P_0)-E_0(Q_0)\}-(1/r)(k_1 t)^{\frac{1}{2}}\{E_1(P_0)-E_1(Q_0)\},$$

$$T_2/T_0 = (a/2r)\{E_0(R_0)+E_0(R_1)\}-(1/r)(k_1 t)^{\frac{1}{2}}\{E_1(R_0)-E_1(R_1)\},$$

with

$$P_0 = -R_0 = \tfrac{1}{2}(a-r)/(k_1 t)^{\frac{1}{2}}, \qquad Q_0 = R_1 = \tfrac{1}{2}(a+r)/(k_1 t)^{\frac{1}{2}}.$$

Using the relations

$$E_0(-x) = 2-E_0(x),$$

$$E_1(-x) = 2x+E_1(x),$$

$$E_1(x) = -x\,E_0(x)+\pi^{-\frac{1}{2}}\exp(-x^2),$$

it is easy to verify that

$$T_1 = T_2 = \tfrac{1}{2}T_0(\operatorname{erf} P_0 + \operatorname{erf} Q_0)-(T_0/r)(k_1 t/\pi)^{\frac{1}{2}}\{\exp(-P_0^2)-\exp(-Q_0^2)\},$$

which agrees with Lovering's solution.

When $K_1 = K_2$, the integral in equation (7) simplifies slightly, since $L = 0$ and $Q = 1/\sigma$. Hence, for $K_1 = K_2$,

$$\frac{T_1}{T_0} = \frac{2\sigma a}{\pi r}\int_0^\infty \frac{(\sin u - u\cos u)\sin(ur/a)\exp(-k_1 u^2 t/a^2)}{u^2(\sigma^2\cos^2 u+\sin^2 u)}\,du. \qquad (17)$$

Equations (15) and (17) now give two strikingly different expressions for the ratio T_1/T_0. Similarly, equation (8) may be used to give an infinite integral for T_2/T_0 as an alternative to the series on the right-hand side of equation (16).

Temperature and Heat Flow at Interface for $\mathrm{K}_1 = \mathrm{K}_2$

The temperature at the interface can be obtained by putting $r = a$ in either equation (15) or (16). Since $E_0(0) = 1$ and $E_1(0) = \pi^{-\frac{1}{2}}$, we get

$$T^* = \frac{\sigma T_0}{1+\sigma}\left\{1-\left(\frac{2}{a}\right)\left(\frac{k_1 t}{\pi}\right)^{\frac{1}{2}}\right\}+\frac{2\sigma T_0}{(1+\sigma)^2}\sum_{N=1}^{\infty}\left(\frac{1-\sigma}{1+\sigma}\right)^{N-1}\left\{E_0(P_N^*)+\frac{2(k_2 t)^{\frac{1}{2}}}{a}E_1(P_N^*)\right\},$$

where $\qquad P_N^* =$ value of P_N at interface $= Na/(k_1 t)^{\frac{1}{2}}$.

Similarly, the heat flux from the core can be obtained from either equation (15) or equation (16). This gives

$$H'(t) = \frac{4\pi a K_1 T_0}{1+\sigma}\left[(\sigma-1)+\frac{a^2-2\sigma k_1 t}{a(\pi k_1 t)^{\frac{1}{2}}}\right.$$
$$\left.+\sum_{N=1}^{\infty}\frac{2(1-\sigma)^{N-1}}{(1+\sigma)^N}\left\{\frac{Na^2+2\sigma k_1 t}{k_1 t}E_0(P_N^*)+\frac{a^2+2k_2 t}{a(k_1 t)^{\frac{1}{2}}}E_1(P_N^*)\right\}\right].$$

These expressions for T^* and $H'(t)$ can be compared with equations (7.2) and (7.3) of Philip's paper (Philip 1964), noting that Philip's symbols B, τ, $\vartheta(1)$, and Φ

are equal, respectively, to $\sigma/(1+\sigma)$, $k_1 t/a^2$, T^*/T_0, and $(4\pi a K_1 T_0)^{-1} H'(t)$ of the present paper. The comparison shows, in the higher order terms, discrepancies which arise because of the omission of a bracket in equation (4.1) of Philip's paper. Dr. Philip (personal communication; see also Philip 1965) has kindly supplied me with amended forms of the equations affected by the missing bracket, and our results are now in agreement.

Related Problems for $K_1 = K_2$

A well-known device for dealing with heat conduction problems where there is spherical symmetry is to use variables $U_1 = rT_1$ and $U_2 = rT_2$, in place of T_1 and T_2. Then U_1 and U_2 satisfy the standard diffusion equation for linear flow of heat, that is, instead of equations (1) and (2) we get

$$\frac{\partial U_1}{\partial t} = k_1 \frac{\partial^2 U_1}{\partial r^2}, \qquad \frac{\partial U_2}{\partial t} = k_2 \frac{\partial^2 U_2}{\partial r^2}.$$

In general, linear flow solutions cannot be taken over unaltered, because the boundary conditions at the interface are

$$U_1 = U_2, \qquad K_1 \frac{\partial}{\partial r}\left(\frac{U_1}{r}\right) = K_2 \frac{\partial}{\partial r}\left(\frac{U_2}{r}\right), \tag{18}$$

whereas in a linear flow problem the boundary conditions are

$$U_1 = U_2, \qquad K_1(\partial U_1/\partial r) = K_2(\partial U_2/\partial r). \tag{19}$$

Carslaw (1921) illustrates this point by quoting a Cambridge tripos question in which the answer supplied was wrong because (19) had been used when (18) was the appropriate pair of equations. But in the special case where $K_1 = K_2$, the distinction between (18) and (19) disappears and the corresponding linear flow solution can be taken over unchanged, if a linear flow solution is available. Where a solution of the corresponding linear flow problem is not immediately available, there may be standard techniques which give a solution readily. Thus, in any heat conduction problem involving a composite material with spherical symmetry, it may be possible to obtain a detailed solution for the case $K_1 = K_2$, and thus obtain some preliminary information about the heat flow, even where it is difficult to find a solution in the general case.

In the problem with which we are concerned, the initial conditions are that $U_1 = rT_0$, for $0 \leqslant r < a$, and $U_2 = 0$, for $r > a$. In addition, U_1 must be zero at $r = 0$, and U_2 must approach zero as $r \to \infty$, for $t > 0$. The justification for the latter requirement is that, for large values of r, T_2 should behave like the solution for a heat source at the origin at $t = 0$, with subsequent diffusion into an infinite medium. Hence, we can expect to have $T_2 \sim t^{-3/2} \exp(-r^2/4k_2 t)$ for large values of r and t greater than zero. It follows that U_2 must tend to zero as r approaches infinity.

An equivalent problem is to find the temperature in an infinite rod with a central portion, $-a < x < a$, which is of different material from the remainder, given that the initial temperature is xT_0 in the central portion and zero outside the central portion. To correspond to the restriction $K_1 = K_2$, the conductivity must be unchanged along the rod. Then the solution of the linear flow problem for $0 < x < a$ corresponds to U_1, and the solution for $x > a$ corresponds to U_2. In the linear flow problem, taking the conductivity to be different in the two media adds no essential difficulty; if the Laplace transform method of solution is used, the transforms that have to be inverted are of the same type as those in equations (13) and (14).

The heat flow problem where the core is initially at a uniform temperature can be related to problems where the core contains a heat source. For example, if heat is produced at a constant rate in the core, and if the core and its surroundings are initially at zero temperature, the subsequent temperature distribution can be obtained by integrating T_1 and T_2 with respect to t, and multiplying by a suitable factor to allow for the strength of the source. This solution in turn can be used to solve the case where the strength of the source decays exponentially with time. Thus, although the model considered is restrictive in its assumptions, it can be regarded as fundamental to a wider range of problems.

References

Carslaw, H. S. (1921).—*Proc. Camb. Phil. Soc. Math. Phys. Sci.* **20**: 399.

Carslaw, H. S., and Jaeger, J. C. (1939).—*Proc. Camb. Phil. Soc. Math. Phys. Sci.* **35**: 394.

Carslaw, H. S., and Jaeger, J. C. (1959).—"Conduction of Heat in Solids." 2nd Ed. (Clarendon Press: Oxford.)

Churchill, R. V. (1958).—"Operational Mathematics." 2nd Ed. (McGraw-Hill: New York.)

Lovering, T. S. (1935).—*Bull. Geol. Soc. Am.* **46**: 69.

Lovering, T. S. (1936).—*Bull. Geol. Soc. Am.* **47**: 87.

Philip, J. R. (1964).—*Aust. J. Phys.* **17**: 423.

Philip, J. R. (1965).—*Aust. J. Phys.* **18**: 393.

ANGULAR DISTRIBUTIONS IN THE REACTIONS $^{11}B(d,p)^{12}B$ AND $^{11}B(d,\alpha)^{9}Be$†

By D. G. Sargood‡ and G. D. Putt‡

In recent years considerable interest has centred on the reaction mechanism in nuclear reactions. At bombarding energies of above about 5 MeV, it has been apparent for many years that (d, p) and (d, n) reactions tend to be dominated by the direct stripping reaction. With the advent of distorted wave stripping theories such as those of Tobocman (1959) and Robson (1961), it now appears that those reactions may proceed by a direct mechanism even at very low bombarding energies. Robson and Weigold (1963) have satisfactorily analysed the angular distributions obtained in the reaction $^{11}B(d,p)^{12}B$ at bombarding energies of 1·02 MeV and 700 keV.

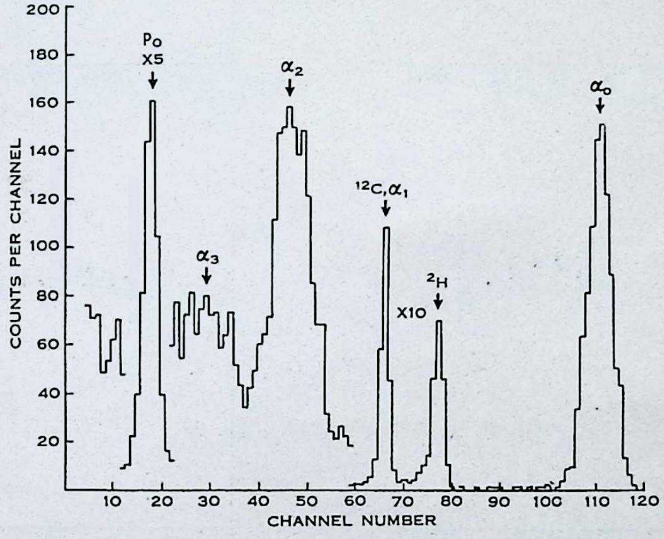

Fig. 1.—Typical pulse height spectrum (taken at 75° and deuteron energy 390 keV). The peaks marked ^{12}C and ^{2}H are attributed to protons from (d, p) reactions in those contaminant nuclei. There is also a small contribution to the ^{12}C peak, at this angle, from the α_1 group leading to the 1·75 MeV state of ^{9}Be. The energy scale for the proton groups is different from that for the alpha groups owing to the effect of the aluminium foil in front of the counter.

Similar attempts have been made to describe (α, d) reactions as two-particle stripping and (d, α) as two-particle pick-up reactions. These theories, due to El Nadi (1957), Newns (1960), Glendenning (1962), are all based on the plane wave approximation used by Butler (1957) for (d, p) and (d, n) stripping, and so, although they have had a certain degree of success at rather large bombarding energies, they are expected to break down at low bombarding energies. However, since it appears that

---

† Manuscript received June 1, 1965.

‡ School of Physics, University of Melbourne.

Aust. J. Phys., 1965, 18, 491–6

direct interaction does dominate (d, p) and (d, n) reactions even at very low energies, it is of interest to determine whether this might be true also for the (d, α) reaction.

Distinction between compound nucleus and direct interaction mechanisms can often be made from an examination of angular distributions of the outgoing particle over a range of bombarding energies. If a compound nucleus is formed by deuteron bombardment, it frequently happens that the energy of such a compound state is greater than about 15 MeV, where the density of states is very large. It therefore follows that several interfering compound states are likely to participate in any compound nucleus process, and the resulting angular distributions may be expected to depend critically on the particular mixture of states involved. Hence, the shape of an angular distribution should vary rapidly with changing bombarding energy. In the case of direct interaction, on the other hand, since no compound nucleus state is involved, the angular distribution should vary only slowly with changing bombarding energy. In the present experiment, this technique was used to carry the investigation from a bombarding energy of 700 keV down to 390 keV in the reactions $^{11}B(d, \alpha)^{9}Be$ and $^{11}B(d, p)^{12}B$.

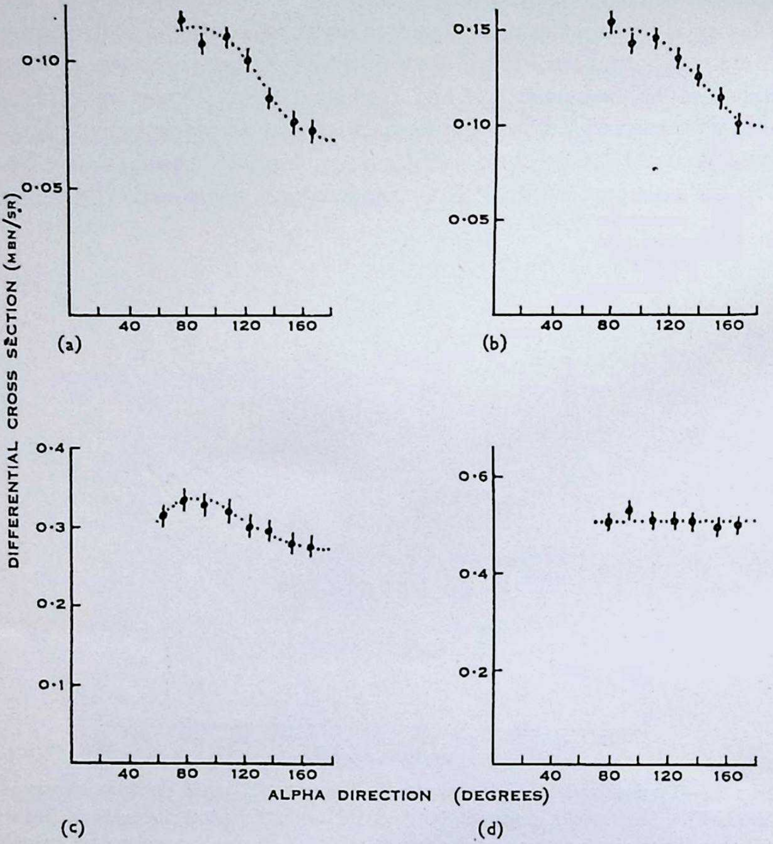

Fig. 2.—Angular distributions of the ground state alpha group, α_0. Deuteron bombarding energy (*a*) 390 keV, (*b*) 490 keV, (*c*) 600 keV, (*d*) 700 keV.

Deuteron Bombardment of ^{11}B

The target, which consisted of separated ^{11}B isotope deposited to a thickness of 16 μg/cm^2 on a thick nickel backing, and supplied by AERE, Harwell, was bombarded by a deuteron beam from the Melbourne 1 MeV electrostatic generator at energies of 700, 600, 490, and 390 keV. Charged particles resulting from this bombardment were detected with an ORTEC model SBC J050–60 silicon surface barrier detector, over the front of which aluminium foil of thickness 10 μm was mounted to stop the very high flux of elastically scattered deuterons. The detector was mounted at a distance of 13·2 cm from the target and was free to rotate between all angles up to 165°. The solid angle subtended by the counter at the target was $2 \cdot 8 \times 10^{-3}$ sr. The target was oriented such that the beam made a glancing angle of 37·5° with it, and particles were observed at intervals of 15° in directions from 75° to 165°. The particle groups, with their identifications, are shown in Figure 1.

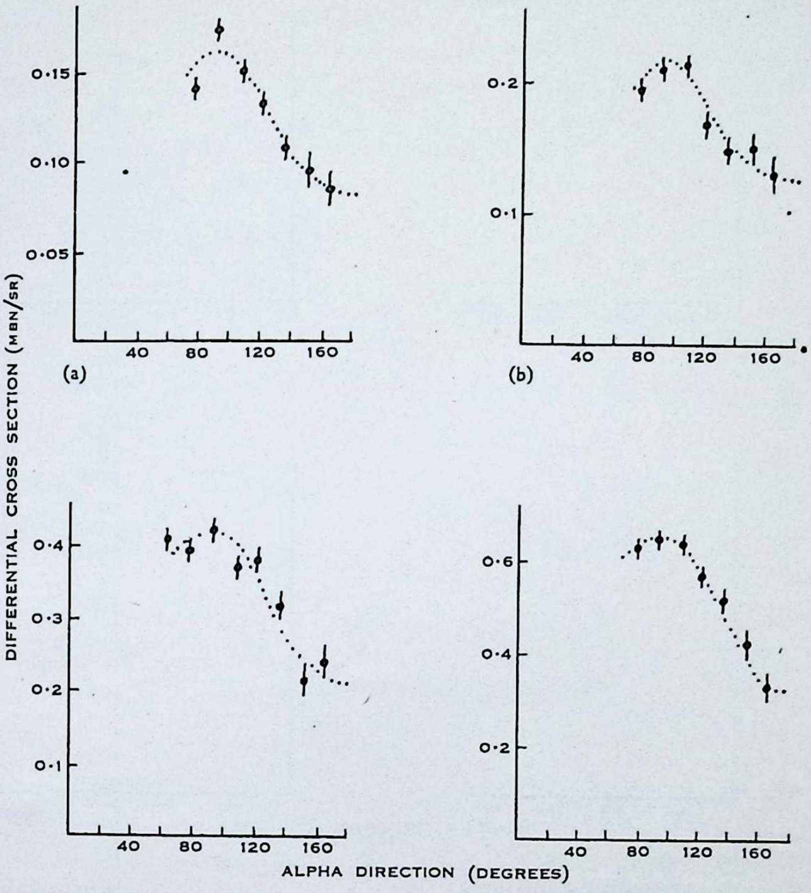

Fig. 3.—Angular distributions of the alpha group, α_2, leading to the 2·43 MeV state of ^{9}Be. Deuteron bombarding energy (*a*) 390 keV, (*b*) 490 keV, (*c*) 600 keV, (*d*) 700 keV.

Angular distributions were extracted for the α-particle groups leading to the ground state and 2·43 MeV state of ^{9}Be, and for the proton group leading to the ground state of ^{12}B. These angular distributions are shown in Figures 2, 3, and 4. Figure 5 shows the three excitation functions measured in the 90° direction normalized to the same value at 550 keV.

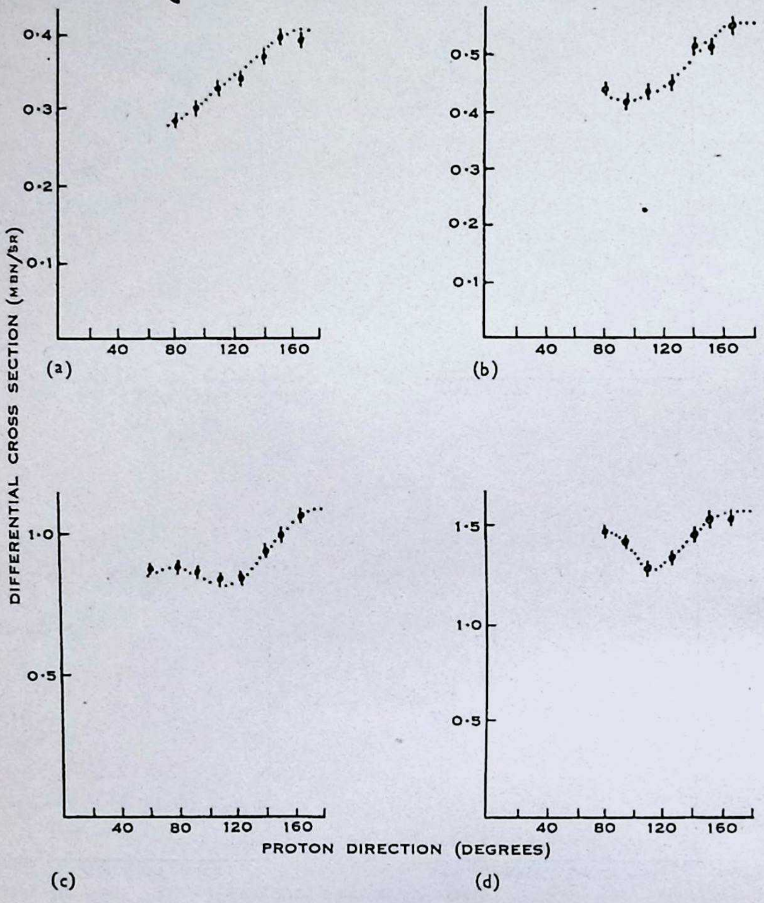

Fig. 4.—Angular distributions of the ground state proton group, p_0. Deuteron bombarding energy (*a*) 390 keV, (*b*) 490 keV, (*c*) 600 keV, (*d*) 700 keV.

Discussion

The angular distributions for the p_0 group have very much the same shape over the whole range of bombarding energies. The backward peaking persists in all the distributions measured, the main change over this energy range being a steady rise in the relative count rate around 90°. This insensitivity of the shape of an asymmetric angular distribution to energy is strongly suggestive of direct interaction. Further, the shape and its variation are consistent with the observations of Robson and Weigold (1963) at energies of 700 keV and 1·02 MeV, which they have successfully described with distorted wave direct interaction theory.

With the angular distributions for the α_0 group, on the other hand, the degree of anisotropy changes rapidly, suggesting a compound nucleus type interaction.

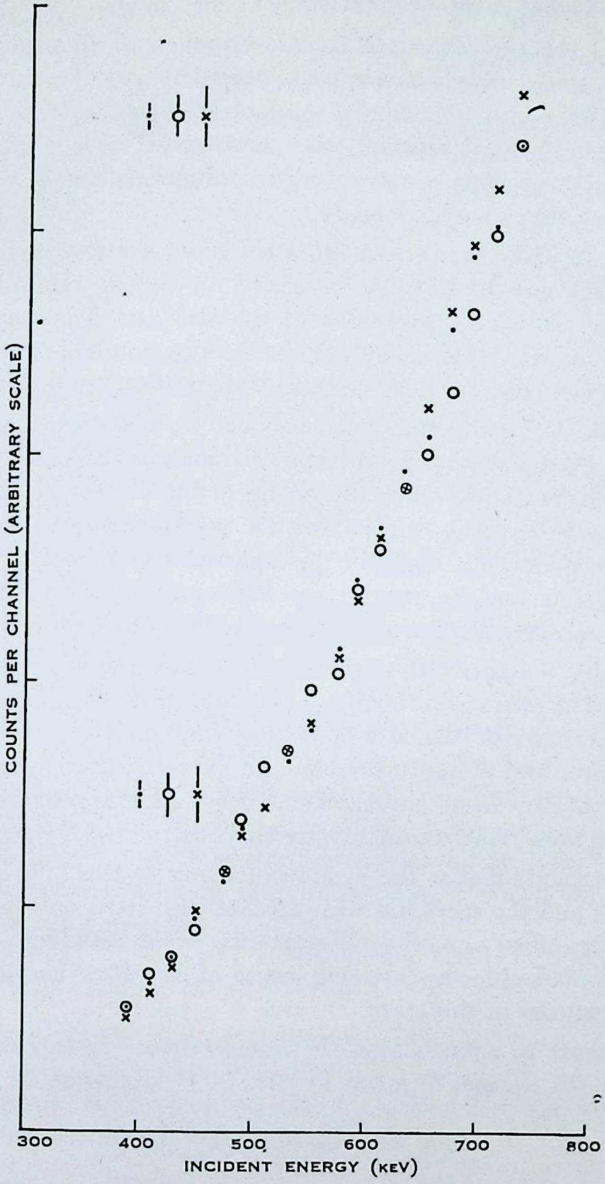

Fig. 5.—Excitation functions for the p_0 (•), α_0 (○), and α_2 (×) groups. The three curves of best fit have been normalized to the same value at a bombarding energy of 550 keV.

This group was also observed by Robson and Weigold at 700 keV and 1·02 MeV, and the trend in shape observed here is continued in their measurements, which were taken over an almost full range of angles and show symmetry about 90°.

The shape of the α_2 angular distributions is, to the accuracy of the measurements, virtually unchanged over the whole energy range from 390 to 700 keV. This is indicative of a direct interaction mechanism, particularly in view of the rapid change of shape observed for the α_0 group over the same energy range.

The fact that the one excitation function applied to all three particle groups observed is strange, since the various reactions proceed by way of different mechanisms. The explanation of this probably lies in the fact that the bombarding energy is so very low, and both types of reaction will be governed to a great extent by the Coulomb barrier, and the sharply rising excitation function simply reflects increasing barrier penetration with increasing energy.

From Figures 2 and 4 it is evident that the cross section for compound nucleus formation is certainly one-third of that for the (d, p_0) reaction, and yet the compound nucleus apparently plays no part in the (d, p_0) reaction. The three most obvious factors that might govern this behaviour are energy available for the compound nucleus to emit a particular particle, nuclear configuration, and angular momentum.

The fact that the compound nucleus, once formed, appears to decay overwhelmingly by alpha emission rather than proton emission can probably be accounted for on energy considerations. Thus the energy available for α_0 emission from the compound nucleus is 8·0 MeV whilst that for proton emission is only 1·1 MeV. When Coulomb barriers of 2·2 MeV for the α-particles and 1·6 MeV for the protons, together with possible angular momentum barriers, are taken into account, it is clear that energy considerations favour the alpha emission quite strongly.

We are unable to explain the apparent dominance of direct interaction in the (d, α_2) reaction and its absence in the (d, α_0) reaction. Both shell model and rotational model attempts to describe ^{9}Be ascribe similar configurations to the ground state and 2·43 MeV state, and it would therefore be expected that both reactions would proceed by way of the same mechanism. There also appear to be no angular momentum restrictions that would favour the observed difference of mechanism.

Finally, we mention that the α_1 group leading to the 1·75 MeV state in ^{9}Be was also observed and the spectrum was satisfactorily fitted on the assumption that the state can be described as an S-wave scattering event between a neutron and ^{8}Be. The best fit was obtained for a scattering length of 20×10^{-13} cm, in agreement with most other observations of this state.

It is a pleasure to acknowledge the interest taken in this work by Professor D. E. Caro, and the assistance given by Mr. G. P. Johnston in carrying out the measurements.

References

Butler, S. T. (1957).—"Nuclear Stripping Reactions." (Horwitz: Sydney.)
El Nadi, M. (1957).—*Proc. Phys. Soc.* A **70**: 62.
Glendenning, N. K. (1962).—*Nucl. Phys.* **29**: 109.
Newns, H. C. (1960).—*Proc. Phys. Soc.* **76**: 489.
Robson, D. (1961).—*Nucl. Phys.* **22**: 34.
Robson, B., and Weigold, E. (1963).—*Nucl. Phys.* **46**: 321.
Tobocman, W. (1959).—*Phys. Rev.* **115**: 98.

ON BOWEN'S HYPOTHESIS*

By T. R. VISVANATHAN†

Bowen (1953) examined daily rainfall at Sydney for January for the years 1859–1940, and found exceptional peaks to occur on the 12th and 22nd days of that month. He extended his investigations to other months and other stations, and concluded that there is a marked tendency for heavy falls of rain to occur on certain dates rather than on others and the pattern to be repeated year after year. He argued that if the feature is noticed in rainfall at a large number of stations over the globe the influence should be extraterrestrial. He put forward the now well-known hypothesis that on some calendar dates the Earth crosses a meteoric stream, and the meteoric dust entering the top of the atmosphere reaches the troposphere about 30 days later, to induce heavy rainfall, the influx of meteoric dust being supposed to provide the necessary condensation nuclei. He further strengthened his hypothesis by showing that such other occurrences as concentration of freezing nuclei counts, cirrus clouds, noctilucent clouds, and the dates on which snow first covered the ground at Tokyo all showed a tendency for maxima to fall on the preferred dates of singularity in rainfall.

During the last decade a number of papers have appeared, some supporting but others criticizing Bowen's hypothesis. Strangely enough the argument against Bowen's hypothesis appears to have come from Bowen himself. Adderley and Bowen (1962) showed that the heaviest falls in New Zealand occurred on certain days of the lunar month, notably about three days after the Full Moon and New Moon. Apparently heavy rainfall cannot have a preference for a calendar date as well as for a lunar day, since the event of New Moon can occur on any calendar date. Thus, there appears to be a contradiction between Bowen's meteor hypothesis and his lunar hypothesis to explain rainfall singularities. The purpose of the present paper is to reconcile the apparent contradiction.

Data

Sydney rainfall for January for the years 1861–1960 has been given by O'Mahony (1962). Of these data, only the rainfall pertaining to the period 1870–1960 was examined, as the decimal ephemeris of the Sun and the Moon (Carpenter 1962) gives the synodic decimals from 1870 onwards only.

Analysis of the Data and Discussion

The angular difference between the longitudes of the Sun and the Moon gives the phase of the Moon in degrees, and if the phase angle is divided by 3·6 the resultant number is the synodic decimal. The synodic decimal for each day is given in the

---

* Manuscript received January 4, 1965.

† Meteorological Office, New Delhi, India; present address: U.S. Weather Bureau, Washington 25 D.C., U.S.A.

Aust. J. Phys., 1965, 18, 497–501

ephemeris of Carpenter (1962). In the present analysis, the 100 synodic decimals are grouped into 30 class intervals to correspond nearly to 30 days of the lunar month. The rainfall amounts falling in each class were added and are shown against the class. Successive 3-lunar-day totals were then made, which gives 10-unit moving totals, and these totals are shown against the central lunar day. This procedure is set out in Table 1.

TABLE 1

ANALYTICAL PROCEDURE

Synodic Decimal Class	Corresponding Lunar Day	10-unit Moving Totals of Synodic Decimals	3-lunar-day Totals*	Shown against Lunar Day:
99, 00, 01	0 NM†	96 to 15	29, 0, 1	0 NM
02, 03, 04, 05	1	99 to 08	0, 1, 2	1
06, 07, 08	2	02 to 11	1, 2, 3	2
09, 10, 11	3	06 to 15	2, 3, 4	3
12, 13, 14, 15	4	09 to 18	3, 4, 5	4
16, 17, 18	5	12 to 21	4, 5, 6	5
19, 20, 21	6	16 to 25	5, 6, 7	6
22, 23, 24, 25	7	19 to 28	6, 7, 8	7
26, 27, 28	8	22 to 31	7, 8, 9	8
29, 30, 31	9	26 to 35	8, 9, 10	9
etc.		etc.	etc.	

* Although the class intervals of individual lunar days are unequal, 3-lunar-day moving totals have all equal class intervals of 10 units.

† NM = New Moon.

Ten-unit moving totals of rainfall for each calendar date are shown in Figure 1, where the horizontal axis represents the calendar dates and the vertical axis the lunar days. The entry 126 against the calendar date January 23 shows that a total of 12·6 in. of rain fell on those days having a calendar date January 23 and synodic decimal between 92 and 01. For the sake of clarity the amounts of rainfall less than 1·0 in. have been left out of the figure.

The rainfall distribution during the synodic month is shown in Figures 2(*a*)–2(*d*), while the total daily rainfall for days in January (1870–1960) is given in Figure 2(*e*). Figures 1 and 2 reveal the following features.

(1) The two rainfall peaks are near the 12th and 22nd, as pointed out by Bowen.

(2) The maximum rainfall on these two dates, 12th and 22nd, has occurred only when these dates happened to be near New Moon or Full Moon.

(3) From Figures 2(*a*)–2(*d*) it is seen that the peaks occurring near New Moon and Full Moon are the main feature of rainfall distribution during the synodic month.

(4) There is no support for the contention that "year after year" on specified dates heavy rainfall occurs. On the other hand it is seen that very little rain has fallen on those days when the preferred dates 12th and 22nd happened to be near the First Quarter or the Last Quarter.

Conclusion

There seems to be supporting evidence to show that Bowen's meteor hypothesis is not inconsistent with the lunar hypothesis. Heavy rainfall appears to prefer not only calendar dates but lunar days as well, and the heaviest rainfall is likely to occur when these two factors combine. The physical explanation adduced by Bowen to explain rainfall on the 12th and 22nd is plausible, though evidence presented herein goes against his statement that the rainfall is repeated "year after year" on the meteor dates. This paper seeks to revive an issue which appears to have been almost settled: "Is the influence of meteoric dust on heavy rainfall, or increased rainfall activity, real?" The author is not unaware of the serious difficulties into which Bowen's meteor hypothesis enters, and the arguments for and against it by several writers. Still, the evidence presented by Bowen in support of his meteor hypothesis is not such as can be satisfactorily ignored. However, caution is necessary in extending the conclusions based on the analysis of rainfall of a month or a place to other periods and other places.

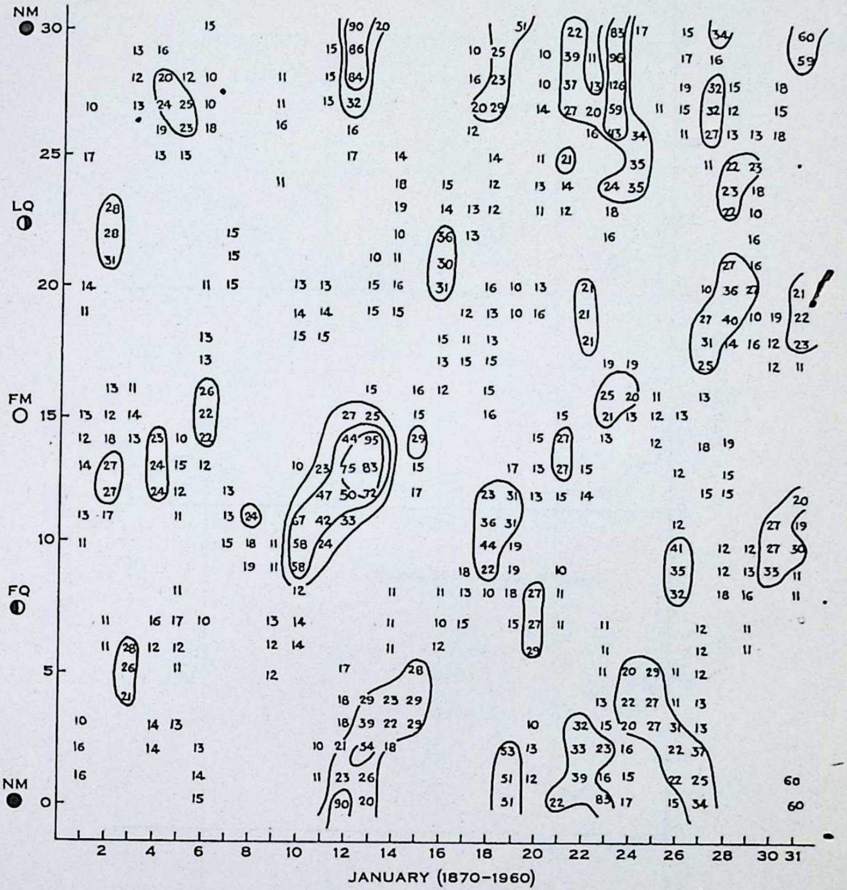

Fig. 1.—Sydney rainfall for January (1870–1960) analysed by calendar date and lunar day.

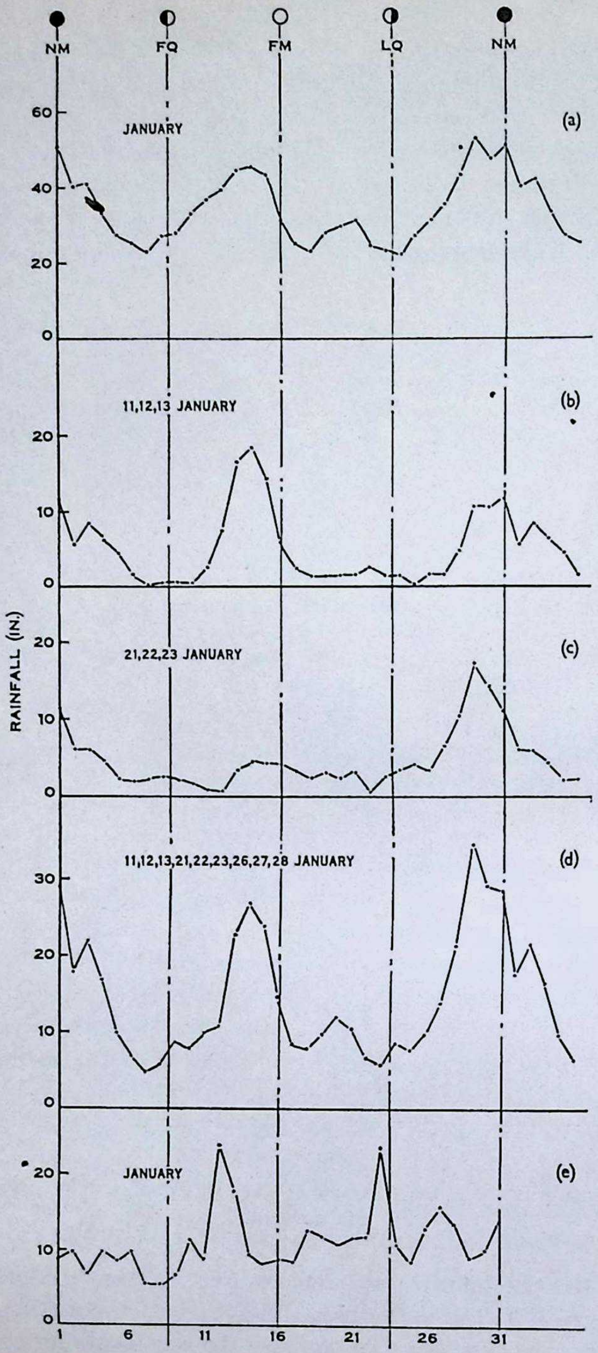

Fig. 2.—Rainfall at Sydney in January (1870–1960). (*a*) Ten-unit moving totals analysed according to lunar month; (*b*) ten-unit moving totals for the calendar dates 11, 12, and 13, analysed according to lunar month; (*c*) ten-unit moving totals for the calendar dates 21, 22, and 23, analysed according to lunar month; (*d*) ten-unit moving totals for the calendar dates 11, 12, 13, 21, 22, 23, 26, 27, and 28, analysed according to lunar month; (*e*) total daily rainfall.

References

ADDERLEY, E. E., and BOWEN, E. G. (1962).—*Science* **137**: 749.

BOWEN, E. G. (1953).—*Aust. J. Phys.* **6**: 490–7.

CARPENTER, T. H. (1962).—"Decimal Ephemeris of the Sun and Moon 1870–1962." (U.S. Weath. Bur.: Washington.)

O'MAHONY, G. (1962).—*Aust. J. Phys.* **15**: 301–23.

REMARKS ON THE PAPER BY T. R. VISVANATHAN ENTITLED "ON BOWEN'S HYPOTHESIS"*

By G. W. Brier†

Visvanathan's paper (1965) has reopened the controversial question of rainfall calendaricities that has stimulated so much research and discussion since the paper by Bowen (1953). Visvanathan's suggestion that anomalous rainfall at Sydney results from the joint effects associated with the lunar month and the calendar date is an interesting one, and depends upon the conclusion that the correlations between the curves of his Figures 2(*b*), 2(*c*), and 2(*d*) are significant. Although these curves are based on data that have been smoothed, thus introducing serial correlation into them, an appropriate significance test can be made which does in fact show that the conclusions are valid. However, his findings led the writer to examine the Sydney data from another point of view, and this investigation led to results giving a different interpretation from that given by Visvanathan.

Evidence presented by Brier (1965) shows that the precipitation variations in the United States are related to the lunar tidal forces, which depend upon the synodic cycle, i.e. the time from one New Moon to the next. In addition, these forces depend upon the anomalistic cycle (from perigee to perigee) and upon the nodical cycle (the period between ascending nodal passages, i.e. crossing of the ecliptic from south to north). Visvanathan's analysis considers the lunar synodic cycle but, since the anomalistic and nodical cycles might show some influence, it seemed reasonable to determine whether or not the rainfall data were random in respect to these cycles. The data chosen were all cases of rainfall exceeding 1 in. at Sydney on January 12, 13, 14, 21, 22, and 23 during the period 1859–1952, the record available at the time this investigation began. The dates January 12–14 and January 21–23 were chosen because these periods show the largest and most pronounced peaks both in Bowen's curves and in the independent analysis of O'Mahony (1962). Furthermore, they are at least 7 days apart, helping to assure independence of the data in the statistical analysis. Further independence was assured by choosing only one day from each of the 3-day periods. The selection of rainfall exceeding 1 in. was based on several reasons. First, the heavy rainfalls contribute most to the variation in the daily averages, and secondly, the heavy rainfalls are of potential physical, meteorological, and economic importance. Another reason follows from the analysis by Brier (1965), which shows the advantage of using extreme values to detect the influence of periodic factors.

There were 22 cases of rainfall greater than 1 in., and the dates and amounts are shown in Table 1. The table also shows the rank (1–22), as well as the values of the synodic, anomalistic, and nodical cycles expressed in terms of 100 decimal classes. The data in this table were plotted on polar diagrams to test whether there was any tendency for the points to distribute in a non-random fashion; the highest values should be of particular interest. Using a test for the consistency of phase on a polar

---

* Manuscript received March 22, 1965.

† U.S. Weather Bureau, Washington 25 D.C., U.S.A.

Aust. J. Phys., 1965, 18, 503–9

diagram, the synodic cycle (Fig. 1) showed a distribution which departed from chance with the highest significance ($p < 0\cdot01$). For example, considering the 12 highest rainfalls, all of which were greater than 1½ in., the probability is 0·01 that the largest "gap" on the circle will be equal to or greater than 171°. The observed gap as shown is over 180°, and in fact the first 16 highest-ranking rainfalls are distributed on the syzygy half of the circle. In addition, although this analysis was not concerned with rainfall during the other days of the month, it is interesting to note that the greatest extreme was on January 31, 1938, the day of a New Moon. The two next highest values, both over 4 in., had an average position near point 11 on Figure 1, between 2 and 3 days before syzygy.* The nodical cycle (Fig. 2) showed the next greatest departure, also highly significant, while a less pronounced but still highly significant departure from chance was found for the anomalistic cycle (Fig. 3). In each figure, the phase and amplitude rainfall amount are plotted as well as the rank for the amounts exceeding 1½ in. Upon reference first to Figure 1, it is seen that there are only four cases falling in the left half of the circle, and these are the smaller rainfalls. Obviously, there is a preference in respect to a New or Full Moon, or a few days before. Figure 2 shows a preference in respect to the time of the cycle when the Moon is going from south to

TABLE 1

DATES OF RAINFALL EXCEEDING 1 IN. AT SYDNEY BETWEEN JANUARY 12–14 AND JANUARY 21–23 DURING THE PERIOD 1859–1952

Rank	Rainfall (in.)	Date	Decimal Class		
			Synodic	Nodical	Anomalistic
1	7·08	Jan. 13, 1911	0·45	0·13	0·08
2	6·53	12, 1918	0·98	0·04	0·83
3	3·75	22, 1863	0·11	0·24	0·19
4	3·72	23, 1933	0·91	0·81	0·08
5	3·06	22, 1901	0·07	0·24	0·86
6	2·80	13, 1872	0·11	0·70	0·16
7	2·51	12, 1873	0·46	0·11	0·40
8	2·13	23, 1895	0·93	0·78	0·40
9	1·94	21, 1887	0·92	0·34	0·29
10	1·70	12, 1883	0·12	0·30	0·92
11	1·67	12, 1892	0·44	0·11	0·23
12	1·56	12, 1885	0·88	0·17	0·46
13	1·56	21, 1879	0·97	0·96	0·24
14	1·34	21, 1924	0·48	0·89	0·67
15	1·31	21, 1951	0·45	0·31	0·58
16	1·29	12, 1910	0·04	0·66	0·78
17	1·15	21, 1922	0·79	0·09	0·21
18	1·15	22, 1927	0·64	0·21	0·49
19	1·09	14, 1920	0·80	0·97	0·42
20	1·05	23, 1893	0·19	0·94	0·89
21	1·02	13, 1922	0·50	0·77	0·89
22	1·02	14, 1948	0·10	0·77	0·55

* Data for more recent years are given by O'Mahony (1962). The date of highest rainfall is January 23, 1955, synodic decimal 0·98 or one half-day before New Moon.

north. The 5 highest rainfalls are distributed in this half of the circle, and only 5 of the 22 cases are in the opposite half. In Figure 3, it is seen that ranks numbered 1–6

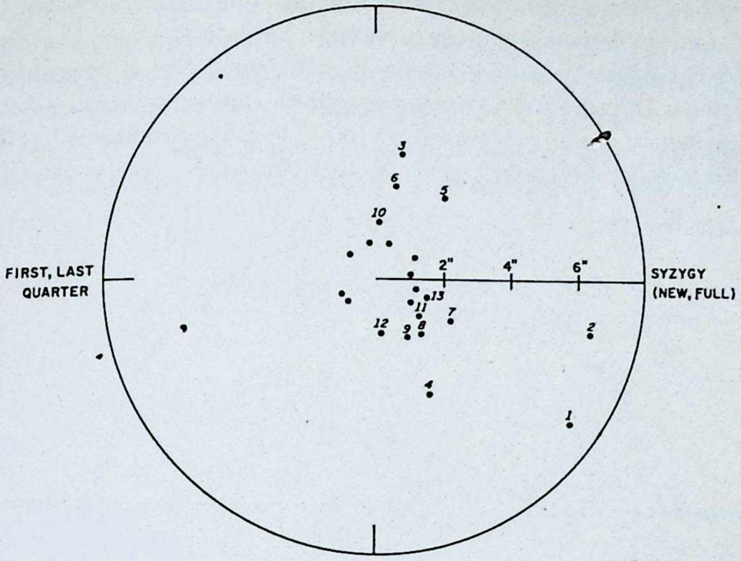

Fig. 1.—Excessive rainfalls at Sydney plotted on a polar diagram to show amplitude and phase with respect to the lunar synodic cycle. Numbers plotted next to the points are the ranks for the rainfalls exceeding 1½ in.

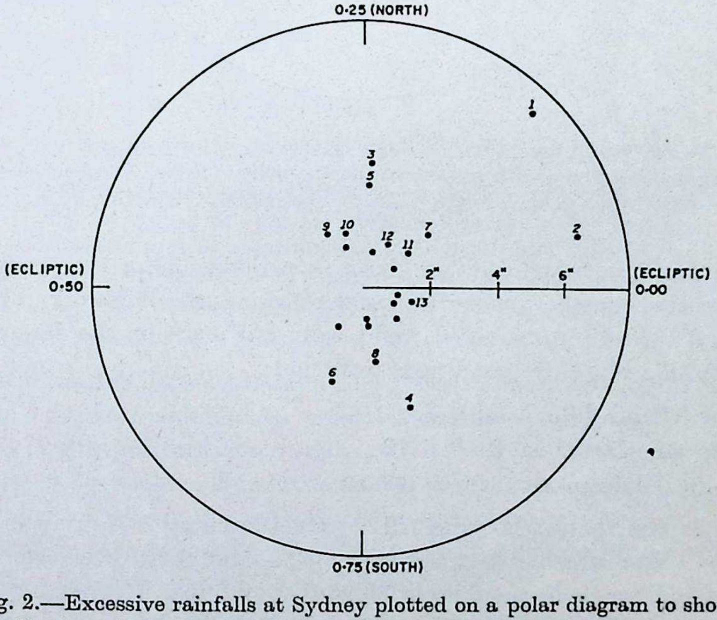

Fig. 2.—Excessive rainfalls at Sydney plotted on a polar diagram to show amplitude and phase with respect to the nodical cycle. Numbers plotted next to the points are the ranks for the rainfalls exceeding 1½ in.

fall nearer perigee than apogee. This is expected since the tidal forces are greatest near perigee.

The foregoing suggests that the necessary conditions for extreme rainfall are related to the tidal influences as they are reflected in the synodic cycle of 29·53 days, the anomalistic cycle of 27·55 days, and the nodical cycle of 27·21 days. Once a particular combination of these cycles occurs, it is a relatively long time before these conditions, or conditions close to these, recur. One such period is about 27 months, and another one is 18 years and 11 days, the well-known Saros period. It is enlightening to inquire whether a given set of "favourable tidal conditions" (FTC) will be distributed uniformly with respect to some other time scale, say the calendar year. In particular, it might be asked whether, during a period of 50 or 100 years, the events FTC have occurred equally frequently on each calendar date of January. To determine this the period 1900–49 was selected, and a tally was made on the January calendar whenever the following three conditions were met:

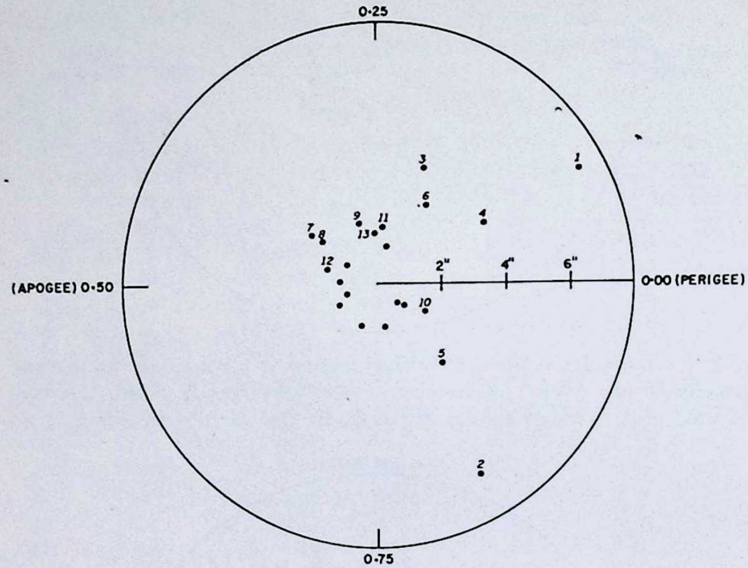

Fig. 3.—Excessive rainfalls at Sydney plotted on a polar diagram to show amplitude and phase with respect to the anomalistic cycle. Numbers plotted next to the points are the ranks for the rainfalls exceeding $1\frac{1}{2}$ in.

(i) phase 0·35–0·45, 0·85–0·95;
(ii) anomalistic decimal 0·90–0·10;
(iii) nodical decimal 0·40–0·60, 0·90–0·10.

The results showed that eight cases fell between January 1–5, nine cases between January 11–14, five cases between January 20–22, and eight cases between January 30–February 3. There were no cases between these groups. The mean dates are January 3, 12, 21, and February 1. *These are the singularity dates* given by the various articles of Bowen, and shown in his world rainfall curve as published by Brier (1961).

The relation between the events of FTC and calendar date is illustrated in another way by Figure 4. On this chart the synodic decimal is plotted as a function of the anomalistic and nodical decimals for each January 13 from 1900 to 1949. A number with a line under it means the particular day was five classes or less from a New (0·00) or Full (0·50) Moon, and it is noticed that no underlined number occurs between anomalistic decimal classes 0·10 and 0·65. It is obvious that the numbers plotted in this figure are not uniformly or randomly distributed, but fall in a systematic pattern determined by the astronomical factors involved. Similar results would be obtained if other conditions were specified.

To complete this phase of the study, the remaining months of the year were examined in the same way. The results are shown in Table 2. The mean date, shown in italics in each group, was selected as a key day for use in a superposed epoch analysis,

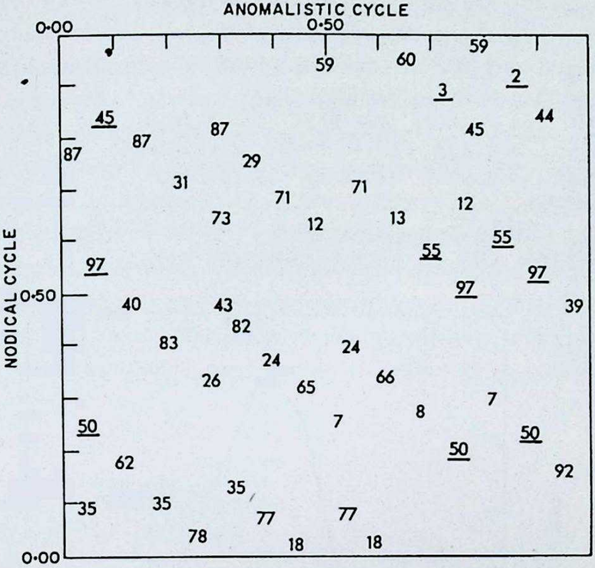

Fig. 4.—Relationship between the synodic, anomalistic, and nodical cycles for January 13 for the period 1900–49. The numbers plotted are the synodic decimals, and underlined numbers represent cases where the synodic decimal is within 5 classes of a New or Full Moon.

using the world rainfall data summarized by Bowen. Averages were obtained for the key dates and 5 days on each side, the results being shown in Figure 5. The amplitude for January is larger than for the remainder of the year, but this may be due in part to the smaller size of the sample. Furthermore, the Earth is at perihelion during January, and an amplification of any tidal effects would be expected at this time. This may be the reason that the January data gave the greatest evidence of departure from randomness in the analysis reported by O'Mahony (1962).

An examination of the tidal cycles and of the ephemeris reveals that the dates shown in Table 2 are "slipping" at the rate of about 9 days every 102 years. These are completely predictable, of course, and for the half-century 1950–99 the dates will average about 4½ days later than those shown in Table 2. However, it would take 400 or 500 years, or more, for things to average out in such a way that every calendar date would have a reasonable chance of being represented by all significant combinations of the three tidal cycles.

TABLE 2

RANGES OF DATES UPON WHICH CERTAIN "FAVOURABLE TIDAL CONDITIONS" OCCURRED DURING THE PERIOD 1900–49

Jan. : 1–*3*–5 [8],* 11–*12*–14 [9], 20–*21*–22 [5], 30–*1*–3 [8]
Feb. : 9–*11*–12 [6], 18–*20*–22 [8], 28–*1*–4 [11]
Mar. : 10–*11*–12 [6], 19–*20*–21 [8], 28–*30*–1 [5]
Apr. : 8–*9*–11 [2], 17–*18*–19 [4], 28–*29*–30 [3]
May : 6–*8*–10 [6], *16*–17 [2], 27–*28*–29 [5]
June : 4–*5*–7 [3], 14–*15*–16 [3], 23–*25*–27 [4]
July : 4–*5*–6 [3], 13–*14*–16 [4], 22–*24*–26 [6]
Aug. : *1*–2 [2], 11–*12*–14 [4], 19–*21*–23 [4], 30–*31*–1 [3]
Sept. : 7–*9*–12 [5], *19* [2], *29* [2]
Oct. : 4–*8*–11 [7], *17*–18 [2], 27–*28*–29 [4]
Nov. : 4–*6*–8 [5], 15–*16*–17 [3], 23–*25*–27 [6]
Dec. : 3–*4*–5 [4], *13*–14 [2], 21–*23*–26 [5]

* The mean date is given in italics, and the number of events is shown in brackets after the dates.

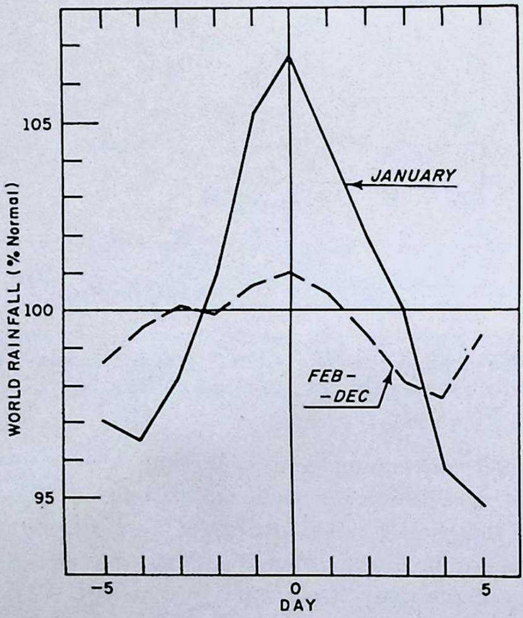

Fig. 5.—Results of superposed epoch analysis, showing average rainfall for 5 days before and after key dates shown in Table 2. Rainfall data used were worldwide averages prepared by Bowen and published by Brier (1961).

Conclusions

It now seems possible to conclude the following, from the analysis of Visvanathan and the results presented here.

(1) There is a highly significant lunar component in the Sydney records of excessive rainfall for days in January over the past 100 years.

(2) When a period as short as 50 or 100 years is considered, particular conditions that are determined by the three lunar tidal cycles do not occur uniformly throughout the year, but tend to occur in groups that are about 10 days apart.

These extreme rainfall data show beyond any reasonable doubt that Bowen (1953) was essentially correct in concluding that the January rainfall data for Sydney showed significant departures from randomness. Some independent supporting evidence was provided by the analysis of O'Mahony (1962) of the heavy rainfalls for Rockhampton, Qld., but some other stations failed to show significant departures from randomness. Some of Bowen's critics have claimed that the departures from expectation were most likely spurious and due to the influence of a relatively few large rainfalls. Actually, these extreme rainfall occurrences demonstrate that significant departures from randomness do exist, but that these anomalies are closely associated with the lunar calendar, rather than with the calendar date. However, in fairness to the pioneering work of these earlier investigators, it should be emphasized that there was at that time no reason to suspect any lunar influence on precipitation or that the solilunar tidal cycles might have any appreciable aliasing effect with calendar date. These effects must be considered in testing for any possible calendaricities, and although the foregoing points do not rule out the possible influence of meteoritic dust on rainfall, they do mean that such an hypothesis is not necessary to explain any apparent tendency for particular meteorological events to occur on some calendar dates more than on others.

References

Bowen, E. G. (1953).—*Aust. J. Phys.* **6**: 490–7.
Brier, G. W. (1961).—*J. Met.* **13**: 142–51.
Brier, G. W. (1965).—*Mon. Weath. Rev. U.S. Dept. Agric.* **93**: 93–100.
O'Mahony, G. (1962).—*Aust. J. Phys.* **15**: 301–26.
Visvanathan, T. R. (1965).—*Aust. J. Phys.* **18**: 497–501.

7791

A SYMMETRIC DECOMPOSITION OF THE TWO-ELECTRON WAVE EQUATION FOR FINITE NUCLEAR MASS

By T. M. Kalotas*

[*Manuscript received June 25, 1965*]

Summary

A complete classification of the state of two-electron atoms is given in terms of a set of symmetrized Euler-angle functions, and the matrix of the kinetic energy derived for this choice of states. For a state of given L, π, P_S the non-relativistic Schrödinger equation reduces to a finite set of coupled equations in the internal coordinates r_1, r_2, r_{12}; these equations are given for arbitrary L, π, P_S. The results apply to atomic two-electron systems with nuclei of finite mass, and more generally to any non-relativistic three-body system in which two of the particles have equal mass.

I. Introduction

Recently (Kalotas and Delves 1964) a complete classification of the states of the three-nucleon system in terms of a set of symmetrized spin-isospin Euler-angle functions Y_i has been given. Such a classification has the advantage that for a state of given total angular momentum J, parity π, and neutron excess T_z, the wave function ψ has the form

$$\psi^{J,\pi,T_z} = \sum_i f_i(r_{12}, r_{23}, r_{31}) Y_i. \tag{1}$$

The sum in (1) is *finite* and so the non-relativistic Schrodinger equation for ψ in the centre-of-mass system, reduces from a six-dimensional to a *finite* set of three-dimensional coupled equations, with consequent overwhelming saving in labour.

A similar classification is possible for the two-electron system, which in general aspects is simpler. The non-relativistic Hamiltonian for two electrons in the Coulomb field of a nucleus is spin independent; hence we need not consider the electron spins. We give then a complete symmetric classification of the Euler-angle states of the two electrons, together with the resulting set of differential equations for the internal functions f_i of equation (1).

There is no unique choice of Euler-angle functions; however, it is desirable that any choice made should take note of the exact constants of motion for the problem. These constants of motion include

(i) the orbital angular momentum L and projection m_L,

(ii) the parity π,

(iii) the symmetry P_S of the space state under permutation of the two electrons. Here a symmetric space function is associated with a singlet (para) spin function and an antisymmetric space function with a triplet (ortho) spin function.

---

* Physics Laboratory, University of Sussex, Falmer, Brighton, Sussex, England.

Aust. J. Phys., 1965, 18, 511–20

The standard classification of two-electron states is due to Breit (1930), who wrote an expression of the form (1) for P-states. However, his choice of Euler angles was quite unsymmetrical, making the construction of eigenfunctions with the correct symmetry very difficult. With our choice of Euler angles each term in (1) will have the appropriate symmetry and we shall therefore be able to deal with the state of general (L, π, P_S). Recently, Bhatia and Temkin (1964) have made an analysis similar to ours but assumed the nucleus to be fixed. Although their method of construction of the Euler-angle functions is different, the actual Euler angles they use are only trivially different and our results reduce to theirs in the limit of infinite nuclear mass.

In the following section we define our choice of Euler angles and construct a set of angular eigenfunctions Y_i of L^2 and L_Z with appropriate behaviour under the operations of time reversal, parity, and particle permutation. In Section III we give the kinetic energy operator in terms of the triangle Euler-angle coordinates and calculate the internal kinetic energy matrix.

II. THE CHOICE OF BODY AXES AND THE SYMMETRIZED EULER-ANGLE FUNCTIONS

The configuration of two-electron atoms in the centre-of-mass system, is determined by the six coordinates in $\mathbf{r}_1$, $\mathbf{r}_2$ representing the electron positions relative to the nucleus, or alternatively by the triangle Euler-angle coordinates r_1, r_2, r_{12}, α, β, γ. These coordinates are defined by

$$r_1 = |\mathbf{r}_1|, \qquad r_2 = |\mathbf{r}_2|, \qquad r_{12} = |\mathbf{r}_1 - \mathbf{r}_2|,$$

while we define the Euler angles α, β, γ as in Derrick and Blatt (1958); that is, a set of body vectors $\mathbf{b}_1$, $\mathbf{b}_2$ giving the positions of the electrons relative to body axes, are related to the vectors $\mathbf{r}_1$, $\mathbf{r}_2$ in the space frame by

$$\mathbf{b}_k = A(\alpha)B(\beta)C(\gamma)\mathbf{r}_k; \qquad k = 1, 2,$$

where A, B, C are elementary rotation matrices given by

$$A(\alpha) = \begin{bmatrix} \cos\alpha & \sin\alpha & . \\ -\sin\alpha & \cos\alpha & . \\ . & . & 1 \end{bmatrix}, \qquad B(\beta) = \begin{bmatrix} 1 & . & . \\ . & \cos\beta & \sin\beta \\ . & -\sin\beta & \cos\beta \end{bmatrix},$$

$$C(\gamma) = A(\gamma).$$

The criteria for a useful set of body axes are:

- (a) simple behaviour of the angular functions Y_i of (1) under operations of parity and electron exchange,
- (b) simple form for the kinetic energy.

We shall choose the body axes in the following way.

- (i) The two electrons lie in the body x–y plane with the nucleus at the origin.
- (ii) The positive body x-axis bisects the smaller angle θ_{12} subtended at the nucleus by the two electrons.

(iii) Particle numbering is such that a rotation from 1 to 2 is clockwise when looking along the positive body z-axis.

A typical triangle body axis configuration is shown in Figure 1.

The above specification of coordinates is unique except when the nucleus and the two electrons lie in a straight line, in which case the body axes and hence the Euler angles remain undefined. The singular region of phase space requires special care in calculations involving the above coordinates. As in the three-nucleon case, this imposes restrictions on the form of the internal functions f_i in this region; these restrictions will be considered in later work.

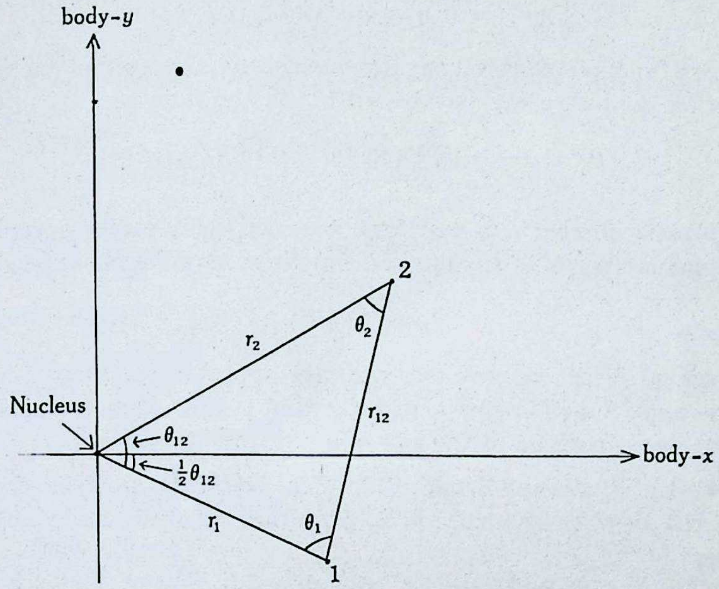

Fig. 1.—A typical configuration showing the position of the body axes.

We now proceed, as in Kalotas and Delves (1964) to construct a set of symmetrized Euler-angle functions of given angular momentum L and z component m_L. Explicitly we define the function

$$Y^L_{m_L}(P_E,|\mu|,(\pi)) = \mathrm{i}^{|\mu|+\bar{P}_E}\{(2L+1)^{\frac{1}{2}}/4\pi\}\epsilon_{\mu,0}\times[D^L_{|\mu|,m_L}(\alpha,\beta,\gamma)+(-1)^{L+\bar{P}_E}D^L_{-|\mu|,m_L}(\alpha,\beta,\gamma)]. \tag{2}$$

Here the $D^L_{\kappa\nu}(\alpha,\beta,\gamma)$ are the representation coefficients of the three-dimensional rotation group appearing in Kalotas and Delves (1964). Further

$$\begin{aligned} \bar{P}_E &= 0, \qquad \text{if } P_E = \text{symmetric } (s), \\ &= 1, \qquad \text{if } P_E = \text{antisymmetric } (a), \\ \epsilon_{\mu,\nu} &= 1/\sqrt{(2^{\delta_{\mu,\nu}})}. \end{aligned}$$

π is a superfluous index denoting the parity and is $+\,(-)$ if μ is even (odd). Thus of the $2L+1$ functions Y_i of fixed L and m_L, $L+1$ (or L) are of even parity if L is even (or odd) and the remainder have odd parity.

The various functions Y_i are orthonormal, that is,

$$\int \mathrm{d(Euler)}\ Y^{L*}_{m_L}(P_E,|\mu|,(\pi))\,Y^{L'}_{m_L'}(P'_E,|\mu'|,(\pi')) = \delta_{L,L'}\,\delta_{m_L,m_L'}\,\delta_{|\mu|,|\mu'|}\,\delta_{P_E,P_E'},$$

and satisfy the time reversal reality condition

$$UY^L_{m_L}(P_E,|\mu|,(\pi)) = (-1)^{L-m_L}\,Y^L_{m_L}(P_E,|\mu|,(\pi)). \tag{3}$$

The functions are either symmetric or antisymmetric under interchange of the two electrons (the mixed representation is irrelevant to our case)

$$P_{12}Y^L_{m_L}(P_E,|\mu|,(\pi)) = (-1)^{\bar{P}_E}\,Y^L_{m_L}(P_E,|\mu|,(\pi)).$$

Hence any wave function of orbital angular momentum L, z component m_L, parity π, and permutation symmetry P_S, may be written in the form

$$\psi^L_{m_L}(P_S,\pi) = \sum_{P_E,|\mu|} f^L_{m_L}(P_R,|\mu|,(\pi))\,Y^L_{m_L}(P_E,|\mu|,(\pi)). \tag{4}$$

In the sum (4) the number μ is restricted to even (odd) values according as π is $+$ $(-)$. The symmetry P_R of the internal functions must be chosen so that

$$P_R \times P_E = P_S.$$

Hence the internal functions have the same (or opposite) symmetry as the corresponding Euler-angle functions for para (or ortho) states. Equation (4) constitutes our symmetric decomposition of the two-electron wave function.

In the work of Bhatia and Temkin (1964), the body axes are defined in a different way to ours but their Euler angles θ, ϕ, ψ are nevertheless closely related to our α, β, γ through

$$\alpha = \psi - \tfrac{1}{2}\pi; \qquad \beta = \theta; \qquad \gamma = \phi.$$

This leads to symmetrized angle functions that are very similar to our Y_i.

III. THE KINETIC ENERGY

For the situation corresponding to two electrons each of mass m and a nucleus of mass M, the kinetic energy operator in the centre-of-mass system may be written

$$T = -(\hbar^2/2\mu)(\nabla_1^2+\nabla_2^2) - (\hbar^2/M)\nabla_1 . \nabla_2. \tag{5}$$

Here μ is the reduced electron mass $mM/(m+M)$, while for $k = 1, 2$

$$\nabla_k \equiv \partial/\partial \mathbf{r}_k$$

We give here the form of the kinetic energy in triangle Euler-angle coordinates.

In the fixed nucleus approximation $M \to \infty$ and

$$T \to -(\hbar^2/2m)(\nabla_1^2+\nabla_2^2).$$

For energy calculations of the helium isoelectronic series it is reasonable to consider the mass polarization operator $-(\hbar^2/M)\nabla_1 . \nabla_2$ as a perturbation term. We shall treat this term exactly but for convenience deal separately with the two operators

$$T_0 \equiv (\nabla_1^2+\nabla_2^2),$$
$$T_{12} \equiv \nabla_1 . \nabla_2.$$

As the transformations are lengthy, we give only the final results. For convenience we give also the matrix elements of these operators defined by

$$\Omega_{ij} \equiv \int \mathrm{d(Euler)}\, Y_i^* \,\Omega Y_j, \tag{6}$$

where Ω is any operator in general. The essential results are given below.

(*a*) *The Transformed Operators* T$_0$, T$_{12}$

(i) We find that the operator T_0 takes the following form in triangle Euler-angle coordinates

$$T_0 = T_0^1+T_0^2+T_0^3+T_0^4,$$

where

$$T_0^1 = \frac{\partial^2}{\partial r_1^2}+\frac{\partial^2}{\partial r_2^2}+2\frac{\partial^2}{\partial r_{12}^2}+2\cos\theta_1\frac{\partial^2}{\partial r_1\,\partial r_{12}}+2\cos\theta_2\frac{\partial^2}{\partial r_2\,\partial r_{12}}+\frac{2}{r_1}\frac{\partial}{\partial r_1}+\frac{2}{r_2}\frac{\partial}{\partial r_2}+\frac{4}{r_{12}}\frac{\partial}{\partial r_{12}}, \tag{7}$$

$$T_0^2 = \frac{(r_1^2-r_2^2)\sin\theta_{12}}{r_1\,r_2\,r_{12}}\left(\frac{\partial}{\partial r_{12}}\right)\left(\frac{L_z^B}{-\mathrm{i}\hbar}\right), \tag{8}$$

$$T_0^3 = \frac{R^2\cos^2\tfrac{1}{2}\theta_{12}}{4\Delta^2}\left(\frac{L_x^B}{-\mathrm{i}\hbar}\right)^2+\frac{R^2\sin^2\tfrac{1}{2}\theta_{12}}{4\Delta^2}\left(\frac{L_y^B}{-\mathrm{i}\hbar}\right)^2+\frac{R^2}{4r_1^2\,r_2^2}\left(\frac{L_z^B}{-\mathrm{i}\hbar}\right)^2$$
$$+\frac{(r_2^2-r_1^2)}{4r_1\,r_2\,\Delta}\left\{\left(\frac{L_x^B}{-\mathrm{i}\hbar}\right)\left(\frac{L_y^B}{-\mathrm{i}\hbar}\right)+\left(\frac{L_y^B}{-\mathrm{i}\hbar}\right)\left(\frac{L_x^B}{-\mathrm{i}\hbar}\right)\right\}, \tag{9}$$

$$T_0^4 = \frac{(r_1^2-r_2^2)\cos\theta_{12}}{4r_1\,r_2\,\Delta}\left(\frac{L_z^B}{-\mathrm{i}\hbar}\right). \tag{10}$$

The components of the angular momentum operator $\mathbf{L}^B$ appearing in the above expressions, are discussed in the Appendix. We have also used the notation

$$R^2 \equiv r_1^2+r_2^2,$$
$$\Delta \equiv \text{triangle area} = \tfrac{1}{2}r_1\,r_2\sin\theta_{12},$$

while θ_1 and θ_2 are angles defined through Figure 1. T_0^1 is a pure *S*-state operator, while T_0^2, T_0^3, and T_0^4 contain angular derivatives and so give zero when applied to *S*-state functions.

(ii) Similarly we find that T_{12} takes the form

$$T_{12} = T_{12}^1+T_{12}^2+T_{12}^3,$$

where

$$T_{12}^1 = -\frac{2}{r_{12}}\frac{\partial}{\partial r_{12}}-\frac{\partial^2}{\partial r_{12}^2}-\cos\theta_1\frac{\partial^2}{\partial r_1\,\partial r_{12}}-\cos\theta_2\frac{\partial^2}{\partial r_2\,\partial r_{12}}+\cos\theta_{12}\frac{\partial^2}{\partial r_1\,\partial r_2}, \tag{11}$$

$$T_{12}^2 = \frac{\Delta}{r_1\,r_2}\left\{\frac{1}{r_1}\frac{\partial}{\partial r_2}-\frac{1}{r_2}\frac{\partial}{\partial r_1}+\frac{(r_2^2-r_1^2)}{r_1\,r_2\,r_{12}}\frac{\partial}{\partial r_{12}}\right\}\left(\frac{L_z^B}{-\mathrm{i}\hbar}\right), \tag{12}$$

$$T^3_{12} = \frac{\cos\theta_{12}}{4r_1r_2}\left(\frac{L^B_z}{-i\hbar}\right)^2 - \frac{r_1r_2}{16\Delta^2}\left\{\left(\frac{L^B_+}{-i\hbar}\right)^2 + \left(\frac{L^B_-}{-i\hbar}\right)^2\right\} - \frac{r_1r_2\cos\theta_{12}}{16\Delta^2}$$
$$\times\left\{\left(\frac{L^B_+}{-i\hbar}\right)\left(\frac{L^B_-}{-i\hbar}\right) + \left(\frac{L^B_-}{-i\hbar}\right)\left(\frac{L^B_+}{-i\hbar}\right)\right\}. \tag{13}$$

T^1_{12} is here the S-state part of T_{12}.

(b) *The Matrix Elements of* T_0 *and* T_{12}

As noted above, the orthogonality of the Euler-angle functions allows us to integrate out the Euler-angle dependence. We give here the reduced matrices of the operators T_0 and T_{12} as defined by equation (6).

(i) We let i, j stand for the groups of indices L, m_L, $|\mu|$, P_E and L, m_L, $|\mu'|$, P'_E respectively and calculate the matrix elements T^w_{0ij} for $w = 1, 2, 3, 4$. Since L^2 and L_z commute with the kinetic energy, L and m_L are taken the same in i and j. Thus we get

$$T_{0ij} = \sum_{w=1}^{4} T^w_{0ij},$$

with

$$T^1_{0ij} = \delta_{|\mu|,|\mu'|}\,\delta_{P_E,P_E'}\,T^1_0, \tag{14}$$

$$T^2_{0ij} = \delta_{|\mu|,|\mu'|}\,\delta_{P_E,\bar{P}_E'}\left\{(-1)^{\bar{\bar{P}}_E}|\mu|\frac{(r_1^2-r_2^2)\sin\theta_{12}}{r_1r_2r_{12}}\frac{\partial}{\partial r_{12}}\right\}, \tag{15}$$

$$T^3_{0ij} = \delta_{|\mu|,|\mu'|}\,\delta_{P_E,P_E'}\left\{\frac{R^2\{|\mu|^2-L(L+1)\}}{8\Delta^2} - \frac{R^2|\mu|^2}{4r_1^2r_2^2}\right\}$$
$$+\delta_{|\mu|,|\mu'|+2}\,\delta_{P_E,P_E'}\left\{\epsilon_{|\mu|,2}\,N_L(-|\mu|)\frac{R^2\cos\theta_{12}}{16\Delta^2}\right\}$$
$$+\delta_{|\mu|,|\mu'|-2}\,\delta_{P_E,P_E'}\left\{\epsilon_{\mu,0}\,N_L(|\mu|)\frac{R^2\cos\theta_{12}}{16\Delta^2}\right\}$$
$$+\delta_{|\mu|,2-|\mu'|}\,\delta_{P_E,P_E'}\left\{\epsilon_{\mu,0}\,\epsilon_{|\mu|,2}(-1)^{L+|\mu|+\bar{P}_E}N_L(-|\mu|)\frac{R^2\cos\theta_{12}}{16\Delta^2}\right\}$$
$$+\delta_{|\mu|,|\mu'|+2}\,\delta_{P_E,\bar{P}_E'}\left\{\epsilon_{|\mu|,2}(-1)^{\bar{\bar{P}}_E}N_L(-|\mu|)\frac{r_2^2-r_1^2}{8r_1r_2\Delta}\right\}$$
$$+\delta_{|\mu|,|\mu'|-2}\,\delta_{P_E,\bar{P}_E'}\left\{\epsilon_{\mu,0}(-1)^{\bar{P}_E}N_L(|\mu|)\frac{r_2^2-r_1^2}{8r_1r_2\Delta}\right\}$$
$$+\delta_{|\mu|,2-|\mu'|}\,\delta_{P_E,\bar{P}_E'}\left\{\epsilon_{\mu,0}\,\epsilon_{|\mu|,2}(-1)^{L+|\mu|}N_L(-|\mu|)\frac{r_2^2-r_1^2}{8r_1r_2\Delta}\right\}, \tag{16}$$

$$T^4_{0ij} = \delta_{|\mu|,|\mu'|}\,\delta_{P_E,\bar{P}_E'}\left\{(-1)^{\bar{\bar{P}}_E}|\mu|\frac{(r_1^2-r_2^2)\cos\theta_{12}}{4r_1r_2\Delta}\right\}. \tag{17}$$

We have used the shorthand

$$N_L(\mu) \equiv [(L-\mu)(L+\mu+1)(L-\mu-1)(L+\mu+2)]^{\frac{1}{2}}.$$

Also

$$\widetilde{P}_E \equiv \text{adjoint symmetry of } P_E = a, \qquad \text{if } P_E = s,$$
$$= s, \qquad \text{if } P_E = a.$$

(ii) With i, j as in (a) above, we write the matrix elements $T^{w}_{12\,ij}$ for $w = 1$, 2, 3 as

$$T^{1}_{12\,ij} = \delta_{|\mu|,|\mu'|}\,\delta_{P_E,P_E'}\,T^{1}_{12}, \tag{18}$$

$$T^{2}_{12\,ij} = \delta_{|\mu|,|\mu'|}\,\delta_{P_E,\tilde{P}_E'}\left\{(-1)^{\bar{\tilde{P}}_E}\,|\mu|\,\frac{\Delta}{r_1 r_2}\left(\frac{1}{r_1}\frac{\partial}{\partial r_2}-\frac{1}{r_2}\frac{\partial}{\partial r_1}+\frac{r_2^2-r_1^2}{r_1 r_2 r_{12}}\frac{\partial}{\partial r_{12}}\right)\right\}, \tag{19}$$

$$\begin{aligned}T^{3}_{12\,ij} = {} & \delta_{|\mu|,|\mu'|}\,\delta_{P_E,P_E'}\left\{|\mu|^2\frac{\cos\theta_{12}}{4r_1 r_2}+\{L(L+1)-|\mu|^2\}\frac{r_1 r_2\cos\theta_{12}}{8\Delta^2}\right\}\\ & +\delta_{|\mu|,|\mu'|+2}\,\delta_{P_E,P_E'}\left\{N_L(-|\mu|)\,\epsilon_{|\mu|,2}\left(-\frac{r_1 r_2}{16\Delta^2}\right)\right\}\\ & +\delta_{|\mu|,|\mu'|-2}\,\delta_{P_E,P_E'}\left\{N_L(|\mu|)\,\epsilon_{\mu,0}\left(-\frac{r_1 r_2}{16\Delta^2}\right)\right\}\\ & +\delta_{|\mu|,2-|\mu'|}\,\delta_{P_E,P_E'}\left\{(-1)^{L+|\mu|+\tilde{P}_E}N_1(-|\mu|)\,\epsilon_{|\mu|,2}\,\epsilon_{\mu,0}\left(\frac{-r_1 r_2}{16\Delta^2}\right)\right\}.\end{aligned} \tag{20}$$

IV. The Coupled Equations for the Internal Functions

The non-relativistic Hamiltonian for two-electron atoms has the form

$$H = \frac{-\hbar^2}{2\mu}T_0-\frac{\hbar^2}{M}T_{12}+e^2\left(\frac{1}{r_{12}}-\frac{Z}{r_1}-\frac{Z}{r_2}\right), \tag{21}$$

where Z is the nuclear charge parameter and $-e$ the electron charge. We decompose the wave function in the form (4) above and write

$$i = L,\ m_L,\ |\mu|,\ P_E,$$
$$j = L,\ m_L,\ |\mu'|,\ P_E'.$$

Then for any operator Ω we may write

$$\Omega\psi = \Omega\left(\sum_i f_i Y_i\right)$$
$$= \sum_j \sum_i \Omega_{ji} f_i Y_j,$$

where Ω_{ji} is the reduced matrix of the operator Ω as defined by (6). In $\sum_i$, i runs over a set of variables V, determined by specified L, m_L, P_S, and π. Setting

$$\Omega = T \equiv -\frac{\hbar^2}{2\mu}T_0-\frac{\hbar^2}{M}T_{12}$$

leads to $\Omega_{ij} = 0$, unless j is in the set V and, further, j exhausts V for all non-zero Ω_{ji}. We may thus write the Schrödinger equation in reduced form as

$$\sum_{i\epsilon v}\left[\sum_{j\epsilon v}\left(-\frac{\hbar^2}{2\mu}T_{0ij}-\frac{\hbar^2}{M}T_{12\,ij}\right)f_j-\left\{e^2\left(\frac{Z}{r_1}+\frac{Z}{r_2}-\frac{1}{r_{12}}\right)+E\right\}f_i\right]Y_i = 0, \tag{22}$$

and hence for all i in V

$$\sum_{j\epsilon v}\left(-\frac{\hbar^2}{2\mu}T_{0ij}-\frac{\hbar^2}{M}T_{12\,ij}\right)f_i-\left\{e^2\left(\frac{Z}{r_1}+\frac{Z}{r_2}-\frac{1}{r_{12}}\right)+E\right\}f_i=0. \tag{23}$$

Equation (23) constitutes a set of coupled equations for the internal functions f_i. For later convenience we also give here explicitly the form that these coupled equations take on carrying out the implied matrix multiplication, in the limit of infinite nuclear mass (that is, keeping the operator T_0 only). A typical member of the coupled set has the form

$$\begin{aligned}
&\left[T_0^1+\left\{\frac{R^2\{|\mu|^2-L(L+1)\}}{8\Delta^2}-\frac{R^2|\mu|^2}{4r_1^2r_2^2}\right\}+\frac{2me^2}{\hbar^2}\left(\frac{Z}{r_1}+\frac{Z}{r_2}-\frac{1}{r_{12}}\right)+\frac{2mE}{\hbar^2}\right]f_{m_L}^L(P_R,\,|\mu|)\\
&+\left[(-1)^{\bar{\bar{P}}_E}|\mu|\left(\frac{r_1^2-r_2^2}{r_1r_2}\right)\left\{\frac{\cos\theta_{12}}{4\Delta}+\frac{\sin\theta_{12}}{r_{12}}\frac{\partial}{\partial r_{12}}\right\}\right]f_{m_L}^L(\widetilde{P}_R,\,|\mu|)\\
&+\left[\epsilon_{|\mu|,2}N_L(-|\mu|)\frac{R^2\cos\theta_{12}}{16\Delta^2}\right]f_{m_L}^L(P_R,\,|\mu|-2)\\
&+\left[\epsilon_{\mu,0}N_L(|\mu|)\frac{R^2\cos\theta_{12}}{16\Delta^2}\right]f_{m_L}^L(P_R,\,|\mu|+2)\\
&+\left[(-1)^{L+|\mu|+\bar{P}_E}\,\epsilon_{\mu,0}\,\epsilon_{|\mu|,2}\,N_L(-|\mu|)\frac{R^2\cos\theta_{12}}{16\Delta^2}\right]f_{m_L}^L(P_R,\,2-|\mu|)\\
&+\left[(-1)^{\bar{\bar{P}}_E}\,\epsilon_{|\mu|,2}\,N_L(-|\mu|)\frac{r_2^2-r_1^2}{8r_1r_2\Delta}\right]f_{m_L}^L(\widetilde{P}_R,\,|\mu|-2)\\
&+\left[(-1)^{\bar{P}_E}\,\epsilon_{\mu,0}\,N_L(|\mu|)\frac{r_2^2-r_1^2}{8r_1r_2\Delta}\right]f_{m_L}^L(\widetilde{P}_R,\,|\mu|+2)\\
&+\left[(-1)^{L+|\mu|}\,\epsilon_{\mu,0}\,\epsilon_{|\mu|,2}\,N_L(-|\mu|)\frac{r_2^2-r_1^2}{8r_1r_2\Delta}\right]f_{m_L}^L(\widetilde{P}_R,\,2-|\mu|)=0.
\end{aligned} \tag{24}$$

On interpreting this equation, the following points should be noted.

(i) We have used the convention

$$f_{m_L}^L(P_R,\,\kappa)=0, \qquad \text{if } \kappa<0 \text{ or } \kappa>L.$$

(ii) Apparently eight functions are coupled into a single general equation (24) but this is reduced to six when it is noted that if $|\mu|\neq 2$ one of $|\mu|-2$ or $2-|\mu|$ is negative and hence the corresponding two functions are identically zero by (i).

(iii) The set of equations is explicitly real and hence the set of functions f_i may be chosen to be real. This is a consequence of the choice of phase for the Y_i satisfying the time reversal reality condition (3).

V. ACKNOWLEDGMENTS

The author is much indebted to his supervisor Dr. L. M. Delves for suggesting the problem and for his willing help and inspiration. Thanks are also greatly due to Dr. G. H. Derrick for making available much of his original work on the ground

state of H^3. Finally, the author is grateful for the Australian and British Commonwealth Scholarship which made this research possible.

VI. References

Bhatia, A. K., and Temkin, A. (1964).—*Rev. Mod. Phys.* **35**: 1050.

Breit, G. (1930).—*Phys. Rev.* **35**: 569.

Derrick, G. H., and Blatt, J. M. (1958).—*Nucl. Phys.* **8**: 130.

Goldstein, H. (1959).—"Classical Mechanics." p. 134. (Addison-Wesley: Reading, Mass.)

Kalotas, T., and Delves, L. M. (1964).—*Nucl. Phys.* **60**: 363.

Appendix

Angular Momentum Operators referred to Body Axes

Let $\mathrm{d}\alpha$, $\mathrm{d}\beta$, $\mathrm{d}\gamma$ be infinitesimal increments in the Euler angles α, β, γ and use the vector notation to write

$$\mathbf{da} \equiv \begin{bmatrix} \mathrm{d}\alpha \\ \mathrm{d}\beta \\ \mathrm{d}\gamma \end{bmatrix}; \qquad \frac{\partial}{\partial \mathbf{a}} \equiv \begin{bmatrix} \dfrac{\partial}{\partial \alpha} \\ \dfrac{\partial}{\partial \beta} \\ \dfrac{\partial}{\partial \gamma} \end{bmatrix}.$$

It follows readily (Goldstein 1959) that the resulting infinitesimal rotation referred to body axes is given by

$$\mathrm{d}\boldsymbol{\theta}^B = S\,\mathbf{da},$$

where S is the matrix

$$S = \begin{bmatrix} \cdot & \cos\alpha & \sin\alpha\sin\beta \\ \cdot & -\sin\alpha & \cos\alpha\sin\beta \\ 1 & \cdot & \cos\beta \end{bmatrix}. \tag{A 1}$$

Let $\mathbf{L}$ be the orbital angular momentum for the two electrons (in the space system) and refer it to body axes by

$$\mathbf{L}^B \equiv \begin{bmatrix} \hat{\mathbf{x}}_B \,.\, \mathbf{L} \\ \mathbf{y}_B \,.\, \mathbf{L} \\ \hat{\mathbf{z}}_B \,.\, \mathbf{L} \end{bmatrix},$$

where $\mathbf{x}_B$, $\hat{\mathbf{y}}_B$, $\hat{\mathbf{z}}_B$ are body axis unit vectors. Then it follows, after some elementary analysis that,

$$\mathbf{L}^B = -\mathrm{i}\hbar(S^{-1})^T\frac{\partial}{\partial \mathbf{a}}. \tag{A 2}$$

We define the useful operators L_0^B, L_+^B, L_-^B by

$$\left.\begin{aligned} L_0^B &= L_z^B, \\ L_\pm^B &= L_x^B \mp \mathrm{i} L_y^B, \end{aligned}\right\} \tag{A 3}$$

and these operators give the following results when acting on the representation coefficients $D^L_{\mu,m_L}(\alpha, \beta, \gamma)$

$$\left.\begin{aligned} L_0^B D^L_{\mu,m_L} &= \hbar\mu D^L_{\mu,m_L}, \\ L_\pm^B D^L_{\mu,m_L} &= \hbar[(L\mp\mu)(L\pm\mu+1)]^{\frac{1}{2}} D^L_{\mu\pm1,m_L}. \end{aligned}\right\} \tag{A 4}$$

A THEORETICAL ANALYSIS OF THE TOWNSEND–HUXLEY SWARM TECHNIQUE FOR ELECTRONS

By C. A. Hurst* and B. S. Liley†

[*Manuscript received August* 18, 1965]

Summary

The Townsend–Huxley swarm technique for electrons is analysed in detail. Particular emphasis is placed on boundary conditions, and those conditions appropriate to the Huxley–Crompton empirical relationship are derived and explained. Secondary emission at the electrodes due to both positive ion and photon bombardment is also taken into account. The principal result is an integral expression for the current ratio received at the circumferentially split anode. From this may be deduced the energy factor k_1 and the secondary emission coefficients. It is shown that it is possible to distinguish between positive ion and photon secondary emission and to determine the associated coefficients simultaneously in the stationary state. Highly accurate conditions for electrical breakdown are also obtained, secondary emission at the anode being taken into account.

I. Introduction

Using a modification due to Huxley (1940) of Townsend's technique for analysing the lateral diffusion of electrons in gases, Crompton and Jory (1962) showed that the ratio of electron drift velocity to the diffusion coefficient, and the associated energy factor k_1, could be determined to a high degree of accuracy. Their results were, however, dependent on the use of an essentially empirical relationship (Huxley and Crompton 1955), while the range of E/p covered was such that the effects of ionization and excitation were unimportant.

The object of the present paper is to analyse the experimental method of Crompton and Jory in detail, particular emphasis being placed on boundary conditions. Those conditions appropriate to the Huxley–Crompton empirical relationship are derived and a physical explanation given. The emission of secondary electrons at the electrodes due to both photon and positive ion bombardment is also taken into account.

The principal result is an integral expression for the current ratio received at the circumferentially split anode. From this and the experimental measurements the energy factor k_1 may be deduced. In general, the integral does not reduce to a simple analytic form, but this is of little consequence since it may be readily computed. In addition to giving an expression from which k_1 may be determined, the results of this analysis have several other important applications. Highly accurate expressions for breakdown are obtained, while it is shown that the swarm technique, as employed by the previously mentioned authors, can be adapted to give secondary emission coefficients. Furthermore, and this is the most important application, it is possible

---

* Mathematical Physics Department, University of Adelaide.
† Department of Engineering Physics, Australian National University, Canberra.

Aust. J. Phys., 1965, **18**, 521–40

using this technique to distinguish between photon and positive ion secondary electrons in the stationary state.

As already implied, only a theoretical treatment is given in the present paper. The application of the results obtained is given elsewhere, in particular for low values of E/p in the paper of Crompton and Jory (1962) and for high values of E/p in the paper by Crompton *et al.* (1965).

Throughout the present paper, continual reference is made to the second edition of Watson's text on Bessel functions (1944). For the sake of brevity, such references will be denoted by the initials WBF followed by the appropriate page number.

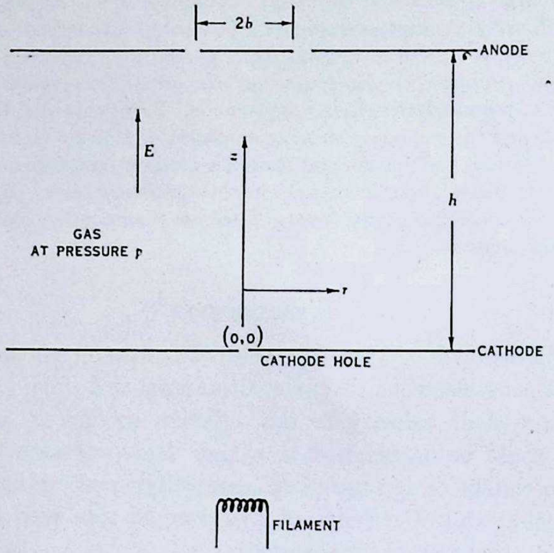

Fig. 1.—Experimental arrangement and geometry.

II. General Theory

(a) *Statement of the Problem*

The essential elements of the experimental arrangement are shown in Figure 1, details being given in the paper by Crompton and Jory. For theoretical purposes, the diffusion chamber is bounded by two infinite plane electrodes separated by a distance h. The anode is circumferentially split at the radius b. Electrons are generated by a heated filament and enter the chamber through a small hole in the cathode; they then drift under the action of a uniform electric field towards the anode, diffusing radially and ionizing and exciting the gas in transit. Any positive ions formed drift to the cathode leading to the emission of secondary electrons, while further secondaries are produced by photon bombardment of both the anode and cathode.

The experimental results are expressed in terms of R, the ratio of the current received by the central anode disk to the total anode current, as a function of p and of E/p. The prime object of the theory is to present R in terms of the various parameters of the problem, including boundary conditions, such that the energy factor k_1 may be deduced from this ratio.

(*b*) *General Solution of the Diffusion Equation*

The basic equations governing the drift and diffusion of the electrons are the continuity and flux equations

$$\operatorname{div}\mathbf{j} = \alpha' n, \tag{1}$$

$$\mathbf{j} = n\mu\mathbf{E} - D\operatorname{grad} n, \tag{2}$$

where $\mathbf{j}$ = electron flux density,
n = electron number density,
α' = ionization coefficient,
μ = electron mobility coefficient,
D = electron diffusion coefficient,
$\mathbf{E}$ = electric field vector.

Since the problem is cylindrically symmetric, substitution of equation (2) in equation (1) gives for $\mathbf{E} = (0, 0, E)$:

$$\frac{1}{r}\frac{\partial}{\partial r}\left(r\frac{\partial n}{\partial r}\right) + \frac{\partial^2 n}{\partial z^2} - 2\lambda\frac{\partial n}{\partial z} + 2\alpha\lambda n = 0, \tag{3}$$

where $\lambda = W/2D$,
$W = \mu E$ = electron drift velocity,
$\alpha = \alpha'/W$ [$= \alpha_T(1-\alpha_T/2\lambda)$, α_T being Townsend's first ionization coefficient; see equation (95)].

Substitution will readily confirm that a general solution of (3) is

$$n = \int_0^\infty J_0(\xi r)\{A(\xi)\exp\beta_1 z + B(\xi)\exp\beta_2 z\}\,\xi\,d\xi, \tag{4}$$

where ξ^2 = a separation constant in equation (3),
$\beta_1 = \lambda - (\xi^2 + \lambda'^2)^{\frac{1}{2}}$,
$\beta_2 = \lambda + (\xi^2 + \lambda'^2)^{\frac{1}{2}}$,
$\lambda'^2 = \lambda^2 - 2\alpha\lambda$ (or $\lambda - \lambda' = \alpha_T$).

In particular, it now follows from equations (2) and (4) that

$$j_z = D\int_0^\infty J_0(\xi r)\{\beta_2 A(\xi)\exp\beta_1 z + \beta_1 B(\xi)\exp\beta_2 z\}\,\xi\,d\xi. \tag{5}$$

$A(\xi)$ and $B(\xi)$ are to be determined from the imposition of boundary conditions at the cathode and anode of the diffusion chamber.

(c) *The Ratio* R

The ratio R is defined as

$$R = \frac{i_z(b,h)}{i_z(\infty,h)}, \tag{6}$$

where

$$i_z(r,h) = 2\pi \int_0^r j_z(r,h)\, r\, \mathrm{d}r. \tag{7}$$

Substitution from equation (5) shows that

$$i_z(b,h) = 2\pi D \int_0^\infty \mathrm{J}_1(\xi b)\, \psi(\xi,h)\, \mathrm{d}(\xi b), \tag{8}$$

where

$$\psi(\xi,h) = \beta_2 A(\xi) \exp \beta_1 h + \beta_1 B(\xi) \exp \beta_2 h. \tag{9}$$

In principle, taking the limit $b \to \infty$ should give $i_z(\infty,h)$. However, there is a simpler method available for deriving this quantity. Since

$$i_z(\infty,h) = 2\pi \int_0^\infty j_z(r,h)\, r\, \mathrm{d}r \tag{10}$$

$$= \lim_{\xi\to 0} 2\pi \int_0^\infty j_z(r,h)\, \mathrm{J}_0(\xi r)\, r\, \mathrm{d}r, \tag{11}$$

an application of the Hankel inversion theorem (WBF, p. 453) to equation (5) immediately gives

$$i_z(\infty,h) = 2\pi D \lim_{\xi\to 0} \psi(\xi,h) = 2\pi D\, \psi(0,h). \tag{12}$$

Therefore,

$$R = \int_0^\infty \mathrm{J}_1(\xi b) \frac{\psi(\xi,h)}{\psi(0,h)}\, \mathrm{d}(\xi b), \tag{13}$$

where $\psi(\xi,h)$ is given by equation (9).

(d) *Scaling Factors*

In the application of the final results of this analysis, the dependence of the various parameters of the problem on E/p is of major importance. Therefore, the scaling laws for the relevant quantities will be recorded. To understand these, however, the following definitions and relationships should be noted.

$$\left.\begin{gathered} \alpha' \equiv n_\mathrm{g} f_1(T_\mathrm{e}); \qquad \mu \equiv e_\mathrm{e}/m_\mathrm{e}\nu; \qquad D \equiv \Lambda k T_\mathrm{e}/m_\mathrm{e}\nu; \qquad \nu \equiv n_\mathrm{g} f_2(T_\mathrm{e}); \\ k_1 \equiv e_\mathrm{e} D/\mu k T_\mathrm{g} = e_\mathrm{e} E/2\lambda k T_\mathrm{g} \\ = \Lambda k T_\mathrm{e}/k T_\mathrm{g}; \end{gathered}\right\} \tag{14}$$

where T_e = electron temperature,
$f_1(T_\mathrm{e})$, $f_2(T_\mathrm{e})$ = functions depending on T_e,
T_g = gas temperature,
e_e = electronic charge,

m_e = electronic mass,
n_g = number density of gas atoms or molecules,
ν = effective electron momentum-transfer collision frequency,
k = Boltzmann's constant,
k_1 = Townsend's energy factor,
Λ = form factor of the order of unity, characteristic of the electron velocity distribution (see Huxley and Crompton 1962).

Subject to certain assumptions, which are briefly discussed in Section V, we have

$$\begin{aligned} T_e &\equiv T_e(E/n_g;\, T_g) \\ &= T_e(E/p) \qquad \text{for a given } T_g. \end{aligned} \tag{15}$$

Therefore, from the definitions of Section II(*b*), equations (14), and subsequent definitions still to be introduced, for a given gas at a given temperature the following parameters are functions of E/p only:

μp	α/p	λ/p	W	γ_i	Γ_i	ζ_c
Dp	α_T/p	λ'/p	$\bar{c}$	γ_p	Γ_p	ζ_a
k_1	η/p	λ_T/p	v_z			

(It is, of course, to be noted that the "secondary emission" coefficients, that is the γ's and Γ's, are also dependent on the nature of the electrode material.)

III. Boundary Conditions

For expression (4) to be the required solution it must satisfy the appropriate boundary conditions. The choice of $J_0(\xi r)$ as the relevant Bessel function, in the solution of equation (3), ensured that ξ^2 was a positive quantity and that n was everywhere finite, except perhaps at the cathode hole. Therefore, the only boundary conditions to be imposed are those at the electrodes. Since the effects of secondary emission at these electrodes have to be taken into account, such conditions will inevitably involve the particle flux density rather than the particle number density.

(*a*) *General*

The electrons in the diffusion chamber have random velocities. Hence, n and $\mathbf{j}$ are variables which are essentially defined in terms of a velocity distribution function $f(\mathbf{c},\mathbf{r})$. That is,

$$n = \int_{\mathbf{c}} f(\mathbf{c},\mathbf{r})\,\mathrm{d}\mathbf{c}, \tag{16}$$

$$\mathbf{j} = \int_{\mathbf{c}} f(\mathbf{c},\mathbf{r})\,\mathbf{c}\,\mathrm{d}\mathbf{c}, \tag{17}$$

where $\mathbf{c}$ = particle velocity,
$\mathrm{d}\mathbf{c}$ = volume element of velocity space.

The integrals extend over all velocity space.

Referring $f(\mathbf{c},\mathbf{r})$ to a system of spherical coordinates in velocity space, with the c_z axis parallel to the axial direction of the diffusion chamber, j_z may be redefined as follows:

$$j_z = j_{z+} + j_{z-}, \tag{18}$$

where

$$j_{z+} = \int_0^\infty \int_0^{2\pi} \int_0^{\frac{1}{2}\pi} f(\mathbf{c},\mathbf{r})\, c\cos\theta\, \mathrm{d}\mathbf{c}, \tag{19}$$

$$j_{z-} = \int_0^\infty \int_0^{2\pi} \int_{\frac{1}{2}\pi}^{\pi} f(\mathbf{c},\mathbf{r})\, c\cos\theta\, \mathrm{d}\mathbf{c}, \tag{20}$$

and

$$\mathrm{d}\mathbf{c} = c^2 \sin\theta\, \mathrm{d}\theta\, \mathrm{d}\epsilon\, \mathrm{d}c.$$

That is, at a given point, j_{z+} is the flux density associated with those particles moving towards the anode, and j_{z-} is the flux density associated with those moving towards the cathode.

To the same degree of approximation as equation (2), the velocity distribution function is given by (Huxley and Crompton 1962)

$$f(\mathbf{c},\mathbf{r}) = f^0(c,\mathbf{r}) + \mathbf{v}\,.\,\mathbf{c}\, f^1(c,\mathbf{r}), \tag{21}$$

where $\mathbf{v}$ = electron mean mass velocity,

$n\mathbf{v} = \mathbf{j}$.

Therefore, it follows from equations (19) and (20) that

$$j_{z+} = \tfrac{1}{4} n\bar{c} + \tfrac{1}{2} j_z, \tag{22}$$

$$j_{z-} = -\tfrac{1}{4} n\bar{c} + \tfrac{1}{2} j_z, \tag{23}$$

with

$$n\bar{c} = \int_{\mathbf{c}} f^0(c,\mathbf{r})\, c\, \mathrm{d}\mathbf{c}. \tag{24}$$

The boundary conditions at the electrodes can now be expressed in terms of "reflection" coefficients and source functions. If the "reflection" coefficient at the cathode is ζ_{c}, then

$$j_{z+}(r,0) = -\zeta_{\mathrm{c}} j_{z-}(r,0) + S_{\mathrm{c}}(r,0), \tag{25}$$

where $S_{\mathrm{c}}(r,0)$ = axial component of the source function, consisting of both primary and secondary electrons.

From use of (22) and (23) the boundary condition on j_z at the cathode is, therefore,

$$j_z(r,0) = -\tfrac{1}{2} n(r,0)\, \bar{c} a_{\mathrm{c}} + \frac{2 S_{\mathrm{c}}(r,0)}{1+\zeta_{\mathrm{c}}}, \tag{26}$$

where

$$a_{\mathrm{c}} = (1-\zeta_{\mathrm{c}})(1+\zeta_{\mathrm{c}})^{-1}. \tag{27}$$

Similarly, it may be shown that at the anode

$$j_z(r,h) = \tfrac{1}{2} n(r,h)\, \bar{c} a_{\mathrm{a}} - \frac{2 S_{\mathrm{a}}(r,h)}{1+\zeta_{\mathrm{a}}}. \tag{28}$$

The problem therefore reduces to one of giving expressions for the source functions and assigning values to the "reflection" coefficients ζ_c and ζ_a.

(b) *The Source Functions*

From the qualitative description given in Section II(*a*), we write

$$S_c(r,0) = p(r,0)+S_i(r,0)+S_p(r,0), \tag{29}$$

$$S_a(r,h) = S_p(r,h), \tag{30}$$

where $p(r,0) =$ primary source axial flux density,

$S_i(r,0) =$ secondary source axial flux density due to bombardment of the cathode by positive ions,

$S_p(r,0) =$ secondary source axial flux density due to bombardment of the cathode by photons,

$S_p(r,h) =$ secondary source axial flux density due to bombardment of the anode by photons.

It is to be noted that, as defined, the functions S account only for the axial components of flux at the electrode surfaces.

(i) *The Primary Source.*—The primary source consists of those electrons generated by the heated filament that enter the diffusion chamber through the small hole in the cathode. In order to avoid mathematical difficulties associated with discontinuous reflection coefficients, it will be assumed that this source may be approximated by a point function. That is,

$$p(r,0) = p'(r,0)\,\delta(r), \tag{31}$$

where

$$2\pi\int_0^\infty p'(r,0)\,\delta(r)\,r\,\mathrm{d}r = P, \tag{32}$$

P being the axial component of the total primary flux at the source hole.

(ii) *The Secondary Source* $S_i(r,0)$.—Associated with ionization processes there is a continuity equation for the ions of the form

$$\operatorname{div}\mathbf{j}_i = \alpha' n, \tag{33}$$

where $\mathbf{j}_i =$ positive ion flux density.

Even for values of E/p approaching breakdown, radial diffusion of the ions will be small. Therefore, for the particular problem in hand, equation (33) is:

$$\frac{\partial j_{iz}}{\partial z} = \alpha' n. \tag{34}$$

Integrating this equation over z, subject to the boundary condition $j_{iz}(r,h) = 0$, this being consistent with the neglect of j_{ir}, we have

$$j_{iz}(r,0) = -\alpha'\int_0^h n\,\mathrm{d}z.$$

A secondary emission coefficient γ_{1c} is now defined such that

$$S_1(r,0) = -\gamma_{1c}\, j_{1z}(r,0) = \alpha'\gamma_{1c}\int_0^h n\,\mathrm{d}z, \tag{35}$$

or, using equation (4),

$$S_1(r,0) = \alpha W\gamma_{1c}\int_0^\infty J_0(\xi r)\{A(\xi)(\exp\beta_1 h-1)\beta_1^{-1}+B(\xi)(\exp\beta_2 h-1)\beta_2^{-1}\}\,\xi\,\mathrm{d}\xi. \tag{36}$$

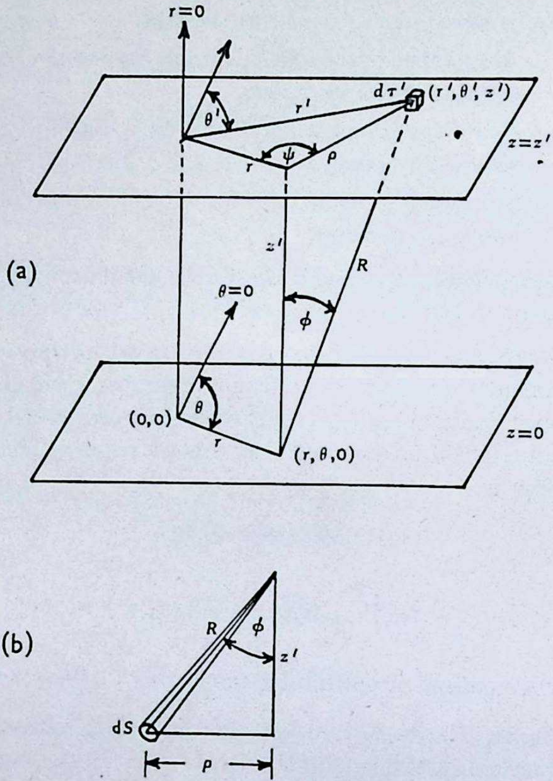

Fig. 2.—Geometry associated with cathode photo-emission.

(iii) *The Secondary Source* $S_p(r,0)$.—Referring to Figure 2, the flux of photons δF, produced in a small volume element $\mathrm{d}\tau'$ about the point (r',θ',z'), is given by

$$\delta F = \eta'\, n(r',\theta',z')\,\mathrm{d}\tau', \tag{37}$$

where

$$\eta' = n_g f_3(T_e), \tag{38}$$

$f_3(T_e)$ being dependent on the electron temperature only.

The associated flux passing through an element of area $\mathrm{d}S$, on the surface of a sphere of radius R centred at the point (r',θ',z'), is given by

$$\delta f_R\,\mathrm{d}S = (\delta F/4\pi R^2)\,\mathrm{d}S. \tag{39}$$

If this element of area $\mathrm{d}S$ intersects the cathode at the point $(r, \theta, 0)$, then this same flux will also pass through an area $\mathrm{d}A$, $\mathrm{d}A$ being the projection of $\mathrm{d}S$ on to the cathode. Therefore, since

$$\mathrm{d}A \cos\phi = \mathrm{d}S, \qquad \cos\phi = z'/R, \tag{40}$$

the flux of photons per unit area of the cathode surface at the point $(r, \theta, 0)$, due to excitation collisions in the volume element $\mathrm{d}\tau'$ about the point (r', θ', z'), is

$$\delta f_{\mathrm{c}} = \frac{\eta' n(r', \theta', z') z'}{4\pi R^3} \mathrm{d}\tau'. \tag{41}$$

Hence, the total flux density $f_{\mathrm{c}}(r, \theta, 0)$ is given by

$$f_{\mathrm{c}}(r, \theta, 0) = \int_{\tau'} \frac{\eta' n(r', \theta', z') z'}{4\pi R^3} \mathrm{d}\tau', \tag{42}$$

the integration being over the entire volume of the diffusion chamber. As in the positive ion case, a secondary emission coefficient γ_{pc} is now defined such that

$$S_{\mathrm{p}}(r, 0) = \gamma_{\mathrm{pc}} f_{\mathrm{c}}(r, \theta, 0), \tag{43}$$

it being noted that f_{c} is in fact independent of θ. But n is given by equation (4), and equation (43) becomes

$$S_{\mathrm{p}}(r, 0) = \gamma_{\mathrm{pc}} W \eta \int_{\tau'} \int_0^\infty \frac{\mathrm{J}_0(\xi r')\{A(\xi) \exp \beta_1 z' + B(\xi) \exp \beta_2 z'\}}{4\pi R^3} z' \xi \,\mathrm{d}\xi \,\mathrm{d}\tau', \tag{44}$$

where, by analogy with the ionization coefficient α,

$$\eta = \eta'/W.$$

In carrying out the integration over $\mathrm{d}\tau'$, it is convenient to take as origin the point $(r, \theta, 0)$ and as integration variables ρ, ψ, and z'. Noting that

$$r'^2 = r^2 + \rho^2 - 2r\rho\cos\psi, \tag{45}$$

the integral in equation (44) may be re-written in the form

$$S_{\mathrm{p}}(r, 0) = \gamma_{\mathrm{pc}} W \eta \int_0^\infty \int_0^h K(r, 0; \xi; z')\{A(\xi) \exp \beta_1 z' + B(\xi) \exp \beta_2 z'\} \,\mathrm{d}z' \,\xi \,\mathrm{d}\xi, \tag{46}$$

where $$K(r, 0; \xi; z') = \int_0^\infty \int_0^{2\pi} \frac{\mathrm{J}_0\{\xi(r^2 + \rho^2 - 2r\rho\cos\psi)^{\frac{1}{2}}\}}{4\pi(\rho^2 + z'^2)^{3/2}} z' \rho \,\mathrm{d}\rho \,\mathrm{d}\psi. \tag{47}$$

The integration over ψ is a particular case of a Sonine–Gegenbauer integral (WBF, p. 367), and K reduces to

$$K(r, 0; \xi; z') = \frac{z' \mathrm{J}_0(\xi r)}{2} \int_0^\infty \frac{\mathrm{J}_0(\xi\rho)}{(\rho^2 + z'^2)^{3/2}} \rho \,\mathrm{d}\rho. \tag{48}$$

This second integral is also known (WBF, p. 434), and we obtain

$$K(r, 0; \xi; z') = \tfrac{1}{2} \mathrm{J}_0(\xi r) \exp(-\xi z'). \tag{49}$$

By substitution of this expression for K in equation (46) and integration over z', the source function $S_{\mathrm{p}}(r,0)$ finally becomes

$$S_{\mathrm{p}}(r,0)=\frac{\gamma_{\mathrm{pc}}\,\eta W}{2}\int_0^\infty \mathrm{J}_0(\xi r)\left(\frac{A(\xi)}{\beta_1-\xi}\{\exp(\beta_1-\xi)h-1\}+\frac{B(\xi)}{\beta_2-\xi}\{\exp(\beta_2-\xi)h-1\}\right)\xi\,\mathrm{d}\xi. \tag{50}$$

(iv) *The Secondary Source* $\mathrm{S}_p(\mathrm{r},\mathrm{h})$.—This source function is similar to $S_{\mathrm{p}}(r,0)$ and may be derived in an identical manner. The result is

$$S_{\mathrm{p}}(r,h)=\frac{\gamma_{\mathrm{pa}}\,\eta W}{2}\int_0^\infty \mathrm{J}_0(\xi r)\left(\frac{A(\xi)}{\beta_1+\xi}\{\exp\beta_1 h-\exp(-\xi h)\}\right.$$
$$\left.+\frac{B(\xi)}{\beta_2+\xi}\{\exp\beta_2 h-\exp(-\xi h)\}\right)\xi\,\mathrm{d}\xi, \tag{51}$$

where $\gamma_{\mathrm{pa}}=$ secondary emission coefficient characteristic of the anode material.

(c) *The "Reflection" Coefficients*

As defined by equation (25) and the corresponding equation for the anode surface, the "reflection" coefficients are no different from any of the other coefficients so far introduced. They are quantities that must be determined by experiment, the correct values being those which subsequently lead to consistent agreement between the experimental results and theoretical predictions. To be completely general, the final expressions derived in this analysis should be expressed in terms of the ζ's. However, such expressions are extremely complex and, in order to simplify the algebra, certain experimental results will be used at this stage to determine the ζ's explicitly.

Crompton and Jory showed that, in the absence of ionization and secondary processes, the ratio R is given to a remarkable degree of accuracy by the Huxley–Crompton empirical relationship

$$R=1-\frac{h}{(h^2+b^2)^{\frac{1}{2}}}\exp[-\lambda\{(h^2+b^2)^{\frac{1}{2}}-h\}]. \tag{52}$$

Since this is essentially an empirical result, it will be used to determine the reflection coefficients. By use of a result given by Watson (WBF, p. 416), this expression for R may be rewritten in the integral form

$$R=\int_0^\infty \mathrm{J}_1(\xi b)\exp[\{\lambda-(\xi^2+\lambda^2)^{\frac{1}{2}}\}h]\,\mathrm{d}(\xi b). \tag{53}$$

Upon comparison of this with equation (13), it follows that

$$\frac{\psi(\xi,h)}{\psi(0,h)}=\exp\beta_1 h. \tag{54}$$

However, according to Section III(a), this result should be consistent with the boundary conditions

$$j_z(r,0)=-\tfrac{1}{2}n(r,0)\,\bar{c}a_{\mathrm{c}}+\frac{2p'(r,0)\,\delta(r)}{1+\zeta_{\mathrm{c}}}, \tag{55}$$

$$j_z(r,h)=\tfrac{1}{2}n(r,0)\,\bar{c}a_{\mathrm{a}}. \tag{56}$$

By use of equations (4) and (5), these boundary conditions may be written in the form

$$\int_0^\infty \mathrm{J}_0(\xi r)\{A(\xi)(\beta_2+a_\mathrm{c}\lambda_\mathrm{T})+B(\xi)(\beta_1+a_\mathrm{c}\lambda_\mathrm{T})\}\,\xi\,\mathrm{d}\xi=\frac{2p'(r,0)\,\delta(r)}{D(1+\zeta_\mathrm{c})}, \tag{57}$$

$$\int_0^\infty \mathrm{J}_0(\xi r)\{A(\xi)(\beta_2-a_\mathrm{a}\lambda_\mathrm{T})\exp\beta_1 h+B(\xi)(\beta_1-a_\mathrm{a}\lambda_\mathrm{T})\exp\beta_2 h\}\,\xi\,\mathrm{d}\xi=0, \tag{58}$$

where

$$\lambda_\mathrm{T}=\bar{c}/2D. \tag{59}$$

Upon use of the Hankel inversion theorem, two algebraic equations can now be obtained for $A(\xi)$ and $B(\xi)$. These may be readily solved and, from equations (9) and (13), the ratio R determined. The result is

$$R=\int_0^\infty \mathrm{J}_1(\xi b)\frac{\psi(\xi,h)}{\psi(0,h)}\,\xi\,\mathrm{d}\xi, \tag{60}$$

where

$$\frac{\psi(\xi,h)}{\psi(0,h)}=\frac{(\xi^2+\lambda^2)^{\frac{1}{2}}}{\lambda}\,\frac{d(0)-c(0)\exp(-2\lambda h)}{d(\xi)-c(\xi)\exp\{-2(\xi^2+\lambda^2)^{\frac{1}{2}}h\}}\exp\beta_1 h, \tag{61}$$

$$d(\xi)=\xi^2+a_\mathrm{a}a_\mathrm{c}\lambda_\mathrm{T}^2+a_\mathrm{a}\lambda_\mathrm{T}\beta_2-a_\mathrm{c}\lambda_\mathrm{T}\beta_1,$$

$$c(\xi)=\xi^2+a_\mathrm{a}a_\mathrm{c}\lambda_\mathrm{T}^2+a_\mathrm{a}\lambda_\mathrm{T}\beta_1-a_\mathrm{c}\lambda_\mathrm{T}\beta_2.$$

In the experiments of Crompton and Jory, λh is greater than 20, hence, to the degree of accuracy to which they worked,

$$\frac{\psi(\xi,h)}{\psi(0,h)}=\frac{(\xi^2+\lambda^2)^{\frac{1}{2}}}{\lambda}\,\frac{d(0)}{d(\xi)}\exp\beta_1 h. \tag{62}$$

On comparison of this expression with equation (54), it follows that

$$d(0)\,(\xi^2+\lambda^2)^{\frac{1}{2}}=\lambda\,d(\xi). \tag{63}$$

If we regard this now as an equation for the "reflection" coefficients, there is only one possible solution, namely

$$\left.\begin{aligned} a_\mathrm{c}\lambda_\mathrm{T}&=-\lambda, &&\text{or } \zeta_\mathrm{c}=(\bar{c}+W)(\bar{c}-W)^{-1};\\ a_\mathrm{a}&\to\infty, &&\text{or } \zeta_\mathrm{a}=-1.\end{aligned}\right\} \tag{64}$$

(The conditions $a_\mathrm{a}\lambda_\mathrm{T}=\lambda$, $a_\mathrm{c}\to\infty$ will also satisfy equation (63). However, these conditions correspond to a positive density gradient at the anode and are not, therefore, realistic.)

In terms of the actual boundary conditions (55) and (56), these results correspond to

$$j_z(r,0)=\tfrac{1}{2}n(r,0)\,W+(1-\lambda/\lambda_\mathrm{T})\,p(r,0), \tag{65}$$

$$0\doteq n(r,h). \tag{66}$$

On the assumption that ionization and secondary effects in no way alter the "reflection" coefficients, the general boundary conditions, corresponding to equations

(64), therefore are

$$j_z(r,0) = \tfrac{1}{2}n(r,0)\,W + (1-\lambda/\lambda_{\mathrm{T}})\,S_{\mathrm{c}}(r,0), \tag{67}$$

$$(2/\bar{c})\,S_{\mathrm{a}}(r,h) = n(r,h). \tag{68}$$

These are the boundary conditions appropriate to the problem in hand.

IV. Solutions

(a) *Particle Flux and Particle Number Densities*

From the expressions given for the source functions in Section III(*b*) and equations (4) and (5), the general boundary conditions (67) and (68) may be written in integral forms similar to equations (57) and (58). Therefore, by applying the Hankel inversion theorem, two algebraic equations for $A(\xi)$ and $B(\xi)$ may again be obtained. The solution of these is:

$$A(\xi) = -\frac{(1-\lambda/\lambda_{\mathrm{T}})(P/2\pi D)\,X(\xi)\exp(-\beta_1 h)}{C(\xi)-D(\xi)}, \tag{69}$$

$$B(\xi) = \frac{(1-\lambda/\lambda_{\mathrm{T}})(P/2\pi D)\,Y(\xi)\exp(-\beta_2 h)}{C(\xi)-D(\xi)}, \tag{70}$$

where
$$X(\xi) = 1-\frac{\lambda'(\lambda-\lambda')}{(\lambda_{\mathrm{T}}-\lambda)(\beta_2+\xi)}\Gamma_{\mathrm{pa}}[1-\exp\{-(\xi+\beta_2)h\}], \tag{71}$$

$$Y(\xi) = 1-\frac{\lambda'(\lambda-\lambda')}{(\lambda_{\mathrm{T}}-\lambda)(\beta_1+\xi)}\Gamma_{\mathrm{pa}}[1-\exp\{-(\xi+\beta_1)h\}], \tag{72}$$

$$C(\xi) = \exp(-\beta_1 h)\,X(\xi)\left(\lambda-\beta_2+\frac{\lambda'(\lambda-\lambda')}{\beta_1}\Gamma_{\mathrm{ic}}(\exp\beta_1 h-1)\right.$$
$$\left.+\frac{\lambda'(\lambda-\lambda')}{\beta_1-\xi}\Gamma_{\mathrm{pc}}\{\exp(\beta_1-\xi)h-1\}\right), \tag{73}$$

$$D(\xi) = \exp(-\beta_2 h)\,Y(\xi)\left(\lambda-\beta_1+\frac{\lambda'(\lambda-\lambda')}{\beta_2}\Gamma_{\mathrm{ic}}(\exp\beta_2 h-1)\right.$$
$$\left.+\frac{\lambda'(\lambda-\lambda')}{\beta_2-\xi}\Gamma_{\mathrm{pc}}\{\exp(\beta_2-\xi)h-1\}\right), \tag{74}$$

$$\Gamma_{\mathrm{i}} = \frac{2\alpha\lambda}{\lambda'\lambda_{\mathrm{T}}}\cdot\frac{\lambda_{\mathrm{T}}-\lambda}{\lambda-\lambda'}\gamma_{\mathrm{i}}, \tag{75}$$

$$\Gamma_{\mathrm{p}} = \frac{\eta\lambda}{\lambda'\lambda_{\mathrm{T}}}\cdot\frac{\lambda_{\mathrm{T}}-\lambda}{\lambda-\lambda'}\gamma_{\mathrm{p}}. \tag{76}$$

The additional subscripts a and c refer to the anode and cathode respectively.

(The formal difference of a factor of 2 between (75) and (76) arises from the fact that whereas all positive ions formed bombard the cathode, only one half of the photons produced do likewise, the other half bombarding the anode.)

Upon insertion of these expressions for $A(\xi)$ and $B(\xi)$ in equations (4) and (5), the solutions for n and j_z are essentially complete. Since, however, the principal quantity of interest is R, there is no value in presenting either of these results in full, except in the case corresponding to a complete absence of ionization and excitation. This case is of particular interest, since it emphasizes the peculiar role of the "reflection" coefficients and the true physical nature of the boundary conditions. These are discussed in Section V.

For the case $\alpha = 0$, $\eta = 0$, it may be shown that

$$n = \left(1-\frac{\lambda}{\lambda_{\mathrm{T}}}\right)\frac{P}{2\pi D}\int_0^\infty \mathrm{J}_0(\xi r)\frac{2\exp\beta_1 z}{\beta_2-\beta_1}\cdot\frac{1-\exp(\beta_1-\beta_2)(h-z)}{1+\exp(\beta_1-\beta_2)h}\,\xi\,\mathrm{d}\xi, \tag{77}$$

where $\beta_1 = \lambda-(\xi^2+\lambda^2)^{\frac{1}{2}}, \qquad \beta_2 = \lambda+(\xi^2+\lambda^2)^{\frac{1}{2}},$

λ' being equal to λ.

Upon expansion of the denominator of the integrand in powers of $\exp(\beta_1-\beta_2)h$, the resulting series may be integrated term by term (see WBF, p. 416). The result is

$$n = (1-\lambda/\lambda_{\mathrm{T}})(P/2\pi D)\,\mathrm{e}^{\lambda z}\sum_{N=-\infty}^{+\infty}(-1)^N\exp(-\lambda d_N)/d_N, \tag{78}$$

where $d_N^2 = r^2+(z+2Nh)^2,$

and N takes all integer values between plus and minus infinity, including $N = 0$.

From this expression for n, j_z and j_r may be readily obtained. However, the only quantity of real interest is $j_z(r,0)$. From the boundary condition, equation (65), we have

$$j_z(r,0) = \tfrac{1}{2}n(r,0)\,W + (1-\lambda/\lambda_{\mathrm{T}})\,p'(r,0)\,\delta(r). \tag{79}$$

Upon integration of this equation over the cathode surface, or noting that $i_z(\infty,0) = i_z(\infty,h)$ and using equation (12), it follows that

$$i_z(\infty,0) = \left(1-\frac{\lambda}{\lambda_{\mathrm{T}}}\right)P\frac{1-\mathrm{e}^{-2\lambda h}}{1+\mathrm{e}^{-2\lambda h}}+\left(1-\frac{\lambda}{\lambda_{\mathrm{T}}}\right)P. \tag{80}$$

The physical significance of these results is readily understood. Referring to the series terms in equation (78), we see that this solution corresponds to a pole source ($N = 0$) of strength ($+1$) at the origin, with image terms at $z = \pm 2Nh$ of strengths $(-1)^N$. The images at $\pm 2Nh$ ensure that (79) is satisfied, while complementary terms at $-2Nh$ and $2(N+1)h$ ensure that the boundary condition $n = 0$ is satisfied at the anode. Since n is not equal to zero at $z = 0$, equation (79) states that the true source of axial flux, as seen by the anode, consists of a point source plus a distributed source, and not a simple point source as originally postulated. For large λh these two sources are of equal strength, but as λh approaches zero the distributed source diminishes and the point source dominates.

(*b*) *The Ratio* R

It was shown in Section II(*c*) that this ratio is given by

$$R = \int_0^\infty \mathrm{J}_1(\xi b)\frac{\psi(\xi,h)}{\psi(0,h)}\,\mathrm{d}(\xi b),$$

where $\psi(\xi,h) = \beta_2 A(\xi)\exp\beta_1 h + \beta_1 B(\xi)\exp\beta_2 h.$

Upon use of expressions (69) and (70) for $A(\xi)$ and $B(\xi)$, this becomes

$$\psi(\xi,h) = -\left(1-\frac{\lambda}{\lambda_T}\right)\frac{P}{2\pi D}\cdot\frac{\beta_2 X(\xi)-\beta_1 Y(\xi)}{C(\xi)-D(\xi)}. \tag{81}$$

For $\alpha = 0, \eta = 0$, this reduces to a relatively simple expression and, in particular,

$$\frac{\psi(\xi,h)}{\psi(0,h)} = \frac{\exp\{\lambda-(\xi^2+\lambda^2)^{\frac{1}{2}}\}h+\exp[-\{\lambda+(\xi^2+\lambda^2)^{\frac{1}{2}}\}h]}{1+\exp\{-2(\xi^2+\lambda^2)^{\frac{1}{2}}h\}}. \tag{82}$$

This is of course the semi-empirical result (54) from which the "reflection" coefficients were determined. Disregard of the factor $\exp\{-2(\xi^2+\lambda^2)^{\frac{1}{2}}h\}$ corresponds to neglect of all image sources except that at $z = 2h$. As already remarked, this is a valid approximation in most practical applications. In the more general case a similar approximation is also valid, and this is considered in the next paragraph.

(i) *First Approximation.*—Although (81) could be written out exactly, there is no value in doing so since certain approximations are clearly justifiable. Since λh will be at least of the order of 10 in all practical cases, terms containing $\exp(-\beta_2 h)$ ($< e^{-\lambda h}$) may be ignored. In this case, (81) reduces to

$$\psi(\xi,h) = -\left(1-\frac{\lambda}{\lambda_T}\right)\frac{P}{2\pi D}\frac{\{\beta_2-\beta_1 Y(\xi)/X(\xi)\}\exp\beta_1 h}{\lambda-\beta_2+\lambda'(\lambda-\lambda')M_1(\xi)}, \tag{83}$$

where

$$M_1(\xi) = \frac{(\exp\beta_1 h-1)\Gamma_{1c}}{\beta_1}+\frac{\{\exp(\beta_1-\xi)h-1\}\Gamma_{pc}}{\beta_1-\xi}$$

$$-\exp(\beta_1 h)\frac{Y(\xi)}{X(\xi)}\left(\frac{\Gamma_{1c}}{\beta_2}+\frac{\Gamma_{pc}}{\beta_2-\xi}\exp(-\xi h)\right), \tag{84}$$

$$\frac{Y(\xi)}{X(\xi)} = \left[1-\frac{\lambda'(\lambda-\lambda')}{(\lambda_T-\lambda)(\beta_1+\xi)}\Gamma_{pa}[1-\exp\{-(\xi+\beta_1)h\}]\right]$$

$$\times\left[1-\frac{\lambda'(\lambda-\lambda')}{(\lambda_T-\lambda)(\beta_2+\xi)}\Gamma_{pa}\right]^{-1}. \tag{85}$$

A further simplification could be achieved by ignoring secondary effects at the anode, that is, by putting

$$\Gamma_{pa} = 0,$$

or

$$Y(\xi)/X(\xi) = 1.$$

Except in cases requiring extreme accuracy this will be a valid step.

(ii) *Second Approximation.*—For larger values of λh still, a further approximation is justified, this involving the neglect of all image terms. The associated simplification is achieved by assuming that

$$\lambda^2 \gg |\xi^2-2\alpha\lambda| \tag{86}$$

for all significant values of ξ (see (iv) below).

Subject to this condition,

$$\beta_1 = \alpha - \xi^2/2\lambda; \qquad \beta_2 = 2\lambda; \qquad \alpha_T = \alpha;$$

while

$$|\beta_2/\beta_1| \gg 1.$$

Using these values for β_1 and β_2, equation (83) reduces to

$$\psi(\xi, h) = \left(1 - \frac{\lambda}{\lambda_T}\right)\frac{P}{2\pi D}\cdot\frac{2\exp(\alpha - \xi^2/2\lambda)h}{1 - \alpha M_2(\xi)}, \tag{87}$$

where
$$M_2(\xi) = \frac{\Gamma_{1c}}{\alpha - \xi^2/2\lambda}\{\exp(\alpha - \xi^2/2\lambda)h - 1\} + \frac{\Gamma_{pc}}{\alpha - \xi^2/2\lambda}\{\exp(\alpha - \xi^2/2\lambda - \xi)h - 1\}, \tag{88}$$

with

$$\Gamma_{1c} = 2(1 - W/\bar{c})\gamma_{1c} \simeq 2\gamma_{1c}, \tag{89}$$

$$\Gamma_{pc} = (\eta/\alpha)(1 - W/\bar{c})\gamma_{pc} \simeq (\eta/\alpha)\gamma_{pc}. \tag{90}$$

The limitation (86) can be expressed in terms of λh, this being done in (iv) below.

(iii) *Low Pressure Limit.*—For sufficiently low pressures, a somewhat different type of approximation is possible. Using the scaling laws given in Section II(d), inspection of equations (83), (84), and (85) shows that for a given E/p the terms involving the Γ's are more pressure dependent than the associated terms $\lambda - \beta_2$ and 1. The difference between the two sets of terms is not simple but involves at least one order of p. This means that for sufficiently low p, secondary emission is unimportant and (83) reduces to

$$\psi(\xi, h) = -(1 - \lambda/\lambda_T)(P/2\pi D)\,2\exp\beta_1 h. \tag{91}$$

It follows that

$$\frac{\psi(\xi, h)}{\psi(0, h)} = \exp\{\lambda' - (\xi^2 + \lambda'^2)^{\frac{1}{2}}\}h, \tag{92}$$

this leading to the Huxley–Crompton relationship with, however, λ' replacing λ. This result was originally derived by Huxley (1959).

An associated result of equal importance defines the Townsend first ionization coefficient α_T. From equations (12), (80), and (91)

$$\frac{i_z(\infty, h)}{i_z(\infty, 0)} = \exp(\lambda - \lambda')h \tag{93}$$

in the limit $p \to 0$. (It is to be noted that in the absence of secondary effects, ionization does not alter the cathode source distribution.) Therefore, by definition,

$$\lambda - \lambda' = \alpha_T \qquad \text{(Townsend's coefficient)}. \tag{94}$$

Since $\lambda'^2 = \lambda^2 - 2\alpha\lambda$, it follows that

$$\alpha = \alpha_T(1 - \alpha_T/2\lambda). \tag{95}$$

(iv) *Numerical Integration.*—In the general case, R cannot be expressed in a simple analytic form. Instead, even though an infinite integral, it must be evaluated by numerical methods. That this can be done to any required degree of accuracy is readily confirmed. Consider

$$R(x_r) = \int_0^{x_r} \mathrm{J}_1(x)\, F(x)\, \mathrm{d}x,$$

where x_r is the rth root of $\mathrm{J}_1(x)$. Then provided $F(x)$ is a monotonically decreasing function of x for $x > x_0$, where $x_0 < x_r$, the damped oscillatory nature of $\mathrm{J}_1(x)$ ensures that

$$\begin{aligned} |R(\infty) - R(x_r)| &< \left| \int_{x_r}^{x_{r+1}} \mathrm{J}_1(x)\, F(x)\, \mathrm{d}x \right| \\ &< |\mathrm{J}_1(x_\mathrm{m})\,(x_{r+1} - x_r)|\; |F(x_r)|, \end{aligned}$$

x_{r+1} being the $(r+1)$th root of $\mathrm{J}_1(x)$. $\mathrm{J}_1(x_\mathrm{m})$ is the maximum value of $\mathrm{J}_1(x)$ in the interval $x_r < x < x_{r+1}$.

If the maximum tolerable error in the computation is denoted by ϵ, then

$$\frac{|R(\infty) - R(x_r)|}{R(\infty)} \leqslant \epsilon.$$

This is satisfied provided

$$\frac{|\mathrm{J}_1(x_\mathrm{m})\,(x_{r+1} - x_r)|\; |F(x_r)|}{R(\infty)} \leqslant \epsilon.$$

This inequality may now be regarded as an equation for x_r, defining the greatest significant value of x. The maximum value of $|\mathrm{J}_1(x_\mathrm{m})\,(x_{r+1} - x_r)|$ occurs between the first and second roots of $\mathrm{J}_1(x)$, being $2\cdot 22$. Hence, we may write

$$F(x_r) = \frac{\epsilon\, R(\infty)}{2\cdot 22}. \tag{96}$$

In the application of the results of this analysis, $R(\infty)$ is given, being an experimentally determined quantity. Again,

$$F(x_r) \equiv \frac{\psi(\xi, h)}{\psi(0, h)},$$

with

$$x_r = \xi_r\, b.$$

Therefore, from equation (83),

$$F(x_r) = K(x_r) \exp \beta_1 h, \tag{97}$$

where $K(x_r)$ is of the order of unity. Using this expression for $F(x_r)$ in (96), it may be shown that

$$(\xi_r^2 - 2\lambda\alpha) h^2 \simeq \left(\ln \frac{2\cdot 22}{\epsilon\, R(\infty)} \right)^2 + 2\lambda h \left(\ln \frac{2\cdot 22}{\epsilon\, R(\infty)} \right). \tag{98}$$

Upon insertion of values of practical interest in this equation, it is found that x_r should never have to be greater than the third root of $J_1(x)$, that is $7\cdot 02$, while the inequality (86) can be rewritten as

$$\lambda h \gg 20. \tag{99}$$

(c) *Breakdown Phenomena*

Conditions in the diffusion chamber will approach those of electrical breakdown when

$$i_z(\infty, h) \to \infty, \tag{100}$$

or, referring to equation (12),

$$\psi(0, h) \to \infty. \tag{101}$$

From equation (81) it follows that the actual breakdown condition is

$$C(0) = D(0). \tag{102}$$

There is nothing to be gained by recording this relationship in detail, and only the conditions corresponding to the approximations (83) and (87) will be considered.

(i) *First Approximation.*—For values of λh of the order of 10 or greater, it follows from equations (83), (84), and (85) that the breakdown condition is

$$(\Gamma_{1c}+\Gamma_{pc})\left(\{\exp(\lambda-\lambda')h-1\}-\frac{Y(0)}{X(0)}\frac{\lambda-\lambda'}{\lambda+\lambda'}\exp(\lambda-\lambda')h\right) = 1, \tag{103}$$

where
$$\frac{Y(0)}{X(0)} = \left[1-\frac{\lambda'}{\lambda_T-\lambda}\Gamma_{pa}[1-\exp\{-(\lambda-\lambda')h\}]\right]\left[1-\frac{\lambda'(\lambda-\lambda')}{(\lambda_T-\lambda)(\lambda+\lambda')}\Gamma_{pa}\right]^{-1} \tag{104}$$

and $\lambda-\lambda' = \alpha_T$.

(ii) *Second Approximation.*—For $\lambda h \gg 20$, the corresponding approximation immediately follows, being

$$1 = (\Gamma_{1c}+\Gamma_{pc})(e^{\alpha h}-1), \tag{105}$$

$$\alpha = \alpha_T,$$

with
$$\Gamma_{1c} \simeq 2\gamma_{1c}, \tag{106}$$

$$\Gamma_{pc} \simeq (\eta/\alpha)\gamma_{pc} \qquad (\equiv \delta/\alpha). \tag{107}$$

The factor of 2 in (106), and which is also implicit in (107), is due to the fact that γ_{1c} was defined in terms of the axial component of flux only. If secondary electrons are emitted isotropically from the cathode surface, then the associated axial component of flux will only account for one half of the total secondaries introduced. This effect is similar to that already noted in equation (80), being clearly dependent on the true nature of the "reflection" coefficients.

(iii) *The Ratio* R.—As $\psi(0,h)$ approaches infinity, R approaches zero, this being due to the spread of the secondary source at the cathode. If in such circumstances the effects of secondary emission are ignored, and equation (52) is used to determine λ or λ', the corresponding values of k_1 will also tend to infinity as $\psi(0, h)$ approaches infinity. That is, unless realized, the spread of the secondary source of electrons at the cathode would be misinterpreted, being explained as a rapid radial diffusion associated with a high electron temperature.

(*d*) *Applications*

As already remarked in the Introduction, the application of the results of this analysis is given elsewhere. It is, however, worth noting here how these results may be applied.

For low values of E/p, $i_z(\infty, h) = i_z(\infty, 0)$. Denote this value of $i_z(\infty, 0)$ by $i_z^1(\infty, 0)$, then for higher values of E/p the ratio

$$\frac{i_z(\infty, h)}{i_z^1(\infty, 0)}$$

may be found from experiment. If now, for a given value of E/p, this ratio is determined as a function of p, apparent values of α_T/p may be obtained by using equation (93). These values will tend to an asymptotic limit as p approaches zero, this limit being the real value of α_T/p for the particular value of E/p chosen. In a similar manner, the real value of λ'/p may be found as a low pressure limit from the Huxley–Crompton relationship, R being experimentally determined as a function of p for given E/p. Hence λ/p, k_1, and α/p may also be found.

Again, since R approaches zero at breakdown, the value of p at which breakdown occurs, for a given E/p, may be experimentally determined. Knowing α_T/p and λ'/p, and ignoring secondary emission at the anode, we may then find $\Gamma_{1c}+\Gamma_{pc}$, from equation (103). Therefore, at an intermediate pressure value, R may be evaluated as a function of either Γ_{1c} or Γ_{pc} by using (13) and (83). Comparison with the corresponding experimental value of R then determines Γ_{1c} and Γ_{pc}. Finally, since W is known from other experiments, while assuming a Maxwellian distribution (i.e. $\Lambda = 1$) $\bar{c}$ may be found from k_1, the secondary coefficients $2\gamma_{1c}$ and $(\eta/\alpha)\gamma_{pc}$ may also be determined.

(If higher accuracy is required, Γ_{pa} in equations (103) and (83) could now be put equal to the value of Γ_{pc} already found, and the cycle of calculations repeated.)

V. DISCUSSION

Although apparently well defined by equation (25), and the corresponding equation at the anode, the subsequent analysis proved that the "reflection" coefficients have no simple physical meaning. They appear as parameters that can be chosen only after experiment. This is not particularly surprising since they actually account for a variety of phenomena, the most important of which are:

(1) The true physical reflecting properties of the electrodes.

(2) In general, in the vicinity of a boundary it is to be expected that the electron velocity distribution will be anisotropic, while relatively large density gradients could occur. Such effects could lead to non-uniform and non-scalar electron temperatures and associated transport coefficients. This means that

within a few mean free paths of a boundary, equations (2), (3), and (21) will inadequately describe the behaviour of the electrons. Therefore, if a solution of these particular equations is to be used to determine n, j_z, R etc., it follows that the boundary conditions, that is the "reflection" coefficients, must be of an artificial nature.

(3) The ζ's have only been defined in terms of the axial components of flux. Since, at a boundary, particles may also be introduced as a pure radial component, the ζ's must be capable of accounting for this.

(4) Associated with (2) and (3), but still an independent possibility, the source of axial flux could be inadequately defined, the true nature and distribution of this source only being accounted for by the ζ's.

As previously emphasized, it follows that the ζ's must be experimentally determined quantities. Their value, however, as meaningful theoretical parameters, depends on their behaviour with varying E/p and p and, in particular, with changes in geometrical dimensions and the magnitude of the total particle flux. The very fact that they are dependent only on E/p, as proved in Section III(c), and do not depend on the geometrical dimensions or particle flux, justifies their definition. The fact that the experimentally determined values, or the associated boundary conditions, appear to be unrealistic is quite immaterial. This does not mean to say, however, that a physical explanation of the associated results cannot be given. For instance, consider the case $\alpha = 0$, $\eta = 0$ of Section IV(a). In the absence of an electric field, particles leaving the cathode source hole can diffuse in a given time t into a half sphere of effective radius

$$x_D = 2(Dt)^{\frac{1}{2}}.$$

On the other hand, in the absence of diffusion but in the presence of an axial electric field, particles will drift in the same time a distance

$$Z = Wt.$$

On elimination of t from these two expressions, it follows that

$$x_D/Z = 2/\lambda x_D;$$

that is, for distances less than $2/\lambda$ in the vicinity of the source hole, diffusion processes dominate. Thus, particles leaving the source hole may diffuse into a half sphere of an effective radius of the order of $1/\lambda$ before the electric field has a major effect. For large λh, the effective radius of the distributed source is just $1/\lambda$ (cf. equations (78) and (79)) and, as seen by the anode, the true source of primary flux is simply the projection of this half sphere on to the cathode surface. However, as λh approaches zero, the anode boundary condition $n(r, h) = 0$ inhibits the formation of this diffusion region, and the effective source appears to be a true point of axial flux. Implicit in this explanation are two physical properties. The first is that the cathode surface is completely reflecting, as borne out by the basic pole-type solution ($N = 0$; equation (78)). The second is that electrons leaving the cathode hole have thermal energies characteristic of the electrons already in the diffusion chamber.

Associated with statement (2) above, the assumption of a uniform T_e and uniform associated transport coefficients has been implicit throughout this analysis. It is neither obvious nor certain that such an assumption is valid. If it is, then the energy equation per unit volume is of the form

$$n_e n_g f(T_e, T_g) = n_e e_e E_z v_z; \tag{108}$$

that is, the energy gained by the electrons from the electric field is exactly equal to that lost in binary collisions with the gas atoms or molecules. Since $j_z = nv_z$, it follows from equations (4) and (5) that v_z scales as $D\lambda$, that is as W which is a function of E/p and T_e. Therefore, from (108),

$$T_e \equiv T_e(E/p, T_g).$$

However, the assumption of uniform T_e depends now on the assumption of uniform v_z. This latter assumption is obviously incorrect, at least near the anode where n is rapidly changing. It is not clear, however, to what extent, if any, this invalidates or restricts the results derived in this paper. Since these non-uniformities will be most marked near the boundaries, such effects could be accounted for by the correct choice of "reflection" coefficients and a choice of sufficiently large λh. This being the case, it follows that the real test of the adequacy of any such assumption finally rests with experiment. That is, the validity of the results derived in the present paper depends solely on the consistency of the theoretical predictions with the experimental results. In particular, if the deduced values of k_1, Γ_1, λ/p, etc. depend only on E/p and not on either p or b/h, then it may be assumed that these are the correct values. That this has been shown to be the case (see Crompton and Jory 1962; Crompton *et al.* 1965) proves the adequacy of the theory and of the associated assumptions.

VI. ACKNOWLEDGMENTS

The authors would like to thank Dr. R. W. Crompton for many helpful discussions and for suggesting this particular problem. They would also like to thank Mr. A. I. McIntosh for similar discussions and for doing the many numerical computations that were necessary before the adequacy of the theoretical results could be confirmed by experiment.

VII. REFERENCES

CROMPTON, R. W., and JORY, R. L. (1962).—*Aust. J. Phys.* **15**: 451.

CROMPTON, R. W., LILEY, B. S., MCINTOSH, A. I., and HURST, C. A. (1965).—*Int. Conf. Ioniz. Phenom. Gases* 7. (In press.)

HUXLEY, L. G. H. (1940).—*Phil. Mag.* **30**: 396.

HUXLEY, L. G. H. (1959).—*Aust. J. Phys.* **12**: 171.

HUXLEY, L. G. H., and CROMPTON, R. W. (1955).—*Proc. Phys. Soc. Lond.* B **68**: 381.

HUXLEY, L. G. H., and CROMPTON, R. W. (1962).—*In* "Atomic and Molecular Processes". (Ed. D. R. Bates.) p. 335. (Academic Press: New York.)

WATSON, G. N. (1944).—"A Treatise on the Theory of Bessel Functions." 2nd. Ed. (Cambridge Univ. Press.)

THE DIFFUSION AND ATTACHMENT OF ELECTRONS IN WATER VAPOUR

By R. W. Crompton,* J. A. Rees,*† and R. L. Jory*‡

[*Manuscript received July* 1, 1965]

Summary

The energy ratio and attachment coefficient for electrons in water vapour have been determined in the range $20 < E/p < 60$ V cm^{-1} torr^{-1}. The results for the attachment coefficient are in general agreement with other recent determinations, but those for the energy ratio differ significantly from the results of Bailey and Duncanson. The use of these new data, in conjunction with values of the drift velocity determined by Pack, Voshall, and Phelps, is shown to remove the serious discrepancy which previously existed between the results of single-collision and swarm experiments.

I. Introduction

When electrons having energies of the order of 5 eV pass through water vapour at a pressure of a few torr, an appreciable fraction of the electrons form negative ions by electron attachment. According to Laidler (1954), Craggs and McDowell (1955), and others, the dominant attachment process for energies up to about 10 eV is the following resonance capture process:

$$e+H_2O \rightarrow H^-+OH. \tag{1}$$

Laidler states that the water molecule is first raised to a repulsive $^2A_1$ or $^2A_2$ state of H_2O^- which at once dissociates into $H^-(^1S)$ and $OH(^2\pi)$. The appearance potential is of the order of 5·5 eV, and the cross section is a maximum for electrons having energies of about 6·5 eV.

The curve showing the variation with electron energy of the rate of production of H^- ions from H_2O shows a second, smaller peak which has a maximum value at an energy of about 8·5 eV (Mann, Hustrulid, and Tate 1940; Buchel'nikova 1959). For electrons of energy greater than about 7·5 eV, O^- ions may also be produced, the reaction being

$$e+H_2O \rightarrow O^-+2H. \tag{2}$$

It is widely believed (see, for example, Cottin 1959) that the H^- ions formed as above are rapidly converted to negative hydroxyl ions by the following process:

$$H^-+H_2O \rightarrow OH^-+H_2. \tag{3}$$

At gas pressures of the order of 1 torr, Branscomb and Smith (1955) and Muschlitz and Bailey (1956) observed that the OH^- ions so formed were considerably more abundant than either H^- or O^- ions.

---

* Ion Diffusion Unit, Australian National University, Canberra.

† Present address: Department of Electrical Engineering, University of Liverpool, England.

‡ Present address: Department of Chemistry, Institute of Molecular Biophysics, Florida State University, Tallahassee, Florida, U.S.A.

Aust. J. Phys., 1965, **18**, 541–51

The dependence of the cross sections for the various attachment processes on the energy of the incident electrons has been investigated in low-pressure beam-scattering experiments by Mann, Hustrulid, and Tate (1940), Buchel'nikova (1959), Schulz (1960), and others. In addition to these investigations, studies have been made of the behaviour of electrons in water vapour by Bailey and Duncanson (1930), Bradbury and Tatel (1934), Kuffel (1959), and Prasad and Craggs (1960), while Hurst, O'Kelly, and Bortner (1961) have carried out a series of experiments with argon–water-vapour mixtures. The experiments in this second group were carried out using swarms of electrons having energies distributed about some mean value $\bar{\epsilon}$. The method adopted by Kuffel was that used earlier by Bradbury and yielded values of the attachment coefficient α_a/p, where α_a is defined as the fraction of the population of an electron swarm that forms negative ions in drifting 1 cm in the direction of an applied electric field E, and p is the gas pressure. Kuffel's measurements were made for values of the parameter E/p lying between 1 and 28, E being measured in V/cm and p in torr. Bailey and Duncanson also measured values of the attachment coefficient, and in addition obtained values of the energy ratio k_1 from which the Townsend energy factor can be derived. Prasad and Craggs studied the growth of electron current between plane-parallel electrodes for $25 < E/p < 40$ and obtained values of the attachment and primary ionization coefficients. Using a parallel-plate ionization chamber, Hurst, O'Kelly, and Bortner measured pulse heights and drift velocities and analysed these data to obtain values of the attachment coefficient for argon containing small concentrations of water vapour. The measurements were made for a series of values of E/p and for varying concentrations of water vapour at each value. By extrapolating the data to zero concentration, they were able to obtain the cross section for electron attachment in water vapour averaged over the energy distribution appropriate to pure argon at each value of E/p. This method does not, however, enable the attachment coefficient for electrons in water vapour to be determined as a function of E/p.

Although Hurst, O'Kelly, and Bortner were able to show that the data from their experiments with mixtures were consistent with the data from Buchel'nikova's beam experiment, the agreement between the results of other investigations in water vapour, particularly between the results of swarm and beam experiments, is in general poor (Prasad and Craggs 1960). The present investigation was undertaken in an attempt to remove some of the major discrepancies. In particular, measurements have been made of the variation with E/p of the energy ratio k_1 and the attachment coefficient α_a/p. The results obtained for $20 < E/p < 60$ are given in the present paper.

II. Experimental Method

The method adopted in the present investigation for the determination of k_1 and α_a/p was that proposed by Huxley (1959) (see also Hurst and Huxley 1960) and applied hitherto to measurements in oxygen (Huxley, Crompton, and Bagot 1959; Rees 1965). The apparatus used for the investigation has been fully described by Crompton and Jory (1962) and is shown schematically in Figure 1. The experimental method need only be outlined here and may be understood by referring to the figure.

Electrons from the heated platinum filament F passed through a small hole (1 mm diam.) in the cathode C and travelled under the influence of the applied electric field E to the anode A, some of the electrons becoming attached to molecules of water vapour in their passage between the electrodes. The experimental parameters were adjusted so that any negative ions formed between the filament and cathode fell eventually on the centre disk A_1 of the collecting electrode, A_1 being connected to earth during the taking of all the measurements. For given values of the gas pressure and of the parameter E/p, the ratio R of the current received by the annular section A_2 to the sum of currents received by the sections A_2 and A_3 of the collecting electrode was determined for two values of the length h of the diffusion chamber. The currents to the sections of the collecting electrode resulted, of course, from the incidence of free electrons and of negative ions formed by attachment in the diffusion chamber. From the pair of measurements of R taken at the two values of h, it was possible to determine the values of k_1 and α_a/p appropriate to the particular value of E/p. For all the values of E/p used, it was necessary to allow for the influence of ionization in the diffusion chamber, and for this purpose values of α_i/p (the Townsend primary ionization coefficient) determined by Prasad and Craggs (1960) were adopted. The evaluation of k_1 and α_a/p was carried out with the aid of an IBM 1620 computer.

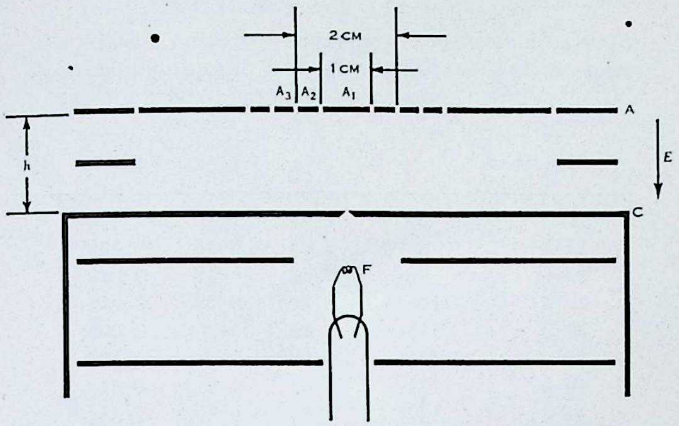

Fig. 1.—Schematic diagram of diffusion apparatus.

It was not possible to heat the diffusion apparatus to degas the electrodes and Pyrex envelope. However, with no liquid-air trap on the vacuum system, the background outgassing rate of the entire apparatus was 1×10^{-7} torr/min, and the system was evacuated to a pressure of the order of 5×10^{-5} torr before the gas samples were introduced. The water vapour was obtained from distilled water which had been further purified by passage through a mixed-bed resin. After being introduced to the vacuum system, the water was carefully treated by repeated pumping over the sample, both when liquid and when frozen, to remove any dissolved gases such as oxygen and carbon dioxide. When the whole of the vacuum system was connected to a liquid-air trap, the pressure in the system was gradually reduced to the background pressure of less than 10^{-4} torr, showing that the level of impurity from non-condensible gases in the samples of water vapour was less than about 100 p.p.m. Since there is some controversy as to the level of impurity that can significantly affect the attachment cross section in water vapour (Branscomb 1961; Pack, Voshall, and Phelps 1962), the level of impurity present in these experiments should be borne in mind when assessing the reliability of the measurements of the attachment coefficient. On the other hand, the consistency of the results with change in pressure as shown in Figure 3 should also be noted, together with the agreement found with the data from single-scattering experiments as discussed in Section IV. It seems unlikely that the measured values of k_1 will be sensitive to an impurity level of this magnitude, so that these values are considered reliable within the limits of experimental error discussed in Section III.

TABLE 1

VARIATION OF k_1 AND α_a/p WITH E/p IN WATER VAPOUR IN THE RANGE $20 < E/p < 60$ AT 293°K

Equivalent values of D/μ appropriate to each value of k_1 are shown, and also the values of α_i/p used in the computation of the results for α_a/p

E/p	k_1	D/μ	α_a/p	α_i/p*
20	63·0	1·59	—	0·022
22·5	82·0	2·07	0·15	0·033
25·0	96·0	2·43	0·17	0·049
27·5	105·4	2·66	0·19	0·072
30·0	113	2·85	0·20	0·098
35·0	124	3·13	$0·21_5$	0·162
40·0	131	3·31	$0·21_5$	0·245
45·0	137	3·46	$0·20_5$	0·35
50·0	142	3·58	0·19	0·46
55·0	144	3·64	0·17	0·60
60·0	147	3·71	0·15	0·79

* The values of α_i/p in the range $30 < E/p < 50$ are those of Prasad and Craggs (1960); the other values were obtained by extrapolation from this range.

III. RESULTS

Measurements of the ratio of currents, R, were made with $h = 2$, 4, and 5 cm at pressures of 1·17, 1·38, and 2·13 torr, and with $h = 2$, 4, and 6 cm at pressure 1·23 torr. The measurements were made over the range $20 < E/p < 60$ and were taken at a temperature of 20°C. From the measured values of R, the values of k_1 and α_a/p were determined. These values are summarized in Table 1 together with values of D/μ equivalent to each value of k_1, D being the diffusion coefficient for the electrons and μ the ratio of the drift velocity W to the electric field E. The table contains also the values of the ionization coefficient α_i/p that were adopted in the calculation of α_a/p. At the intermediate values of E/p the values of α_i/p used are those given by Prasad and Craggs (1960), while for lower and higher values of E/p extrapolations of those workers' data have been used. It should be emphasized that the results given in Table 1 for k_1 and α_a/p could be readily recomputed if later determinations of α_i/p differ markedly from the values shown in the table.

(*a*) *Results for* k_1

The results obtained for k_1, which are shown in Figure 2, were subject to a maximum scatter of less than 3% and were independent of the gas pressure used. Further, the results were independent of the way in which the measured values of the ratios R were combined in the analysis; for example, the same values of k_1 were obtained when the values of R determined at $h = 2$ cm were combined with those determined at either $h = 4$ or 6 cm. The main sources of error in the measurements were those arising from inaccuracies in the measurement of the relatively low gas pressures employed (measured to within ±1%) and from the heating of the gas in the diffusion chamber as a result of the high temperature at which it was necessary to operate the filament if adequate emission currents were to be obtained.

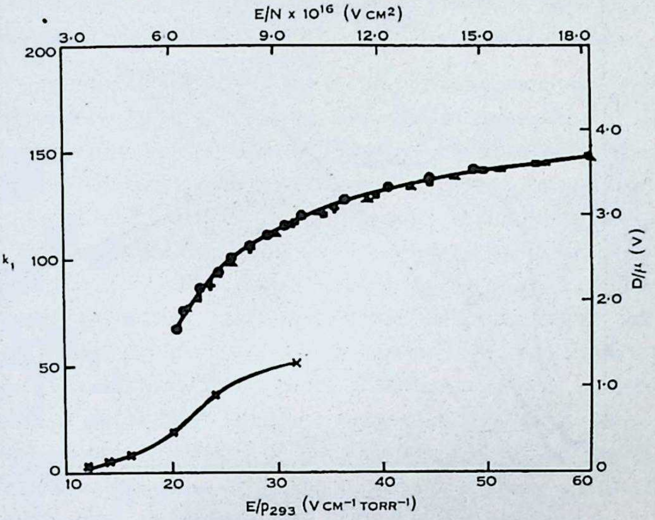

Fig. 2.—Experimental results for the energy ratio k_1 in water vapour. ▲ 1·17 torr; ● 1·23 torr; ■ 1·38 torr; + 2·13 torr; × Bailey and Duncanson. (Note: Conversion factor between E/p_{293} and E/N is $3 \cdot 03 \times 10^{15}$.)

The use of a receiving electrode of the configuration shown in Figure 1, in conjunction with a diffusion chamber of length 2 cm, enhances errors arising from the spatial dependence of the energy distribution as discussed by Parker (1963), but the magnitude of these errors is difficult to assess in specified instances in the absence of a complete theory. Nevertheless, it should be noted that the agreement between the results obtained by analysing the data obtained for different values of h is an indication that these errors are not serious.

In addition to the present results, Figure 2 includes the data obtained earlier by Bailey and Duncanson (1930), which we believe to be the only other data available. It is seen from Figure 2 that the present results lie well above the earlier data. One important consequence of this is discussed in Section IV.

(b) *Results for* α_a/p

The results obtained for α_a/p, which are shown in Figure 3, are subject to an r.m.s. error of ±5%. The major sources of this error were

(i) errors in pressure measurement and fluctuations in gas pressure;

(ii) errors in the measured values of the ratio R.

Both sources of error, in addition to influencing the accuracy of the values of α_a/p directly, also influenced the results indirectly through errors introduced into the values of k_1 used when calculating the values of α_a/p. The errors introduced directly were less than ±5%, while the error arising from an error of ±1% in the value for k_1 at a particular value of E/p was typically ±10%.

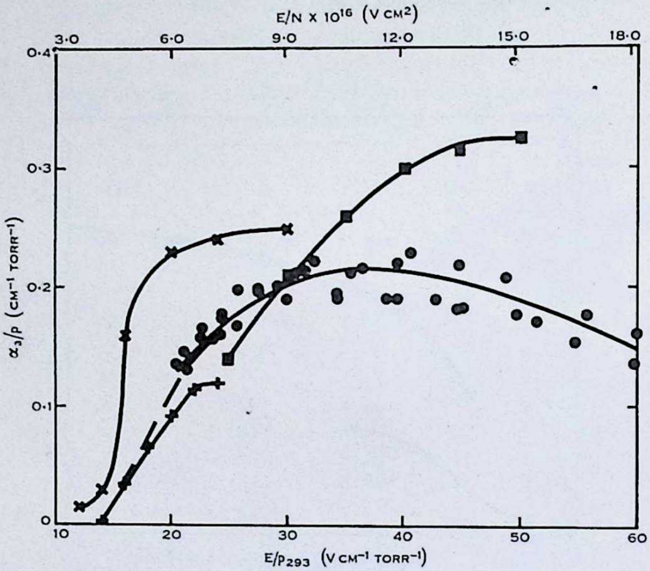

Fig. 3.—Experimental results for the attachment coefficient α_a/p in water vapour. ● Present results; × Bailey and Duncanson (1930); + Kuffel (1959); – – – Kuffel's data corrected for ionization; ■ Prasad and Craggs (1960). (Note: Conversion factor between E/p_{293} and E/N is $3\cdot03\times10^{15}$.)

In addition to the present results for α_a/p, Figure 3 shows the data obtained by Bailey and Duncanson (1930), Kuffel (1959), and Prasad and Craggs (1960). The present results lie up to 40% below those of Bailey and Duncanson; their results are in any case considerably higher than those of the other investigations. The values given by Kuffel for α_a/p are more accurately taken as being the values of $(\alpha_a/p-\alpha_i/p)$, and an attempt has been made in Figure 3 to adjust Kuffel's published data for α_a/p to allow for the influence of ionization, an extrapolation of the data of Prasad and Craggs for α_i/p being used in the correction. It is seen from Figure 3 that a smooth curve can be drawn through Kuffel's adjusted values and the present results. The results obtained by Prasad and Craggs for α_a/p are in fair agreement with our results at low values of E/p, but there is considerable divergence between the two sets of data at higher values of E/p.

IV. COMPARISON OF ATTACHMENT DATA FROM BEAM AND SWARM EXPERIMENTS

It is of interest to compare the results of single scattering experiments such as those of Buchel'nikova (1959) with those of swarm experiments. The most straightforward way of making such comparisons is to use the energy-dependent values of attachment cross section found from beam experiments to compute values of α_a/p for a series of values of E/p (e.g. Emeléus, Lunt, and Meek 1936; Asundi and Craggs 1964), the calculations depending on a known or postulated energy distribution within the swarm. Frequently, however, comparisons have been made (e.g. Craggs, Thorburn, and Tozer 1957; Bhalla and Craggs 1960; Prasad and Craggs 1960; Chanin, Phelps, and Biondi 1962; Rees 1964; Rees and Jory 1964) by comparing a "mean attachment cross section" $\bar{\sigma}_a$, derived from the swarm data, with values of the same quantity calculated by averaging the monoenergetic attachment cross section over the energy distribution of the swarm. This procedure is perhaps less satisfactory because of the difficulty in assigning a physical significance to $\bar{\sigma}_a$ (see equation (6)).

Although in general the results of these comparisons for several gases (e.g. Prasad and Craggs 1961; Rees 1964; Rees and Jory 1964) have shown discrepancies no greater than might be expected as a result of imprecise knowledge of the appropriate energy distributions, the comparisons for water vapour (Prasad and Craggs 1960) were a notable exception. For this gas, values of $\bar{\sigma}_a$ calculated from swarm experiments exceeded the corresponding values calculated from Buchel'nikova's data by a factor of 5 in some instances. The calculations described below suggest that the major part of this discrepancy can be attributed to the difference between the values of k_1 as a function of E/p given by Bailey and Duncanson (1930) and those given in Table 1. The calculations of Prasad and Craggs were, of course, based on the data of Bailey and Duncanson, which were at that time the only data available. Because of several factors which will become apparent in the discussion, we have thought it advisable to repeat the earlier calculations with the new data to demonstrate the removal of the earlier discrepancies, in addition to adopting the alternative, somewhat more straightforward, method of comparison. The results of the alternative method of comparison are given in the Appendix. As will be shown, the result of any method of comparison cannot be regarded as highly significant at the present time because of the lack of some of the necessary data.

The method of calculating "mean attachment cross sections" from the two types of experiment has been described by Bhalla and Craggs (1960) and is briefly as follows. The collision frequency for attachment of electrons of energy ϵ is given by $\nu_{a\epsilon} = N\sigma_{a\epsilon} c_\epsilon$, where N is the molecular number density and σ_a is the attachment cross section for electrons of speed c, the subscript ϵ denoting that each value is appropriate to an energy ϵ. If $\mathrm{d}n_\epsilon$ is the number of electrons per unit volume in the swarm with energy between ϵ and $\epsilon+\mathrm{d}\epsilon$, it follows from the definition of the attachment coefficient α_a that

$$N\int \sigma_{a\epsilon} c_\epsilon \,\mathrm{d}n_\epsilon = n_0 \alpha_a W, \qquad (4)$$

where $n_0\,(=\int \mathrm{d}n_\epsilon)$ is the number density of electrons in the swarm.

The "mean attachment cross section" $\bar{\sigma}_a$ can be defined through the equation (cf. Bhalla and Craggs 1960)

$$\bar{\sigma}_a = \frac{\alpha_a W}{N\bar{c}}. \tag{5}$$

Comparison of equations (4) and (5) shows that

$$n_0 \bar{\sigma}_a \bar{c} = \int \sigma_{a\epsilon} c_\epsilon \, dn_\epsilon,$$

so that

$$\bar{\sigma}_a = \frac{\overline{\sigma_a c}}{\bar{c}}. \tag{6}$$

Equation (5) can be rewritten

$$\begin{aligned} \bar{\sigma}_a &= \frac{1}{N_0}\left(\frac{W}{\bar{c}}\right)\left(\frac{\alpha_a}{p}\right) \\ &= \frac{A}{\bar{\epsilon}^{\frac{1}{2}}} W\left(\frac{\alpha_a}{p}\right), \end{aligned} \tag{7}$$

where N_0 is the gas molecular number density corresponding to unit pressure at some temperature, and A is a constant whose value depends in part on the form of the energy distribution in the swarm. Provided that k_1, W, α_a/p, and the form of the energy distribution are known as functions of E/p from swarm experiments, values of $\bar{\epsilon}$ can be calculated from the values of k_1 (e.g. Huxley and Crompton 1962) and values of $\bar{\sigma}_a$ then obtained by use of equation (7). A curve of $\bar{\sigma}_a$ versus $\bar{\epsilon}$ can then be plotted.*

Equation (6) likewise enables $\bar{\sigma}_a$ to be calculated for a series of values of $\bar{\epsilon}$ from the data provided by single collision experiments, the integrations being carried out for the same form of energy distribution as was used for the evaluation of $\bar{\sigma}_a$ from the swarm data.

In the absence of precise information on the form of the electron energy distribution in water vapour, comparisons have usually been made for typical energy distributions, for example the Maxwellian or Druyvesteyn distributions, although these may or may not resemble the true energy distribution in the gas (compare, for example, the energy distributions that have been reported for other molecular gases by Engelhardt and Phelps (1963), and by Engelhardt, Phelps, and Risk (1964)). Figure 4 shows such a comparison between Buchel'nikova's data and the data from our experiments where the data have been analysed on the basis of a Maxwellian distribution, using the values of k_1 given in Table 1 and the values of Pack, Voshall, and Phelps for W. A difficulty exists in carrying out the calculations in that there are no values of the drift velocity in water vapour measured by a time-of-flight technique for E/p greater than 27. The computation of the values of $\bar{\sigma}_a$ from the measured values of α_a/p requires values of W for E/p as high as 40; those portions of the curves in

---

* The values of $\bar{\sigma}_a$ computed from data for α_a/p for dry air and carbon dioxide by Rees (1964) and Rees and Jory (1964) are in error by 7%, the correct values being 7% higher than those quoted. This systematic error does not in any way affect the conclusions drawn from the comparisons of the values of $\bar{\sigma}_a$ with corresponding values deduced from beam data for $\bar{\sigma}_{a\epsilon}$, the latter values of $\bar{\sigma}_a$ being correctly given.

Figure 4 represented by broken lines result from the use of values of W that have been extrapolated in the range $27 < E/p < 40$, so that less reliance should be placed upon these sections of the curves.

Also plotted in Figure 4 is the curve for $\bar{\sigma}_a$ versus $\bar{\epsilon}$ calculated by Prasad and Craggs (again for a Maxwellian distribution) from their measured values of α_a/p and using values of k_1 and W published by Bailey and Duncanson.* The curve resulting from a recalculation of these data using the newer data for k_1 and W is also shown. It can be seen that the use of the new auxiliary data results in very much closer agreement between the results of Buchel'nikova and those of Prasad and Craggs, the newer data for k_1 being mainly responsible for this closer agreement, since the data for W of Bailey and Duncanson are not very different from the later results of Pack, Voshall, and Phelps for E/p greater than 20. Still better agreement exists, however, between the data of Buchel'nikova and those from our experiments, but the

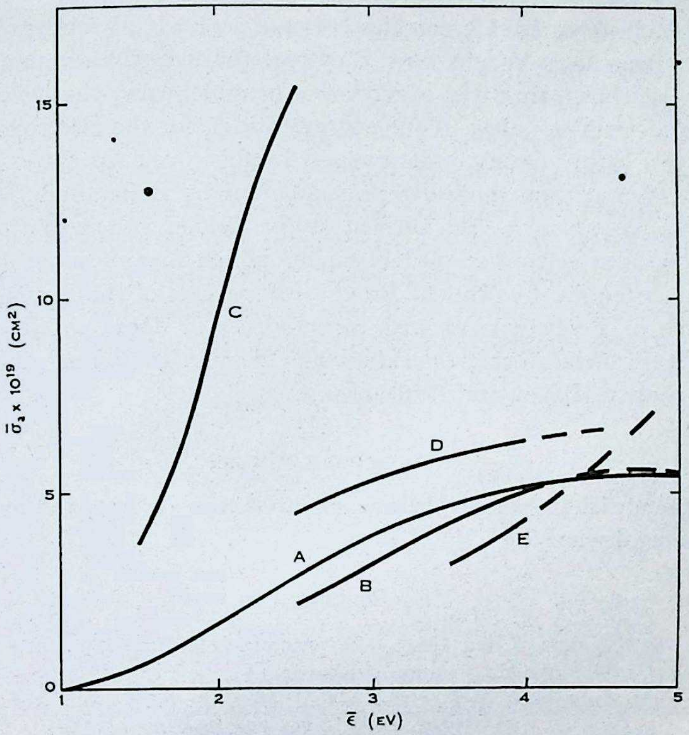

Fig. 4.—Comparison of the results of beam and swarm experiments for the "mean attachment cross section" $\bar{\sigma}_a$ in water vapour (assuming a Maxwellian distribution). A, from Buchel'nikova's (1959) data; B, from the present data; C, Prasad and Craggs (1960); D, from the data of Bailey and Duncanson (1930) for α_a/p, and the new data for k_1 and W; E, curve C recalculated using the new data for k_1 and W.

---

* The values of W given by Bailey and Duncanson were obtained using the magnetic deflection method. There exists, therefore, the possibility of large errors apart from experimental errors (see, for example, Jory 1965).

sensitivity of the comparisons to the form of energy distribution adopted (cf. Bhalla and Craggs 1960), together with the need to use extrapolated values of W for part of the curves, should be borne in mind when assessing the significance of the agreement. It is for these reasons that we do not feel justified in claiming more than the removal of a serious discrepancy between the results of single collision and swarm experiments.

V. Conclusion

Although electrons having energies between 5 and 10 eV undergo considerable attachment to form negative ions when they pass through water vapour, the present investigation has shown that it is nevertheless possible, using the method suggested by Huxley, to determine values of the energy ratio k_1 for the electrons. The values of k_1 (or of the parameter D/μ) determined in this work for $20 < E/p < 60$ are considerably different from those determined earlier by Bailey and Duncanson. In addition to the values of k_1, the present study yielded values of the attachment coefficient α_a/p for electrons in water vapour which merge smoothly with those determined at lower E/p by Kuffel. From a comparison of the results of the single scattering data of Buchel'nikova with various sets of data for α_a/p from swarm experiments, it is concluded that the values of k_1 given in Table 1 are likely to be more reliable than those of Bailey and Duncanson.

VI. Acknowledgment

The authors wish to express their thanks to their colleagues in the Ion Diffusion Unit for valuable discussions.

VII. References

Asundi, R. K., and Craggs, J. D. (1964).—*In* "Atomic Collision Processes". (Ed. M. R. C. McDowell.) p. 549. (North-Holland: Amsterdam.)
Bailey, V. A., and Duncanson, W. E. (1930).—*Phil. Mag.* **10**: 145.
Bhalla, M. S., and Craggs, J. D. (1960).—*Proc. Phys. Soc.* **76**: 369.
Bradbury, N. E., and Tatel, H. E. (1934).—*J. Chem. Phys.* **2**: 835.
Branscomb, L. M. (1961).—*Int. Conf. Ioniz. Phenom. Gases* **5**: 1.
Branscomb, L. M., and Smith, S. J. (1955).—*Phys. Rev.* **98**: 1028.
Buchel'nikova, N. S. (1959).—*Soviet Phys.–J.E.T.P.* **8**: 783.
Chanin, L. M., Phelps, A. V., and Biondi, M. A. (1962).—*Phys. Rev.* **128**: 219.
Cottin, M. (1959).—*J. Chim. Phys.* **56**: 1024.
Craggs, J. D., and McDowell, C. A. (1955).—*Rep. Prog. Phys.* **18**: 374.
Craggs, J. D., Thorburn, R., and Tozer, B. A. (1957).—*Proc. R. Soc.* A **240**: 473.
Crompton, R. W., and Jory, R. L. (1962).—*Aust. J. Phys.* **15**: 451.
Emeléus, K. G., Lunt, R. W., and Meek, C. A. (1936).—*Proc. R. Soc.* A **156**: 394.
Engelhardt, A. G., and Phelps, A. V. (1963).—*Phys. Rev.* **131**: 2115.
Engelhardt, A. G., Phelps, A. V., and Risk, C. G. (1964).—*Phys. Rev.* **135**: A 1566.
Hurst, C. A., and Huxley, L. G. H. (1960).—*Aust. J. Phys.* **13**: 21.
Hurst, G. S., O'Kelly, L. B., and Bortner, T. E. (1961).—*Phys. Rev.* **123**: 1715.
Huxley, L. G. H. (1959).—*Aust. J. Phys.* **12**: 171.
Huxley, L. G. H., and Crompton, R. W. (1962).—The motions of slow electrons in gases. *In* "Atomic and Molecular Processes". (Ed. D. R. Bates.) (Academic Press: New York.)
Huxley, L. G. H., Crompton, R. W., and Bagot, C. H. (1959).—*Aust. J. Phys.* **12**: 303.
Jory, R. L. (1965).—*Aust. J. Phys.* **18**: 237.
Kuffel, E. (1959).—*Proc. Phys. Soc.* **74**: 297.

LAIDLER, K. J. (1954).—*J. Chem. Phys.* **22**: 1740.

MANN, M. M., HUSTRULID, A., and TATE, J. T. (1940).—*Phys. Rev.* **58**: 340.

MUSCHLITZ, E. E., and BAILEY, T. L. (1956).—*J. Phys. Chem.* **60**: 681.

PACK, J. L., VOSHALL, R. E., and PHELPS, A. V. (1962).—*Phys. Rev.* **127**: 2084.

PARKER, J. H. (1963).—*Phys. Rev.* **132**: 2096.

PRASAD, A. N., and CRAGGS, J. D. (1960).—*Proc. Phys. Soc.* **76**: 223.

PRASAD, A. N., and CRAGGS, J. D. (1961).—*Proc. Phys. Soc.* **77**: 385.

REES, J. A. (1964).—*Aust. J. Phys.* **17**: 462.

REES, J. A. (1965).—*Aust. J. Phys.* **18**: 41.

REES, J. A., and JORY, R. L. (1964).—*Aust. J. Phys.* **17**: 307.

SCHULZ, G. J. (1960).—*J. Chem. Phys.* **33**: 1661.

APPENDIX

Using the data of Table 1 for k_1 and the values of Pack, Voshall, and Phelps for W as auxiliary data, values of α_a/p have been calculated from Buchel'nikova's data for σ_{a_ϵ} by use of equation (4). The calculations were carried out for both Maxwellian and Druyvesteyn energy distributions The resulting values of α_a/p are compared in Table 2 with the data obtained in swarm experiments. The remarks made in Sections IV and V above in discussing the data of Figure 4 apply equally to the results of Table 2.

TABLE 2

COMPARISON OF EXPERIMENTAL VALUES OF α_a/p WITH COMPUTED VALUES DERIVED FROM THE DATA OF BUCHEL'NIKOVA

E/p_{293}	α_a/p_{293}				
	Bailey and Duncanson	Prasad and Craggs	Crompton, Rees, and Jory	Buchel'nikova (Maxwellian Distribution)	(Druyvesteyn Distribution)
22·5	0·236	—	0·15	0·18	$0{\cdot}10_5$
25	0·24	0·14	0·17	0·195	$0{\cdot}16_5$
27·5	$0{\cdot}24_5$	$0{\cdot}17_5$	0·19	0·20	0·20
30	0·25	0·21	0·20	$0{\cdot}20_5$	0·22
35	0·25	0·26	$0{\cdot}21_5$	0·21	$0{\cdot}24_5$
40	—	0·30	$0{\cdot}21_5$	0·22	0·26

CHARGED PARTICLE MOTION IN A TIME-DEPENDENT AXIALLY SYMMETRIC MAGNETIC FIELD

By P. W. Seymour,* R. B. Leipnik,† and A. F. Nicholson‡

[*Manuscript received May* 31, 1965]

Summary

Following a short review of the drift theory of plasma radial compression, an exact solution for the motion of a charged particle in an axially symmetric time-dependent magnetic field is obtained. The method gives forms for the cylindrical coordinates r and θ of the charged particle that have a simple interpretation, the z-motion being of constant velocity. As examples, the exact results are discussed for a simple power law and an exponential time dependence of the magnetic field and, using the latter results, the drift theory of plasma radial compression is qualitatively verified.

I. Introduction

In an earlier paper (Seymour 1963), a review was included of the drift theory of radial compression of a tenuous plasma suitably contained within a long, straight solenoid through which is passing a time-dependent electric current, and this was followed by a trajectory approach to the same problem using the equations of motion for a charged particle moving in a time-dependent axially symmetric magnetic field, $\mathbf{B}(t)$. A simple, but not very adequate, approximation then led to a flux-conserving result similar in form to, but different in nature from, that obtained by the drift analysis. At that stage it was evident that an exact solution for the trajectory approach would be helpful, since it should permit determination of the various charged particle motions that may occur in collisionless plasma approximation, but mathematical difficulties were encountered.

In the present paper, the general form of the exact microscopic solution for the motion of a charged particle in a time-dependent axially symmetric magnetic field is obtained, and applied to particular cases of interest. This gives insight into the macroscopic motions of charged particles in a plasma of low number density, in which interparticle collisions are rare. For the convenience of the reader, the salient features of the particle drift and trajectory approaches described by Seymour (1963, pp. 436–43) appear in the next section, prior to the derivation of the exact solution.

II. Charged Particle Guiding-Centre and Trajectory Approaches to Plasma Radial Compression

As is well known, drift analysis is primarily concerned with the motion of the guiding centre of a spiralling charged particle, whereas the trajectory approach seeks to determine the classical path traversed by the charged particle. For the magnetic field specified in Section I, we consider the above approaches separately.

---

* Department of Mathematical Physics, University of Adelaide.
† NOTS, China Lake, California, U.S.A.
‡ Philips Research Laboratory, Hendon, S. Aust.

(a) *Guiding-Centre Approach*

The geometry of interest is that of a long, straight solenoid through which is passing a current that varies with time. Within the solenoid, clear of the ends, the resulting time-dependent magnetic field possesses axial symmetry, and is simply $\mathbf{B}(t) = \mathbf{k}B_z(t)$, in the usual notation. Accordingly, it is plausible to assume that the induced electric field, **E**, has circular field lines, concentric with the longitudinal axis of symmetry of the solenoid. To calculate E_θ, we evaluate the line integral of **E** around a circular path P of radius r, bounding a surface S lying in a plane normal to the z axis of the solenoid. Employing electromagnetic units, we have from Maxwell's equation for the curl of **E**, and Stokes's theorem,

$$\oint_P \mathbf{E}.\mathrm{d}\mathbf{l} = -\int_S \dot{\mathbf{B}}.\mathbf{k}\,\mathrm{d}S, \tag{2.1}$$

where dl is taken along the boundary of P. Since $\dot{\mathbf{B}}$ has the same value at all points on the surface S, and also has the z direction of the unit vector **k**, (2.1) yields

$$E_\theta = -\tfrac{1}{2}r\dot{B}, \tag{2.2}$$

where for convenience we omit the subscript z from B_z.

The effect of this induced electric field in the presence of the magnetic field is to produce a drift of a charged particle's guiding centre at a velocity

$$\mathbf{v}_\mathrm{d} = \frac{\mathbf{E}\times\mathbf{B}}{B^2}. \tag{2.3}$$

Since a tenuous plasma is under consideration, we assume, for a reasonably strong magnetic field, a collisionless approximation in which the charged particles spiral about the magnetic field lines and do not transfer from one magnetic field line to another. In other words, diffusion transverse to the magnetic field is absent in this approximation, and typically, at some instant of time, guiding centres of certain plasma particles would be found lying on the path P of radius r, used in the calculation of E_θ. In the dynamic situation encountered here the time rate of change of r must therefore be equated to the radial drift velocity E_θ/B, to obtain the equation

$$\frac{2}{r}\dot{r}+\frac{1}{B}\dot{B} = 0, \tag{2.4}$$

with the solution

$$Br^2 = \text{constant}. \tag{2.5}$$

For the case of interest, $\dot{B} > 0$, this result states that the total flux, $\phi = \pi r^2 B$ enclosed by a circle of radius r, concentric with the solenoid axis, is conserved as r shrinks, and guiding centres lying on this circle move inward in the axially symmetric time-dependent magnetic field. Graphically, the particle guiding centres stick to the surface of some collapsing flux tube of the time-dependent magnetic field.

Bearing in mind the assumptions made above, one now wonders whether it is possible to demonstrate radial compression of the plasma under consideration by a non-drift analysis.

(b) *Trajectory Approach*

Using cylindrical coordinates, the velocity of a particle at r, θ, z may be written as

$$\mathbf{v} = \mathbf{r}_0 v_r + \boldsymbol{\theta}_0 v_\theta + \mathbf{k} v_z, \tag{2.6}$$

where $\mathbf{r}_0$, $\boldsymbol{\theta}_0$, $\mathbf{k}$ are unit vectors, and

$$v_r = \dot{r}, \qquad v_\theta = r\dot{\theta}, \qquad v_z = \dot{z}. \tag{2.7}$$

With similar resolution of $\mathbf{E}$ and $\mathbf{B}$, and recalling that $\mathrm{d}\mathbf{r}_0/\mathrm{d}\theta = \boldsymbol{\theta}_0$, $\mathrm{d}\boldsymbol{\theta}_0/\mathrm{d}\theta = -\mathbf{r}_0$, the non-relativistic equation of motion for a particle of charge q, mass m,

$$m\dot{\mathbf{v}} = q(\mathbf{E}+\mathbf{v}\times\mathbf{B}) \qquad \text{(e.m.u.)}, \tag{2.8}$$

in which radiation damping has been permissibly neglected, yields the component equations

$$\ddot{r} - r\dot{\theta}^2 = (q/m)[E_r + (r\dot{\theta}B_z - \dot{z}B_\theta)], \tag{2.9}$$

$$2\dot{r}\dot{\theta} + r\ddot{\theta} = (q/m)[E_\theta + (\dot{z}B_r - \dot{r}B_z)], \tag{2.10}$$

$$\ddot{z} = (q/m)[E_z + (\dot{r}B_\theta - r\dot{\theta}B_r)]. \tag{2.11}$$

To facilitate analysis, the current in the solenoid may be reasonably approximated as $\mathbf{j} = \boldsymbol{\theta}_0 j_\theta$, whereupon symmetry considerations (see, for example, Smythe 1950) suggest that the magnetic vector potential is simply

$$\mathbf{A} = \boldsymbol{\theta}_0 A_\theta. \tag{2.12}$$

Then, neglecting contributions to $\mathbf{E}$ from the scalar potential ϕ in

$$\mathbf{E} = -\dot{\mathbf{A}} - \nabla\phi, \tag{2.13}$$

we obtain (cf. Seymour 1963, pp. 437–9)

$$A_\theta = \tfrac{1}{2} r B_z, \tag{2.14}$$

and

$$E_\theta = -\tfrac{1}{2} r \dot{B}_z \qquad \text{as in (2.2)}, \tag{2.15}$$

by means of a proof which shows formally that the induced electric field lines are circles concentric with the z axis of the solenoid. The result (2.14) depends on the fact that B_z has no spatial dependence here, as can be deduced from the Maxwell field equations

$$\operatorname{div}\mathbf{B} = 0, \tag{2.16}$$

$$\operatorname{curl}\mathbf{B} = 0, \tag{2.17}$$

the latter equation applying inside the solenoid, where it is assumed that the displacement current may be neglected, and that the charged particle motions do not contribute to the magnetic field, so that $\mathbf{B}(t) = \mathbf{k}B_z(t)$ has $j_\theta(t)$ alone as its source.

If we now specialize the equations of motion (2.9), (2.10), and (2.11) to accord with the fields

$$\mathbf{E} = (0, -\tfrac{1}{2}r\dot{B}_z, 0), \tag{2.18}$$

$$\mathbf{B} = (0, 0, B_z), \tag{2.19}$$

we obtain, for the solenoid problem outlined,

$$\ddot{r} - r\dot{\theta}^2 = (q/m)B_z r\dot{\theta}, \tag{2.20}$$

$$2\dot{r}\dot{\theta} + r\ddot{\theta} = -(q/m)(\tfrac{1}{2}r\dot{B}_z + \dot{r}B_z), \tag{2.21}$$

$$\ddot{z} = 0. \tag{2.22}$$

Equation (2.21) immediately yields a first integral

$$\dot{\theta} = \omega_{\mathrm{L}}(t) + Cr^{-2}, \tag{2.23}$$

where $\omega_{\mathrm{L}}(t)$ is the Larmor angular frequency

$$\omega_{\mathrm{L}}(t) = -(q/2m)\,B_z(t), \tag{2.24}$$

and C is a real constant. Elimination of $\dot{\theta}$ from equation (2.20) by means of (2.23) gives the differential equation governing the behaviour of r,

$$\ddot{r} + \omega_{\mathrm{L}}^2 r - C^2 r^{-3} = 0. \tag{2.25}$$

From (2.22) it is seen that the z-direction motion is trivial in this case, v_z being constant. The significant results representing charged particle motions in this particular time-dependent magnetic field are therefore the integrated form of (2.23),

$$\theta = \int_0^t \omega_{\mathrm{L}}\,\mathrm{d}t' + C\int_0^t \frac{\mathrm{d}t'}{r^2} + \theta_0, \tag{2.26}$$

where θ_0 is the value of θ at $t = 0$, and the solution of equation (2.25) for r.

III. Solution of the r Equation and Modification of the θ Equation

To obtain the general solution of equation (2.25), we commence with the *ansatz*

$$\dot{r} = M(t)\,r + N(t)\,r^{-1}, \tag{3.1}$$

where M and N are functions of time to be determined, so that

$$\ddot{r} = (M^2 + \dot{M})r + \dot{N}r^{-1} - N^2 r^{-3} \tag{3.2}$$

contains terms in r of the type appearing in (2.25). In fact, for (3.2) to assume precisely the form of (2.25), we see at once that the relationships

$$M^2 + \dot{M} = -\omega_{\mathrm{L}}^2, \tag{3.3}$$

$$\dot{N} = 0, \tag{3.4}$$

$$N^2 = -C^2, \tag{3.5}$$

must hold. The last two equations are consistent, and give

$$N = \pm \mathrm{i}C, \tag{3.6}$$

where, from equation (2.23), C is a real constant.

Equation (3.3) is a particular form of Riccati's differential equation. The introduction of a new variable $s(t)$, such that

$$(\ln s)^{\cdot} = M, \tag{3.7}$$

transforms (3.3) to the form

$$\ddot{s} + \omega_{\mathrm{L}}^2 s = 0. \tag{3.8}$$

To express r in terms of s, where s is determined by equation (3.8) for chosen forms of $\omega_{\mathrm{L}}(t)$, we integrate (3.1), modified by insertion of $N = +\mathrm{i}C$, say, and M from equations (3.6) and (3.7) respectively, by use of the integrating factor s^{-2}, to obtain

$$r = s\left(A + 2\mathrm{i}C \int_0^t \frac{\mathrm{d}t'}{s^2}\right)^{\frac{1}{2}}, \tag{3.9}$$

from which it is evident that, in general, $s(t)$ and the integration constant A are complex quantities. Clearly, the form of this equation can be simplified by the introduction of a further complex variable

$$u(t) = A^{\frac{1}{2}} s(t). \tag{3.10}$$

Then (3.9) becomes

$$r = u\left(1 + 2\mathrm{i}C \int_0^t \frac{\mathrm{d}t'}{u^2}\right)^{\frac{1}{2}}, \tag{3.11}$$

and (3.8) transforms to

$$\ddot{u} + \omega_{\mathrm{L}}^2 u = 0. \tag{3.12}$$

Equation (2.25) is now represented by the pair of equations (3.11) and (3.12). The integral appearing in equation (3.11) can be performed in some cases of interest (an example will be given in Section VI), but in fact it can be avoided by developing an alternative form of solution for r. The equation

$$\dot{r} = \frac{\dot{s}}{s} r + \frac{\mathrm{i}C}{r}, \tag{3.13}$$

which led, through the use of the integrating factor s^{-2}, to (3.9), can also be rearranged to the form

$$\frac{\dot{r}}{r} - \frac{\dot{u}}{u} = \frac{\mathrm{i}C}{r^2}, \tag{3.14}$$

where (3.10) has been used to eliminate $s(t)$.

Equation (3.14) immediately yields by integration the inverted form of (3.9)

$$u = r \exp\left(-\mathrm{i}C \int_0^t \frac{\mathrm{d}t'}{r^2}\right), \tag{3.15}$$

where the multiplicative constant of integration can be seen to be unity by comparing (3.15) with (3.11) at $t = 0$.

Since r, C, and t are real quantities, we see at once that

$$r = (uu^*)^{\frac{1}{2}}, \qquad r \geqq 0, \tag{3.16}$$

where the equation

$$u^* = r\exp\left(\mathrm{i}C\int_0^t \frac{\mathrm{d}t'}{r^2}\right) \tag{3.17}$$

corresponds to the choice $N = -\mathrm{i}C$ in equation (3.6).

Writing

$$u(t) = \alpha(t) + \mathrm{i}\beta(t), \tag{3.18}$$

where α and β are real quantities, we have from (3.15)

$$C\int_0^t \frac{\mathrm{d}t'}{r^2} = -\tan^{-1}(\beta/\alpha). \tag{3.19}$$

Hence the expression for θ given by (2.26) becomes

$$\theta = \int_0^t \omega_{\mathrm{L}}\,\mathrm{d}t' - \tan^{-1}(\beta/\alpha) + \theta_0. \tag{3.20}$$

A useful identification of the constant C is obtained as follows. Insertion of (3.18) into (3.14), use of (3.16), and equation of imaginary parts shows that

$$W(\alpha, \beta) = -C, \tag{3.21}$$

where $W(\alpha, \beta)$ is the Wronskian determinant $\begin{vmatrix} \alpha & \beta \\ \dot{\alpha} & \dot{\beta} \end{vmatrix}$.

Let now $I_1(t)$ and $I_2(t)$ be linearly independent, real solutions of equation (3.12), such that

$$\alpha = a_{11} I_1 + a_{12} I_2, \tag{3.22}$$

$$\beta = a_{21} I_1 + a_{22} I_2, \tag{3.23}$$

the a_{ij} being arbitrary real constants. Then (3.21) gives

$$W(I_1, I_2) = \begin{vmatrix} I_1 & I_2 \\ \dot{I}_1 & \dot{I}_2 \end{vmatrix} = -\frac{C}{|a_{ij}|}. \tag{3.24}$$

From (3.18) and the form of α and β,

$$u = \mu I_1 + \rho I_2, \tag{3.25}$$

where

$$\mu = a_{11} + \mathrm{i}a_{21} = |\mu| \exp \mathrm{i}\epsilon_1, \qquad \rho = a_{12} + \mathrm{i}a_{22} = |\rho| \exp \mathrm{i}\epsilon_2,$$

and so (3.16) gives, as the general solution of (2.25),

$$r = \{|\mu|^2 I_1^2 + |\rho|^2 I_2^2 + 2|\mu||\rho|\, I_1 I_2 \cos(\epsilon_1 - \epsilon_2)\}^{\frac{1}{2}}, \tag{3.26}$$

where, from (3.24),

$$\sin(\epsilon_1 - \epsilon_2) = \frac{C}{|\mu||\rho|\, W(I_1, I_2)}. \tag{3.27}$$

Further, in view of (3.22) and (3.23), θ of (3.20) can be written as

$$\theta = \int_0^t \omega_{\mathrm{L}}\, \mathrm{d}t' - \tan^{-1}\left\{\frac{|\mu|\, I_1 \sin\epsilon_1 + |\rho|\, I_2 \sin\epsilon_2}{|\mu|\, I_1 \cos\epsilon_1 + |\rho|\, I_2 \cos\epsilon_2}\right\} + \theta_0. \tag{3.28}$$

Although these results for r and θ are of complicated appearance, they can, in fact, be interpreted in a simple manner. From (3.26) we see that at any instant of time r can be regarded as the resultant of two vectors, of lengths $|\mu|\, I_1(t)$ and $|\rho|\, I_2(t)$, having a constant angle $\epsilon_1 - \epsilon_2$ between them. If we now set $|\mu|\, I_1$ at angle ϵ_1 ($\epsilon_1 > \epsilon_2$, say) to an axis moving in the $r\theta$-plane with angular velocity $\omega_{\mathrm{L}}(t)$ about the z axis, and set $|\rho|\, I_2$ at angle ϵ_2 to this moving axis, then it is readily verified that the angle between the resultant r measured relative to the moving axis is the second term on the right-hand side of (3.28). The general solution for the charged particle motion in the $r\theta$-plane is thus pictorially represented by the vectors of lengths $|\mu|\, I_1$ and $|\rho|\, I_2$, with constant angle $\epsilon_1 - \epsilon_2$ between them, moving about the origin of coordinates at the angular velocity $\omega_{\mathrm{L}}(t)$.

IV. PARTICULAR SOLUTIONS OF THE u EQUATION, AND CORRESPONDING FORMS OF r AND θ

In this section we develop solutions for some simple time dependences of $\omega_{\mathrm{L}}(t)$.

Case (a) $\omega_L(\mathrm{t})$ *Obeys the Power Law* $\pm\gamma \mathrm{t}^{\mathrm{k}}$, $\mathrm{k} \neq -1$

If we adopt the functional transformation

$$v(t) = t^{-\frac{1}{2}}\, u(t), \tag{4.1}$$

equation (3.12) assumes the form

$$\frac{\ddot{v}}{\omega_{\mathrm{L}}^2} + \frac{\dot{v}}{t\omega_{\mathrm{L}}^2} + \left(1 - \frac{1}{4t^2\omega_{\mathrm{L}}^2}\right) v = 0, \tag{4.2}$$

which bears some resemblance to Bessel's differential equation

$$y'' + \frac{y'}{x} + \left(1 - \frac{p^2}{x^2}\right) y = 0, \tag{4.3}$$

where the prime denotes differentiation with respect to x. Comparison of (4.2) and (4.3) suggests a further transformation

$$y(x) = v(t), \tag{4.4}$$

where the new variable $x = x(t)$. Then (4.2) becomes

$$\frac{\dot{x}^2}{\omega_{\mathrm{L}}^2} y'' + \frac{1}{\omega_{\mathrm{L}}^2}\left(\ddot{x} + \frac{\dot{x}}{t}\right) y' + \left(1 - \frac{1}{4t^2\omega_{\mathrm{L}}^2}\right) y = 0, \tag{4.5}$$

and this assumes the Bessel form if

$$\dot{x} = \pm\omega_{\mathrm{L}}, \tag{4.6}$$

$$\ddot{x} + \frac{\dot{x}}{t} = \frac{\omega_{\mathrm{L}}^2}{x}, \tag{4.7}$$

$$\frac{p}{x} = \pm\frac{1}{2t\omega_{\mathrm{L}}}. \tag{4.8}$$

From (4.6) and (4.8) we find that

$$x = \frac{\gamma}{k+1} t^{k+1}, \tag{4.9}$$

where γ and k are constants, with $p = \frac{1}{2}(k+1)^{-1}$. From (4.6) it follows immediately that

$$\omega_{\mathrm{L}} = \pm \gamma t^{k}, \tag{4.10}$$

so that ω_{L} obeys a simple power law here, and $x = \pm \omega_{\mathrm{L}} t(1+k)^{-1}$. We note that (4.7) is consistent with (4.9) and (4.10).

In terms of the real cylindrical functions $\mathrm{J}_p(x)$ and $\mathrm{Y}_p(x)$, the Bessel functions of the first and second kind respectively, of order p and real argument x, the solution of (3.12) may be written, by use of (4.1) and (4.4), as

$$u(t) = t^{\frac{1}{2}}\{\lambda\, \mathrm{J}_p(x) + \sigma\, \mathrm{Y}_p(x)\}, \tag{4.11}$$

where, in general, $\lambda = |\lambda| \exp \mathrm{i}\psi_1$ and $\sigma = |\sigma| \exp \mathrm{i}\psi_2$ are complex constants. Since

$$\mathrm{Y}_p(x) = \frac{\mathrm{J}_p(x)\cos p\pi - \mathrm{J}_{-p}(x)}{\sin p\pi}, \tag{4.12}$$

we recall that, when p is not an integer, $\mathrm{Y}_p(x)$ in (4.11) can be replaced by J_{-p} to again give the general solution. However, when $p = n$, an integer, J_n and J_{-n} are no longer linearly independent, being related by

$$\mathrm{J}_{-n} = (-1)^n \mathrm{J}_n, \tag{4.13}$$

and so we retain the form (4.11), modified by introduction of J_n and Y_n, where

$$\mathrm{Y}_n(x) = \lim_{p \to n} \mathrm{Y}_p(x). \tag{4.14}$$

Considering, for example, non-integral p, (3.16) and the appropriate form of u described above give

$$r = [t\{|\lambda|^2 \mathrm{J}_p^2 + |\sigma|^2 \mathrm{J}_{-p}^2 + 2|\lambda||\sigma|\, \mathrm{J}_p \mathrm{J}_{-p} \cos(\psi_1 - \psi_2)\}]^{\frac{1}{2}}. \tag{4.15}$$

The associated angle, θ, is obtained from (3.20), (4.10), and the appropriate u as

$$\theta = \pm \frac{\gamma}{k+1} t^{k+1} - \tan^{-1}\left(\frac{|\lambda|\, \mathrm{J}_p \sin\psi_1 + |\sigma|\, \mathrm{J}_{-p} \sin\psi_2}{|\lambda|\, \mathrm{J}_p \cos\psi_1 + |\sigma|\, \mathrm{J}_{-p} \cos\psi_2}\right) + \theta_0. \tag{4.16}$$

Similar results are obtained for p an integer.

When $k = -1$, we see from $p = \frac{1}{2}(k+1)^{-1}$ that the Bessel functions are of infinite order. In this case we proceed as follows.

Case (b) ω_L(t) Varies Inversely with the Time

For $k = -1$, equation (4.10) gives

$$\omega_{\mathrm{L}}(t) = \pm \gamma / t, \tag{4.17}$$

and hence equation (3.12) becomes

$$t^2 \ddot{u} + \gamma^2 u = 0, \tag{4.18}$$

a simplified form of the Euler–Cauchy equation. The usual procedure here is to let

$$u(t) = v(x), \tag{4.19}$$

where

$$x = \ln t, \tag{4.20}$$

whereupon (4.18) transforms to the second-order linear differential equation with constant coefficients

$$v'' - v' + \gamma^2 v = 0, \tag{4.21}$$

with characteristic equation

$$\xi^2 - \xi + \gamma^2 = 0. \tag{4.22}$$

The general solution of (4.21) is, of course,

$$v = K_1 \exp \xi_1 x + K_2 \exp \xi_2 x, \tag{4.23}$$

where

$$\xi_1 = \tfrac{1}{2} + \eta, \qquad \xi_2 = \tfrac{1}{2} - \eta, \tag{4.24}$$

with

$$\eta = (\tfrac{1}{4} - \gamma^2)^{\frac{1}{2}}. \tag{4.25}$$

Using (4.19), (4.20), and (4.24), equation (4.23) becomes

$$u = t^{\frac{1}{2}}(K_1 t^{\eta} + K_2 t^{-\eta}), \tag{4.26}$$

where K_1 and K_2 are, in general, complex constants.

Three particular forms of (4.26) must now be considered:

(i) $\tfrac{1}{4} > \gamma^2, \quad \eta > 0.$ (4.27)

Equation (4.26) applies as it stands.

(ii) $\tfrac{1}{4} = \gamma^2, \quad \eta = 0.$ (4.28)

Equation (4.26) assumes the form

$$u = t^{\frac{1}{2}}(K_3 + K_4 \ln t), \tag{4.29}$$

where K_3 and K_4 are complex constants.

(iii) $\tfrac{1}{4} < \gamma^2, \quad \eta = \mathrm{i}\eta_0$, where $\eta_0 = (\gamma^2 - \tfrac{1}{4})^{\frac{1}{2}} > 0.$ (4.30)

Equation (4.26) here becomes

$$u = t^{\frac{1}{2}}\{K_5 \cos(\eta_0 \ln t) + K_6 \sin(\eta_0 \ln t)\}, \tag{4.31}$$

where K_5 and K_6 are complex constants.

The forms of r and θ associated with (i), (ii), and (iii) above are readily obtained from (3.16) and (3.20) respectively. As can be seen, the charged particle motions in each instance are markedly different.

Case (c) $\omega_L(t)$ *Varies Exponentially with the Time*

In this case we first transform (3.12) by assuming

$$u(t) = v(x), \tag{4.32}$$

where, with D and G real constants,

$$x = D\mathrm{e}^{Gt}. \tag{4.33}$$

The result,

$$G^2(x^2v''+xv')+\omega_L^2\, v = 0, \tag{4.34}$$

can then be converted to the form of Bessel's equation (4.3), by a particular choice of ω_L, namely,

$$\omega_L^2 = G^2(x^2-p^2). \tag{4.35}$$

Then, for $G \neq 0$, (4.34) yields the required form

$$x^2v''+xv'+(x^2-p^2)v = 0, \tag{4.36}$$

and so from (4.32) the general solution of (3.12) for ω_L varying exponentially as in (4.35) is

$$u(t) = \mu\, J_p + \rho\, Y_p, \tag{4.37}$$

where μ and ρ are complex constants. For p not an integer the solution for r here is

$$r = \{|\lambda|^2 J_p^2 + |\sigma|^2 J_{-p}^2 + 2|\lambda||\sigma|\, J_p\, J_{-p} \cos(\psi_1-\psi_2)\}^{\frac{1}{2}}, \tag{4.38}$$

in the notation of Case (a) of this section. Correspondingly, the equation for θ becomes, from (3.20), (4.33), and (4.35),

$$\theta = \frac{\omega_L}{G} \mp p \sec^{-1}\left|\frac{x}{p}\right| - \tan^{-1}\left(\frac{|\lambda|\, J_p \sin\psi_1 + |\sigma|\, J_{-p} \sin\psi_2}{|\lambda|\, J_p \cos\psi_1 + |\sigma|\, J_{-p} \cos\psi_2}\right) + \theta_0, \tag{4.39}$$

after the performance of an elementary integration to obtain the first two terms on the right-hand side. Proceeding as in Case (a), we similarly obtain r and θ here for $p = n$, an integer.

V. DISCUSSION OF RESULTS

When $p = \frac{1}{2}$, the Bessel functions J_p and J_{-p} become simply

$$J_{\frac{1}{2}} = \left(\frac{2}{\pi x}\right)^{\frac{1}{2}} \sin x, \tag{5.1}$$

and

$$J_{-\frac{1}{2}} = \left(\frac{2}{\pi x}\right)^{\frac{1}{2}} \cos x. \tag{5.2}$$

From the hierarchy of charged particle motions covered by the results derived above, it serves our purpose here to restrict the discussion to results for $p = \frac{1}{2}$. Thus, in Case (a) of the previous section, $k = 0$, and so from (4.10)

$$\omega_L = \pm\gamma, \quad \text{a constant}, \tag{5.3}$$

corresponding to a magnetic field B_z independent of the time (cf. equation (2.24)). Further, from (4.9),

$$x = \gamma t = \pm\omega_L t. \tag{5.4}$$

Thus, for charged particle motion in a constant magnetic field, expression (4.15) yields the required result

$$r = \{P + Q\cos(\omega_g t + \phi)\}^{\frac{1}{2}}, \tag{5.5}$$

where P, Q, and ϕ are constants, restricted by $\omega_g^2(P^2-Q^2) = 4C^2$, ω_g being the familiar gyrofrequency given by

$$\omega_g = 2\omega_L. \tag{5.6}$$

Further, from (4.16),

$$\theta = \pm\tfrac{1}{2}\omega_{\mathrm{g}}t - \tan^{-1}\left(\frac{|\sigma|\sin\psi_2 + |\lambda|\sin\psi_1\tan(\frac{1}{2}\omega_{\mathrm{g}}t)}{|\sigma|\cos\psi_2 + |\lambda|\cos\psi_1\tan(\frac{1}{2}\omega_{\mathrm{g}}t)}\right) + \theta_0. \tag{5.7}$$

For $p = \frac{1}{2}$, Case (*c*) of Section IV is of particular interest, because the simple trigonometrical nature of the constant magnetic field solution is retained, but the time dependence of B_z is not lost. From (4.33) and (4.38),

$$r = \mathrm{e}^{-\frac{1}{2}Gt}\{L + R\cos(2D\,\mathrm{e}^{Gt} + \xi)\}^{\frac{1}{2}}, \tag{5.8}$$

where L, R, and ξ are constants, restricted by $D^2G^2(L^2-R^2) = C^2$; and from (4.33), (4.39), and (5.6),

$$\theta = \frac{\omega_{\mathrm{g}}}{2G} \mp \tfrac{1}{2}\sec^{-1}|2D\,\mathrm{e}^{Gt}| - \tan^{-1}\left(\frac{|\sigma|\sin\psi_2 + |\lambda|\sin\psi_1\tan(D\,\mathrm{e}^{Gt})}{|\sigma|\cos\psi_2 + |\lambda|\cos\psi_1\tan(D\,\mathrm{e}^{Gt})}\right) + \theta_0, \tag{5.9}$$

where, from (4.33), (4.35), and (5.6),

$$\omega_{\mathrm{g}} = \pm G(4D^2\,\mathrm{e}^{2Gt} - 1)^{\frac{1}{2}}. \tag{5.10}$$

We see immediately from equation (5.8) that for $G > 0$, corresponding to a magnetic field B_z whose magnitude increases with the time, r decreases with time, thus supporting, for $p = \frac{1}{2}$, the drift theory hypothesis of radial compression of the plasma particles under such conditions. The approximate treatment given by Seymour (1963, p. 443) can be recovered from (5.8) by giving the constant G a sufficiently small value.

VI. Alternative Method of Calculating r

As mentioned in Section III, r can also be obtained from equation (3.11) if the integral $\int \mathrm{d}t'/u^2$ can be evaluated. As a consistency check, this calculation was carried out for the exponential-law ω_{L}, Case (*c*) of Section IV. Briefly, we define a quantity

$$\Sigma = \frac{\mathrm{J}_p}{u}, \tag{6.1}$$

where u is given by (4.37), and then calculate

$$\frac{\mathrm{d}\Sigma}{\mathrm{d}x} = -\frac{\rho\, W(\mathrm{J}_p, \mathrm{Y}_p)}{u^2}. \tag{6.2}$$

Since the Wronskian

$$W(\mathrm{J}_p(x), \mathrm{Y}_p(x)) = \begin{vmatrix} \mathrm{J}_p & \mathrm{Y}_p \\ \mathrm{J}_p' & \mathrm{Y}_p' \end{vmatrix} = \frac{2}{\pi x}, \tag{6.3}$$

where the prime denotes differentiation with respect to x, we obtain, with the help of (4.33),

$$\int \frac{\mathrm{d}t'}{u^2} = \frac{1}{G}\int \frac{\mathrm{d}x'}{x'u^2} = -\frac{\pi}{2G\rho}\frac{\mathrm{J}_p}{u}. \tag{6.4}$$

Then, from equation (3.11),

$$r = \left\{ (\mu \mathrm{J}_p + \rho \mathrm{Y}_p)^2 - \frac{\mathrm{i} C \pi}{G \rho} \mathrm{J}_p (\mu \mathrm{J}_p + \rho \mathrm{Y}_p) \right\}^{\frac{1}{2}}. \tag{6.5}$$

Again writing $\mu = |\mu| \exp \mathrm{i}\epsilon_1$ and $\rho = |\rho| \exp \mathrm{i}\epsilon_2$, we equate the imaginary part of (6.5) to zero to obtain real r, with the independent results

$$\left. \begin{aligned} |\mu||\rho| \sin 2\epsilon_1 - \frac{\pi C}{G} \cos(\epsilon_1 - \epsilon_2) = 0, \\ \sin 2\epsilon_2 = 0. \end{aligned} \right\} \tag{6.6}$$

Use of these results in the real part of (6.5) yields real r, of the general form given by (4.38). Thus we have a satisfactory consistency check in the exponential-law case, and a similar procedure confirms consistency in the case of power-law ω_L.

VII. Wronskian Relationships

From the equations (3.18), (3.22), (3.23) and, say, (4.11) for the power-law ω_L, it follows that

$$I_1 = t^{\frac{1}{2}}(c_{11} \mathrm{J}_p + c_{12} \mathrm{Y}_p), \tag{7.1}$$

$$I_2 = t^{\frac{1}{2}}(c_{21} \mathrm{J}_p + c_{22} \mathrm{Y}_p), \tag{7.2}$$

where the c_{ij} are constants. Hence the Wronskian determinant in (3.24) can also be written as

$$W(I_1(t), I_2(t)) = |c_{ij}| \, W(\mathrm{J}_p(x), \mathrm{Y}_p(x)) \, \dot{x} t. \tag{7.3}$$

With the help of (6.3), (3.24) and (7.3) can be combined to give

$$t (\ln x)^{\cdot} = \text{constant}. \tag{7.4}$$

Integration immediately yields the form of (4.9), a useful consistency check. Similarly, if (4.11) is replaced by (4.37) of the exponential ω_L case, we obtain

$$(\ln x)^{\cdot} = \text{constant}, \tag{7.5}$$

the integral of which is in agreement with (4.33).

VIII. Conclusions

In this analysis we have provided the general form of solution for the motion of a charged particle in the time-dependent magnetic field within a long solenoid, together with a simple pictorial interpretation. However, the particular examples we have discussed do not include the following important cases. First, approximation of the exact solution for quasi-static variation of the magnetic field, with the object of identifying the associated adiabatic invariants; secondly, examination of the case corresponding to harmonic variation of ω_L with time. These cases will be covered in a paper shortly to be published by one of the present authors (P.W.S.).

IX. ACKNOWLEDGMENTS

During this investigation the authors have received encouragement and valuable advice from Professors H. S. Green and C. A. Hurst, to whom they are much indebted.

X. REFERENCES

SEYMOUR, P. W. (1963).—Motions of charged particles in plasmas. *Int. J. Engng Sci.* **1**: 423–51.

SMYTHE, W. R. (1950).—"Static and Dynamic Electricity." pp. 268–70. (McGraw-Hill: New York.)

THE LUNAR MAGNETIC VARIATIONS AT TOOLANGI

By H. F. PETERSONS,* D. E. WINCH,* and L. SLAUCITAJS*†

[*Manuscript received March* 9, 1965]

Summary

The lunar semi-diurnal variations in H, D, and Z at Toolangi observatory have been analysed for the 4-yr period 1952–55 of the sunspot minimum.

Three methods of analysis of the lunar semi-diurnal component of D have been compared. It was found that the Chapman–Miller method was the most suitable and that the initial removal of the solar daily variation used in earlier methods is not essential.

I. INTRODUCTION

The lunar diurnal variation, L, of the Earth's magnetic field is of special interest owing to the relatively simple and regular distribution of the lunar tide which produces it. The significance of lunar influences on geophysical parameters in general can be seen in the recent works of Bradley (1962), Adderley (1963), Bartels (1963), Bigg (1963*a*, 1963*b*), and Bowen (1963). Knowledge of the behaviour of L, especially of a world-wide nature, is therefore likely to be of value even though its small magnitude, and the fact that its period is close to that of the solar transient daily variations, makes its calculation laborious.

Data available from the Toolangi (37° 32′ S., 145° 28′ E.) observatory were analysed. Furthermore, a comparison of three methods of computation, of which one was the Chapman–Miller method, was undertaken in order to determine the most suitable method. The results obtained were then arranged according to the seasons to obtain the seasonal variation in the amplitude and phase of L. Comparison of the amplitude C_2 of the lunar semidiurnal term from Tables 1, 2, and 4 shows that they are not significantly different, the differences between the amplitudes calculated by any one method and either of the other two being within the probable error range of any one of them.

II. PROCEDURE

(*a*) *First Method*

The first method described here is that used by Chapman (1914) in his calculation of L for Pavlovsk and Pola (1857–1903).

The published geomagnetic data usually consist of hourly mean values of the three magnetic elements H, D, and Z, arranged in columns according to the hour, from 1 to 24, and in rows according to the day of the month, from the first of the month to the end of the month. The solar daily variation, S, is assumed to be independent of the lunar daily variation, so that in one month (or more correctly 29·5306 days) the lunar disturbance characteristic of any lunar hour affects in turn each group

---

* Department of Applied Mathematics, University of Sydney.

† On leave from Observatorio Astronomico, Universidad Nacional de La Plata, Argentina.

Aust. J. Phys., 1965, **18**, 567–78

of 28–31 solar hours in like degree. This also assumes that the variation of L from day to day is small; the statistical fluctuations could, however, be considerable (Bartels and Johnston 1940; Schneider 1941).

If from each hourly value is subtracted the solar daily variation for that hour, the remainder will be due to causes not regularly solar, that is, to irregular disturbance, secular variation, and any lunar action. Where work can be carried out using computers, the computation of the mean hourly values for each day of the month centred at that day is not very difficult.

The hourly mean values minus their monthly mean hourly values are next arranged according to lunar time, and it is assumed that, if a sufficiently large number of days are taken, the irregular disturbance will average out, even though on individual days the magnitude of the disturbance may be greater than the lunar variation.

The length of the lunar day is on the average 24 hr 50 min, and it usually does not vary from this by more than half an hour. It is therefore convenient to treat the lunar day as being of duration 25 solar hours. Commencement of the lunar day is taken at the lower local transit of the Moon (lunar hour 0). The times for the upper and lower transit of the Moon at Greenwich can be obtained from the "Nautical Almanac", and interpolation to any other longitude will yield the local mean time of transit. These times do not as a rule fall at an exact solar hour, and the nearest solar hour is used. The difference for this hour (that is, the hourly mean value minus the monthly mean hourly value) and the differences for the 24 succeeding hours are arranged in a row on a lunar sheet, and represent the lunar variations together with accidental variations.

A further hourly difference is added at the end of the row to correct for the non-cyclic variation. The solar times which are adopted as most nearly corresponding to the time of lower lunar transit generally differ from one day to the next by 25 hr, so that the last entry on the row for one lunar day is the first in the row for the next day. When, however, the interval is 24 hr, further 2-hourly differences are added at the end of the row, and these will be the first two on the next row.

All the lunar days for one calendar month are written on the one lunar sheet, and a few hours are taken each from the preceding and following month to make all the rows on the lunar sheet complete. Totals and means of all the columns are then formed, and the resulting hourly means are then corrected for non-cyclic variation. These then give the mean lunar variation for the month but will usually include considerable accidental error due to magnetic disturbance. It is, therefore, necessary to combine the results from many months before a well-determined lunar daily variation can be expected to be obtained.

A computer program was written for an IBM 1620 machine, which calculated the lunar variation by the above method. Small modifications, which it was assumed would not significantly affect the results, were introduced to simplify the program and to make it possible for a single program to do the complete computation.

The first modification was to correct each solar day for the non-cyclic variation in order to remove any linear trends (e.g. non-cyclic variation) in the data. This was done using Chapman's formula for midnight local time, which is magnetically the quietest period, where the non-cyclic variation (NCV) in G.M.T. is given by

$$\mathrm{NCV} = \tfrac{1}{2}\{(14\tfrac{1}{2})+(13\tfrac{1}{2})-(-10\tfrac{1}{2})-(-9\tfrac{1}{2})\},$$

in which the numbers in the round brackets refer to the hourly means centred at the epochs indicated. Hourly values n ($n = 1$–24) were then corrected by adding

$$(n-0\cdot 5)\times(\mathrm{NCV})$$

to the original hourly values, and finally these were adjusted to have zero mean.

The second modification was to take exactly 30 solar days, starting with January 1, and organize them in five rows of 25 and one of 24, in order to make the deviation from the mean lunar day (taken as 24 hr 50 min) not more than half an hour. It was found that 30 solar days could be exactly arranged in 29 lunar days, which simplified the computer program considerably and is a good approximation to one complete lunation.

Means of the 25 columns were formed, and these were taken to represent the mean lunar daily variation for the month of January. The 11 succeeding lots of 30 days were taken to give values of L for the corresponding remaining months. This left 5 or 6 days (depending on whether the year was not or was a leap year) at the end of the year untreated, for treatment of the next year was started on January 1. This was done so that the lunations could be more easily classified according to the seasons.

(*b*) *Second Method*

The second method is the same as the first, except that the solar daily variation is not subtracted from the data. It is assumed that the arrangement of the data according to lunar time over 29 lunar days (approximately 1 complete lunation) is sufficient to average out the solar daily variation.

To show why the greater part of S is eliminated by arrangements of 30 solar days according to lunar time, consider data y_j such that

$$y_j = \alpha_1 \cos\{(2\pi j/24)+\epsilon_1\} + \alpha_2 \cos\{(2\pi j/24\cdot 84)+\epsilon_2\},$$

that is, where y_j contains the first harmonics of S and L respectively.

Let $\theta_1 = 2\pi/24$, and $\theta_2 = 2\pi/24\cdot 84$, then the lunar Fourier coefficient (in complex variable notation) from $N+1$ solar hourly values is given by

$$\begin{aligned}\sum_{j=0}^{N} y_j \exp \mathrm{i}\theta_2 j &= \sum_{j=0}^{N} \tfrac{1}{2}\alpha_1\Big(\exp \mathrm{i}\{j(\theta_1+\theta_2)+\epsilon_1\} + \exp[-\mathrm{i}\{j(\theta_1-\theta_2)+\epsilon_1\}]\Big)\\ &\quad + \sum_{j=0}^{N} \tfrac{1}{2}\alpha_2\Big(\exp \mathrm{i}(2j\theta_2+\epsilon_2) + \exp(-\mathrm{i}\epsilon_2)\Big)\\ &= \tfrac{1}{2}\alpha_2 \exp \mathrm{i}\epsilon_2 \frac{1-\exp 2\mathrm{i}\theta_2(N+1)}{1-\exp 2\mathrm{i}\theta_2} + \tfrac{1}{2}\alpha_2 \exp\{-\mathrm{i}\epsilon_2(N+1)\}\\ &\quad + \tfrac{1}{2}\alpha_1 \exp \mathrm{i}\epsilon_1 \frac{1-\exp \mathrm{i}(\theta_1+\theta_2)(N+1)}{1-\exp \mathrm{i}(\theta_1+\theta_2)}\\ &\quad + \tfrac{1}{2}\alpha_1 \exp(-\mathrm{i}\epsilon_1) \frac{1-\exp\{-\mathrm{i}(\theta_1-\theta_2)(N+1)\}}{1-\exp\{-\mathrm{i}(\theta_1-\theta_2)\}}.\end{aligned}$$

If k is the number of lunar days used, then $N+1 = k\times 24\cdot 84$. Now, to eliminate the contribution of S one must eliminate the terms containing α_1 without eliminating α_2. This is the case when $(0\cdot 842/24)k = 1, 2, 3, \ldots$, that is,

$$k = 28\cdot 50,\ 57\cdot 00,\ 85\cdot 50, \ldots \text{ (lunar days)}$$

$$= 29\cdot 50,\ 59\cdot 00,\ 88\cdot 50, \ldots \text{ (solar days),}$$

so that S should be completely eliminated (if it remains constant in amplitude from day to day) over periods that are multiples of $29\cdot 50$ solar days. This is only approximately true if 30 solar days are taken, but the approximation appears to be a good one, as shown by the result of Figure 1.

A similar proof holds for the other harmonics of S and L.

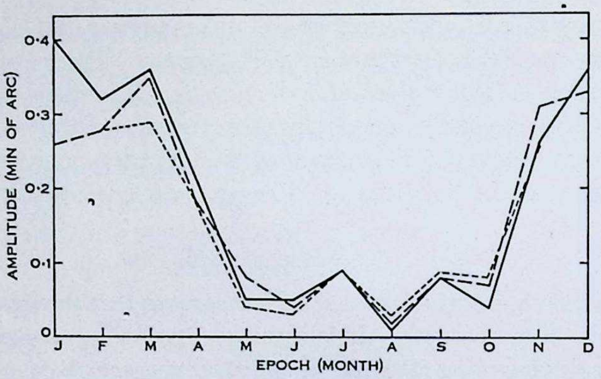

Fig. 1.—Amplitude of lunar semi-diurnal variation of declination for Toolangi, 1952–55. - - - - First method; — — — second method; —— third method.

(c) *Third Method*

The third method employed, the Chapman–Miller method, was developed by Chapman and Miller (1940), and later Tschu (1949) described the computations required in the practical applications of it. The geomagnetic data at Toolangi were analysed following Tschu, and the probable errors were calculated as outlined by him and later by Chapman (1952). The method is briefly as follows.

Daily sequences of hourly values are arranged in 12 groups ($r = 0$–11) according to the ages as assigned to each day from "Geophysikalische Mond-Tafeln" by Bartels and Fanselau (1937). Thus the group r contains days for which the age of the Moon is r and $r+12$. To each daily sequence the hour from the preceding daily sequence is then added, so that allowance for the non-cyclic variations can be made. The number of daily sequences for the group r is N_r, and $\Sigma N_r = N$ (N = total number of daily sequences used).

For each group r, the hourly values are summed and the 12 group-sum sequences $g_{s,r}$ ($s = 0$–S, $r = 0$–11) are obtained; $S = 24$, 12, or 8 depending on whether 1-hourly, 2-hourly, or 3-hourly data are used. (This S is not to be confused with the S used above to denote solar daily variation.) These group-sum sequences are then harmonically analysed, giving

$$A_{p,r} = \sum_{s=0}^{S} g_{s,r}\cos(2\pi sp/S) + \tfrac{1}{2}(g_{S,r}-g_{0,r}),$$

$$B_{p,r} = \sum_{s=0}^{S} g_{s,r}\sin(2\pi sp/S) + \tfrac{1}{2}(g_{S,r}-g_{0,r})\cot(\pi p/S).$$

Here the last terms in the expressions for $A_{p,r}$ and $B_{p,r}$ correct the data for non-cyclic variation. The value of p determines which harmonic is to be analysed. For the calculation of the lunar semi-diurnal variation, $p = 2$.

A secondary harmonic analysis now gives

$$N_{1,A} = \sum_{r=0}^{11} N_r\cos(2\pi r/R), \qquad N_{1,B} = \sum_{r=0}^{11} N_r\sin(2\pi r/R),$$

$$A_{p,A} = \sum_{r=0}^{11} A_{p,r}\cos(2\pi r/R), \qquad A_{p,B} = \sum_{r=0}^{11} A_{p,r}\sin(2\pi r/R),$$

$$B_{p,A} = \sum_{r=0}^{11} B_{p,r}\cos(2\pi r/R), \qquad B_{p,B} = \sum_{r=0}^{11} B_{p,r}\sin(2\pi r/R).$$

where $R = 12$, the number of lunar age groups.

Finally,

$$U_p = (A_{p,A}-B_{p,B}) - N^{-1}(A_{p,N}N_{1,A} - B_{p,N}N_{1,B}),$$

$$V_p = (B_{p,A}+A_{p,B}) - N^{-1}(B_{p,N}N_{1,A} + A_{p,N}N_{1,B}),$$

from which the lunar amplitude L_2 and phase λ_2 are given by the equations

$$L_2\sin\lambda_2 = U_2/Kd_{mpS}, \qquad L_2\cos\lambda_2 = V_2/Kd_{mpS},$$

$$K = 0\cdot4943\,NS[1-\{(N_{1,A})^2+(N_{1,B})^2\}N^{-2}],$$

$$d_{mpS} = (1/S)\sin\pi(m-p)\,[\cot\{\pi(m-p)/S\} + \cot(\pi p/S)],$$

$$m = 2(1-M^{-1}),$$

where M ($= 29\cdot5306$) is the number of mean solar days in the mean synodic period of the Moon.

A correction δ to the phase must now be carried out if the data are not tabulated for Greenwich mean time and at the latitude of Greenwich, given by

$$\delta = 2L/M - 15mH' + m(L-L') \quad \text{degrees},$$

where L denotes the longitude from Greenwich (measured positive if westward and negative if eastward) of the station to which the data refer. L' is similarly the meridian to which the data are tabulated, and H' is the initial solar hour used for the calculation.

(*d*) *Probable Errors*

(i) *First Method*.—The probable error in the amplitude of the lunar semi-diurnal variation L_2 was obtained using the simple probability theory given by Guest (1961). Here the variance of the Fourier coefficients a_n and b_n, and hence of $c_n = (a_n^2+b_n^2)^{\frac{1}{2}}$, is given by $2\sigma^2/r$, where σ is the standard deviation of an observation, r is the number of data points, and c_n is the amplitude of the nth harmonic. The probable error for c_n is therefore taken to be $2\cdot06(2\sigma^2/r)^{\frac{1}{2}}$.

(ii) *Second Method.*—The theory used to calculate the probable error in the values of L obtained by using the second method was the one developed by Miller (1934). This theory also served as the basis of the determination by Tschu (1949) of the probable error in L using the Chapman–Miller method.

Let $\mathbf{R}_m$ $(m = 1, \ldots, n)$ denote a set of vectors representing the set of lunar semi-diurnal harmonic components. These vectors can be considered as consisting of two parts, namely, a vector $\mathbf{L}_m$ which is the mean value of the $\mathbf{R}_m$'s, and the vector $\mathbf{A}_m$ which represents the errors in the lunar variation. The vector $\mathbf{L}_m$ is assumed to represent the true lunar variation of the set of $\mathbf{R}_m$ vectors.

Further, let the vector $\mathbf{L}_m$ have a constant amplitude L and a known variable phase angle l_m, and let $\mathbf{A}_m$ have an amplitude A'_m and phase $(l_m+\theta_m)$, where θ_m is independent of l_m. Consider vectors $\mathbf{R}'_m$, $\mathbf{L}$, and $\mathbf{A}'_m$ which are equal to $\mathbf{R}_m$, $\mathbf{L}_m$, and $\mathbf{A}_m$ except that they are reduced in phase by l_m. Therefore,

$$R_m = R'_m, \qquad A_m = A'_m,$$

and

$$\mathbf{R}'_m = \mathbf{L}+\mathbf{A}'_m,$$

where $\mathbf{L}$ is a constant vector with zero phase.

Next, assume that the n vectors $\mathbf{A}'_m$ have a Gaussian distribution, so that the distribution function for any one of the vectors is given by

$$(1/2\pi\sigma^2)\exp(-r^2/2\sigma^2)\, r\, \mathrm{d}\theta\, \mathrm{d}r,$$

where r is the amplitude and θ the phase angle, so that the probable error r_0 in the amplitude A_m is

$$\frac{1}{2\pi\sigma^2}\int_0^{r_0}\int_0^{2\pi} \exp(-r^2/2\sigma^2)\, r\, \mathrm{d}\theta\, \mathrm{d}r = \tfrac{1}{2},$$

that is,

$$1-\exp(-r_0^2/2\sigma^2) = \tfrac{1}{2},$$

and therefore $r_0 = 0\cdot8326\sqrt{2}\,\sigma$.

To calculate σ, first the r_i were found, where

$$r_i = \{(a_i-\bar{a})^2+(b_i-\bar{b})^2\}^{\frac{1}{2}},$$

and where the a_i and b_i are the harmonic coefficients of the lunar semi-diurnal variation, and $\bar{a}$ and $\bar{b}$ are the corresponding mean values. Then the variance is given by

$$\sigma^2 = (1/n)\sum_i r_i^2 - \bar{r}^2,$$

where $\bar{r} = (1/n)\sum_i r_i$.

The value of σ then enables the r_0 to be calculated.

TABLE 1

HARMONIC COMPONENTS* OF THE LUNAR SEMI-DIURNAL VARIATION OF DECLINATION D, FROM THE FIRST METHOD

Values are monthly means, February–November, for the period 1952–55

	C_2 (tenths of min of arc)	ϵ_2 (degrees)	Probable Error in C_2 (same units)
Feb.:	2·75	159	1·84
Mar.:	2·88	108	1·60
Apr.:	1·83	145	1·39
May:	0·40	345	2·02
June:	0·34	204	0·31
July:	0·89	35	0·73
Aug.:	0·29	236	0·41
Sept.:	0·89	245	0·58
Oct.:	0·67	218	0·63
Nov.:	2·46	222	0·70

* Expressed in the form $C_2 \sin(2\tau + \epsilon_2)$, where τ = mean lunar time in angular measure reckoned from lower lunar transit at Toolangi.

TABLE 2

HARMONIC COMPONENTS* OF THE LUNAR SEMI-DIURNAL VARIATION OF DECLINATION D, FROM THE SECOND METHOD

Values are monthly means for the period 1952–55

	C_2 (tenths of min of arc)	ϵ_2 (degrees)	Probable Error in C_2 (same units)
Jan.:	2·62	284	1·24
Feb.:	2·77	291	0·74
Mar.:	3·46	336	1·06
Apr.:	1·76	307	0·57
May:	0·82	166	0·87
June:	0·42	242	0·58
July:	0·85	45	0·38
Aug.:	0·18	220	0·65
Sept.:	0·81	213	0·57
Oct.:	0·72	236	0·40
Nov.:	3·14	229	1·09
Dec.:	3·31	271	0·85

* Expressed in the form $C_2 \sin(2\tau + \epsilon_2)$, where τ = mean lunar time in angular measure reckoned from lower lunar transit at Toolangi.

TABLE 3

HARMONIC COMPONENTS* OF THE LUNAR SEMI-DIURNAL VARIATION OF HORIZONTAL INTENSITY H, FROM THE THIRD METHOD

Values are monthly, seasonal, and yearly means respectively for the period 1952–55

	C_2 (gammas)	ϵ_2 (degrees)	Probable Error in C_2 (same units)
Jan.:	0·89	64	0·65
Feb.:	0·90	19	0·64
Mar.:	0·87	44	0·69
Apr.:	0·10	20	0·80
May:	0·04	307	0·82
June:	0·57	301	0·57
July:	0·20	255	0·44
Aug.:	0·64	346	0·53
Sept.:	0·42	319	0·89
Oct.:	0·46	349	0·50
Nov.:	1·31	352	0·89
Dec.:	2·23	24	0·63
Summer:	1·23	21	0·36
Equinox:	0·38	10	0·37
Winter:	0·31	316	0·30
Year:	0·59	10	0·20

* Expressed in the form $C_2 \sin(2\tau + \epsilon_2)$, where τ = mean lunar time in angular measure reckoned from lower lunar transit at Toolangi.

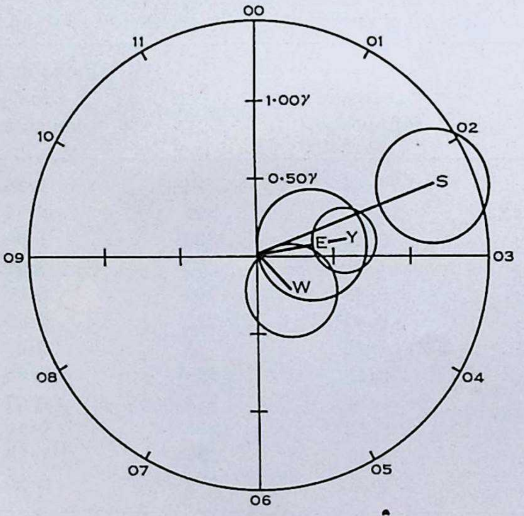

Fig. 2.—Harmonic dial for second Fourier component of lunar daily variation of H at Toolangi, 1952–55. S, summer; E, equinox; W, winter; Y, year.

TABLE 4

HARMONIC COMPONENTS* OF THE LUNAR SEMI-DIURNAL VARIATION OF DECLINATION D, FROM THE THIRD METHOD

Values are monthly, seasonal, and yearly means respectively for the period 1952–55

	C_2 (tenths of min of arc)	ϵ_2 (degrees)	Probable Error in C_2 (same units)
Jan.:	4·02	82	3·41
Feb.:	3·19	140	1·27
Mar.:	3·59	352	1·99
Apr.:	2·06	155	1·28
May:	0·52	149	0·95
June:	0·49	80	0·63
July:	0·94	60	0·66
Aug.:	0·11	114	1·15
Sept.:	0·81	49	1·28
Oct.:	0·40	118	1·11
Nov.:	2·63	86	1·07
Dec.:	3·59	126	1·61
Summer:	3·04	108	1·03
Equinox:	1·31	165	0·73
Winter:	0·42	87	0·44
Year:	1·42	121	0·45

* Expressed in the form $C_2 \sin(2\tau + \epsilon_2)$, where τ = mean lunar time in angular measure reckoned from lower lunar transit at Toolangi.

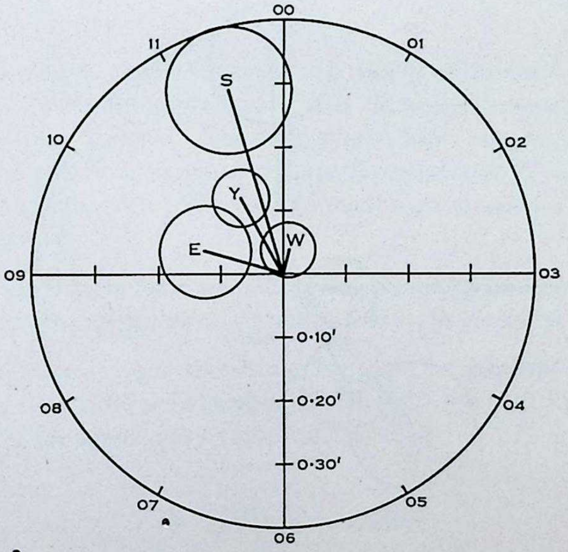

Fig. 3.—Harmonic dial for second Fourier component of lunar daily variation of D at Toolangi, 1952–55. S, summer; E, equinox; W, winter; Y, year.

TABLE 5

HARMONIC COMPONENTS* OF THE LUNAR SEMI-DIURNAL VARIATION OF VERTICAL INTENSITY Z, FROM THE THIRD METHOD

Values are monthly, seasonal, and yearly means respectively for the period 1952–55

	C_2 (gammas)	ϵ_2 (degrees)	Probable Error in C_2 (same units)
Jan.:	1·18	74	0·29
Feb.:	1·11	79	0·37
Mar.:	0·81	228	0·40
Apr.:	0·55	242	0·45
May:	0·69	245	0·32
June:	0·68	244	0·31
July:	0·64	72	0·21
Aug.:	0·83	240	0·24
Sept.:	0·66	219	0·35
Oct.:	0·48	225	0·35
Nov.:	0·91	239	0·45
Dec.:	1·32	79	0·34
Summer:	0·69	84	0·19
Equinox:	0·62	228	0·20
Winter:	0·39	239	0·14
Year:	0·18	192	0·10

* Expressed in the form $C_2 \sin(2\tau+\epsilon_2)$, where $\tau =$ mean lunar time in angular measure reckoned from lower lunar transit at Toolangi.

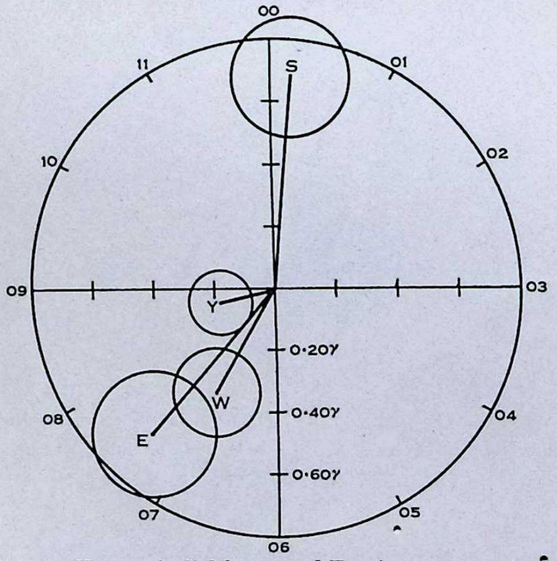

Fig. 4.—Harmonic dial for second Fourier component of Z at Toolangi, 1952–55. S, summer; E, equinox; W, winter; Y, year.

III. Results and Discussion

Figure 1 and Tables 1, 2, and 4 show the great difference in amplitude of the semi-diurnal variation of declination between the summer and winter months, over the 4-yr period 1952–55. It also shows how nearly equivalent are the values of the amplitude of the semi-diurnal variation obtained from the three methods of computation of L, in spite of the fact that the probable errors are so large. The probable errors for the three methods were all themselves of the same order.

Table 6

AMPLITUDE AND PHASE OF LUNAR SEMI-DIURNAL VARIATION OBTAINED AT BOTH NORTHERN AND SOUTHERN STATIONS ON LATITUDES NEAR THAT OF TOOLANGI

Units of C_2 and ϵ_2 are the same as in Tables 3 and 4

		Val-Joyeux	Pola	Amberley, N.Z.
Geographical latitude		48°·3 N.	44°·9 N.	43°·2 S.
Geomagnetic latitude		51°·3 N.	45°·1 N.	47°·7 S.
Variation of H	C_2	—	0·79	1·09
	ϵ_2	—	39	339
Variation of D	C_2	1·3	0·9	2·4
	ϵ_2	9	68	29
Worker		Rougerie (1950)	Chapman (1914)	Bullen and Cummack (1954)

Figures 2, 3, and 4, which illustrate the results of Tables 3, 4, and 5, are harmonic dials showing the seasonal variation in H, D, and Z, respectively, as computed by the Chapman–Miller method. The error circles have also been included. Where the radius of the error circle is greater than the amplitude of L, little significance can be given to the value of L. The time of maximum amplitude can be easily read from the harmonic dials.

Table 6 has been included to enable a comparison to be made with some of the values obtained by other workers at stations of latitude similar to that of Toolangi.

Figure 1 also shows that the initial inclusion or removal of the solar daily variation from the data does not significantly alter the value of the amplitude of the second harmonic of the lunar daily variation.

IV. Acknowledgment

We wish to acknowledge the helpful criticism of our work by Dr. O. Schneider of Buenos Aires, Argentina.

V. REFERENCES

ADDERLEY, E. E. (1963).—The influence of the Moon on atmospheric ozone. *J. Geophys. Res.* **68**: 1405.

BARTELS, J. (1963).—Statistische Hintergründe für geophysikalische Synchronisierungs-Versuche und Kritik an behaupteten Mond-Einflüssen auf die erdmagnetische Aktivität. *Nachr. Akad. Wiss. Göttingen* (Math. Phys. Klasse) **23**: 1.

BARTELS, J., and FANSELAU, G. (1937).—Geophysikalische Mond-Tafeln 1850–1975. *Z. Geophys.* **13**: 311.

BARTELS, J., and JOHNSTON, H. F. (1940).—Geomagnetic tides in horizontal intensity at Huancayo. *Terr. Magn. Atmos. Elect.* **45**: 269.

BIGG, E. K. (1963*a*).—Influence of the Moon on geomagnetic disturbance. *J. Geophys. Res.* **68**: 1409.

BIGG, E. K. (1963*b*).—Lunar and planetary influence on geomagnetic disturbance. *J. Geophys. Res.* **68**: 4099.

BOWEN, E. C. (1963).—A lunar effect on the incoming meteor rate. *J. Geophys. Res.* **68**: 1401.

BRADLEY, D. H., *et al.* (1962).—Lunar synodic period and widespread precipitation. *Science, N.Y.* **137**: 748.

BULLEN, J. M., and CUMMACK, C. H. (1954).—The lunar diurnal variations of the Earth's magnetic field for all elements at Amberley, N.Z., based on five years' observations. *N.Z. Jl Sci. Technol.* B **35**(5): 371.

CHAPMAN, S. (1914).—*L* at Pavlovsk and Pola. *Phil. Trans. R. Soc.* A **214**: 295.

CHAPMAN, S. (1952).—The calculation of the probable error of determinations of lunar daily harmonic component variations in geophysical data: a correction. *Aust. J. Scient. Res.* A **5**: 218.

CHAPMAN, S., and MILLER, J. C. P. (1940).—The statistical determination of lunar daily variations in geomagnetic and meteorological elements. *Mon. Not. R. Astr. Soc. Geophys. Suppl.* **4**: 649.

GUEST, P. (1961).—"Numerical Methods of Curve Fitting." (Cambridge Univ. Press.)

MILLER, J. C. P. (1934).—On a special case in the determination of probable errors. *Mon. Not. R. Astr. Soc.* **94**: 860. (Suppl.)

ROUGERIE, P. (1950).—Variation diurne lunaire de la déclinaison magnétique et de la composante verticale du champ terrestre au Val-Joyeux. *Annls Géophys.* **6**: 300.

SCHNEIDER, O. (1941).—The variability of lunar magnetic variation. *Terr. Magn. Atmos. Elect.* **46**: 283.

TSCHU, K. K. (1949).—On the practical determination of lunar and luni-solar daily variations in certain geophysical data. *Aust. J. Scient. Res.* A **2**: 1.

STRATOSPHERIC TEMPERATURES OVER AUSTRALIA

By J. G. Sparrow*

[*Manuscript received June* 18, 1965]

Summary

A study of the stratospheric temperatures over Australia has revealed apparent anomalously high temperatures during 1963–64. Although a change in the radiosonde type was made near the beginning of this period, it is unlikely that this change can have introduced a discontinuity of the magnitude observed. It is tentatively proposed that the anomaly may be related either to the effects of the Bali volcanic debris which appeared over Australia during the same period or to a change in the nature of the biennial oscillation.

I. Introduction

In a previous paper (Sparrow and Unthank 1964), a preliminary examination of the biennial temperature oscillation over Australia was reported. The Laverton and Hobart data at 60 and 50 mb had been shown to exhibit the quasi-biennial cycle reported by Reed (1960). However, this oscillation appeared to break down towards the end of 1962. It was then suggested that this may have been due to a temperature discontinuity arising from the introduction of the external-thermistor radiosonde at about this time. Further investigation has shown, however, that, although these sondes were introduced at about this time, many stations were carrying large stocks of the ducted-thermistor sondes, so that the change took place at different times at the different stations. It therefore seems likely that the change is an actual change of stratospheric temperature, and tentative suggestions are made as to the possible cause of this change. The occurrence of the temperature change at about the time of the Bali volcanic eruption is noted. An alternative mechanism relates to a breakdown in the biennial cycle during the same period.

II. Australian and New Zealand Temperatures

Table 1 shows the latitude and longitude of the Australian stations and the approximate times of introduction of the external thermistor sondes, as well as the same data for several New Zealand stations used in this analysis. Figures 1 and 2 show the monthly mean "2300 Z"† (daytime) temperatures for Darwin and Port Hedland, respectively, at 100, 60, and 50 mb; at Darwin, although the change of radiosonde took place in January 1963, the temperature anomaly was not apparent until after the Bali eruption several months later. The 12-month running mean temperatures at 100 and 60 mb for both Woomera and Charleville are shown in

---

* Physics Department (RAAF Academy), University of Melbourne.

† Z = G.M.T.

Figure 3. This presentation in the form of moving averages effectively removes the annual temperature variation while allowing the biennial cycle and the high temperatures during 1963–64 to be seen. The time of occurence of the Bali volcanic eruption (March 17, 1963) is indicated in each figure.

As monthly mean temperatures are used here, it was useful to estimate the consistency (or relative accuracy) of data sampled in this way. Data from several Antarctic stations ("Climatological Data for Antarctic Stations"*) were examined for those stations making twice-daily temperature soundings. Although the observations were made usually at 12-hourly intervals, it was considered that at these latitudes both radiation corrections to the sonde and diurnal temperature fluctuations should be negligible. Comparison of the monthly means for the two release times showed

TABLE 1

POSITIONS OF STATIONS AND APPROXIMATE DATE OF CHANGE OF RADIOSONDE

Station	Latitude	Longitude	Sonde Changed
AUSTRALIA			
Adelaide	34° 57′ S.	138° 31′ E.	10. x.62
Alice Springs	23 48	133 53	25. xi.62
Carnarvon	24 53	119 39	11. i.63
Charleville	26 25	146 17	26. v.63
Cloncurry	20 40	140 30	10. vii.63
Cocos Island*	12 11	96 50	6. iv.63
Darwin	12 28	130 55	25. i.63
Garbutt	19 15	146 46	9. x.62
Guildford	31 56	115 57	14. v.63
Hobart	42 50	147 28	26. ii.63
Honiara*	9 25	159 58	20. v.63
Lae*	6 43	147 00	3. iv.63
Laverton	37 52	144 46	13. iii.63
Port Hedland*	20 23	118 37	24. iii.63
Williamtown	32 48	151 51	29. xii.62
Willis	49 59	160 18	20.viii.63
Woomera	31 20	135 55	15. i.63
NEW ZEALAND			
Auckland	36 51	174 46	20. ii.62
Christchurch	43 29	172 32	20. ii.62
Invercargill	46 25	168 19	27. ii.62
Nandi (Fiji)	17 45	177 27	17. iii.62
ANTARCTICA			
Amundsen–Scott	90 00	—	
Byrd	80 00	120 00 (W.)	
Hallett	72 12	170 12	
Wilkes	66 18	110 36	

* These stations use a 403 Mc/s radiosonde, while the other stations, in general, use 72 Mc/s. The Antarctic stations use GMD-1 equipment.

---

* Published at intervals by the United States Weather Bureau, Washington, D.C.

that, in general, when the number of observations is greater than, say, 15, the difference between the two means seldom exceeds 0·5 degC. However, when the number of observations at one or other of the release times is less than 10, the difference often amounts to more than 1 degC. These observations appear consistent

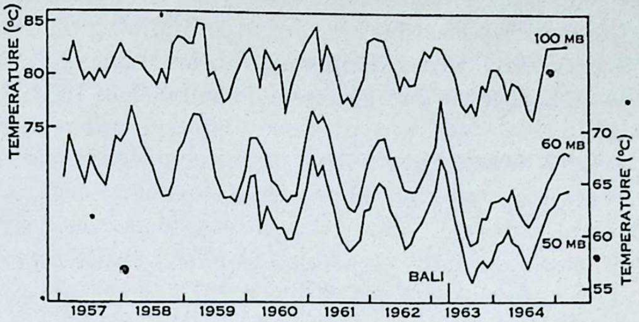

Fig. 1.—Monthly mean 2300 Z temperatures for Darwin at 100, 60, and 50 mb. The temperature scale (negative) is shown at left for 100 mb and at right for 60 and 50 mb. The time of occurrence of the Bali eruption is indicated.

with the daily temperature fluctuations that have been examined both for these Antarctic stations and, of course, for the Australian stations.

Temperature data above 60 mb were not recorded in Australia prior to November 1959. Sufficient 60 mb data (more than 10 observations per month) are available at most stations to enable examination of several years prior to 1959.

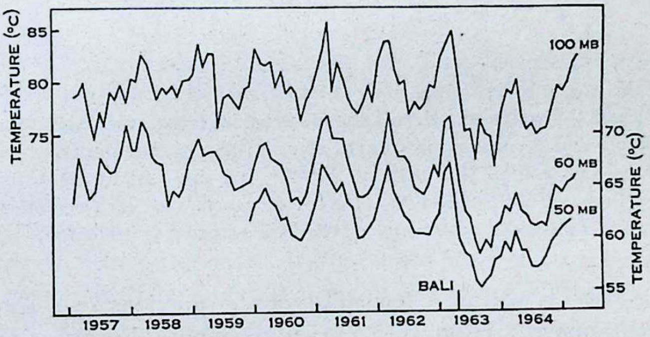

Fig. 2.—Monthly mean 2300 Z temperatures for Port Hedland at 100, 60, and 50 mb. The temperature scale (negative) is shown at left for 100 mb and at right for 60 and 50 mb. The time of occurrence of the Bali eruption is indicated.

However, it should be noted that, although the sparseness of data at 60 mb for some months gives rise to an "uncertainty" of perhaps 1 or 2 degC in the mean value for that month, it is unlikely that this uncertainty will be biased in either direction. Thus, the use of extensive smoothing (for example, 12-month running means) should make it possible to consider those months having more than 10 observations per month.

Where this criterion cannot be fulfilled, the value for that month has been obtained by linear interpolation between adjacent months.

The scheduled time of the daily release of the radiosonde has changed during the period being discussed (1953–65), being successively at 0400, 0330, and now at 2300 Z. The last change took place at about June 1957. The data prior to 1953 have been examined, but the sonde release time (0830 or 0730 Z) during that period makes the application of the radiation correction (discussed below) difficult. Similarly, several of the stations have changed their locations (and names) since 1953; however in each case the new station is within a few miles of the previous one, so this positional change has been ignored. From 1957 until the change of radiosonde occurred, the radiation correction (see "Manual of Radiosonde Observations, Circular P"; United States Weather Bureau 1950) was applied to the daily observations by the observer at each station. For the data prior to 1957, the author has applied the radiation correction to the monthly mean data, based upon station latitude and longitude, time of year, and a mean rate of rise of the sonde. The corrections applied to the temperatures at several of the stations are illustrated in Table 2, where the radiation corrections at 60 and 100 mb are given for a month typical of each season.

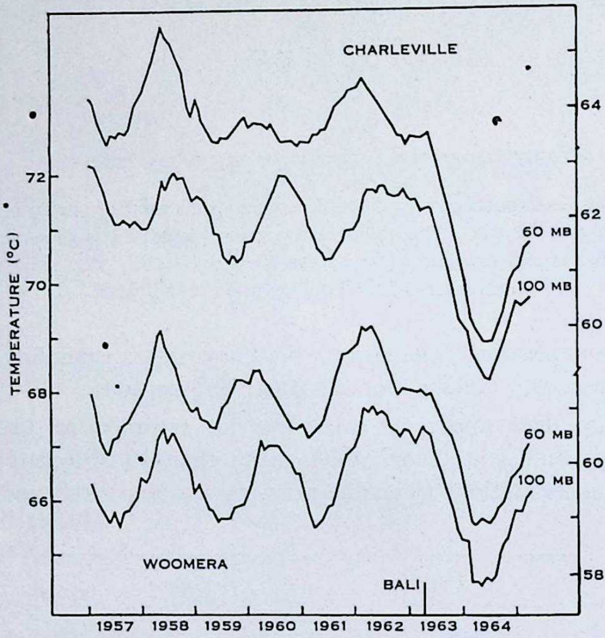

Fig. 3.—Twelve-month running mean temperatures for Charleville (top) and Woomera (bottom) at 60 and 100 mb. The temperature scale (negative) is shown at left for 100 mb and at right for 60 mb. Data for January–December are plotted as December. The time of occurrence of the Bali eruption is indicated.

The question remains whether the anomalously high temperatures indicated during 1963–64 are due simply to the lack of compatibility of the data taken from the two types of sonde, or to a real change in stratospheric temperature. That the former is unlikely is seen when it is realized that this infers the necessity for a radiation correction of several degrees to be applied to temperatures measured with the external white-coated thermistor. Unfortunately, night-time observations have been taken at only a few of the more southerly stations, and continuously only since late 1962. Insufficient night-time observations do not allow satisfactory comparison of the monthly means. This comparison would have enabled a check to be made on whether the new radiosonde was free of radiation errors.

Nevertheless, as the Australian radiosonde uses the same white thermistor and is built to the specifications of the equivalent United States Weather Bureau sonde, it is unlikely that the two sondes will exhibit different properties. The previous ducted-thermistor sonde should also be comparable to the sonde used in the United States. Teweles and Finger (1960) and McBirney (personal communication) give the radiation error in the exposed thermistor sonde as less than 1 degC at the heights considered here. Rofe (1963) has assessed the various sources of error inherent in the measurement of temperature with the ducted-thermistor sonde, and gives a combined standard error at these heights of the order of 1·5 degC.

TABLE 2

RADIATION CORRECTIONS APPLIED TO MONTHLY MEAN TEMPERATURES AT 60 AND 100 MB FOR THREE OF THE STATIONS

	Darwin		Guildford		Laverton	
	60 mb	100 mb	60 mb	100 mb	60 mb	100 mb
January	4·4°C	2·4°C	4·7°C	2·6°C	4·2°C	2·3°C
April	4·2	2·3	3·7	2·0	3·2	1·8
July	3·8	2·1	3·3	1·9	2·6	1·5
October	4·4	2·5	4·4	2·4	3·8	2·1

The data for three of the New Zealand stations also show an anomaly during 1963–64. In Figure 4, the 30 and 50 mb running means for Auckland and Christchurch are shown. In these graphs, the anomaly appears as a breakdown in the biennial cycle, the temperature being several degrees higher than one might have expected. At Nandi, Fiji, no definite change could be seen; the biennial cycle also could not be seen. At lower heights (100 and 200 mb) for all of these stations, again no definite change could be seen.

Examination of the temperature records from a large number of stations in the northern hemisphere failed to reveal the anomaly shown above for the Australian and New Zealand stations. Unfortunately, suitable data from South America and South Africa have not yet become available to the author.

III. TOTAL OZONE AMOUNTS

The total ozone data from Aspendale (38·0° S., 145·1° E.) and Brisbane (27·5° S., 153·0° E.) are shown in Figure 5. It is again seen that anomalous values have been obtained in 1963–64. This is noticed as an apparent breakdown of the biennial oscillation in total ozone reported by Funk and Garnham (1962). On the other hand, it was found that the similar data for the Indian stations New Delhi (28·6° N., 77·2° E.), Ahmedabad–Mount Abu (24·5° N., 72·7° E.), and Kodaikanal (10·2° N., 77·5° E.) showed no significant change during 1963–64. It would appear that the anomaly occurred only in the southern hemisphere. It is interesting to speculate

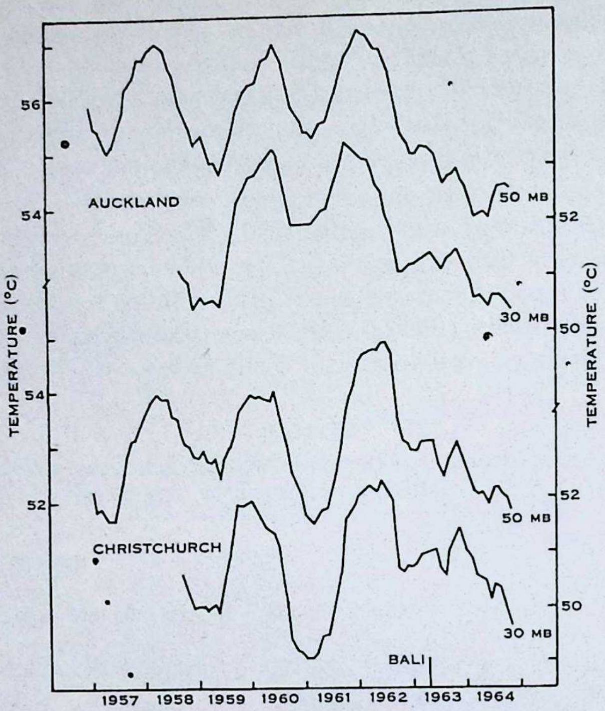

Fig. 4.—Twelve-month running mean temperatures for Auckland (top) and Christchurch (bottom) at 30 and 50 mb. The temperature scale (negative) is shown at left for 50 mb and at right for 30 mb. Data for January–December are plotted as December. The time of occurrence of the Bali eruption is indicated.

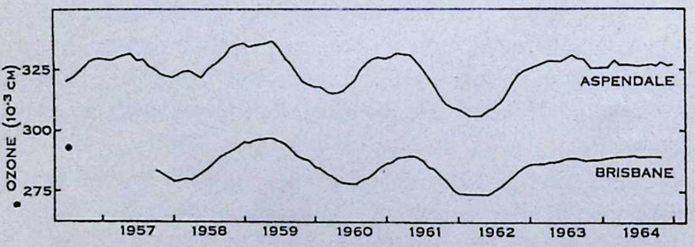

Fig. 5.—Twelve-month running means of total ozone amount at Aspendale and at Brisbane. Data for January–December are plotted as December.

whether these effects could have been due to the presence in the stratosphere of considerable amounts of volcanic debris from the Mount Agung eruption, which occurred on March 17, 1963, or alternatively, whether the anomaly may just reflect a change in the nature of the quasi-biennial oscillation.

IV. VOLCANIC DEBRIS FROM THE MOUNT AGUNG ERUPTION

The volcanic dust from the Mount Agung eruption spread rapidly throughout the southern hemisphere, although taking a longer time to diffuse into the northern hemisphere. Photometric observations (and the occurrence of brilliant sunsets) showed that the dust had reached Chile, South Africa, and New Zealand within a month or so of the eruption (Hill 1964) and had spread throughout Australia (Hogg 1963; Harris 1965). Diffusion of the ash into the northern hemisphere did not occur until September or October 1963. Mossop (1964), using particle impactors on U-2 aircraft, has made collections of the volcanic dust over Australia. He has reported that the ash was present in appreciable quantities in early April 1963 and persisted for over a year. It has been reported that the presence of this ash at high levels depressed the amount of direct solar radiation received at the ground in New Zealand and Fiji by as much as 5% in comparison with previous years (Hogg 1963). Even larger depletion of solar radiation had been recorded for the Katmai and Krakatoa eruptions (Wexler 1951). Dyer (personal communication) has reported a depletion of direct sunlight of some 25% over Aspendale after the Bali eruption. The effects of volcanic dust on insolation and surface weather have been discussed by Wexler (1951).

It is difficult at this stage to postulate any definite mechanism whereby volcanic dust could affect the stratospheric temperature. Stagg (1964), in discussing the similar problem of the effects of rocket exhausts, was unable to decide the direction that any climatic change might take. However, Pittock (1964) has suggested the direct destruction of stratospheric ozone by a thin layer of volcanic dust. He has invoked this mechanism to explain a persistent dip, at 50 mb, in the vertical ozone distribution during March 1964 over Colorado, U.S.A. It is conceivable that this mechanism may be of importance particularly if the dust is in highly stratified layers. Kroening (1965) has also suggested the importance of direct ozone destruction by dust in the lower stratosphere.

V. QUASI-BIENNIAL TEMPERATURE OSCILLATION

The quasi-biennial oscillation (henceforth called biennial, for simplicity) in stratospheric temperatures was first reported by Ebdon and Veryard (1961). Since that time the characteristics of the oscillation in the tropical regions have been extensively studied. However, the picture in mid latitudes has not yet been firmly established. Indeed, it would seem surprising that more attention has not been paid to the data available in the southern hemisphere. Although these data are not as extensive as those for the northern hemisphere, it is apparent that the biennial oscillation is more clearly defined in the southern hemisphere (Reed 1965). Angell and Korshover (1964) have studied the data from a small number of stations in the southern hemisphere but have considered only two in the Australian region. For this reason, it seemed desirable to study the records of those stations in Australia having records of any significant length. As mentioned previously, data above 60 mb were not recorded in Australia prior to 1959. However, sufficient data are available at 60 mb to enable the comparisons shown in Figure 6 to be made. In this figure, the 12-month running means of the 60 mb temperatures (50 mb in the case of Canton Island, Hallett, and Wilkes) are shown, covering a range of latitudes from 3° to 72° S. (see also Figs. 3 and 4). It is interesting to compare these graphs with similar ones for different longitudes, as shown by Angell and Korshover (1964).

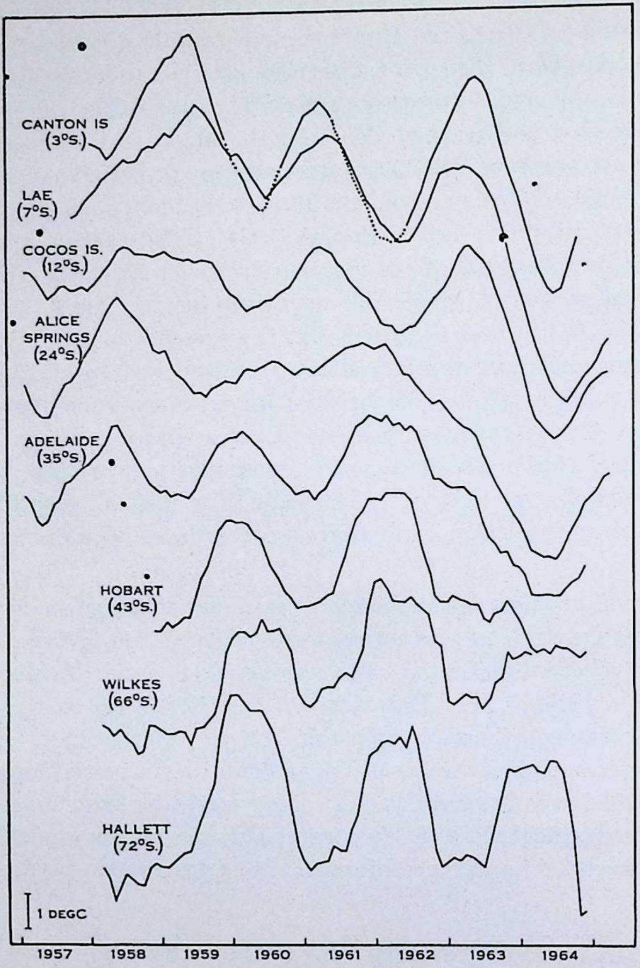

Fig. 6.—Twelve-month running means of 60 mb temperatures (50 mb in the case of Canton, Wilkes, and Hallett). Data for January–December are plotted as December. The temperature scale is indicated at lower left, negative magnitude increasing upward.

Figure 6 shows clearly the rather abrupt phase change in the vicinity of 15°–20° S. The three stations equatorwards of this latitude are in phase with one another; the stations of higher latitude are in phase with one another but approximately 180° out of phase with the three "equatorial" stations. The amplitude of the oscillation decreases from the equator to a latitude of about 20° S., but then increases again at higher latitudes. Comparison of the phases of the New Zealand and Australian stations shows no significant difference, in agreement with the observation of Angell and Korshover of the invariance of phase with respect to longitude. Examination of the data at lower levels for Canton Island shows that the magnitude of the oscillation decreases rapidly with decreasing height, so that it has almost disappeared at 200 mb. Downward phase propagation of about 1 km per month is also seen, similar to that for the zonal wind oscillation. However, this phase propagation disappears southward of about 15° or 20° S., the oscillation then appearing in phase at all levels. At mid-latitudes over Australia, an oscillation is still apparent at 200 mb at most stations. It is interesting to note, however, that these oscillations at 200 mb have a period significantly longer than 2 yr, and would appear to be closer to $3\frac{1}{2}$ yr. Further poleward, at Wilkes, the biennial oscillation is readily apparent at all heights between 50 and 200 mb.

The ozone and temperature cycles are more or less in phase, low temperature being coincident with low total ozone amounts. It has been shown previously (Sparrow and Unthank 1964) that, at the same time, the zonal wind cycle has its strongest west winds.

At the present time, data are available to study the biennial temperature oscillation only for a limited number of years. Thus it would not be altogether surprising if the apparent anomaly during 1963–64 were a change in the biennial cycle related to the solar sunspot minimum occurring during the same period. However, the anomaly did not appear in the northern hemisphere, nor has a similar anomaly been reported in the northern hemisphere for those stations with observations extending back to the previous solar minimum.

VI. CONCLUSION

It has been shown that, during 1963–64, temperatures in the lower stratosphere over Australia and New Zealand were several degrees higher than usual. Furthermore, total ozone amounts over Australia showed a similar increase. It has been suggested that these effects may be related to the presence in the stratosphere of volcanic debris from the Mount Agung eruption, or to a change in the nature of the biennial oscillation occurring during solar minimum.

VII. ACKNOWLEDGMENTS

The author is indebted to Miss B. J. Harris for assistance in the initial phases of this work. The receipt of data from the following organizations is gratefully acknowledged: Commonwealth Bureau of Meteorology; International Antarctic Analysis Centre, Melbourne; Division of Meteorological Physics, CSIRO; New Zealand Meteorological Service; United States Weather Bureau; and Indian Meteorological Department. The author has received a University of Melbourne Research Grant during the period of this work.

VIII. REFERENCES

ANGELL, J. K., and KORSHOVER, J. (1964).—*J. Atmos. Sci.* **21**: 479.

EBDON, R. A., and VERYARD, R. G. (1961).—*Nature* **189**: 791.

FUNK, J. P., and GARNHAM, G. L. (1962).—*Tellus* **14**: 378.

HARRIS, B. J. (1965).—M.Sc. thesis, University of Melbourne.

HILL, P. W. (1964).—*Mon. Notes Astr. Soc. Sth. Afr.* **23**: 148.

HOGG, A. R. (1963).—*Aust. J. Sci.* **26**: 119.

KROENING, J. L. (1965).—*Science, N.Y.* **147**: 862.

MOSSOP, S. C. (1964).—*Nature* **203**: 824.

PITTOCK, A. B. (1964).—Proc. Intern. Ozone Conf., Albuquerque, New Mexico, September 1964. (In press.)

REED, R. J. (1960).—The circulation of the stratosphere. Paper presented at 40th Anniversary Meeting of the American Meteorological Society, Boston, Jan. 1960 (unpublished).

REED, R. J. (1965).—*Bull. Am. Met. Soc.* **46**: 374–87.

ROFE, B. (1963).—W.R.E. Tech. Note SAD-127. (Department of Supply: Salisbury, S. Aust.)

SPARROW, J. G., and UNTHANK, E. L. (1964).—*J. Atmos. Sci.* **21**: 592.

STAGG, J. M. (1964).—*New Scient.* **23**: 627.

TEWELES, S., and FINGER, F. G. (1960).—*J. Met.* **17**: 177.

UNITED STATES WEATHER BUREAU (1950).—"Manual of Radiosonde Observations." Circular P. (U.S. Weath. Bur.: Washington.)

WEXLER, H. (1951).—*Bull. Am. Met. Soc.* **32**: 10.

A STUDY OF THE DECIMETRIC EMISSION AND POLARIZATION OF CENTAURUS A

By B. F. C. Cooper,* R. M. Price,† and D. J. Cole*

[*Manuscript received June 25, 1965*]

Summary

The results of a study of Centaurus A in the wavelength range 6–74 cm are presented. From observations at 11, 21, and 31 cm the intrinsic polarization and Faraday rotation have been determined for much of the source.

Of the two sources that form the central component, the north-following source is strongly polarized at wavelengths shorter than about 31 cm. The south-preceding source is 3% polarized at 6 cm and not more than 3% polarized at 11 cm.

At 11 and 21 cm the degree of polarization in extended regions of the source is typically 10–20% and in places as high as 40%. The orientation of the intrinsic polarization is quite uniform over large areas but appears to bear no constant relationship to the axis of symmetry of the source.

In general the rotation measure varies slowly over the source, and values lie in the range -36 to -84 rad/m^2, with most values lying between -50 and -70 rad/m^2. Possible relationships between Faraday rotation and depolarization effects are discussed.

All parts of the source have an essentially constant spectral index of $-0\cdot6$ at decimetric wavelengths. The central component contributes approximately 22% of the total flux density, the remainder being equally divided between the northern and southern extended sources.

I. Introduction

Centaurus A was one of the first of the "discrete" sources of radio emission to be identified. The intense central sources were detected, although unresolved, in 1947, and reported by Bolton (1948). Soon afterwards, more precise measurements with their cliff interferometer at 100 Mc/s allowed Bolton, Stanley, and Slee (1949) to tentatively identify the peculiar radio emission with an unusual optical object, NGC 5128. Continued measurements showed that the source actually consisted of two components, a region of intense radio emission thought to be less than 7′ in extent, surrounded by a lower brightness envelope of approximately 30′ (Stanley and Slee 1950).

As equipment and techniques improved, knowledge of the complicated brightness distribution of this radio source increased, although major changes were not effected in the picture derived from earlier observations. Mills (1953) reported that interferometry showed the intense source to be 5′ wide in the east–west coordinate, while increased sensitivity allowed the extended source in the same region to be traced out to more than a degree. Bolton *et al.* (1954) confirmed these results and traced the regions of low brightness, which were believed to be physically associated with the intense source, out to a total width of more than 2° in the east–west direction.

---

* Division of Radiophysics, CSIRO, University Grounds, Chippendale, N.S.W.

† Division of Radiophysics, CSIRO, University Grounds, Chippendale, N.S.W., and Mount Stromlo Observatory, Canberra.

Aust. J. Phys., 1965, **18**, 589–625

Position measurements were now accurate enough to consider the radio source as definitely identified with NGC 5128. Further measurements by McGee, Slee, and Stanley (1955) at 400 Mc/s, and by Piddington and Trent (1956) at 600 Mc/s, served to confirm that the general brightness distribution of the source was similar over a wide range of frequencies.

Further surveys at various frequencies showed the extent of the source in the north–south direction. Sheridan (1958) investigated Centaurus A at 85 Mc/s (3·5 m) using a 50′ pencil beam and showed that the source extended over some 8° in declination. Thus at the presently accepted distance of 4 Mpc the projected linear extent of the source is 600 kpc, a dimension that is large, but not exceptional for radio galaxies. Measurements by Shain (1958) at 19·7 Mc/s showed essentially the same structure as that found at 85 Mc/s. By this time, the general structure of the source had been determined, and further measurement was primarily for the investigation of the brightness distribution with the higher resolution instruments that were coming into use, and for the study of the brightness distribution as a function of frequency. Hindman and Wade (1959) studied the source at 1400 Mc/s and further confirmed the previously determined structure, their observations bearing "a remarkably close resemblance" to findings at lower frequencies. Wade (1959) interpreted previous investigations as indicating that the extended source of low brightness temperature was a "double" source of radio emission, with the intense source (and NGC 5128) lying approximately midway between the two peaks of the extended source. Bolton and Clark (1960) applied a similar analysis to their 960 Mc/s observations and derived a similar brightness distribution for the extended source.

Further interferometry by several groups showed the intense central component to be double also. As most of the interpretations were based on information obtained with east–west base lines only, they seemed consistent with an earlier suggestion that the central radio source was closely associated with the dark lane of obscuring matter clearly visible on plates of NGC 5128. However, Maltby (1961) showed the central component to consist of two sources, each of about 2′ diameter, separated by about 7′ in position angle 46°·5. Each source appeared to be slightly elongated in the direction of the line joining their centres. The ratio of brightness of the two sources was estimated to be of the order of 1·3 to 1·0, at 960 Mc/s.

With the greatly improved resolution of the Parkes 210 ft telescope it has proved possible to delineate fine details of the source structure and to reveal the previously unsuspected polarization and Faraday rotation that is associated with the radio emission (Bracewell, Cooper, and Cousins 1962; Cooper and Price 1962). In the following sections the results of a detailed study of the source at wavelengths of 74, 31, 21, and 11·3 cm are presented, together with some restricted observations at 6 cm. From the 31, 21, and 11·3 cm observations the distribution of intrinsic polarization and Faraday rotation over the source has been delineated.

South-eastern Extension

Observations in the southern part of the extended source have shown that the absolute intensity on the east-following side of the source is significantly higher than on the west-preceding side. Piddington and Trent (1956) traced this feature in a south-easterly direction until it merged with the Galaxy some 20° away. They speculated that it was in fact a bridge between our Galaxy and Centaurus A (a suggestion that was not unreasonable at a time when the estimated distance was 700 kpc, but is difficult to accept in view of the present accepted distance of 4 Mpc). Also Bolton and Clark (1960) suggested that the south-east extension in the declination range −44° to −48° was physically associated with Centaurus A, but they were unable to trace its full extent from their northern observing site in California.

Observations at 74 cm with the 210 ft telescope have verified the continuity of this feature down to the galactic plane and its large angular extent. The extent and placing of the feature make it highly probable that it is a galactic spur, similar to those observed in other parts of the sky but extending for some distance in front of Centaurus A before fading out. If there is radio emission physically associated with Centaurus A in this region, it should be possible to identify it with the aid of polarization and Faraday rotation measurements. Such measurements have not yet been carried out owing to the extremely low brightness temperatures encountered there. For the present we have chosen to establish a boundary on the eastern side of Centaurus A where the emission shows a shallow minimum before rising again towards the galactic plane.

Optical NGC 5128

The optical object associated with the radio source Centaurus A is NGC 5128, one of the five extragalactic objects in the sky brighter than sixth total photographic magnitude (de Vaucouleurs 1953, 1956). NGC 5128 appears, on a medium exposure plate (Plate 1) as an unresolved E0 type galaxy bifurcated by a very strong absorption lane lying approximately along position angle 120°. This lane becomes more diffuse at both ends and curves in a manner that would suggest it is wrapped around the edge of the bright regions of the object. The brightest portions of the object are more than 10′ in extent and on long-exposure, high-contrast prints can be traced out to 1° with a noticeable elongation along position angle 45°. Composite photographic techniques have been applied to the object by Johnson (1963) and the results indicate a helical or "corkscrew" structure extending 45′ in position angle 40° and some 30′ along position angle 220°. This structure seems to involve both the dust lane in the central part of the optical object and the faint optical extensions on either side of the bright source.

Studies of spectrograms of the object indicate a velocity of about 400 km/s (with respect to the centre of our Galaxy). Turbulence is noted in the dust lane while the bright portions of the object appear to be rotating about an axis perpendicular to the dust lane (Burbidge and Burbidge 1959). The object is not resolved into stars although Sérsic (1958) has reported chains of stars or perhaps HII regions within the dust lane. From estimates of the absolute magnitudes of the observed regions and the probable absorption, Sérsic (1961) derives a distance of 4 Mpc and an absolute magnitude of −20·8 for NGC 5128, in agreement with estimates derived from the observed radial velocity.

Polarization studies of NGC 5128 by Elvius and Hall (1964) have shown light in the region of the obscuring dark band to be up to 6% polarized with the E vector approximately parallel to the band. It is not clear whether this polarization is due to the absorption in the dark clouds or to the observation of optical synchrotron emission, although the former seems the more likely suggestion.

II. Observing Methods

The observing techniques used were essentially the same at all of the wavelengths. However, the variations in resolution of the telescope at different wavelengths and the sensitivity of the various receivers used governed the rates at which the source was scanned and the spacing of the scan tracks. In general the source was scanned in right ascension at fixed declinations. Because of the large extent of the source in declination, right ascension scans could be kept shorter and receiver base-line drifts were more easily detected and corrected. Two sets of declination scans, at $13^h 19^m 30^s$ and $13^h 24^m 00^s$, were used for checks on both the brightness distribution and the polarization parameters determined with the right ascension scans.

To determine the intensity and polarization of the source each scan was repeated six times, with the feed of the telescope in a different orientation each time. The interval between feed angles was 30°, so that for each set of scans the feed angles used normally were 0°, 30°, 60°, 90°, 120°, and 150°. In the context of the altazimuth mounting of the 210 ft telescope, a feed orientation of 0° corresponds to the electric vector of the feed horn lying in the vertical plane containing the beam axis, while increasing feed angles imply anticlockwise rotation of the feed looking outwards along the beam. The position angle of the electric vector projected on the sky is then equal to the feed angle plus the parallactic angle, where the parallactic angle is the position angle of the vertical circle of the telescope measured east of north.

Since Centaurus A transits close to the zenith at Parkes and the parallactic angle changes rapidly near the zenith, scans were taken at large hour angles whenever possible so that correction for changes of parallactic angle would be small within the set of scans. When observations were taken close to transit, the separation of the feed angles was adjusted so that the resulting position angles of observation were very nearly 30° apart.

Scans were extended on either side of the source until it became apparent that the base level had been reached, or to a point related to the predetermined base level. On the preceding (early right ascension) side this was easily done. However, on the following side, particularly for the southern part of the source, confusion with the galactic spur in the region made the selection of a base level for the source more complicated and introduced a small uncertainty in the level of brightness temperature contours near that area.

The average of the six scans within a set was used to determine the brightness distribution along each scan track, while plots of feed (or position) angle versus intensity for individual points along the track were used to determine the polarization parameters for the given point at the observing frequency. Corrections for time constant and base line were applied to the intensity values where necessary, and a sine wave was then fitted by eye to the six intensity values plotted.

Many regions were further investigated for polarization using a feed-rotation technique. In these observations, the feed was rotated through 300° and back while the telescope was tracking a given point in the source. Similar rotations were taken at the same hour angle and declination (to ensure the same ground radiation effects) at points off the source. Rotations could be integrated to give a more accurate result than the scans at discrete feed angles provided, and were not prone to the same baseline effects that might result if the background were polarized in some unknown manner.

III. Total Emission and Polarization–Brightness Temperature Calibration

The measurement of the flux densities and brightness temperatures of partially linearly polarized sources has been discussed by Westerhout *et al.* (1962), and we follow their definitions and terminology with some variations. The isophotes presented in the following sections are of full-beam brightness temperature, which is equivalent to the aerial temperature that would be observed if the aerial received energy only within the confines of its full beam and had zero response elsewhere. The extent of the full beam is a somewhat arbitrary quantity, but it is taken here to extend out to a distance from the beam axis at which the aerial power response is not more than a few tenths of 1% of its maximum value.

The flux density of a source may then be obtained with good accuracy by integrating the contours of full-beam brightness temperature according to the relationship

$$S = (2k/\lambda^2)\int_{\text{source}} T_{\mathrm{B}}\,\mathrm{d}\Omega\,, \tag{1}$$

where k is the Boltzmann constant, λ is the wavelength, and T_{B} is the full-beam brightness temperature observed in the direction of the element of solid angle $\mathrm{d}\Omega$.

To establish a full-beam brightness temperature scale a point source of known flux density may be observed, in which case (1) reduces to

$$S = 2kT_{\mathrm{BP}}\,\Omega_{\mathrm{FB}}/\lambda^2, \tag{2}$$

where Ω_{FB} is the effective full-beam solid angle obtained by integrating the beam contours, and T_{BP} is the peak apparent brightness temperature of the point source, i.e. as smoothed by the beam. T_{BP} is then calculated from (2) to establish the relationship between receiver output and source brightness temperature.

Where a partially linearly polarized source is observed with a rotating linearly polarized feed, the apparent brightness temperature will vary between the limits $\max T_{\mathrm{B}}$ and $\min T_{\mathrm{B}}$, in which case the mean value $\frac{1}{2}(\max T_{\mathrm{B}}+\min T_{\mathrm{B}})$ is applied in (1). We define this mean value as the *full-beam total emission brightness temperature.* To specify the polarized component we define $\max T_{\mathrm{B}}-\min T_{\mathrm{B}}$ as the *full-beam polarization brightness temperature*. The degree of linear polarization p at that point is then given by

$$p = \frac{\max T_{\mathrm{B}}-\min T_{\mathrm{B}}}{\max T_{\mathrm{B}}+\min T_{\mathrm{B}}}.$$

In the present paper the adopted unit of flux density is $10^{-26}\,\mathrm{W\,m^{-2}\,(c/s)^{-1}}$, which will be referred to hereafter as 1 *flux unit*.

At all observing wavelengths, brightness temperature scales were determined as described above. A noise step coupled into the aerial feeder from an argon discharge tube was used as a transfer calibrator between the standard sources and the unknown sources. The receiver non-linearity was measured by applying this noise step in the manner described by Komesaroff and Mathewson (1962).

The standard source flux densities adopted in the following sections are close to the values derived by Conway, Kellermann, and Long (1963), but are modified slightly in the light of more recent work at Parkes and elsewhere. The characteristics of the receivers used at the various frequencies are summarized in Table 1, together with beam dimensions and the assumed flux densities of the reference sources.

TABLE 1

EQUIPMENT SUMMARY

Frequency (Mc/s):	406	960	1410	2650	5000
Receiver:					
Type	Crystal mixer	Crystal mixer	Parametric	Parametric	Crystal mixer
Bandwidth (Mc/s)	8	8	10	100	10
System noise temp. (°K)	350	400	105	180	650
Beamwidth at half intensity (min of arc)	48·0	20·0	14·0	7·35	4·1
Full-beam solid angle (sr)	$2{\cdot}08\times10^{-4}$	$3{\cdot}96\times10^{-5}$	$1{\cdot}83\times10^{-5}$	$5{\cdot}15\times10^{-6}$	—
Assumed flux densities ($10^{-26}\,\mathrm{W\,m^{-2}\,(c/s)^{-1}}$)					
Hydra A	135	64	45	23·5	12·4
Virgo A	560	285	210	120	76

IV. OBSERVATIONS AT 74 CM

The receiver (Mackey 1964) used for the 74 cm observations was a crystal mixer type, which accepted two sidebands, each 8 Mc/s wide, centred on 396 and 416 Mc/s. Its sensitivity was more than adequate for observing the high brightness temperatures encountered in Centaurus A. The passband characteristic of this receiver was satisfactory for determining the isophotes of the source, but was not suitable for observing any polarization that might have been present, as the observations at shorter wavelengths showed that a differential Faraday rotation of about 250° was to be expected across the sidebands. However, some 74 cm polarization checks have been made independently by F. F. Gardner and A. G. Little (personal communications) using a receiver that accepted a single sideband only 4 Mc/s wide. The differential Faraday rotation across this bandwidth would cause no more than 10% depolarization in the case of Centaurus A. Their observations showed that the regions strongly polarized at short wavelengths were virtually unpolarized at 74 cm, either by internal depolarization in the source, by confusion effects in the larger beam at this wavelength, or by differential Faraday rotation across the telescope beam.

Scans were made at half-beamwidth intervals, and the isophotes constructed from them are presented in Figure 1. By comparison with the shorter wavelength maps much of the fine detail has been smoothed out by the increase in beamwidth to 48′. However, the foreground structure surrounding Centaurus A becomes relatively bright at 74 cm, and it is easier to distinguish the intensity rise that occurs in crossing

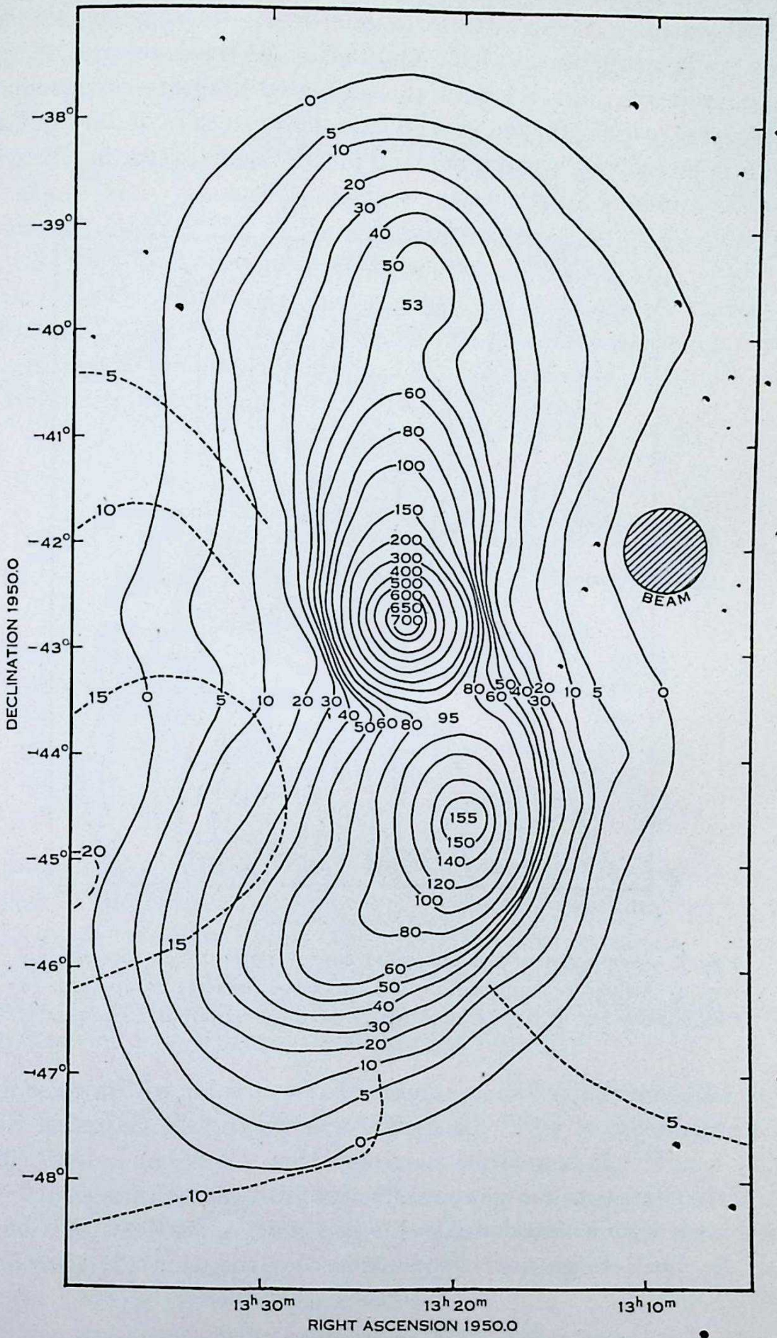
−38°
−39°
−40°
−41°
−42°
−43°
−44°
−45°
−46°
−47°
−48°
DECLINATION 1950.0
13h 30m
13h 20m
13h 10m
RIGHT ASCENSION 1950.0
BEAM
0
5
10
20
30
40
50
53
60
80
100
150
200
300
400
500
600
650
700
95
155
150
140
120
100
80
60
50
40
30
20
10
5
0
15
20
10
5

Fig. 1.—Isophotes of full-beam total emission brightness temperature at 406 Mc/s. Full-line contours show brightness temperature (in °K) above the estimated galactic foreground structure (indicated by the dashed contours). Epoch 1950.0. Observed with a 48′·0 beam.

the southern part of the source from west to east. As discussed earlier, we have tentatively concluded that this intensity rise is due to a galactic spur that extends upwards in a north-westerly direction from the galactic plane and fades out in front of Centaurus A. This spur was traced by several scans in the direction of the galactic plane, and its general structure was evident in more detail in the 400 Mc/s survey scans kindly made available by J. G. Bolton, F. F. Gardner, and M. B. Mackey. The dashed contours in Figure 1 show the estimated intensity of this spur above an arbitrary zero level, which is taken just outside the western boundary of Centaurus A. A fairly uniform intensity plateau was found in this region extending from declination −37° to −47°.

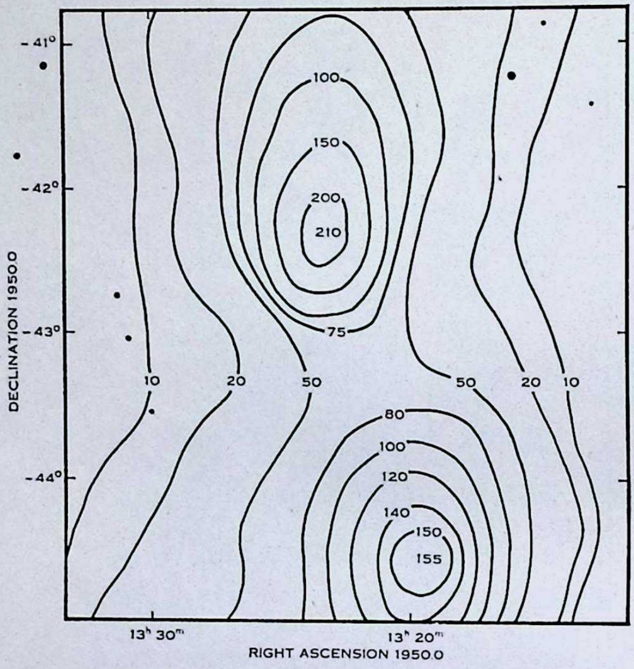

Fig. 2.—Isophotes of the extended source structure in the central region, derived by subtracting the estimated central component of flux density 595×10^{-26} W m^{-2} (c/s)$^{-1}$ from the isophotes of Figure 1.

The aerial beam shape was determined to be circular within close limits with a half-intensity diameter of 48′. Its shape was accurately Gaussian down to the half-intensity point, but somewhat narrower than Gaussian below this intensity. Integration of the beam contours gave an effective full-beam solid angle of $2\cdot08\times10^{-4}$ sr. For a point source with a flux density of 1 flux unit, observed with a beam of these dimensions, the peak brightness temperature by equation (2) (Section III) was 0·94°K.

The contribution of the central component to the isophotes was determined by subtracting patterns of various peak intensities, corresponding to the central double source convolved with the main beam, until a set of residual contours, which were consistent with the known structure and spectrum of the extended source in this region, was obtained. After subtraction of a pattern of 550°K peak brightness temperature, corresponding to a combined flux of 595 flux units from the two central sources, the residual contours of Figure 2 were obtained. These are considered to be consistent with the structure observed at 21 and 11 cm after allowing for a 0·6 spectral index and the dilution effect of the 48′ beam. The flux contributions from the north, south, and central portions of the source, obtained by integrating the T_B contours, are listed in Table 2.

V. OBSERVATIONS AT 31 CM

Observations at 31 cm were carried out using a total-power radiometer of the crystal mixer type. Both sidebands (each of 8 Mc/s bandwidth with centre frequencies separated by 20 Mc/s) were accepted by the receiver. With the 2 s output time constant used in the observations, the peak-to-peak fluctuations on the records were 0·6 degK of aerial temperature. The primary feed was a pyramidal horn, which was designed to illuminate the dish equally on both the E and H planes and to provide low ground radiation "spill-over".

TABLE 2

CENTAURUS-A FLUX DENSITIES AT 406 Mc/s

Region	Flux Density (10^{-26} W m^{-2} (c/s)$^{-1}$)	Fraction of Total (%)
North of centre	1075	39
Central component	595	22
South of centre	1070	39
Total	2740	100

At a wavelength of 31 cm, the half-power beamwidth of the telescope was measured to be 20′·0. With this resolution, a scan rate of 1°/min with a time constant of 2 s was adequate to follow the steepest intensity changes found in the extended portions of the source without distortion. A special survey was carried out over the central source, using slower scans and a calibration procedure that allowed its peak temperature to be compared with that of Virgo A.

Scans were placed 15′ apart in most parts of the source, following the same declination values used in the other wavelength surveys, whenever possible, for direct comparison.

The observed brightness distribution over the source at 31 cm is shown in Figure 3(*a*). Figure 3(*b*) shows the distribution of polarization brightness temperature and the observed directions of the E vectors of the polarized emission. Position angles for these E vectors are given in Table 3.

Polarization was measurable over some 30% of the source area, but by comparison with the shorter-wavelength maps it is apparent that depolarizing effects are beginning to operate rather strongly at this wavelength. However, there are several areas where the degree of polarization is still as high as 10% and one area

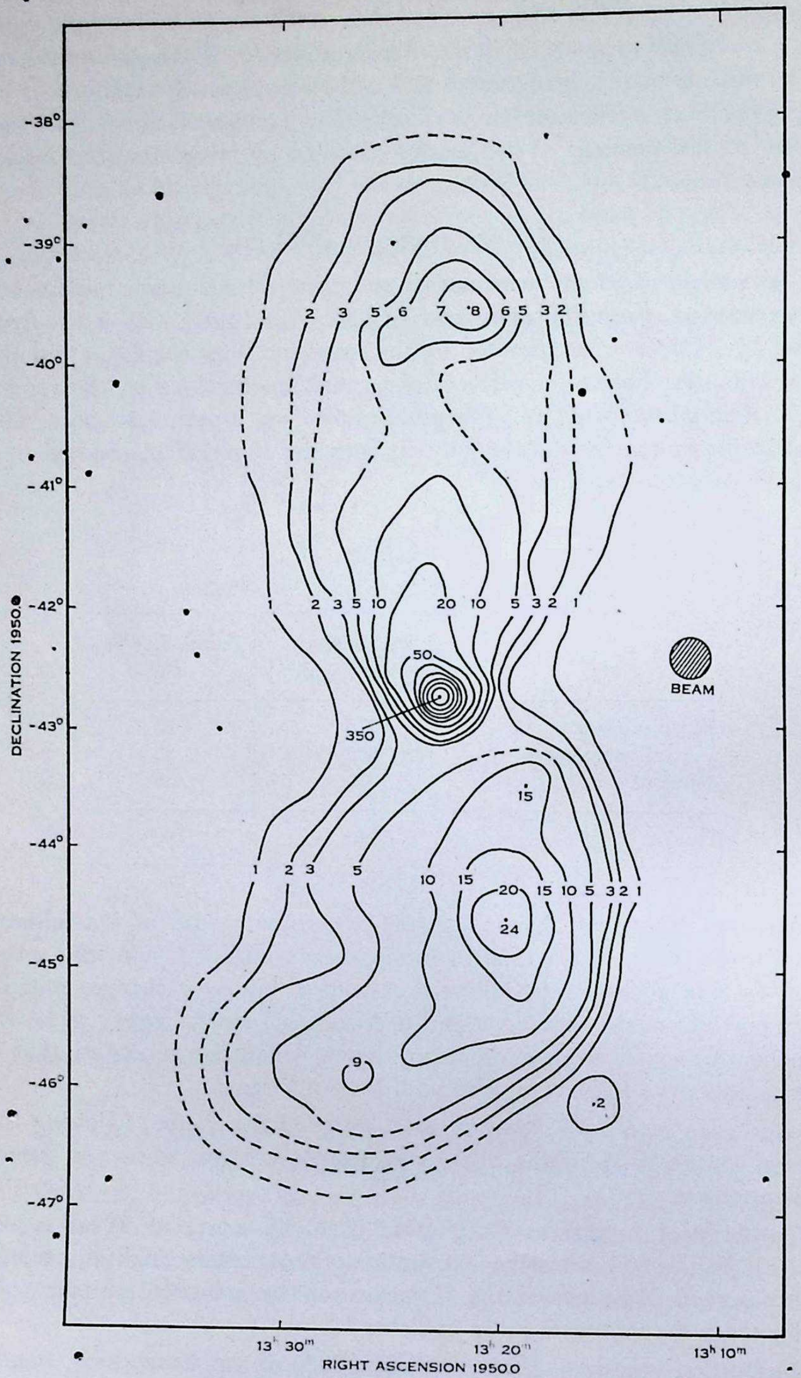

Fig. 3(*a*).—Isophotes of full-beam total emission brightness temperature at 960 Mc/s (in °K); beamwidth 20′·0 at half intensity. Contour interval for the central component is 50 degK.

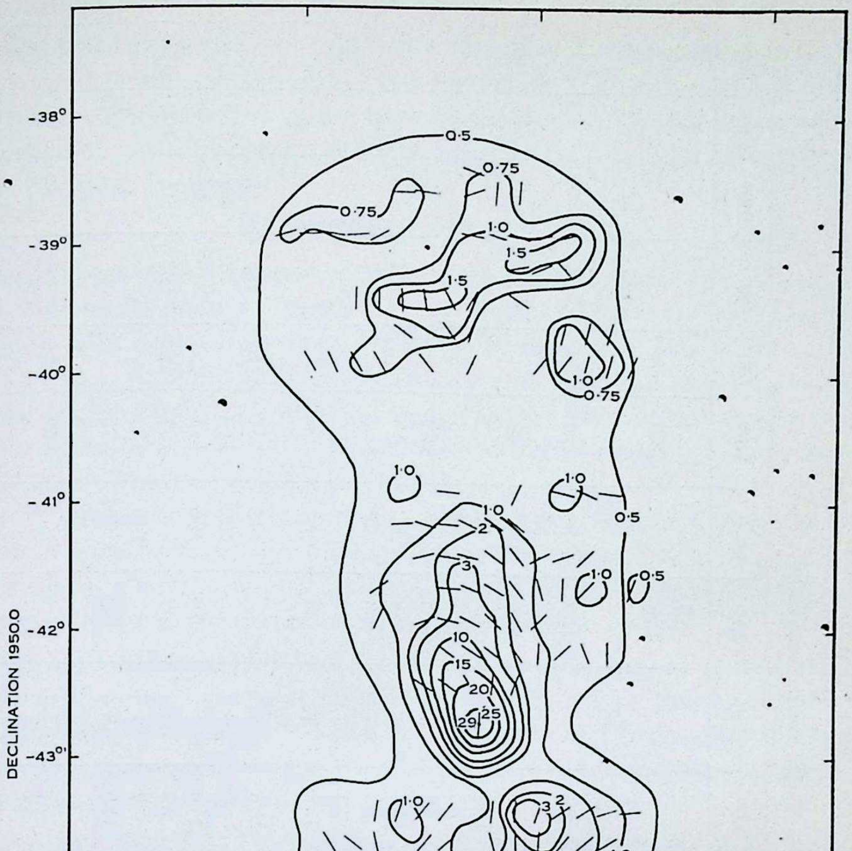
-38°
-39°
-40°
-41°
-42°
-43°
-44°
-45°
-46°
-47°
DECLINATION 1950.0
13h 30m
13h 20m
13h 10m
RIGHT ASCENSION 1950.0
0·5
0·75
0·75
1·0
1·5
1·5
1·0
0·75
1·0
1·0
1·0
0·5
2
3
1·0
0·5
10
15
20
25
29
1·0
3
2
1·0
1·0
1·5
2
3
3
1·0
1·0
1·5
2
3
1·0

Fig. 3(*b*).—Isophotes of full-beam polarization brightness temperature at 960 Mc/s (in °K). The position angles of the observed E vectors of the polarized emission are indicated by short lines.

TABLE 3

CENTAURUS-A POLARIZATION POSITION ANGLES IN DEGREES AT 960 Mc/s

Add 20ˢ to indicated minute of right ascension

Declination 1950.0	Right Ascension 1950.0																
	13ʰ15ᵐ	16ᵐ	17ᵐ	18ᵐ	19ᵐ	20ᵐ	21ᵐ	22ᵐ	23ᵐ	24ᵐ	25ᵐ	26ᵐ	27ᵐ	28ᵐ	29ᵐ	30ᵐ	31ᵐ
−38° 26′									73								
36									108		80	89?					
56					104	96	71	74	80				117	94	84	89	104
−39° 11′					47	112	100										
26							60		150	30	10	3	178	0			
41			165	166	164				158	35		56					
56		158	165	165	145	140			153		40		30	30	25	30	
−40° 56′			83	66	77		156			85							
−41° 11′							50	56	66	86	75	95					
26				134	108	118	41	56	76	82	102						
41		161		137	175		14	38	59	68	88		123				
56						136	29	48	63	76	107		157				
−42° 11′			0	20	133	175	34	52	56	53							
26							159	177	32	53	57						
Central peak								0±5									
−43° 26′		96	106	123	126	161	175	173		142	141	161	171				
41			122	130	140	175	0	15		132	140		14	50	30		
56	162	115	10	93	155	162	170	174	176	165	146	147		58	58		
−44° 11′			22	37	32	50	55	35	167		131	134	122	97	102	122	112
21			12	2	6	32	57	57		104	107						
41	160		153	144	146	145	150	148	80	75?	75?						
56			141	156	156	156		16		16	6	6					
−45° 11′		19				169		157			139	164					
26		120	50	160		17	11	23									
41				158?	8	15	13	8	0				5	16	33	21	
56					135	150?		34	21	5	172	3	0	7		132	140
−46° 16′													42				

near right ascension $13^h 24^m$, declination $-42° 15'$, where the degree of polarization is as high as 20%.

In Table 3 and the following Tables 4, 5, and 6, the position angles have been tabulated at the points where observations were made. It was considered undesirable to smooth and interpolate the angles to neat minutes of right ascension and degrees of declination (1950.0 epoch), as in many places rapid changes of angle occurred in a short distance.

VI. OBSERVATIONS AT 21 CM

Observations of the source at 21 cm wavelength were carried out using a switched radiometer with a degenerate parametric r.f. preamplifier (Gardner and Milne 1963). Its centre frequency was 1410 Mc/s with a bandwidth of 10 Mc/s. With the 2 s time constant used in the observations, the peak-to-peak noise fluctuations observed were 0·2 degK of aerial temperature. Most of the observations were carried out using combined feeds, which allowed simultaneous observations at both 21 and 74 cm. However, a few observations were carried out with a single 21 cm feed. In all cases, the feeds were designed for similar illumination of the reflector in both the *E* and *H* planes, the primary feed response being 14 dB at the edge of the reflector surface to minimize ground effects. Calibrator sources were observed with all of the feeds used to ensure accuracy in calibrations.

At 21 cm, the measured beamwidth of the telescope, to half-power points, was 14′·0 with a high degree of circular symmetry. With this beamwidth and a 2 s time constant for the receiver output, a scan rate of 1°/min allowed 7 time constants per beam passage over a point, and permitted accurate determination of the brightness distribution over the track of the scan.

Scans were spaced at 15′ intervals in the extended portions of the source, this spacing being reduced to 10′ in regions of higher brightness, and further reduced to 7′ in the region of the central component. The scans were extended from $13^h 05^m$ to $13^h 40^m$ right ascension to allow accurate determination of the base levels. A slight change in aerial temperature with changing zenith angle due to ground spill-over was observed, but this was assumed to be linear over the small zenith-angle ranges for any one scan and its effect was removed in the reduction of the records. To determine the polarization parameters of this spur region, declination scans at six feed angles were made from −42° to −48° at right ascension $13^h 38^m$. In analysis of these parameters it was assumed that their end-points were in regions that exhibited negligible polarization at 1410 Mc/s. The region was found to be slightly polarized with average polarization temperatures of 0·2°K and a few values up to 0·4°K. At intermediate points along the right ascension scans that were terminated in this spur region, a correction vector was applied whose amplitude was taken to vary linearly from zero at right ascension $13^h 12^m$ to the measured amplitude at $13^h 38^m$. Notwithstanding these corrections, it is possible that residual uncertainties due to foreground polarization averaging 0·2 to 0·3 degK remain on the south-following side of the source. Since the foreground polarization may compound with the source polarization at arbitrary angles, the observed polarization may be modified in amplitude or orientation, or partly in both, to an extent appropriate to the amount of foreground polarization estimated above.

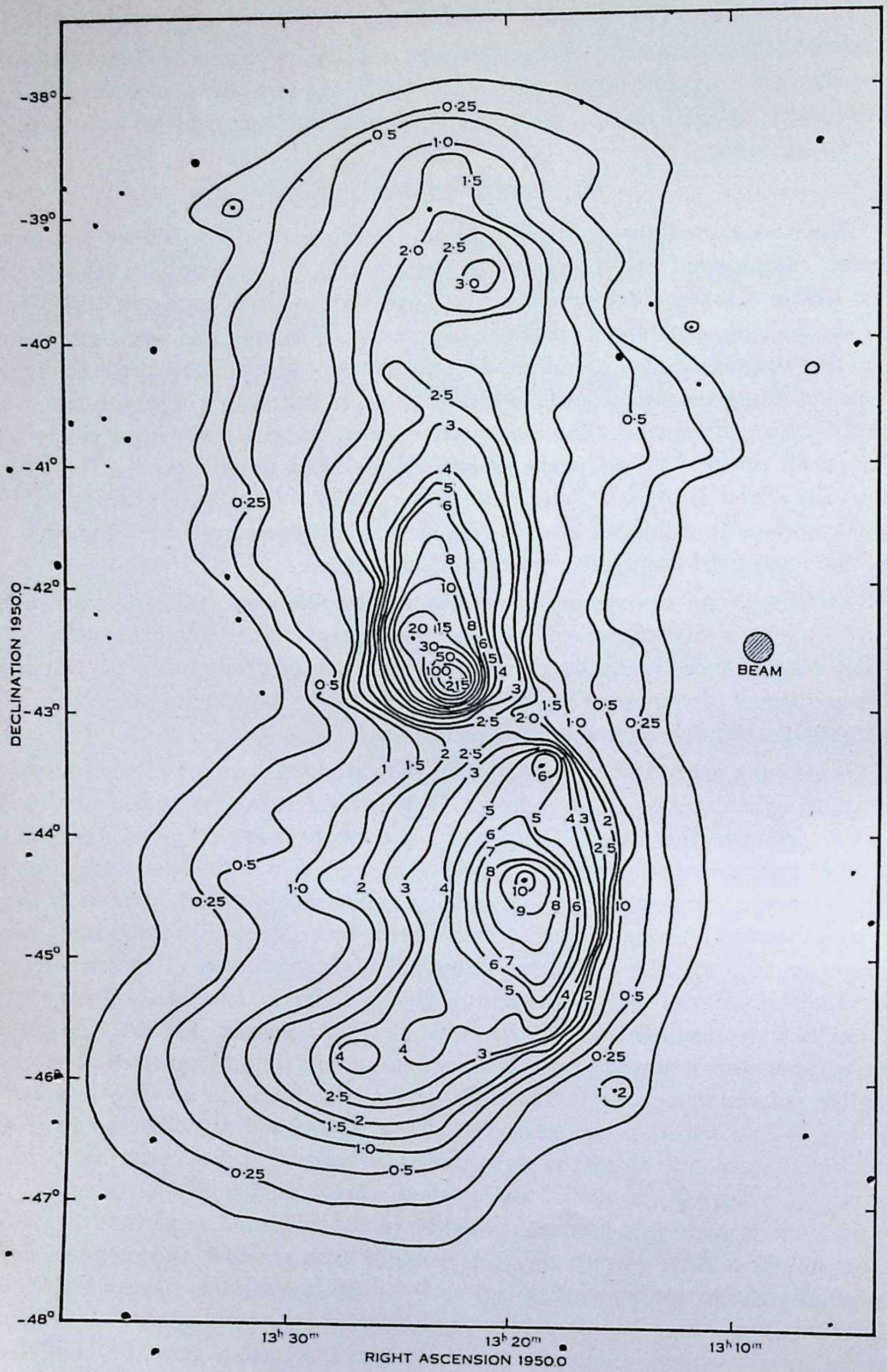

Fig. 4(a).—Isophotes of full-beam total emission brightness temperature at 1410 Mc/s (in °K); beamwidth 14′·0 at half intensity.

Figure 4(*a*) shows the observed brightness distribution over the source at 21 cm, while Figure 4(*b*) shows the distribution of polarization brightness temperature across the source and the observed directions of the *E* vectors of the polarized emission. Position angles for these *E* vectors are given in Table 4. The peak in Figure 4 near right ascension $13^h\,18^m$, declination $-43°\,26'$, is due to an extraneous source,

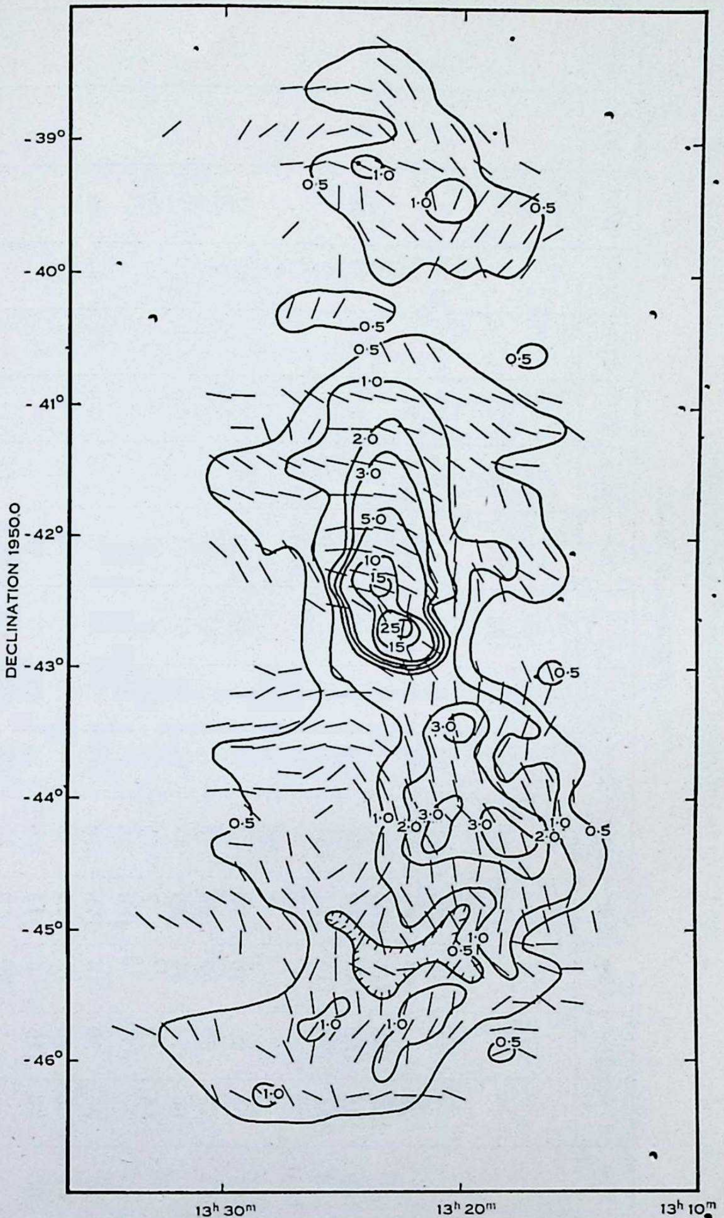

Fig. 4(*b*).—Isophotes of full-beam polarization brightness at 1410 Mc/s (in °K). Short lines indicate the observed directions of the *E* vectors.

TABLE 4

CENTAURUS-A POLARIZATION POSITION ANGLES IN DEGREES AT 1410 Mc/s

Add 20 s to indicated minute of right ascension

Declination 1950.0	Right Ascension 1950.0																			
	13h 15m	16m	17m	18m	19m	20m	21m	22m	23m	24m	25m	26m	27m	28m	29m	30m	31m	32m	33m	34m
−38° 16′									62											
26									55											
36								30	49	73	94	96								
46									45											
56				11	41	36	21	26	45	66	11	41	145	20	146					
−39° 11′			78		55	40	61	74	63	66	73	105	95							
26			125	135	145	160	25		45	5?	1?									
41		120	145	150	145	150	50	50	63	30				135	110	75				
56		118	144	134	115	124	154		64		0									
−40° 16′		154?							69		150	160	160							
36							35	30	50											
56		75	60	70	70	70	65	75	78	75	70	60	55		90	85				
−41° 11′	53?	82	72	52	52	62	62	72	76	91	90	150	10	20	0					
26			86	76	54	56	49	66	79	81	81		66	56	56	56				
41			24	19		3	55	55	82	86	91	116	80	80	67	69				
56						156	39	59	80	80	102									
−42° 06′		35	35	30	15	178	19	63	75	82	95	178	39	69	34	49				
16		60	60	45	10	174	25	50	75	77	75	30?		29	29					
24		36	36	15	5	15	36	35	66	71	76									
32					30	0	25	170	40	60	80	60								
38								164	24											
44								173*												
52							55	25												

−43° 01′		19	24		12	7	34	31	60	32	44		99	69						
11		160	170	173	175	7	175	164	65	90	100	103	105	120	95					
26		151	161	156	13	15	19	17	59	102	116	110	97	107	107	110				
36	34	30	27	25	15	13	10	10	42	33	130	120	85							
48			175	155	160	15	20	20	56	75	80	105	100	100	100	90				
56	0	12	27	36	20	14	17	18	20	36	96	96	90	87	80	93	96	96	102	
−44° 06′		8	31	50	33	45	45	28	22	8		126			44					
21			16	17	14	25	32	15	175			129	7		85					
33			38	15	170	9	7	174	151	150	125	36	18	22	30					
46	160	15	12	175	46	15	25	30	130	126		30	41	32	56	60				
56	12	3	0	168	172	30	32	32	170	146	6	24	40	38	18	30	56	60	48?	
−45° 06′		90	80	175	170	160	90?	35	16	150	0									
18	89	70	51	51	36	146	146	97	66	62	2	158	29							
32	82	52	87	127		172	169	162	177	7	10	7								
36		62			93	172	170	165				15								
46			86	98		140	155	153	145	134	144	157	166			12	27	44	64	69
56			63	110				175	162	150		170	25	60						
−46° 16′						68	83	90	110	98	18		30	49	63	23				
26									63											

---

* North-following central source.

which is described separately in Section XIII. Other minor point sources may be noted around the periphery of Centaurus A.

Figure 5 shows the distribution of the source polarization at 1410 Mc/s in percentage groups. Apart from the highly polarized region just north of the central component, it is seen that highly polarized regions are concentrated towards the edges of the source. This is to be expected as the depth of the emitting regions should be least near the edges of the source.

VII. OBSERVATIONS AT 11·3 CM

The receiver used for the 11·3 cm observations was a parametric type (Cooper, Cousins, and Gruner 1964) that accepted a band of frequencies 100 Mc/s wide centred on 2650 Mc/s. A 2 s output time constant was used during most of the observations, allowing the telescope to be driven at up to 0°·5/min without significant loss of detail in the source. With this time constant the peak-to-peak output fluctuations were of the order of 0·2 degK. In view of the low signal-to-noise ratio encountered over much of the extended regions of Centaurus A, the 11 cm observations were limited to areas where significant polarization was observable at 21 cm.

Figure 6(*a*) shows the isophotes of total emission observed at 11·3 cm while Figure 6(*b*) shows the distribution of polarization brightness temperature and the observed directions of the *E* vectors. Position angles for these *E* vectors are given in Table 5(*a*). Details of the central structure are shown in expanded form in Figures 7(*a*) and 7(*b*). Polarization position angles for the central region are tabulated in Table 5(*b*). The extraneous sources that are present in Figure 4 have been removed from Figure 6.

At 11 cm the beam shape was not quite circular, being 7′·5 wide in the *E* plane and 7′·2 wide in the *H* plane at half intensity. Its effective full-beam solid angle was determined to be $5\cdot15\times10^{-6}$ sr, so that by equation (2) (Section III) the observed peak brightness temperature of a source of 1 flux unit would be 0·9°K.

In observing the polarization of the central component, corrections were made for spurious instrumental effects produced by the elliptical beam section. These occurred whenever one of the central sources was situated on the steep sides of the aerial beam pattern. Corrections were made by subtracting polarization vectors determined from the measured beam sections in the *E* and *H* planes. Another minor correction was necessitated by a small variation of aerial gain with feed orientation. This produced a spurious polarization component of 1·3% of the source intensity with its maximum always coinciding with vertical polarization of the feed. When corrected for these effects, the contours for the total emission and the polarized emission of the central region are as shown in Figure 7. The centres of the north-following and south-preceding sources are marked A and B respectively.

The north-following source is 14% polarized at this wavelength and its polarized flux shows a well-defined pattern corresponding to the beam shape. At distances more than one beamwidth from A, the polarization vectors swing abruptly to the general north–south orientation that applies to the surrounding areas. As shown later, this cannot be due to a change in Faraday rotation, but must be due to a sudden shift in the magnetic field orientation at the boundary of the north-east source. A

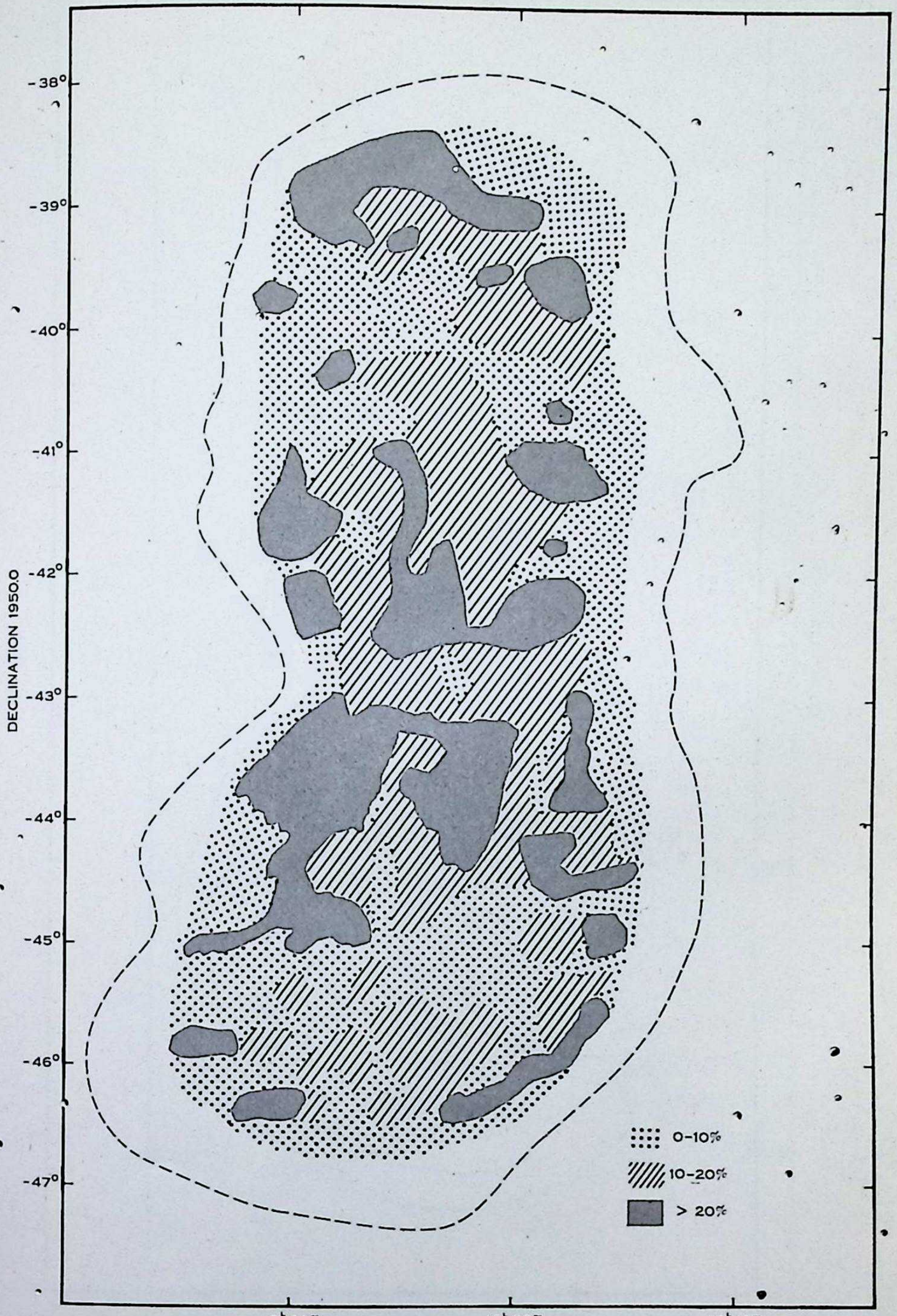
-38°
-39°
-40°
-41°
-42°
-43°
-44°
-45°
-46°
-47°
DECLINATION 1950.0
13h 30m
13h 20m
13h 10m
RIGHT ASCENSION 1950.0
0-10%
10-20%
> 20%

Fig. 5.—Distribution of the source polarization at 1410 Mc/s in percentage polarization groups 0–10, 10–20, and greater than 20%.

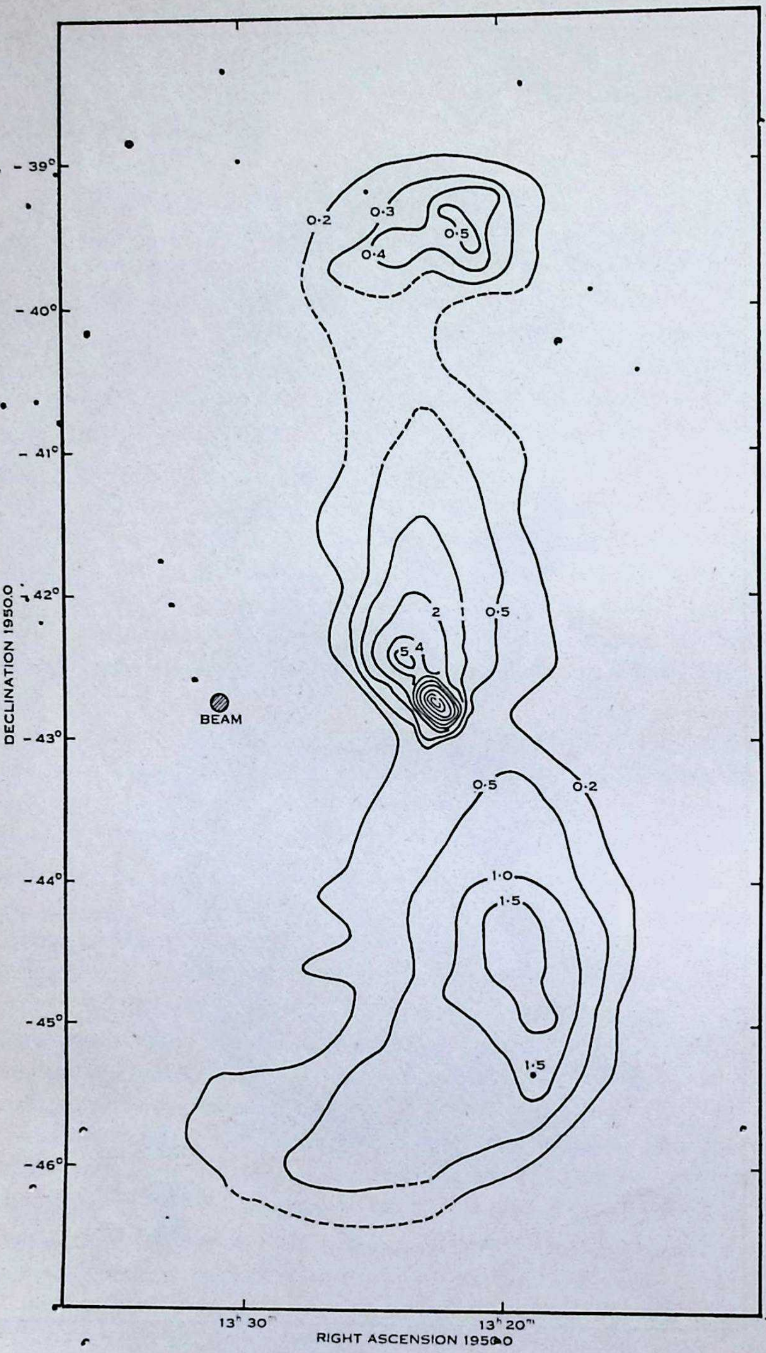

Fig. 6(*a*).—Isophotes of full-beam total emission brightness temperature at 2650 Mc/s (in °K); beamwidth 7′·4 at half intensity. Details of the central region are shown in Figure 7.

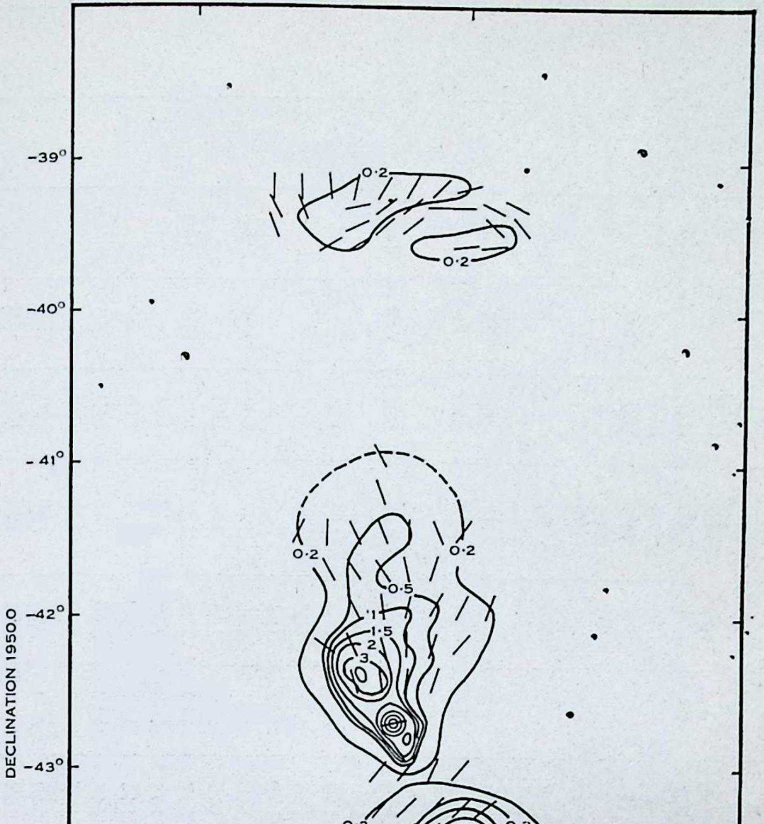

Fig. 6(*b*).—Isophotes of full-beam polarization brightness temperature at 2650 Mc/s (in °K). Short lines indicate the observed directions of the *E* vectors.

Table 5

CENTAURUS-A POLARIZATION POSITION ANGLES IN DEGREES AT 2650 Mc/s

(*a*) *Outer Regions*

Add 20 s to indicated minute of right ascension. Boldface numbers also observed by the rotating-feed method

Declination 1950.0	Right Ascension 1950.0														
	13h 15m	16m	17m	18m	19m	20m	21m	22m	23m	24m	25m	26m	27m	28m	29m
−39° 11′·0						105?	135?	150	135	168?	5?	0?	0?		
18′·5				65?	65?	90	90	108	123	100		20	25	15	
26′·0				40?	50?			130	130	114			20		
33′·5					95	90			125	120	120				
41′·0					96				120						
56′·0									95						
−40° 56′·0									30						
−41° 11′·0									**19**						
26′·0						145	23	0	**19**	26	176	160			
41′·0					128?	68?	162	12	25	34	35				
See Table 5(*b*) for central region															
−43° 01′·0					128	138	158	143	143	153	143	143			
06′·0						158	168	158							
11′·0						149	164	154	164	179					
16′·0					125	135	135	135	140						
26′·0					124	142	139	124							
36′·0		116	100	110	125	150	160	150	145	160	160	154			
46′·0		119	119	119	128	145	150	145	144	135					
56′·0	135	135	135	149	**140**	142	140	139	132	126	137	140			
−44° 03′·5		114	134	143	143	153	153	143	133	144					
11′·0		150	153	140	135	145	147	140	135	115	80				
21′·0	140	150	165	146	**130**	146	142	145	130	140					
36′·0	31	162	28	0	20	175	0	152	125	130					
46′·0		0	5	125	120	150	155	165	130	120	130				
56′·0		42	161	130		42		11	126	125	110				
−45° 06′·0		66		114	83	36	40	5	148	154	165	5			
16′·0		30	165	136	110	62	62	62	44			102?			
26′·0	9	4	173	173	147	64	74	74	74	105	112	112	112	112?	112?
36′·0		10	10	5		95	72	80	80	90	100	110	110		
46′·0						80	**72**	72	**72**	87	80	97			
56′·0								88	81	91		96	101	135	136
−46° 06′·0									88			93	126	148	133
16′·0													161		

TABLE 5 (*Continued*)

(*b*) *Central Region*

Declination* 1950.0	Right Ascension 1950.0																
	$13^{h} 20^{m}$		$13^{h} 21^{m}$			$13^{h} 22^{m}$			$13^{h} 23^{m}$			$13^{h} 24^{m}$			$13^{h} 25^{m}$		
—41° 56′ (a)	155		150			167			9			25					
—42° 06′ (b)	145	153	156		168	8		9	16		24	26		26	25		
—42° 11′ (b)	140	162	162		162	0		3	15		23	23		36	56		56
—42° 16′ (b)	9	9	157		177	4		9	16		24	29		28	37		50
—42° 21′ (c)		147	145	157	164	170	171	2	9	13	19	22	30	38	52	52	71
—42° 26′ (b)					158	168		0	6		11	16		31	34		34
—42° 31′ (b)	165		175		160	168		165	177		5	158		25	56		
—42° 36′ (d)				174	3	15	110	112	105	0	170	168	3	178			
—42° 39′·3 (d)					10	15	120	102	92	90	10	15	10				
—42° 42′·6 (d)					155	170	80	103†	100	95	105						
—42° 46′·0 (d)					150	145	50	100	110	125	15						
—42° 49′·3 (d)						175	155	136	125								
—42° 52′·6 (d)						170	165	155	20								
—42° 56′·0 (d)				120		3	3	168									

* Position angles tabulated at (a) 20 s, (b) 20 and 50 s, (c) 15, 35, and 55 s, (d) 0, 20, and 40 s after indicated minute of right ascension.

† Position angle for point A in Figure 7.

localized ridge of weak polarization is seen to overlap the south-preceding source, but, as this ridge shows elongation in a north–south direction greater than the known dimensions of the south-preceding source, its coincidence with the source may be fortuitous. The continuity of polarization orientation from here to the area north of the central sources suggests that this ridge is in fact a local intensification of the extended region of polarized emission in which the central sources are situated.

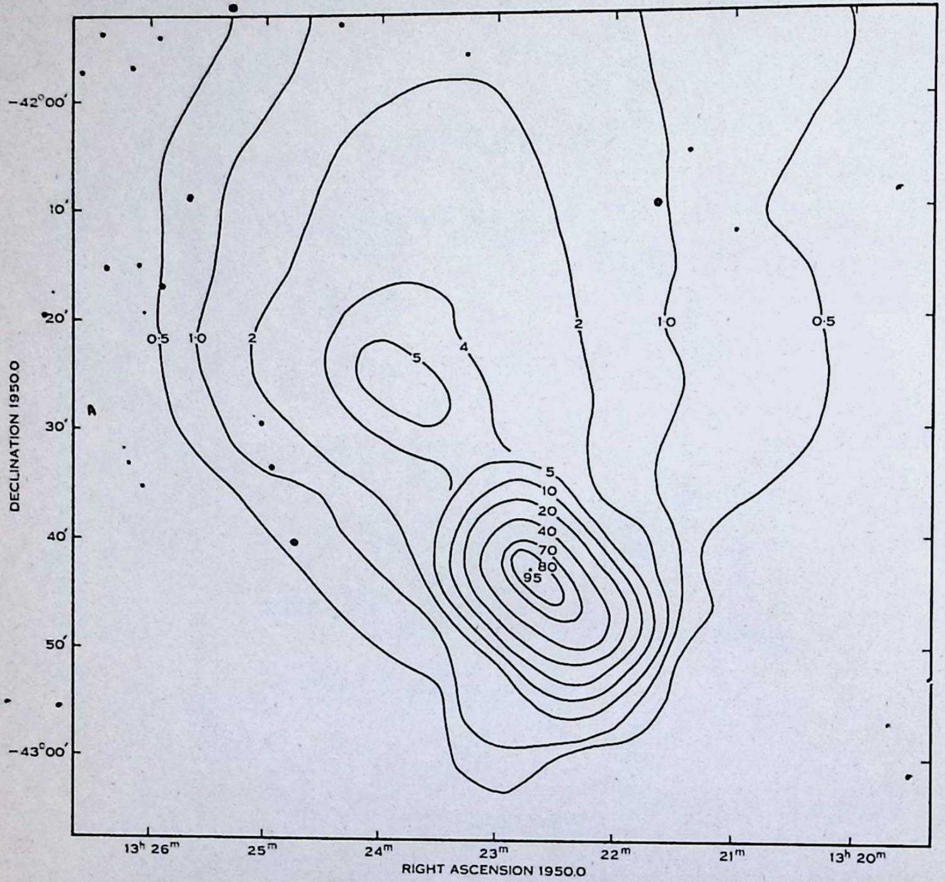

Fig. 7(*a*).—Isophotes of full-beam total emission brightness temperature at 2650 Mc/s for the central region of Figure 6.

Morris, Radhakrishnan, and Seielstad (1964), using a twin 90 ft interferometer at 2840 Mc/s, concluded that the south-west source was 5% polarized at this frequency. We are led to the conclusion, however, that the source is not more than 3% polarized in this frequency range; and we would emphasize the complexity of the polarization in the immediate vicinity of the source.

The isophotes in the central region are consistent with a double source having unpolarized components each of flux density 95 flux units, while the polarized contribution from the north-following source augments its total flux density to 108 flux units.

Beyond the central region there is very little improvement in the total intensity detail seen with the 7′·4 beam as compared with the 14′ beam at 1410 Mc/s. However, there are some regions, particularly near declination −45°, where the polarization orientation is changing rapidly and the polarization can therefore be followed more satisfactorily with the 7′·4 beam.

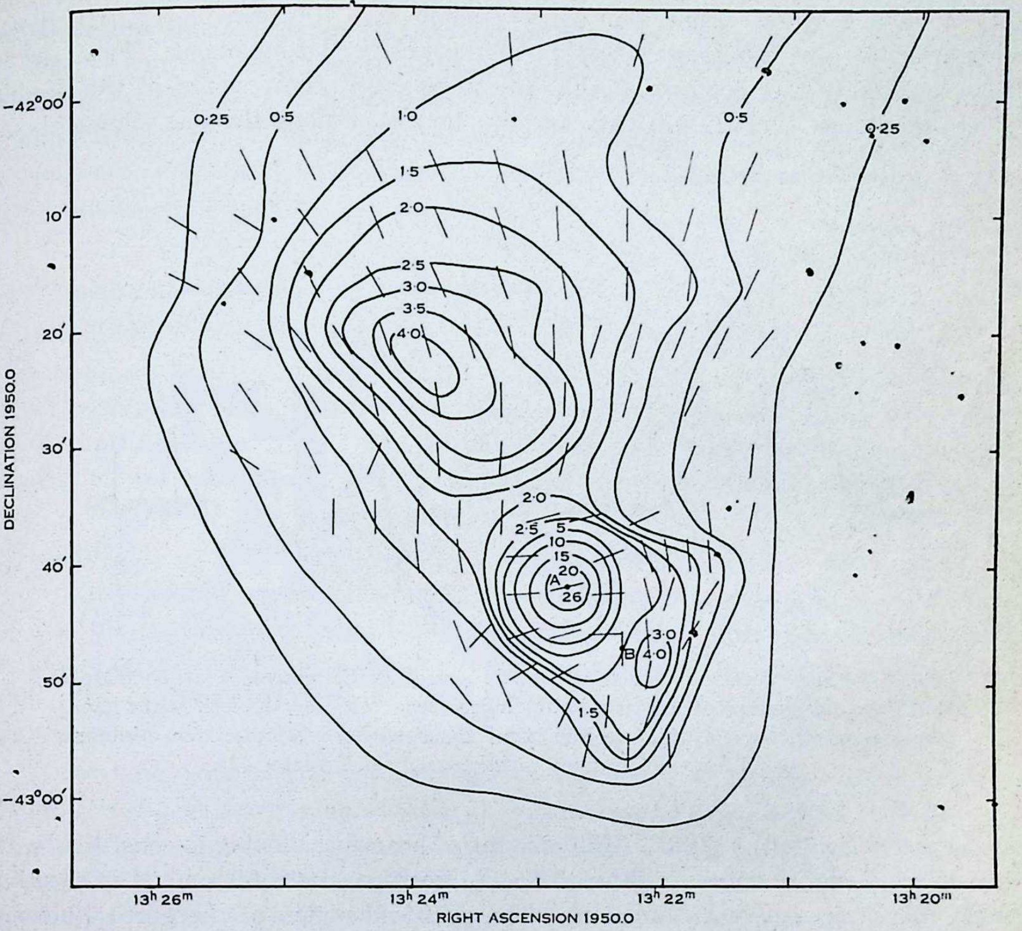
-42°00′
10′
20′
30′
40′
50′
-43°00′
DECLINATION 1950.0
13h 26m
13h 24m
13h 22m
13h 20m
RIGHT ASCENSION 1950.0
0·25
0·5
1·0
1·5
2·0
2·5
3·0
3·5
4·0
0·5
0·25
2·0
2·5
5
10
15
20
A
26
3·0
B
4·0
1·5

Fig. 7(*b*).—Isophotes of full-beam polarization brightness temperature at 2650 Mc/s. Short lines indicate the observed directions of the *E* vectors. The centres of the bright central sources are indicated by A and B on the map.

The dimensions of the secondary maximum centred at declination −42°30′ can be determined with some accuracy by subtracting the emission of the central component. This secondary source falls to half intensity in a distance of approximately 15′ from the maximum intensity in the east, south, and west directions and merges in the north with the remainder of the northern extended source.

VIII. Observations at 6 cm

Limited observations of the central double source have been carried out at a wavelength of 6·0 cm. For these observations a crystal mixer receiver of 650°K double-sideband noise temperature and a 10 Mc/s bandwidth was used. With a 2 s time constant the peak-to-peak fluctuations were 1·5 degK in aerial temperature.

This sensitivity was adequate for observing the central sources but not for the extended source. The beamwidth at half intensity was 4′·1 so that the central sources were well resolved. This is illustrated by Figure 8, which shows scans made along a track passing close to the centres of the double source. Scan (*a*) was made with the feed horn oriented to give maximum reception of the polarized component in the north-following source, while scan (*b*) was made with the feed in the orthogonal orientation to give minimum reception of the polarized component. From scans such as these it was determined that the unpolarized components of the double source are almost equal in intensity and are elongated along the line joining them, as suggested by Maltby (1961). The amount of beam broadening is consistent with equivalent Gaussian source widths of 3′·5 in position angle 45° and 2′ in position angle 135° (the transverse direction). The polarized region of the north-following source is noticeably smaller than the unpolarized region, and its equivalent Gaussian diameter is not more than 2′. This is consistent with measurements made with an interferometer at 10·6 cm by Morris, Radhakrishnan, and Seielstad (1964).

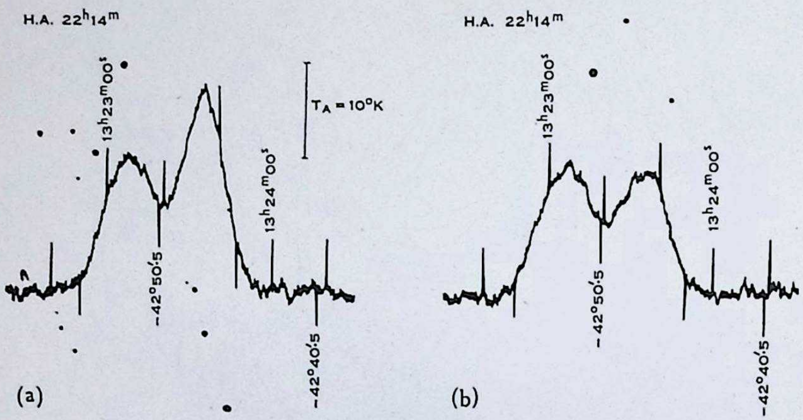

Fig. 8.—Scans through the central double source of Centaurus A at 5000 Mc/s. (*a*) Feed horn oriented for maximum signal from the north-east (right-hand) source; position angle of *E* vector 132°. (*b*) Feed horn oriented for minimum signal from this source; position angle of *E* vector 42°.

Observations made with the rotating feed showed that the north-following source is 18(±2)% polarized in position angle 132°(±5°), while the south-preceding source is 3(±1·5)% polarized in position angle 103°(±10°). These percentages are not corrected for resolution effects, and the actual percentage polarization in the polarized region of the north-following source must be considerably higher than 18%.

The 6·0 cm flux density of the north-following source is calculated to be 71 flux units and that of the south-preceding source to be 55 flux units. The probable error of these flux densities may be as high as 25%, due partly to uncertainties in the flux densities of calibrator sources and partly to a zenith-angle dependence of aerial gain, which made accurate intercomparison of source intensities difficult.

IX. Intrinsic Structure and Polarization

Figure 9 shows the intrinsic structure of the source as deduced from the present series of observations and supplemented by other published interferometric data for the central component. The contours represent equally spaced intensities in arbitrary units (dashed contour is one half unit in value). Since the spectral index is essentially constant throughout the wavelength range 3·5 m to 11 cm, and possibly down to 6 cm, the map should also be applicable throughout this range. An inset enlarged by a factor of five shows the central double source in relation to the optical disk of NGC 5128. Position measurements in which the pointing errors of the telescope were determined as accurately as possible by reference to identified sources gave the following position for the central component:

	R.A. 1950.0	Declination 1950.0
North-following source	$13^h 22^m 47^s\cdot 0 \pm 2^s$	$-42° 42'\cdot 5 \pm 0'\cdot 5$
South-preceding source	$13^h 22^m 20^s\cdot 5 \pm 2^s$	$-42° 47'\cdot 4 \pm 0'\cdot 5$

The two sources lie on a line in position angle 44° ±1° at a spacing of $6'\cdot 8 \pm 0'\cdot 2$. Their positions are approximately, but not quite, symmetrically placed with respect to the optical disk of NGC 5128. Bracewell (personal communication) has reviewed available positional data for NGC 5128 and has given a position for its optical centre as:

R.A. 1950.0 $\quad 13^h 22^m 31^s\cdot 6 \pm 0^s\cdot 5 \qquad$ Declination 1950.0 $\quad -42° 45'\cdot 4 \pm 0'\cdot 1$

Thus the mid point of the radio sources appears to be displaced approximately $0'\cdot 5$ to the north and by 2^s of R.A. to the east of the optical centre of NGC 5128. It should be noted that the accurately known position calibrators were at a considerable distance from Centaurus A, and the displacement quoted above should, for the present, be regarded as barely significant in relation to the probable errors.

Intrinsic polarization position angles and Faraday rotation measures were determined for as many points as possible in the source, as described in Section X. The polarization position angles are listed in Table 6. In Figure 9, vectors have been drawn at right angles to the intrinsic polarization E vectors to show the projected orientation of the magnetic field at the source. The numbers on the map are Faraday rotation measures in radians per metre squared and are negative in value.

The source appears to consist of a number of ejecta that have originated in NGC 5128 and have streamed away from it in a very open spiral. The initial direction of motion on the north side is towards the north-east, changing in the space of about half a degree to a general northerly direction and maintaining this up to the northern boundary of the source. On the south side, the spiral changes direction by about 90° in a more gradual fashion, starting in a south-westerly direction and finishing in a south-easterly direction. A high degree of symmetry is shown in the size and placing of the central components on the periphery of NGC 5128 and in their approximately equal flux densities, but this structural symmetry is not maintained in the outer extensions, although, as has been noted earlier, the total power emission is very evenly divided between the northern and southern regions. Apart from this lack of symmetry, the well-defined intensity maximum near declination −42° 30′ may be paired off with the broad maximum at −44° 20′, and the weak feature at declination

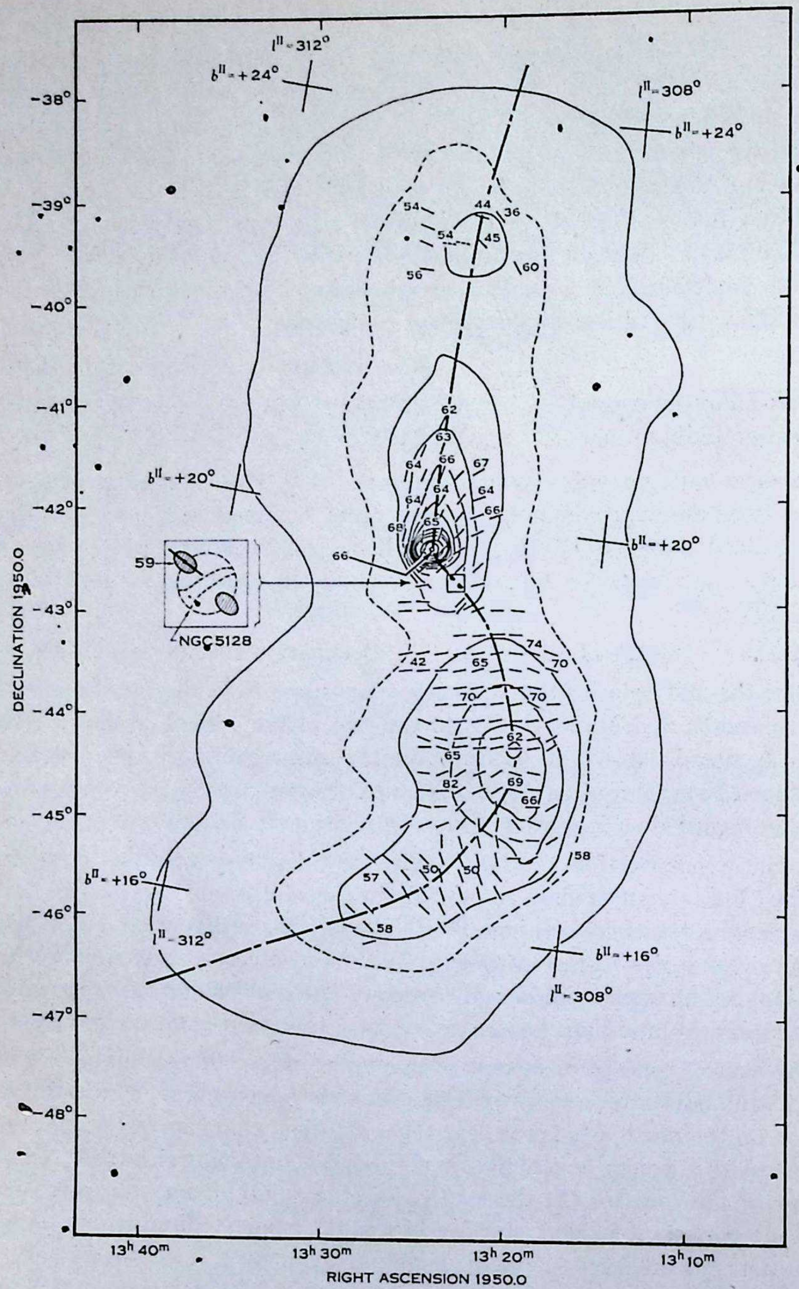
l^{II} = 312°
b^{II} = +24°
l^{II} = 308°
b^{II} = +24°
−38°
−39°
−40°
−41°
−42°
−43°
−44°
−45°
−46°
−47°
−48°
DECLINATION 1950.0
54
44
36
54
45
56
60
62
63
66
67
64
64
64
64
66
68
65
66
59
NGC 5128
b^{II} = +20°
b^{II} = +20°
74
42
65
70
70
70
62
65
82
69
66
58
57
50
50
58
b^{II} = +16°
l^{II} = 312°
b^{II} = +16°
l^{II} = 308°
13h 40m
13h 30m
13h 20m
13h 10m
RIGHT ASCENSION 1950.0

Fig. 9.—Intrinsic structure of Centaurus A seen in projection. Solid contours represent equally spaced values of intensity in arbitrary units (dashed contour is one half unit in value). Enlarged inset shows central components (shaded) in relation to NGC 5128. Vectors are at right angles to the intrinsic *E* vectors of the source to indicate the direction of the projected magnetic field at the source. Numbers indicate magnitudes of Faraday rotation measures, negative in sign in all cases. The heavy broken line shows the ridge line of the source.

TABLE 6

CENTAURUS-A INTRINSIC POLARIZATION POSITION ANGLES IN DEGREES

Add 20 s to indicated minute of right ascension

Declination 1950.0	Right Ascension 1950.0													
	$13^h 16^m$	17^m	18^m	19^m	20^m	21^m	22^m	23^m	24^m	25^m	26^m	27^m	28^m	29^m
−38° 26′								0						
56								153						
−39° 11′					135	171	174	5						
26				82	148	130	172	142						
41		115	115	120				135	155					
56		115	115											
−41° 11′								62						
26									66					
41						30	46	75		80				
56′						20	42	52	68					
−42° 11′					0	23	41	61	75					
16				20	10	25	53	60	73	70				
26							30	55	60	80				
36						40	160	40	40					
41							147*							
46						10			5					
−43° 01′				175	0	23	50		175	15				
26			170	177	7	175	170	0	8	8				
36	165	158	161	174	15	8	5	5	10	10				
46	165	168	166	13	18	13								
56		177	17	4	4	2	0							
−44° 11′					5	5								
21	15	30	4	178	8	8	11							
36	30	80	50	173	55	55	40							
46	54	174	169				20	10						
56			163	163				6						
−45° 26′	40	33	34	7	92	107	102	102	145	152	152	152		
41	50	50	45		122	97	107	107	130	140	140	150		
56							125	120	130		132	145		
−46° 06′													12	177
16											135	4		

* North-following central source.

$-39°30'$ with the feature near declination $-46°00'$. The latter may well have been a separate feature at an earlier stage in the development of the source.

The polarization of the source shows considerable variety, both in uniformity and orientation relative to the spiral structure. In view of the prevalence of strong polarization elsewhere in the source, it is surprising that the south-preceding central source is so weakly polarized. It is possible that the magnetic field in this source is relatively disordered at its present stage of development.

Alternatively, the three-dimensional structure of the source may be such that the north-following source lies partly in front of NGC 5128 while the south-preceding source lies partly behind NGC 5128. Differential Faraday rotation in the outer regions of NGC 5128 may then account for the depolarization.

In the north-following source there appears to be a core of strong polarization, but with presently available resolution it is not known in detail how the polarization varies across the source. However, it does appear that the polarization orientation changes suddenly by about 90° at the boundary of the north-following source.

In the region immediately north of the central component, the projected magnetic field vectors run generally along the source extension and some fanning out of the vectors may be noted. It is quite possible that this fanning out is connected with the elongation of the intensity contours in this region. North of declination $-41°00'$ the polarization is generally more confused than elsewhere in the source and it is difficult to discern any systematic pattern. On the other hand, there are some very large areas of uniform polarization in the southern extended source. For example, in the region around declination $-44°00'$ there is an area of about 2 square degrees where the field vectors are uniformly transverse. At an assumed distance of 4 Mpc this would represent a projected area of about 10^{10} square parsecs. There is a region of confused polarization near declination $-45°00'$, which divides the above region from a region around declination $-46°00'$ where the field vectors again become transverse to the spiral axis. This division lends additional support to the suggestion that the two regions in question have partly intermingled after being originally separate.

The integrated polarization of the whole source is of some interest for comparison with other unresolved sources. This integration has been done at 21 cm where the polarization data for the source are reasonably complete. The source was divided into small areas over which the polarization was substantially uniform. By adding up the Stokes "*Q*" and "*U*" parameters for these regions the integrated degree of polarization was determined to be approximately 7% with the *E* vector in position angle 38°. Since the polarization data were less complete at 31 and 11 cm, the integrated polarization was not determined at these wavelengths. However, taking an average Faraday rotation of 150° for the whole source at 21 cm, the intrinsic position angle for the integrated polarization would be approximately 8°.

X. FARADAY ROTATION

The rotation of the position angle of the electric vector with a wavelength squared dependence, the well-known phenomenon of Faraday rotation, has already been noted at three points in the source (Cooper and Price 1962). Subsequent determination

TABLE 7

CENTAURUS-A FARADAY ROTATION MEASURES

Values in units of rad/m². Add 20 s to indicated minute of right ascension

Declination 1950.0	Right Ascension 1950.0											
	13h 16m	17m	18m	19m	20m	21m	22m	23m	24m	25m	26m	27m
−38° 26′								53				
−38° 56′								48				
−39° 11′					36	45						
−39° 26′						42	53	54	54			
−39° 41′				60				29	54?			
−40° 56′												
−41° 11′								64				
−41° 26′								63				
−41° 41′						68	67	67	65			
−41° 56′						64	64	64	64			
−42° 11′					67	66	63	66	69			
−42° 41′								59*				
−43° 26′			75	74					42	42	35	
−43° 41′		70				66			41			
−43° 56′			71	71	71	71	71					
−44° 21′			63	63	63		65					
−44° 41′				70				84				
−44° 56′			67	67								
−45° 26′	58				51	51	51	51				
−45° 41′					51	51	51	51			58	
−45° 56′												59
−46° 16′												59

* North-following central source.

of the polarization parameters over the entire source at several wavelengths have enabled us to study the Faraday rotation characteristics over a region of approximately 12 square degrees in the more intense regions of the source.

Using polarization data from 31, 21, and 11 cm surveys, the electric vector position angles for each point investigated were plotted as a function of wavelength squared. These plots gave the intrinsic polarization angle, by extrapolation to zero wavelength, and the rotation measure (as defined by Gardner and Whiteoak 1963) for each point. For each position angle there was an ambiguity of $n\pi$, and a best fit to the position angle versus wavelength squared plot was effected, accepting the lowest rotation measure consistent with the observational data. Values of rotation measure were derived for some 63 points distributed over the entire source, taken in regions where the total brightness and the polarization brightness allowed a good signal-to-noise ratio in the observations.

Table 7 lists these rotation measures in units of radians per metre squared, and a representative number of them are included in Figure 9.

The origin of the Faraday rotation in this and other radio sources has been the subject of previous discussion (Cooper and Price 1962; Sciama 1962; Gardner and Whiteoak 1963; Gardner 1964) and it is now generally accepted that the rotation occurs in the galactic halo. It is possible that a small amount of Faraday rotation occurs in the source itself, but from depolarization considerations, as discussed in Section XII, the amount of rotation occurring in the source can only be a small fraction of the observed total.

To account for a rotation measure R.M. we need an electron density and magnetic field such that

$$\text{R.M.} = 8\cdot 1\times 10^5 \int N_e H_l \, \mathrm{d}l,$$

where N_e is the electron density in electrons/cm^3, H_l is the longitudinal component of the magnetic field in gauss, and dl is an element of path length measured in parsecs. Estimates of the path length over which the Faraday rotation may be occurring range from a few hundred parsecs to about 10 kpc. For the short path length, electron densities of $\sim 10^{-2}$ electrons/cm^3 and magnetic fields of $\sim 10^{-5}$ G are indicated, while for the longer path length the field strength and electron density may be reduced accordingly.

Since Centaurus A provides by far the largest continuous area of extragalactic polarization, it affords a unique opportunity to study the scale on which rotation measures, and hence magnetic field strengths and electron densities, vary in the galactic halo. This is the more so since it has turned out that a specially interesting span of galactic latitude is covered. It may be seen from Figure 9 that the rotation measures tend to maximize near $b^{\text{II}} \simeq +18°$ and fall off in an irregular manner towards the northern and southern boundaries of the source at $b^{\text{II}} = +24°$ and $+16°$ respectively. The fall-off at lower and higher latitudes is consistent with the conclusion reached by Gardner and Davies (personal communication) from a general study of galactic Faraday rotation that, in the vicinity of $l^{\text{II}} = 310°$, the rotation measure passes through zero and changes sign at $b^{\text{II}} \simeq +10°$ and $+50°$.

In more than half of the Centaurus-A area where rotation measures have been obtained, the value does not change more than 10–15% in the space of a degree, but some small regions may be noted in Figure 9 where a change of the order of 30% in rotation measure occurs in the space of one-quarter to one-half of a degree. The boundaries of these regions are revealed in several places on the 31 cm polarization map of Figure 3 by the lack of polarization due to differential Faraday rotation across the telescope beam.

In regions of fairly uniform rotation measure the estimated accuracy is ±5%. For points that have been given special study, such as the central component, the point at right ascension $13^{\mathrm{h}}\,24^{\mathrm{m}}$, declination $-42°\,30'$, and the point at right ascension $13^{\mathrm{h}}\,20^{\mathrm{m}}$, declination $-42°\,25'$, the accuracy is estimated to be ±2%.

XI. Spectral Analysis

Flux densities derived in previous sections are summarized in Table 8 and a logarithmic plot of these flux densities is presented in Figure 10 together with other published data on Centaurus A. At frequencies below our lowest value of 406 Mc/s the most recent data are those of Sheridan (1958) at 85 Mc/s and Shain (1958) at 19·7 Mc/s.

Table 8

CENTAURUS-A FLUX DENSITIES AT SEVERAL WAVELENGTHS

Values in units of $10^{-26}\,\mathrm{W\,m^{-2}\,(c/s)^{-1}}$

Wavelength (cm)	Total Emission	Central Component Emission	Extended Component Emission	
			North	South
74	2740	595 (22%)	1075 (39%)	1070 (39%)
31		370		
21	1330	288 (22%)	510 (38%)	532 (40%)
11		203		
6		126		

The plot of total source flux density (curve 2) indicates strong curvature of the spectrum, with an index of approximately −0·9 at the low frequency end, decreasing to −0·6 at the high frequency end. On the other hand, the plot for the central component (curve 1) shows a fairly uniform average slope with an index of −0·6. If the 85 Mc/s flux densities are multiplied by 0·82, as has been suggested by Kellermann (1964) to harmonize the flux scale of the 85 Mc/s survey of Mills, Slee, and Hill (1958, 1960) with the currently accepted flux scale for northern sources, the resulting 85 Mc/s flux densities for the whole source and for the central component fall quite close to a straight line plot through our higher frequency data. The rise in total flux density at 19·7 Mc/s then becomes even more pronounced, but in the absence of independent measurements in the 19 Mc/s region we are unable to assess the reality of this rise. The uncertainty of the 19·7 Mc/s absolute intensity scale was estimated by Shain to be up to 20%. However, the assessment of the proportion of the total emission that is contributed by the central component should be subject to much smaller uncertainties, and we note that this proportion decreases from 22% at frequencies of 85 Mc/s and above to 11% at 19·7 Mc/s. This decrease may possibly be explained by the mechanism, which has been discussed by Kellermann (1964), whereby, in the early life of certain sources, the rate of injection of energetic particles has not come into equilibrium with the radiation losses. In such a case the spectral slope is expected to flatten towards the low frequency end, but as the source ages and equilibrium is reached the spectral curvature disappears. Thus the central component of Centaurus A may be at such an early stage of development, while the outer parts have reached equilibrium.

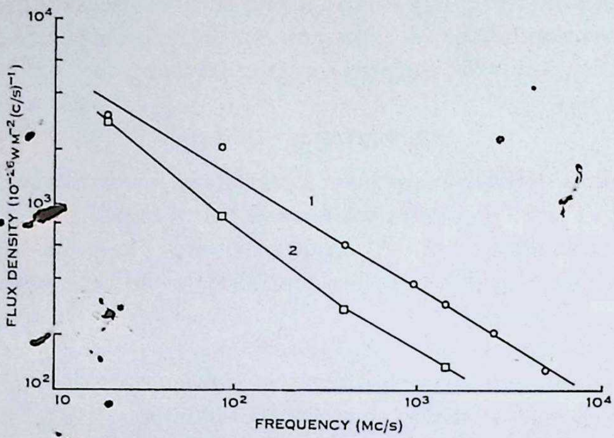

Fig. 10.—Spectrum of the total emission of Centaurus A, curve 2 (÷ 10), and the central component emission, curve 1, plotted from the data of Table 7 together with data at 19·7 Mc/s from Shain (1958) and at 85 Mc/s from Sheridan (1958).

A value of 1765 flux units for the combined emission of the central component and the northern and southern parts of the extended source at 960 Mc/s has been given by Bolton and Clark (1960). Recent adjustments to the Caltech flux density scale indicate that this value should be multiplied by 0·95, bringing it closely into line with our own flux density for this frequency. The same authors estimated a flux density for the central component of 460 flux units at 960 Mc/s, but they appear to have overestimated the contribution of the central component to their isophotes, which were observed with a 0°·8 beam. In the light of our improved knowledge of the source structure, a value of 370 flux units seems more reasonable.

XII. Depolarization Effects

As the observing wavelength increases, a number of effects come into play to decrease the degree of polarization observed in the source. Firstly, the larger beam may encompass areas of differing polarization orientation with the result that the net polarization decreases. The differing polarization orientations may be inherent in the source or may be due to differential Faraday rotation between the source and the observer. The latter effect certainly operates in some areas of Centaurus A.

Even in areas of uniform polarization there may be depolarization due to Faraday rotation occurring in the source along with the emission process. If the emission and rotation are uniformly distributed in depth through the source and the radiation from the most distant part of the source is subjected to a total rotation of x degrees before emerging from the source, it may readily be shown that there will be a net Faraday rotation of $\frac{1}{2}x$ degrees for the integrated emission, and a depolarization factor $(\sin x)/x$ applicable to this emission. Thus depolarization will become very pronounced as x approaches 180°. A uniform distribution of rotation with depth in the source is not to be expected in practice, but for more tapered distributions the depolarization factor will still be much the same for a given total Faraday rotation.

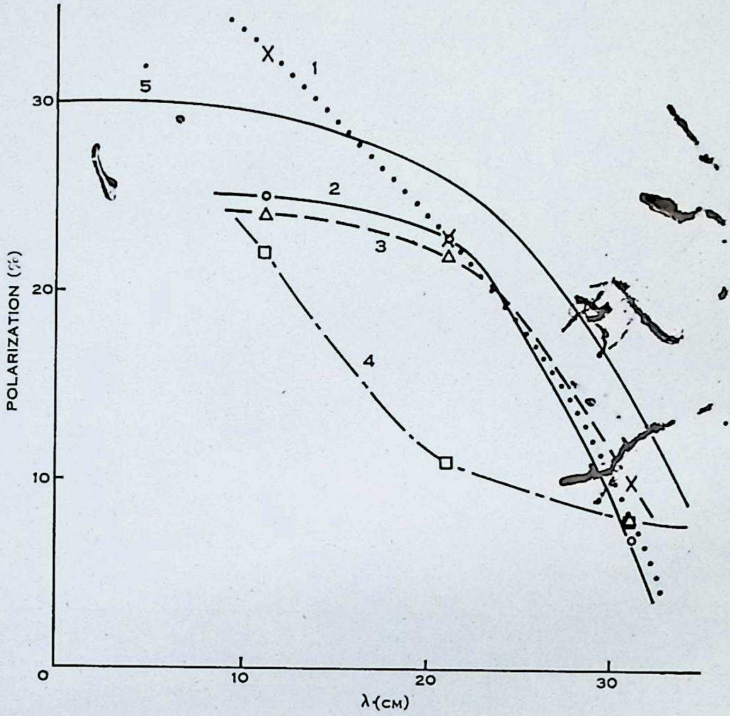

Fig. 11.—Plots of the percent polarization at several points in Centaurus A as a function of wavelength: curve 1, R.A. $13^{h} 22^{m}$, dec. $-43° 45'$; curve 2, R.A. $13^{h} 24^{m}$, dec. $-41° 15'$; curve 3, R.A. $13^{h} 21^{m} \cdot 5$, dec. $-44° 25'$; curve 4, R.A. $13^{h} 21^{m} \cdot 5$, dec. $-45° 30'$; curve 5, a plot of the function $P_0(\sin R\lambda^2)/R\lambda^2$, where $P_0 = 30\%$ and $R = 20$ rad/m^2.

In an attempt to set a limit to the amount of Faraday rotation occurring in Centaurus A, the variation in percent polarization with wavelength is plotted in Figure 11 for four regions where confusion effects in the beam are small at wavelengths up to 31 cm. For comparison a plot of the depolarization to be expected due to a rotation measure of 20 rad/m^2 distributed uniformly in depth through the emitting region is shown in Figure 11, curve 5. This plot has been arbitrarily drawn for 30% polarization at zero wavelength.

Curve 5 suggests that the upper limit for the internal rotation measure of the source is about 20 rad/m^2 and therefore that the net rotation in the source has an upper limit of about 10 rad/m^2, that is, about one-sixth of the observed rotation.

XIII. EXTRANEOUS SOURCES

In the course of the observations two extraneous sources of moderate intensity were discovered within the boundaries of Centaurus A, and a third was discovered just outside the south-preceding extremity of Centaurus A. These sources are listed in Table 9 in order of increasing right ascension. The resolution at 74 cm wavelength was not sufficient to distinguish any of these sources, but the first and second were quite clearly defined at 21 cm. The third source was only distinguishable at 11 cm.

TABLE 9

EXTRANEOUS SOURCES IN THE CENTAURUS-A REGION

Source:	1315–46	1318–43	1320–44
Position (1950.0)			
Right ascension	$13^h 15^m 35^s$	$13^h 18^m 13^s$	$13^h 20^m 07^s$
Declination	$-46° 05'·5$	$-43° 26'·3$	$-44° 35'·1$
Annual precession			
$\Delta\alpha$ (s/yr)	3·53	3·49	3·52
$\Delta\delta$ ('/yr)	−0·32	−0·32	−0·31
Flux density (10^{-26} W m^{-2} $(c/s)^{-1}$)			
1410 Mc/s	2·65	5·8	—
2650 Mc/s	1·32	4·75	1·45
Spectral index			
1410 → 2650 Mc/s	−1·0	−0·31	—
Angular size			
N.–S.	P	5'·0	P
E.–W.	P	6'·3	P
Degree of polarization at 1410 Mc/s	< 3%	See text	See text

The source 1318–43 has equivalent Gaussian dimensions of $4'·5 \times 6'·3$ and is identified with an elliptical galaxy of approximately $14^m·5$ found on a plate taken by Dr. J. B. Whiteoak with the Mt Palomar 48 in. Schmidt telescope. Within the position error rectangle of 1320–44 no nebular images can be distinguished to the plate limit, and there are no stellar images brighter than about 17^m. The position of the source 1315–46 has not been examined yet, as no high definition plates are available for the region.

The source 1315–46 is less than 3% polarized at 21 cm and the other two sources show no polarization that can be distinguished from the strong polarization of Centaurus A and of the foreground, which surrounds them.

XIV. CONCLUSIONS

The work described here has revealed Centaurus A as a unique object for studying the processes by which radio galaxies evolve. Its polarized emission enables the distribution of magnetic fields to be traced over the extremely large volume of space occupied by the source, while at the same time allowing the details of galactic Faraday rotation to be traced over a particularly interesting region of the sky.

POLARIZATION OF CENTAURUS A

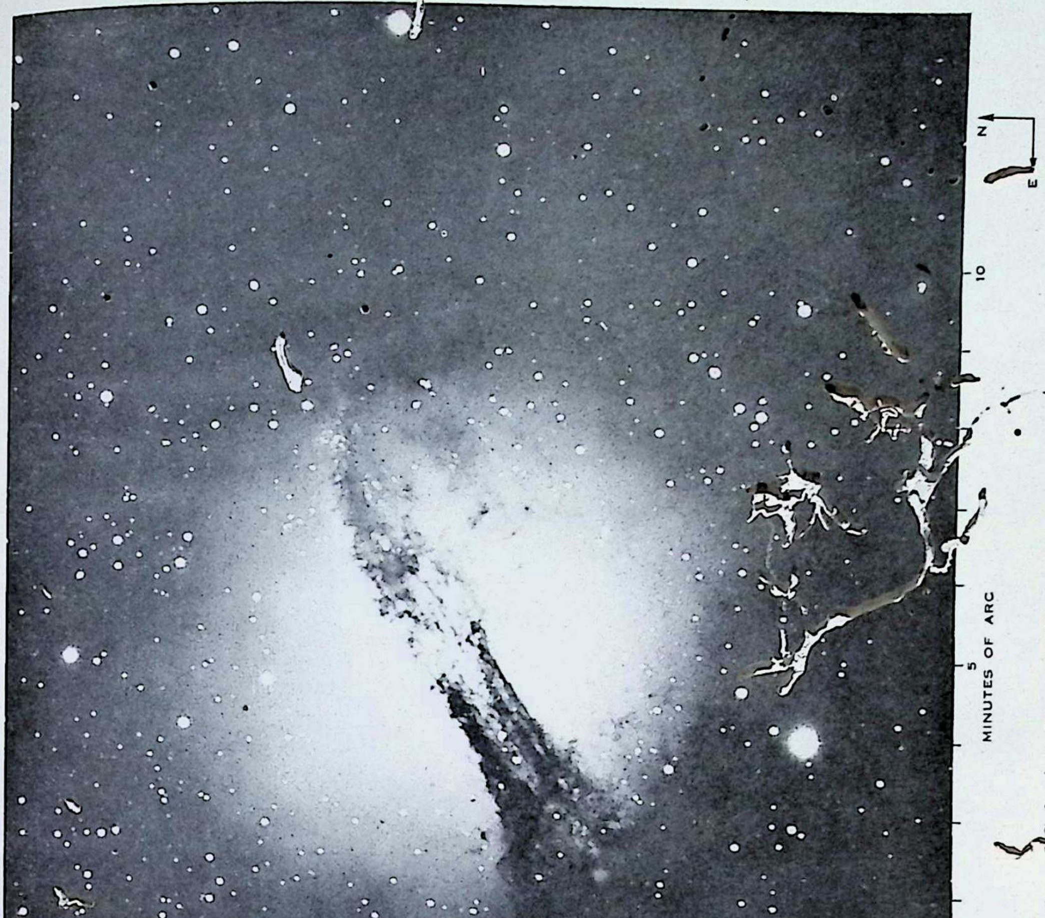

NGC 5128. From the Hubble Atlas of Galaxies, Carnegie Institute of Washington, 1961. (Note that the orientation of the galaxy given in the Hubble Atlas is incorrect.)

Aust. J. Phys., 1965, **18**, 589–625

The basic features of the source and the Faraday rotation are now apparent, and it remains for further studies employing higher sensitivity and resolution to build up a more detailed picture. Observations that will be of special interest concern the polarization of the south-preceding central source at wavelengths below 6 cm, and the regions in the extended source where the Faraday rotation appears to be changing rapidly. A definite answer to the question, whether or not Centaurus A extends further on its south-following side than we have assumed in the present paper, is also needed.

XV. Acknowledgments

We thank Mr. J. G. Bolton and Dr. F. F. Gardner for critical readings of the manuscript and for their helpful suggestions on points of interpretation. One of us (R.M.P.) is at present the holder of a National Science Foundation Fellowship.

XVI. References

Bolton, J. G. (1948).—*Nature* **162**: 141.
Bolton, J. G., and Clark, B. G. (1960).—*Publs Astr. Soc. Pacif.* **72**: 29.
Bolton, J. G., Stanley, G. J., and Slee, O. B. (1949).—*Nature* **164**: 101.
Bolton, J. G., Westfold, K. E., Stanley, G. J., and Slee, O. B. [illegible]—*Aust. J. Phys.* **7**: 96.
Bracewell, R. N., Cooper, B. F. C., and Cousins, T. E. (1962).—*Nature* **195**: 12[illegible]9.
Burbidge, E. M., and Burbidge, G. R. (1959).—*Astrophys. J.* **129**: 271.
Conway, R. G., Kellermann, K. I., and Long, R. J. (1963).—*Mon. Not. R. Astr. Soc.* **125**: 261.
Cooper, B. F. C., Cousins, T. E., and Gruner, L. (1964).—*Proc. Instn Radio Engrs Aust.* **25**: 221.
Cooper, B. F. C., and Price, R. M. (1962).—*Nature* **195**: 1084.
Elvius, A., and Hall, J. S. (1964).—*Bull. Lowell Observ.* **6**: 123.
Gardner, F. F. (1964).—Symp. IAU–URSI No. 20 (Canberra 1963). p. 143.
Gardner, F. F., and Milne, D. K. (1963).—*Proc. Instn Radio Engrs Aust.* **24**: 127.
Gardner, F. F., and Whiteoak, J. B. (1963).—*Nature* **197**: 1162.
Hindman, J. V., and Wade, C. M. (1959).—*Aust. J. Phys.* **12**: 258.
Johnson, H. M. (1963).—Pubs NRAO, Volume 1, No. 15.
Kellermann, K. I. (1964).—*Astrophys. J.* **140**: 969.
Komesaroff, M. M., and Mathewson, D. S. (1962).—*Aust. J. Phys.* **15**: 572.
McGee, R. X., Slee, O. B., and Stanley, G. J. (1955).—*Aust. J. Phys.* **8**: 347.
Mackey, M. B. (1964).—*Proc. Instn Radio Engrs Aust.* **25**: 515.
Maltby, P. (1961).—*Nature* **191**: 793.
Mills, B. Y. (1953).—*Aust. J. Phys.* **6**: 452.
Mills, B. Y., Slee, O. B., and Hill, E. R. (1958).—*Aust. J. Phys.* **11**: 360.
Mills, B. Y., Slee, O. B., and Hill, E. R. (1960).—*Aust. J. Phys.* **13**: 676.
Morris, D., Radhakrishnan, V., and Seielstad, G. A. (1964).—*Astrophys. J.* **139**: 560.
Piddington, J. H., and Trent, G. H. (1956).—*Aust. J. Phys.* **9**: 74.
Sciama, D. W. (1962).—*Nature* **196**: 760.
Sersic, J. L. (1958).—*Observatory* **78**: 24.
Sérsic, J. L. (1961).—*Revta Univ. Nac. Córdoba* **11**: No. 3.
Shain, C. A. (1958).—*Aust. J. Phys.* **11**: 517.
Sheridan, K. V. (1958).—*Aust. J. Phys.* **11**: 400.
Stanley, G. J., and Slee, O. B. (1950).—*Aust. J. Sci. Res.* A **3**: 234.
de Vaucouleurs, G. (1953).—*Observatory* **73**: 252.
de Vaucouleurs, G. (1956).—*Occ. Notes R. Astr. Soc.* **3**: 118.
Wade, C. M. (1959).—*Aust. J. Phys.* **12**: 471.
Westerhout, G., Seeger, C. L., Brouw, W. N., and Tinbergen, J. (1962).—*Bull. Astr. Insts Neth.* **16**: 187.

IDENTIFICATION OF EXTRAGALACTIC RADIO SOURCES BETWEEN DECLINATIONS −20° AND −44°

By J. G. Bolton,* Margaret E. Clarke,* and R. D. Ekers*

[*Manuscript received June 29, 1965*]

Summary

Identifications with extragalactic objects are suggested for 5[illegible] radio sources with declinations between −20° and −44°. The identifications are based on a search of the Palomar Sky Survey plates in the position of sources in the Parkes catalogue. Eight of the identifications are with suspected quasi-stellar objects and the remainder with galaxies. Finding charts are provided for the fainter objects.

I. The Search for Identifications

The recently published Parkes catalogue of radio sources with declinations between −20° and −60° (Bolton, Gardner, and Mackey 1964; subsequently referred to as BGM) lists 297 sources with flux densities greater than $4\times10^{[illegible]}$ W m^{-2} (c/s)$^{-1}$ at 408 Mc/s. For the area north of −50° the accuracy claimed for the source positions is such that there is a 90% chance that both coordinates are within 0·6 min of arc of the true position. With this accuracy it is possible to make unique identifications with galaxies as faint as $m_{\mathrm{pg}} = 17$, and, under favourable conditions, even as faint as $m_{\mathrm{pg}} = 18$.

One hundred and eleven of the catalogue sources lie between declinations −20° and −33°, for which two-colour plates of the Palomar Sky Survey exist, and a further 101 sources lie between declinations −33° and −45°. In 1962 Dr. I. S. Bowen, then Director of the Mount Wilson and Palomar Observatories, agreed to the use of the 48 in. Schmidt telescope for an extension of the Sky Survey to this more southerly zone. He suggested a combination of 103a–E plates and an orange filter. With this combination, a limiting magnitude of about 19·5 is reached in the short exposure time of 20 min and effects of differential refraction are kept as small as possible. These extension plates have been taken by Dr. J. B. Whiteoak and many of them are of as high a quality as those of the standard survey, in spite of the unfavourable zenith distance. As plates of only one colour are available, quasi-stellar objects cannot be recognized by their characteristic blue colour, and thus identifications in this zone are restricted to galaxies. The declination limit of the survey is not uniform and varies between 44°·5 for the early hours of right ascension and about −45° near 20 hr.

To aid in a rapid examination of the Sky Atlas prints or plates, transparent overlays were prepared on which were marked the position of the source and the positions of between 6 and 10 reference stars from either the Yale or Cape photographic catalogues. Examination was made of an area 2 min of arc square, centred on the

---

* Division of Radiophysics, CSIRO, University Grounds, Chippendale, N.S.W.

Aust. J. Phys., 1965, 18, 62[illegible]

source position. Positions of sources in the region from −20° to −33° were examined initially on prints of the Sky Atlas and later, together with those south of −33°, on the original plates at the California Institute of Technology.

Suggested identifications were found for 55 sources out of a total of 192. Of the remaining 137 fields: 21 contain objects that could be galaxies near the plate limit (no identifications were made in these cases as either the radio position was not sufficiently accurate to distinguish between several possible objects or the peak quality was too poor to be sure the images were those of galaxies); 21 fields are either heavily crowded or obscured; 95 fields contain stars only, 37 of these in the northern zone contain no abnormally blue stars.

Radio positions for most of those sources for which an identification appeared likely have since been determined more precisely in a series of "transit" measurements with the 210 ft telescope at a frequency of 2650 Mc/s (Shimmins, Clarke, and Ekers, to be published). Calibration was obtained from well-accepted, but more northerly, identifications and the assumption of identification of a small number of objects in the present list. The right ascensions were measured from meridian transit observations with the telescope azimuth set on 0° or 180° (the 210 ft telescope has an altazimuth mounting but can be driven in equatorial coordinates through a *master equatorial* unit). Declination observations were made with the telescope under control of its master equatorial, but observations were restricted to a range of 10 min of hour angle either side of the meridian. The accuracy achieved in these transit measurements is at least a factor of three better than those of the position measurements of the BGM catalogue. This is because the method of observation ensured that the errors were a function of only one coordinate, and this error function could be precisely determined from the observation of calibrator sources.

Positions of the optical counterparts were estimated from the 48 in. plates with the aid of the transparent overlays. For plates of good image quality, where either the overlay fitted precisely or where the object was close to a reference star, the estimated position is probably accurate to 0·1 min of arc in both coordinates. In less favourable cases the error could be two or even three times this. These positions are given in the table of identifications (Table 1) and the final digit stated is some guide to the relevant accuracy. The accuracy of the radio transit positions is of the same order, and in most cases the radio and optical positions agree to well within the sum of possible errors. The exceptions are a few cases where the optical position lies within the area covered by an extended radio source, or where the radio position lies within the image of a galaxy of large angular extent (e.g. NGC 253).

II. The Identified Sources

Details of the identified sources are given in Table 1. For the sake of completeness the list includes all previously suggested identifications that are substantiated by the present observations. In these cases references to original publications are given in column 10 and the footnote. The first column of Table 1 contains the Parkes

---

Plate 1 to 6.—Finding charts for identified sources. Scale is 5 mm = 1 min of arc. North-east is top left-hand corner.

EXTRAGALACTIC SOURCES BETWEEN −20° AND −44°

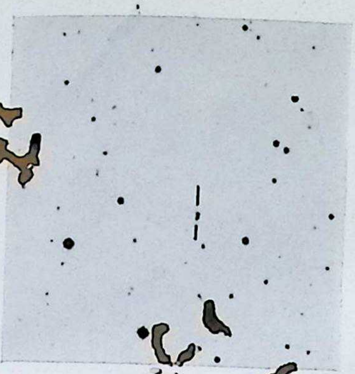

0114−21

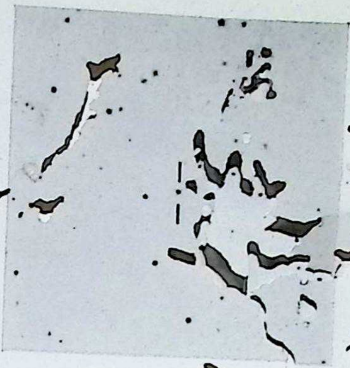

215−5

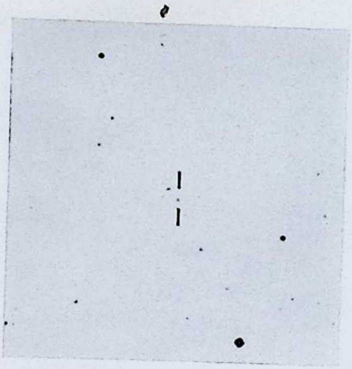

0043−42

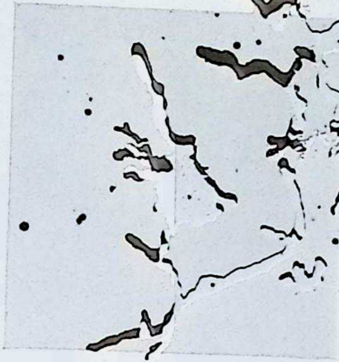

0157−31

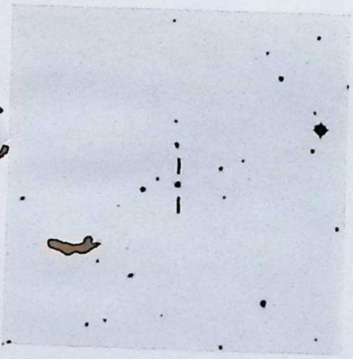

0023−33

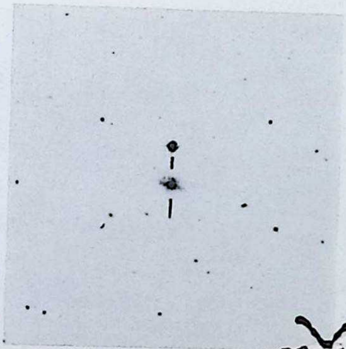

0131−36

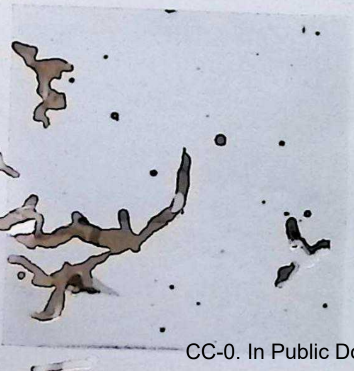

0022−29

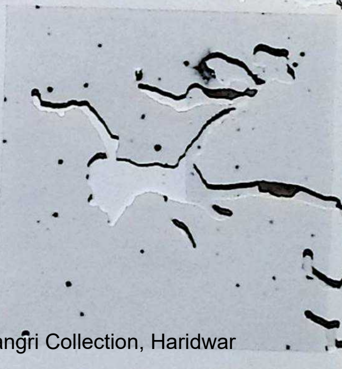

0[illegible]2−25

EXTRAGALACTIC SOURCES BETWEEN −20° AND −44°

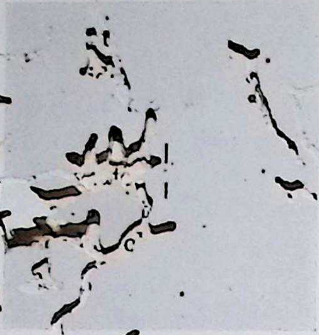

0331−39

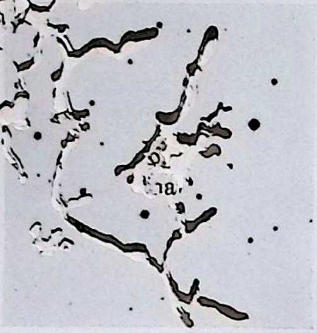

0231−23

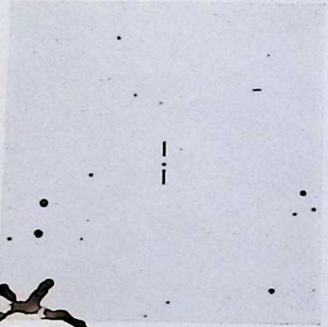

0222−23

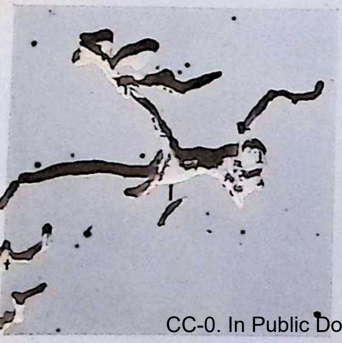

0220−42

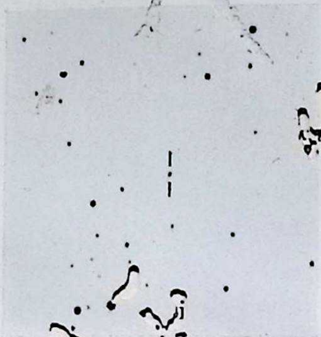

0442−26

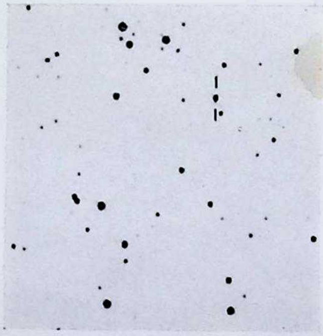

0424−26

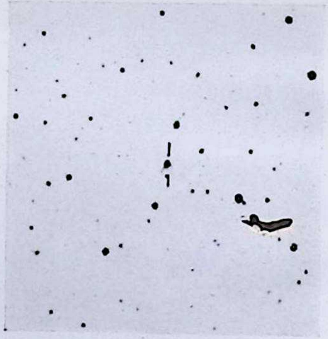

0349−2

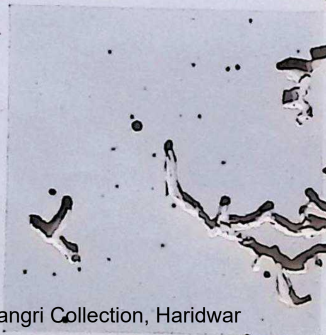

0[illegible]44−

EXTRAGALACTIC SOURCES BETWEEN −20° AND −44°

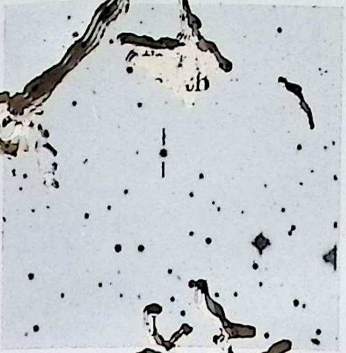
0511−30

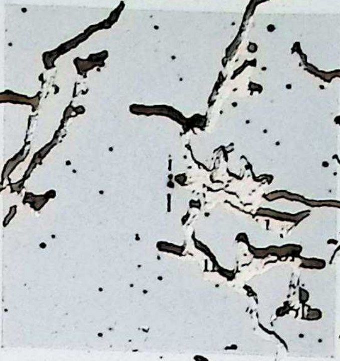
061[illegible]−[illegible]7

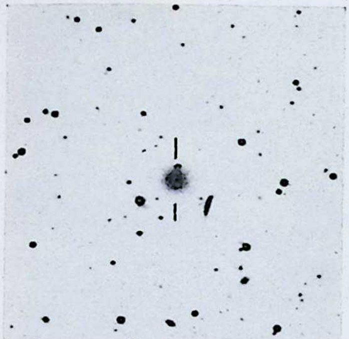
0453−20

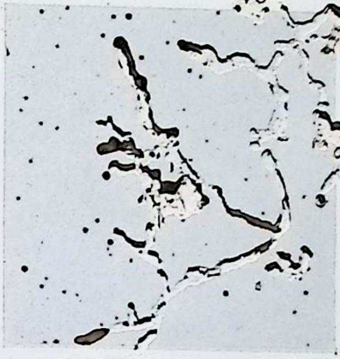
0614−34

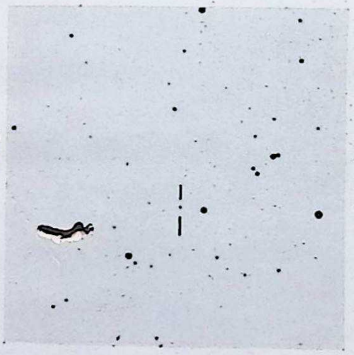
0451−28

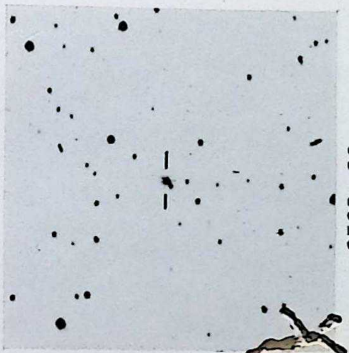
0523−32

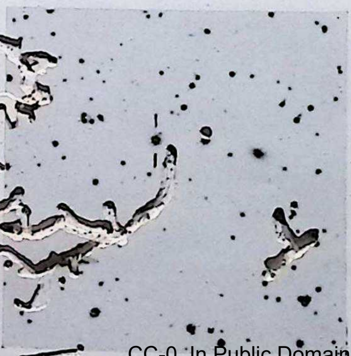
0446−20

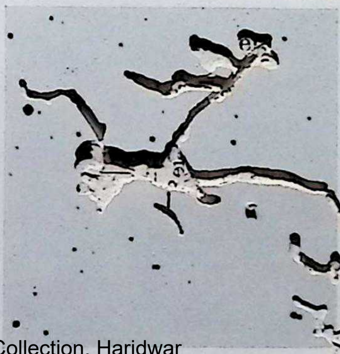
0[illegible]21−36

EXTRAGALACTIC SOURCES BETWEEN −20° AND −44°

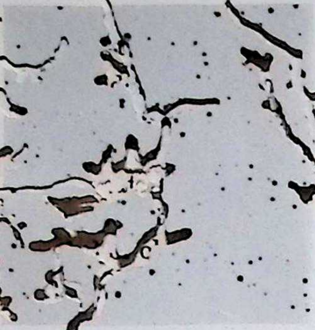

36

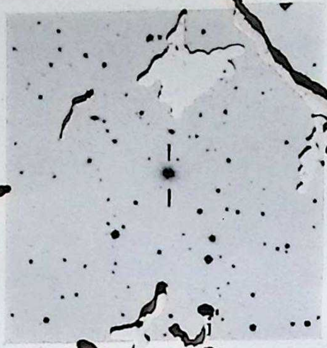

1123−3

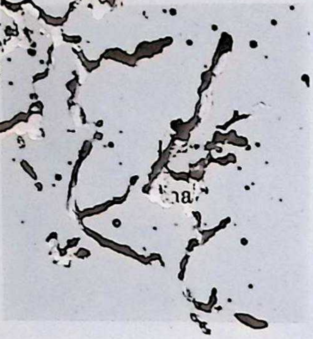

0642−43

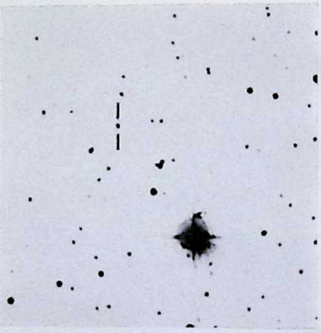

1103−20

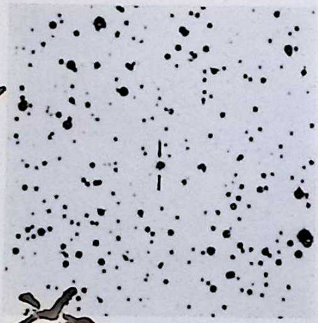

0634−20

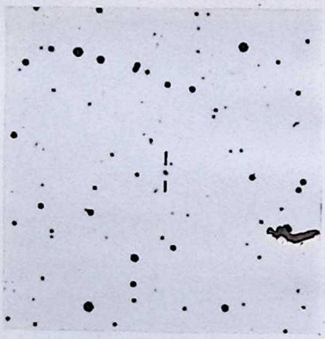

1103−24

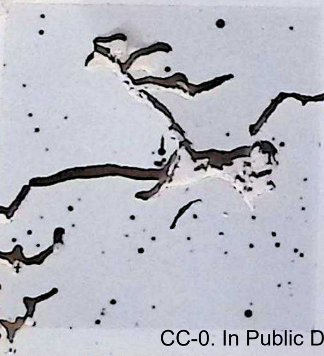

0625−35

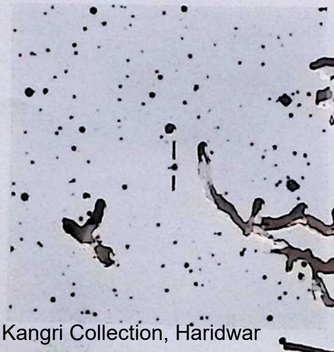

−34

Aust. J. Phys., 1965, 18, 627–33

EXTRAGALACTIC SOURCES BETWEEN −20° AND −4

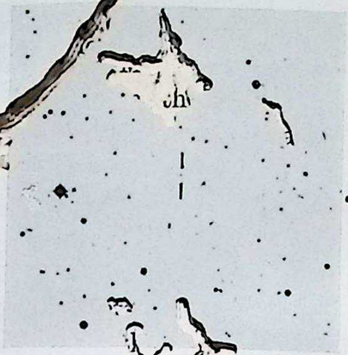
141[illegible]−36

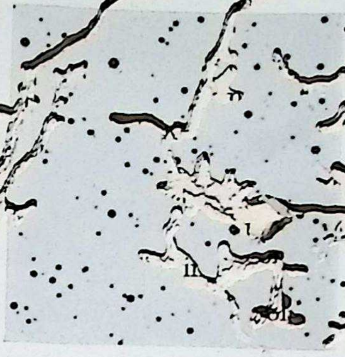
[illegible]20

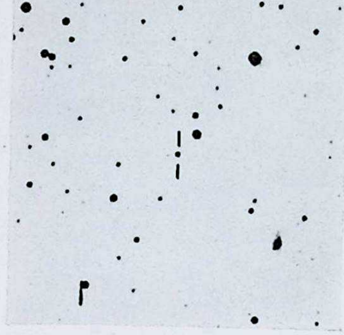
1327−21

2040−2[illegible]

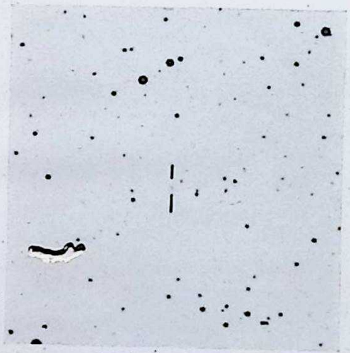
1221−42

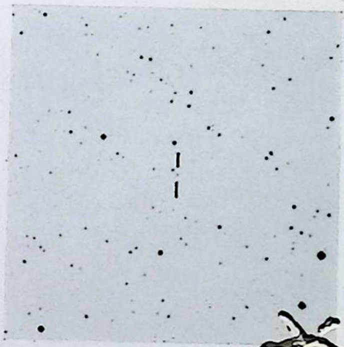
1928−34

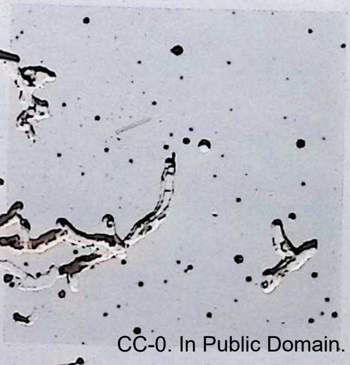
1211−41

[illegible]14−24

Aust. J. Phys., 1965, **18**, 627–33

BOLTON, CLARKE, AND EKERS

EXTRAGALACTIC SOURCES BETWEEN −20° AND −44°

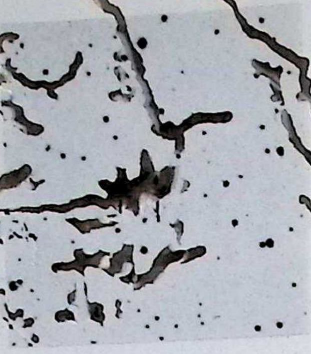

21[illegible]30

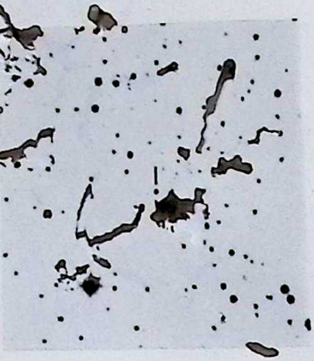

2115−30

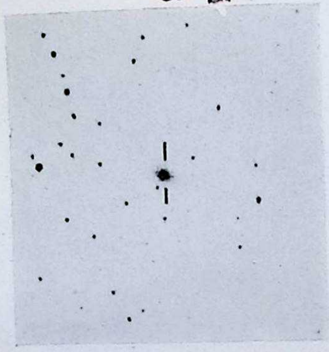

2354−35

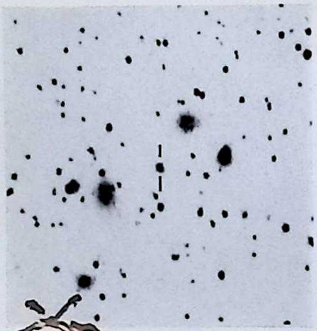

2104−25

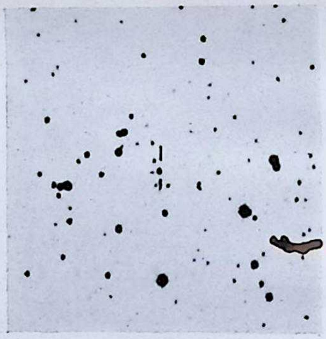

2317−27

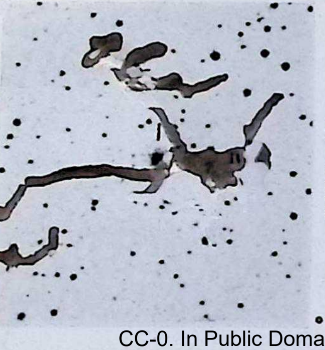

2058−28

catalogue number for the source, and the final column, the equivalent number in the MSH catalogue (Mills, Slee, and Hill 1960). Columns 2 and 3 give the optical position for epoch 1950.0. Columns 4 and 5 contain the flux density of the radio source at a frequency of 1410 Mc/s and its spectral index, taken from BGM. For a source with a power-law spectrum, the flux density at 1410 Mc/s is approximately proportional to the total power emitted in the available radio spectrum (85–2050 Mc/s). Columns 6 and 7 give the type of galaxy and an estimated photographic magnitude. For galaxies the classification follows that of Matthews, Morgan, and Schmidt (1964). E, elliptical; D, spherical with an extended diffuse envelope; db, dumb-bell or double system; and N, compact galaxy with a very bright nucleus. QSO indicates suspected quasi-stellar objects for which identification is suggested on the basis of a marked blue excess relative to the surrounding star images on the plates. Particularly for faint objects, colour differences are difficult to estimate and confirmation through photometric detection of an ultraviolet excess is necessary. Magnitudes have been visually estimated by comparing the plate images with those of galaxies in the list of Maltby, Matthews, and Moffet (1963). For relatively bright objects in unobscured regions the magnitudes are perhaps accurate to a few tenths, but for fainter objects in low galactic latitudes they may be in error by as much as one magnitude. Hence, photometric measurements are desirable. Columns 8 and 9 give the new galactic coordinates of the object. Additional points of interest on individual sources are given in column 11.

III. Finding Charts

Plates 1–6 contain finding charts for the 46 identified objects that are fainter than fourteenth magnitude. These charts were prepared photographically from the Sky Survey prints for objects north of declination −33°, and from Polaroid prints made from the extension plates for objects south of −33°. Contrast has been deliberately increased over that of the original prints.

IV. Some Interesting Galaxies

Three sources of particular interest are those apparently associated with the bright galaxies NGC 253, NGC 1399, and NGC 5419. In all three cases the radio sources are of small diameter (< 2 min of arc) but, although they are within the visible limits of the galaxies, they are not centred. The discrepancy in position for NGC 253 is quite small, only about 1% of the optical diameter, but for the other two sources it is of the order of the optical diameter. In these cases the sources may be associated with singular events such as supernovae rather than with the nuclei of galaxies. This possibility was first suggested to us by Dr. J. A. Roberts, who noted the position discrepancy for NGC 253.

Fourteen of the identified galaxies are in small or medium clusters and in all cases but one, the identified galaxy is the brightest member. The exception is the source 2104–25 and, as can be seen from the finding chart in Plate 6, there are three other [illegible] systems that are at least a magnitude brighter. It appears possible that this source could be an exception to the generally accepted rule that the radio source

TABLE 1

LIST OF IDENTIFICATIONS

Catalogue Number	Position (1950.0) R.A. h	m	s	Dec. °	′	Flux Density at 1410 Mc/s (10^{-26} W m^{-2} (c/s)$^{-1}$)	Spectral Index	Type	m_{pg}	Galactic Coordinates l^{II}	b^{II}	Reference	Remarks	MSH Cat. No.
0022–29	00	22	01	−29	45·5	3·3	−1·0	QSO?	20	13	−84	7		00–[illegible]
0023–33	00	23	02·2	−33	19·7	1·7	−1·0	E	[illegible]	346	−82	1		00–37
0043–42	00	43	55·9	−42	24·3	9·1	−0·7	E	18	[illegible]	−75	1		00–*411*
0045–25	00	45	06	−25	33·6	6·3	−0·7	Sc	7·0	96	[illegible]	5	NGC 253	00–*222*
0114–21	01	14	22	−21	07·3	4·1	−0·8	db	19	106	−81	1	Curved spectrum	01–*26*
0122–25	01	22	23·5	−25	33·7	1·3	−0·8	E3	17·8	200	−88			01–*29*
0131–36	01	31	43·6	−36	44·9	7·1	−0·7	SO	14·2	261	−77	1		01–*36*
0157–31	01	57	58·4	−31	07·9	3·7	−0·7	QSO?	19	230	−74			[illegible]*15*
0216–25	02	16	24·8	−25	03·6	1·3	−1·0	QSO?	18	270	−63			[illegible]
0220–42	02	20	18·5	−42	13·4	1·9	−0·7	db	19	257	−66			02–*45*
0222–23	02	22	46	−23	26·2	1·8	−0·9	QSO?	18	208	−68			02–*27*
0231–23	02	31	06·5	−23	33·7	1·3	−1·0	QSO?	15	251	−65			02–*211*
0320–37	03	20·7		−37	25	150	−0·7	SO	10	239	−57	4	NGC 1316	03–*31*
0332–39	03	32	14	−39	10·7	1·7	−0·8	E	17·4	243	−54		Curved spectrum. In small cluster	03–*32*
03[illegible]35	03	36·6		−35	37	2·5	−0·8	E	10·9	236	−54		May be associated with NGC 1399. Source is 3′ north following	03–*33*
0344–34	03	44	36	−34	32·0	3·0	−0·9	E	17·4	234	−52		In small cluster	03–[illegible]
0349–[illegible]7	03	49	32	−27	53·4	5·2	−0·8	E	16·8	224	−50			03–[illegible]
042[illegible]6	04	24	37	−26	50·6	1·2	−1·0	E3	17·2	225	−43		Identification based on catalogue position only	
044[illegible]8	04	[illegible]	[illegible]8	−28	15·3	7·1	−0·9	E	18·2	228	−39			04–*218*
0446–[illegible]0	04	46	20·7	−20	36·0	0·9	−1·2	E	16·2	219	−36		In small cluster. Identi[illegible]ation based on cata[illegible]position only	04–*219*

0451–28	04	51	[illegible]	−28	12·6	2·5	−0·1	QSO?	19	229	−37			
0453–20	04	53	14	−20	39·2	4·7	−0·5	E	14	220	−34	2		04–222
0511–30	05	11	37·2	−30	32·2	2·7	−1·0	E	17	223	−33		Curved spectrum	05–35
0521–36	05	21	13·7	−36	30·2	19	−0·6	N	16·8	240	−33		Curved spectrum	05–36
0523–32	05	23	35·7	−32	44·9	1·2	−0·5	E	16·6	236	−31			
0614–34	06	14	48	−34	55·1	2·8	−0·4	db	19	242	−22			06–3
0618–37	06	18	19	−37	10·3	3·0	−0·7	db	16·6	244	−22		Highly polarized	06–37
0625–35	06	25	21	−35	27·2	4·5	−0·6	db	17·6	243	−20		Optically, close triple	06–38
0634–20	06	34	23	−20	32·2	7·0	−0·8	E	16·8	230	−12	2	Extended radio source	06–210
0642–43	06	42	55	−43	40·6	1·8	−0·7	E	17	253	−19			06–412
0715–36	07	15	22·5	−36	16·4	2·2	−0·9	E	17·8	248	−11			07–35
0718–34	07	18	57	−34	01·5	2·1	−0·9	E	16·5	246	−9			07–37
0843–33	08	43	08·5	−33	37·1	2·0	−0·7	E3	12·3	256	6		NGC 2663	08–38
1103–24	11	03	45·5	−24	28·5	1·3	−0·9	D	17·5	274	32		In small cluster. Identification based on catalogue position only	11–21
1103–20	11	03	51·5	−20	51·7	2·4	−0·7	E3	18·2	272	35			[illegible]
1123–35	11	23	28	−35	07·3	2·6	−0·7	E3	16·0	284	24		In cluster	11–33
1211–41	12	11	42	−41	43·2	1·6	−0·8	E	19	296	21			12–41
1221–42	12	21	04	−42	18·7	2·7	−0·6		18	298	20		Low surface brightness object with double nucleus	

* References to previous identifications are:

1, Bolton, Gardner, and Mackey (1964); identification based on 74 in. plates by Westerlund.
2, Bolton, Gardner, and Mackey (1964).
3, Bolton, Stanley, and Slee (1949).
4, Mills (1954).
5, Mills (1955).
6, Mills, Slee, and Hill (1960).
7, P. Veron (personal communication).

TABLE 1 (*Continued*)

Catalogue Number	Position (1950·0)					Flux Density at 1410 Mc/s (10^{-26} W m^{-2} (c/s)$^{-1}$)	Spectral Index	Type	m_{pg}	Galactic Coordinates		Reference	Remarks	MSH Cat. No.
	R.A. h	m	s	Dec. °	′					l^{II}	b^{II}			
1246–41	12	46	03·6	−41	02·3	4·1	−0·9	Sc	12·2	302	22	2, 6	NGC 4696	12–45
1322–42	13	22	28	−42	45·6	1330	−0·6	SO	6·1	309	19	3	NGC 5128	13–42
1327–21	13	27	23·7	−21	26·6	2·0	−0·7	QSO?	17	315	40			
1333–33	13	33	47	−33	42·7	7·0	−0·8	E	11·9	313	28	2, 6	Ic 4296. Triple radio source	13–33
1334–29	13	34	11·3	−29	36·7	2·6	−1·0	Sc	8·0	315	32	2, 5	NGC 5236	13–25
1400–33	14	00	42·2	−33	44·3	0·8		E	12·4	320	27		NGC 5419. Source centred 3′ north following	14–32
1413–36	14	13	32	−36	27·3	2·4	−0·7	D	18·5	321	23		In cluster	
1514–24	15	14	45·6	−24	11·3	2·7	−0·4	E	16·2	341	28			
192[illegible]–34	19	28	23·5	−34	01·2	1·2	−0·8	E	17	5	−22			
2[illegible]40–26	20	40	46	−26	44·0	2·3	−0·8	E	15·4	19	−35	2		20–*212*
2053–20	20	53	12·5	−20	08·1	2·8	−0·7	E2	17·8	27	−36		In cluster	20–*214*
2058–28	20	58	38	−28	13·5	6·7	−0·8	E	15·6	18	−39	2	In small cluster	20–*215*
2104–25	21	04	26	−25	39·5	12	−0·8	E	16·8	21	−40		In cluster	21–*21*
2115–30	21	15	10·4	−30	32·1	2·4	−0·7	QSO?	17·5	16	−43			21–3[illegible]
2216–28	22	16	55	−28	10·5	2·6	−0·9	E	18	22	−56		In cluster	
231[illegible]–27	23	17	16	−27	44·5	3·3	−0·8	E	18	28	−69		In cluster	23–24
2354–35	23	54	26·5	−35	02·3	1·3	−1·2	D	15·5	356	−76			23–37

is the brightest member of a cluster. An alternate explanation is that the three bright galaxies belong to a small foreground group and that the radio source is the brightest member of a more distant cluster.

V. Acknowledgments

The authors wish to thank Dr. Horace Babcock and Dr. Jesse Greenstein for use of the facilities at the Mount Wilson and Palomar Observatories; Dr. J. B. Whiteoak, Dr. E. Herzog, and Mrs. Margaret Hayden for assistance; and Dr. A. R. Sandage, Dr. M. Schmidt, Dr. J. D. Wyndham, and Dr. F. Zwicky for discussion during the examination of the 48 in. Palomar Sky Survey Plates. This examination was made while one of us (J.G.B.) was a guest investigator at the Mount Wilson and Palomar Observatories. One of us (R.D.E.) wishes to acknowledge the support of a Graduate Fellowship at the Australian National University.

VI. References

Bolton, J. G., Gardner, F. F., and Mackey, M. B. (1964).—*Aust. J. Phys.* **17**: 340.
Bolton, J. G., Stanley, G. J., and Slee, O. B. (1949).—*Nature* **164**: 101.
Maltby, P., Matthews, T. A., and Moffet, A. T. (1963).—*Astrophys. J.* **137**: 153.
Matthews, T. A., Morgan, W. W., and Schmidt, M. (1964).—*Astrophys. J.* **140**: 35.
Mills, B. Y. (1954).—*Observatory* **74**: 248.
Mills, B. Y. (1955).—*Aust. J. Phys.* **8**: 368.
Mills, B. Y., Slee, O. B., and Hill, E. R. (1960).—*Aust. J. Phys.* **13**: 676.

A LINEAR POLARIZATION SURVEY OF THE SOUTHERN SKY AT 408 MC/S

By D. S. Mathewson* and D. K. Milne*

[*Manuscript received July 26, 1965*]

Summary

The results of 408 Mc/s linear polarization observations of the southern sky using the 210 ft steerable reflector at Parkes are presented. Combination of this survey with the northern sky survey of the Leiden group shows that almost all of the polarization at this frequency lies in a band about 60° wide, which contains the great circle that passes through the galactic poles and intersects the plane at $l^{\mathrm{II}} = 340°$ and 160°. This large-scale distribution of linear polarization at 408 Mc/s may be explained on the basis of synchrotron radiation theory if the Sun lies almost at the centre of a spiral arm that has a magnetic field directed along it towards $l^{\mathrm{II}} = 70°$ and 250°. The concentrations of relativistic electrons may be confined to regions of higher than average magnetic field strength (5×10^{-5} G) elongated in the direction of the arm. The observations show that the magnetic fields in these "synchrotron" regions are very ordered. The distance to the polarized regions may be about 150 pc. At high latitudes, close correlation is observed between features of the distribution of background polarization and Faraday rotation of extragalactic sources.

Evidence from other observations such as the rotation measures of sources, polarization of starlight, and the H-line Zeeman experiment suggest that the magnetic fields in the HII regions, dust clouds, and concentrations of neutral hydrogen are ordered and lie in approximately the same direction as the magnetic fields in the synchrotron regions. It appears that the local synchrotron regions are manifestations of a larger-scale field extending throughout the spiral arms.

I. Introduction

In 1961, the Leiden group (Westerhout *et al.* 1962) using the 80 ft reflector at Dwingeloo showed beyond doubt that at 408 Mc/s the galactic radio emission had a linearly polarized component. Shortly afterwards, Wielebinski, Shakeshaft, and Pauliny-Toth (1962) confirmed this result using a 30 ft reflector. These positive results (together with the spectral index of the radiation) showed almost conclusively that the synchrotron mechanism was responsible for the non-thermal radio emission from the Galaxy. A large-scale survey of the 408 Mc/s polarization of the northern sky was then carried out at Leiden by Brouw, Muller, and Tinbergen (1962) and Berkhuijsen and Brouw (1963), and at Cambridge by Wielebinski and Shakeshaft (1964).

This paper presents the results of a linear polarization survey of the southern sky at 408 Mc/s using the 210 ft steerable reflector at Parkes during 1963–4. Combination of the northern and southern sky surveys gives the large-scale distribution of the polarized radio emission, which should provide much information on the structure of the magnetic fields in the local spiral arm of the Galaxy, for at 408 Mc/s,

---

* Division of Radiophysics, CSIRO, University Grounds, Chippendale, N.S.W.

Aust. J. Phys., 1965, 18, 635–53

the polarized component probably originates within a few hundred parsecs (see Westerhout *et al.* 1962; and Section V).

Previous knowledge about galactic magnetic fields was derived mainly from polarization measurements of starlight (Hall 1958) and the Zeeman experiment (Davies *et al.* 1964). Other more indirect forms of evidence such as stability of the spiral arms, retention of high energy cosmic rays in the Galaxy, intensity of non-thermal continuum radio emission, and star formation have been used in attempts to estimate the strength and the distribution of the magnetic fields in the Galaxy.

The starlight polarization and Zeeman measurements only give information about the magnetic fields in localized regions of dust clouds and dense neutral hydrogen clouds respectively. It is unlikely that either of these regions is the source of synchrotron radio emission (i.e. a region of relativistic electrons and magnetic fields). Therefore, the study of the polarization of the more widely distributed synchrotron radiation can provide information on the field structure in the more tenuous general medium of interstellar space.

Recent studies of the polarization of discrete sources provide a powerful method of investigating the magnetic fields in the Galaxy. It is now certain that most of the observed Faraday rotation occurs in regions of ionized hydrogen and magnetic fields within the Galaxy (Gardner and Davies 1966). The rotation measure of a radio source (most of which are extragalactic) provides information about the sense of the magnetic field and the product of the electron density and the field strength through the Galaxy in the particular direction of the source. In Section V, a comparison is made between the distribution of the 408 Mc/s polarization and the rotation measures of the radio sources, which shows that at high latitudes the rotating medium for the source radiation is fairly local.

II. Equipment

The 210 ft steerable reflector was fed by a pair of parallel dipoles with a plane reflector giving a tapered illumination that fell to approximately 4% at the edge of the aperture. The resulting main beam was circular and 48 min of arc between half-power points. The aerial feed could be rotated at 3°/s through one complete revolution in either direction.

The receiver was a double sideband crystal mixer (local oscillator frequency, 408 Mc/s) with an input temperature of 300°K and a bandwidth of 8 Mc/s. The receiver was switched between the aerial feed and a reference load at liquid nitrogen temperature. With a 2 s time constant, peak-to-peak noise fluctuations were about 0·5 degK. A constant noise-source signal could be injected through a directional coupler into the aerial side of the switch to check the sensitivity of the receiver during the observations.

The whole system was calibrated using the radio source Hydra A. The flux density of Hydra A at 408 Mc/s was taken to be $134\times10^{-26}\,\mathrm{W\,m^{-2}\,(c/s)^{-1}}$, following Kellermann (1964). This gave a main beam brightness temperature T_b of 118°K when the source was at the centre of the aerial beam.

III. Observational Procedure and Data Reduction

The observational procedures and data reduction processes used in the present survey are similar to those described by previous workers (Brouw *et al.* 1962; Westerhout *et al.* 1962; Weilebinski and Shakeshaft 1964). They are outlined below under the headings of (*a*) the instrumental polarized component, (*b*) the survey, (*c*) data reduction, (*d*) calibration points, and (*e*) correction for Faraday rotation in the ionosphere.

(*a*) *The Instrumental Polarized Component*

If the radio emission incident on the reflector has a linearly polarized component, one full rotation of the dipole feed should produce a double sine wave in the output of the receiver. However, radiation from the ground in far side lobes or spillover of the primary feed usually produces a similar double sine wave output. In order to determine the spurious component, scans across a number of regions well removed from the galactic plane were made with different orientations of the primary feed. Two positions were selected from those scans that showed no variation with feed orientation. These positions at $04^{\mathrm{h}}\,00^{\mathrm{m}}$, -46°, and $04^{\mathrm{h}}\,30^{\mathrm{m}}$, -4°, were then tracked from rising to setting. During this period, the primary feed was rotated continuously backwards and forwards through an angle of about 360°. Each rotation produced a double sine wave pattern at the recorder. The feed angle of the maximum of this pattern remained constant to within $\pm 7^\circ$ showing that no real polarized component was present. As the Parkes reflector has an altazimuth mount, the feed angle (which is the angle between the dipoles and the vertical plane containing the beam axis) changes with respect to the position angle in celestial coordinates so that the feed angle of maximum should be a function of hour angle for a source with a real component of linear polarization.

All the observations were carried out at zenith angles greater than 30°. At 30° the amplitude of this instrumental polarized component was about 2·5 degK and decreased with increasing zenith angle to less than 1 degK at a zenith angle of 60° (the telescope's horizon). This remained the same both before and after transit and it was concluded that there was no effect due to change of azimuth. As the survey progressed, two other unpolarized regions at $12^{\mathrm{h}}\,10^{\mathrm{m}}$, -12°, and $06^{\mathrm{h}}\,10^{\mathrm{m}}$, -28°, were also used to determine the spurious polarized component.

Rotations were also made while the reflector tracked a strong radio source, 30 Doradus, known to be unpolarized at higher frequencies, to see if increase in aerial temperature caused any modification of the spurious polarization rotation curve. No such effect was found.

(*b*) *The Survey*

The survey was carried out over four intervals of 10 days each during the months of February, July, and September 1963 and February 1964. The survey covers from declinations -90° to $+14^\circ$ for right ascensions 0^{h} to 3^{h} and 22^{h} to 24^{h}, $+26^\circ$ for right ascensions 3^{h} to 14^{h}, and -6° for right ascensions 14^{h} to 22^{h}.

Observations were made only at night, generally commencing about 1 hr after sunset and finishing at sunrise. Thus, the effect of solar radiation and rapid changes in the ionosphere were avoided. The observational procedure was to track a point whilst rotating the dipoles through about 300°. Such rotations were made at a 2° grid of points over the survey region.

In general, the measured points were spaced at intervals of approximately 2° in right ascension along even-degree declination circles, although in some interesting regions a closer spacing was used in both right ascension and declination. The bracket of declinations covered at a particular right ascension was such that the aerial remained approximately at the same azimuth and zenith angle during the night's observation (i.e. the average rate at which right ascension increased was equal to the sidereal rate). Thus, the spurious polarization component to be subtracted from the survey rotation curves was approximately the same throughout the night. This procedure also simplified correction for ionospheric Faraday rotation (see (*e*) of this section). The following night, some of the previous night's measurements were repeated, interlaced among the new positions. Most observations were made near zenith angle 50° as the amplitude of the spurious polarization component was smaller than at higher elevations. At the beginning of each observing period, the spurious polarized component was determined as a function of zenith distance by continuously tracking, whilst rotating the feed, one of the positions given above in (*a*) of this section. On subsequent nights, this calibration was checked at a particular zenith angle every 3–4 hr.

TABLE 1

SECONDARY CALIBRATION POINTS

Position (1963)	Position Angle of E Vector θ_{oq} (outside-ionosphere)	Polarization Brightness Temperature T_b^p (°K)
$01^h 11^m$, −64° 30′	157	5·0
$01^h 40^m$, −34°	148	6·1
$14^h 00^m$, −20°	135	4·5
$15^h 10^m$, −40°	92	3·6
$18^h 40^m$, −14°	154	7·0
$20^h 48^m$, −36°	87	5·2
$23^h 20^m$, −16°	65	5·9

A number of strongly polarized positions distributed over the survey region were chosen for checking the overall system. Initially two positions ($14^h 28^m$, +14°, and $02^h 00^m$, +09° 30′) were selected from the Leiden survey as primary calibration points (see (*d*) of this section) and one or the other was observed at least once every night. As the survey progressed, a number of newly detected positions of strong polarization were chosen to act as secondary calibration points (see Table 1). Some of them were measured at two-hourly intervals during each night and the records were reduced immediately as a running check on the observations.

(c) *Data Reduction*

The spurious polarization component was subtracted vectorially from the rotation curves of the survey points (see Fig. 1). The amplitude of the resulting sine wave and the feed angle of maximum were determined. This amplitude, when measured in units of brightness temperature, is the polarization brightness temperature T_b^p. The position angle of the plane of vibration of the incident E vector (θ_{eq}) was obtained by adding the parallactic angle for the particular hour angle and declination of measurement to the feed angle of maximum. These results are presented in Table 3 (Section IV).

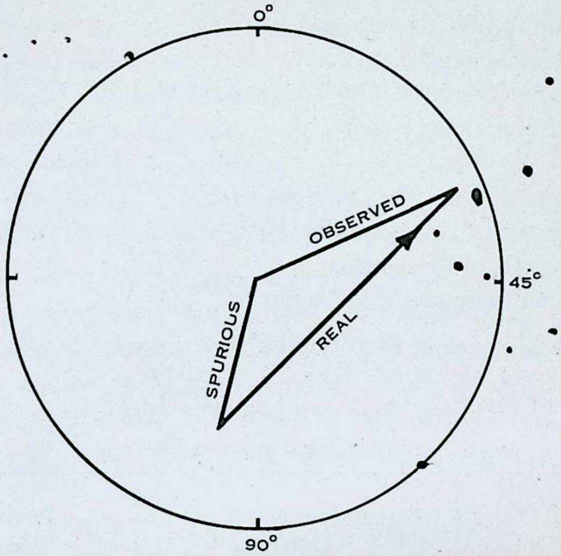

Fig. 1.—Vectorial subtraction of the spurious polarized component from the observed double sine wave rotation curve.

The probable error for points with polarization brightness temperatures between 1·6 and 2·6°K is about 10° for θ_{eq} and 0·6 degK for T_b^p (the errors arise mainly in the measurement of the observed and instrumental polarization components); for points greater than 2·6°K, the probable error is about 5° for θ_{eq} and 0·4 degK for T_b^p. The increase of accuracy for these points is due to the increased ratio of real to spurious polarization component, and to the fact that most of them were measured at least twice.

(d) *Calibration Points*

The primary calibration points were at $14^h 28^m$, +14°, and $02^h 00^m$, +09° 30′. The first of these was observed by the Leiden group more than 500 times and was one of their main calibration points.

The secondary calibration points at southern declinations are listed in Table 1. These were observed over a wide range of hour angles during the observations. Measurements at some of these positions were also made around sunset or sunrise when a variation of θ_{eq} due to changing Faraday rotation in the ionosphere was observed. As pointed out by the Leiden and Cambridge workers such observations provide an excellent test of the genuine nature of the polarized radiation.

(e) *Correction for Ionospheric Faraday Rotation*

To obtain the polarization angles outside the ionosphere, it is necessary to correct for ionospheric Faraday rotation. At 408 Mc/s, it is given by the relation

$$\xi = 1 \cdot 42 \times 10^{-13} H_{300} F \int N \, \mathrm{d}h \qquad \text{radians,} \qquad (1)$$

where N = number of electrons/cm^3,
h = height above Earth (cm),
H_{300} = magnetic field at 300 km (gauss), and
$F = \sin i + \cos i \tan z \cos(a - \beta)$,

with

i = angle of dip of the magnetic field,
β = magnetic declination (east),
a = azimuth of the source, and
z = zenith distance of the source.

The magnetic constants used were $i = 64°$ and $\beta = 11°$ (east).

TABLE 2

PRIMARY CALIBRATION POINTS

Position (1963)	Berkhuijsen and Brouw (1963)		Present Survey (smoothed)	
	θ_{eq} (outside-ionosphere)	T_b^p (°K)	θ_{eq} (inside-ionosphere)	T_b^p (°K)
$14^h 28^m$, $+14°$	126	5·0	104	5·9
$02^h 00^m$, $+09° 30'$	28	5·3	7	6·5

The sense of rotation was such that for all points in the survey the observed values of the polarization angle were less than the values outside the ionosphere.

The "outside-ionosphere" polarization angles for our primary calibration points ($14^h 28^m$, $+14°$; $02^h 00^m$, $+09° 30'$) were known from the work of Brouw and Berkhuijsen (1962) and Berkhuijsen and Brouw (1963). To compare our measurements (0°·8 aerial beam) with those of the Leiden group (2° beam), rotations were made over a $\frac{1}{2}°$ grid of points covering an area of 16 sq degrees around these two positions. The Stokes parameters for the linearly polarized component of the radiation, $Q = T_b^p \cos 2\theta_{eq}$ and $U = T_b^p \sin 2\theta_{eq}$, were integrated using a weighting function appropriate to the 2° aerial beam pattern. The results are shown in Table 2 for a measurement in July 1963.

A total electron content of 4×10^{12} electrons/cm³ is required to account for the observed difference in θ_{eq} in terms of Faraday rotation in the ionosphere. This value is in good agreement with the observations of Berkhuijsen *et al.* (1964). If this Faraday rotation (ξ_1) is known for one position at some particular time, then from equation (1) it may be seen that the Faraday rotation for any other part of the sky is given by

$$\xi_2 = \frac{F_2}{F_1}\xi_1. \qquad (2)$$

In this way the value of the Faraday rotation obtained by observations of the primary calibration points was used to determine the outside-ionosphere polarization angles for the secondary calibration points (Table 1). Repeated observation of these points during each night plus at least one observation of a primary calibration point enabled the ionospheric Faraday rotation to be calculated for the survey points using the same relation. A subsequent inspection of the $f_0 F_2$ records provided by the Ionospheric Prediction Service showed that the ionosphere had in fact remained fairly constant in the periods between the calibration observations.

This correction for Faraday rotation in the ionosphere was rather small, particularly in the southern sky where the component of the Earth's magnetic field along the line-of-sight is small. For example, the correction to be added to the observed polarization angles for regions around the south pole was about 5°, increasing to about 20° at the equator and 30° at the declination of +26°. There could be systematic errors of up to 7° in some of the polarization angles measured at positive declinations.

(*f*) *The Johnston Island Explosion*

During the initial setting-up period for the polarization survey, a violent disturbance of the ionosphere occurred during the observations. This was produced by the explosion at 1210 U.T. (2210 E.A.S.T.) on November 1, 1962, of a 1 megaton bomb 10 km above Johnston Island. Measurements of some polarized points between declinations −60° and −80° before (2000 E.A.S.T.) and after (0300 E.A.S.T.) the explosion showed rotations of the polarization angles of some 80°. If this was due purely to an increase in electron density, it would indicate a total electron content for the ionosphere greater than its noonday value.

(*g*) *An Attempt to detect the Magnetosphere*

At the suggestion of Dr. E. G. Bowen, for several hours each night for a period of 5 days in October 1964, 408 Mc/s polarization measurements of an extended region of polarization that happened to coincide with the direction of the anti-solar point at that time were made in an attempt to detect Faraday rotation in the tail of the magnetosphere. The attempt was unsuccessful.

Similarly, it may be possible to use these regions emitting polarized 408 Mc/s radio waves to study the magnetic fields in the solar corona, if compensation can be made for the spurious effects arising from the Sun in the aerial side lobes.

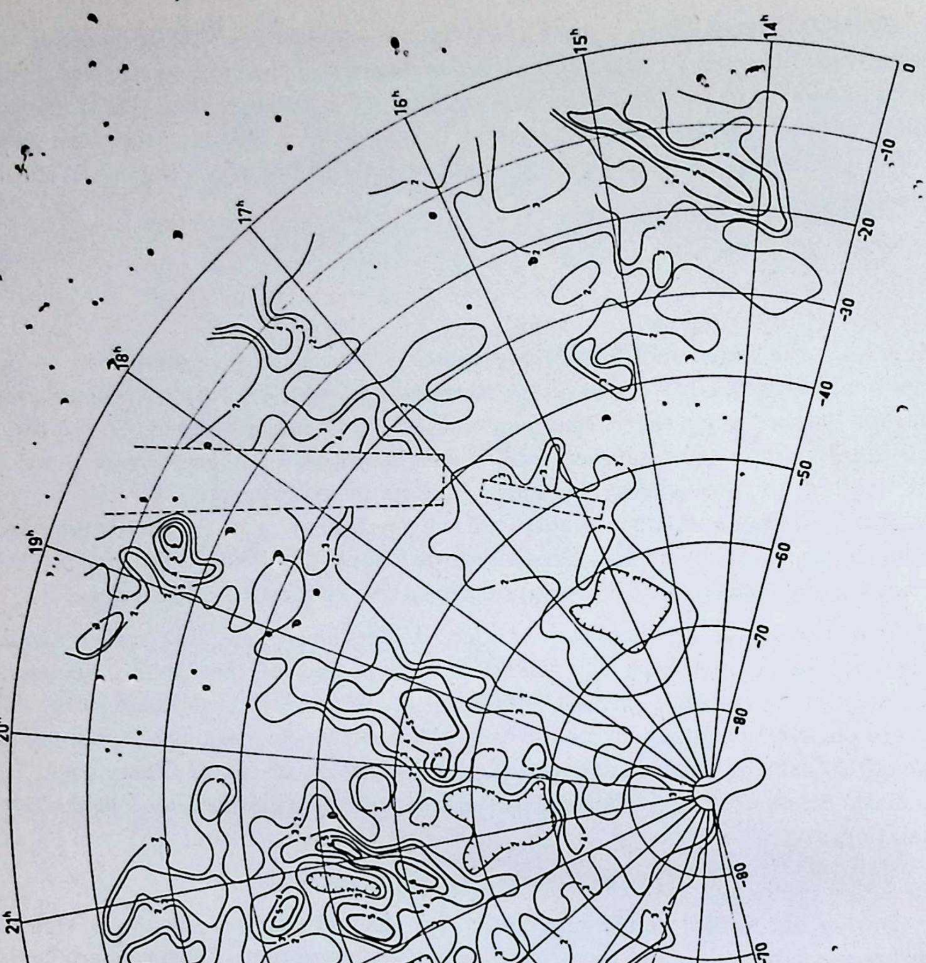
14h
15h
16h
17h
18h
19h
20h
21h
22h
23h
0h
1h
2h
3h
0
-10
-20
-30
-40
-50
-60
-70
-80
-80
-70
-60
-50
-40
-30
-20
-10
0

Fig. 2(a)

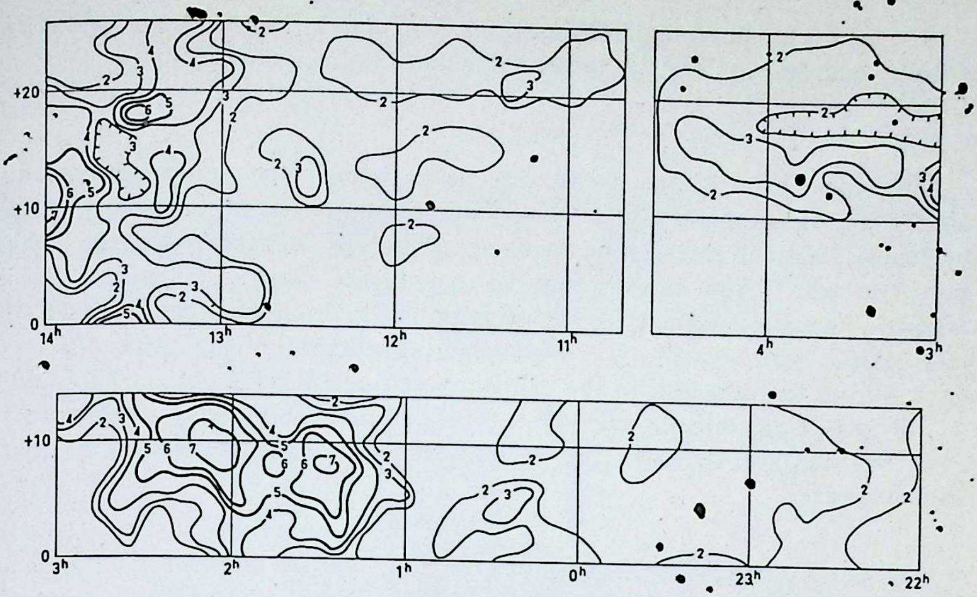

Fig. 2(b)

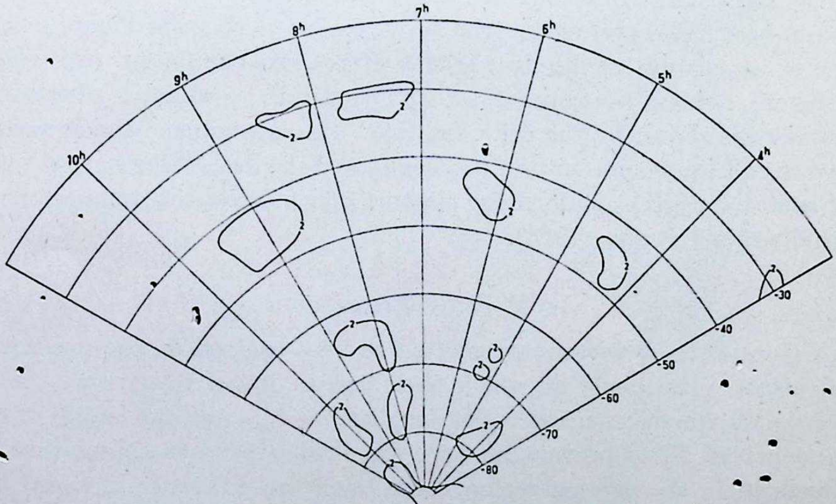

Fig. 2(c)

Figs 2(a) to 2(c).—Schematic contours in equatorial coordinates of polarization brightness temperature obtained from measurements at 408 Mc/s with the 210 ft telescope at a 2° grid of points over the survey region. The contour unit is 0·8 degK.

IV. PRESENTATION OF RESULTS

The results are presented in three forms, (*a*) Table 3, (*b*) contours of polarization brightness temperature, and (*c*) vector presentation of θ_{gal} and T_b^p.

(*a*) *Table* 3*

This table lists (1) the declination circles along which measurements were made (2° steps in general) with a corresponding group of right ascensions for each value (epoch 1963), (2) the position angles θ_{eq} of the plane of vibration of the incident E vector measured from the direction to the celestial north pole (uncorrected for ionospheric Faraday rotation), (3) the polarization brightness temperatures T_b^p (°K), (4) the galactic position angles θ_{gal} of the plane of vibration of the incident E vector measured from the direction to the galactic north pole (this is obtained by adding to θ_{eq} the galactic parallactic angle and the correction for Faraday rotation in the ionosphere), and (5) the new galactic longitudes and latitudes l^{II} and b^{II} to the nearest degree.

(*b*) *The Contours*

The polarization brightness temperatures are plotted both in equatorial and galactic coordinates. The isophotes are shown in Figures 2(*a*), 2(*b*), and 2(*c*) (equatorial) and Figure 3 (galactic). The contour unit of polarization brightness temperature is 0·8 degK. To conserve space, some of the unpolarized regions have not been included in the contour maps in equatorial coordinates. Contour number 1, i.e. the 0·8 degK contour, has been omitted. It was felt that at this low level of T_b^p the results were not significant.

As the contours are based on a network of points whose separation is about two and a half times the half-power aerial beamwidth, some fine structure may have been missed. However, some trial scans similar to those in Figure 5 show that they give a fair picture of the distribution of polarized radiation over the survey region. Figure 3 shows the contours of T_b^p in galactic coordinates where the limits of the survey are shown by the thick full line. The isophotes of the present survey are drawn in full lines (contour unit 0·8 degK) and the dashed lines are the isophotes (contour unit 1·0 degK) obtained by plotting the polarization temperatures given by Berkhuijsen and Brouw (1963).

(*c*) E *Vector Presentation*

In Figure 4 the E vectors are plotted as lines centred on the positions of the observed points. The angle at which each line is drawn relative to the galactic north pole in the direction of increasing longitude is θ_{gal}, and the length of each line is proportional to T_b^p. Comparison with the Leiden surveys shows that there is good agreement in the overlap region, considering the difference in aerial beams of the two surveys.

A striking demonstration of the polarization at 408 Mc/s is shown in Figure 5, which presents the results of scanning the telescope through one of the highly polarized

---

* This table is available on request to the Chief, Division of Radiophysics, CSIRO, University Grounds, Chippendale, N.S.W.

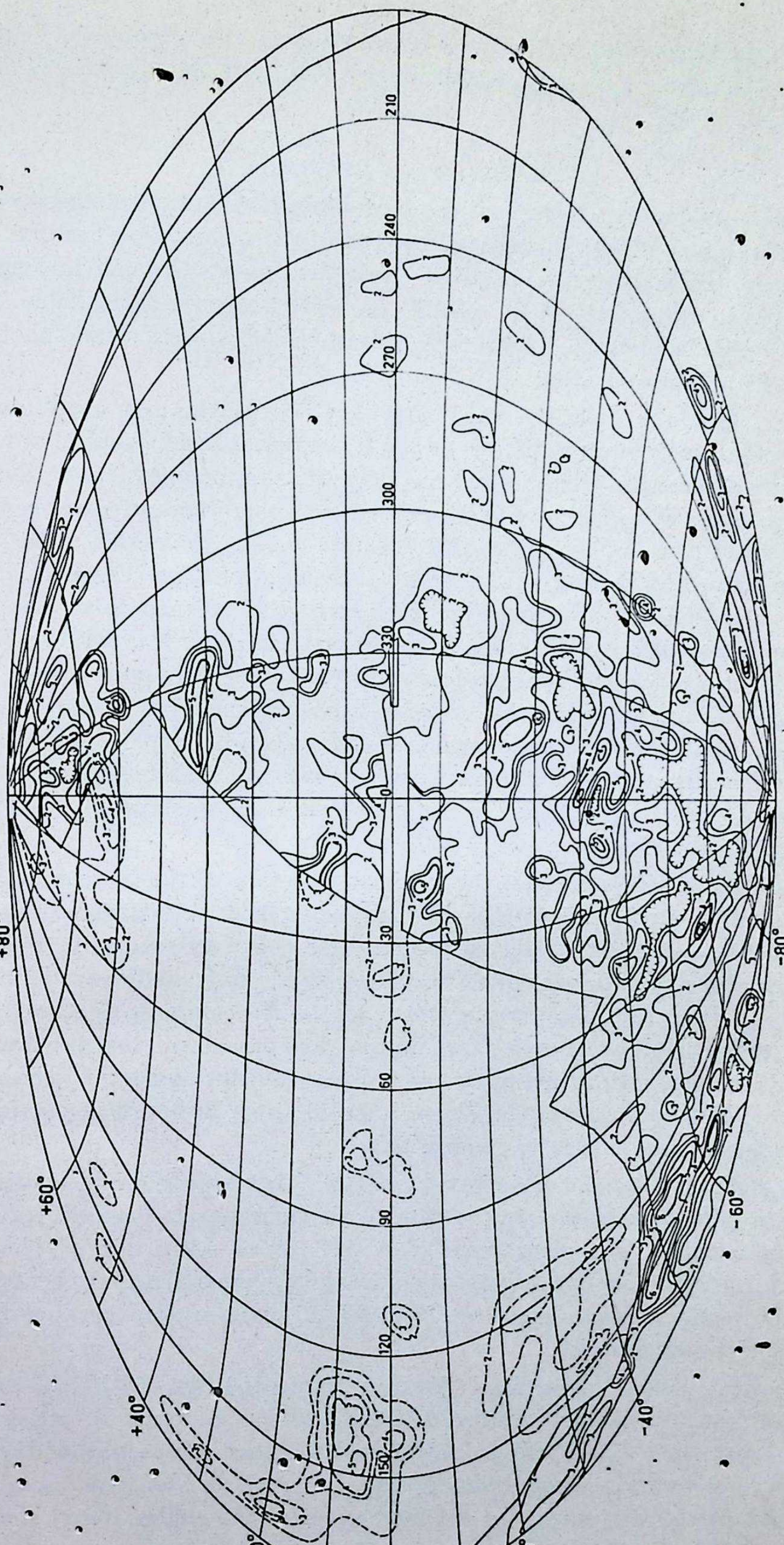
210
240
270
300
330
0
30
60
90
120
150
+80°
+60°
+40°
+20°
0°
-20°
-40°
-60°
-80°

Fig. 3.—The contours of polarization brightness temperature at 408 Mc/s are drawn on this Aitoff projection in new galactic coordinates. The thick line represents the limits of the Parkes survey. The full contour lines are the isophotes of the Parkes survey (contour unit 0·8 degK). The broken lines are the isophotes of the Leiden survey (obtained by plotting the results of Berkhuijsen and Brouw 1963; contour unit 1·0 degK).

regions shown in Figure 2(*a*) with different orientations of the dipole feed; (*a*) was obtained with the dipoles set at a position angle of 50° and (*b*) with the dipoles at a position angle of 140°.

V. Discussion of Results

The most outstanding feature of the large-scale distribution of the 408 Mc/s polarized radio emission (Fig. 3) is that almost all of the polarization lies in a band about 60° wide, which contains the great circle that passes through the galactic poles and intercepts the plane at $l^{\mathrm{II}} = 340°$ and 160° (Mathewson and Milne 1964). The centre of this band is the small circle (parallel to this great circle) that cuts the plane at $l^{\mathrm{II}} = 350°$ and 150°.

The fact that the polarized radio emission lies within this band may be explained by the synchrotron radiation theory if the Sun is inside a spiral arm that has relativistic electrons moving around magnetic lines of force, which are directed along the arm towards $l^{\mathrm{II}} = 70°$ and 250°. Under such conditions an observer would see a bright band of radiation about him (Tunmer 1958). The width of the band would be determined by the degree of isotropy of the electron flux. The most intense part of the band would be where the line-of-sight is perpendicular to the magnetic field, i.e. along the great circle through the poles and the plane $l^{\mathrm{II}} = 340°$ and 160°. Optimum conditions for the detection of polarization of the synchrotron radio emission would also exist where the line-of-sight is perpendicular to the magnetic field, as there would be no depolarization of the radiation by Faraday rotation. (The reason for the polarized regions being distributed slightly asymmetrically about the great circle may be that the magnetic field lines are expanding outwards about the axis in the direction of $l^{\mathrm{II}} = 250°$.)

If this explanation is correct, the intrinsic direction of the *E* vectors of the radiation, which are perpendicular to the magnetic field at emission, would be nearly parallel to this great circle. In the stronger polarized regions in Figure 4, the *E* vectors of the 408 Mc/s emission do indeed lie approximately parallel to this great circle. In fact the ordered arrangement of the *E* vectors in these regions is remarkable (each region covers over 300 sq degrees) and must mean that the magnetic fields in the emission regions are very ordered as they run along the spiral arm. This evidence strongly supports the above interpretation, although measurements at other frequencies are needed to confirm this.

Muller *et al.* (1963) and Berkhuijsen *et al.* (1964) have made linear polarization measurements of the northern sky at 610 Mc/s. Their results show a region of zero Faraday rotation extending from $l^{\mathrm{II}} = 130°$, $b^{\mathrm{II}} = -40°$, up to $l^{\mathrm{II}} = 140°$, $b^{\mathrm{II}} = +10°$. The *E* vectors in this band are approximately parallel to the great circle that cuts the plane at right angles at $l^{\mathrm{II}} = 160°$. These results give additional support to the proposed model.

In the north galactic polar map shown in Figure 4(*c*) the 408 Mc/s *E* vectors are orientated roughly parallel to the line joining $l^{\mathrm{II}} = 290°$ and 110° rather than to $l^{\mathrm{II}} = 340°$ and 160°. The Leiden group found that in their section of the map the 610 Mc/s *E* vectors were more ordered than the 408 Mc/s *E* vectors. Combining their 408 and 610 Mc/s results, the intrinsic polarization angles were calculated

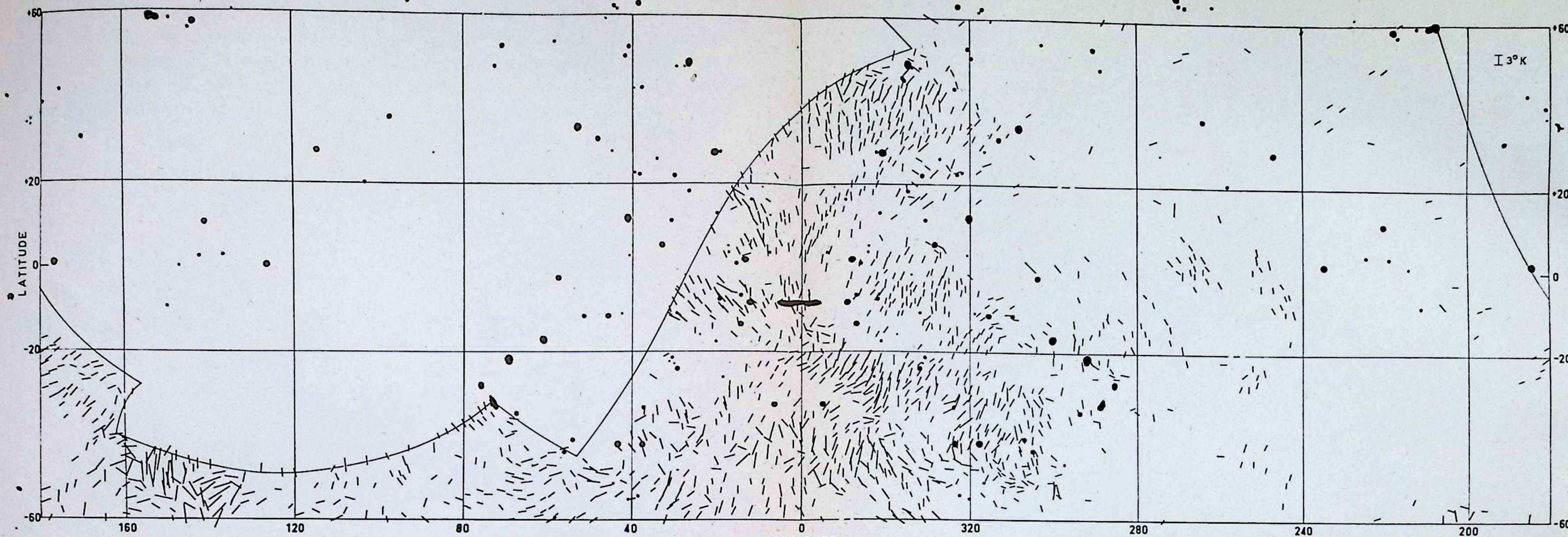

Fig. 4(*a*)

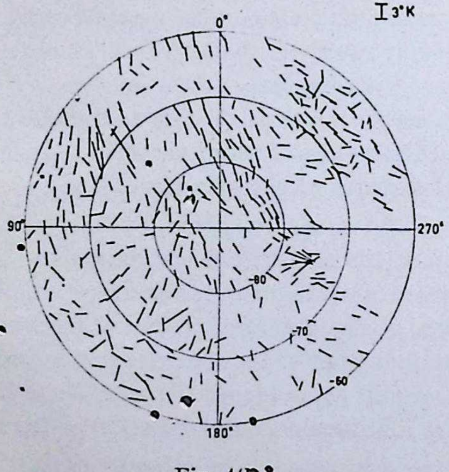

Fig. 4(*b*)

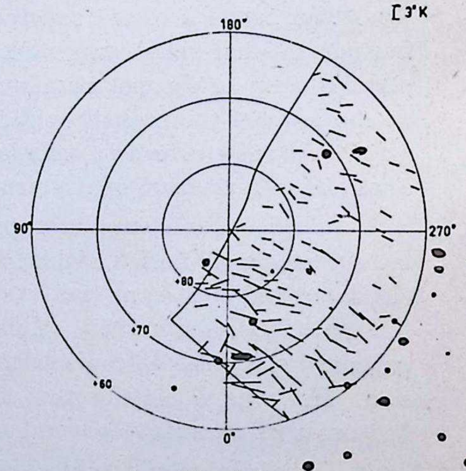

Fig. 4(*c*)

Figs 4(*a*) to 4(*c*).—The 408 Mc/s polarization results are plotted as lines centred on the positions (new galactic coordinates) of the observed points. The angle at which each line is drawn relative to the galactic north pole in the direction of increasing longitude is θ_{gal} and the length of each line is proportional to the polarization brightness temperature (Table 3).

on the assumption that only one polarized component was in the aerial beam. They were found to lie parallel to the line joining $l^{\mathrm{II}} = 340^\circ$ and 160°. Apparently there must be some ionized region with a component of magnetic field towards the Sun in front of the emitting region in this part of the band. It is interesting to note that the well-known northern spur (Hanbury Brown, Davies, and Hazard 1960) cuts across the polarized band in the area, and it may well produce this rotation of the 408 Mc/s *E* vectors.

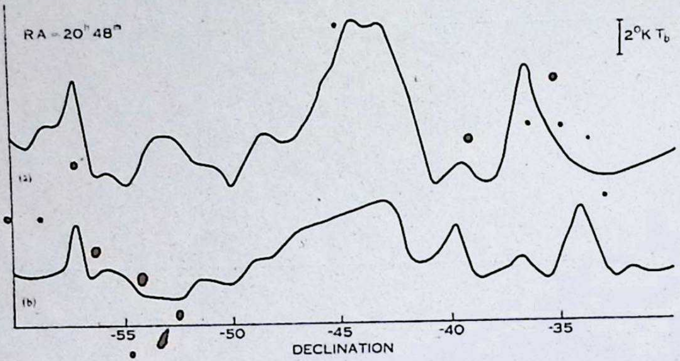

Fig. 5.—The profiles of two scans in declination at R.A. $20^{\mathrm{h}} 48^{\mathrm{m}}$ with different orientations of the 408 Mc/s primary feed; (*a*) dipoles set at a position angle of 50°, (*b*) dipoles at a position angle of 140°.

Davies and Hazard (1962) have suggested that the radio emission from a spiral arm is due to old fragments of supernovae remnants. However, if this is the case, it is difficult to explain why the preferred direction of the *E* vectors in the stronger polarized regions is approximately parallel to the great circle passing through the poles and cutting the plane at $l^{\mathrm{II}} = 340^\circ$ and 160°. It is also difficult to explain the degree of order of the *E* vectors, as great turbulence is expected in the magnetic fields of old supernovae remnants. Of course, some contribution to the non-thermal spiral arm radio emission must be made by these objects, and perhaps some of the polarization observed at 408 Mc/s arises in them. However, on the basis of the present evidence, it seems more reasonable to assume that the majority of the synchrotron emission arises in regions of magnetic fields and relativistic electrons that are part of the structural features of the spiral arm itself.

Additional evidence in support of the model is given by the polarization measurements of starlight, which show that the magnetic fields associated with dust clouds in the spiral arm are very ordered and aligned in the direction $l^{\mathrm{II}} = 60^\circ$ and $l^{\mathrm{II}} = 240^\circ$ (Smith 1956). This is close to the direction predicted from the radio polarization results. Of course, dust clouds may not be the source of synchrotron emission. However, it may be that the magnetic fields associated with these different features that constitute a spiral arm are all aligned in the direction of the arm.

The direction of the local spiral arm estimated from other evidence (e.g. the concentrations of neutral hydrogen, bright O and B stars, and HII regions) ranges from $l^{\mathrm{II}} = 70^\circ$ to $l^{\mathrm{II}} = 90^\circ$ (Weaver 1953; Westerhout 1957). This is in good agreement with that predicted from the polarization studies. It is also interesting to note that the low velocity H-line studies of McGee and Murray (1961) place the Sun inside the local spiral arm, in agreement with the model put forward on the basis of the polarization results. They find that the Sun is almost on the plane of the Galaxy. The 408 Mc/s polarization temperatures are higher on the anti-centre side of the band, which may mean that the Sun lies towards the inner edge of the local arm.

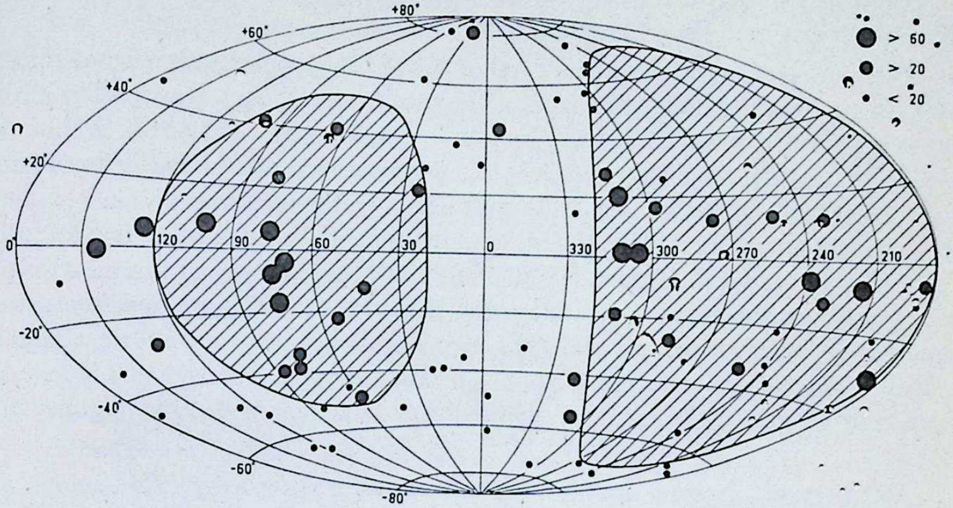

Fig. 6.—The rotation measures of the discrete radio sources (Gardner and Davies 1966) are separated into three groups (> 60, > 20, < 20), irrespective of the sense of rotation, and plotted on this Aitoff projection in new galactic coordinates. The unshaded area is the 60° wide band that contains most of the 408 Mc/s polarization.

The rotation measures for discrete radio sources provide information about the distribution of magnetic fields and ionized hydrogen through the Galaxy in the directions of the sources. Morris and Berge (1964) concluded from a study of the rotation measures of 37 sources that the direction of the local field was towards $l^{\text{II}} = 70°$ and $250°$. Gardner and Davies (1966) using 86 sources obtained the direction of the field as $l^{\text{II}} = 90°$ and $270°$. (The sense of the magnetic field above the plane $b^{\text{II}} > 20°$ is opposite to the field at southern latitudes, but here we are concerned more with the general alignment of the magnetic field.) These directions are in fair agreement with the direction of the field in the synchrotron regions of the local arm. This agreement must mean that the fields in the ionized-hydrogen regions producing the source Faraday rotation at latitudes greater than about 10° must be fairly local and directed along the same spiral arm as the synchrotron regions.

To demonstrate the close agreement between the source and background polarization results, we have drawn in the 60° wide band (unshaded) that contains most of the 408 Mc/s polarization onto Figure 6, where the rotation measure data of Gardner and Davies (1966) are plotted. It is quite striking how the sources with low rotation measure fall outside the shaded areas. Altogether 36 sources fall inside the band at latitudes greater than 10°. Their mean rotation measure is 11. Gardner and Davies place an upper limit of 5 on the rotation measure due to Faraday rotation in the source itself, so the remainder occurs in the ionized hydrogen and magnetic fields in the local spiral arm.

The available observational evidence indicates that the magnetic fields that permeate the various regions constituting a spiral arm (i.e. HII regions, dust clouds, neutral hydrogen clouds, and synchrotron regions) are roughly aligned along the same general direction as the spiral arm. It also appears that the local magnetic field revealed by the distribution of 408 Mc/s polarization is part of a larger-scale field extending throughout the spiral arms.

It is noticed from Figures 3 and 4 that the 408 Mc/s polarization is not smoothly distributed over the band but has a patchy, almost striated, appearance. The stronger regions appear to be extended in the longitude direction by some 30° to 50°, but only 10° to 15° in the latitude direction. Does this patchy distribution reflect concentrations of the relativistic electrons, or is it produced by depolarizing regions of ionized hydrogen and magnetic fields in the intervening space? In this regard, it is interesting to note that Davies and Hazard (1962) from a 237 Mc/s survey of the galactic plane near the anti-centre found that a large fraction of the continuum emission arises in a number of localized regions and that any contribution by a uniform component is small. This evidence suggests that the areas of the observed 408 Mc/s polarization may delineate the intrinsic shape of the nearby synchrotron regions in the local arm.

However, it appears that in some places at least nearby HII regions cause depolarization of the radiation from the synchrotron regions. Evidence for this may be found in a comparison of the high and low frequency galactic continuum surveys where absorption of the low frequency radio emission reveals the presence of local concentrations of electrons. The 400 Mc/s (Pauliny-Toth and Shakeshaft 1962) and 178 Mc/s (Turtle and Baldwin 1962) continuum surveys clearly show a band of radiation centred on $l^{\mathrm{II}} = 150°$ and extending up to high latitudes on either side of the plane that is identified here with the band of 408 Mc/s polarization. However, comparison with the 38 Mc/s isophotes of Blythe (1957) shows absorption features along parts of the band. As an example, the intense feature on the high frequency surveys of the southern spur centred on $l^{\mathrm{II}} = 153°$, $b^{\mathrm{II}} = -32°$, occurs in absorption on the 38 Mc/s survey. This same area shows no polarization at 408 Mc/s although the adjoining regions are polarized. This strongly suggests that the HII region causing the absorption is also responsible for depolarizing the radio emission by Faraday rotation. It is interesting to note that, in principle, a combination of measurements of Faraday rotation and the absorption of the radiation in a HII region provides a method for the determination of magnetic field strengths in the region. This is based on the fact that Faraday rotation is proportional to the electron density, the component of the magnetic field in the line-of-sight, and the depth of the region, while the absorption of the background radio emission in the region is proportional to the square of the electron density and the depth of the region.

In an attempt to gain more information on this question of the distribution of polarization within the band, the rotation measures of sources were examined to see if the lowest rotation measures occurred in the same direction as the 408 Mc/s polarized patches. However, no such systematic trend could be detected with the small number of sources available.

We have seen that the mean rotation measure of the radio sources in the band at latitudes greater than 10° is 11, whereas an upper limit of 5 has been placed on the contribution to the rotation measure by the source itself. Recent polarization measurements at 620 Mc/s by Mathewson, Broten, and Cole (1966) at Parkes give an average of 1·5 for the rotation measures of the stronger extended regions in Figure 3. Therefore, the contribution to the rotation measures of the sources by the local arm is definitely greater than for the 408 Mc/s polarized regions. It appears likely that the 408 Mc/s polarized regions lie closer to the Sun than a fair proportion of the ionized hydrogen and magnetic fields causing the Faraday rotation of the source radiation. If the mean radius of the local arm is 400 pc (Mills 1959; McGee and Milton 1964), then the distance to the polarized regions may be only 100–200 pc. It should also be noted that, if more extended synchrotron regions exist at greater distances such that their radiation experiences a similar amount of Faraday rotation as the source radiation, polarization could probably not be detected for these regions owing to rapid depolarization by differential Faraday rotation in the aerial beam.

Some further evidence for a distance determination may be obtained from a comparison of the 408 Mc/s polarization temperatures with the temperatures that might be expected from a spiral arm on the basis of other evidence. Continuum surveys clearly show the existence of the band of radiation about us due to the local spiral arm. This band of local emission together with the integrated radiation from the other spiral arms should theoretically produce four broad minima centred at $l^{\mathrm{II}} = 70°$, $b^{\mathrm{II}} = \pm 35°$, and $l^{\mathrm{II}} = 250°$, $b^{\mathrm{II}} = \pm 35°$. On most surveys, three minima are clearly seen at $l^{\mathrm{II}} = 80°$, $b^{\mathrm{II}} = -55°$, $l^{\mathrm{II}} = 240°$, $b^{\mathrm{II}} = +35°$, and $l^{\mathrm{II}} = 230°$, $b^{\mathrm{II}} = -40°$, which lie close to the predicted positions (e.g. see Dröge and Priester 1956; Pauliny-Toth and Shakeshaft 1962). A possible fourth minimum may be masked by a nearby spur of emission from the galactic plane. From these surveys, the brightness temperature at 408 Mc/s of the band of radiation is estimated at 10°K using a spectral index of $-0·6$ for the radiation emission. (This temperature estimate, made on the basis of lower frequency surveys, would be for unpolarized radiation.)

Additional information is obtained from the observations of Davies and Hazard (1962) at low galactic latitudes in the anti-centre region in the vicinity of $l^{\mathrm{II}} = 200°$. The observed average temperature of the disk component was about 80°K at 237 Mc/s. In this direction, this probably represents the total contribution from the outer spiral arm. This would give a brightness temperature of about 20°K at 408 Mc/s, which agrees well with the estimate of 10°K for the "half-arm" contribution obtained from high latitude observations of the local emission. The polarization brightness temperatures (Fig. 3) in the stronger regions of 408 Mc/s polarization vary from about 5°K to 8°K, which gives a percentage polarization of about 30%. This is quite large, particularly as the maximum percentage polarization to be expected under ideal conditions is about 70% (LeRoux 1961). The polarized radiation must therefore come from a fair proportion of the whole spiral arm and is not an extremely local feature. Taking into account the evidence from the rotation measure studies given above, a very tentative distance of 150 pc is suggested for the 408 Mc/s polarized regions, assuming as before that the mean radius of the local spiral arm is 400 pc.

A knowledge of the distance makes it possible to make a rough calculation of the magnetic field strength in the 408 Mc/s polarized regions. The assumptions involved in this calculation are that

(1) the distance to the polarized region is 150 pc,

(2) the radio emission is confined to filaments of circular cross section of diameter 25 pc,

(3) the spectral index of the radiation is $-0\cdot6$,

(4) the high and low frequency cut-offs for the synchrotron emission are 10^{10} and 10^7 c/s respectively, and

(5) there is equipartition between the energy in the relativistic particles and the magnetic field, and that the protons have 100 times the energy of the electrons (Burbidge and Burbidge 1959).

A field strength of 5×10^{-5} G was obtained. This is high compared with 7×10^{-6} G measured in the Zeeman experiment (Davies *et al.* 1964). It is quite possible that the radio emitting regions in the spiral arms have higher magnetic field strengths than the dense HI regions. A field of this strength is in accord with that predicted on the basis of the total intensity of the non-thermal radio emission from the galactic disk.

VI. Conclusions

Summing up, the large-scale distribution of linear polarization at 408 Mc/s may be explained on the basis of synchrotron radiation theory if the Sun lies almost at the centre of a spiral arm that has a magnetic field directed along it towards $l^{\mathrm{II}} = 70°$ and 250°. The concentrations of relativistic electrons may be confined to regions of higher than average magnetic field strength (5×10^{-5} G) elongated in the direction of the arm. The observations show that the magnetic fields in these synchrotron regions are very ordered. The distance to the polarized regions may be about 150 pc.

Evidence from other observations such as the rotation measures of sources, polarization of starlight, and the H-line Zeeman experiment suggests that the magnetic fields in HII regions, dust clouds, and concentrations of neutral hydrogen are ordered and lie in approximately (within 20°) the same direction as the magnetic fields in the synchrotron regions. It appears that the local synchrotron regions are manifestations of a larger-scale field extending throughout the spiral arms.

These polarization studies enable the near emission to be separated from the more distant emission. Past continuum surveys reveal clearly the existence of the local band of radio emission and the positions of the three observed minima agree well with those predicted on the basis of the proposed model. This local emission should be removed before estimates are made of any coronal or extragalactic component.

At high latitudes, close correlation is observed between features of the distribution of background polarization and Faraday rotation of extragalactic sources.

It will be of great interest to compare the fine detail of these distributions when rotation measures are available for a much greater number of sources.

Multifrequency measurements of the background polarization are also required to give the Faraday rotation of the radiating regions and the intervening medium. These will provide data on field directions and strengths and, in combination with rotation measures for radio sources, estimates of the distances to the synchrotron regions.

VII. Acknowledgments

The authors wish to thank Mr. J. R. Healy and Mr. M. James for their assistance in part of the observations and reduction of the records, Miss J. E. Leveleky for her help in the preparation of the Tables and Figure 4, Miss V. Rowntree for the preparation of the diagrams, and Mr. J. G. Bolton for his critical reading of the manuscript and many helpful comments.

VIII. References

Berkhuijsen, E. M., and Brouw, W. N. (1963).—*Bull. Astr. Insts Neth.* **17**: 185.

Berkhuijsen, E. M., Brouw, W. N., Muller, C. A., and Tinbergen, J. (1964).—*Bull. Astr. Insts Neth.* **17**: 465.

Blythe, J. H. (1957).—*Mon. Not. R. Astr. Soc.* **117**: 657.

Brouw, W. N., and Berkhuijsen, E. M. (1962).—*Nature* **196**: 757.

Brouw, W. N., Muller, C. A., and Tinbergen, J. (1962).—*Bull. Astr. Insts Neth.* **16**: 213.

Burbidge, E. M., and Burbidge, G. R. (1959).—Symp. IAU No. 9 (Paris 1958). p. 323.

Davies, R. D., and Hazard, C. (1962).—*Mon. Not. R. Astr. Soc.* **124**: 147.

Davies, R. D., Shuter, W. L. H., Slater, C. H., and Wild, P. A. T. (1964).—*Mon. Not. R. Astr. Soc.* **126**: 353.

Dröge, F., and Priester, W. (1956).—*Z. Astrophys.* **40**: 236.

Gardner, F. F., and Davies, R. D. (1966).—*Aust. J. Phys.* **19** (in press).

Hall, J. S. (1958).—*Publs U.S. Nav. Obs.* (2nd series) **17**: 275.

Hanbury Brown, R., Davies, R. D., and Hazard, C. (1960).—*Observatory* **80**: 191.

Kellermann, K. I. (1964).—*Publ. Owens Valley Radio Obs.* **1**: 1.

LeRoux, E. (1961).—*Annls Astrophys.* **24**: 71.

McGee, R. X., and Milton, J. A. (1964).—*Aust. J. Phys.* **17**: 128.

McGee, R. X., and Murray, J. D. (1961).—*Aust. J. Phys.* **14**: 260.

Mathewson, D. S., Broten, N. W., and Cole, D. J. (1966).—*Aust. J. Phys.* **19** (in press).

Mathewson, D. S., and Milne, D. K. (1964).—*Nature* **203**: 1273.

Mills, B. Y. (1959).—Symp. IAU No. 9 (Paris 1958). p. 431.

Morris, D., and Berge, G. L. (1964).—*Astrophys. J.* **139**: 1388.

Muller, C. A., Berkhuijsen, E. M., Brouw, W. N., and Tinbergen, J. (1963).—*Nature* **200**: 155.

Pauliny-Toth, I. I. K., and Shakeshaft, J. R. (1962).—*Mon. Not. R. Astr. Soc.* **124**: 61.

Smith, Elske Von P. (1956).—*Astrophys. J.* **124**: 43.

Tunmer, H. (1958).—*Phil. Mag.* **3**: 370.

Turtle, A. J., and Baldwin, J. E. (1962).—*Mon. Not. R. Astr. Soc.* **124**: 459.

Weaver, H. F. (1953).—*Astrophys. J.* **58**: 177.

Westerhout, G. (1957).—*Bull. Astr. Insts Neth.* **13**: 201.

Westerhout, G., Seeger, Ch. L., Brouw, W. N., and Tinbergen, J. (1962).—*Bull. Astr. Insts Neth.* **16**: 187.

Wielebinski, R., and Shakeshaft, J. R. (1964).—*Mon. Not. R. Astr. Soc.* **128**: 19.

Wielebinski, R., Shakeshaft, J. R., and Pauliny-Toth, I. I. K. (1962).—*Observatory* **82**: 158.

EFFECT OF GRAVITATION IN THE ORIGIN OF COSMIC PARTICLES

By M. C. Durgapal* and G. L. Gehlot*

[*Manuscript received August 2, 1965*]

Summary

Following on Infeld's (1963) proposal of the dependence of the physical constants on the gravitational field, we apply this idea to quantum mechanics and other physical phenomena and suggest a possible explanation of the origin of cosmic rays.

I. Introduction

Gravitation can always play a significant role in the explanation of so many phenomena because it is universal. The cause of the very large number of cosmic particles in our Galaxy has yet to be properly explained. We consider the possible effects of gravitation in the origin of these particles.

If we consider a gravitational field such that in the metric

$$ds^2 = g_{00}\,dt^2 - g_{kl}\,dx^k\,dx^l.$$

g_{00} and g_{kl} are independent of time, we call it static. In such a case we have to modify Planck's constant and the inertial mass of the particle (Infeld 1963) as

$$h = h_0/g_{00} \tag{1}$$

and

$$\mu = \mu_0/g_{00}, \tag{2}$$

where the velocity of light is assumed to be unity and h_0 and μ_0 correspond to Planck's constant and the inertial mass of the particle when $g_{00} = 1$. The mass of the particle is such that it does not affect the gravitational field.

Infeld (1963) has given a possible explanation of the red-shift by using these relations. We have extended the utility of the results to other physical phenomena.

II. Utility in Some Quantum Phenomena

(a) *Uncertainty Principle*

Heisenberg's uncertainty relation at a place where $g_{00} \neq 1$ becomes

$$\Delta x\,\Delta p_x \geqslant \hbar_0/2g_{00}. \tag{3}$$

Suppose that $g_{00} = 1-\chi$, then

$$\begin{aligned}\Delta x\,\Delta p_x &\geqslant \hbar_0/2(1-\chi)\\ &\geqslant \tfrac{1}{2}\hbar_0(1+\chi) \qquad \text{if } \chi \text{ is small.}\end{aligned}$$

We see that the uncertainty increases if the gravitation is large. If χ is comparable to unity, the uncertainty will increase so much that it will be observable under normal conditions. If $\chi \to 1$, then even if we find the momentum of a particle to a poor approximation it will be impossible to know where the particle is situated.

---

* Department of Physics, University of Jodhpur, Jodhpur, India.

Aust. J. Phys., 1965, **18**, 655–60

(b) *Schrödinger's Wave Equation*

Let us first consider the one-dimensional Schrödinger wave equation

$$-\frac{\hbar^2}{2\mu}\frac{\mathrm{d}^2\psi(x,t)}{\mathrm{d}x^2}+V(x)\psi(x,t)=-\frac{\hbar}{\mathrm{i}}\frac{\mathrm{d}\psi}{\mathrm{d}t}. \tag{4}$$

If $\psi(x,t)=U(x)\phi(t)$, then from the expression $\phi=\exp(\mathrm{i}Wt/\hbar_0)$ and equation (1) we have

$$\frac{\mathrm{d}^2U}{\mathrm{d}x^2}+\frac{2\mu g_{00}}{\hbar_0^2}\Big\{W \quad g_{00}\,V(x)\Big\}U=0,$$

and from (2)

$$\frac{\mathrm{d}^2U}{\mathrm{d}x^2}+\frac{2\mu_0}{\hbar_0^2}\Big\{W-g_{00}\,V(x)\Big\}U=0. \tag{5}$$

In a similar manner we can find the equation in three dimensions. We see that the g_{00} term appears only with the potential. It may be pointed out that Einstein's theory of gravitation as a first approximation to Newton's theory leads to the derivatives of g_{00} as the intensity of the gravitational field, and to g_{00} itself as the gravitational potential. Hence equation (5) having the g_{00} term with the potential seems to be consistent with Einstein's theory.

(c) *Electric Potentials*

The effective potential for a particle in a static gravitational field becomes

$$V'=g_{00}\,V. \tag{6}$$

Relation (6) is of great importance, for it shows that gravitational potential has a dominating effect on all types of potentials encountered by charged particles. If a particle has to cross a potential barrier and it happens to be in a gravitational field, the effective barrier will become $g_{00}\,V$; that is, the probability of penetration for the same type of particle, the interaction between similar particles, and the escape of certain particles from a potential well will differ in different gravitational fields. If g_{00} becomes very small, the effective potential V' will be small whatever may be the value of V. In such a case, e.g. α-particle emission, we see that the probability of emission will greatly increase due to the effective reduction of the potential barrier. Similarly, other nuclear particles will also experience a loosening in such a gravitational field. If $g_{00}\to 0$, all types of particles will behave as free particles, even though the potential V may have any value. Schrödinger's equation will approach the relation

$$\frac{\mathrm{d}^2U}{\mathrm{d}x^2}+\frac{2\mu_0}{\hbar_0^2}\,WU(x)=0,$$

which is the equation for a free particle.

III. ORIGIN OF COSMIC RAYS

In order to illustrate the theory clearly, we must choose a particular field as a model. Although not necessarily the correct model, we choose the Schwarzschild interior field in isotropic coordinates, which gives the values of g_{00} and g_{kl} (Wyman 1946) as

$$\begin{aligned} g_{00} &= \{2a-2m+m(4a-m)r^2/2a^3\}^2\times\{(2a+m)(1+mr^2/2a^3)\}^{-2}, \qquad (7)\\ g_{kl} &= \{1+m/2a\}^6\{1+mr^2/2a^3\}^{-2}. \end{aligned}$$

Since both g_{00} and g_{kl} are independent of time, the results are applicable.

The value of $g_{00}\to 0$ at the centre as $m\to a$, and at $r=a$ the value of $g_{00}=0\cdot 1$. At intermediate values of r, g_{00} will vary from 0 to $0\cdot 1$. If we assume homogeneity in a star with density ρ_c, we have under such conditions $\rho_c = 3/4\pi a^2$ when $g_{00}=0$. Let us consider two extreme cases.

(i) *Stars with a Radius* a $\simeq 10^4$ *times that of the Sun.*—For such stars with $g_{00}=0$ at the centre

$$\rho_c = \frac{3}{4\pi}\times 10^{-8}\simeq\frac{1}{30}\quad\text{times that of water}$$

(standard density of water is $6\cdot 665\times 10^{-8}\,\mathrm{s}^{-2}$; Synge 1960), that is, a star with such a large radius cannot have a density greater than $1/30\,\mathrm{g/cm^3}$ on average. When such a density is attained in this type of star, the value of $g_{00}=0$ at the centre reduces the effective potential barriers to zero near the centre. The matter in this neighbourhood will be most unstable, and it will be only in the form of freely moving neutrons, protons, electrons, mesons, hyperons, etc., the so-called fifth and sixth states of matter. Near the surface, the effective potential is not zero but is reduced to one-tenth of its value. Here we have ionized masses (together with many nuclei, α-particles, etc.), the so-called fourth state of matter or plasma. It is very difficult to confine a plasma to this shape when the core of the star is filled with elementary particles, and the star breaks up due to the instability of the plasma and emits a very large number of cosmic particles.

(ii) *Stars with a Density of* $\sim 10^5$.—In such cases

$$a^2 = \frac{3\pi}{4}\times\frac{1}{6\cdot 665\times 10^{-3}} = (3\cdot 456)^2,$$

or

$$a\simeq 3\cdot 456,$$

that is, a star with such a high density cannot have a radius less than one and a half times that of the Sun.

According to prevailing theories, when the entire hydrogen of a star is consumed the star first expands and then contracts more and more until it ultimately loses its brightness and is lost.

Here we introduce the new idea that, as the star shrinks, it tends to attain a minimum size. Before this minimum size is reached the interior of the star is converted into freely moving elementary particles and, near the surface, into plasma.

This arrangement is very unstable and the star breaks up into ionized particles and the freely moving particles, which are scattered in the Galaxy. Thus we see that the star is not lost as a block but rather as a dust.

(iii) *The Origin of Cosmic Rays.*—We have now seen that when the stars decay the ultimate product is a large number of particles, which are scattered at random in the Galaxy. Some of these particles enter the Earth's atmosphere and fall in the form of cosmic rays. This is the proposed theory of the origin of cosmic rays.

IV. ILLUSTRATIONS

(a) α-*Decay Process*

Here we examine the process by which particles are emitted from the nucleus under the effect of gravitation. As an example we consider the process of α-decay. The probability of emission of an α-particle from the nucleus is given by

$$P = e^{-x},$$

where

$$x = 4\pi(2\mu)^{\frac{1}{2}} h^{-1} \int_{R_0}^{R'} (V-E)^{\frac{1}{2}}\, dR.$$

However, using the modified equation of the form (5), we obtain

$$x = 4\pi(2\mu_0)^{\frac{1}{2}} h_0^{-1} \int_{R_0}^{R'} (g_{00} V-E)^{\frac{1}{2}}\, dR,$$

or

$$x = 4\pi(2\mu_0)^{\frac{1}{2}} h_0^{-1}(zZe^2/E^{\frac{1}{2}})\{\cos^{-1} y^{\frac{1}{2}} - y^{\frac{1}{2}}(1-y)^{\frac{1}{2}}\},$$

where $y = E/g_{00}B$ and $B = 2Ze^2/R_0$. R_0 is the radius of the nucleus and E is the energy of the α-particle.

We shall now calculate the period of emission of an α-particle in the case of nuclei that do not give detectable emission ordinarily, i.e. for $g_{00} = 1$. Bethe (1947), assuming that an α-emitter with a period greater than 10^{14} years would be undetectable, has computed the smallest energy expected for the emitted particles for various values of Z as:

Z	10	30	50	70	90
E	0·13	0·8	1·7	2·7	3·7

The period T $(= T_0/P,\ T_0$ constant) of an α-emitter, taking $Z = 50$ and $E = 1{\cdot}7$, has been calculated from the above formulae for values of g_{00} of 0·6, 0·4, 0·2, 0·1. The results are shown in Table 1 together with calculated values of the disintegration constant λ $(= \lambda_t P,\ \lambda_t$ constant) for a Pa–Ac source.

If $g_{00} < 0{\cdot}1$, the energy E becomes greater than $g_{00}B$ and there is no question of penetration since the α-particle is free to emerge from the nucleus. Similar calculations can be made for any other value of Z and also for protons and other particles.

(*b*) *Solutions of the Einstein Field Equations*

Solutions of the Einstein field equations for contracting Schwarzschild static models are possible. Bondi (1964) has shown that the gravitating sphere contracts without radiating any energy. The limits to the contraction allowed by physical assumptions are

(1) $a > 9m/4$ for the central pressure to be finite, and

(2) $a > 18m/5$ for the central-energy invariant $(3p-\rho)$ to be positive.

TABLE 1

CALCULATED VALUES OF PERIOD AND DISINTEGRATION CONSTANT FOR VARIOUS VALUES OF g_{00}

g_{00}	Period T (for $Z = 50$, $E = 1 \cdot 7$)	Disintegration Constant λ for Pa–Ac (s^{-1})
1·0	$\simeq 10^{14}$ yr	$5 \cdot 5 \times 10^{-13}$
0·6	$\simeq 10^{9}$ yr	$5 \cdot 5 \times 10^{-8}$
0·4	$\simeq 10^{2}$ yr	$2 \cdot 57 \times 10^{-2}$
0·2	$\simeq 10^{4}$ s	$2 \cdot 5 \times 10^{18}$
0·1	$\simeq 10^{-6}$ s	$E > g_{00} B$

If the limiting values of a are substituted in the expression for g_{00} (equation (7)) in the Schwarzschild internal solutions, we see that the limiting values of g_{00} are

(1) $a > 9m/4$ at $r = 0$ $g_{00} \simeq 0 \cdot 2$

at $r = a$ $g_{00} \simeq 0 \cdot 4$

(2) $a > 18m/5$ at $r = 0$ $g_{00} \simeq 0 \cdot 4$

at $r = a$ $g_{00} \simeq 0 \cdot 6$

In Table 1 we have seen the effect of these values of g_{00} on α-decay. After attaining the limiting size the sphere cannot contract further and the material composing it is mostly in the form of unstable nuclei that give spontaneous emission of particles.

(*c*) *Further Reactions*

For radiative contraction no such limit has been proposed, and a large number of phenomena await investigation. The value of g_{00} may go down to 0·1 or even less. It may be that, owing to contraction, the value of g_{00} is reduced and gives rise to radiation of nuclear particles. Calculations for other nuclear reactions are beyond the scope of the present paper.

V. CONCLUSION

We have presented here a possible solution for the origin of cosmic rays. The theory put forward may find its proper application in explaining various phenomena in cosmology. By taking some suitable metric, detailed calculations could be made.

VI. REFERENCES

BETHE, H. A. (1947).—"Elementary Nuclear Theory." (Wiley: New York.)

BONDI, H. (1964).—*Proc. R. Soc.* A **281**: 39.

INFELD, L. (1963).—*Z. Phys.* **171**: 34.

SYNGE, J. L. (1960).—"Relativity: the General Theory." (Interscience: New York.)

WYMAN, M. (1946).—*Phys. Rev.* **70**: 74.

SHORT COMMUNICATIONS

THE $^{16}O(\gamma, p_0)^{15}N$ CROSS SECTION BETWEEN 14 AND 16 MeV*†

By R. J. J. Stewart,‡ P. H. Cannington,‡ and B. M. Spicer‡

This paper reports an investigation of the 90° differential cross section for the $^{16}O(\gamma, p_0)^{15}N$ reaction from 14 to 16 MeV.

The work was undertaken in an attempt to resolve an apparent discrepancy between the published $^{16}O(\gamma, p_0)^{15}N$ and $^{15}N(p, \gamma_0)^{16}O$ cross sections in this energy region. The early (γ, p) work indicated a resonance at 14·7 MeV (Spicer 1955; Johansson and Forkman 1957; Shoda 1961), which was assigned a spin and parity of 2^+ and was suspected of being a collective quadrupole state predicted to be in this energy region (Barton 1959; Fallieros and Ferrell 1959; Raz 1960; Gillet and Vinh-Mau 1964). However, the (p, γ_0) measurements failed to confirm the existence of this state, so throwing some doubt on the existing data, or, alternatively, on the validity of the principle of detailed balance, which relates the cross sections of the two reactions.

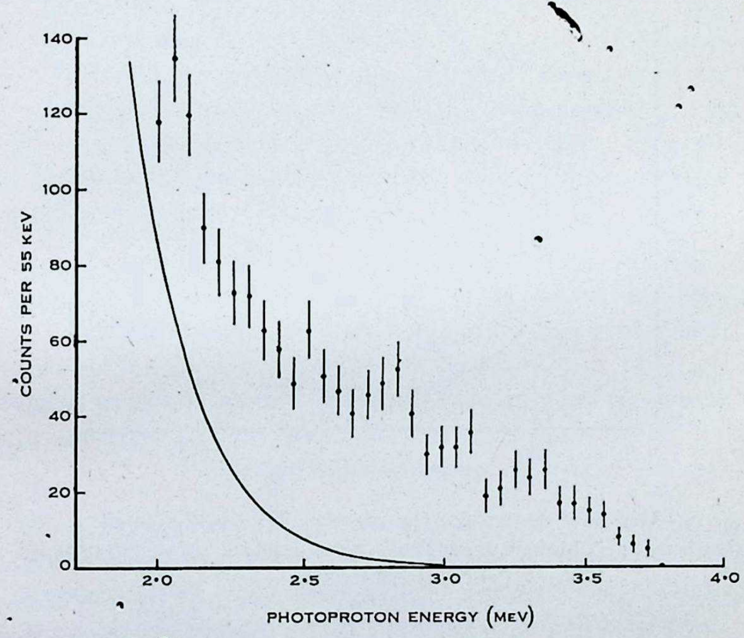

Fig. 1.—The energy spectrum of photoprotons from ^{16}O following bombardment by 16 MeV bremsstrahlung.

---

* Work supported by a Research Grant from the United States Army Research Office

† Manuscript received September 9, 1965.

‡ School of Physics, University of Melbourne.

Aust. J. Phys., 1965, 18, 661–4

It was noted that in all the early (γ, p) experiments the protons were detected in nuclear emulsions, allowing the possibility of spurious counts from neutron–proton scatterings by the hydrogen of the emulsion. The present experiment repeated these measurements using a different method of detection to remove this possibility.

Experimental Details and Treatment of Data

A silicon surface barrier detector (ORTEC type SCIJ300–60) was mounted in a target chamber filled with oxygen to $\frac{1}{2}$ atm pressure. A collimated γ-ray beam of 16 MeV end point energy from the Melbourne betatron was passed axially through the chamber, the cylinder of irradiated gas seen by the detector acting as target. The detector was 3·6 cm from the chamber axis. The time duration of the γ-ray pulse was lengthened to about 150 μs to reduce pile-up. The background was further minimized by ensuring that the detector depletion layer was just deep enough (110 μm) to stop the most energetic protons produced in the reaction. The pulses were amplified, shaped, and presented to a 256 channel pulse-height analyser, which was gated on only during the betatron beam burst. Alpha particles from a ThC+C′ source were used to calibrate the system, which had a measured resolution of about 70 keV. The energy lost by a proton in traversing the gas was determined using the range–energy relations of Whaling (1957). The corrected energy spectrum is shown in Figure 1, where the indicated errors are statistical only.

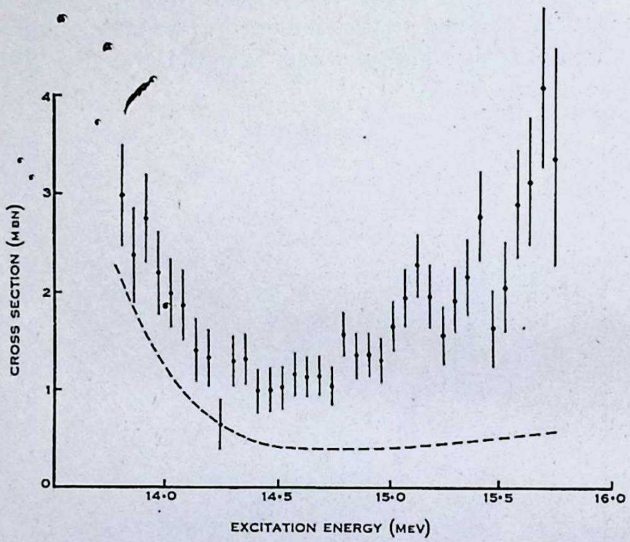

Fig. 2.—The cross section for the reaction $^{16}O(\gamma, p_0)^{15}N$, together with a cross section obtained from the inverse reaction using the principle of detailed balance.

The dose was monitored by placing in the beam a Victoreen thimble at the centre of a cylinder of Lucite of radius 7·5 cm. A dose of 2594 r was recorded in accumulating the data of Figure 1. The background was determined in a separate run performed with the chamber evacuated. In this run a dose of 1170 r was recorded.

The spectrum was converted to a cross section using a bremsstrahlung number distribution function based on the zero-degree spectrum of Schiff (1951), with $C = 111$, but modified suitably to take account of the extended duration of the γ-ray beam pulse.

The dosemeter reading was used to fit an absolute scale to the cross section, in the manner described by Johns *et al.* (1950). This cross section is presented in Figure 2, together with a cross section derived from the $^{15}N(p,\gamma_0)^{16}O$ work of Wilkinson and Bloom (1956) using the principle of detailed balance. In making this derivation, the peak cross section for the $^{15}N(p,\gamma_0)^{16}O$ reaction leading to the 13·1 MeV level of ^{16}O was taken to be 1 mbn (Schardt, Fowler, and Lauritsen 1952).

Discussion

The feature of interest in the results presented is the absence of any peak in the region of 14·7 MeV. This strongly suggests that the earlier (γ, p) work is incorrect, and that there is no real discrepancy between the (γ, p_0) and (p, γ_0) results. A possible explanation of the earlier (γ, p) results may be given in terms of neutron–proton scatterings in the detector material, the neutrons being formed in large quantities in the lead collimators used to define the γ-ray beam. However, this does not explain the angular distribution obtained by Spicer (1955), who observed appreciable numbers of protons at backward angles.

There is good agreement in shape between the cross section obtained in the present work and that derived from the (p, γ_0) cross section using the principle of detailed balance. The difference in absolute magnitudes may be ascribed to uncertainties in the assumed bremsstrahlung spectral shape, and in the determination of detector efficiency. Such uncertainties have not been included in the errors (statistical only) shown in Figure 2.

Conclusion

It is concluded that there is no essential disagreement in shape between the $^{16}O(\gamma, p_0)^{15}N$ and $^{15}N(p, \gamma_0)^{16}O$ cross sections in the region 14–16 MeV; hence the data give no cause to query the validity of the principle of detailed balance. The absence of a 2^+ state in ^{16}O at 14·7 MeV excitation is substantiated by a recent calculation of $T = 0$, 2^+ states (Eisenberg, Spicer, and Rose 1965), which shows that the inclusion of two-particle–two-hole excitations radically changes the predictions of the simpler calculations that include only one-particle–one-hole excitations (see Gillet and Vinh-Mau 1964).

The authors gratefully acknowledge the technical assistance of G. Haertal and U. Flego and the facilities made available by the University of Melbourne Computation Department. Financial assistance was provided in the form of a CSIRO Post-graduate Studentship (P.H.C.) and a Commonwealth Post-graduate Award (R.J.J.S.).

References

BARTON, G. (1959).—*Nucl. Phys.* **11**: 466.

EISENBERG, J. M., SPICER, B. M., and ROSE, M. E. (1965).—*Nucl. Phys.* **71**: 273.

FALLIEROS, S., and FERRELL, R. A. (1959).—*Phys. Rev.* **116**: 660.

GILLET, V., and VINH-MAU, N. (1964).—*Nucl. Phys.* **54**: 321.

JOHANSSON, S. A. E., and FORKMAN, B. (1957).—*Ark. Fys.* **12**: 359.

JOHNS, H. E., KATZ, L., DOUGLAS, R. A., and HASLAM, R. N. H. (1950).—*Phys. Rev.* **80**: 1061.

RAZ, B. J. (1960).—*Phys. Rev.* **120**: 169.

SCHARDT, A., FOWLER, W. A., and LAURITSEN, C. C. (1952).—*Phys. Rev.* **86**: 527.

SCHIFF, L. I. (1951).—*Phys. Rev.* **83**: 252.

SHODA, K. (1961).—*J. Phys. Soc. Japan* **16**: 1841.

SPICER, B. M. (1955).—*Phys. Rev.* **99**: 33.

WHABING, W. (1957).—"Handbuch der Physik." Vol. 34, p. 193. (Springer: Berlin.)

WILKINSON, D. H., and BLOOM, S. D. (1956).—*Phys. Rev.* **105**: 683.

A SURVEY OF THE SOUTHERN SKY AT 30 Mc/s*

By D. S. Mathewson,† N. W. Broten,† and D. J. Cole†

This paper presents the results of a 30 Mc/s survey of the southern sky using the 210 ft steerable reflector at Parkes, N.S.W. The aerial was fed by a right-handed helix with plane reflector giving a tapered illumination that fell to approximately 10% at the edge of the aperture. The resulting main beam was circular and approximately 11° between half-power points. The aerial measured left-handed circular polarization relative to the direction of propagation.

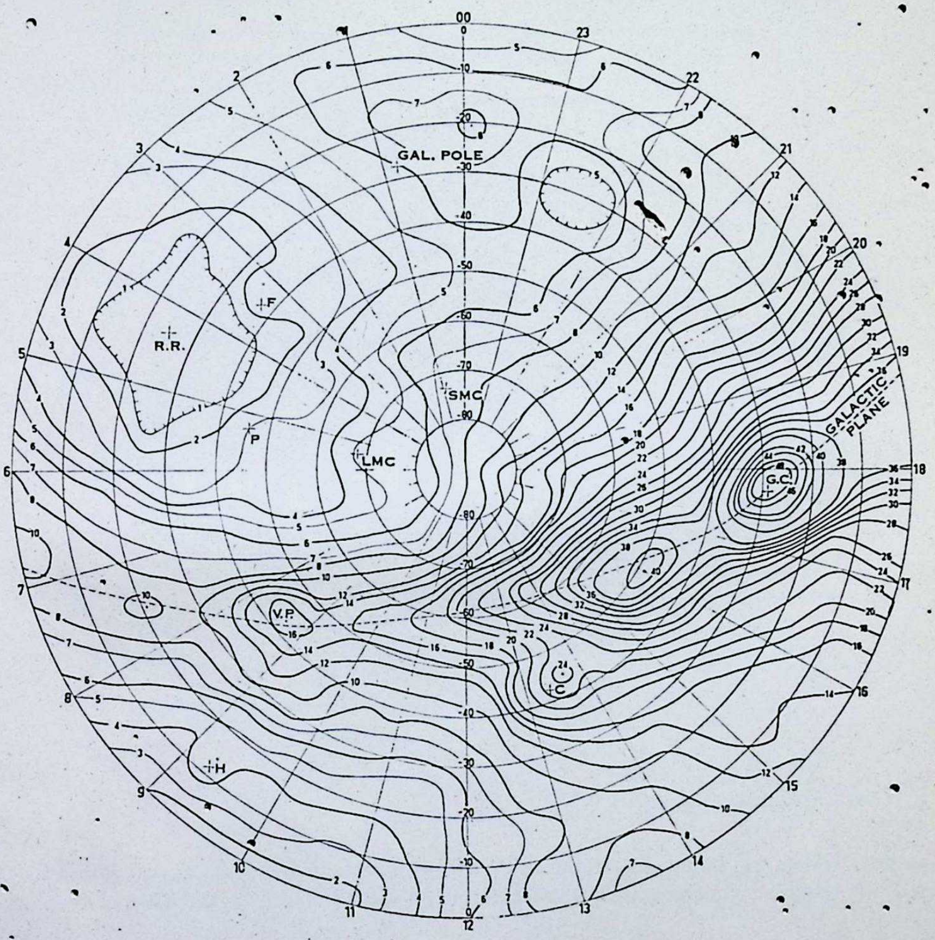

Fig. 1.—30 Mc/s isophotes in equatorial coordinates (epoch 1964). The brightness temperature contour unit is 1800 degK. The point above which all temperatures are measured is at R.A. 04h 20m, dec. −25°, which is indicated by R.R. in the figure. The positions of the stronger radio sources are marked and identified by their initials: the galactic centre (G.C.), the Vela Puppis region (V.P.), Centaurus A (C), Hydra A (H), Fornax A (F), Pictor A (P), the Large Magellanic Cloud (LMC), and the Small Magellanic Cloud (SMC).

* Manuscript received September 7, 1965.

† Division of Radiophysics, CSIRO, University Grounds, Chippendale, N.S.W.

The receiver was a cascade amplifier with a noise temperature of less than 100°K and a bandwidth of 2 Mc/s. At this low frequency the main contribution to the total noise of the system was produced by the sky temperature and, with a 2 s time constant, the peak-to-peak noise was about 60 degK. The system was calibrated using the radio source Fornax A, which was assumed to have a flux density of 2700×10^{-26} W m^{-2} (c/s)$^{-1}$ at 30 Mc/s. This value has been derived from a combination of the results of Bolton, Gardner, and Mackey (1964) at 408 Mc/s, of Sheridan (1958) at 85·5 Mc/s, and of Shain (1959) at 19·7 Mc/s. Fornax A gave a main beam brightness temperature T_b of 2300°K when at the centre of the aerial beam.

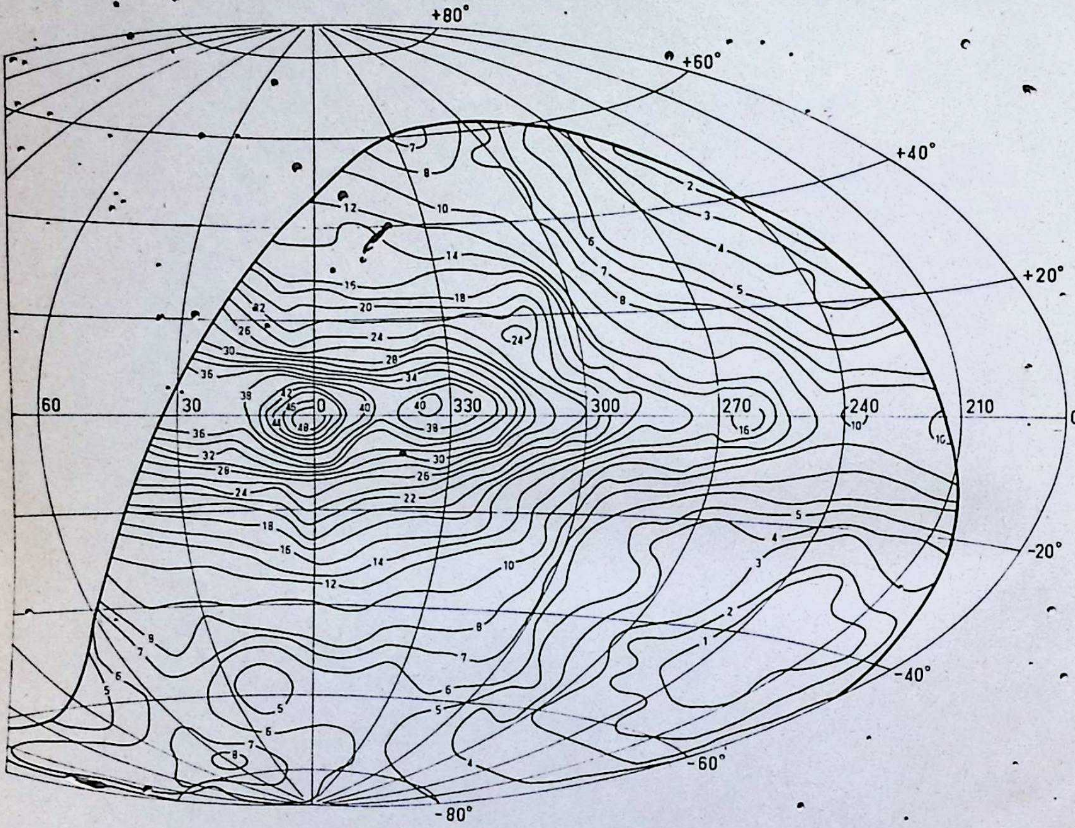

Fig. 2.—The 30 Mc/s isophotes plotted on an Aitoff projection in new galactic coordinates. The brightness temperature contour unit is 1800 degK. The thick line marks the limit of the survey.

The survey, which was carried out in October 1964, covers the sky from the celestial equator to the south celestial pole. The observations were taken by scanning the telescope in azimuth at 16°/min from azimuth 70°, through 180°, to 290° and back again. This process was repeated continuously from 1600 to 0930 hr, Local Solar Time. The zenith distance of the telescope was kept constant at 57° so that the south celestial pole was passed through at the middle of each scan. This point was used as the reference region of the survey. Fornax A, the calibration source, was observed three times during the night to check on the overall sensitivity of the measuring system.

The isophotes are drawn in equatorial coordinates in Figure 1. The brightness temperature contour unit is 1800 degK. The point above which all temperatures are measured is at R.A. 04^h 20^m, Dec. −25°. Wielebinski (personal communication) has estimated the absolute brightness temperature at 30 Mc/s of this position to be 14 800°K. The estimated probable error of the measurement of brightness temperature is 1000 degK. In Figure 2, the contours have been redrawn in new galactic coordinates on an Aitoff projection. The thick line marks the limit of the Survey.

References

BOLTON, J. G., GARDNER, F. F., and MACKEY, M. B. (1964).—*Aust. J. Phys.* **17**: 340.

SHAIN, C. A. (1959).—"Paris Symposium on Radio Astronomy." (Ed. R. N. Bracewell.) p. 328. (Stanford Univ. Press.)

SHERIDAN, K. V. (1958).—*Aust. J. Phys.* **11**: 400.

IDENTIFICATION OF TWO SOUTHERN QUASI-STELLAR OBJECTS*

By R. D. Ekers† and J. G. Bolton‡

A number of possible quasi-stellar objects have been found from a search of the Palomar Sky Survey plates for identification of radio sources in the Parkes catalogue (Bolton, Clarke, and Ekers 1965). Confirmation of the identification of two of these sources, 1327−21 and 2115−30, has now been obtained from both precise position measurements and photoelectric observations. As quasi-stellar objects generally are of very small radio diameter, the optical positions can be used as primary calibration points for southern radio telescopes.

Table 1

POSITIONS OF SOURCES

Source	Optical Position (1950)		Radio Position (1950)	
	R.A.	Dec.	R.A.	Dec.
1327−21	$13^{\mathrm{h}}\,27^{\mathrm{m}}\,23^{\mathrm{s}}\cdot2\pm0^{\mathrm{s}}\cdot1$	$-21°\,26'\,34\pm1''$	$13^{\mathrm{h}}\,27^{\mathrm{m}}\,23^{\mathrm{s}}\cdot7\pm0^{\mathrm{s}}\cdot6$	$-21°\,26'\,41\pm10''$
2115−30	$21\;\;15\;\;11\cdot1\pm0\cdot1$	$-30\;\;31\;\;50\pm1$	$21\;\;15\;\;10\cdot1\pm0\cdot6$	$-30\;\;32\;\;01\pm12$

The optical positions were measured on plates taken with the 20/26 in. Schmidt telescope of the Uppsala Southern Station. Reference stars for 1327−21 were taken from the Yale Catalogue and for 2115−30 from the Cape Photographic Catalogue. Radio positions were determined from measurements with the 210 ft telescope using an extrapolation of the calibration curve for the best northern calibrators (Shimmins, Clarke, and Ekers, unpublished data). The optical and radio positions are given in Table 1 together with the probable errors of the determinations.

Table 2

PHOTOELECTRIC AND RADIO DATA

Source	Photoelectric Data			Flux Density at 1410 Mc/s (10^{-26} W m^{-2}(c/s)$^{-1}$)	Spectral Index	b^{II}
	V	B−V	U−B			
1327−21	$16\cdot74\pm0\cdot05$	$+0\cdot10\pm0\cdot06$	$-0\cdot54\pm0\cdot06$	$2\cdot0$	$-0\cdot76$	+40°
2115−30	$16\cdot47\pm0\cdot04$	$+0\cdot49\pm0\cdot05$	$-0\cdot54\pm0\cdot07$	$2\cdot4$	$-0\cdot63$	−43°

---

* Manuscript received September 16, 1965.

† Division of Radiophysics, CSIRO, University Grounds, Chippendale, N.S.W., and Mt. Stromlo Observatory, Canberra.

‡ Division of Radiophysics, CSIRO, University Grounds, Chippendale, N.S.W.

Aust. J. Phys., 1965, 18, 669–70

The photoelectric observations were made with the 40 in. reflector at the Siding Spring Station of the Mount Stromlo Observatory and have been reduced to the Johnson UBV system using the standard stars in IC4665 (Johnson 1954). Table 2 gives the photoelectric magnitudes and colours, together with radio data for the sources from the Parkes Catalogue (Bolton, Gardner, and Mackey 1964).

Both objects show a high ultraviolet excess and lie within the area on the U−B, B−V diagram defined by the northern quasi-stellar objects (Sandage 1965). One of them, 2115−30, lies near the lower boundary of the diagram and below the black-body line, the other well above the black-body line.

We wish to thank Dr. Bengt Westerlund for his interest in these observations and his assistance in providing extinction corrections, Professor Bart J. Bok for permission to use the 40 in. reflector, and Dr. C. Roslund and Professor E. Holmberg for making the Uppsala telescope available.

References

Bolton, J. G., Clarke, M. E., and Ekers, R. D. (1965).—*Aust. J. Phys.* **18**: 627.
Bolton, J. G., Gardner, F. F., and Mackey, M. B. (1964).—*Aust. J. Phys.* **17**: 340.
Johnson, H. L. (1954).—*Astrophys. J.* **119**: 181.
Sandage, A. R. (1965).—*Astrophys. J.* **141**: 1560.

A DOUBLE RADIO SOURCE WITH A WIDE COMPONENT SEPARATION*

By F. F. Gardner† and J. G. Bolton†

Moffet (1964, 1965) has recently drawn attention to two double radio sources which have unusually large ratios of separation to component size. One of these, 3C 33, an interferometric double, has an angular separation of 250″ and a component size of 16″, giving a ratio of 16 : 1. The distance of the parent galaxy is such that the physical separation of the two components is at least 200 kpc. The other double consists of the sources 3C 343 and 3C 343·1 (revised Third Cambridge Catalogue (Bennett 1962)). Their angular separation is 29′, and the size of the components, of the order of 8″, gives a ratio of at least 200 : 1. The parent galaxy is not known; the nearest bright galaxy is a fourteenth-magnitude spiral lying some 8′ NE. of the centre of the two components. Moffet argues that the two sources are a physical double from the fact that they have almost the same flux densities and similarly curved spectra. Since sources with curved spectra are rare, the close proximity of two of them with the same flux density would be unlikely to occur by chance.

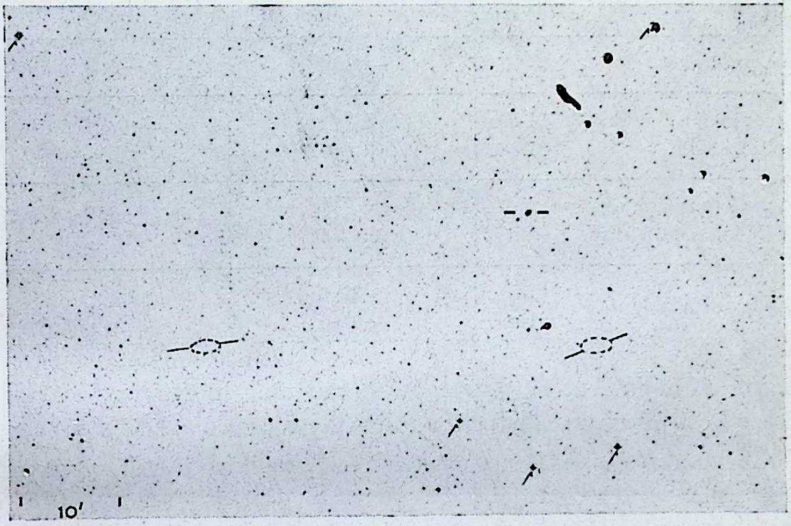

Fig. 1.—The region of the two sources 0453−30 and 0456−30, reproduced from the Palomar Sky Survey print. North-east is at the top left-hand corner. The dotted lines indicate the locations and approximate dimensions of the sources, and the solid lines through them indicate the intrinsic position angle of the linearly polarized components. The suggested parent galaxy is indicated by heavy horizontal bars. Reference stars in the Yale catalogue are shown by short arrows.

---

* Manuscript received August 23, 1965.

† Division of Radiophysics, CSIRO, University Grounds, Chippendale, N.S.W.

Aust. J. Phys., 1965, 18, 671–3

Somewhat similar arguments may be applied to the pair of sources 0453−30 and 0456−30 as listed in "The Parkes catalogue of radio sources, declination zone −20° to −60°" (Bolton, Gardner, and Mackey 1964). The sources were not resolved at the survey wavelength of 75 cm but were clearly seen as individual objects at both 11 and 21 cm wavelength. Both sources show noticeable beam broadening in right ascension at 11 cm but no detectable broadening in declination. The sources are thought to be a physical pair for the following reasons.

Table 1

DATA ON SOURCES 0453−30 AND 0456−30

Source		0453−30	0456−30
Position (1950·0)	R.A. Dec.	$04^h\ 53^m\ 21^s$ $-30°\ 11'\cdot 3$	$04^h\ 56^m\ 33^s$ $-30°\ 10'\cdot 8$
Flux density (10^{-26} W m^{-2} (c/s)$^{-1}$)	11 cm 21 cm	1·9 3·4	1·6 2·7
Spectral index		−0·9	−0·8
Percentage polarization	11 cm 21 cm	6·6±0·8 4·9±0·5	7·0±1·0 5·1±0·8
Intrinsic position angle of linear polarization		100±5°	122±5°
Angular dimensions	R.A. Dec.	$\sim 3'\cdot 5$ $< 2'\cdot 0$	$\sim 3'\cdot 0$ $< 2'\cdot 5$

(1) Both sources have flux densities and spectral indices that are almost the same.

(2) Both sources are elongated, and the directions of elongation are close to that of the line of centres.

(3) Both sources are highly polarized and have the same rate of depolarization with wavelength.

(4) The intrinsic *E* vectors are almost the same and approximately parallel to the line of centres.

Full data are given in Table 1. The region of the two sources, reproduced from a Palomar Sky Survey print, is shown in Figure 1. The brightest galaxy in the area is an elliptical, of apparent magnitude 13·5, at R.A. $04^h\ 53^m\ 54^s$, Dec. −29° 57′. This position is at a considerable distance from either the centroid of the two sources or the line of centres, but it does lie within a circle with the two components as diameter, as does Moffet's suggested identification for 3C 343 and 3C 343·1. If this galaxy is the parent and its absolute magnitude is similar to that of other radio galaxies, namely −21 (Bolton 1960), then its distance modulus is −34·5 and its distance, taking Hubble's constant as 100 km s^{-1} Mpc^{-1}, is 80 Mpc. On this basis, the minimum spatial separation of the two sources is 900 kpc.

If the $13 \cdot 5^{\mathrm{m}}$ galaxy is not the parent, then identification with the next brightest galaxy in the area, at least two magnitudes fainter, would imply a considerable increase in the spatial separation of the components. There always remains the slight possibility that the source is closer but has no optical counterpart, although at present satisfactory identifications have been obtained for all sources greater than a few minutes of arc in diameter.

The possibility of a third component midway between the two, or in the location of the suggested identification, was investigated at 11 cm. However, no other source with a flux density greater than $0 \cdot 2 \times 10^{-26}$ W m^{-2} (c/s)$^{-1}$ was found in the area shown in Figure 1.

References

Bennett, A. S. (1962).—*Mem. R. Astr. Soc.* **68**: 163.

Bolton, J. G. (1960).—Report at XII General Assembly of URSI, London. *Also* Obs. Caltech. Radio Observatory No. 5.

Bolton, J. G., Gardner, F. F., and Mackey, M. B. (1964).—*Aust. J. Phys.* **17**: 340–72.

Moffet, A. T. (1964).—*Science, N.Y.* **146**: 764.

Moffet, A. T. (1965).—*Astrophys. J.* **141**: 1580.

INDEX

PAGE

Aarons, J.—
  On scintillation of radio sources .. 97
Akabane, K., and Kerr, F. J.—
  A distant HII region in the Galaxy .. 91
Alfven waves, attenuation in a laboratory plasma 437
Amethyst, transmission electron microscope study of 135
Attachment of electrons in oxygen .. 41
Attachment of electrons in water vapour 541

Bagnall, F. T., and Haydon, S. C.—
  Pre-breakdown ionization in molecular nitrogen in $E \times B$ fields 227
Barker, A. A.—
  Monte Carlo calculations of the radial distribution functions for a proton–electron plasma 119
Bhanot, V. B.—
  See Kumar, N. 265
Blevin, H. A., and Miller, R. B.—
  Equilibrium of a pinch discharge with a transverse rotating magnetic field 309
Bolton, J. G.—
  See Ekers, R. D. 669
  See Gardner, F. F. 671
Bolton, J. G., Clarke, Margaret E., and Ekers, R. D.—
  Identification of extragalactic sources between declinations −20° and −44° 627
Boron: angular distributions in the reactions $^{11}B(d,p)^{12}B$ and $^{11}B(d,\alpha)^{9}Be$ 491
Bowen's hypothesis 497
Bowen's hypothesis: remarks on the paper by T. R. Visvanathan 503
Breakdown, electrical, in polycrystalline sodium chloride at 350°C 193
Brier, G. W.—
  Remarks on the paper by T. R. Visvanathan entitled "On Bowen's hypothesis" 503
Broten, N. W.—
  See Mathewson, D. S. 665
Broten, N. W., Cooper, B. F. C., Gardner, F. F., Minnett, H. C., Price, R. M., Tonking, F. G., and Yabsley, D. E.—
  Some observations at 6 cm wavelength with the Australian 210-ft radio telescope 85

PAGE

Brown, A.—
  Diffusion of heat from a sphere to a surrounding medium 483
Brown, I. G.—
  Some experimental observations of the attenuation of Alfven waves in a laboratory plasma 437
Buchdahl, H. A., and Tassie, L. J.—
  Gauge-independent theory of symmetry. II 109
Butler, L. A., and Hanscomb, J. R.—
  Electrical breakdown in polycrystalline sodium chloride at 350°C 193

Calibrations and comparisons of reference standards, reliability of 401
Cannington, P. H.—
  See Stewart, R. J. J. 661
Carden, P. O.—
  Gross discontinuities in the magnetization of type II superconductors .. 257
Centaurus A, decimetric emission and polarization of 589
Channels, closed, response to wind stresses 219
Charged particle motion in a time-dependent axially symmetric magnetic field 553
Chow, B. S. K.—
  See Wu, K. K. M. 59
Citrine, transmission electron microscope study of 135
Clarke, Margaret E.—
  See Bolton, J. G. 627
Cole, D. J.—
  See Cooper, B. F. C. 589
  See Mathewson, D. S. 665
Cooper, B. F. C.—
  See Broten, N. W. 85
Cooper, B. F. C., Price, R. M., and Cole, D. J.—
  A study of the decimetric emission and polarization of Centaurus A 589
Corrigenda 99, 393
Cosmic ray solar anisotropy, upper limiting primary rigidity of 451
Cosmic rays: effect of gravitation in the origin of cosmic particles 655
Crab nebula, polarization of 6 cm radiation from 335

PAGE

Crompton, R. W., Elford, M. T., and Gascoigne, J.—
Precision measurements of the Townsend energy ratio for electron swarms in highly uniform electric fields .. 409
Crompton, R. W., Rees, J. A., and Jory, R. L.—
The diffusion and attachment of electrons in water vapour 541

Dallimore, P. J., Lam, K. S., and Thies, H. H.—
The reactions of ^{6}Li(γ,d) and ^{7}Li(γ,t) below 4 MeV 389
Delves, L. M.—
A note on a soluble three-body problem 101
Durgapal, M. C.—
See Gehlot, G. L. 303
Durgapal, M. C., and Gehlot, G. L.—
Effect of gravitation in the origin of cosmic particles 655

Ekers, R. D.—
See Bolton, J. G. 627
Ekers, R. D., and Bolton, J. G.—
Identification of two southern quasi-stellar objects 669
Electromagnetism: force theorem for quasi-stationary currents 195
Electron swarms, precision measurements of the Townsend energy ratio 409
Electrons: diffusion and attachment in water vapour 541
Electrons: equilibrium density distribution with a transverse rotating magnetic field 309
Electrons: radial distribution functions for a proton–electron plasma 119
Electrons: symmetric decomposition of two-electron wave equation 511
Electrons, free and attached, behaviour in oxygen 41
Electrons, low energy, transport coefficients in crossed fields 227
Electrons, theoretical analysis of Townsend–Huxley swarm technique for .. 521
Elford, M. T.—
See Crompton, R. W. 409
Energy and dispersion in electromagnetic systems 287
Energy level spectra for ^{118}Sn and ^{122}Sn 265

PAGE

Fitzgerald, L. M., and Mansfield, W. W.—
The response of closed channels to wind stresses 219
Fletcher, G. C.—
See Powell, D. G. M. 205
Fluorine: parameters of two levels of the ^{17}F nucleus 7
Force theorem, electromagnetic, for quasi-stationary currents 195

Galaxy, distant HII region in the .. 91
Gardner, F. F.—
Polarization of 6 cm radiation from the Crab nebula 385
See also Broten, N. W. 85
Gardner, F. F., and Bolton, J. G.—
A double radio source with a wide component separation 671
Gascoigne, J.—
See Crompton, R. W. 409
Gehlot, G. L.—
See Durgapal, M. C. 655
Gehlot, G. L., and Durgapal, M. C.—
Vector tetrad in cosmological red shift 303
Glow clouds, contaminant, theoretical models for the radiance of 349
Gopala Rao, U. V.—
The polarization structure of type III solar radio bursts 283
Gravitation effect in the origin of cosmic particles 655
Green, B., and May, R. M.—
Magnetohydrodynamic ionizing shock waves in a conducting medium .. 363

Hanscomb, J. R.—
See Butler, L. A. 193
Haydon, S. C.—
See Bagnall, F. T. 227
Heat, diffusion from a sphere to a surrounding medium 483
Humble, J. E.—
See Jacklyn, R. M. 451
Hurst, C. A., and Liley, B. S.—
A theoretical analysis of the Townsend–Huxley swarm technique for electrons 521
Hydrogen: distant HII region in the Galaxy 91
Hydrogen plasma, spectroscopic study of a decaying 23

Ionization in molecular nitrogen in crossed fields 227

PAGE

Irons, F. E., and Millar, D. D.—
A spectroscopic study of a decaying hydrogen plasma 23

Jacklyn, R. M., and Humble, J. E.—
The upper limiting primary rigidity of the cosmic ray solar anisotropy .. 451
Jory, R. L.—
Transport coefficients for low energy electrons in crossed electric and magnetic fields 237
See also Crompton, R. W. 541

Kalotas, T. M.—
A symmetric decomposition of the two-electron wave equation for finite nuclear mass 511
Kerr, F. J.—
See Akabane, K. 91
Krishnamurthi, M., Sivarama Sastry, G., and Seshagiri Rao, T.—
Harmonic structure and band splitting of type II solar radio bursts 473
Kumar, V.—
See Kumar, N. 265
Kumar, N., Kumar, V., and Bhanot, V. B.—
Energy level spectra for ^{118}Sn and ^{122}Sn 265
Kundu, S. K.—
Electromagnetic 2π decay of K_2^0 .. 395
Two-stream instabilities in a plasma .. 271

Lam, K. S.—
See Dallimore, P. J. 389
Leipnik, R. B.—
See Seymour, P. W. 553
Liley, B. S.—
See Hurst, C. A. 521
Lithium: reactions of ^{6}Li(γ,d) and ^{7}Li(γ,t) below 4 MeV 389
Lloyd, K. H.—
Theoretical models for the radiance of contaminant glow clouds in the upper atmosphere 349

McCusker, C. B. A., Peak, L. S., and Woolcott, R. L. S.—
Elastic and electromagnetic proton interactions at 3 TeV 277
McLaren, A. C., and Phakey, P. P.—
A transmission electron microscope study of amethyst and citrine .. 135
Magnetic variations, lunar, at Toolangi 567

PAGE

Magnetization of type II superconductors, discontinuities in 257
Mansfield, W. W.—
See Fitzgerald, L. M. 219
Mathewson, D. S., Broten, N. W., and Cole, D. J.—
A survey of the southern sky at 30 Mc/s 665
Mathewson, D. S., and Milne, D. K.—
A linear polarization survey of the southern sky at 408 Mc/s 635
May, R. M.—
See Green, B. 363
Meggitt, S. M. A.—
Models of massive stars in homologous gravitational contraction 297
Millar, D. D.—
See Irons, F. E. 23
Miller, R. B.—
See Blevin, H. A. 309
Milne, D. K.—
See Mathewson, D. S. 635
See Price, R. M. 329
Minnett, H. C.—
See Broten, N. W. 85

Nebulae, planetary, radio survey of, south of declination 24° 187
Nicholson, A. F.—
See Seymour, P. W. 553
Nitrogen, molecular, pre-breakdown ionization in crossed fields 227
Noyes, R. B.—
Saint-Venant's principle in anisotropic media 479

Orchiston, D. W.—
See Slee, O. B. 187
Oxygen: cross section of ^{16}O(γ,p$_0$)^{15}N between 14 and 16 MeV 661
Oxygen, behaviour of free and attached electrons in 41

Parker, A. W., Whitehead, R. R., and Shute, G. G.—
The photonuclear giant resonance in silicon-28 15
Peak, L. S.—
See McCusker, C. B. A. 277
Petersons, H. F., Winch, D. E., and Slaucitajs, L.—
The lunar magnetic variations at Toolangi 567
Phakey, P. P.—
See McLaren, A. C. 135

PAGE

Photon absorption, electric dipole, in ^{32}S .. 1
Pion decay: electromagnetic 2π decay of K^0_2 395
Plasma: flow parameters in a magnetohydrodynamic shock wave in a conducting medium 363
Plasma: pinch discharge with a transverse rotating magnetic field 309
Plasma, hydrogen, spectroscopic study of a decaying 23
Plasma, laboratory, attenuation of Alfven waves in 437
Plasma, proton–electron, radial distribution functions for 119
Plasma, two-stream instabilities in .. 271
Polarization structure of type III solar radio bursts 283
Powell, D. G. M., and Fletcher, G. C.—
  Thermal expansion and other properties of sodium chloride 205
Price, R. M.—
  See Broten, N. W. 85
  See Cooper, B. F. C. 589
Price, R. M., and Milne, D. K.—
  The Parkes catalogue of radio sources, declination zone −60° to −90° .. 329
Proton–electron plasma, radial distribution functions for 119
Proton flux, variation with atmospheric depth 59
Proton interactions, elastic and electromagnetic, at 3 TeV 277
Putt, G. D.—
  See Sargood, D. G. 491

Quasi-stellar objects, identification .. 669

Radiance of contaminant glow clouds in the upper atmosphere, theoretical models for 349
Radio waves, backscatter from land and sea 317
Radiofrequency radiation, cosmic: decimetric emission and polarization of Centaurus A 589
Radiofrequency radiation, cosmic: distant HII region in the Galaxy 91
Radiofrequency radiation, cosmic: double radio source with wide component separation 671
Radiofrequency radiation, cosmic: extended radio sources 77
Radiofrequency radiation, cosmic: identification of extragalactic sources .. 627
Radiofrequency radiation, cosmic: identification of quasi-stellar objects .. 669
Radiofrequency radiation, cosmic: linear polarization survey of southern sky .. 635
Radiofrequency radiation, cosmic: observations at 6 cm wavelength 85
Radiofrequency radiation, cosmic: Parkes catalogue of radio sources, declinations −60° to −90° 329
Radiofrequency radiation, cosmic: polarization of 6 cm radiation from the Crab nebula 385
Radiofrequency radiation, cosmic: preliminary radio survey of planetary nebulae south of declination 24° .. 187
Radiofrequency radiation, cosmic: scintillation of radio sources 97
Radiofrequency radiation, cosmic: survey of the southern sky at 30 Mc/s .. 665
Red shift, vector tetrad in 303
Rees, J. A.—
  The behaviour of free and attached electrons in oxygen 41
  See also Crompton, R. W. 541
Resonance, photonuclear, in silicon-28 15
Rigidity, upper limiting primary, of cosmic ray solar anisotropy 451

Saint-Venant's principle in anisotropic media 479
Sargood, D. G., and Putt, G. D.—
  Angular distributions in the reactions ^{11}B(d,p)^{12}B and ^{11}B(d,α)^{9}Be 491
Scheuer, P. A. G.—
  Extended radio sources. II 77
Scintillation of radio sources 97
Seshagiri Rao, T.—
  See Krishnamurthi, M. 473
Seymour, P. W., Leipnik, R. B., and Nicholson, A. F.—
  Charged particle motion in a time-dependent axially symmetric magnetic field 553
Shute, G. G.—
  See Parker, A. W. 15
Silicon-28, photonuclear giant resonance 15
Sivarama Sastry, G.—
  See Krishnamurthi, M. 473
Slaucitajs, L.—
  See Petersons, H. F. 567
Slee, O. B., and Orchiston, D. W.—
  A preliminary radio survey of planetary nebulae south of declination 24 degrees 187

PAGE

Smith, W. E.—
An electromagnetic force theorem for quasi-stationary currents 195
Energy and dispersion in electromagnetic systems 287
Sodium chloride, polycrystalline, electrical breakdown in at 350°C 193
Sodium chloride, thermal expansion and other properties 205
Sparrow, J. G.—
Stratospheric temperatures over Australia 579
Spicer, B. M.—
Electric dipole photon absorption in ^{32}S 1
See also Stewart, R. J. J. 661
Standards, reference, reliability of calibrations and comparisons of 401
Stars, massive, in homologous gravitational contraction, models of .. 297
Steele, J. G.—
Backscatter of 16 Mc/s radio waves from land and sea 317
Stewart, R. J. J., Cannington, P. H., and Spicer, B. M.—
The ^{16}O(γ,p$_0$)^{15}N cross section between 14 and 16 MeV 661
Stewart, R. T.—
The speed and acceleration of the sources of type III and type V solar radio bursts over large distances in the corona 67
See also Weiss, A. A. 143
Stratosphere: temperatures over Australia 579
Sulphur: electric dipole photon absorption in ^{32}S 1
Sun: harmonic structure and band splitting of type II radio bursts .. 473
Sun: nature and velocity of the sources of type II radio bursts 167
Sun: radio bursts of spectral type V .. 143
Sun: speed and acceleration of the sources of type III and type V radio bursts .. 67
Sun: type III radio bursts, polarization structure of 283
Superconductors, type II, gross discontinuities in the magnetization of .. 257
Symmetry, gauge-independent theory of 109

Tanner, R. I.—
A new kinetic energy correction for capillary tube viscometers 381

PAGE

Tassie, L. J.—
See Buchdahl, H. A. 109
Thermal expansion, sodium chloride .. 205
Thies, H. H.—
See Dallimore, P. J. 389
Three-body problem, a soluble 101
Thwaite, E. G.—
Reliability of calibrations and comparisons of reference standards with an application to a group of line standards 401
Tin: energy level spectra for ^{118}Sn and ^{122}Sn 265
Tonking, F. G.—
See Broten, N. W. 85
Toutenhoofd, W.—
Parameters of two levels of the ^{17}F nucleus 7
Townsend energy ratio for electron swarms, precision measurements of .. 409
Townsend–Huxley swarm technique for electrons, theoretical analysis of .. 521
Transport coefficients, low energy electrons in crossed fields 237

Viscometers, capillary tube, new kinetic energy correction for 381
Visvanathan, T. R.—
On Bowen's hypothesis 497

Water vapour, diffusion and attachment of electrons in 541
Wave equation, two-electron, symmetric decomposition of 511
Weiss, A. A.—
The nature and velocity of the sources of type II solar radio bursts 167
Weiss, A. A., and Stewart, R. T.—
Solar radio bursts of spectral type V 143
Whitehead, R. R.—
See Parker, A. W. 15
Winch, D. E.—
See Petersons, H. F. 567
Wind stresses, response of closed channels 219
Woolcott, R. L. S.—
See McCusker, C. B. A. 277
Wu, K. K. M., and Chow, B. S. K.—
Variation of proton flux with atmospheric depth between 10 and 50 g/cm^2 at $\lambda = 47°$ S. geomagnetic .. 59

Yabsley, D. E.—
See Broten, N. W. 85

पुस्तकालय
7791
गुरुकुल कांगड़ी वि

पुस्तकालय
गुरुकुल कांगड़ी विश्वविद्यालय
हरिद्वार

यह पुस्तक वितरित न की जाय
NOT TO BE ISSUED

सन्दर्भ ग्रन्थ
REFERENCE BOOK

Compiled
1999-2000